The Structural, Metamorphic and Tectonic Context of Selected Sub-Economic Veining in the Natal Thrust Front and Natal Nappe Zone, Northern Kwazulu-Natal

by

Ian James Basson, B.Sc. (Honours)

Submitted in partial fulfilment of the requirements for the degree of

Doctorate of Philosophy in Science

Department of Geology and Applied Geology

University of Natal (Durban)

DURBAN 2000

I declare that this is my own unaided work except where suitably referenced and acknowledged

Signed: 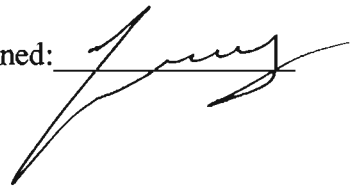 Date: 10/3/2000

Abstract

The eastern portion of the Namaqua-Natal Mobile Belt, the Natal Metamorphic Province is divided into four main tectonostratigraphic units. These units comprise two accreted island arcs: the Mzumbe and Margate Terranes; an imbricately thrust nappe zone consisting of four ophiolitic nappes in a hinterland-dipping duplex; and the highly deformed metavolcaniclastic/metagreywacke Mfongosi Group directly adjacent to the stable northern foreland of the Kaapvaal Craton. Theories of late-tectonic left-lateral movement in the southern island arcs are extrapolated northwards of the southern margin of the Kaapvaal Craton coincident with the Lilani-Matigulu Shear Zone. The relative timing and structural context of vein-hosted mineralization with respect to major recognized tectonic events is resolved in five separate areas, two in the Natal Nappe Zone and three in the Natal Thrust Front.

The Madidima Nappe of the Natal Nappe Zone contains several north-northeast- to northeast-trending and northeast- to east-northeast trending quartzofeldspathic veined reefs considered to have formed in a late-tectonic left-lateral shear system (main shear and synthetic shear orientations, respectively). The northeast- to east-northeast-trending reef is duplicated due to infilling of normally-faulted steep structures in the semi-brittle, incremental normal faulting of the banded amphibolite component of the nappe. Later left-lateral movement has reactivated one of these steep structures along the southern margin of a regional F_2-folded band of granite-gneiss in that a southwest extension of this structure may be responsible for sub-economic veining for a length of up to 9 km. The extensive flat-lying topography of the Mbongolwane Flats area, in which the reefs are situated, is accounted for by the accelerated weathering of rocks which underwent sustained late-tectonic metamorphism in the epidote-actinolite facies, accompanied by pervasive shearing and block rotation to the south of the southern limb of the regional F_2 fold in the granite-gneiss. A large, kilometer-scale, open advective fluid system which provided fluid-mediated exchange between co-existing rocks existed at the time of vein formation. The fluid system was driven by early-tectonic intrusion of a granite-gneiss and amphibole-rich granite.

Two areas in the Mfongosi River valley, the northern and southern Mfongosi Valley areas, contain typical evidence of deformation at the leading edge of collision in a mobile belt. The southern Mfongosi Valley area, at the confluence of the Mfongosi and Tugela Rivers, contains veining which resulted from pressure solution of the host metavolcaniclastic/metagreywacke. Veining occupies predictable shear and tension fractures formed during the initial deformation of a foreland margin sequence, in addition to occupying those fractures formed by buckling on the layer-scale. The structural context of the northern Mfongosi Valley veining is defined by subsequent deformation and vein fragmentation such that the metavolcaniclastic/metagreywacke was reduced to a melange in which vein segments acted as competent clasts; a large-scale porphyroblast/matrix system. Formation of the Manyane Thrust to the south of the Mfongosi Group interrupted the normal retrograde metamorphism of the remainder of the Tugela Nappe and initiated a "hot iron effect" whereby a short-lived thermal pulse acted at the thrust plane, producing a reversed geothermal gradient in the underlying Mfongosi group. This reversed gradient would have been counteracted by a steepened normal geothermal gradient in the Mfongosi Group caused by overloading of the Natal Thrust Front by the Natal Nappe Zone. These geothermal gradients partly account for the concentration of veining in the areas of the Mfongosi Group which are directly adjacent to the Manyane Thrust, and directly adjacent to the Kaapvaal Craton, in the lower portions of the thrust front. Stable isotope studies indicate fractionation between vein and wall rock under a short-lived, mainly rock-buffered, layer-scale fluid-movement system.

Also forming part of the Mfongosi Group of the Natal Thrust Front, the Ngubevu area contains an apparently enigmatic distribution of veining accompanied by gold and base metal mineralization. The structural evolution of the Ngubevu area occurred during consistent left-lateral transpression into which has intruded early-tectonic veins, formed by pressure solution and having the same structural format as the early-tectonic veining in the southern Mfongosi Valley area. Subsequent deformation of the system was accompanied by 190°-trending tension gashes which were continually ptygmatically-folded, sheared and offset to form occasionally mineralized quartzofeldspathic "blows" and along-strike stringers in the epidote-

actinolite schist. Where veining cross-cuts narrow calcite - graphite - sericite - quartz - albite - tourmaline ± chlorite schist layers, gold mineralization occurred. The late-tectonic tension gashes, antitaxially filled by quartz and amorphous calcite, cross-cut the entire range of lithologies. The fluid system during vein deposition varied: during infilling of early-tectonic fractures a short-lived fluid-flow system dominated, with the emplacement of recrystallized wallrock occurring in a closed, non-advective regime under the influence of diffusion caused by pressure solution. The fluid system changed to a more open, advective, greater than layer-scale rock-buffered one with a decreasing contribution of material from immediate host rocks. An internal fluid source is implied for the entire period of vein emplacement, derived from structural analyses which indicates negative dilation across the Mfongosi Group in this area and by comparison of vein:wallrock $\delta^{18}O$ values which indicate a lack of igneous-derived fluids.

The Phoenix Mine, in the central portion of the Tugela Nappe, and the Ayres Reef, hosted in Manyane amphibolite adjacent to the Manyane Thrust, are grouped together on the basis of their cross-cutting nature and timing with respect to metamorphism and deformation of the host rock, and also due to their similarity in isotopic plots. Both vein sets occur in approximately east-west to east-northeast-trending zones which show evidence of late-tectonic left-lateral movement. Phoenix Mine veining occurs in weakly-metamorphosed meta-gabbro/meta-norite of the Tugela Rand Complex. The Manyane amphibolite demonstrates the amphibolite facies of metamorphism due to the short-lived thermal pulse at the Manyane Thrust. Both sets of veining display slickenlines which are indicative of their emplacement prior to the late-tectonic left-lateral movement. The unusually thick quartz veins of both deposits are the results of late- to post-Tugela Rand Complex fluids or the tapping of late-tectonic metamorphic fluid reservoirs. This caused silica metasomatism and redeposition of material in post-thrusting collapse features. A highly channelized, single-pass fluid system is proposed in the absence of intrusion-derived fluids.

Whole rock geochemical data allow a distinction to be made between the Natal Thrust Front and the Natal Nappe Zone: the foremost nappe of the nappe zone consists primarily of N-type mid-ocean ridge basalts/ocean-floor to within-plate basalts which were intruded prior to nappe emplacement by metaluminous orogenic volcanic arc granitiods. The thrust front displays a lateral variation in metabasite/metasediment ratio, with the ratio increasing from east to west in this inlier. In the east, in the Nkandlha area, melanged metagreywackes dominate and there is a marked paucity of associated metabasites. In the central portions of the thrust front, in the vicinity of the Mfongosi area, active continental margin/continental arc magmatogenic greywackes and arkoses are interlayered with calk-alkaline volcanic arc basalts (volcaniclastics). The greywacke geochemistry indicates little to no mafic/ultramafic influences in sediment contribution and the source of sediment is inferred to be the southern portions of the Kaapvaal Craton. The Nkandlha and Mfongosi area Mfongosi Group segments are considered to be in-situ or para-autochthonous. The western-most Ngubevu area predominantly hosts metabasites. The geochemistry of the metabasites indicates that they are N-type mid-ocean ridge basalts/ocean floor basalts from a destructive plate margin setting. The metabasites are interbanded with metapelitic/metacalcsilicate layers produced in a shallow water oxic environment, here inferred as a spatially-restricted shallow, marginal basin. The metabasites in the Ngubevu area are notably similar to those of the Madidima Nappe, indicating a similar provenance and pre-collisional mode of formation. It is proposed that the variation in the Natal Thrust Front was due to a north-east/south-west distribution of lithological proportions or mixing, with greywackes dominating in the northeast (in proximity to the Kaapvaal Craton) and metabasites dominating in the southwest. Left-lateral transpressional movement within the Mfongosi Group of the Natal Thrust Front, and the Natal Nappe Zone, was continuous throughout plate collision and obduction.

Contents

Chapter 1 - Introduction

Chapter 2 - The Mbongolwane Flats Area

Chapter 6 - Phoenix Mine Page

Chapter 7 - Oxygen Stable Isotope Study

Chapter 8 - Geochemistry

Chapter 9 - Summation Page

Appendices

"To the best of my knowledge, the most continually-visited area lies in the Tugela Valley where the deep clefts cut by the river through the ages act as the pages of a book which the geologist can study to determine the various formations. Many will remember, in particular, the old Ngubevu working on the Zululand bank of the Tugela River between the Ferry and Jamesons Drift, where a small animal-driven stamp battery used to crush the quartz extracted from a shaft, and gold dust was taken to the bank in Greytown in Vaseline bottles. Subsequently a small company was formed to continue operations, but this suffered the same fate as dozens of other attempts to find that big pot of gold."

- There's Gold in Them Thar Hills - But Natal Lacks It In Payable Quantities -

S. P. Horning, Natal Witness, March 27, 1963

"Today, the attitude seems to be that as no gold is expected, no intensive prospecting and drilling is worthwhile. So sceptical is officialdom, in fact, that no comprehensive geological map seems to have been produced to indicate where the gold can be found in Natal."

- Mfongosi Gold Fields - Original Discovery by Fred Markham -

D. Robbins, Natal Witness, January 23, 1985

Chapter 1

1.1) Introduction

The province of Kwazulu-Natal has been prospected for gold for almost its entire populated history. This ongoing prospecting, together with the study of the distribution of localised deposits, sampling, drilling, and the construction of a multitude of genetic models for ore deposit formation, has resulted in limited gold production. This study attempts to elucidate the origin and formation of a selection of gold- and base metal-bearing veining in the northern part of Kwazulu-Natal, in the tectonostratigraphic terranes of the Natal Thrust Front and the Natal Nappe Zone, each being units of the Natal Metamorphic Province.

1.2) Regional Geology

The Namaqua-Natal Metamorphic Province (NNMP) is interpreted to be a Mesoproterozoic mobile belt formed by the collision between the southern margin of the Archaean Kaapvaal Craton and a plate or sub-plate to the south (African azimuths; Du Toit, 1931; Matthews, 1959, 1981 a, b). The NNMP extends from the southeastern coast of South Africa in northern Kwazulu-Natal to the west coast of South Africa in the northwestern Cape (Figure 1.1). The east-west continuation of the NNMP beneath Palaeozoic and Phanerozoic cover is inferred and the mobile belt may be divided into two parts in South Africa; the western portion consisting of the Namaqua Metamorphic Province in Namaqualand and the Natal Metamorphic Province (NMP) in the east (Figure 1.1).

The NMP is a regionally metamorphosed and deformed mobile belt incorporating ophiolite and ocean floor material, "geosynclinal" sequences, island arc assemblages and para-autochthonous granite-gneiss basement (Du Toit, 1931; Matthews, 1959, 1972, 1981 a, b; Cain, 1973, 1975; Thomas, 1989 a, b). These observations are based on regional lithological, geophysical and preliminary geochemical grounds (*op. cit.*; Barkhuizen and Matthews, 1990) The regional outcrop of the NMP is restricted to a narrow, 220-kilometre long, north-south trending erosional inlier (Matthews, 1981 b; Figure 1.1) in the province of Kwazulu-Natal.

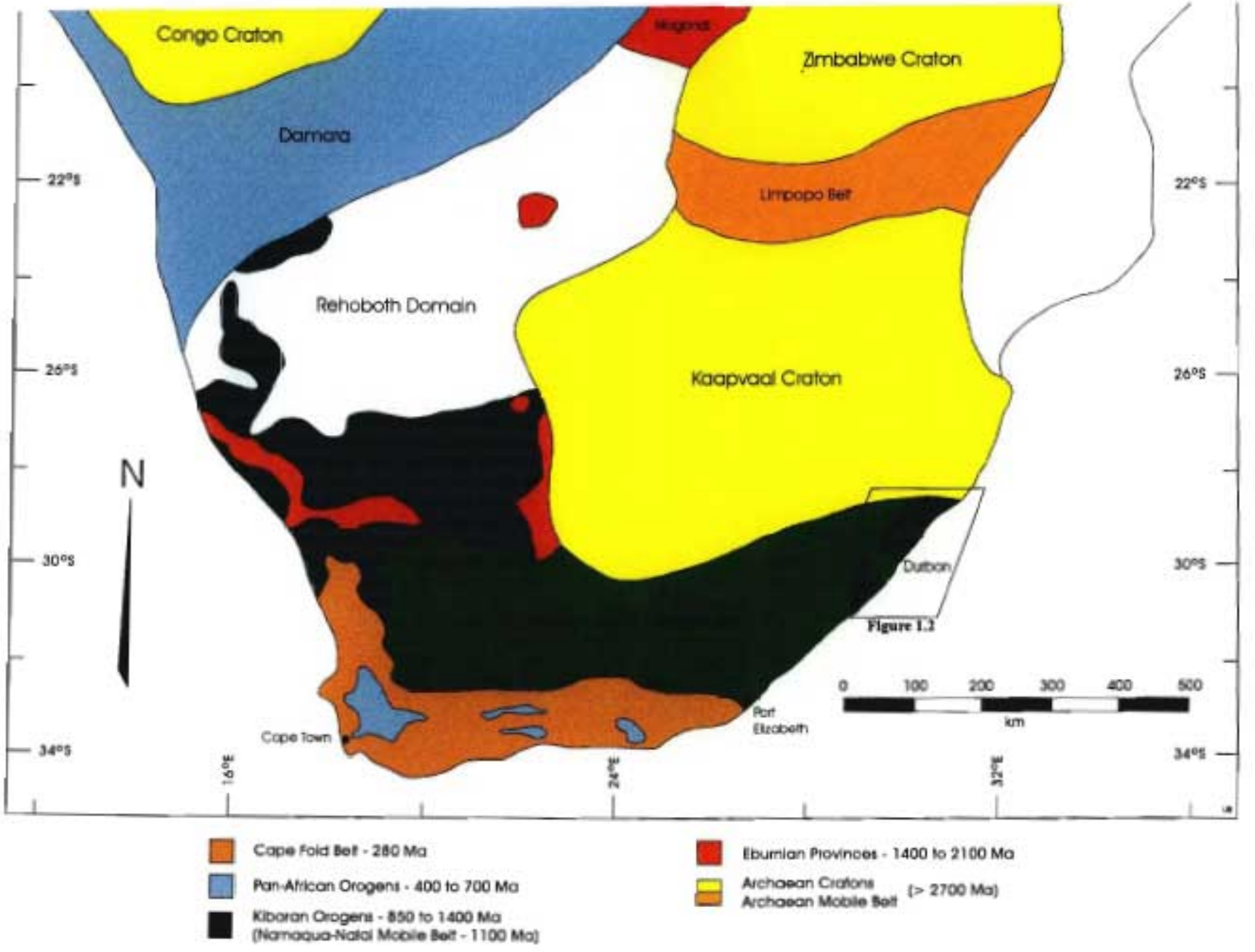

Figure 1.1 The main structural elements of southern Africa. Adapted from Saggerson (1973); Saggerson and Turner (1980); SACS (1980); Martin and Hartnady (1986); Groenewald *et al.* (1991); Jacobs *et al.* (1993) and Jacobs and Thomas (1994). The positions of the Natal Metamorphic Province and Figure 1.2 are indicated.

1.3) Subdivisions of the Natal Metamorphic Province

Numerous subdivisions of the Natal Metamorphic Province (Figure 1.2), based on tectonostratigraphic and/or metamorphic variations across the province of Kwazulu-Natal, have been proposed and are summarized in Table 1.1, modified after Matthews (1959, 1972), Cain (1973, 1975), Matthews and Charlesworth (1981) and Thomas (1989 b). The regional strike of these zones varies from east-west to east-northeast. The stable Kaapvaal Craton to the north of the NMP consists mainly of granite-gneiss basement which apparently has not been affected by a major regional metamorphic event for at least 2600 my (Matthews, 1972). The Kaapvaal Craton contains infolded greenschists and amphibolites of the Nondweni Greenstone Belt and is overlain by the 6000 m-thick Archaean Pongola Supergroup consisting of the basal Nsuzi and upper Mozaan Groups (eg. Tankard *et al.*, 1982). The Pongola Supergroup has a minimum age of 2900 Ma and consists of thick units of orthoquartzites, alternating with subordinate units of sheared volcanic rocks and phyllitic metasediments.

The north-south extent of the NMP is divisible into four main zones (Figure 1.2 - inset, Table 1.1). These are, from north to south, the Natal Thrust Front, The Natal Nappe Zone, the Mzumbe Terrane and the Margate Terrane (Matthews, 1959, 1972; Cain, 1975; Thomas, 1989 b). The tectonostratigraphic nomenclature adopted in this study is that of Matthews and Charlesworth (1981), that of the 1:250 000 scale Geological Series map, Dundee, No. 2830 and that of SACS (1980) including descriptions of units derived from Matthews (1959, 1972) and Thomas (1989b). In this scheme the NMP is divided into groups, intrusive complexes and nappes, the latter being further subdivided into formations. The area previously known as the Tugela Terrane comprises that portion of the Natal Thrust Front and Natal nappe Zone in the immediate vicinity of the Tugela River.

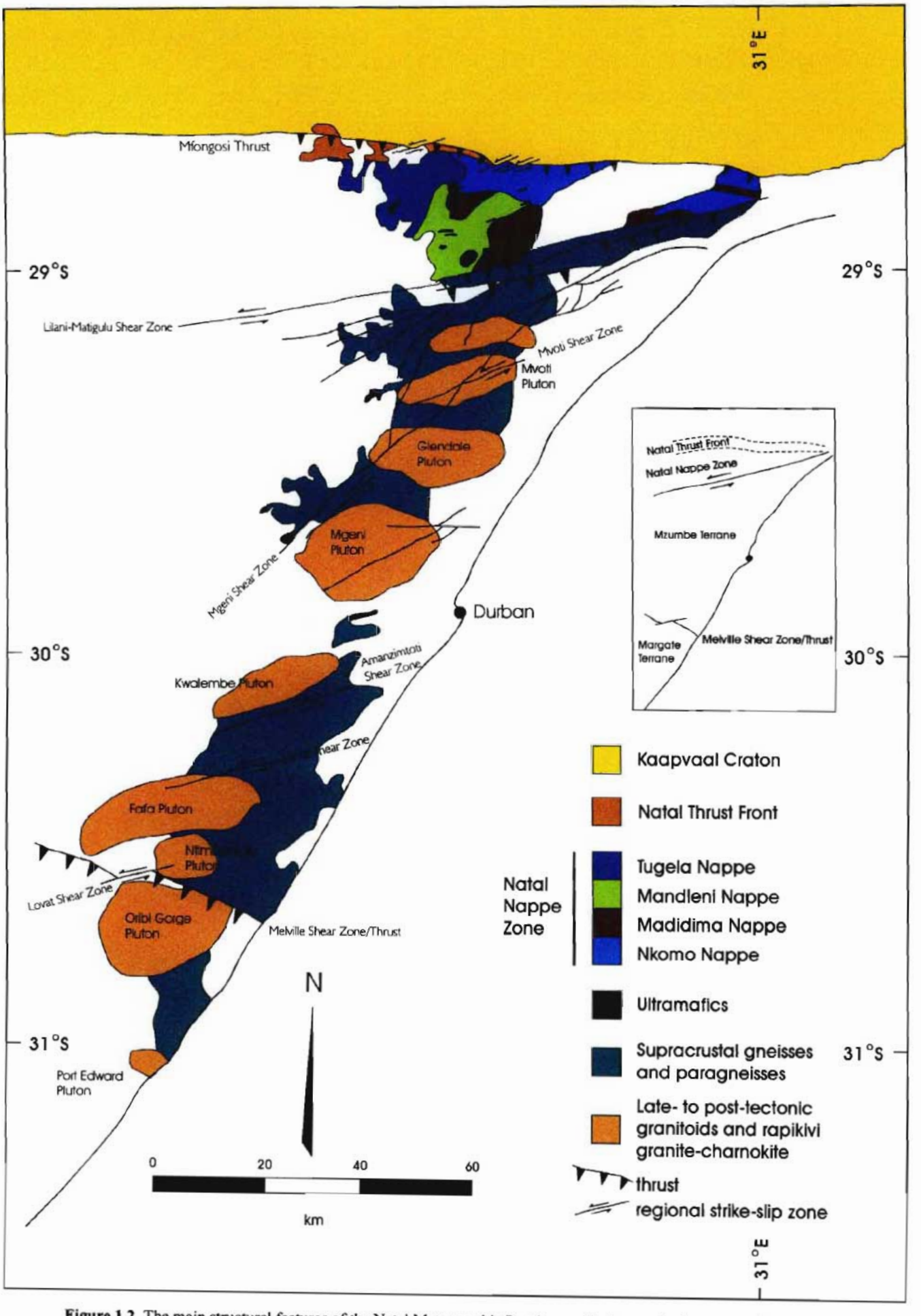

Figure 1.2 The main structural features of the Natal Metamorphic Province, with the terminology as used in the text (inset shows the subdivision of terranes). After Cain (1973, 1975); Matthews and Charlesworth (1981); Thomas (1989b) and Jacobs *et al.* (1993).

Table 1.1 Tectonostratigraphic subdivision of the Natal Metamorphic Province, compiled from Matthews (1959, 1972), Cain (1975), Matthews and Charlesworth (1981) and Thomas (1989 b).

	Kaapvaal Craton	*Natal Thrust Front*	*Natal Nappe Zone (Imbricate thrust zone)*	*Accreted Volcanic Arc Sequences*	
Tectonostratigraphic Unit	Cratonic rocks Infolded greenstone belts Archaean supracrustal sequences	Ntingwe Group Mfongosi Group	Tugela Terrane Tugela Nappe Mandleni Nappe Madidima Nappe Nkomo Nappe	*Mzumbe Terrane* Mapumulo Group metavolcanics	*Margate Terrane* Mzimkulu Group meta-volcanics
Orogenic Facies	Stable crystalline foreland or foundation	Shallow water or shelf facies Marginal volcani-clastic/pyroclastic series	Gneissic amphibolite complex with mafics/ultramafics, layered amphibolites and subordinate quartzofeldspathic gneisses and plagiogranites	Arc-related felsic to mafic metavolcanic gneisses and subordinate paragneisses intruded by plutons in which mega- crystic granites, charnokites and enderbites dominate	
Tectonic Unit	Continental crust	Miogeosynclinal limestones and sediments Upper-ophiolite seq.	Post-Ntingwe Thrust Units derived from the "Tugela Trough"	Arc-related metavolcanic sequences	
General Regional Metamorphism		Upper Greenschist Facies	Lower Amphibolite Facies (*c.f.* this study)	Upper Amphibolite Facies - locally to Granulite facies adjacent to plutons Granulite Facies	
Metamorphic Facies Series (Cain, 1975; Matthews, 1981 a, b)		High-Pressure/ Intermediate	Intermediate-Pressure/ Intermediate	Low-Pressure/ High-Temperature (fluid-rich?), widespread migmatization	
Pressure-Temperature estimates		Chlorite-garnet zone 500-550°C 12-16 kb	lower almandine-amphibolite 440-650°C 6-10 kb	almandine-amphibolite 600-700°C 5-6 kb (Mapumulo Group)	

Tectonic Unconformity (Basal/Mfongosi Thrust)

Lilani-Matigulu Shear Zone

Separated by Melville shear zone and hosting ENE-trending sinistral shears

a) Natal Thrust Front

The Natal Thrust Front consists of the Ntingwe and Mfongosi Groups which occur at the leading edge of the collision zone, immediately south of and overlying the southern margin of the Kaapvaal Craton. This zone defines a 2-12 km wide, south-dipping imbricate complex of low-grade, apparently high-pressure metamorphic formations (Matthews, 1959; Cain, 1975). The structures prevalent in this zone are east-trending tight isoclinal folds, with south-dipping axial planes, which are disrupted by overthrusting towards the northern foreland (*op. cit.*). The northernmost Ntingwe Group consists of dolomite, limestone, shale and mudstone, overlying conglomerates and breccias (Matthews, 1959; Matthews and Charlesworth, 1981).

The Mfongosi Group, immediately to the south of the Ntingwe Group, consists chiefly of phyllitic quartzite, quartz-chlorite schist, carbonate-rich quartz-chlorite schist, epidote-actinolite schist, quartz-albite-carbonate-chlorite schist and garnet-staurolite-mica schist (Matthews, 1959; Matthews and Charlesworth, 1981; Cain, 1973, 1975; this study). These rock types represent interlayered schistose meta-argillites and metalavas with rare relict pillow structures and amygdaloidal textures (Matthews, 1981a) such as remnant epidote-chlorite and alkali feldspar glomeroporphyroblasts (Cain, 1975) which are possibly recrystallized amygdales previously containing zeolites. Minor quartzites, limestones and banded iron formations also occur. This imbricate zone was transported northwards in an ascending sequence (i.e. the youngest lithologies at the deepest part of the tectonostratigraphic succession) and was thought to contain displaced para-autochonous slices of foreland material (Matthews, 1972). Studies of the Kaapvaal Craton have concentrated on late- and post-Pongola granitoids (eg Matthews, 1985, 1987, 1988, 1991), the Pongola Basin to the north of the Natal Thrust Front (eg Matthews, 1990) and intrusives to the northwest of the Mbongolwane Flats area (eg Scogings, 1986, 1989).

The Ntingwe and Mfongosi Groups are highly deformed and separated from the Kaapvaal Craton in the north by the basal Mfongosi Thrust (= Post-Ntingwe Thrust of Matthews, 1959; Figure 1.2). The dip of the Mfongosi Thrust, immediately adjacent thrust units and possibly the southern margin of the Kaapvaal Craton, increases from west to east along the Natal Thrust Front: in the western sector, the major thrusts are inclined to the south at low angles (10-20°) while progressively eastwards the inclination increases to 45-60°, a situation inferred to imply differential downwarping of the thrust front (Matthews, 1981 b).

Metamorphic rocks of the Natal Thrust Front are dominated by indicator assemblages in the chlorite-garnet zone that conform to the upper greenschist facies of Winkler (1967) and Liou *et al.*, (1985) and show characteristic high-pressure, intermediate facies series (Cain, 1975). The amphibole in the Mfongosi Group is mainly actinolite which becomes more hornblendic southwards. Thus an increase in the grade of metamorphism of the Natal Thrust Front towards the contact with the Natal Nappe Zone has been recognised although the mechanisms effecting this change have not been explained. Pressure-temperature conditions for the Natal Thrust Front are conservatively estimated to be in the order of 500-550°C at 12-16 Kb (*op. cit.*).

b) Natal Nappe Zone

To the south of the frontal collision zone (the Natal Thrust Front - *sensu stricto*) is the Natal Nappe Zone (Matthews, 1959, 1981 a, b) which consists of four flat lying thrust sheets composed mainly of granitic gneiss, para-amphibolite, meta-basalt and bands of granitic gneiss, magnetite quartzite and ultramafic pods and lenses. Pre-tectonic serpentinites include podiform chromites, pyroxenites and peridotites. The thrust sheets outcrop in an ascending tectonostratigraphic sequence from east to west (Matthews, 1959; Smalley, 1980) and conform regionally to an antiformal stack plunging shallowly westwards in a typical horse-emplacement scenario (Rigotti, 1977; Schulze-Hulbe, 1977; Smalley, 1980). The thrust units collectively cover a width of 25-30 km and are separated by zones of talc schist which contain sepentinite pods (*op. cit.*). From the base of the thrust stack upwards, the thrust units are named as follows: Nkomo, Madidima, Mandleni and Tugela (Matthews and Charlesworth, 1981; Table 1.1). The grade of metamorphism in the thrust units is proposed to be of upper-amphibolite to migmatitic (gneiss) grade (Matthews, 1981 b) while Cain (1975) found widespread evidence for the almandine-amphibolite facies of Winkler (1967). The average P-T conditions are thus estimated to be in the order of 440-650°C and 6-10 kb. The grade of metamorphism over an individual thrust sheet is variable due to any combination of the following factors; depth of the thrust unit in the thrust stack, proximity to the Kaapvaal Craton and late-tectonic retrograde metamorphism which acted to varying degrees in each unit. The Tugela Rand Complex in the Tugela Nappe is regarded as the only major early- to syn-tectonic intrusive (Lambert, 1962).

Based on comparisons with analogous terranes, the obduction of an ophiolite sequence was proposed for the Tugela terrane with the Mfongosi schist representing the upper, metamorphosed part of an ophiolite suite (Matthews, 1972). Despite partial anatexis and compositional banding, the majority of the Natal Nappe Zone may still be recognised as metamorphosed basalts with the mafic-ultramafic association characteristic of the intermediate layers of a complete ophiolite suite (*op. cit.*). These associations are regarded as representing a transformed, inverted, metamorphosed ophiolite complex (*op. cit.*). Furthermore, the Ntingwe Group is proposed to represent a displaced shallow-water or shelf facies while the Mapumulo Complex to the south is regarded as an intensely folded, predominantly meta-greywacke sequence which was accreted onto the leading edge of a northward-moving continental plate (*op. cit.*).

The *Lilani-Matigulu Shear Zone* (Table 1.1; Figure 1.2) is a 1 km-wide, approximately 140 km-long shear zone which separates the Natal Nappe Zone to the north from the arc-dominated Mzumbe Terrane (Mapumulo Group) to the south (Thomas, 1988 b; Thomas, 1989 b; Jacobs and Thomas, 1994; Figure 1.2). The Lilani-Matigulu Shear Zone is the largest of a number of parallel shears which trend east-northeast, parallel to the strike of regional structures described above although shears are abundant within the Mzumbe and Margate Terranes. These similarly-oriented minor shears which have the same sense of movement as the Lilani-Matigulu Shear Zone include the Mvoti, Amanzimtoti, Jolivet and Loval Shears (Figure 1.2; Thomas, 1989b; Jacobs *et al.*, 1993; Jacobs and Thomas, 1994). The Lilani-Matigulu Shear Zone dips southward at about 80°, stretching lineations indicate a sinistral sense of movement consistent with the oblique collision model proposed by Jacobs and Thomas (1994) where the NMP utilized continental margin-parallel sinistral shear zones while moving in a mainly north-easterly direction.

Gravity modelling by Barkhuizen and Matthews (1990) indicates that the Lilani-Matigulu Shear Zone is the southern limit of the nappe-dominated Natal Nappe Zone and is co-incident with the southern margin of the Kaapvaal Craton. It was formerly believed that late-tectonic sinistral transpressive motion as described by Jacobs *et al.* (1993) and Jacobs and Thomas (1994) only prevailed to the south of the Lilani-Matigulu Shear Zone. The inferred competency contrast at the vertical portion of this discontinuity is interpreted as a deep crustal suture, similar to several other Precambrian crustal sutures (eg Gibb and Thomas, 1976; De Beer and Meyer, 1984; Barkhuizen and Matthews, 1990). Transcurrent shearing has thus been concentrated along the

Lilani-Matigulu Shear Zone (Jacobs *et al.*, 1993) although it has persisted to the north of this tectonic boundary (this study). This transpressional deformation is one of the factors controlling the distribution of mineralization in selected areas as will be shown in this study.

c) Mzumbe and Margate Terranes

Thomas (1989 a, b) subdivided the southern portion of the NMP into two recognisable major tectonostratigraphic terranes; the Mzumbe and Margate Terranes. These terranes are separated by the southerly-dipping ductile Melville Shear Zone (Figure 1.2) which is thought to represent a deeply eroded suture zone between two Mesoproterozoic volcanic island arcs (Table 1.1, Jacobs and Thomas, 1994). This terrane division is based on a lack of correlation between the older rocks across the shear zone and differs to that proposed by Thomas (1988 a) and SACS (1980) where all the supracrustal gneisses were consigned to the Mapumulo Group. This subdivision is further supported by the grade of metamorphism of each domain; a northern amphibolitic terrane and a southern granulitic terrane (Thomas, 1988 a, b). The Mzumbe and Margate Terranes are made up of relatively old, arc-related felsic to mafic metavolcanic gneisses and subordinate paragneisses which were intruded by multiple plutonic suites from 1200 to 1025 Ma (Jacobs and Thomas, 1994). The lithologically distinct older gneisses of the Margate Terrane are not included in the Mapumulo Group; rather, the older gneisses of the Mzumbe Terrane, which extends northwards of the Melville Shear to the Mapumulo Thrust, comprise the Mapumulo Group (Thomas, 1989 b). The protoliths of the gneisses pre-dated the first deformation event while the emplacement of almost invariably megacrystic plutons spanned the entire post-supracrustal evolution of gneissose rocks.

1.4) Age and Mesoproterozoic Position of the Natal Metamorphic Province

An exact age for the formation of the mobile belt is not known. Mineral and whole rock Rb/Sr and U/Pb zircon ages from 900 Ma to 1194 Ma (Nicholayson and Burger, 1965; Burger and Coertze, 1973) must be regarded with caution as these authors used whole-zircon dating methods. The tectonic setting and age of late megacrystic granites, enderbites and charnockites of the southern NMP, based on a range of related textures which include unfoliated intrusives, augen gneisses and mylonites, is also controversial (Cain, 1975; Eglington *et al.*, 1986; 1989).

The Mapumulo and Mzimkulu Groups in the Mzumbe and Margate Terranes, respectively, were intruded by plutonic suites over the period between 1200 ma to 1025 ma (Thomas and Eglington, 1990).

The early, *pre-tectonic* Mzumbe Suite, emplaced at about 1200 Ma (U-Pb zircon, Thomas and Eglington, 1990) consists of calk-alkaline, tonalite-trondjemite orthogneiss which was intruded by mafic dykes of the Equefa Suite prior to shearing by the Melville Shear Zone (Thomas and Eglington, 1990; Jacobs and Thomas, 1994). *Syntectonic* intrusions in both terranes occur as sheet-like leucocratic granites, emplaced at 1100 ma (Thomas, 1989 b).

The *syn- to post-tectonic* Oribi Gorge Suite is the youngest plutonic phase occurring in both the Mzumbe and Margate Terranes and consists of large plutons of late-tectonic rapakivi-textured granitoid and charnockite plutons (Thomas, 1988 c) dated at about 1050 ma (Thomas, 1988 b, c).

In a larger context the NMP occurred at the centre of the Namaqua-Natal-Heimefrontfjella mobile belt in Mesoproterozoic times (Smith and Hallam, 1970; Matthews, 1981 a; Martin and Hartnady, 1986; Groenewald *et al.*, 1991 and Jacobs *et al.*, 1993). Indeed, the break-up of the super-continent Rhodinia, which contained the mobile belts, is proposed to have centred on the NMP (*op. cit.*). To the south of the southernmost outcrops of the NMP is an east-west trending geophysical anomaly termed the Southern Cape Conductive Belt (De Beer *et al.*, 1982). This anomaly strikes westwards from the Transkei coast and is inferred to represent the continuation of the NMP beneath cover rock. An interesting aside: the normal/strike-slip faults which were strongly controlled by the angle of the collision of craton and plate/microplate may have been influential in the break-up of Gondwana. In particular, the faults which have arcuate east-northeast trends, with coastward concavity, seem to have exerted a strong influence on the beak-up pattern (Von Veh and Anderson, 1990). A late-break-up coastline fault set is associated with dolerite dykes which define the prominent north-east trending magnetic lineaments (pers. comm. M.K. Watkeys).

1.5) Methodology

A study of known gold and base metal occurrences in the Natal Thrust Front and the Natal Nappe Zone was limited to five field areas, comprising three areas in the Natal Thrust Front and two areas in the Natal Nappe Zone. The five areas focused upon are shown in Figure 1.3.

a) Mbongolwane Flats

The Mbongolwane Flats area (Mpapala Flats) occurs in the eastern portion of the Madidima Nappe and is an extensive flat-lying alluvial plane with less than 0.5% outcrop by area, in which three definite known gold occurrences, including two mines, are found. The Mbongolwane Flats area was accessed from the Anglican Mbongolwane Mission which is to the west of the field area.

b) Phoenix Mine

The Phoenix Mine shear zone is hosted in a sliver of the chiefly mafic to ultramafic Tugela Rand Complex. The mine occurs near the centre of the exposed part of the Tugela Nappe and was accessed by camping in the vicinity of the main shear zone.

c) Northern Mfongosi Valley

The Northern Mfongosi Valley area contains silver and gold workings from the early part of the century which concentrated on Pb-Ag-Au-carrying veining located within the tectonic melange of a highly deformed distal, bimodal volcanic/volcaniclastic succession within 2 kilometres of the southern margin of the Kaapvaal Craton.

d) Southern Mfongosi Valley

The Southern Mfongosi Valley area is centred on the confluence of the Mfongosi and the Tugela Rivers. The field area encompasses the Ayres Reef in the Manyane amphibolite (Tugela Nappe) and other tunnels and adits in veining in Mfongosi Group rocks. A bimodal volcanic succession may still be distinguished in this area. The Manyane Thrust is the main tectonic feature of this area.

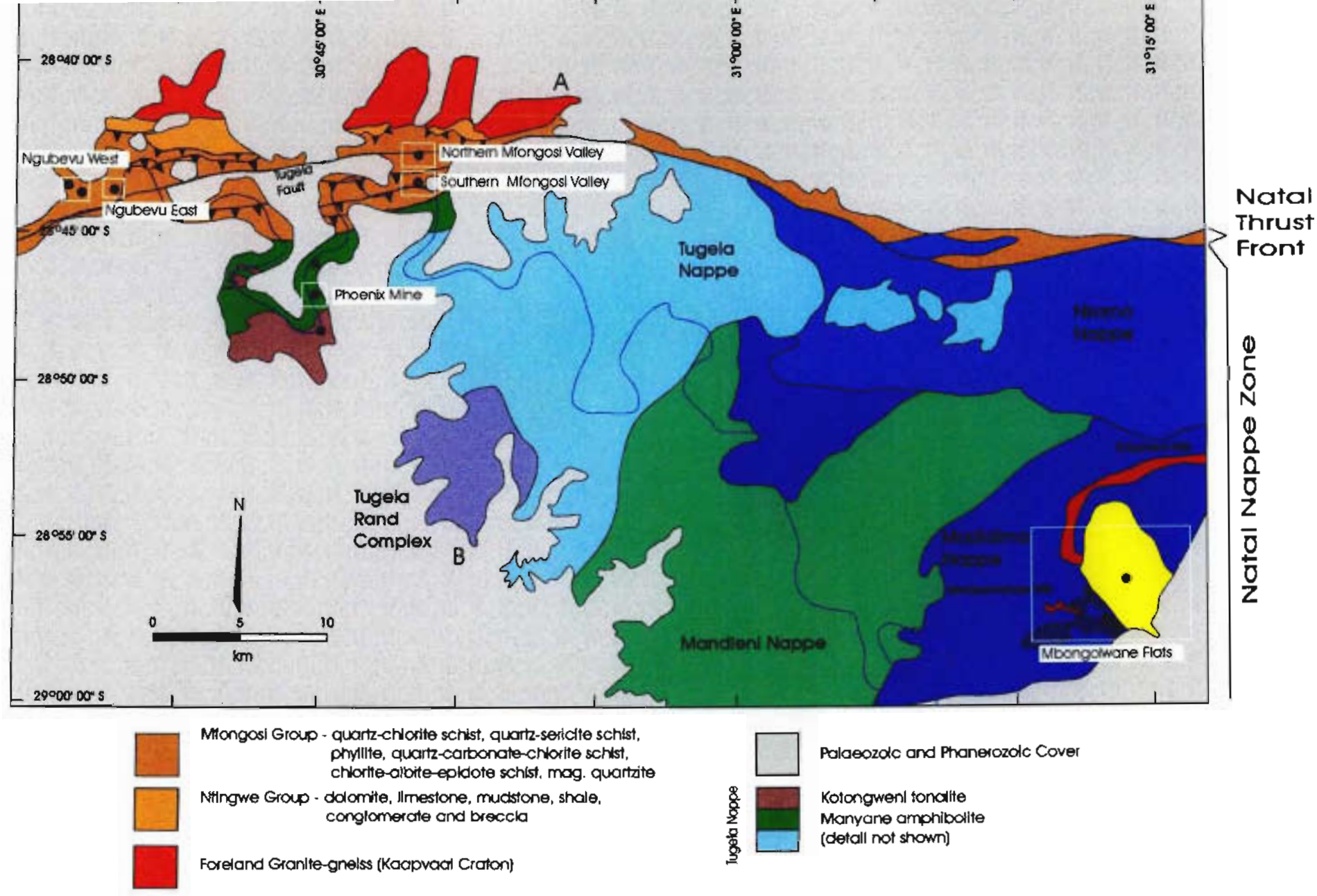

Figure 1.3 Simplified geological map of the Natal Thrust Front and western Natal Nappe Zone showing the distribution of the field areas under consideration in this study. (after Matthews and Charlesworth, 1981; positions of gold and base metal mineralization (●) after the 1:250 000 scale Geological Series map - Dundee - 2830). The position of the cross-section depicted in Figure 1.4 is marked as A-B; although the detailed geology encompassed by the section is not shown here, Figure 1.4 gives some indication

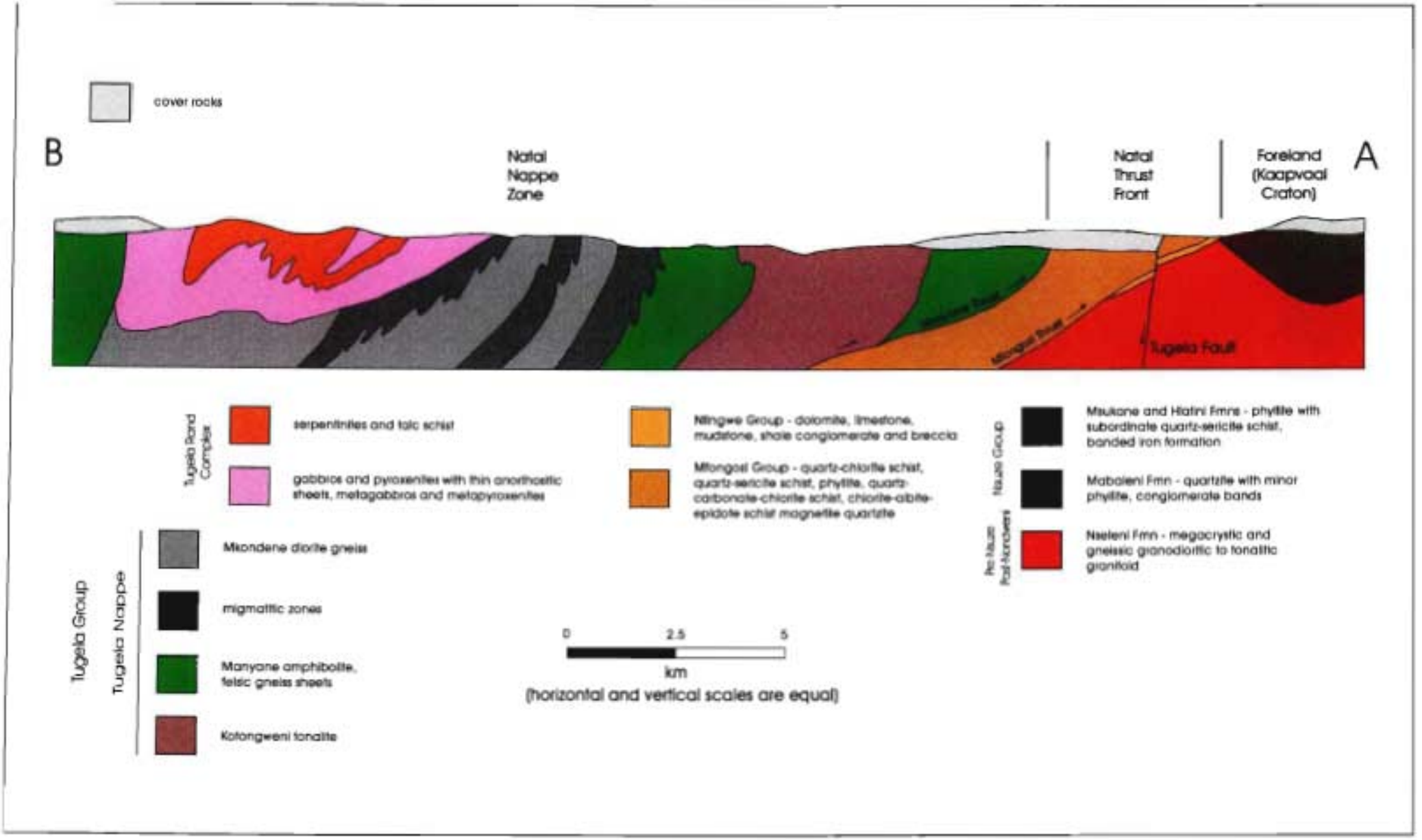

Figure 1.4 Cross-section A-B on Figure 1.3. The tectonostratigraphic succession is evident, as is the position of the Tugela Rand Complex; a deformed metabasic-ultrabasic complex. Note the positions of the Mfongosi and Manyane Thrusts and the downthrow to the south along the Tugela fault which results in cover rocks being laterallyjuxtaposed against elements of the mobile belt (modified after Matthews and Charlesworth, 1981)

Both the northern and the southern Mfongosi Valley areas were accessed from two base camps at different stages; the first camp was situated at the Felix Unite river rafting syndicate which is just to the west of the Mfongosi R.-Tugela R. confluence; the other camp was situated in the Quedeni logging camp, an hours drive from the Mfongosi Valley.

e) Ngubevu Area

The Ngubevu area in the westernmost extremity of the Mfongosi Group is divided into two parts: the Ngubevu West area, which forms the focus of this study, is centred on the Ngubevu River near the Ngubevu R.-Tugela R. confluence. The Blue Spec and Golden Eagle Mines are given a detailed contextural geological examination. The Ngubevu East area, near the Buffalo R.-Tugela R. confluence, hosts the Buffalo River Cu-Au deposit. Both the Ngubevu West and East deposits occur in highly deformed and metamorphosed volcanic and volcaniclastic basalts which are interlayered with metamorphosed volcanic tuffs or metapelites. The Ngubevu west and east field areas were approached from Greytown, via the Greytown-Dundee road.

Two days were dedicated to reconnaissance mapping and orientation surveys to determine the mode of mapping. In the case of the Mbongolwane Flats and Northern Mfongosi Valley areas outcrop mapping was undertaken while the remainder of the field areas were covered by across-strike (and along-strike, where relevant) mapping. Orthophotographs were used in conjunction with 1:10 000 scale contour maps to locate some of the smaller field areas, denoted on the 1:250 000 scale Geological Series map (Dundee 2830) as containing mineralization. Aerial photographs were only used in an ongoing basis for mapping the Mbongolwane Flats area as the size of the remaining four field areas did not justify the use of this technique. In all five areas specific outcrops were selected for detailed structural analysis.

In contrast to De Klerk (1991), Bullen *et al.* (1994) and Bullen *et al.* (in prep), this study concentrates on the context of veining in the structural scheme and attempts to resolve the relative timing of veining with respect to major deformation events. The results obtained for the timing of vein formation are conclusive in terms of the tectonometamorphic mechanisms and mineralization. Following the structural analysis of veining and mineralogy, the grade of metamorphism of the host rocks to veining were resolved and the rocks classified in conjunction with their field descriptions. Thin and polished sections of over 300 samples provided the basis

for rock and vein identification and grouping. In each case, an attempt was made to reconcile the structural features with structural modelling of veining and/or processes in similar tectonic environments.

Oxygen isotope analyses of 94 samples of vein and whole rock material were used in constraining rock/vein interaction such as whether a fluid- or a rock-buffered system was present during vein formation; the degree of contribution from host rock pressure solution; the inferred influence of intrusion-related fluids and basic water:rock ratio estimates. Fluid inclusion studies were abandoned due to the highly deformed nature of veins and the decrepitation and leakage of inclusions which was observed in a comprehensive preliminary study.

Genetic models for each area were constructed, based on the conclusions reached on vein emplacement in a structural context, metamorphism, deformation and oxygen isotope studies. The lack of available detailed structural data necessitated a re-evaluation of the succession of structural and metamorphic events, in addition to determining the timing of veining with respect to the various processes. Only one previous comprehensive study on the Natal Thrust Front was undertaken by Matthews (1959) who concentrated more on the regional distribution of the Mfongosi and Ntingwe Groups while portions of the Natal Nappe Zone were mapped on a regional scale by students working under P.E. Matthews, as part of the Natal portion of the International Geodynamics Project. Schematic three-dimensional diagrams of the present configuration of veining and/or schematic three-dimensional evolutionary diagrams of the deposits are presented. The method of data measurement in the field and a brief description of the program DIPS®, which was used for stereonet generation, are presented in Appendix E. Deductions and recommendations are made concerning the extent of the mineralization and the feasibility of further economic exploitation of each type of vein-hosted deposit. Geochemical data are used to define a pre- to syn-collisional regional tectonic configuration of the NNZ and NTF, by using tectonic and genetic discrimination plots and the various interpretations thereof.

Chapter 2

The Mbongolwane Flats Area

2.1) Introduction

The Mbongolwane Flats area is an extensive flat-lying alluvial to colluvial plane in the center of the Madidima Nappe, which occurs in the eastern portion of the Natal Nappe Zone (Figure 1.3). These flat-lying area is all the more remarkable for its contrast with the surrounding mountains, and due to the fact that it contains a number of gold workings on what is termed the Rebellion Reef. The exact configuration of this reef has not been documented although it is known that gold was mined from quartz reefs which have no apparent consistent orientation. This portion of the study on vein-hosted mineralization in the Natal Nappe Zone concentrates on solving the structural enigma of this area of very poor outcrop. Stable isotopes (Chapter 7) provide some qualitative information on the nature of the fluid phase present during deformation and indicate the extent of the fracture and shear system which operated during the formation of the Rebellion Reef.

2.2) Economic History

The Mbongolwane Flats has had a history of prospecting with limited exploitation. Gray (1907) commented on the extreme scarcity of outcrop which prevented proprietors and visiting commissioners of mines from determining the full extent of the reef during early prospecting Reef orientation seemed variable during early prospecting; at its eastern extremity, to the south of the western termination of the Entumeni Mountains (Figures 1.3, 2.1), the reef trends almost north-south. Further to the southwest, the ridge defining the reef dies out into the relatively flat-lying Mpapala (Mbongolwane) Flats. Limited outcrops of quartz reef were traced in a wide curve with the reef gradually altering its trend to the west and finally attaining a consistent north-northwest strike to the north of the Isiwasamanqe Mountains. The reef was also traced with a consistent east-northeast trend in the direction of the Tugela Valley towards Kranzkop. It is apparent that not one reef, but possibly many, were encountered during early prospecting.

The main Rebellion Reef was found to occur in the local granite and fractures produced by post-cooling deformation of this granite (Gray, 1907). The reef dip was furthermore found to be consistently greater than the dip of the granites' planar foliation implying post-cooling emplacement. The hangingwall to the reef displayed shearing, occasionally showing offsets (of about 30 cm - this study) along near- vertical reverse faults with the downthrown side to the south. The thickness of the Rebellion Reef mined in 1906 varied from 18 to 76 cm with a dip between 68° and 75° to the southwest. Furthermore, reef duplication was noted to the north and south of the main reef being mined at the time. Samples spanning the main reef at its westernmost extremity yielded traces of gold. Gray (1907) presented a range of grades obtained by fire assay on quartz veins, quartz lode, pyritic quartz bands and schistose quartz bands (Table 2.1).

Hatch (1910) documented shaft depths in the Mbongolwane Flats area, but came to no conclusion about the genesis of the reef. A mine operated by the Minoru Gold Exploration Company closed in 1932 due to adverse boring tests (Schurink, 1986). Schurink (1986) proposed that gold is associated with gossaniferous and malachite-stained quartz veins which are continuous for short strike lengths within a sheared meta-gabbro. A poorly-constrained metamorphic overprinting event was dated at 1000 ma (Shurink, 1986) and a metamorphic replacement model was envisaged (e.g. Groves *et al.*, 1985) wherein ore fluids derived from basal devolitization of a volcanic pile in a high-grade metamorphic terrane would transport gold as $HAu(HS)_2$ complexes to deposition (accompanied by sulphurization) in an iron-rich host rock. Fe-sulphide and gold would be deposited in sub-amphibolite facies conditions (1-2 kb, 300-400°C). Two linear arrangements of prospects (R-2/R-3/R-1/R-6 and R-5/R-4 - Figure 2.1) were noted by Schurink (1986). Areas R-1 to R-5 are located in a sheared, K-metasomatized and epidotized meta-gabbro whilst locality R-6 is located in a hornblende-mica schist. The shear zones are not of a consistent thickness (*op. cit.*). Thus, from past reports on the Rebellion Reef, the main targets in this section of the Madidima Nappe are multiple east to east-northeast-trending shear zone-hosted veins. A concise structural analysis of the area will explain this configuration.

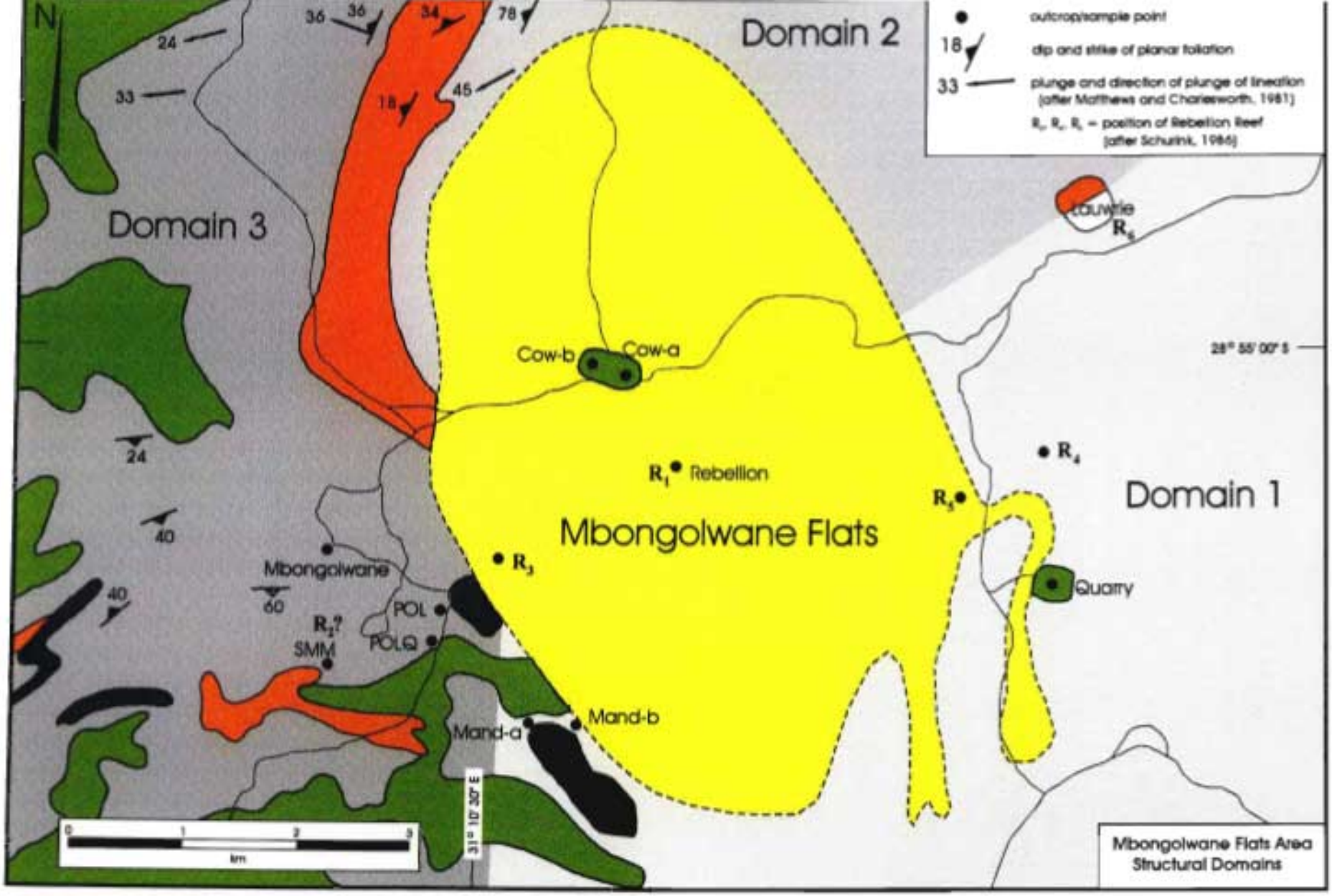

Figure 2.1 The Mbongolwane Flats area, showing the distribution of reef encountered by Schurink (1986). Outcrop names

Table 2.1 Summary of materials sampled and Au grades obtained in Rebellion Reef prospecting

Study	Material Sampled	Grade Obtained (Au)	Averages
Gray (1907)	quartz band	trace	
	pyritic quartz band	3.11 g over 0.38 m	
	quartz	3.11 g over 0.41 m	
	quartz	20.22 g over 0.06 m	17.12 g over 1.42 m
	schistose quartz band	35.77 g over 0.4 m	
	quartz	35.77 g (chip sample)	
	quartz	1.56 g over 0.19 m	
Schurink (1986)	***RT-1***		
	shear zone in unfoliated meta-	50 ppb over 0.5 m	
	gabbro trench float	max. = 4.6 $g.t^{-1}$	
	RT-2 at ***R-1***		
	weakly foliated	average < 0.01 ppm	
	meta-gabbro	max. = 50 ppm	
	RT-5		
	talc-chlorite schist	max. = 320 ppb	
	RT-6 at ***R-4***		
	sheared and veined	average < 1 ppb	
	meta-gabbro	max. = 50 ppb	
	RT-7 at ***R-1***		
	veined, K-metasomatized and	120 ppb over 10 cm	
	epidotised meta-gabbro		
	RR-1 (Borehole)		
	borehole core in veined	average < 0.05 ppm	
	meta-gabbro	max. = 170 ppb over 13 cm	

2.3) Structural Geology

a) Syn- to Late-Tectonic Events in the Natal Metamorphic Province

Recent studies depict the Kaapvaal Craton as a southwest-directed block (Figure 2.2) causing consistent north-northeast- to northeast-verging isoclinal folding and fold-disrupting thrusting onto the southern margin of the Kaapvaal Craton. The sequences immediately adjacent to the Kaapvaal Craton margin, the Ntingwe and Mfongosi Groups and the ophiolite nappe complex derived from the Tugela Basin to the south were emplaced onto the Kaapvaal Craton margin in a northeasterly direction (Matthews, 1972). Subsequently the island arcs, now comprising the Mzumbe and Margate Terranes (Thomas, 1989 b) were accreted onto the southern portions of the nappe zone (Table 1, Figure 2.2). These events were thought to be predominantly ductile and no lateral motion or reverse faulting of tectonic fragments (*cf.* Mancktelow, 1992) had been noted until recently (Jacobs *et al.*, 1993; Jacobs and Thomas, 1994). A number of approximately east-northeast-trending sinistral, transpressional shear zones have now been observed (*op. cit.*). These sub-vertical ductile shear zones separate tectonostratigraphic terranes and host rapakivi-textured granitoids (e.g. the Oribi Gorge Suite) within the Margate and Mzumbe Terranes (Eglington *et al.*, 1986; Thomas, 1989 b; Jacobs and Thomas, 1994; Figure 2.2).

Studies of late transcurrent motion concentrate on the Mzumbe and Margate Terranes whilst overlooking those segments of the mobile belt to the north of the Lilani-Matigulu Shear Zone; the Natal Nappe Zone (Table 1.1, Figure 1.2). The reason for this omission may stem from the findings of De Beer and Meyer (1984) and Barkhuizen and Matthews (1990). Modeling of gravitational anomalies in the mobile belt reveal sub-vertical, crustal-scale displacement zones extending to the crust-mantle boundary (*op. cit.*). The east-northeast-trending Lilani-Matigulu Shear Zone has been informally proposed as the southern sub-surface limit of the Kaapvaal Craton (*op. cit.*). The inferred competency contrast at this boundary is interpreted to indicate a deep crustal suture (e.g. Gibb and Thomas, 1976; Barkhuizen and Matthews, 1990). The rigid Kaapvaal Craton underlying the Natal Nappe Zone is a "stiffener" which resisted overthrusting and late transcurrent shearing. Stresses causing thrusting and transcurrent shearing were consequently dissipated at the Lilani-Matigulu Shear Zone and late-tectonic, sinistral transpressive motion was therefore assumed to have been limited to the Mzumbe and Margate Terranes.

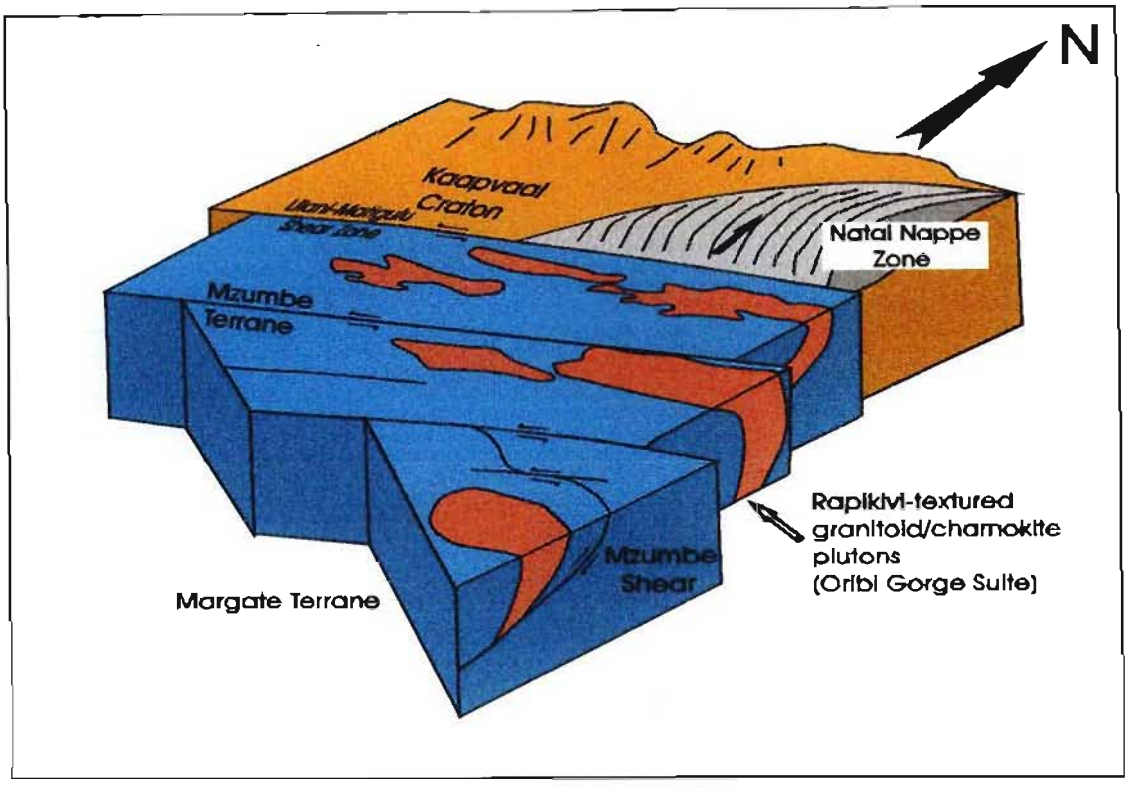

Figure 2.2 Schematic diagram of the configuration of the Natal Metamorphic Province at about 1050 Ma (after Jacobs and Thomas, 1994).

b) The Madidima Nappe

The readily recognizable and predictable features of fold and thrust belts (e.g. Chapple, 1978; Boyer, 1986; Boyer and Elliot, 1982; Mitra, 1986; Gray and Willman, 1991; Ring, 1993) have been extensively documented in the Natal Metamorphic Province (e.g. Matthews, 1959; 1972; Rigotti, 1977; Schulze-Hulbe, 1977; Smalley, 1980; Charlesworth, 1981; Matthews and Charlesworth, 1981) and in particular, in the Natal Nappe Zone.

The Madidima Nappe (Schulze-Hulbe, 1977; Matthews and Charlesworth, 1981) directly overlies the Nkomo Nappe, occupying the majority of the eastern portion of the Natal Nappe Zone adjacent to the Lilani-Matigulu Shear Zone to the south (Figure 1.2). Given the westwards tectonic plunge of the antiformal stack, the Madidima Nappe occupies a large portion of the base of this duplex. The components of the Madidima Nappe in the vicinity of the Mbongolwane Flats are as follows (Schulze-Hulbe, 1977):

- the Silambo banded amphibolite, containing dolomite, limestone and magnetite quartzite layers, displays a wide range of variants including banded epidote-amphibolite, streaky amphibolite and garnetiferous amphibolite
- the Zidoni amphibolitic gneiss, consisting of hornblende-plagioclase gneiss, hornblende-epidote gneiss, hornblende-biotite-plagioclase gneiss, hornblende-biotite-epidote gneiss and hornblende-diopside±epidote gneiss. The Zidoni amphibolitic gneiss intruded the Silambo banded amphibolite in early- to syn-tectonic times (*op. cit.*). Schulze-Hulbe (1977) cites hornblende as the dominant amphibole. However, in the Mbongolwane Flats area the dominant amphibole is actinolite.
- the Thaweni biotite-feldspar granite-gneiss/schist initially intruded the Zidoni amphibolitic gneiss and the Silambo banded amphibolite as thin sheets, often discordant to the first-formed planar foliation. The main components of this unit are; biotite-feldspar gneiss, biotite-microcline gneiss, quartz-muscovite-sillimanite gneiss, quartz-garnet-staurolite-cordierite schist and biotite-hornblende-feldspar gneiss. The Thaweni granite gniess is therefore most likely a para-gneiss.

The Madidima Nappe has undergone a number of deformation events, commencing with D_1 which produced isoclinal folds (F_1) overturned to the north-northeast/northeast (*op. cit.*, this study). D_1 resulted in S_0 (original lithological banding in the Silambo amphibolites) and S_1 (axial planar foliation to F_1) becoming indistinguishable, hence the S_{01} terminology of Schulze-Hulbe (1977) and Smalley (1980) which is also adopted in this study. D_1 and F_1 are pre-thrusting in timing. Originally transgressive offshoots/apophyses of quartzofeldspathic sheets and veining in the Silambo banded amphibolite, defining an agmatic macro-texture, are rotated into near-parallelism with S_{01} indicating that the Zidoni amphibolitic gneiss intrusion was pre- to early thrusting (*op. cit.* Matthews, 1972; Harmer, 1981). Further deformation phases are: D_2 which consisted of northward-verging folds (F_2) with axial planes more steeply inclined to the south than those of F_1; and D_3 which "takes the form of a broad, open, westward-plunging warp (F_3) with a moderately to steeply- (46°-80°) south-dipping axial plane" (Smalley, 1980) that is, possibly in the form of a fault-bend fold or antiformal stack. This sequence of events is similar to those formed in a hinterland-dipping duplex (Boyer and Elliot, 1982; Mitra, 1986). Schulze-Hulbe (1977) proposes a fold generation with axes oriented between those of F_2 and F_3 ($F_{2/3}$).

Deformation events during thrusting are continuous and the features formed thereby are transitional between deformational phases (e.g. D_1 (F_1) and D_2 (F_2) hence the $F_{1/2}$ fold generation used in this study). Intrafolial folds alone may describe a discrete phase of folding which is non-parallel to the stretching lineation (Z) in the early stages of deformation (q.v. Hopwood, 1975). Based on petrographic studies, the formation of the dominant planar foliation in the Zidoni amphibolitic gneiss was a dynamic, continuous process incorporating reversal of shear sense in the overturned limbs of isoclinal folds and the crystallization of several generations of actinolite. Competent layers in the relatively incompetent host rock influenced the style and orientation of folds formed in adjacent, less competent rocks.

Small-scale tensional features, not recorded before in the predominantly collisional tectonics-oriented studies, host the majority of quartz, quartzofeldspathic and epidote-albite veining in the Natal Nappe Zone. No major veining or mineralization is hosted by the south- to southwest-dipping ductile thrust planes (Bullen *et al.* in press) simply because σ_1 due to overloading by thrust units in a ductile regime tends to close thrust planes and potential local release features. Post-peak metamorphic equilibration of thrust units has not been considered although these largely retrograde effects, when combined with a late-collisional structural interpretation, have implications for economic and non-economic mineralization and veining.

The Madidima Nappe was re-examined to determine a late-tectonometamorphic history and to elucidate late-tectonic structural features in the nappe zone north of the Lilani-Matigulu Shear Zone, in addition to deformational events which are not recognized in present models. One of these structural features hosts the Rebellion Reef and is a direct result of a local competency contrast and oblique collision being transmitted north of the Lilani-Matigulu Shear Zone.

c) Structural Features - Planar Foliation, Shearing and Veining

There are four major veining and/or shearing events in the Madidima Nappe and adjacent nappes, two of which have not been formerly recorded in the literature;

i) Transgressive Apophyses, consisting mainly of quartz and quartzofeldspathic veins with aplitic textures, occur as offshoots from the Zidoni amphibolitic gneiss which intruded into the Silambo amphibolite. These pre-thrusting veins have been flattened into the plane of S_{01} (Smalley, 1980) and their orientations are non-systematic, that is measurements of their margins would give approximations of the enclosing planar foliation. This type of vein is rare and occurs only in the southern part of the field area, near and inferred Zidoni amphibolitic gneiss intrusive contact. Metamorphic segregation within the veins often forms a massive hornblendic "fraction" reminiscent of the early veining in the Ngubevu area (see Chapter 6).

ii) Antithetic Quartz Veins, which are up to one meter wide and cross-cuts the thrust-produced planar foliation in many places. The antithetic veins are usually within 20° of being perpendicular to S_{01} and were produced in tensional shears parallel to σ_1 (the maximum principle stress direction) due to superimposed nappe emplacement (Figure 2.3). Antithetic veining formed in tension gashes in the intervals where pressure-temperature conditions entered the brittle-ductile field. The antithetic veins therefore sampled syn-thrusting fluids produced by pressure solution along an embryonic planar foliation (e.g. Etheridge *et al.*, 1983, 1984) and were segmented by continued overthrusting. Antithetic veins in the Natal Nappe Zone are analogous in orientation to landward-dipping seismic reflectors recognized by Cloos (1984) in accretionary wedges.

Landward-dipping reflectors are dewatering conduits which pass fluid upwards from previously accreted lithologies. Although seemingly a dominant vein generation in other nappes, no major antithetic quartz veining was observed in the Mbongolwane flats area and this vein type cannot be considered responsible for hosting mineralization in the Madidima Nappe.

Figure 2.3 Antithetic quartzofeldspathic veins in the Nkomo banded amphibolite and the biotite-plagioclase quartzite of the Nkomo Nappe (Locality : road approaching the Nkadla Forest from the south)

iii) East- to East-Northeast-Trending Complex Shear Zones which potentially extend for up to 10 km (Figure 2.1). These shear zones contain quartzofeldspathic material and are prevalent on a major competency contrast, that is, at a boundary between lithologies of markedly different rheologies. The east-northeast-trending shears appear to be reactivated "steep structures" and may be termed complex shear zones. The type example of these reactivated steep structures hosts the abandoned gold working on the Lauwrie Farm and occurs at a Thaweni granite-gneiss/Silambo banded amphibolite contact (locality : Lauwrie - Figure 2.1). The complex shear zones record an initial ductile reverse movement, with the downthrown side to the south, and take the form of the vertical shears or steep structures described in Apotria *et al.* (1993) (Figure 2.4 a). These shears are interpreted as being a consequence of a hangingwall passing through the lower hinge of a frontal ramp, from pre-ramp flat to ramp, during thrusting along the basal decollement in thin-skinned thrust tectonics (e.g. Chapple, 1978; Coward, 1983; Apotria *et al.*, 1993) such that the vertically-measured thickness of the hangingwall remains approximately constant. Incremental downfaulting to the south is the local expression of this strain distribution and this study infers that a small-scale version of this process occurred at the Thaweni granite-gneiss/Silambo banded amphibolite contact (Figure 2.4 b) allowing quartzofeldspathic wedges to infill spaces in a ductile regime (Figure 2.4 c).

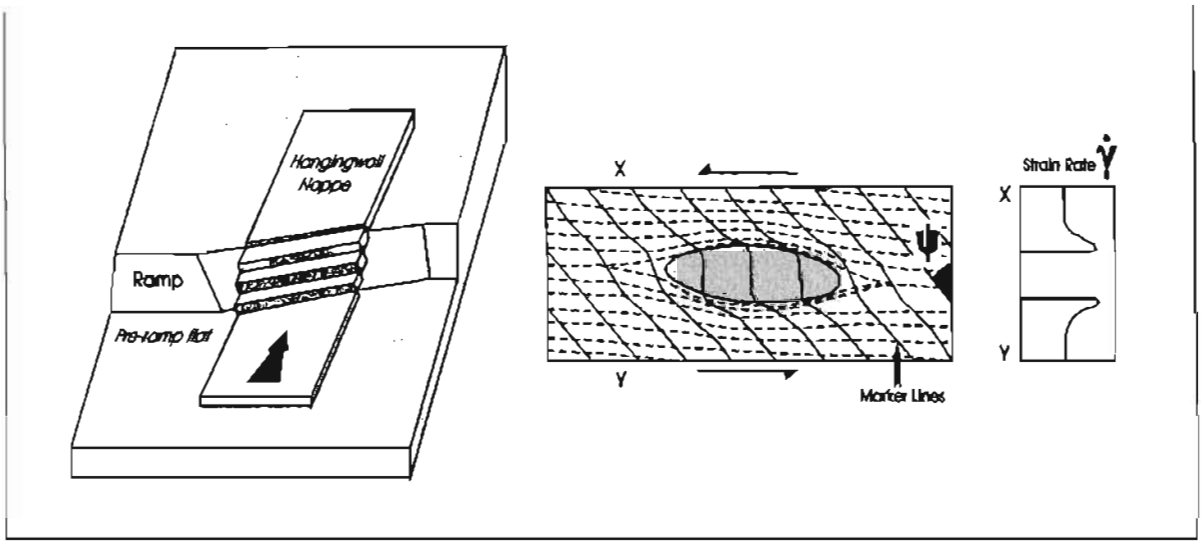

Figure 2.4 a The formation of steep structures during thin-skinned thrust tectonics. Movement of hangingwall material from pre-ramp flat to ramp results in normal faulting with the downthrown side to the hinterland (Apotria *et al.*, 1993). These steep structures result from the fact that stresses in the hangingwall material provide for a constant hangingwall thickness. (Inset - the effect of a competent lens in an incompetent layer undergoing simple shear (Sibson, 1980); Strain and strain rate increase at the contact with the competent lens)

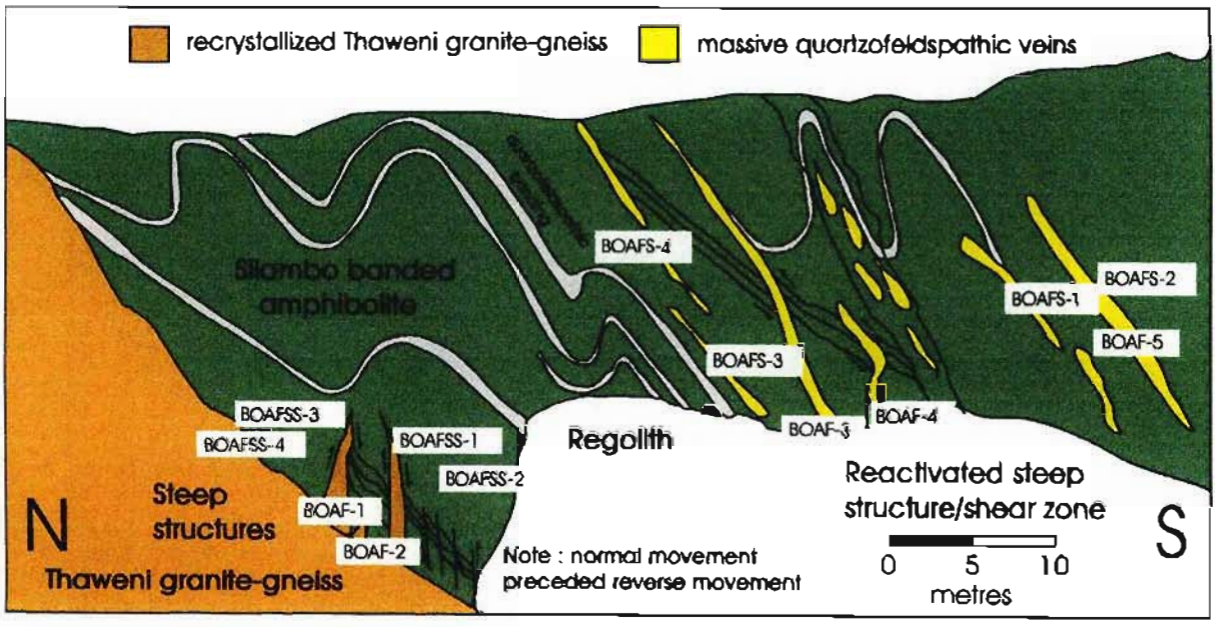

Figure 2.4 b A small-scale analogue of steep structures formed in thin-skinned thrust tectonics. Steep structures at the Thaweni granite-gneiss/Silambo banded amphibolite contact display characteristics of hangingwall movement across an irregular ramp morphology. The Thaweni granite-gneiss may be considered as the footwall/ramp while the Silambo banded amphibolite may be considered as the hangingwall to the minor thrust for Au values of sampling localities (See Appendix B1, Locality : Lauwrie outcrop)

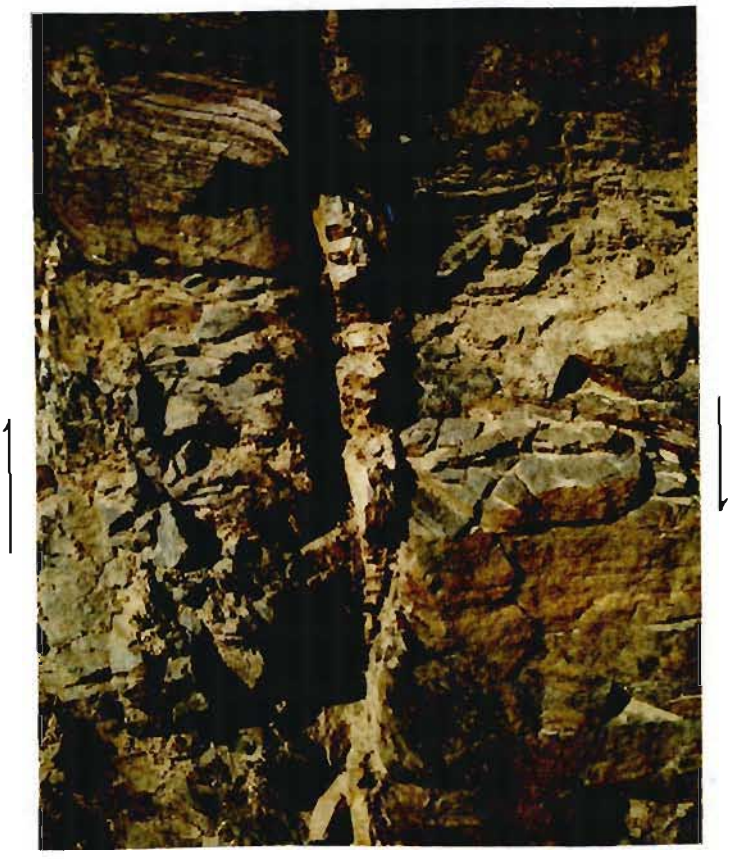

Figure 2.4 c An example of a single steep structure which contains quartzofeldspathic material. Recrystallized Thaweni granite-gneiss may also infill these reverse ductile faults (Locality : Lauwrie outcrop)

In this respect the steep structures follow the location of stress risers (Sibson, 1980). Ramsay and Graham (1970), Ramsay (1980 a) and Sibson (1980), conclude that in uniform simple shear, strain (γ) and strain rate ($\dot{\gamma}$) will be constant across a ductile shear zone except where a more competent lens of rock exists within the shear zone. To preserve strain continuity, strain and strain rate must increase at the competent lens/host shear contact (Figure 2.4 a - inset). Another means of viewing the relationship between the Thaweni granite-gneiss and the hangingwall banded amphibolite is in the form of a spatial synclinorium through which the hangingwall material moves towards the northern foreland. This pleads a special case of discrete sub-units in the thrust sheet, each moving at different rates, and also suggests a means whereby individual thrust / sub-thrust sheets may be initiated at a steep structure. A small component of oblique motion, causing the steep shears to be non-parallel to the southern margin of this Thaweni granite-gneiss layer is due to oblique nappe emplacement and is effectively the conjugate scenario of the oblique ramp of Apotria *et al.* (1993). A summary of orientation data for steep structures/reactivated steep structures, pegmatites and planar foliation in the Thaweni granite-gneiss is given in Figure 2.5 a-d.

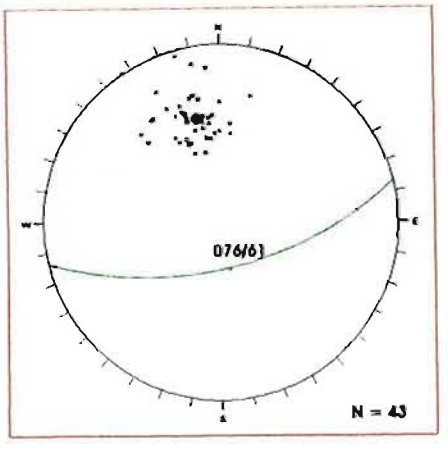

Figure 2.5 a Equal angle plot of poles to quartzofeldspathic veins/re-crystallized Thaweni granite-gneiss in steep structures and reactivated steep structures at Lauwrie outcrop. The general trend of these structures is east-northeast N = 43

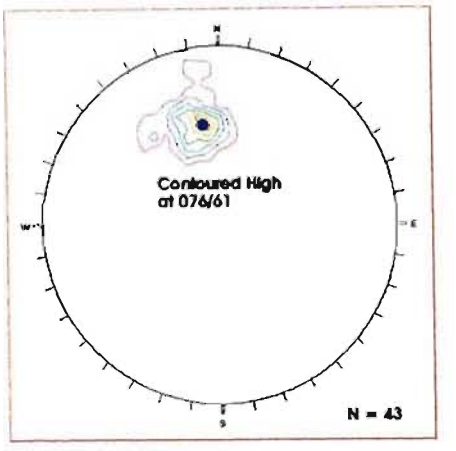

Figure 2.5 b Equal area contour plot of data in a) - contours show % of total area, per 1% area. Contoured high/maximum concentration is at 076/61° N = 43

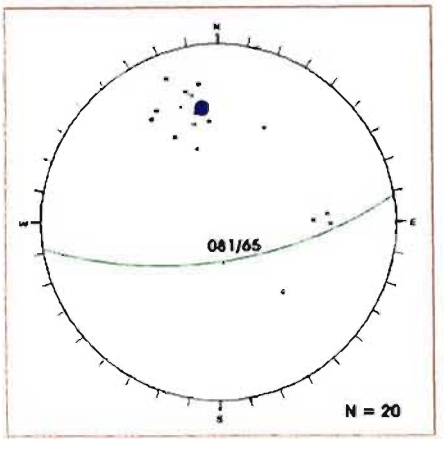

Figure 2.5 c Equal angle plot of poles to highly-deformed pegmatites in the Thaweni granite-gneiss at Lauwrie outcrop. Approximate mean of the data is at 081/65° N = 20

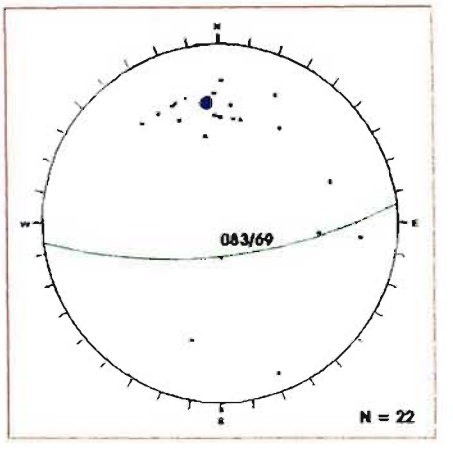

Figure 2.5 d Equal angle plot of poles to planar foliation (S_2) in the Thaweni granite-gneiss at Lauwrie outcrop. Approximate mean of the data is at 083/69° N = 22

The effect of an east-northeast-trending southern limb of a regional F_2 fold in the Thaweni granite-gneiss may be inferred from the change in the dominant fold axes of folded S_{01} as one approaches the southern limb of this regional fold. The Mbongolwane Flats area may therefore be divided into three domains, based on the orientations of the deformed S_{01} planar foliation (Figure 2.1; Figure 2.6 a-f).

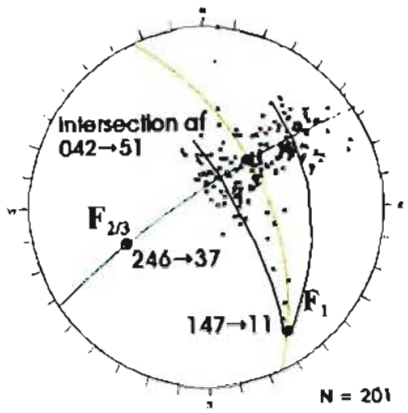

Figure 2.6 a Equal angle plot of poles to S_{01} in infolded Zidoni amphibolitic gneiss and Silambo banded amphibolite in structural ***Domain 1*** of the Mbongolwane Flats area. Poles to two distributions, based on contouring of data, may be fitted: F_1 - 147→11° and $F_{2/3}$ - 246→37° N = 201

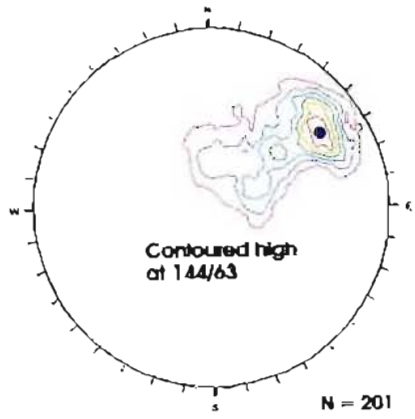

Figure 2.6 b Equal area plot of poles to S_{01} in infolded Zidoni amphibolitic gneiss and Silambo banded amphibolite in ***Domain 1*** of the Mbongolwane Flats area. 0...13% of total area, maximum concentration is at 16%. Contoured high at 144/63°. Note the "bow-tie" distribution of data, indicating two phases of folding N = 201

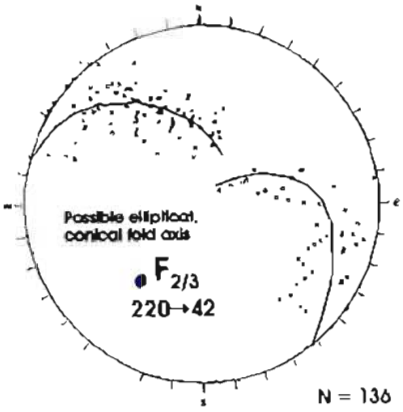

Figure 2.6 c Equal angle plot of poles to S_{01} in Zidoni amphibolitic gneiss in structural ***Domain 2*** of the Mbongolwane Flats area. The distribution of the poles matches that of a linear feature deformed around a non-cylindrical or conical fold with an axis at 220→42° which is parallel to the contoured maximum (222→39°) of the stretching lineations in Domain 2. These azimuths are parallel to $F_{2/3}$ folds N = 136

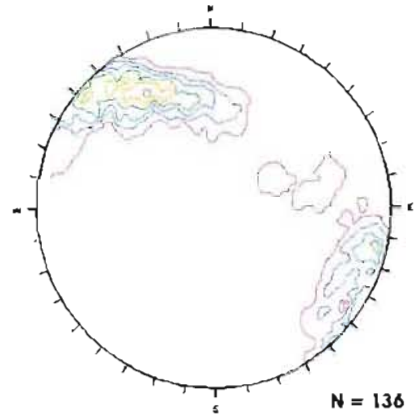

Figure 2.6 d Equal area plot of poles to S_{01} in Zidoni amphibolitic gneiss in structural ***Domain 2*** of the Mbongolwane Flats area. 0...10% of total area, maximum concentration is at 11% N = 136

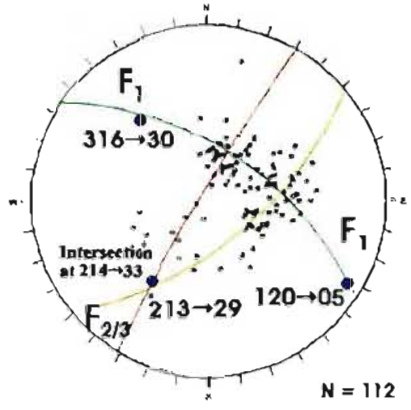

Figure 2.6 e Equal angle plot of poles to S_{01} in Zidoni amphibolitic gneiss and Silambo banded amphibolite in structural ***Domain 3*** of the Mbongolwane Flats area. Possible poles to great circle approximations to data give: F_1 at 120→05° and 316→30°; $F_{2/3}$ at 214→33° and 213→29° (intersection of F_1 great circle fits). It is not, however, strictly correct to apply more than one great circle to data as subsequent folding will not allow earlier great circle distributions to persist N = 112

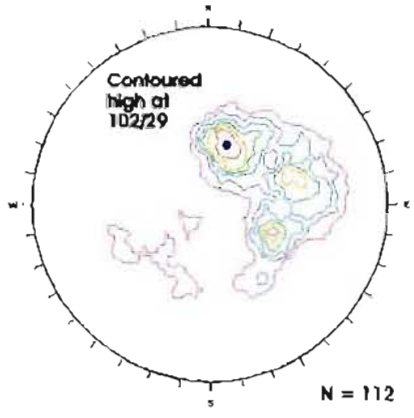

Figure 2.6 f Equal area plot of poles to S_{01} in Zidoni amphibolitic gneiss and Silambo banded amphibolite in structural ***Domain 3*** of the Mbongolwane Flats area. 0...10% of total area, maximum concentration is at 11%. Contoured high is at 102/29° N = 112

iv) Structural Domains in the Mbongolwane Flats Area

Domain 1 - South and Southeast of Regional F_2 Fold in Thaweni Granite-gneiss

There is a progressive change in the orientation of the dominant fold generation from the Mand-a to Quarry to Lauwrie outcrops such that the influence of a large, relatively competent band of Thaweni granite-gneiss in the volumetrically dominant Zidoni amphibolitic gneiss and Silambo banded amphibolite is apparent (Figure 2.7). At the Mand-a outcrop to the north of the sandstone-capped Isiwasamanqe Hill, the dominant fold axes, defined by a great circle approximation to variably-oriented S_{01}, is 321→ 04° which agrees with the F_1/F_2 orientation of Schulze-Hulbe (1977) and Smalley (1980). The latter folds are northward- to northeastward-verging isoclinal and closed folds. However a minor fold axis of 230→66°, matching the regional orientation of $F_{2/3}$, may be present. The intersection of the F_1/F_2 and the $F_{2/3}$ great circles is 053→24° (Figure 2.7). At the Quarry outcrop, two fold axes may be defined by great circle approximations, the dominant fold axes now being 231→21° (F_3) which a subsidiary fold axis at 139→17° (F_1/F_2). The intersection between the two great circles to these fold axes is 011→64°.

At the Lauwrie outcrop, directly adjacent to the competent granite-gneiss, the F_1/F_2 fold generation is least evident. The Silambo banded amphibolite is strongly deformed into closed folds at the amphibolite/granite-gneiss contact (Figure 2.4 b) where the pole to a best-fit great circle to poles to planar foliation in the hangingwall amphibolite approximates the $F_{2/3}$ axes orientation in the literature at 051→33° (Schulze-Hulbe, 1977). The orientations of the planar foliations in Domain 1 are summarized in Figure 2.6 a and b.

Between ***Domain 1*** and ***Domain 2 - Thaweni Granite-gneiss***

The trend of the planar foliation of the Thaweni granite-gneiss (S_2) is sub-parallel to the regional $F_{2/3}$ fold axis plunge direction of the granite gneiss layer in the central to northern part of the Mbongolwane Flats (Figure 2.7). The fold axes are 261→05° and 228→46° The intersections of the poles to great circles (including those surmised from the Thaweni granite-gneiss) and the $F_{2/3}$ axis of 251→33° at the respective outcrops, fall on a

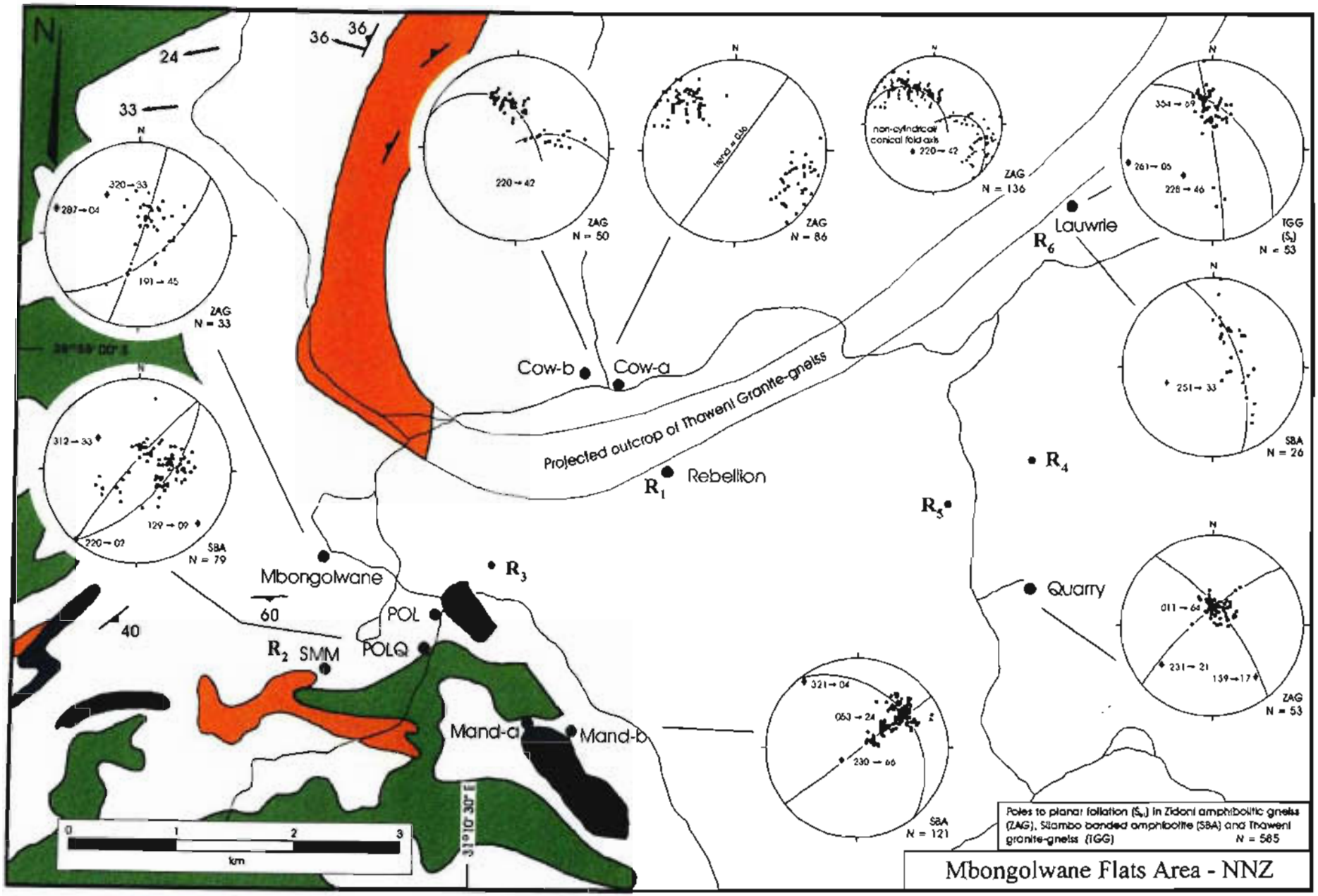

Figure 2.7 The distribution of planar foliation (S_{0i}) in the components of the Madidima Nappe in the Mbongolwane Flats. Note the change in data distribution (and the interpretation thereof) in Domain 1 (Figure 2.1) from south to north.

great circle of 241/67° which is similar to the trend of the margin of the influencing structure; the $F_{2/3}$ fold in Thaweni granite-gneiss.

Domain 2 - Interior/Core of Regional F_2 Fold in Thaweni Granite-gneiss

Domain 2 constitutes the interior of the regional F_2 anticline in the Thaweni granite-gneiss and consists predominantly of Zidoni amphibolitic gneiss with Silambo banded amphibolite xenoliths. At the Cow-a and Cow-b outcrops there are a myriad of approximately 036° to 045°-trending shear zones which display both left and right-lateral offsets, deduced from limited S-C cleavage observations. The proximal parallel planar foliation to these shear zones changes in orientation with increasing distance from the shear, and at a distance greater than 10 cm from the discrete shears the planar foliation segments display distributions on stereonets which do not fit great or small circles. A combination of the orientations of the planar foliations sub-parallel to the shears and the aberrant orientations (Figures 2.7 c and d; Figure 2.7) results in a complex spatial locus of data (Ramsay, 1967), exactly similar to that shown by deformation of lineations during the formation of a circular conical fold (Figure 2.8; Ramsay, 1967). In other words, the distribution of poles to planar foliations at the Cow-a and b outcrops traces the locus of a deformed linear feature on the surface of a non-cylindrical or conical fold. It cannot be ascertained whether syn- or post-folding flattening to form an elliptical conical fold has occurred in non-cylindrical folding.

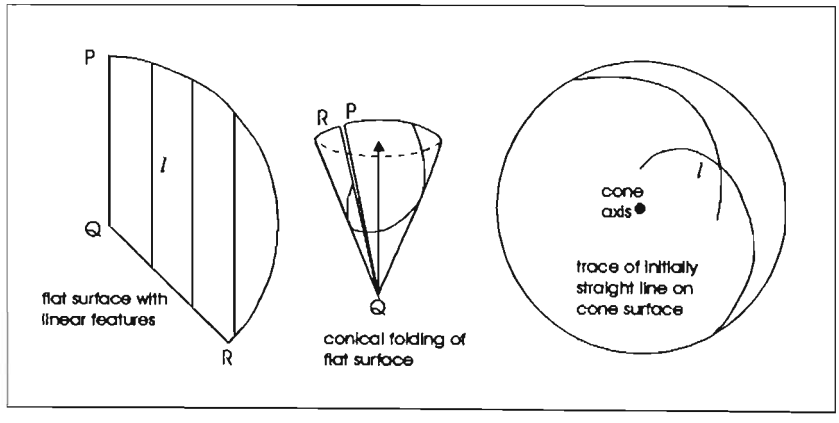

Figure 2.8. Deformation of lineations by formation of a circular conical fold. A) shows the surface on which the initial rectilinear structure was developed and B) shows the deformation of this surface into a cone. C) illustrates the plot of the positions of the deformed lineations in B) (modified after Figure 8-7 of Ramsay , 1967)

Ramsay (1967, Figure 8.7) utilizes a vertical cone axis for the sake of convenience but in this study the conical fold axis is likely to be steeply inclined. An approximate cone axis estimated for the folded planar foliation at the Cow-a and b outcrops is 220→42° which is parallel to the contoured maximum of the plunge and direction of plunge of stretched feldspar and actinolite crystals at the Cow outcrops (Figure 2.9). It may be concluded that folding in ***Domain 2***, at least near the hinge zone of the regional F_2 fold, was non-cylindrical or conical with the long axes of aligned porphyroblasts in Zidoni amphibolite gneiss being parallel to the fold axis.

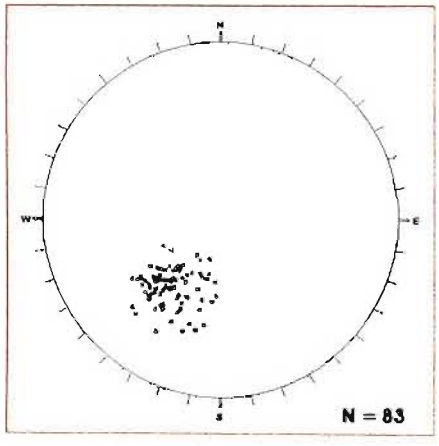

Figure 2.9 a Plunge and direction of plunge of long axes of feldspar and amphibolite porpyroblasts in Zidoni amphibolitic gneiss at Cow-a and b outcrops (***Domain 2***) N = 83

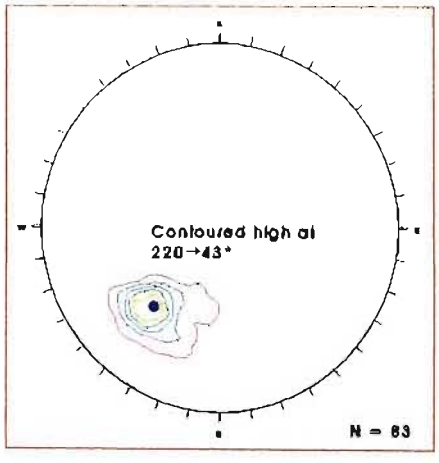

Figure 2.9 b Equal area contour plot of stretching lineations as described in a). 0..28% of total area. Contoured high is at 220→43° (25,3% of total area) N = 83

There are three likely causes of this non-cylindrical or conical folding:

- fold core constriction as the southern limb is pushed towards the northern limb of the regional anticline in Thaweni granite-gneiss within the bulk of the Zidoni amphibolitic gneiss and the Silambo banded amphibolite
- a zone of contact strain and disharmonic folding on the inside (lower) curve of the regional anticline
- shearing and flattening (ie, simple and pure shear) along an axial planar cleavage of the regional fold

Domain 3 - Southwest to West of the Hinge Zone of the Regional F_2 Fold in Thaweni granite-gneiss

Folding is controlled by obliquely-oriented flattening along the margins of the Thaweni granite-gneiss, in a northeasterly-moving thrust sheet. Fold axes are of the F_1/F_2 generation and define northeasterly-verging closed and isoclinal folds. Fold axes are 320→33° and 287→04°, 312→33° and 129→09° (F_1/F_2). The intersection of the first pair is at 191→45° and the intersection of the second pair is 220→02°. The fold axes 191→45° and 220→02°, constitute the F_2/F_3 fold generation for this domain (Figures 2.7 e and f).

♦ *Sinistral Mixed Dilation/Sheared Veins (North-Northeast- to Northeast-trending (shears initiated at a foreland margin or underlying nappe irregularity)*. These minor shear zones are distributed over the deepest part of the Madidima Nappe, predominantly in the Zidoni amphibolitic gneiss where raised temperatures appear to have been maintained in late- to post-thrusting times in a ductile-brittle shearing environment. These minor shear zones contain up to four cross-cutting generations of annealed mylonite and ultramylonite, the formation of which alternated with vein dilation and infilling. Early shear zones contain aligned actinolite almost at right angles to the planar foliation in the host amphibolitic gneiss, indicating commencement of shearing in the epidote-actinolite facies. Albite and epidote usually prevail as the main shear infilling, defining a hydrothermally-introduced "metamorphic" facies (Figure 2.10). Epidote-albite veining is evidence of late dextral shearing in a waning geothermal regime (e.g. Stel, 1986). Epidotization is also evident in the quartzofeldspathic matrix of the host amphibolitic gneiss where the sheared and annealed albite and epidotized plagioclase feldspars are almost totally replaced; only strained quartz polygons remain. Epidotization was post-epidote-actinolite facies in timing as the margins of poikiloblastic actinolite laths are epidotized (Figure 2.11 ***Sample ZAGQ - 20/1a***). Summaries of epidote-albite veining orientation and shear orientations for the three domains are presented in Figures 2.13 and 2.14, respectively, while the distributions of the orientations of veins and shears across the Mbongolwane Flats area are displayed in Figures 2.15 and 2.16, respectively. The great circles to contoured maxima on the equal area stereonets serve only as indications of the general trends of shears and veins in a particular domain.

Figure 2.10 An example of epidote-albite veining in a northeast-trending fracture in Zidoni amphibolitic gneiss (Locality : Quarry outcrop).

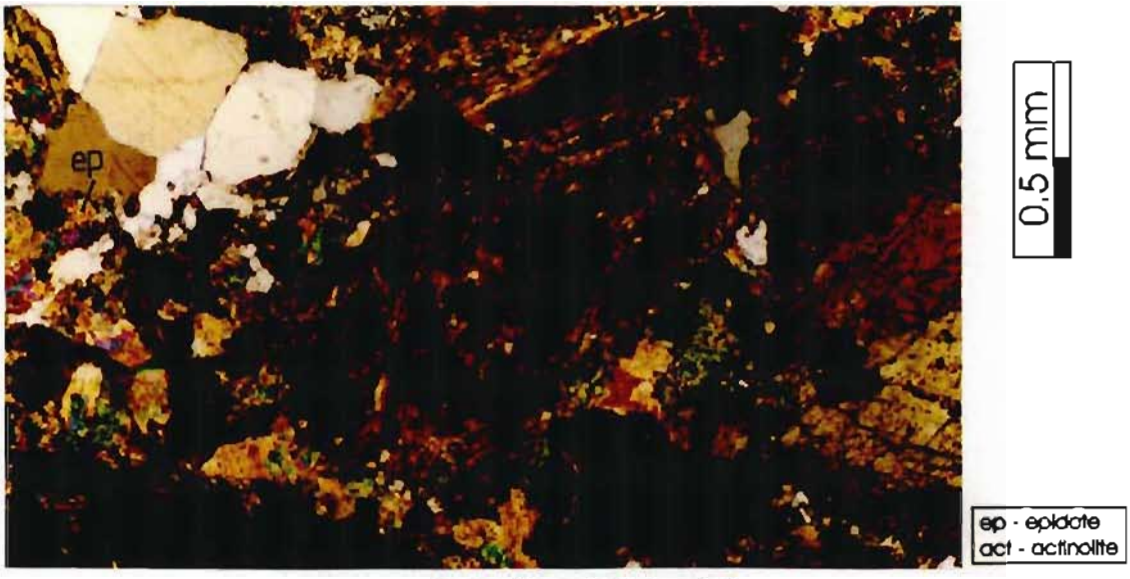

Figure 2.11 Photomicrograph of epidotization of the margins of a poikiloblastic actinolite lath in the Zidoni amphibolitic gneiss (Locality : Quarry outcrop, ***Sample ZAGQ - 20/1a***)

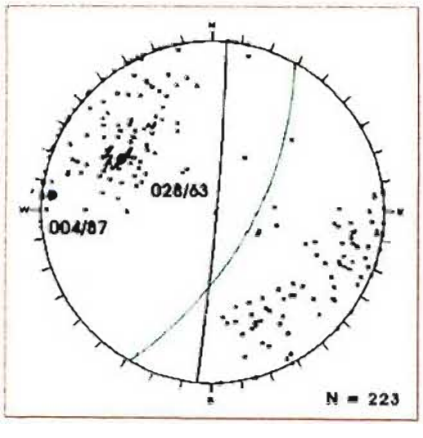

Figure 2.12 a Equal angle plot of poles to sheared epidote-albite veins, and largely unsheared antitaxial quartz veins in ***Domains 1 and 3***. Note the general north-northeast trend N = 223

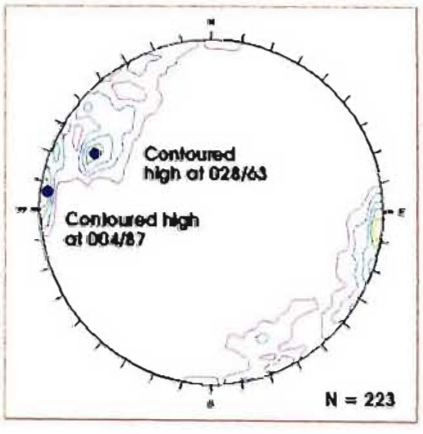

Figure 2.12 b Equal area contour plot of data in **a**). 0...18% of total area. Contoured highs (18% and 16%) are 004/87° and 028/63°, respectively N = 223

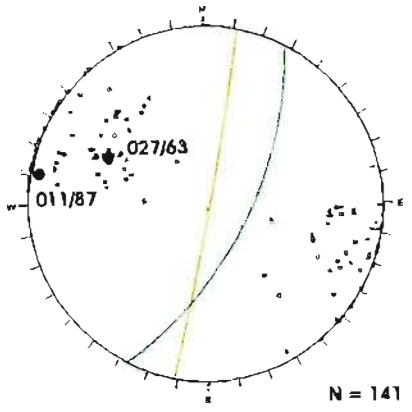

Figure 2.13 a Equal angle plot of poles to brittle-ductile shear zones in Zidoni amphibolitic gneiss in structural ***Domain 1***. Planes to contoured highs are 011/87° and 027/63° N = 141

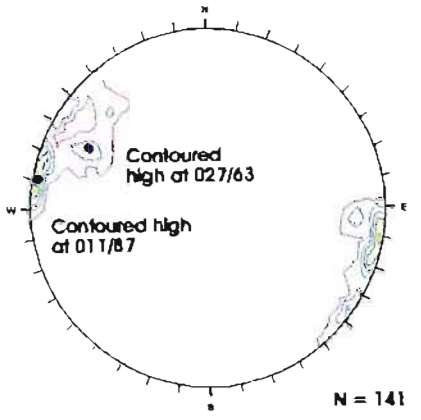

Figure 2.13 b Equal area contour plot of poles to shear zones as described in **a**). 0...17.5% of total area. Contoured high is at 16.3% of total area (011/87°). The other high is at 027/63° N = 141

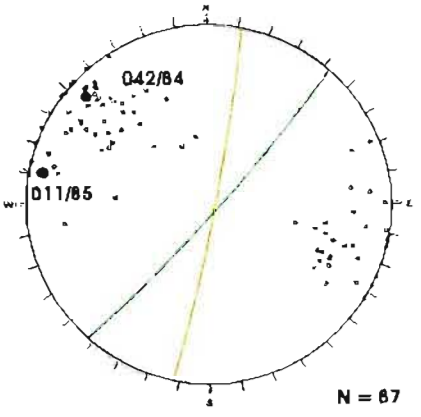

Figure 2.13 c Equal angle plot of poles to brittle, brittle-ductile and ductile epidote-albite-filled shears in ***Domain 2***. Planes to contoured highs are 011/85° and 042/84° N = 87

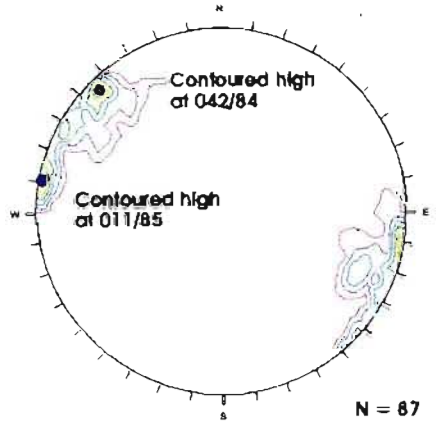

Figure 2.13 d Equal area plot of poles to shear zones as described in **a**). 0...17 % of total area. Contoured high is at 18 % (011/85°). The other high is at 042/84° N = 87

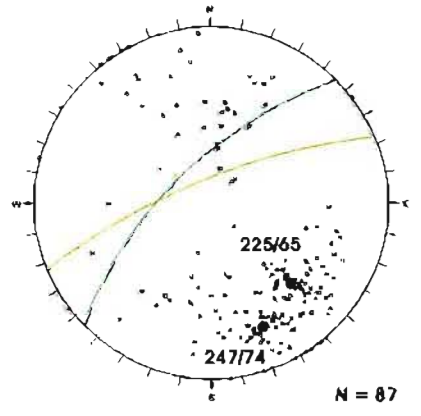

Figure 2.13 e Equal angle plot of poles to brittle-ductile shear zones in Zidoni amphibolitic gneiss in ***Domain 3***. Planes to contoured highs are 225/65° and 247/74° N = 177

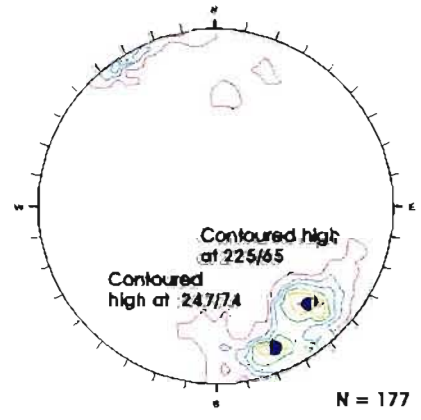

Figure 2.13 f Equal area plot of poles to shear zones as described in **a**). 0...10.5% of total area. Contoured highs are at 9.1% (225/65° and 247/74°) N = 177

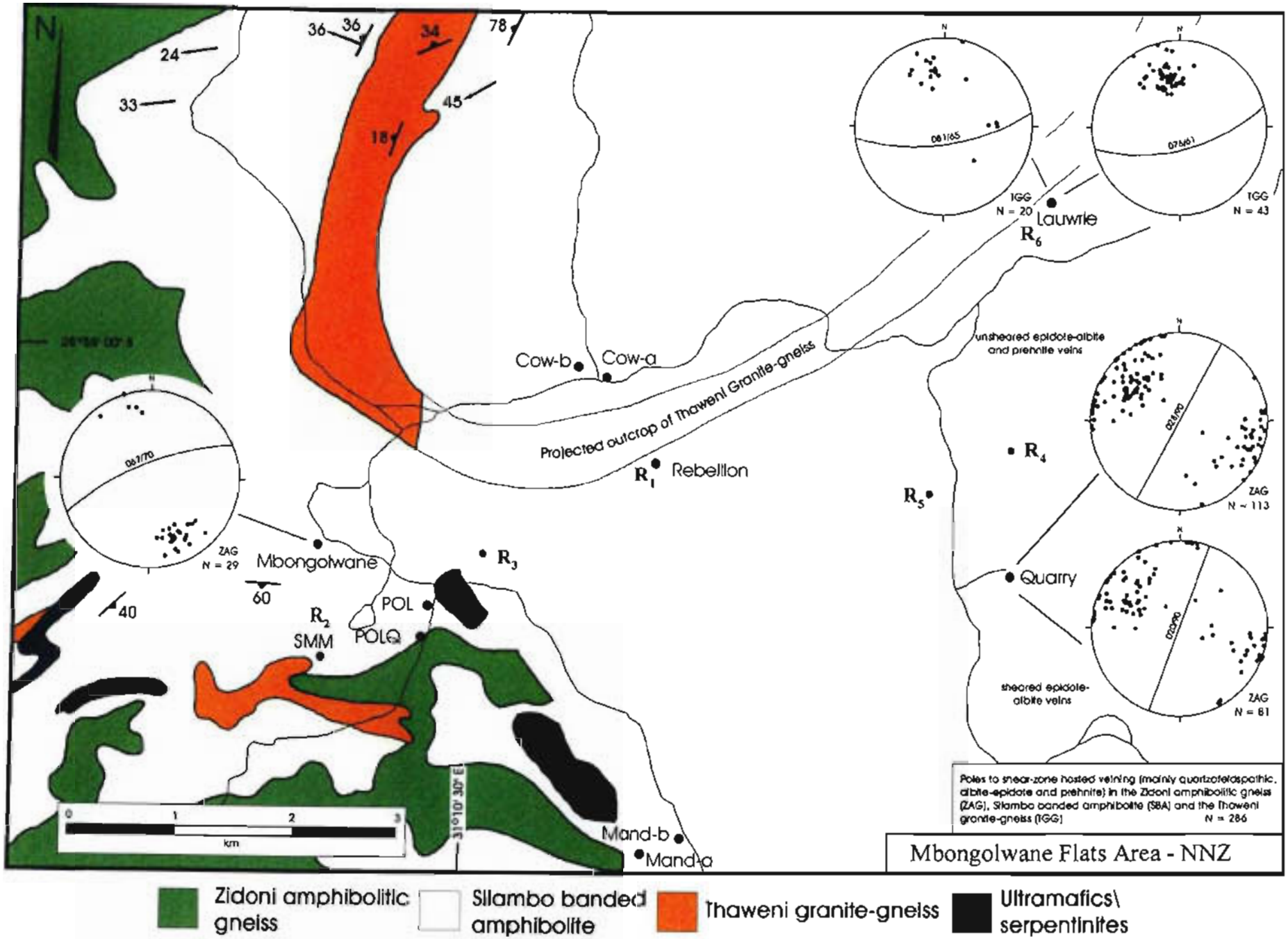

Figure 2.14 Vein orientation in the Mbongolwane Flats. Veins consist mainly of epidote+albite and prehnite. Compare Figure 2.15 with Figure 2.16 (shear orientations). Veins and shears effectively define the edges of rotated tectonic blocks which are described in a later section

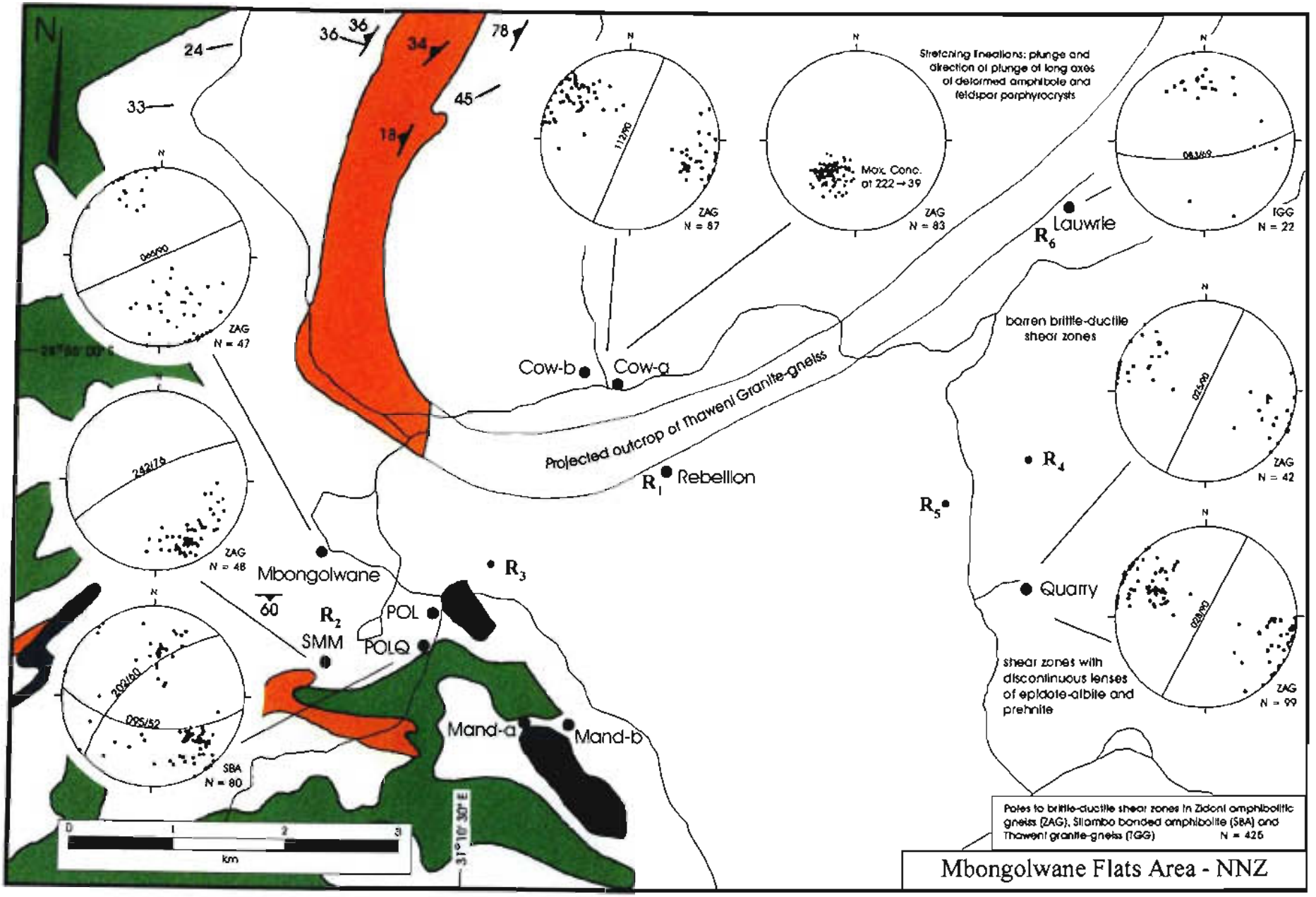

Figure 2.15 Brittle-ductile shear zone orientations across the Mbongolwane Flats. Note the southern limb of Thaweni granite-gneiss effects a change in the orientation of the dominant shear generation. Great circles on stereonets serve as an indication of the general trends of the shear zones

The trend of retrograde metamorphism accompanying vein formation is further indicated by late, selective emplacement of prehnite (Figure 2.16). Prehnite forms radiating tabular and acicular fans at Zidoni amphibolitic gneiss/albite-epidote vein contacts and along albite-albite grain contacts in veins. Prehnitization post-dates albite-epidote veining. Further evidence of mineral emplacement during waning temperatures are shears hosting opportunistic brittle-ductile dilational features with antitaxial crystal growth. The final alteration event consists of sericitization accompanied by sphene formation (Figure 2.17) which overprints the prehnite. The later shears anastomose around the quartzofeldspathic lenses hosted in ductile shear zones. In the regional scheme of shearing (e.g. Wilcox *et al.*, 1973; Mandl, 1988), these 030°-045° shear zones define the R_1/σ_1 orientation, that is R_1 (synthetic sinistral shear to the main sinistral shear) alternated with σ_1 (dilation parallel to maximum principal compressive stress). This implies small changes in the orientations of these shears in a consistently-oriented far-field force caused by a possible southwest-directed movement of the Kaapvaal Craton. These shears may have been initiated at a change in strike and/or dip of the foreland margin or the Nkomo Nappe, that is at a craton margin, intra-nappe or underlying nappe irregularity (Figure 2.18). Variations in shear orientation and alternating shearing/dilation were caused by jostling and rotation of intra-nappe blocks during late-tectonism which further segmented the nappe into blocks due to craton margin/Nkomo Nappe irregularity or the strain variation caused by an escape structure to the east.

Figure 2.16 Selective emplacement of prehnite in epidote-albite veining in Zidoni amphibolitic gneiss (***Slide ZAGQ-20/1b*** - Quarry outcrop). XP light.

Figure 2.17 Sericitization and sphene formation in Zidoni amphibolitic gneiss: the last stage of retrogression (***Slide ZAGQ-2/4*** - Quarry outcrop). PPL.

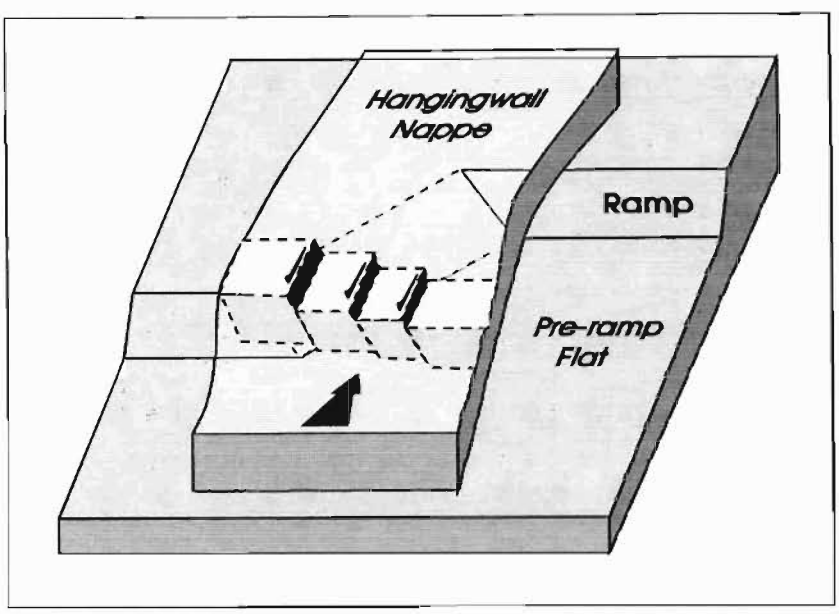

Figure 2.18 The initiation of shears at a foreland margin irregularity in the case of thin-skinned thrust tectonics (Apotria *et al.*, 1993)

The presence of the north-northeast to northeast-trending shears may be recognized by their effect upon the wallrock to shears. Using the Zidoni amphibolitic gneiss as an example, a progression, from foliated amphibolitic gneiss, to an annealed cataclastic (Figures 2.20 a and b ***Slide ZAGQ - 2/3a and 3b***) to a highly altered recrystallized ultracataclastic (Figure 2.19 c ***Slide ZAGQ - 25/1***), may be observed in thin section. The pertinent comments are set out below.

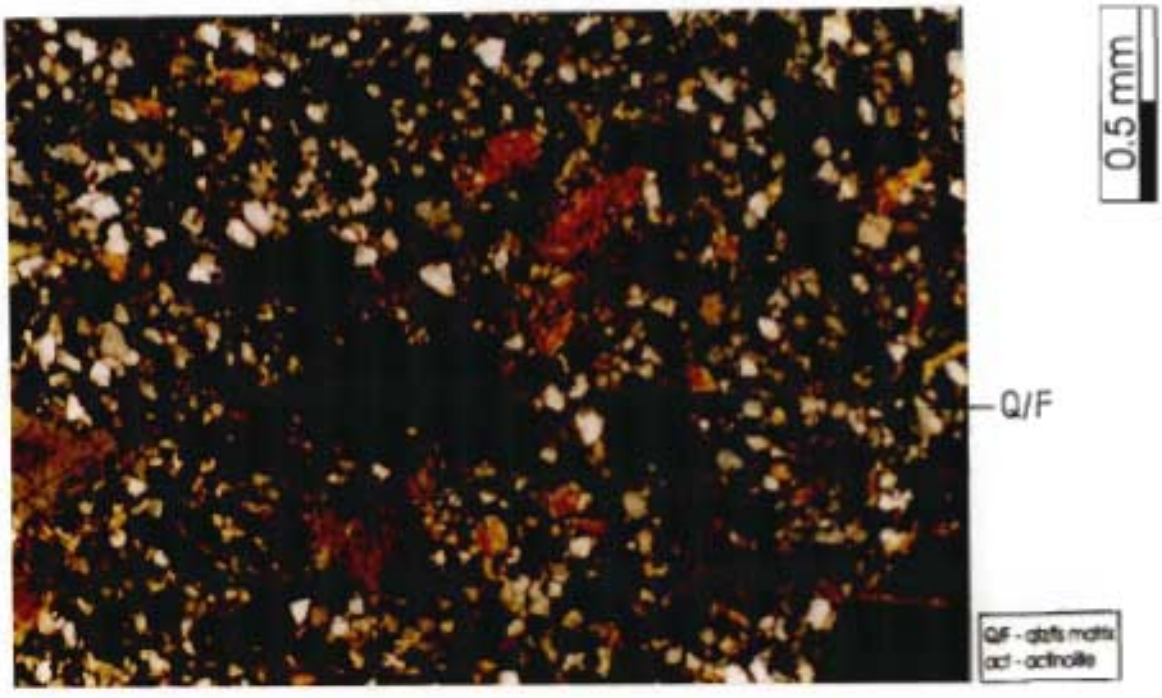

Figure 2.19 a Indications of brittle deformation followed by annealing of the Zidoni amphibolitic gneiss. Mosaic-textured quartz and feldspar with highly fragmented actinolite clast (***Slide ZAGQ-2/3 a*** - Quarry outcrop). XP.

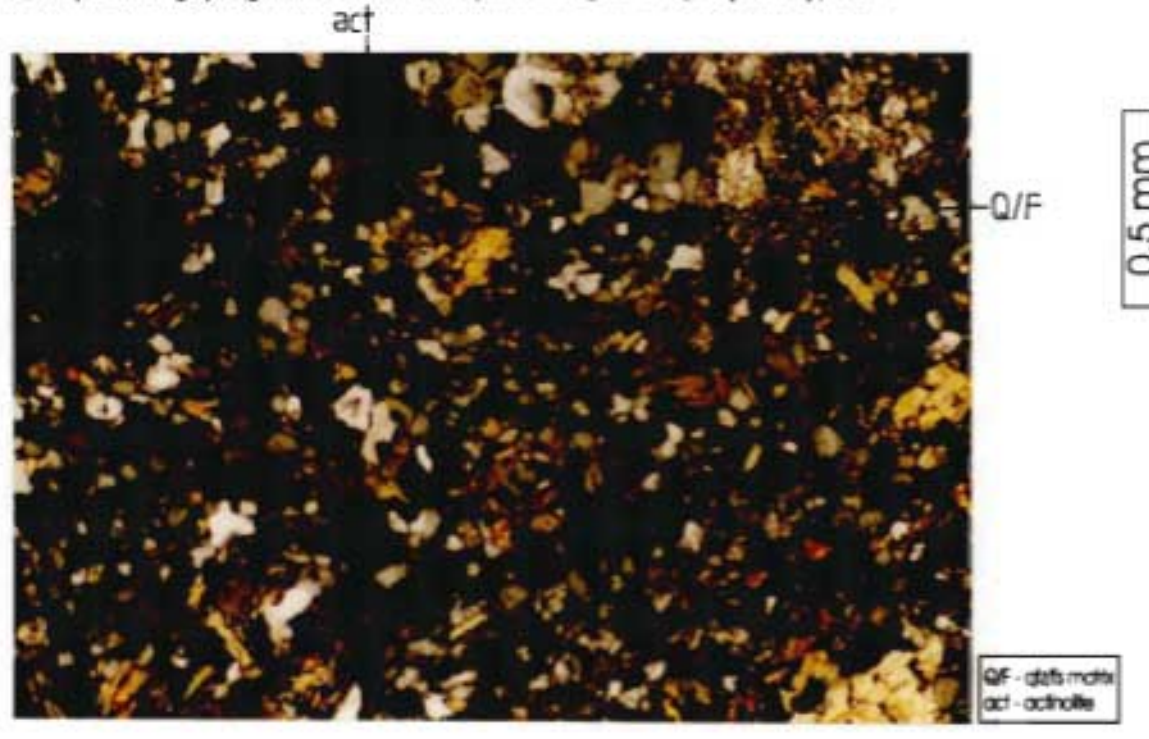

Figure 2.19 b As for Figure 2.19 a, cataclasis has been more pervasive in the amphibolitic gneiss; actinolite is more fragmented and evenly distributed within the matrix (***Slide ZAGQ-2/3 b*** - Quarry outcrop). XP

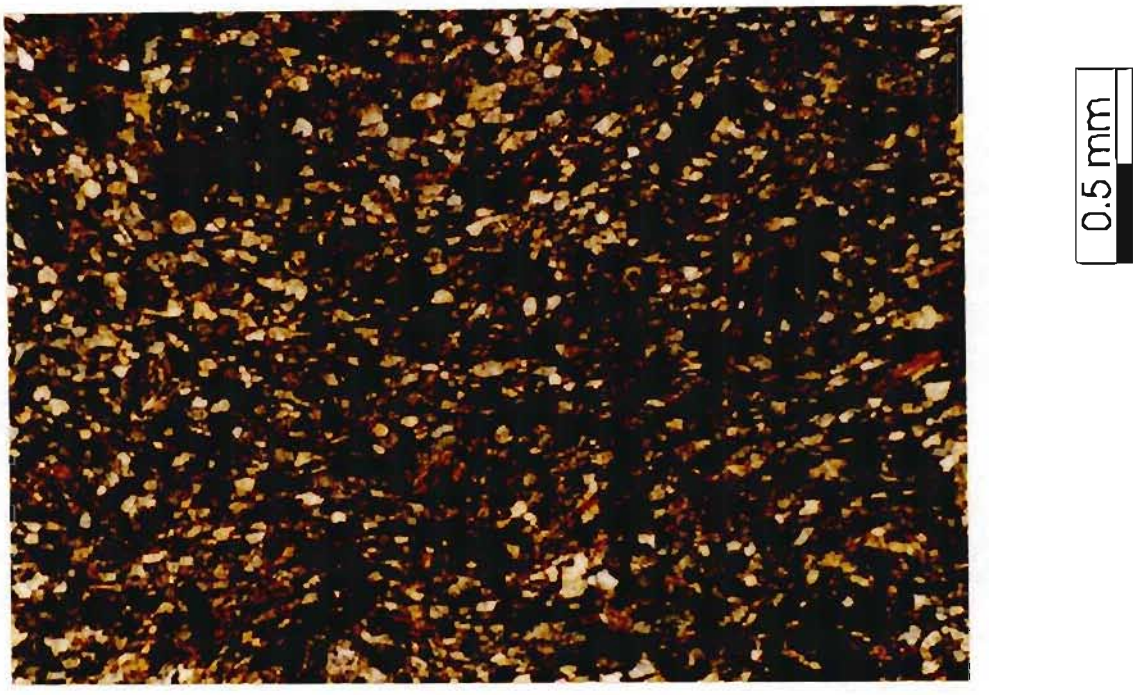

Figure 2.19 c A highly altered, recrystallized ultra-cataclastic of Zidoni amphibolitic gneiss. Note the flattened mosaic-textured quartz and feldspar and the absence of large actinolite porphyroblasts/crysts (***Slide ZAGQ-25/1*** - Quarry outcrop). XP.

- The cataclasite has randomly-oriented porphyroblastic and poikiloblastic actinolite in a matrix of annealed quartz, albite and alkali feldspar (Figure 2.19 a ***Slide ZAGQ - 2/3a***). Opaque minerals, such as sphene, and ilmenite with alteration rims of sphene, are disseminated throughout the mosaic-textured groundmass. Highly strained porphyroclasts and porphyroblasts have cataclastically-deformed margins.

- ***Slide ZAGQ - 2/3b*** (Figure 2.19 b) reveals an increase in strain upon approaching a shear zone. The decussate mosaic of quartz, albite, alkali feldspar and chlorite exhibits flattening and aligning of most minerals. The dominant foliation wraps around epidotized plagioclase feldspar and orthoclase feldspar porphyroclasts.

- ***Slide ZAGQ - 25/1*** (Figure 2.19 c) shows post-shearing recrystallization of actinolite and biotite which are commonly poikiloblastic.

Replacement/retrogression sites prevail in areas of strong deformation; if a shear is active during retrogression of the host rock, the material in the shear zone will attain a new fabric and compositional equilibrium due to enhanced diffusion in crystal lattices (Passchier *et al.*, 1990). Whole rock compositions should be preserved. However, shear zones are instrumental in channeling late-tectonic (low-grade metamorphic) fluids (Liou *et al.*, 1985; Passchier *et al.*, 1990). Furthermore, OH-bearing phases form at the expense of water-free minerals in such sites.

In high-grade sheared terranes, shears tend to be wide (up to 2 metres) as quartz, feldspar, mica and hornblende deform by crystalloplastic flow which is homogeneous on a very small scale (Tullis, 1982; Passchier *et al.*, 1990). In medium- to low-grade terranes, shear zones are of more restricted width. There is a sharply-defined fabric transition to the lower-temperature conditions with quartz and micas deforming by crystalloplastic flow resulting in strain shadows, recrystallization and triple-point junctions between minerals, while feldspar and hornblende often deform predominantly by microfracturing (Sibson, 1977; Passchier *et al.*, 1990).

2.4) Syn- to Late-Tectonic Metamorphism of the Madidima Nappe

a) Establishment of Maximum Metamorphic Grade

The maximum equilibrium metamorphic conditions of lower amphibolite facies (intermediate-P/intermediate facies) proposed for the majority of the Natal Nappe Zone is not evident in the deepest portions of the Madidima Nappe in the Mbongolwane Flats area (Figure 2.1 - Quarry, Cow and Mandrb-Zag outcrops). Petrographic and thin section studies of oriented samples reveal a maximum local metamorphic grade, constrained by the metamorphic assemblages of Silambo banded amphibolite xenoliths in Zidoni amphibolitic gneiss and the Zidoni amphibolitic gneiss itself, of epidote-actinolite (lower greenschist facies - Table 2.2). No abundant metamorphic hornblende indicative of lower to middle amphibolite facies was found in this portion of the Madidima Nappe and the epidote-actinolite grade is proposed as the maximum equilibrium assemblage remaining in the Mbongolwane Flats area although Liou *et al.* (1985) state that it is unwise to assume full equilibrium in the lower greenschist facies. Indeed the low-grade metamorphic assemblages which are described in the section on north-northeast to northeast-trending sinistral shears are implicitly disequilibrium assemblages. The hornblende-in limit from Cain (1975), estimated from Winkler (1974), may have been passed but evidence of this transgression remains rare in that equilibration in the epidote-actinolite facies was complete. The full assemblage for this facies is:

$$\text{actinolite} + \text{epidote} \pm \text{albite} \pm \text{chlorite} \pm \text{stipnomelane} \quad \textbf{(1)}$$

The change from acicular, to prismatic, to equant crystal habit of the amphiboles, from actinolite to hornblende to pargasite (Deer *et al.*, 1992) appears to have been reversed during retrogression. Only igneous and early metamorphic amphiboles have equant shapes. Cross-cutting poikiloblastic actinolite assumes acicular shapes and non-poikiloblastic igneous amphibole is often cataclastically deformed and may define flaser structures with granulated margins. Rounded igneous amphiboles (see Chapter 8) form inclusions in early metamorphic actinolite. The contacts of the igneous amphiboles with actinolite are sharp and are often marked by stringers of quartz blebs, possibly implying only partial mutual miscibility between these amphiboles.

Table 2.2 Metamorphic facies constrained by mineral assemblages in the Silambo banded amphibolite, Zidoni amphibolitic gneiss and banded amphibolite xenoliths in the amphibolitic gneiss. Equilibrium in the Mbongolwane Flats area is evident from the consistent regional metamorphic grade in the Mbongolwane Flats. First-order subdivision is on temperature. Reactions and assemblages are from Winkler (1967), Yardley (1989) and Liou *et al.*, (1985). The implications of the metamorphism are from Norris and Henley (1976), Etheridge *et al.*, (1984) and Fyfe and Kerrich (1985).

Metamorphic Facies, Scale and Mode	**Assemblage**	**Implications (a similar sequence of events occurs in an underthrust plate)**
Lower Greenschist Regional (multiple temperature excursions into the epidote-actinolite facies)	lower temperature part of facies actinolite + epidote ± albite ± chlorite ± stipnomelane *Note*: not high temperature part of facies (hbld ± act ± ab ± chl ± ep ± gt) - the latter may only have been achieved adjacent to Zidoni amphibolitic gneiss intrusions prior to sustained overprinting by the epidote-actinolite facies	EQUILIBRIUM METAMORPHISM (regional, ductile) • higher P and T • initiation of structures in compressional tectonics • locally-derived fluids at low fluid : rock ratios • minimal fluids along thrust planes
Albite-epidote (hornfels) Local hydrothermal veining	albite + epidote ± actinolite ± chlorite or actinolite + oligoclase	DISEQUILIBRIUM METAMORPHISM (ductile-brittle to brittle-ductile) • lower P + T • exotic fluids in partial transtensional tectonics or in local release features • possible leaching • higher fluxes of reduced metamorphic fluids along conduits
Prehnite-(pumpellyite) Local hydrothermal veining	lower temperature part of facies prehnite (+ pumpellyite) ± chlorite ± albite ± epidote *Note*: not high temperature part of facies (pumpellyite + epidote)	

Four generations of actinolite occur in the Zidoni amphibolitic gneiss, each having cross-cutting relationships with the last, and all of which may have bent twin lamellae. Examples of each generation are best displayed by samples from the Quarry outcrop.

a) early, well-twinned actinolite containing well-defined but scarce deformation lamellae; These actinolite crystals parallel quartz stringers, microcrystalline quartz/ feldspar, and biotite which all define S_{01}. This generation of actinolite developed in syn-thrusting times and is deformed around more competent feldspar porphyroclasts. Mortar textures of actinolite, with unbroken cores but finer-grained recrystallized margins, are typical of this generation; bent and strained twins are also prevalent (Figure 2.20 ***Slide ZAGQ 11/1***)

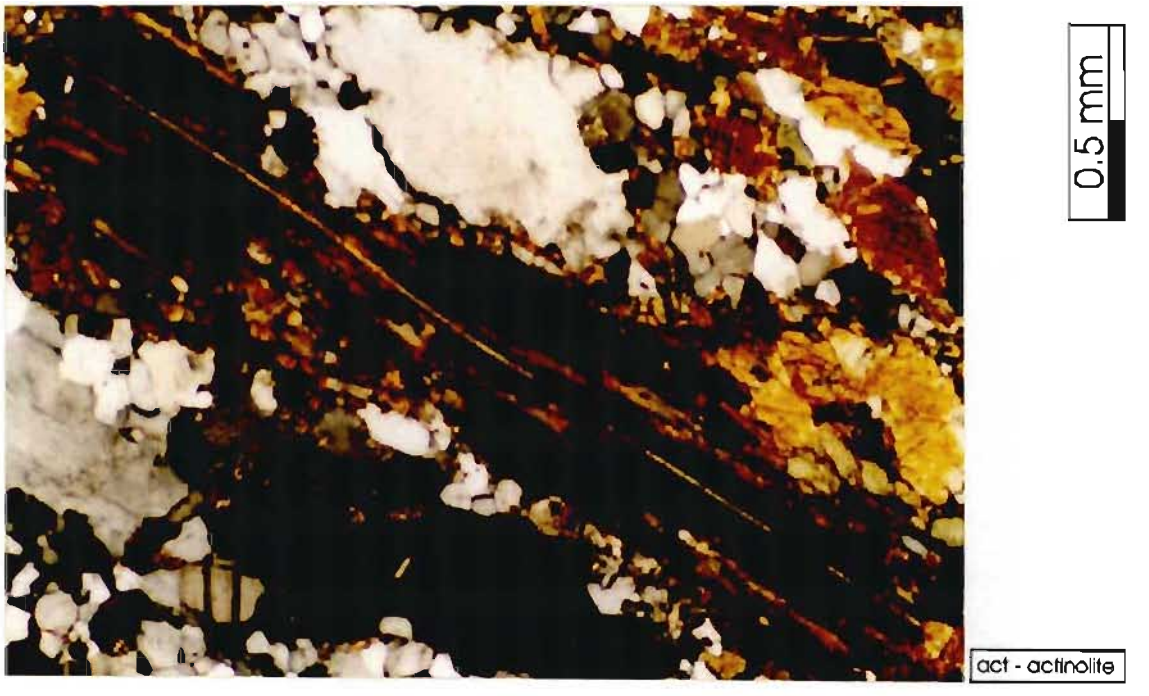

Figure 2.20 Early elongate actinolite with bent twin lamellae and cataclastically-reduced margins (***Slide ZAGQ 6/1*** - Quarry outcrop). XP.

b) syn- to late syn-thrusting actinolite which occurs mainly in the low pressure areas adjacent to feldspar porphyroclasts but is also weakly aligned by continued overthrusting (Figure 2.21 ***Slide ZAGQ -11/1***)

Figure 2.21 Syn- to late-thrusting poikiloblastic actinolite in the strain shadow of a feldspar porphyrocryst (***Slide ZAGQ-11/1*** - Quarry outcrop). XP.

c) non-aligned actinolite consisting of smaller crystals, often poikiloblastic to sieve-textured with inclusions of actinolite (Figure 2.22 ***Slide ZAGQ - 6/1 and 11/1***).

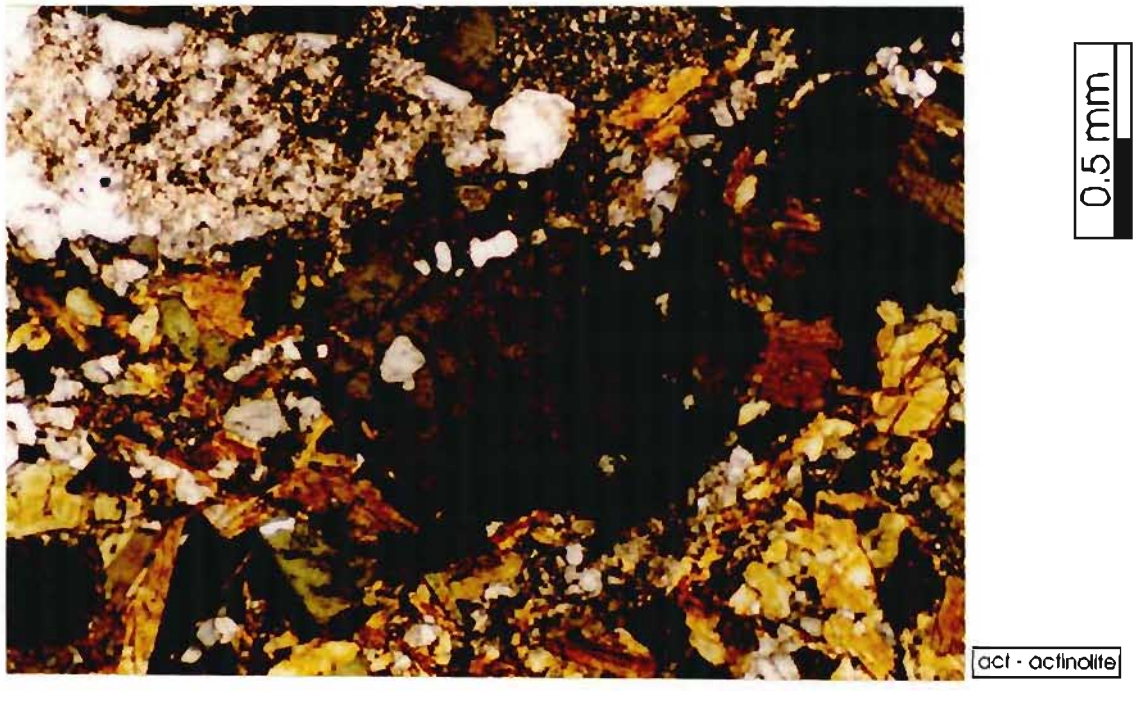

Figure 2.22 Non-aligned, poikiloblastic to sieve-textured actinolite with largely ungranulated margins (***Slide ZAGQ-6/11*** - Quarry Outcrop). XP.

d) actinolite hosted in, and parallel to, discrete synthetic sinistral shear zones with displacements less than 20 mm (Figure 2.23)

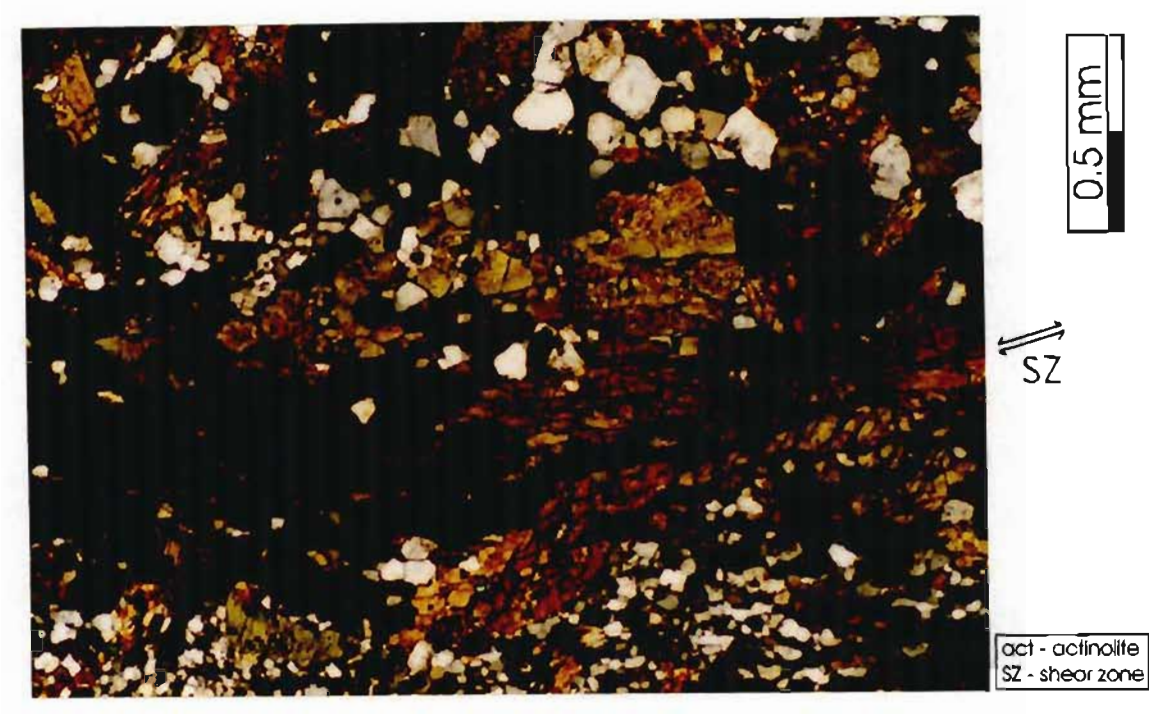

Figure 2.23 Aligned actinolite in narrow, brittle-ductile sinistral shear zone. Note the partially mosaic-textured margins of the shear zone (Slide ZAGQ-1/1 - Quarry outcrop). XP

Lower greenschist regional metamorphism occurred under predominantly ductile to brittle-ductile conditions above the epidote-actinolite limit defined by Schiffman and Liou (1980) and Yardley (1989) (Figure 2.24). Another criterion for constraining this metamorphic episode are the upper and lower boundaries of the semi-brittle or ductile-brittle field in quartzofelspathic rocks, of which the Zidoni amphibolitic gneiss is an example. The upper limit of this field is dictated by feldspar plasticity and the drawing out of feldspar into stringers at 450°C, similarly the lower limit is defined by quartz plasticity at 300°C (White, 1975; Kerrich *et al.*, 1977; Fyfe and Kerrich, 1985; Scholz, 1988; Figure 2.24 a). The upper limit of this field has not been reached in the Zidoni amphibolitic gneiss; plagioclase feldspar still maintains its porphyroclastic configuration, contains deformation lamellae and has cataclastically-deformed margins. However, quartz is drawn out into fully annealed stringers which usually show no strained extinction, excepting in those polycrystalline stringers which were formed below 300°C (in relation to veining in late-tectonic brittle-ductile shears) the lowest annealing temperature of quartz (*op. cit.*). The formation of a planar foliation, deformation lamellae, quartz stringers and annealed

porphyroclast margins appears to have been synchronous. An approximate indication of the grade of metamorphism is gleaned from an ACF plot with the ACF parameters or co-ordinates derived from whole rock major oxide analyses (Figure 2.24 b).

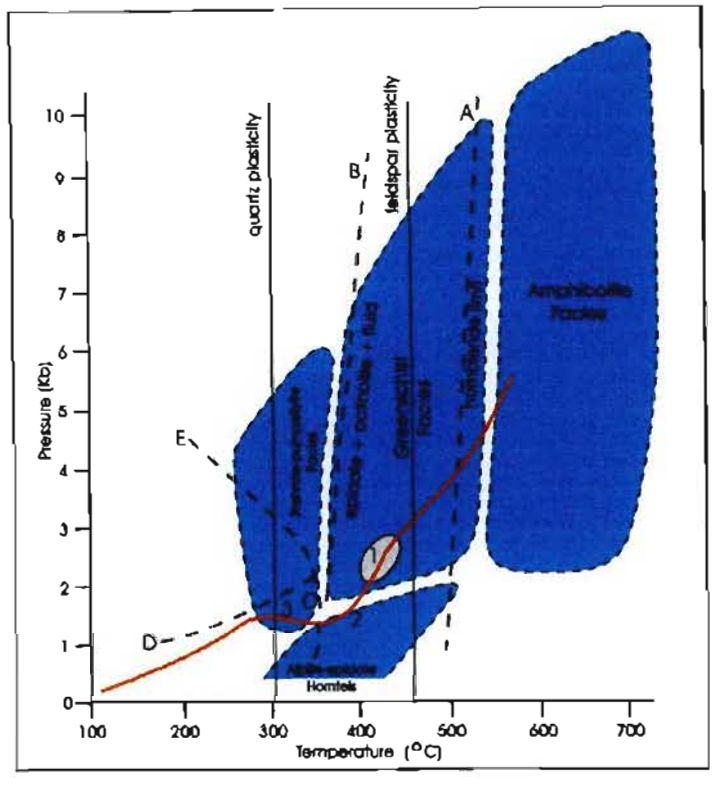

Figure 2.24 a Qualitative, partial pressure-temperature time path for the base of the Madidima Nappe.
A Hornblende-in limit (Winkler, 1974)
B Epidote-actinolite limit (Schiffman and Liou, 1980)
C Reaction line : prehnite + (Mg)Chlorite + fluid → Pumpellyite + Tremolite + Quartz (Liou *et al.*, 1985)
D Reaction line : Prehnite + Epidote + Chlorite → Pumpellyite
E Reaction line : Prehnite + Chlorite + Quartz → Zoisite + Tremolite + Fluid

b) Continued Tectonism in a Waning Geothermal Regime

Evidence for continued deformation in a waning geothermal regime is given by local metamorphic assemblages in discrete, brittle-ductile shear zones. Following on from the brief descriptions of vein mineralogies in the section on shearing, the first such event produced a structurally-controlled albite-epidote facies (Schiffman and Liou, 1980; Liou *et al.*, 1985) with the assemblage;

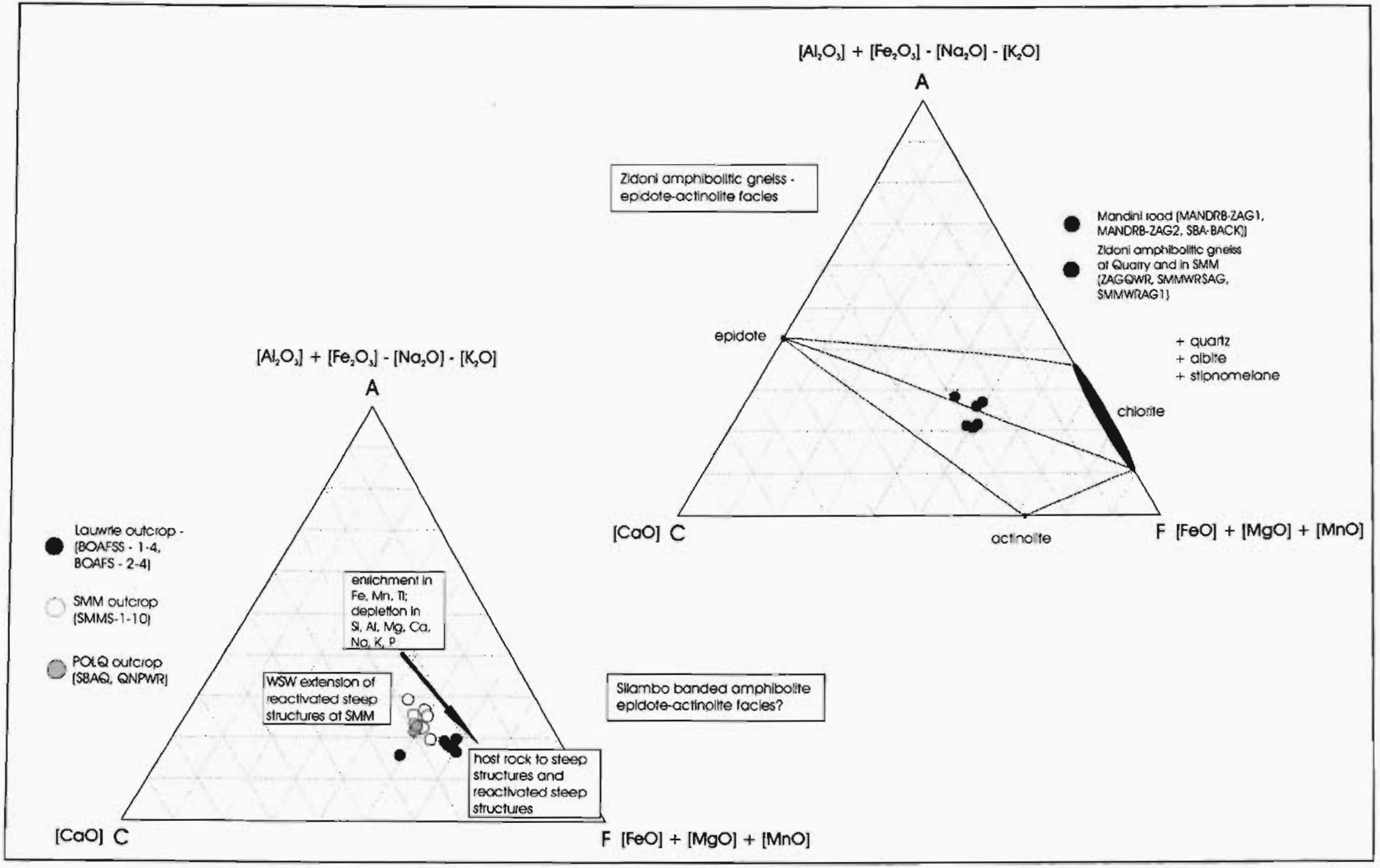

Figure 2.24 b ACF plots of the main components of the Madidima Nappe in the Mbongolwane Flats. The parageneses derived from thin section studies matche the ACF parameters calculated from major oxide whole rock geochemistry (Appendix A1). Note that the Silambo banded amphibolite in the Lauwrie outcrop, adjacent to the type outcrop of the steep structures, is enriched in Fe, Mn and Ti but depleted in Si, Al, Mg, Ca, Na, K and P. Although a detailed mineralogical study has not been performed on the Silambo banded amphibolite, the same state of metamorphism as the amphibolitic gneiss may be inferred, that is, the epidote-actinolite facies or greenschist grade

albite + epidote ± actinolite ± chlorite **(2)**

Albite-epidote veins occur in the mixed brittle-ductile/dilational sinistral shear zones in which cyclic emplacement of albite and epidote ± actinolite and chlorite occurred. This structurally-constrained event cross-cuts S_{01} in the Zidoni amphibolitic gneiss and the Silambo banded amphibolite.

Cross-cutting the albite-epidote veins are a series of very small prehnite domains, occupying the last local transtensional areas made available during sinistral shearing. Liou *et al.* (1985) make a distinction between a prehnite-actinolite facies and the greenschist facies (*sensu stricto*) (Figure 2.24 a, isograd **C**).

prehnite + chlorite + quartz → zoisite (epidote) + tremolite (actinolite) + fluid **(3)**

The albite-epidote and prehnite events exemplify hydrothermal metamorphic mineral emplacement in local spaces in late sinistral shears formed during the last stages of tectonism. The final alteration event consists of sericitization and sphene formation as has been mentioned in a previous section (Figure 2.24 a; Table 2.2). Sphene commonly occurs in low-temperature Alpine-type veins where it may be associated with aduluria, albite and epidote (Deer *et al.*, 1992) and also commonly occurs in metamorphic rocks rich in ferromagnesian minerals, such as gneisses (*op. cit.*). This metamorphic assemblage is best observed in north-northeast- to northeast-trending shear-hosted veins. Because of reactions between veins and wallrocks these last three events are local disequilibrium metamorphic events in a brittle-ductile stage where localized fluid flow was high while the epidote-actinolite facies was achieved by a regional metamorphic event (q.v. Norris and Henley, 1976; Etheridge *et al.*, 1984; Fyfe and Kerrich, 1985; Vrolik *et al.*, 1988, Table 2.2).

There is no evidence in any thin sections for the pumpellyite-tremolite facies (Liou *et al.*, 1985) and thus the reaction line **C** (Figure 2.24 a), has not been crossed. An upper temperature limit defined by the pumpellyite-tremolite facies and a partial upper pressure limit defined by the bivariant reaction line **D** are evident. Prehnite and epidote are in local equilibrium. These lower temperature assemblages and are not strictly retrograde products of the epidote-actinolite facies and have not been overprinted.

2.5) New Model for Rebellion Reef Formation

The Lilani-Matigulu Shear Zone is not the northern delimiter of late-tectonic events in the Natal Nappe Zone. Some features atypical of and succeeding ductile overthrusting persist north of the proposed southern margin of the Kaapvaal Craton, for instance steep discontinuities/steep structures and shears initiated at foreland margin irregularities, intra-nappe irregularities or undulations in an underlying nappe.

Late, east-northeast-trending transcurrent shear zones are strongly controlled by the close proximity of the Kaapvaal Craton and the Lilani-Matigulu Shear Zone to the north of Mapumulo. Further southwards, the trend of shear zones becomes more northeast (Figure 1.2) with a splaying of shear zones such that the orientation of the dominant transcurrent movement plane is influenced by the proximity of the Kaapvaal Craton. In a study of normal-slip faulting in the coastal areas of Natal, Von Veh and Anderson (1990) found similar characteristics and orientations for Jurassic dip-slip faulting caused by the break-up of Gondwana. The expected trend of any major late shears in the Tugela Nappe Zone should therefore be between east and east-northeast provided transcurrent movement was able to entrain portions of the underling Kaapvaal Craton.

A new model for late-tectonic structural features of a portion of the Madidima Nappe on the southern ramp of the Kaapvaal Craton north of the Lilani-Matigulu Shear Zone is proposed here and summarized in Table 2.3, which has a first-order subdivision based on temperature, encompassing the qualitative range of ductile to brittle. In the absence of meta-calcsilicate assemblages, no inferences may be made about pressures during tectonism.

The S_{01} foliation in the Mbongolwane Flats was deformed such that three distinct structural domains are defined. Both the F_1 and the $F_{2/3}$ fold generations were generated during early tectonism and metamorphism which also included a regional-scale $F_{2/3}$ fold in a discordant Thaweni granite-gneiss sheet. Subsequent deformation revolved around the tightening of this regional fold, the competency contrast between the Thaweni granite-gneiss and the volumetrically dominant banded amphibolite and amphibolitic gneiss, and oblique collision. After the formation

of S_1 and S_2 under ductile conditions in the (upper?) epidote-actinolite facies, initiation of two dominant trends of shears occurred. These constitute the east-northeast trending and the northeast- to north-northeast trending shear generations, the former resulted from a reactivation of structural weaknesses (steep structures) which coincided with the Thaweni granite-gneiss/Silambo banded amphibolite contact.

The contact between Domain 1 and Domain 2 hosts steep shears as described by Apotria *et al.* (1993), which were caused by the ductile movement of the hangingwall Silambo banded amphibolite over the southern limb of the regional $F_{2/3}$ fold in Thaweni granite-gneiss. It is apparent that these steep shears and the reactivated steep shears between Domain 1 and 2 constitute the linear array R-1 to R-6 (Figure 2.1) of Schurink (1986). The repetition or duplication of the reef, as noted by earlier prospectors and as observed in this study, is merely a result of the incremental downfaulting of the Silambo banded amphibolite. Subsequent shearing of the steep structures would have resulted in multiple reefs separated by banded amphibolite. The east-northeast trend of the Rebellion Reef seems to have been extended to the west-southwest, to the R-3 and SMM (south of Mbongolwane Mission - R2?) gold occurrences. Quartz, feldspar, muscovite, biotite and mesothermal chalcopyrite were emplaced into these shear zones. An oblique or transverse motion was superimposed upon the initial reverse shearing within the steep structures.

The formation of the limited number of steep shears was followed by synthetic sinistral R_1/σ_1 shearing commencing in the epidote-actinolite facies and continuing through the hydrothermal albite-epidote and then prehnite facies towards the last stages of metamorphism. Albite and epidote emplacement and the epidotization of adjacent feldspars occurred in periods of incremental dilation followed by repeated, almost co-planar shearing which continued into the brittle regime. These features are indicative of late-thrusting/late tectonic deformation in a waning geothermal regime Very late-tectonic brittle features are low angle thrust planes (dipping at about 10° to the south) exhibiting a consistent top-to-north displacement and further minor antithetic veining only occasionally disrupted by thrusting in the zeolite facies.

The formation of the R5/R4 array of Schurink (1986) (Figure 2.1) and the myriad of shear zones in the south of the field area is a result of stress transmission from the Thaweni granite-gneiss contact to another incipient/potential weakness, such as a Silambo banded amphibolite/Zidoni amphibolitic gneiss contact which fortuitously trends east-northeast. It is well known that when portions of the crust or a thrust unit form individual blocks, the imposition of tectonic shearing results in deformation by slip and block rotation, rather than by uniform straining (Nur *et al.*, 1989). Two orders of magnitude exist for block rotation in the terrane under study.; the larger of these comprises blocks of the size of the Margate and Mzumbe Terranes, while the smaller of these comprises blocks within the nappes, the edges of which have been the targets of mineral exploration in the past, unbeknownst to the researchers.

The very fact that many of the northeast-trending shears do not exhibit left-lateral movement allows further consideration of the processes described by Nur *et al.* (1989). A component of left-lateral shearing at the Thaweni granite-gneiss/Silambo banded amphibolite contact, compementary to another sheared contact to the south of the field area and so delimiting a series of kilometre-scale blocks, may be assumed in the Mbongolwane Flats (Figure 2.26). Motion at the individual block contacts is implicitely right-lateral and there is, furthermore, an implied dilation between blocks, such as that noted in the northeast-trending veins. Block rotation may only have served to disrupt the rigidly-defined fold patterns such that fold axes of initially of the same generation are not entirely parallel to one another.

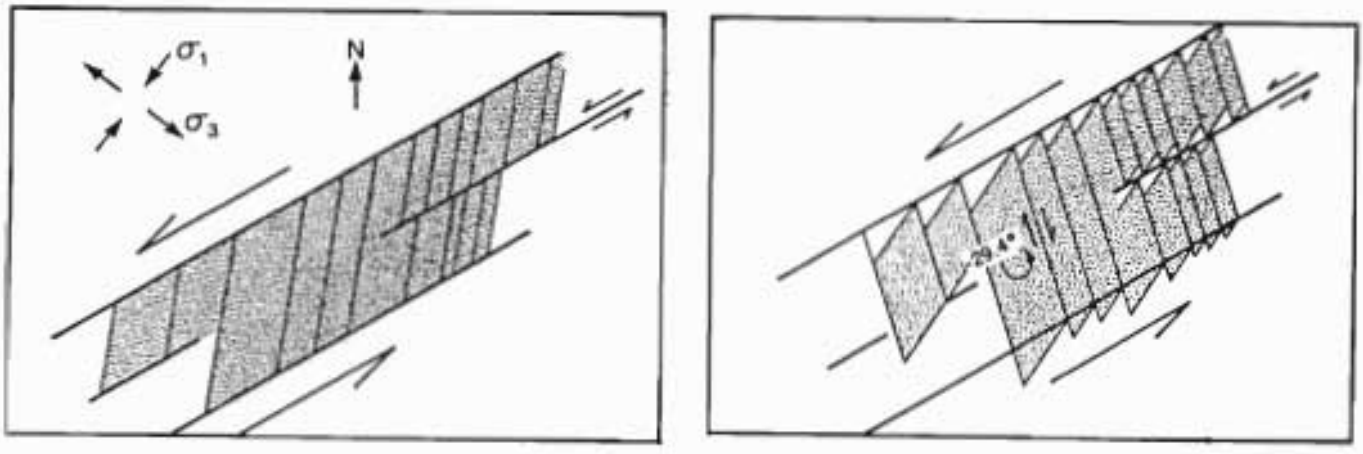

Figure 2.26 Block rotation during the slow transmission of stress in the earths crust (after Nur *et al.*, 1989). Note that right-lateral movement is implied at the block margins, as is dilation between blocks. This may account both for the contradictory movement indicators (eg dextrally-offset agmatic veins) and fracture/shear infilling.

Table 2.3 General model for syn- to late-tectonic features of the Madidima Thrust Unit

General Style of Deformation (ductile vs brittle)	Ductile (pervasive veining, residual fluids from intrusion)	Brittle-ductile (mainly albite and epidote veining)	Brittle (quartz veining)
Remote Force	NNE-SSW compression, southwest-to-top overthrusting and metamorphic inversion	cessation of overthrusting, movement around the Kaapvaal Craton, ENE-trending sinistral shearing focussed on steep structures	halting of active collision partial transtension
Local Features	•oscillation between ductile and brittle deformation •tectonic loading due to thrust sheet emplacement •formation of steep shears with downthrown side to the south	•waning temperature regime •NE-NNE and ENE-trending sinistral strike-slip shear zones in the deepest part of the nappe where higher temperatures persisted •intersection of residual hydrothermal reservoirs and reactivation of steep structures	•"back-sliding" along shallow, south-dipping discontinuities •low angle brittle thrusting •further antithetic veining
Metamorphic Style	Regional	Local Hydrothermal	Local
Metamorphic Facies	Thermal equilibrium between vein and host rock lower greenschist epidote-actinolite facies	Thermal disequilibrium between veins and host rock sub-greenchist grade albite-epidote (hornfels) and low-temperature prehnite-(pumpellyite)	Zeolite zone

2.6) Discussion - Economic Potential

The majority of the whole rock and vein Au assays yield extremely low or insignificant values, usually between 10 and 20 ppb (Appendix B1). The only notable exception in the data are Au values of veining and host rocks to veining at the abandoned gold working on the Lauwri farm/outcrop wherein Au values range from 31 to 221 ppb in reactivated steep structures to less than 10 ppb in steep structures. The accompanying footwall granite-gneiss has Au values of 47 and 211 ppb Au. No raised Au values were found in the host banded amphibolite (usually > 10 ppb). The mine at SMM, inferred to be the west-southwest extension of shearing along the southern limb of the F_2 fold in Thaweni granite-gneiss, situated at a banded amphibolite/amphibolitic gneiss contact, reveals only slightly raised Au values (15 and 27 ppb) in the host amphibolitic gneiss while veins (e.g. SMMV-1 to 3) show insignificant Au values. The poorly mineralized, east-northeast-trending shear zone is potentially 9 km in length, from northeast of the Lauwrie outcrop to southwest of the SMM outcrop. It would appear, from this study, that gold grades are insignificant and Au grades above 10 ppb are limited to the Thaweni granite-gneiss/Silambo banded amphibolite contact.

In this case, the poorly mineralized shear zone should at least have a 6 km extent along the southern regional F_2 fold limb.

Hildreth plots demonstrate enrichment and depletion in the alteration zones adjacent to the extended east-northeast-trending shear zone. The Silambo banded amphibolite adjacent to the steep structure at the Lauwrie outcrop (normalized to a comparatively unaltered sample - SBA-BACK), exhibits enrichment in Si, Fe, Pb, Zn, Ni and As, and consistent depletion in Al, Mg, Ca, Na, Cu and S (Appendix G1). On the contrary, the Zidoni amphibolitic gneiss adjacent to the SBA, at the SMM outcrop (Appendix G1) exhibits notably different trends, with a depletion in Si, Al, Mg, K, Na, Cu, Zn and Ni, and an enrichment in Fe, Ca, Pb, As and S. A fluid-mediated exchange of elements between adjacent rocks, with the possibility of element contribution from the Thaweni granite gneiss (present in the vicinity of both the outcrops) is implicit. Oxygen isotope studies (Chapter 7) suggest that no igneous-derived fluids were active during vein deposition. The enrichment/depletion trends, combined with the mineralogy at the abandoned workings, implies veining similar to Cordilleran-type vein deposits.

2.7) Conclusion

The steep structures in the Mbongolwane Flats area are typically formed during late tectonism of areas with oblique collisional tectonics (Figure 2.26). Knoper *et al.*, (1997) observed that the Steenkampskraal orebody in Namaqualand is affected by late brittle subvertical steep structures with characteristics very similar to those found in the Mbongolwane Flats. Jackson and Harris (1997) found evidence of extensional reactivation of the Hartbees River Thrust Belt in the northeastern Namaqua Tectonic Province. The features observed by Jackson and Harris (1997) include sigmoidal deflection of shear bands due to normal movement being superimposed on the main thrust/reverse movement. It is to be expected that structures which are observed in the Namaqua portion of the Namaqua Metamorphic Province may be reconciled with analogue structures in the Natal portion of this mobile belt even through the shear sense in each terrane is different. It is therefore recommended that further research should endeavor to draw parallels between these two different, but related, structurally complex areas.

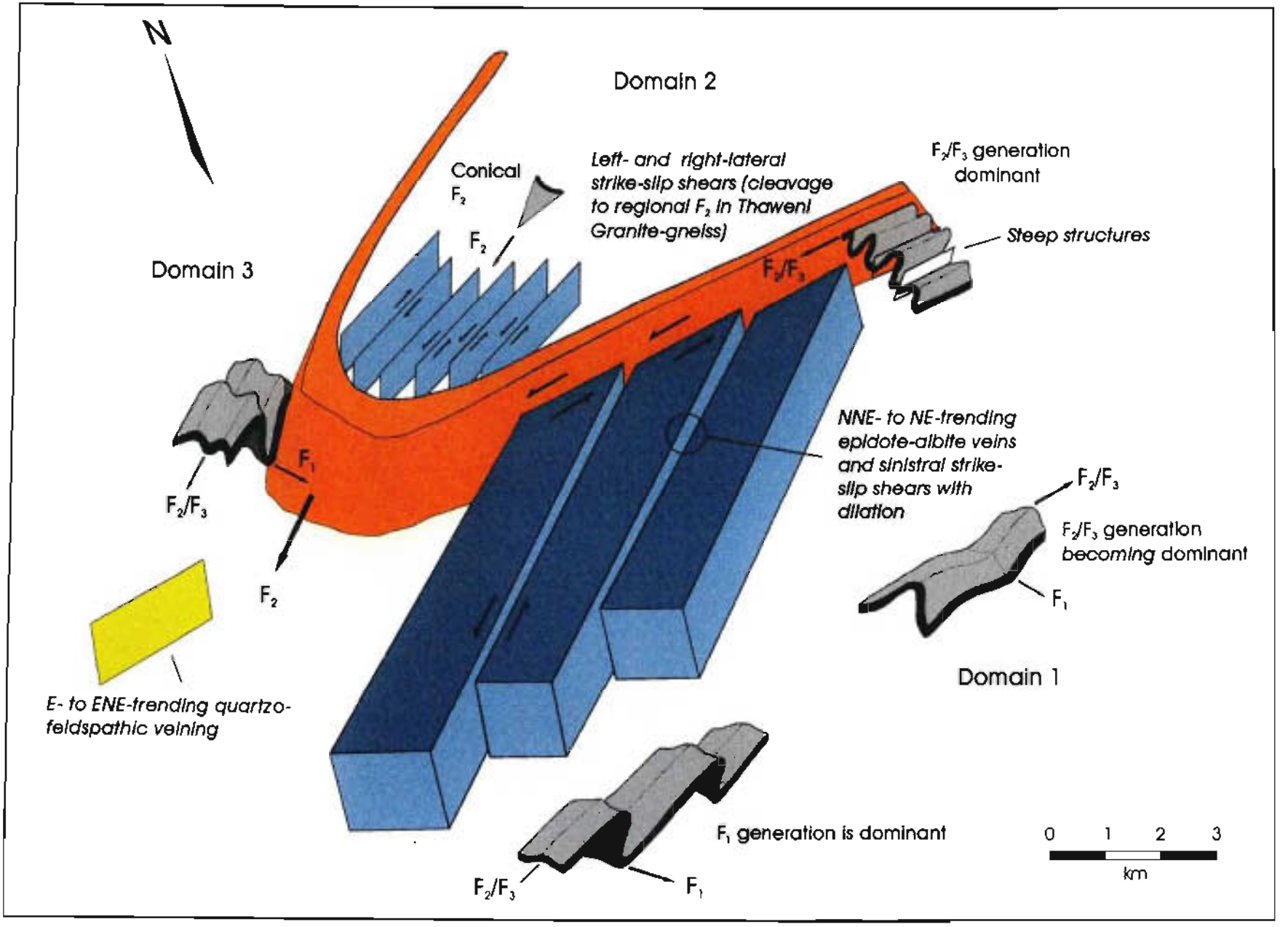

Figure 2.26 Block diagram of the configuration of the structural features in teh Mbongolwane Flats area. An aproximate scale is shown

Northern and Southern Mfongosi Valley Areas

Regional Geology

The Mfongosi Valley near the westernmost extremity of the Natal Thrust Front is an extensive flat-lying area in the Mfongosi Group schist which is part of an imbricately thrust volcanosedimentary wedge (Figures 1.3, 1.4, 3.1; Matthews 1959). The Mfongosi schist forms an inlier within the Permian Ecca Group as does the Ntingwe limestone which overlies the Kaapvaal Craton. The Mfongosi River transgresses the Mfongosi Valley from north to south and is a tributary to the Tugela River. Prospects and workings in the Mfongosi Valley may be divided into two areas; those in the northern Mfongosi Valley consisting of lead-silver-gold prospects and those south of the Mfongosi Valley consisting mainly of gold prospects (Smith, 1987). Although banded iron formation has been found in the valley floor (Matthews, 1959; Harmer, 1979), the outcrop is extremely poor and rocks are largely hidden by regolith.

The area is structurally complex and hosts an estimated six thrusts within the Mfongosi schist and Ntingwe limestone occurring between the northern foreland (the Kaapvaal Craton) and the Manyane Thrust to the south (Matthews and Charlesworth, 1981). The Tugela Fault is a regional feature which transgresses the east-west extent of the Mfongosi Valley about 200 metres north of the northern Mfongosi Valley lead-silver workings. The Tugela Fault is a vertical to steeply south-dipping normal fault with a 240 - 460 m downthrow (Matthews, 1959).

The Mfongosi Valley area will be dealt with in two parts; the northern Mfongosi Valley area, concentrating on lead-silver-gold workings (Chapter 3) and the gold and copper workings in the southern part of the Mfongosi Valley (Chapter 4). Detailed structural analyses of each area will give an indication of the origin, subsequent deformation, and extent of veining in both areas. Models from the northern and southern Mfongosi areas will then be merged to produce a model of vein formation and mineralization which may be applied to the veining in a large portion of the Natal Thrust Front.

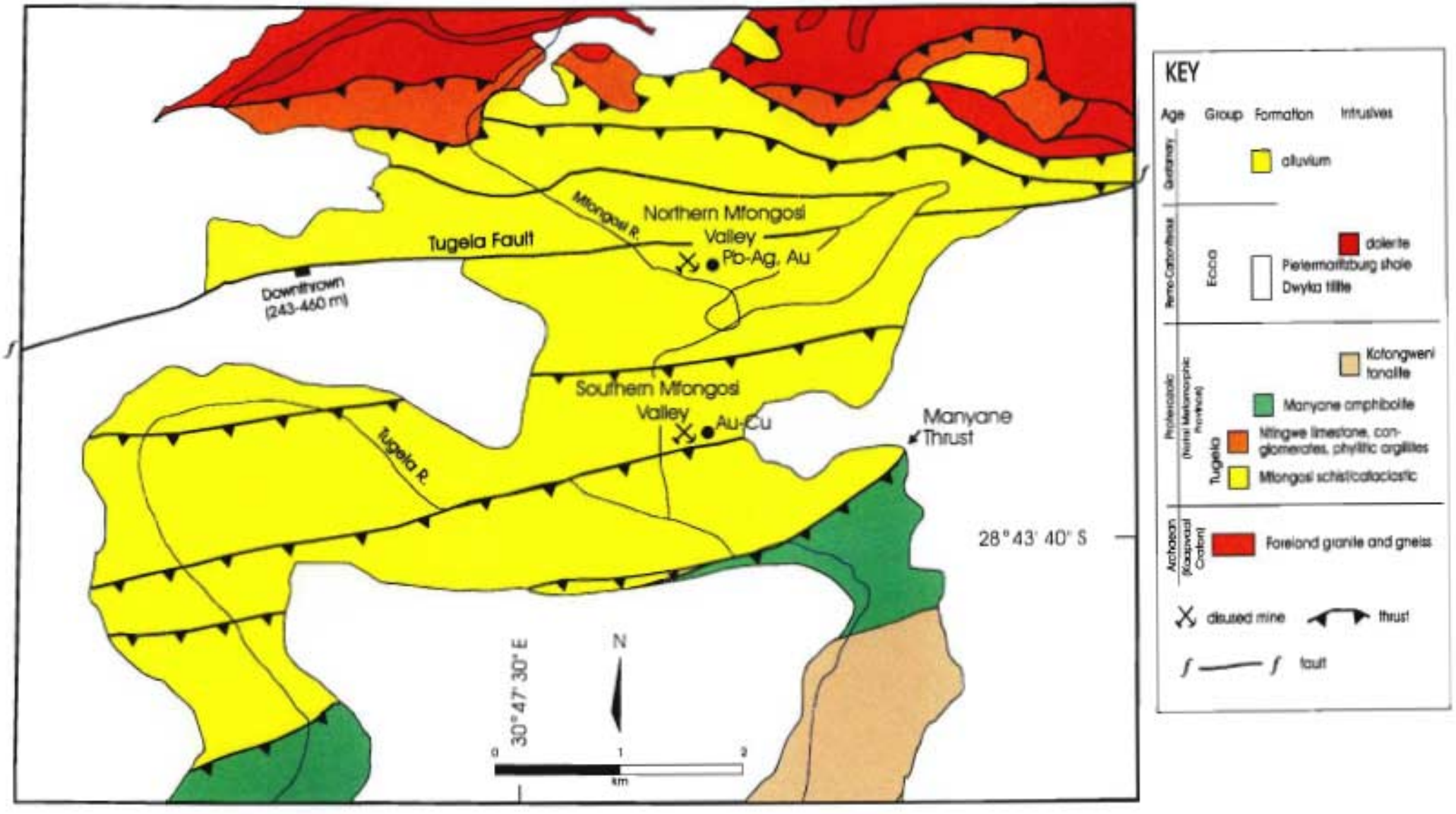

Figure 3.1 The Mfongosi Valley, showing the position of workings in the northern and southern areas. Note that the southern Mfongosi Valley area includes the Ayres Reef in the Manyane amphibolite at the base of the Tugela Nappe. (after Matthews and Charlesworth, 1981 and the 1 : 250 000 scale Geological Series, Dundee, 2830)

Chapter 3

Northern Mfongosi Valley Area

3.1) Economic History

Reports on the mining industry of Natal contain consistent comparisons between the workings in the Nkandla district in the eastern Natal Thrust Front and the workings north of the Mfongosi Valley (Gray, 1899 to 1906). Gray (1899, 1901) refers to a galena ± copper lode occurring in the "northern or lower part of the schists which straddle the whole of the Mfongosi Valley". The quartz lode was observed to be continuous for a maximum strike length of 3000 yards (2743 m) across a number of spurs and showed uniform silver values, contained in galena or as native silver, along its length (Figure 3.2). A massive porphyritic syenite which is likely to be part of the Kaapvaal Craton occurs about 1.5 km to the north of this array of shallow trenches over the workings. Prospecting trenches exposed a 0.6 m width of highly disrupted glassy white quartz veining in the footwall and hangingwall to the quartz lode, both levels containing stringers and veins of galena and quartz fragments entirely suspended in or enclosed by galena. The lode was observed to be lenticular, widening and narrowing along its length. Prior to 1902 the exploitation rights to the northern Mfongosi Valley workings, comprising a main lode at right angles to the north-south extents of five small spurs of the Quedeni mountain, were secured by the South African Federated Mineral Development Syndicate (Figure 3.2). The range of spurs fall between the Amanzawayo River to the west and the Amanzimnyama (Mfongosi) River to the east. Findings on each spur, from east to west across the Syndicate's holdings, were as follows (Gray, 1902; Figure 3.2):

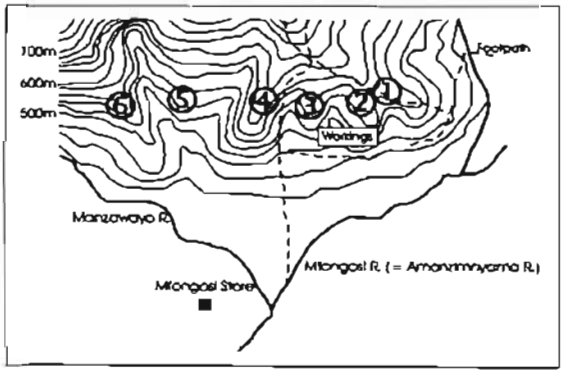

Figure 3.2 The set of spurs in the northern Mfongosi Valley area (Spur 1 - 6 from east to west) which were considered as viable prospecting areas by the South African Federated Mineral Development Syndicate (Gray, 1902). Three of these spurs (2, 3 and 4) form the focus of this study.

Spur ① The thickness of the quartz lode varied from 23 cm to 76 cm in a pinch and swell structure. The quartz lode was fragmented and entrained in the enclosing schist and no lode was discovered on the western slope of the spur despite a 25 m x 3.5 m trench having been excavated.
Spur ② Four trenches were excavated on the eastern side of the spur with no result while on the western side the lode outcropped from summit to base and consisted of a large quartz lens disrupted by entrained stringers of schist. A 15 m shaft was sunk on the lode which was disrupted by several lenses and blocks of schistose host rock. Lead in the shaft occurred as a sulphide (galena) and as a carbonate (cerussite).
Spur ③ A 1.3 m wide ft-wide lode was apparent with galena confined to the hangingwall. Half-way down the western slope a cross-cut at the down-dip extension was barren, implying down-dip lode discontinuity.
Spur ④ A small lode was found to occur on the summit and to a limited extent on either side of the summit.
Spur ⑤ No lode was apparent; schist occurred from the summit to the base of the spur and in dongas on either side.
Spur ⑥ Preliminary trenching showed the lode to be horizontal and dipping progressively more to the south at increasing depth. The thickness of the lode varied from 15 cm to 150 cm but no lode outcrop was discovered or exposed on the Syndicate's claim west of Spur 6.

No further mention of the northern Mfongosi workings is made in reports to the mining commissioner until Hedges (1909) noted galena disseminated throughout the zoned orebody; copper sulphides were concentrated in the hangingwall and pyrite was selectively enriched near the footwall. Recent models regarding the mineralization in the Mfongosi Valley area have been proposed by Winfield (1979), Becker (1986), Thomas *et al.* (1990), and Bullen *et al.* (in prep). These models make no conclusions as to the structural context and origin of veining in this structurally complex terrane and merely attribute mineralization to shear-zone hosted quartz veining in a highly deformed volcaniclastic sequence. Winfield (1979), in a study on the Tugela Fault area, continued the prospecting initiated by Eland Exploration Company, International Nickel, Messina Transvaal Development Company, Billiton Exploration South Africa, Shell South Africa Metals Division and Johnnies Consolidated Investment. Winfield (1979) summarised the findings of the former exploration efforts and concluded the following:

- the Tugela Fault should be the prime target in the Mfongosi Valley and Ngubevu areas
- coincident copper, zinc and nickel anomalies require follow-up work by means of magnetometer surveys, induced polarization and geochemical sampling
- higher than background base metal values are associated with certain rock types rather than being due to simple sulphide mineralization; high-grade metamorphic rocks offer better chances of finding base metal sulphide accumulations
- disseminated sulphide zones are up to 20 m in width. The lengths of these zones were not disclosed although Winfield (1979) estimated a maximum length of 50 m
- high zinc values are associated with andesitic volcanics
- nickel anomalies define the extent of the mafic components of the Mfongosi schist

Based one regional, and limited local mapping, Coldwell (1984) presented preliminary conclusions on the western portion of the Mfongosi Valley encompassing a length of the Tugela Fault. The east-west succession of greenschist, ferruginous phyllite, sericite-muscovite schist, banded magnetite chert, thin carbonate layers and dacitic lava gave variable grades of base and precious metals (*op. cit.*). Coldwell (1984) proposed the average and maximum grades to be expected from a typical portion of the Mfongosi schist straddling a portion of the Tugela Fault and concluded the following:

- copper, lead and silver mineralization occurs in east-west trending quartz vein systems 1 km north of Mfongosi
- malachite- and chalcocite-bearing felsic volcanics (dacitic lavas) have peak copper values
- mica phyllite (≈ phyllitic quartzite) has moderate base metal values while chlorite schist contains the highest zinc values
- lead is preferentially concentrated in gossaniferous quartz siderite veins within laminated mica phyllite and chlorite schist
- minor magnetic anomalies are associated with carbonaceous shale and banded magnetite chert

Other workers (eg Becker, 1986; Pearman, 1994) prefer models which are based on regional lineaments controlling the location of precious and base metal deposits during the formation of the Natal Thrust Front and Natal Nappe Zone. Intersections of these lineaments, particularly a northeast-trending and a northwest-trending set, were considered as viable targets and were proposed to coincide with known gold workings or occurrences (Becker, 1986). This correlation is tenuous at best as the possibility of these linear features remaining linear and undeformed during collision is slim. Pearman (1994) presents qualitative evidence for possible Carlin-type mineralization (Ntingwe limestone) and Hemlo-type mineralization (Mfongosi schist) based on preliminary field observations. Alternative theories for fluid movement, other than those concerning fluids moving along basal décollements and thrust planes (Thomas *et al.*, 1990; Pearman, 1994), have been made (eg. Bullen *et al.*, in prep.). Initial theories on metallization of the Mfongosi schist (e.g.Thomas *et al.*, 1990) depended upon amphibolite grade-generated fluids moving northwards along major, southerly-dipping thrust planes with metal deposition below the amphibolite-greenschist facies boundary where brittle deformation began to dominate during retrograde metamorphic conditions. The highly fractured Mfongosi schist was considered as an ideal host to gold and base metal deposition. Bullen *et al.* (in prep.), using stable isotope data, have proposed an alternative model to that of thrust-controlled mineralization, concentrating on mineralization during a final lateral movement along subvertical shears in the Mfongosi schist.

This chapter serves to illustrate the lack of correlation of structural features with the Tugela Fault. The structural model proposed in this study obviates the need for any large-scale shear zone or thrust-emplaced mineralization. Rather, early tectonic veins were incorporated in later deformation phases, giving the appearance of the veins having been formed during simple shear. The apparently random and irregular distribution of veins, of vastly different thicknesses, cannot be explained by the processes of simple or pure shear alone. This study gives an indication of the extent of veining and mineralization in the northern Mfongosi Valley area.

The origin of the veins described in this chapter is comprehensively dealt with in Chapter 4 wherein the first stages of Mfongosi Group deformation are examined in the light of juxtaposed tectonic terranes.

3.2) Host Rocks to Veining

Initial impressions of the Mfongosi schist within 1-2 km south of the Kaapvaal Craton are that it is both compositionally massive and highly deformed. Predictable features of fold and thrust belts, such as systematic folding, regularly-oriented veining, jointing and discernable lithologies are absent. Furthermore schistosity, being the "oriented or planar structure, mainly seen in schists and sometimes phyllites, due to the parallel alignment of platy or prismatic mineral grains" (Lapidus and Winstanley, 1987) is scarce, and is only observable at host rock/quartz vein contacts. The host rock is a pale blue to dark-yellow, very fine-grained quartzite exhibiting banding across the whole of the northern Mfongosi field area. Banding is defined by small variations in phyllitic mineral and/or calcite and siderite content. The host rock to veining, adjacent lithologies and vein segments may be termed a tectonic melange. The matrix in which these vein segments occur is usually a fine-grained cataclasite to ultracataclasite. The field area is remarkable for two reasons; the extent and apparently non-systematic orientation of veins and the fact that a large portion of the veins are hosted by a rock type which differs from the rock type forming the bulk of the set of spurs (Figure 3.3).

The host rock to the profuse veining is a pale blue to dark yellow *finely-banded quartz-albite-chlorite-calcite-riebeckite ultracataclasite* which has abundant iron staining and calcite banding (Figure 3.4 a, b). Banding is measured as a planar feature and shows extensive deformation or variation in orientation near competent quartz vein segments. In thin section quartz and albite are highly strained with diffuse lobate grain boundaries which are characteristic of dynamically metamorphosed non-annealed rocks (Spry, 1969) and although flattening of grains has been extensive, reduction of strain within clasts has occurred by cataclasis rather than annealing (Mason, 1990). Larger pre-cataclastic clasts are often found preserved in calcite bands which have undergone ductile deformation (eg Scholz, 1988). Cross-cutting the quartz, albite, chlorite and calcite bands are a series of anastomosing and fan-shaped/diverging brittle-ductile fractures which are not evident on the outcrop or hand specimen scale. Opaques, comprising magnetite and haematite, are distributed regularly over the area of a thin section and make up 3-5 % of the rock . The host rock to the mineralization may therefore be termed a *riebeckite-bearing phyllitic quartzite/cataclsite to ultracataclasite.*

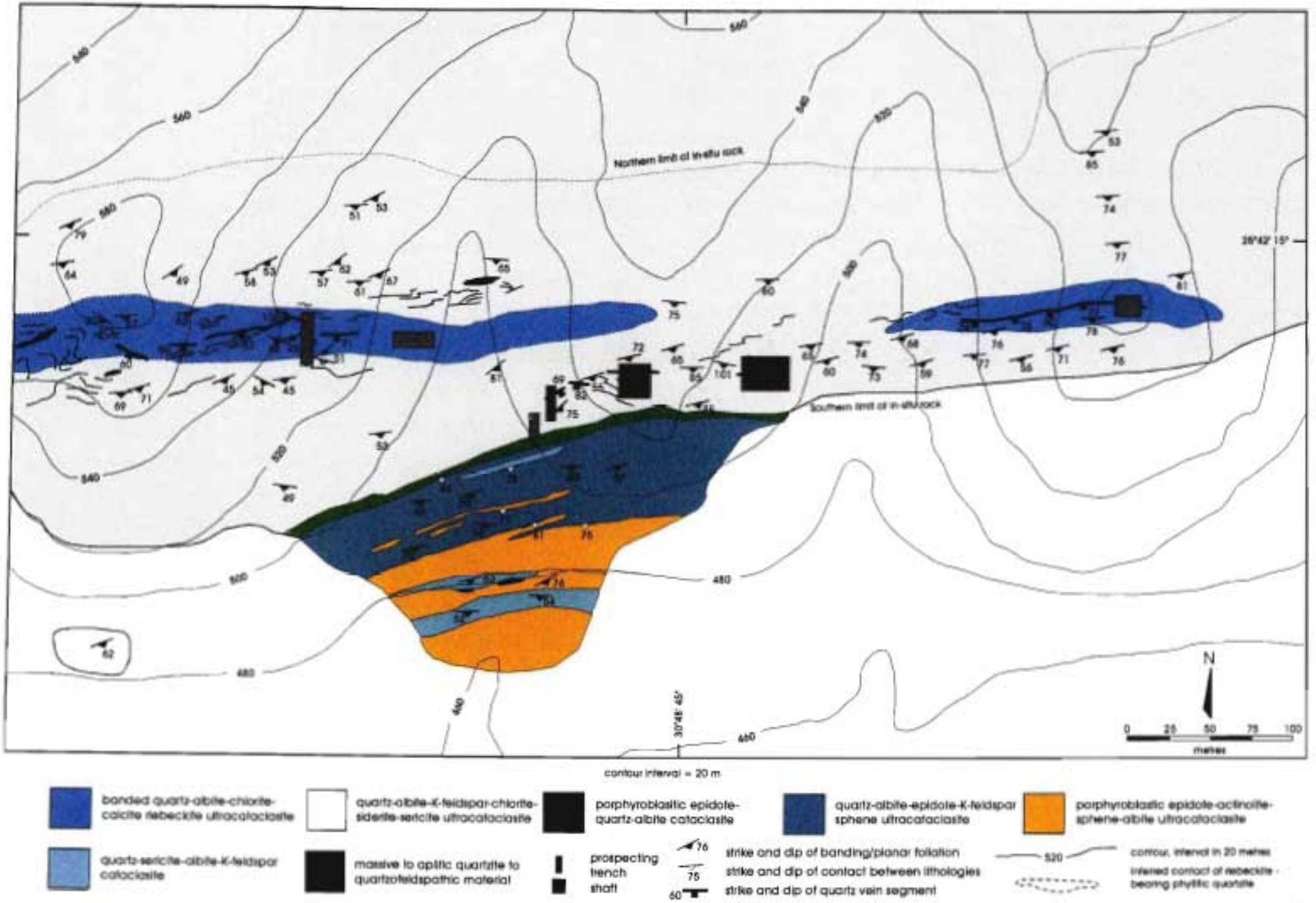

Figure 3.3 The northern Mfongosi Valley field area. Note the lenticular form of the riebeckite-bearing phyllitic quartzite which hosts the abundant veining. The massive to aplitic, quartzitic to quartzofeldspathic veins are at varying attitudes, with the banding/foliation having deformed around them

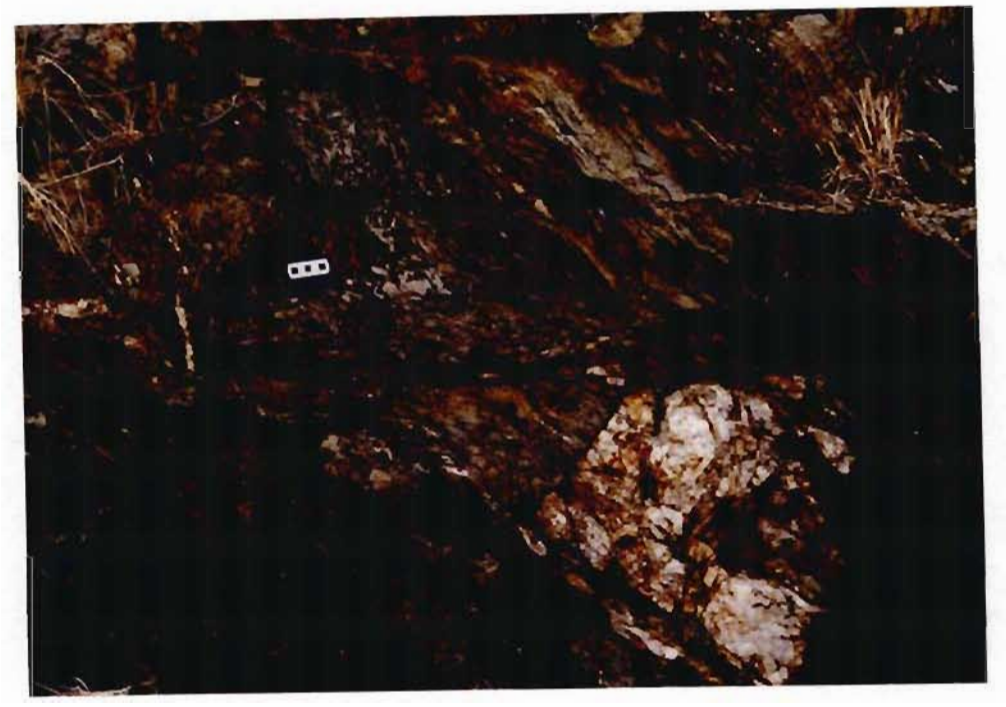

Figure 3.4 a The host rock to veining in the northern Mfongosi Valley area. Note the subtle blue colour imparted by minor quantities of riebeckite

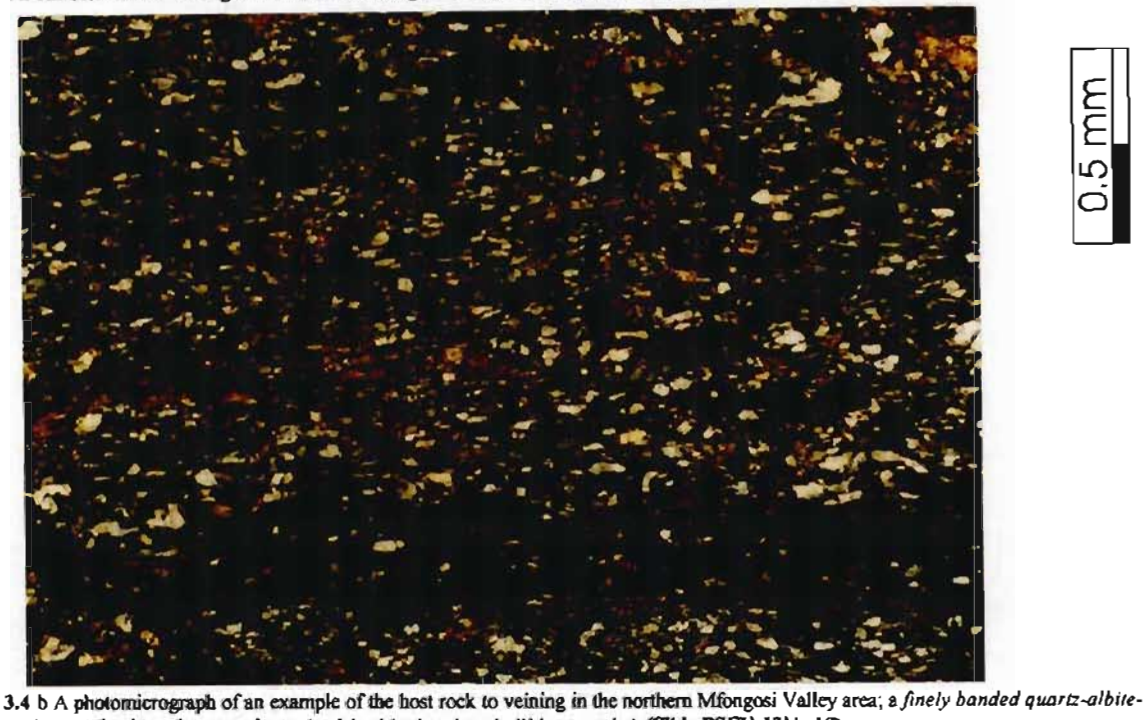

Figure 3.4 b A photomicrograph of an example of the host rock to veining in the northern Mfongosi Valley area; a *finely banded quartz-albite-chlorite-calcite-riebeckite ultracataclasite* (= riebeckite-bearing phyllitic quartzite) ***(Slide PSFU-12b)***. XP.

The rock type surrounding, in turn, the extensive lenses of highly veined host rock is a dark yellow to light reddish orange *quartz-albite-K-feldspar-chlorite-siderite-sericite ultracataclasite* (Figures 3.3 and 3.5 a, b). A very weak schistosity is developed in places although the main texture is one of a cataclastic rock similar to the host rock to veining. This *phyllitic quartzite* constitutes a large portion of the neighbouring spurs. Similarities between the phyllitic quartzite and the riebeckite-bearing phyllitic quartzite include pre-cataclastic quartz and

albite in calcite/siderite stringers, layers of magnetite- and haematite-rich pycnochlorite and a myriad of late fractures and shears. Calcite-chlorite-sericite glomeroporphyroblasts and rare epidote-quartz-calcite palimpsest amygdales (*cf.* Matthews, 1959) are the only kinematic indicators which, unfortunately, display variable senses of movement in σ- and δ-structures presumably due to shearing and cataclasis being accompanied by intense flattening (Passchier and Simpson, 1986). These patterns have furthermore been complicated by cross-faulting along fanning micro-faults.

The contrast between the phyllitic quartzite and the riebeckite-bearing phyllitic quartzite (host rock to veining) is gradational over 10-20 cm and the exact definition of margins to the host rock lenses is difficult. The indicated contacts on Figure 3.3 are therefore approximate.

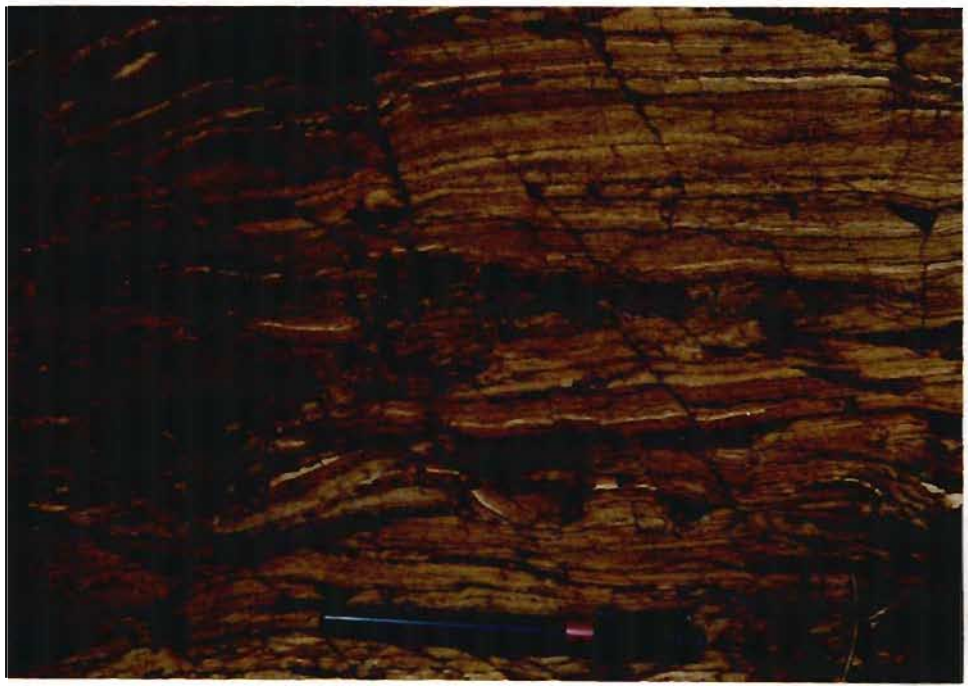

Figure 3.5 ▪ The rock type which surrounds the lensoid riebeckite-bearing phyllitic quartzite; a phyllitic quartzite

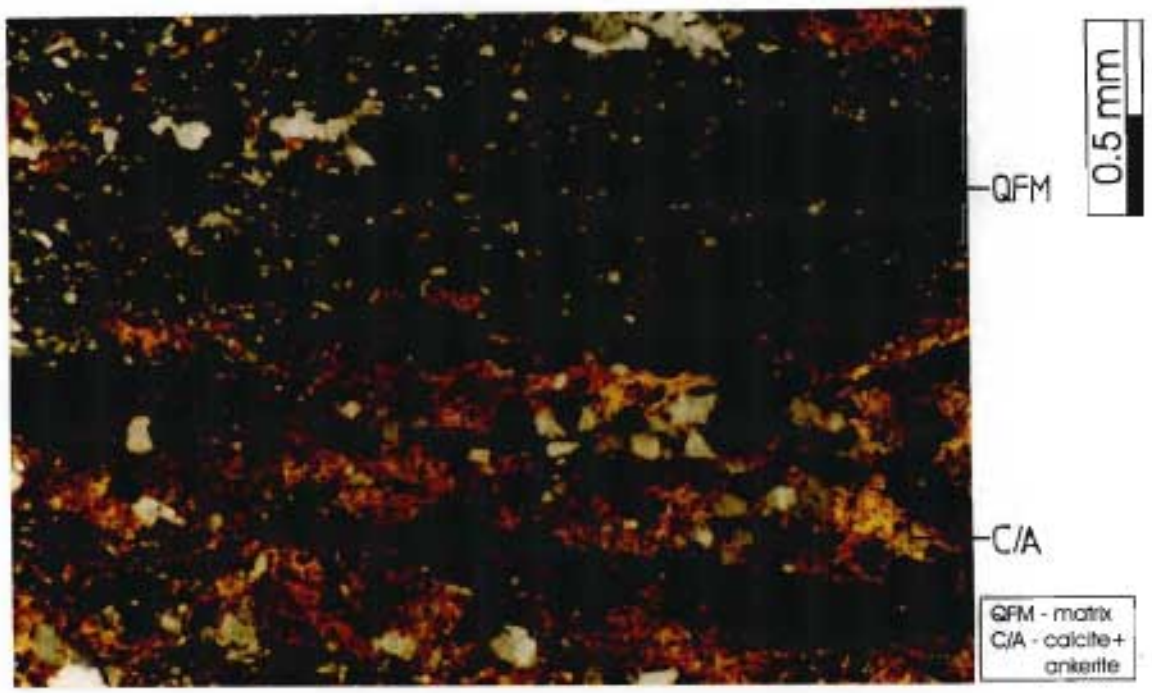

Figure 3.5 b Mfongosi tectonic melange matrix consisting of *quartz-albite-K-feldspar-chlorite-siderite-sericite ultracataclasite*. Note the abundant calcite and ankerite shielding larger quartz and feldspar crystals from the cataclastic deformation which has affected adjacent layers (= phyllitic quartzite) (***Slide PSFU - 2a***). XP.

To the south of the three spurs containing the northern Mfongosi Valley veining is a highly deformed zone in which the remains of individual lithologies are distinguishable (Figure 3.3). Immediately south of the main body of phyllitic quartzite is a tectonically conformable 7 m thick band of retrogressed *porphyroblastic epidote-quartz-albite schist/cataclasite* (Figure 3.6) followed to the south by an extensively veined layer of *quartz-albite-epidote-K-feldspar-sphene ultracataclasite* (Figure 3.7) with lenses of Mn-stained quartzite. To the south of this ultracataclasite is a *porphyroblastic epidote-actinolite-sphene-albite ultracataclasite* (Figure 3.8) with lenses of *quartz-sericite-albite-K-feldspar cataclasite*.

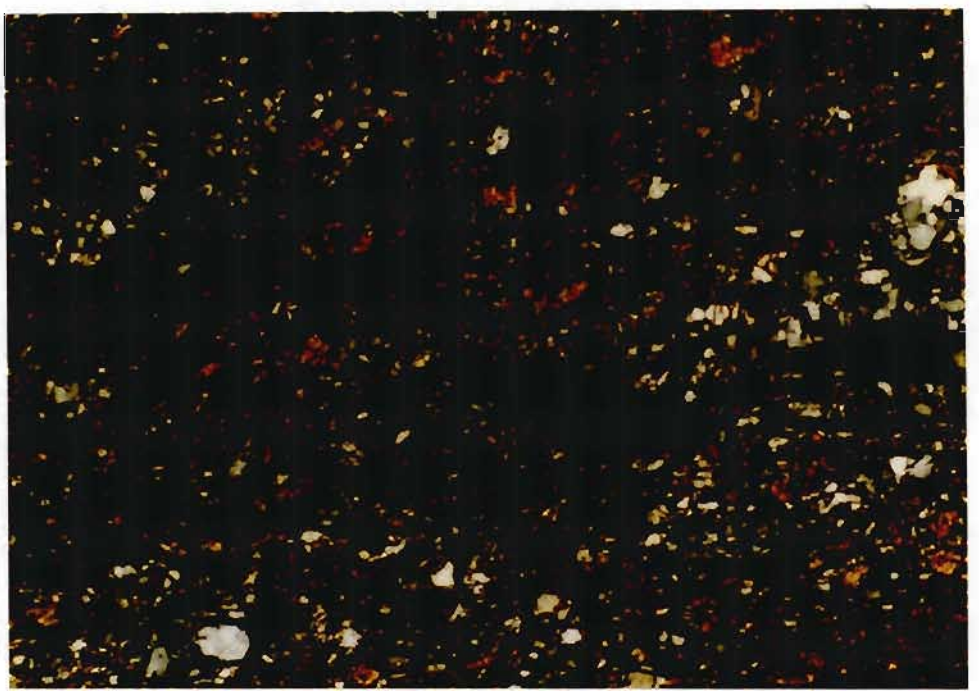

Figure 3.6 Part of the tectonically conformable sequence to the south of the vein-hosted workings; a *porphyroblastic epidote-quartz-albite schist/cataclasite* ***(Slide PSFU-38)***. XP.

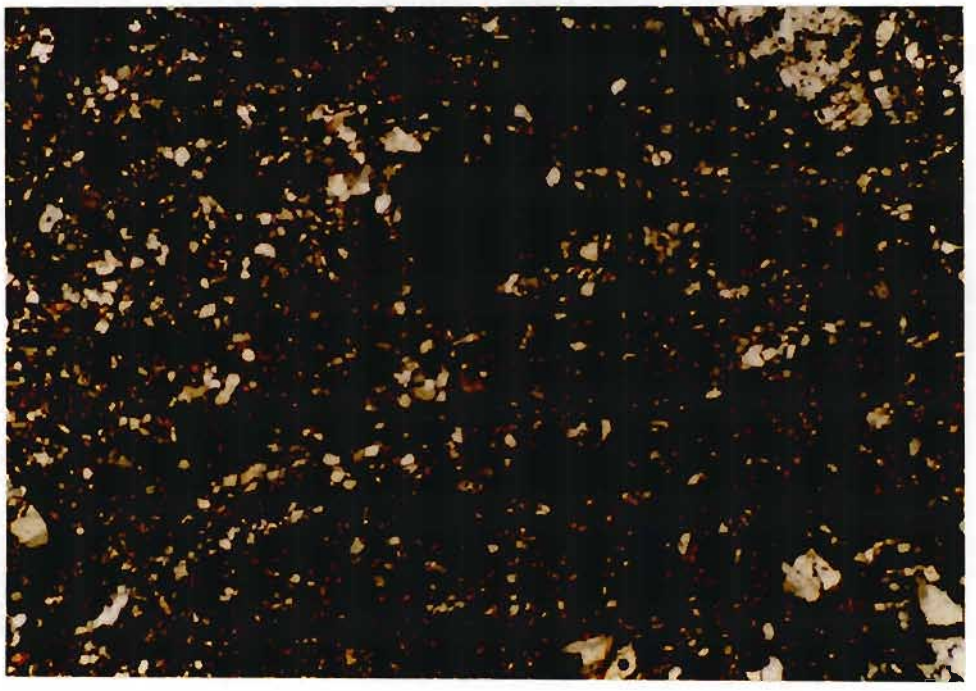

Figure 3.7 Part of the tectonically conformable sequence to the south of the vein-hosted workings; a *quartz-albite-epidote-K-feldspar-sphene ultracataclasite* ***(Slide PSFU-34)***. XP.

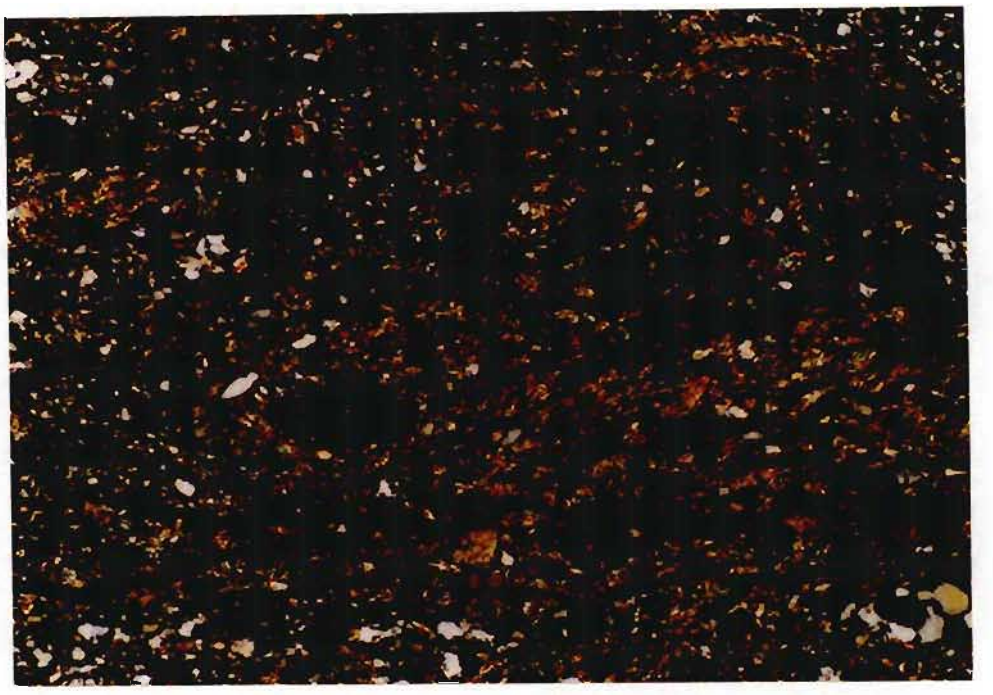

Figure 3.8 Part of the tectonically conformable sequence to the south of the vein-hosted workings; a *porphyroblastic epidote-actinolite-sphene-albite ultracataclasite (Slide PSFU-30)*. XP.

Distinction between layers is difficult in the field and is only possible in thin and polished section. Such examination indicates that a blue-green colour and relatively positive weathering caused by riebeckite and/or epidote; a dark yellow to light reddish-orange colour and relatively negative weathering is due to an abundance of chlorite and/or sericite bands in the phyllitic quartzite. These conclusions are similar to those deduced from outcrops of Mfongosi Group rocks in the southern Mfongosi Valley field area (Chapter 4).

3.3) Structural Geology

a) Banding/Foliation

The general trend of the deposits and workings across the three spurs is 084° which matches the contoured maximum of S_{01} of 083/59° in the riebeckite-bearing phyllitic quartzite and the phyllitic quartzite (Figure 3.9). The banding is refracted or bent around the larger quartzofeldspathic clasts/veins while smaller quartz vein fragments or clasts have been rotated into parallelism with the banding. Consequently the majority of readings on the banding and foliation were taken away from the quartz clast/banding contacts although the orientations and nature of fold structures near quartz vein fragments were recorded.

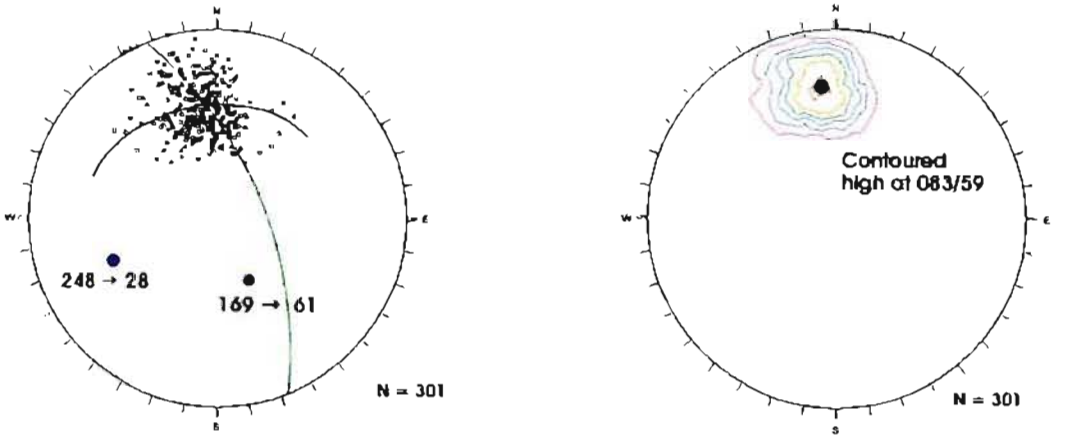

Figure 3.9 Equal angle and contoured equal area lower hemisphere stereonet plots of poles to banding (S_{01}) in the Mfongosi schist in the northern Mfongosi Valley field area. Contoured data indicate a maximum or contoured high at 083/59°. Two possible fold axes may be deduced, one at 248→28° (pole to great circle) and the other at 169→61° (cone axis). Alternatively, deformation of the banding around hidden competent clasts (in the third dimension) may contribute to the spread of data on stereonets N = 301

A foliation discordancy is preserved in several localities (Figure 3.10). The banding in discordant sections was recorded as S_2 and describes a fold axis of 260→47° (Figure 3.11). Two fold axes may be calculated for many of the localities. It appears that S_{01} and S_2 are being folded by the same deformation event.

Figure 3.10 Foliation discordancy in the Mfongosi melange; S_{01} and S_1 occur at acute angles to one another

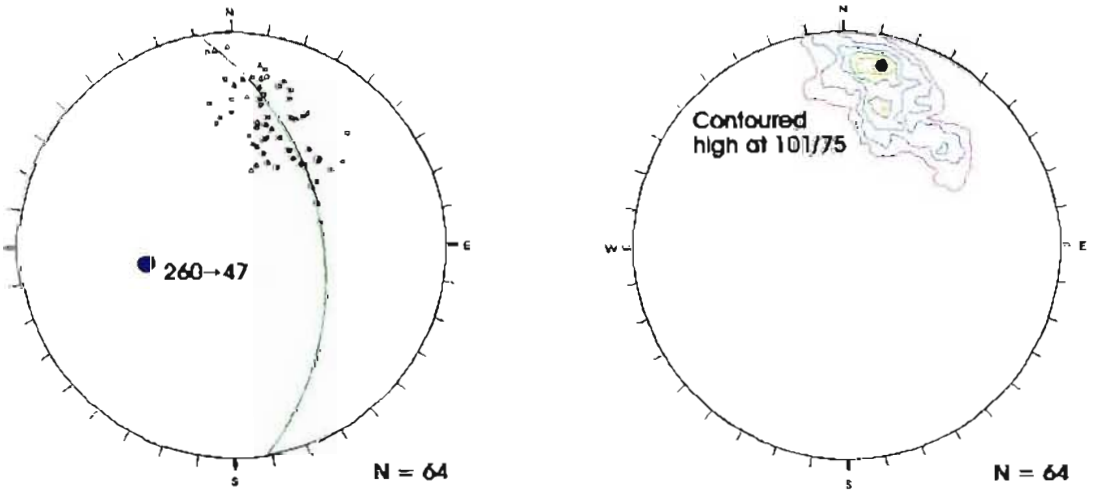

Figure 3.11 Equal angle and contoured equal area lower hemisphere stereonet projections of the discordant foliation (S_1) in the Mfongosi melange. A great circle fitted to the data indicates a cylindrical fold axis plunging at 47° towards 260°. Contoured high at 101/75° N = 64.

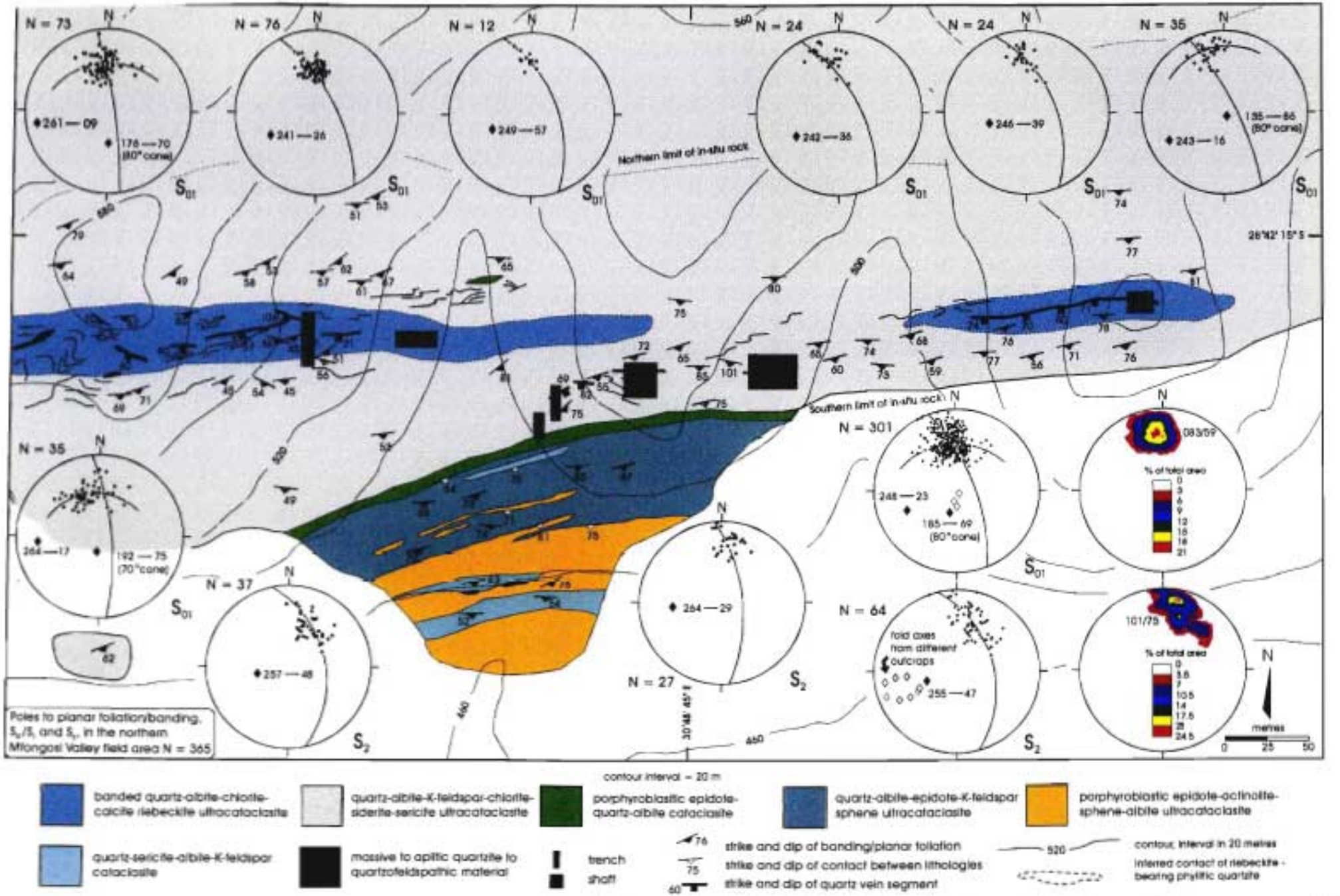

Figure 3.12 Poles to S_{01}, S, and S_2 in the northern Mfongosi Valley area. Best fit great and small circles to data are as depicted. Squares and rectangles outline the prospecting trenches and/or shafts. The summation stereonets are of equal angle poles to planes and contoured equal area plots with maxima as indicated in the text N = 365

b) Folding

Some indication of late-tectonic movement may be gauged from intrafolial folds within banding (Figures 3.13, 3.14 and 3.15; Ramsay and Huber, 1983; Price and Cosgrove, 1990). Left-lateral movement along a shear plane parallel to the banding is dominant despite a contradictory shear sense. This pattern of left- and right-lateral intrafolial folds may occur together to form box folds which are disrupted by brittle-ductile shears. Other than monoclinal, intrafolial kink folds, there are no other shear sense indicators observable in the field. The kink folds usually have minimum dimensions as follows: amplitudes - 4-6 cm, wavelengths - 10 cm, with axes which plunge to the southwest (Figure 3.13, 3.14). Two contoured maxima, on equal area plots, of the plunge and direction of plunge of fold axes are 217→27° and 235→42°. The smaller wavelength kink folds are superimposed on larger buckle folds, usually with amplitudes of 60 cm and wavelengths 3-7m. The larger-amplitude folds plunge preferentially towards the southeast and have a poorly-defined contoured high at 168→53° (Figure 3.15). Kink folds are more abundant in proximity to large quartzofeldspathic vein segments which are markedly discordant to the banding. The variation in fold axis orientation across the northern Mfongosi Valley area is shown in Figure 3.16. All fold generations are not evident at every outcrop whilst larger wavelength flexures occur in the western part of the outcrop where veining is most abundant.

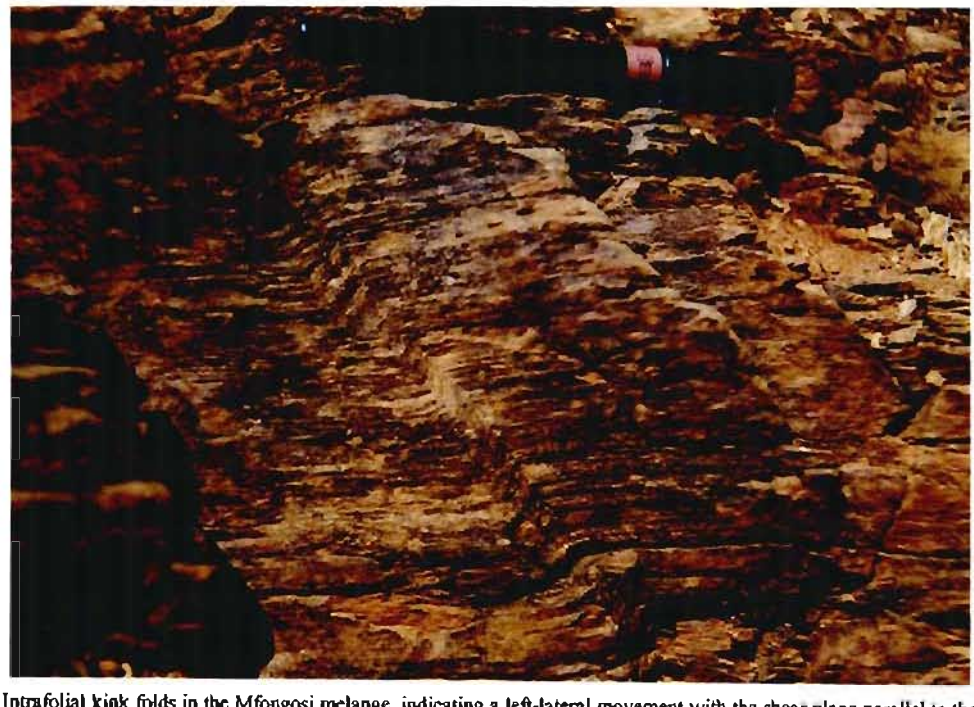

Figure 3.13 Intrafolial kink folds in the Mfongosi melange, indicating a left-lateral movement with the shear plane parallel to the banding in the ultracataclasitic

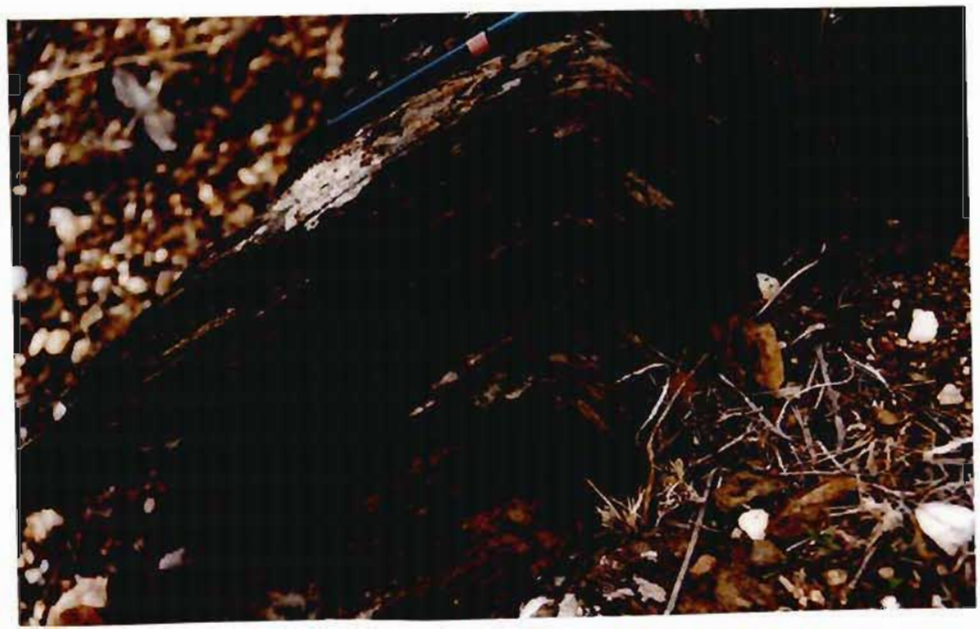

Figure 3.14 Larger kink folds, oriented in the same direction and with similar plunges as the smaller intrafolial kink folds. These folds are usually evident near a large quartzofeldspathic clast.

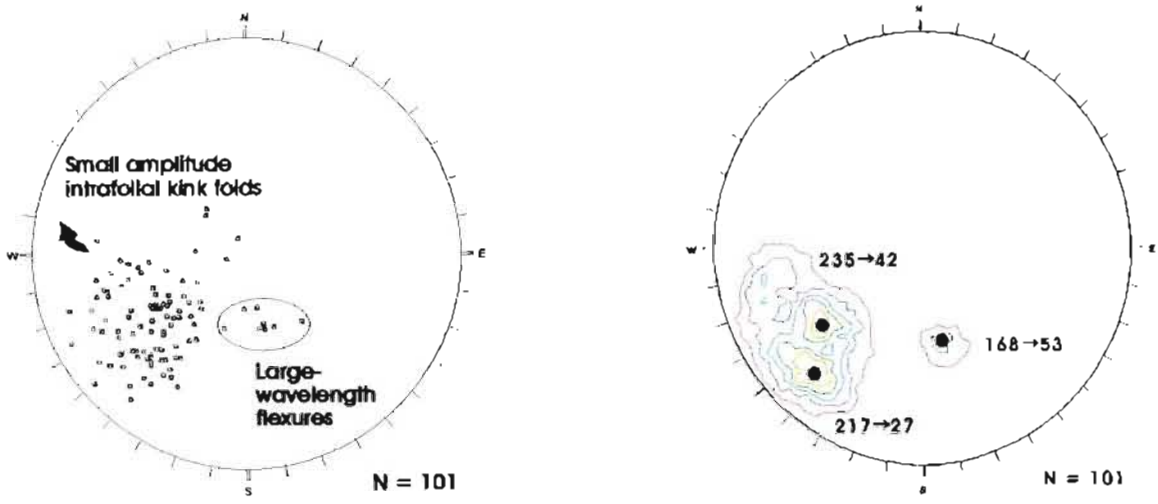

Figure 3.15 Equal angle and contoured equal area lower hemisphere stereonet plots of plunge and direction of plunge of kink folds (dominantly plunging towards the SW) with contoured highs at 217→27° and 235→42°, and larger-wavelength buckle folds or flexures which preferentially plunge towards the SE with a contoured high at 168→53° N = 101

Where vein segments are absent and kink folding persists, no other causal factor for the formation of kink folds need be invoked; examination of dongas between the three spurs indicate that surface folds are caused by larger clasts in sub-outcrop. This factor may explain the variability of intrafolial fold axis orientation, that is, measurements taken at different elevations.

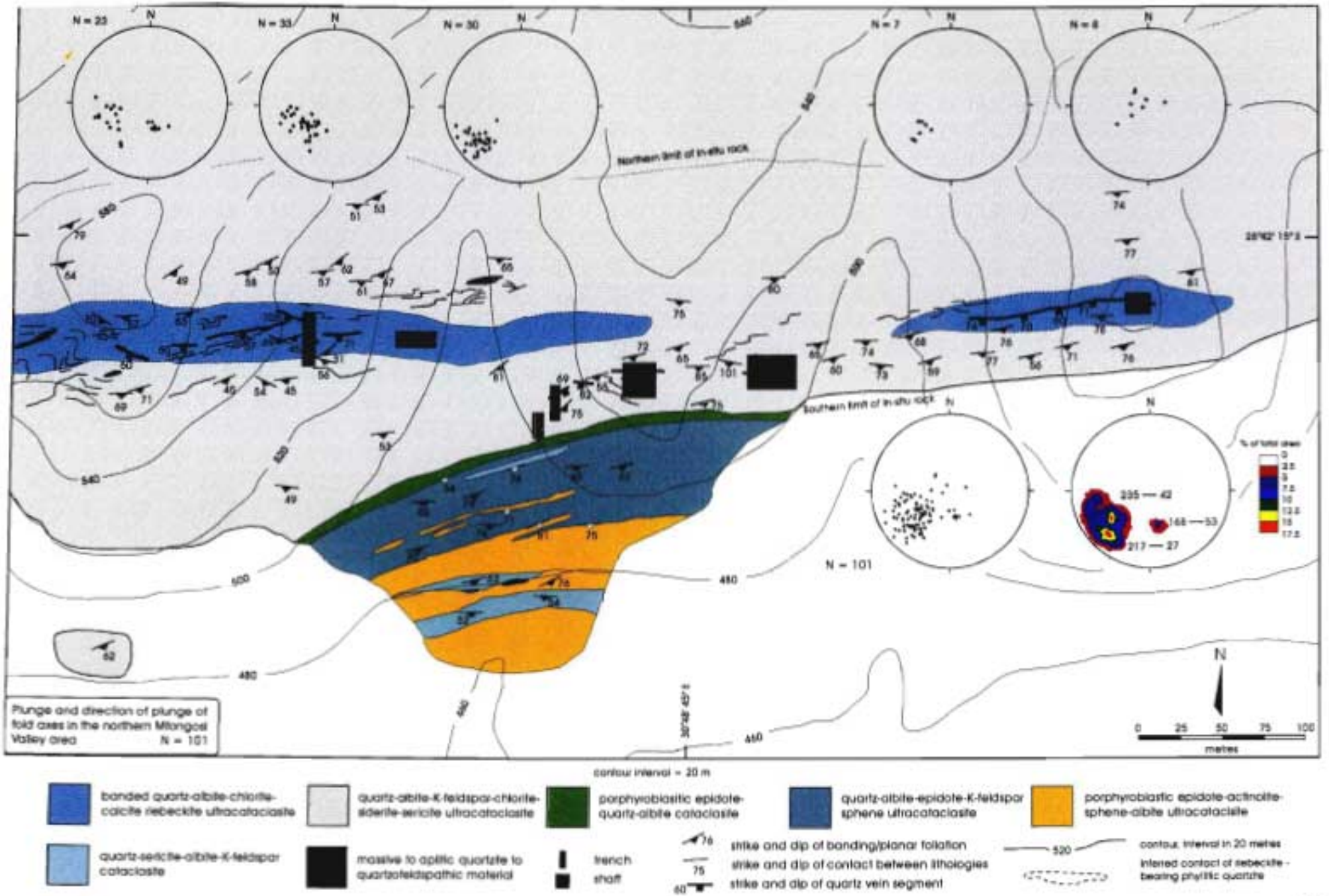

Figure 3.16 Plunge and direction of plunge of fold axes observed in the field. Both intrafolial kink folds and large-wavelength flexures are present. The summation stereonets comprise an equal angle plot of fold axis azimuths and a contoured equal area plot of the same data. Contoured maxima are as discussed in the text N = 101

c) Veining

Veining in the northern Mfongosi Valley area occurs as vein segments which form competent clasts in ultracataclasite. The quartzofeldspathic clasts have distinct vuggy textures due to the weathering out of sulphides and metallic oxides. Field observations and polished section examination of the veins or vein segments across the northern Mfongosi Valley area reveal sparse metallic phases. Magnetite and haematite are the most common opaque minerals in polished section while highly altered euhedral pyrite, galena and argentite occur on vein/clast margins.

Consistent banding orientation versus clast size show an antipathetic relationship; the larger the clasts (0.5 to 4 m long), the greater the effect on banding and the greater the zone of contact strain in the matrix (Figure 3.17). Smaller quartzofeldspathic fragments do not affect banding orientation and are conformable to the banding. The inference is that once continuous veins have acted as competent clasts in a relatively incompetent matrix during the final stages of deformation , i.e. - continued deformation of the Mfongosi melange has completely disrupted any vestige of initial vein orientation and has segmented the veins. Rare rootless fold hinges which acted as clasts substantially disrupted the adjacent banding due to their irregular clast shape (Figure 3.18). Rootless folds are best observed in the prospecting trenches on each hill.

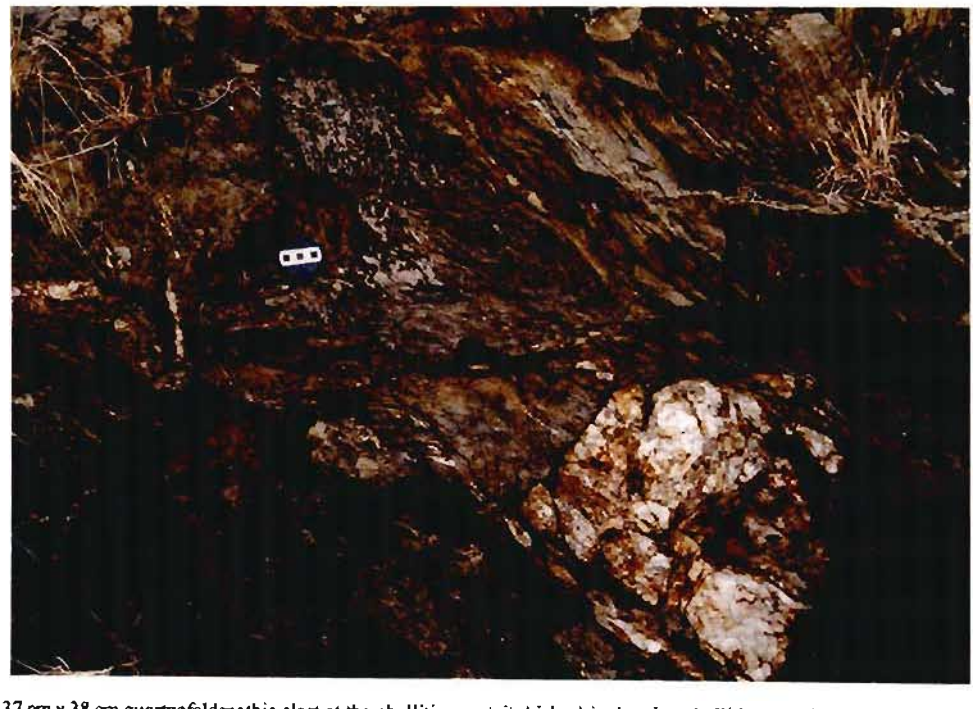

Figure 3.17 A 37 cm x 38 cm quartzofeldspathic clast at the phyllitic quartzite/riebeckite-bearing phyllitic quartzite contact. Note the concordance of the contact between the two phyllitic quartzites and banding. Note also the intense disruption of banding near the clast. Eastern side of westernmost trench of the field area.

Figure 3.18 Rootless fold in competent quartzofeldspathic clast in the western side of the westernmost trench in the PSFU area. The banding could not be traced around the rootless fold. Pen is 15 cm in length.

Discordancy between vein segments/clasts and banding in the ultracataclasite is more pronounced in the eastern portion of the field area where veins are normally 30 cm in thickness. Smaller veins have been compacted and compressed against a large quartzofeldspathic vein (up to 2 m wide) in the eastern part of the field area as the host rock has flowed around this vein. The southern side of the large vein comprises a tectonic melange with greater than 60% vein fragments by volume. Orientations of the long axes of quartz vein segments or clasts show distributions in orientation between those of S_{01} and S_2 (Figure 3.19). A pole to the great circle fit to data plunges at 47° towards 217°. Two contoured highs of the data are evident, one at 082/70° and the other at 102/56°. Outcrop distributions of vein orientations are shown in Figure 3.20. No left-stepping or right-stepping vein patterns of typical shear systems are evident. Vein segments may be considered as clasts which are hosted and rotated in an incompetent matrix of phyllitic quartzite and riebeckite-bearing phyllitic quartzite or cataclasite.

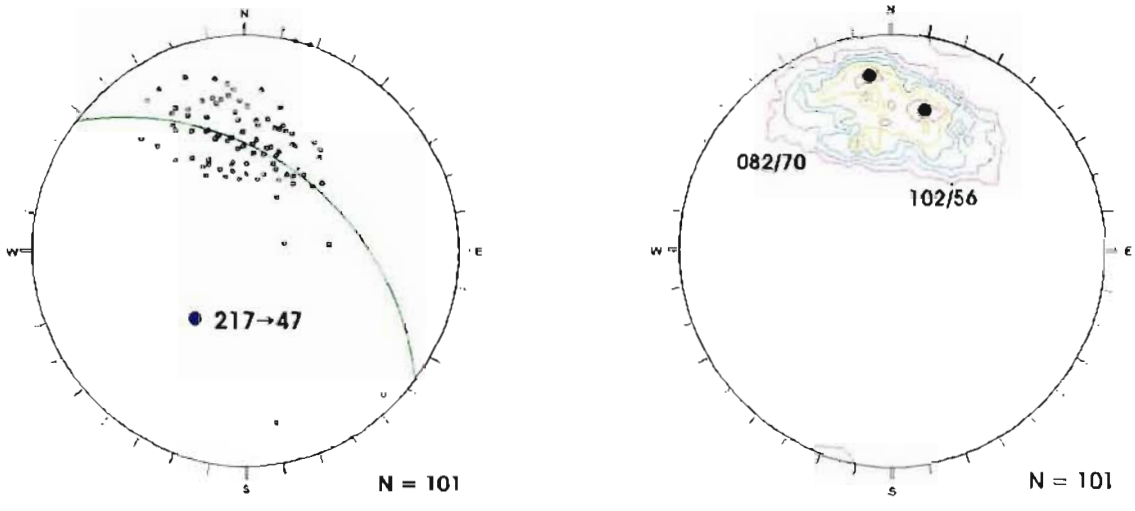

Figure 3.19 Equal angle and contoured equal area lower hemisphere stereonet plots of poles to the margins of quartzofeldspathic clasts. The fold axis form a great circle fit to data is 217→47 N = 101

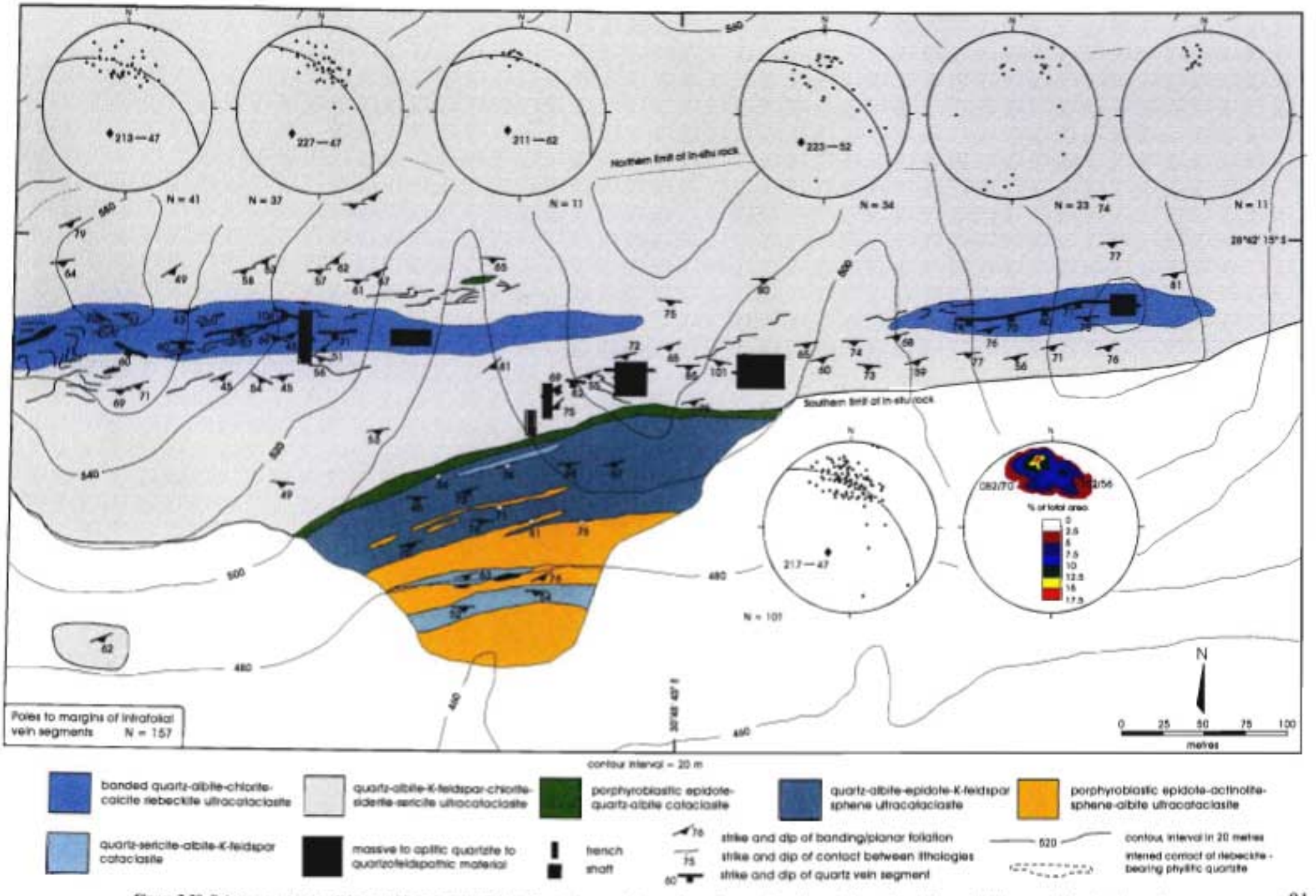

Figure 3.20 Poles to massive to aplitic quartzitic and quartzofeldspathic veining on surface and in underground workings of the northern Mfongosi Valley area. The orientations of the clasts falls between that of S_n and S_1 in three-dimensional space. The summation stereonets utilise only 101 points of the 157 measured data points N = 157

3.4) Comparison of Structural Features with Analogue Models

To the south of the northern Mfongosi valley outcrop is a transitional zone (Harmer, 1979; this study) between conformable, distinct units which have undergone isoclinal folding and shearing, and the northern Mfongosi tectonic melange which is dominated by cataclasites and ultracataclasites wherein little or no distinguishable original lithologies exist. Rectangular particles, as opposed to spherical or circular particles (Berthé *et al.*, 1979; Passchier and Simpson, 1986; Van Den Driessche and Brun, 1987; Bjornerud, 1989) have been modelled in various studies and are considered relevant to the veining in this field area as most vein segments, termed "clasts" in this study, are rectangular in shape. The simplest analogue modelling involves single, isolated, rigid, rectangular particles in a Newtonian fluid undergoing simple or pure shear (Ramsay, 1967; Fernandez, 1987; Ildefonse *et al.*, 1992; Ildefonse and Mancktelow, 1993) while more complex models include multiple interacting rigid particles.

The interaction between adjacent rigid particles at different particle spacing and whether or not the concept of total strain (≈ collective contact strain) around a group of interacting particles is factored into such models (Ildefonse *et al.*, 1992). The condition of coherence or non-slip between a rigid particle and the surrounding matrix is tested as this affects the rate at which particles rotate and/or align themselves with the principal shear direction (Ildefonse and Mancktelow, 1993). The effect of particle rotation on the adjacent matrix and the subsequent extent of the passive matrix deformation in relation to the particle size, that is, what the extent of the zone of contact strain around a rigid particle is (Ramsay and Huber, 1983; Bjornerud, 1989), is ascertained. Finally, the determination of shear strain from the final orientations of initially randomly-oriented rigid, linear particles which have undergone homogeneous two-dimensional deformation will be accomplished by applying the mathematical and graphical solution of (Fernandez, 1987) . First a description will be made of the structural features of modelled small-scale shear systems which are similar to those found in the Mfongosi tectonic melange.

a) Multiple Interacting Rigid Particles

Rigid particles in a Newtonian fluid in a simple shear system produce certain features which become more apparent with increased simple shear (γ). The conditions and results of modelling these systems are directly comparable to the clast/matrix relationship in the field:

- a homogeneous, isotropic fluid matrix with a finite yield strength (Ramsay, 1967; Bjornerud, 1989) under no inertial forces, is assumed. The ultracataclasite is unlikely to be exactly similar in mechanical properties and yield strength to an ideal matrix material. Concentrations of smaller vein segments between the larger quartz clasts detract from matrix homogeneity.
- the presence of differently oriented rigid particles leads to heterogeneous strain distribution in the matrix
- the shear strain value for structure initiation depends strongly upon rigid particle size relative to the spacing of the marker lines (the marker lines on an initially orthogonal grid, of which one direction is parallel to the shear direction, may be equated with S_{01}). As clast radius or size increases relative to the layer thickness or foliation spacing the shear strain required to produce a particular feature decreases (Bjornerud, 1989). The shear strain value assigned to a given structure is thus only valid if the clast size/layer spacing is specified. In the Mfongosi melange clast rotation strongly effects host foliation and a zone of contact strain up to three times the clast length is produced in the adjacent matrix. Contact strain due to clast rotation is pronounced in areas of high clast concentration and/or where large vein segments/clast have been rotated in the cataclasite (eg. the western extent of the westernmost lens of riebeckite-bearing phyllitic quartzite - Figure 3.20). The measured clast size/layer spacing here is in the range 30:1 to 70:1.
- from thin section studies the conditions of no-slip (coherence) and slip ("uncoherence" - Bjornerud, 1989; Ildefonse and Mancktelow, 1993) were operative at the vein/matrix contact. The range of features which developed as a result of both conditions applying is consequently extremely complex, however, strain localization is greater in the case of slipping at the particle/matrix interface (Ildefonse and Mancktelow, 1993).
- interaction of the contact strain zone near individual vein segments has made for a complex deformation history with contradictory shear senses

Clasts in a simple shear system with slip at the particle/matrix contact and separated by a distance less than their lengths produce narrow zones of high shear strain which anastomose and ramp up from one level parallel to the shear plane to another linking parallel zones. The overall pattern in shear box experiments is very similar to that observed in S-C fabrics in shear zones (Berthé *et al.*, 1979; Ildefonse and Mancktelow, 1993). Rigid particles with their long axes initially parallel to the shear plane are important in the nucleation of discrete surfaces. This may explain the weak S_2 fabric in the Mfongosi melange (Figures 3.10, 3.11).

With increased shear strain and limited further rotation, the discrete C planes link up to form a set of continuous bands parallel to the shear direction. This typical feature of shear box models is comparable to the single cleavage/foliation in the tectonic melange adjacent to the 2 m-thick vein in the eastern part of the field area. Similar, but more diffuse features are observed in the case of particle/matrix coherence where a bulk strain zone around a number of rigid particles is more relevant than discrete S-C fabrics (Ildefonse *et al.*, 1992; Ildefonse and Mancktelow, 1993).

Furthermore, particle rotation is significantly disturbed when the distance between adjacent particles of equal size is less than the lengths of those particles, that is, only in very concentrated suspensions of rigid particles (Ildefonse *et al.*, 1992). Ildefonse and Fernandez (1988) and Ildefonse *et al.* (1992) demonstrated that the interactions between particles were responsible for a decrease in the fabric intensity (e.g. S-C cleavage) and, in the case of simple shear, for a perturbation in the cyclic rotation of the fabric axis in addition to rotation of individual clasts. For similar distances between unequal-sized particles (eg. compression of smaller veins against larger veins in the eastern part of the field area) the smaller particles or veins are always more affected (Ildefonse *et al.*, 1992).

b) Single Rotating Object in a Simple Shear System

Other features in the Mfongosi melange may be explained by focussing on structures which form directly adjacent to a single rotating clast:

S_0/S_2 discordancy - in the slipping interface scenario (Figure 3.21) localized high strain zones produce marked discordancies between initially orthogonal marker lines (Ildefonse and Mancktelow, 1993). The discordancies are most pronounced when the particle is initially aligned in the same sense as the long axis of the shear strain ellipsoid (*op. cit.*, this study) and rotates towards the shear direction (Figure 3.21). In this respect the discordancies between previously formed fabrics (Figure 3.10) may be directly analogous to the discordancies between marker lines that were initially co-linear or parallel and the S_2 terminology adopted here may not be valid (ie, S_2 may be transposed S_1 or S_1' ?).

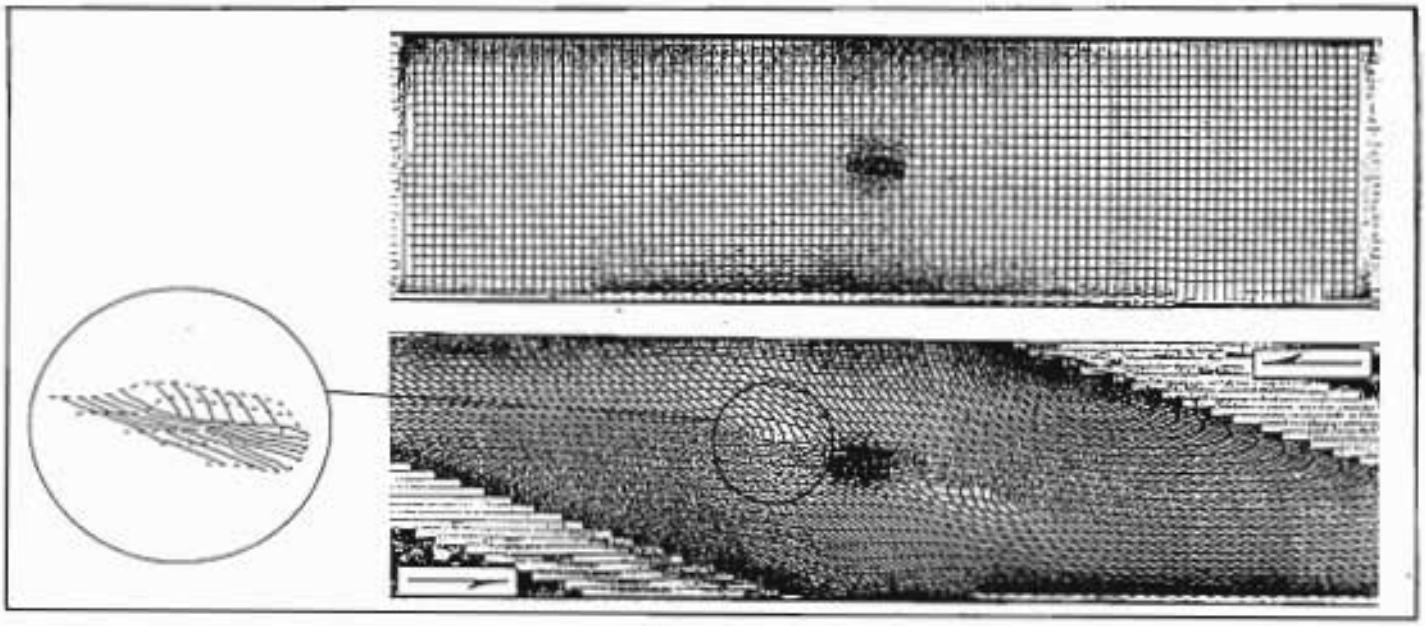

Figure 3.21 Initial and final stages of a simple shear run with a slipping interface at the particle-matrix contact. The effect of initial particle orientation is crucial to the development of fabric discordancies as explained in the text. Bulk shear strain here is 3. (Plate III of Ildefonse and Mancktelow, 1993). Inset shows the manner in which initially co-linear or parallel lines, similar to pre-formed banding in the northern Mfongosi Valley area, may become discordant.

Intrafolial folding - Bjornerud (1989) studied folded layering near rigid circular objects in simple shear deformation and developed ideal fold and strain patterns in the matrix.

The features that develop with increased shear strain are:

Low strains (γ = 0.69 to 1.37) - asymmetrical half folds or monoclines which are convex in the direction of clast rotation develop in the matrix close to the clast (Figure 3.22 - γ = 1.03). This is a direct result of objects undergoing angular rotation which pulls the adjacent matrix with it and therefore assumes coherence at the clast-matrix boundary.

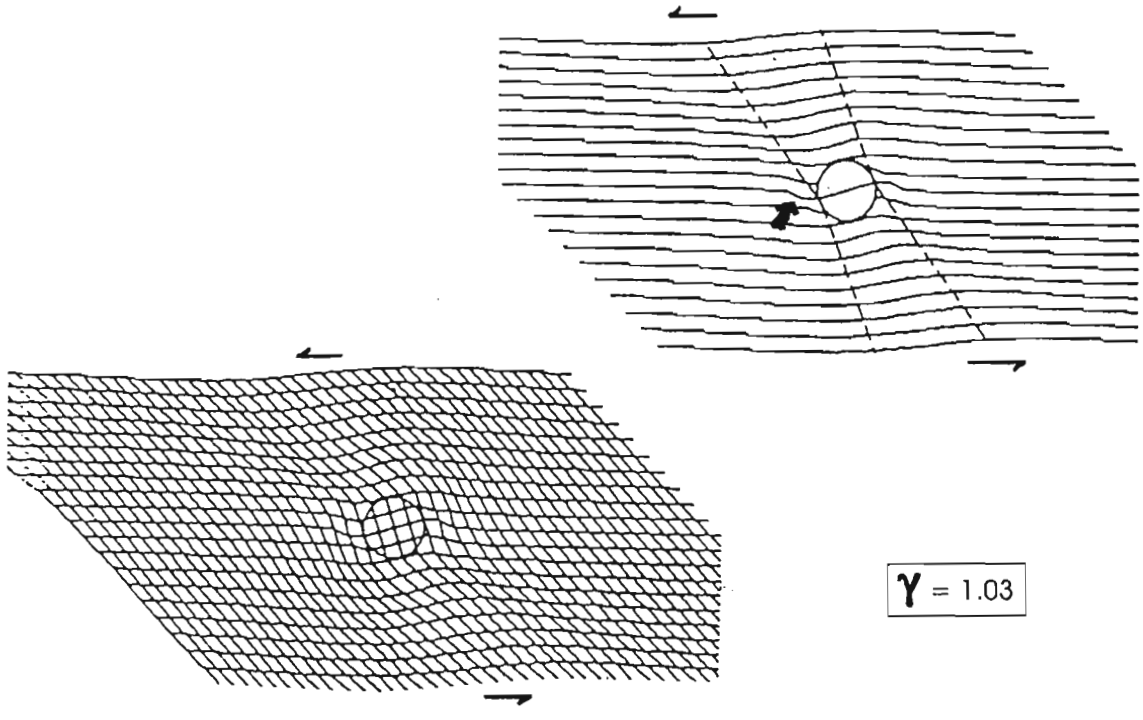

Figure 3.22 Deformation of an initially orthogonal grid in which is embedded a circular rigid object. γ = 1.03. Two folds are formed; a kink fold which indicates the direction of object rotation (arrow) and larger amplitude folds. The amplitudes of such folds grow while the thickness of the limbs decreases with increased strain (Figures 6 C and D of Bjornerud, 1989).

Intermediate strains (γ = 1.67 to 2.72) - with increasing shear strain the competent object continues to rotate and half-folds in adjacent layers begin to amplify while layer spacing in the fold limbs decreases further (Figure 3.23). As observed in the Mfongosi melange at a distance of about 3 times the clast diameter from the clast, open folds (*cf.* kink folds) become visible, the outer inflection points of which define the outer limits of the strain. When flexed zones on either side of the object have been translated out of the original positions of formation they enter a part of the velocity field where there is a significant component of motion perpendicular to the shear zone margins (Figure 3.23 - inset) and the result is the development of small folds in the flexed layering (kink folds).

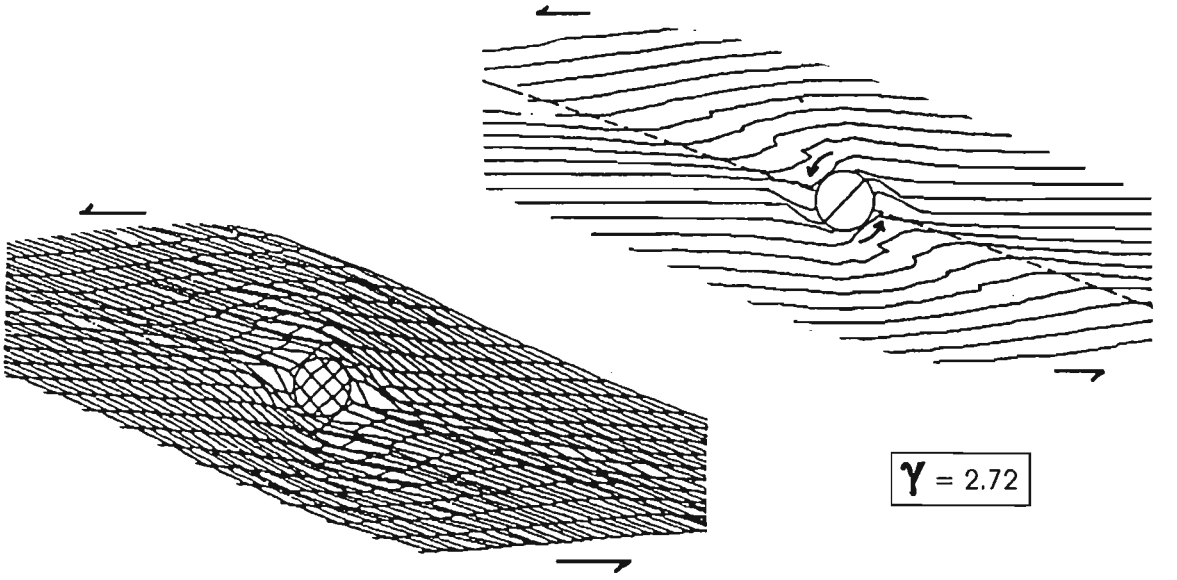

Figure 3.23 Results of intermediate shear strain ($\gamma = 2.72$). The larger wavelength folds become accentuated in the direction of rotation (marked) while the box folds decrease in wavelength and become tighter. Earlier-formed features are themselves passively deformed with increased shear strain. The dashed lines mark the band of thinned layers and the maximum finite strain direction (λ_1) (Figures 7 E and F of Bjornerud, 1989).

Higher shear strains ($\gamma = 5.95$), the "flap fold" zones extend away from the particles and enter fields of nearly homogeneous simple shear deformation with the result that the folds are tightened (Figure 3.24). Note also the potential for box fold development near the rotating particle, imparting a contradictory sense of movement in the field. With increased shear strain, a band of closely-spaced layering becomes visible (Figure 3.24) and persists through $\gamma = 6$. Simply put, the features developed at lower shear strains are themselves passively deformed with increasing shear strain. High finite strain zones are aligned parallel to the direction of the maximum finite stretch (Fernandez, 1987; Ildefonse *et al.*, 1992).

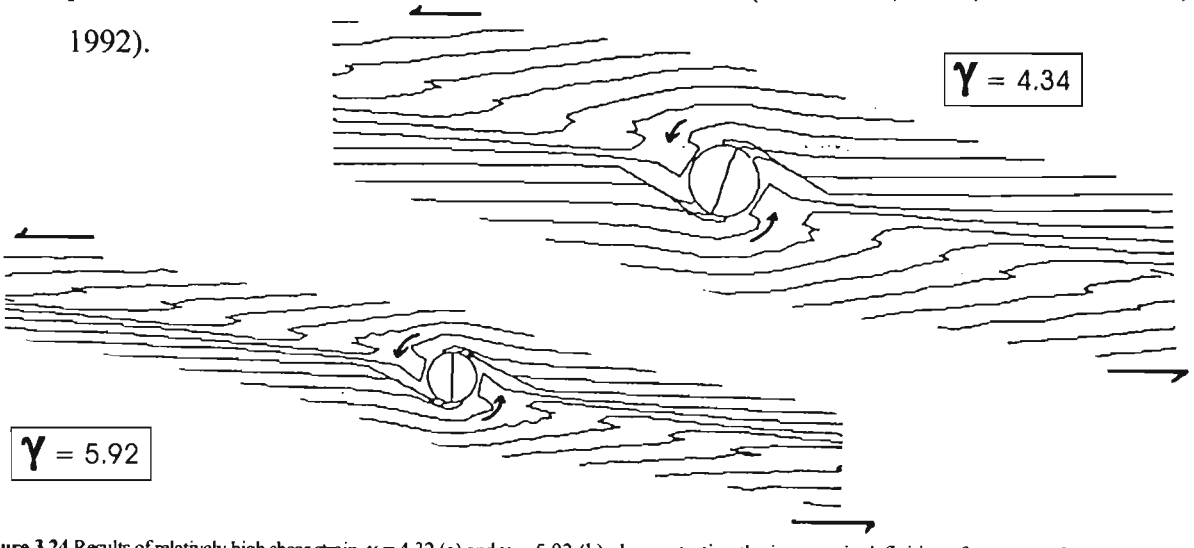

Figure 3.24 Results of relatively high shear strain, $\gamma = 4.32$ (a) and $\gamma = 5.92$ (b), demonstrating the increase in definition of structures formed at lower shear strains (Figures 9 A and B of Bjornerud, 1989).

The characteristic asymmetrical strain pattern around rigid, isolated particles is usually a reliable shear strain criterion but becomes unreliable at high concentrations of rigid particles (Ildefonse *et al.*, 1992) or with pure shear at right angles to the shear direction (Passchier and Simpson, 1986), hence the majority of intrafolial kink folds imply left-lateral movement (Figure 3.20).

c) Estimation of Shear Strain

The distribution of vein segments or clasts may be used to determine the amount of shear strain (or an indication of the amount of pure shear) which acted on the Mfongosi melange. Fernandez (1987) studied analogue models of rigid linear markers embedded in a viscous matrix undergoing homogeneous two-dimensional simple shear. The markers develop a preferred orientation which coincide with the gross orientation of the principal strain ellipse (*op. cit.*).

Simple shear transforms the long axis of a needle-like, passive and/or rigid marker from an angle (α) to an angle (α') with the X direction (the direction of shearing or the displacement direction - Ramsay and Huber, 1983; Fernandez, 1987; Figure 3.25). Note that θ and θ' refer to the angles between the major axis of the strain ellipsoid and the displacement direction. The relationships between these angles and shear strain (γ) are given in Ramsay (1967) and are set out in Appendix C1.

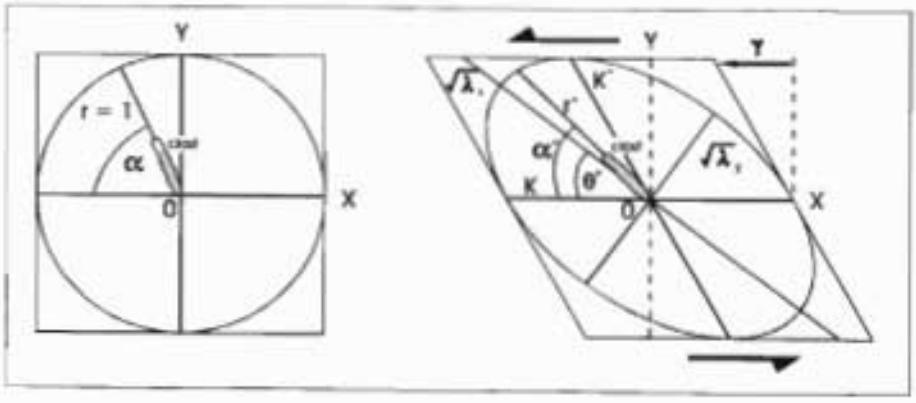

Figure 3.25 Distortion of a unit circle in simple shear. X - displacement direction, K and K' - lines of no finite longitudinal strain, θ and θ' - angle made by a radius r of the unit circle and the corresponding vector radius r' of the strain ellipse with direction X, respectively before and after deformation (after Figure 1 of Fernandez, 1987). α and α' refer to the angle between the clast length and the shear direction before and after shearing, respectively

The orientations of long axes of quartzofeldspathic clasts were used to evaluate the extent of simple shear. The plane with a pole to the contoured maximum of S_{01} data (Figure 3.9- 083/59°), is taken to be the shear plane. The strikes and dips of clast margins were reduced to a single plane which is perpendicular to 083/59° (ie 263/31°) an angle corresponding to α'. These trends, which are the same as the directions of plunge of the intersection lineations between the strike and dip of a clast and the plane 263/31°, were divided into groups at ten degree intervals measured anticlockwise (in a positive sense) from the displacement direction (Figure 3.26 - inset).

The number of veins with trends in the plane 263/31° (the XY plane in shear zone models) was normalized or divided by the average expected density, assuming a random initial orientation of particles prior to shearing. The average expected angular density of veins in a sector prior to shearing ($d\theta$) is 101/180° = 5.6. The use of θ follows Fernandez (1987) rather that Ramsay and Huber (1983). The D value for each interval, centred at ten degree increments anticlockwise from the shear direction 083° is calculated in Table 3.1 (Appendix C2). It is apparent that there are two main maxima, one centred at 283° and the other at 073°. There is therefore no concentration of data along an axis indicative of simple shear, instead, the two maxima signify pure shear along the 083/59° plane. Any evidence of simple shear may have been accentuated by superimposed pure shear. The D vs θ' plot for the different increments, without sufficient evaluation of field data, could be interpreted as evidence of simple shear with the shear plane being at a strike of less than 083°.

A graphical plot of D vs θ', compared with experimentally-derived plots in Fernandez (1987), shows that an apparent shear strain of $\gamma = 1.8$ is indicated by the data distribution with the D_m peak coinciding with the 083° direction (Figure 3.27). The value of D_m(5.04) using equation (7) in Appendix C2 , gives the same value as that obtained from the graphical plot and the best-fit curve (5) (Figure 3.27). An indication of the flattening of an asymmetrical arrangement of veins, the K and K' angles with the X-axis (as defined in Figure 3.25) are not equal. This system is a non-coaxial pure shear system superimposed on simple shear.

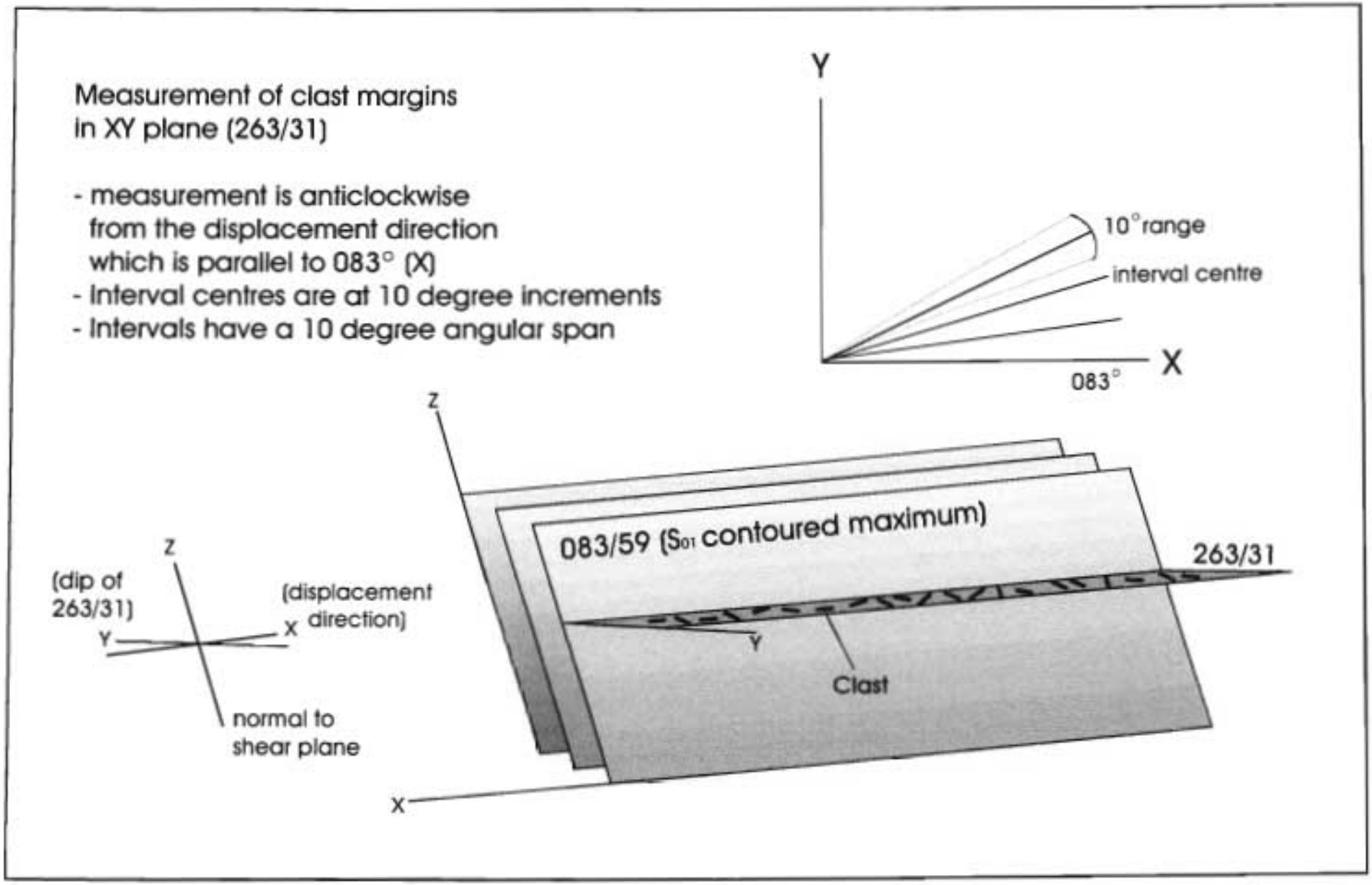

Figure 3.26 Framework of measurement of vein orientations which have been reduced to the plane 263/31 which is perpendicular to the average of the S_{01} plane and thus represents the XY plane in the analogue models of Fernandez (1987), Ildefonse *et al.* (1992) and Ildefonse and Mancktelow (1993)

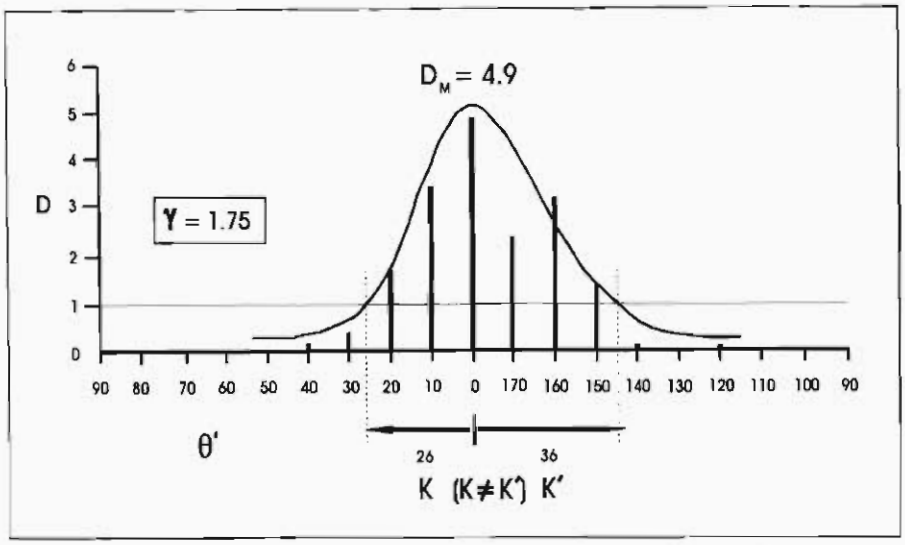

Figure 3.27 Plot of D vs ω' intervals and best fit curve for the northern Mfongosi area clast margins. A similar peak is that of γ = 1.8 (Fernandez, 1987)

Table 3.1 Data derived from the orientation of the long axes of quartzofeldspathic clasts in relation to the shear plane or displacement direction (N = 101).

C (interval centre)	Δθ (interval ranges)	Number of particles in range (f_o)	D (= f_o/5.6) (dθ = 5.6)	Visual Concentration
0	088-078	12	2.14	●●●●●●●●●●●●
10	078-068	19	3.4	●●●●●●●●●●●●●●●●●●●
20	068-058	10	1.78	●●●●●●●●●●
30	058-048	2	0.35	●●
40	048-038	1	0.17	●
50	038-028			
60	028-018			
70	018-008			
80	008-358			
90	358-348			
100	348-338			
110	338-328			
120	328-318	1	0.17	●
130	318-308			
140	308-298	1	0.17	●
150	298-288	8	1.43	●●●●●●●●
160	288-278	18	3.24	●●●●●●●●●●●●●●●●●●
170	278-268	14	2.5	●●●●●●●●●●●●●●
180	268-258	15	2.68	●●●●●●●●●●●●●●●

3.5) Metamorphism

Besides indications of major brittle deformation of the host rock to northern Mfongosi Valley veining, evidence of the maximum temperature conditions are scarce. Figure 3.28 (***Slide 12b***) displays relict riebeckite $\{Na_2Fe_3^{2+}Fe_2^{3+}[Si_8O_{22}](OH)_2\}$, altered to chlorite, indicateing maximum temperatures of 500°C (Deer *et al.*, 1992, Figure 2.29). Furthermore, lowering of riebeckite and magnesioriebeckite stability by Fe^{2+} substitution for Mg^{2+}, and Fe^{3+} substitution for Al^{3+}, makes it a poor indicator of the pressure conditions in the Na-amphiboles; glaucophane is the only exception to this (Deer *et al.*, 1992). "Riebeckite-out" can result from:

- increasing temperature - riebeckite → haematite + magnesioferrite + actinolite + fluid
- by retrogression of riebeckite to : albite + tremolite-actinolite

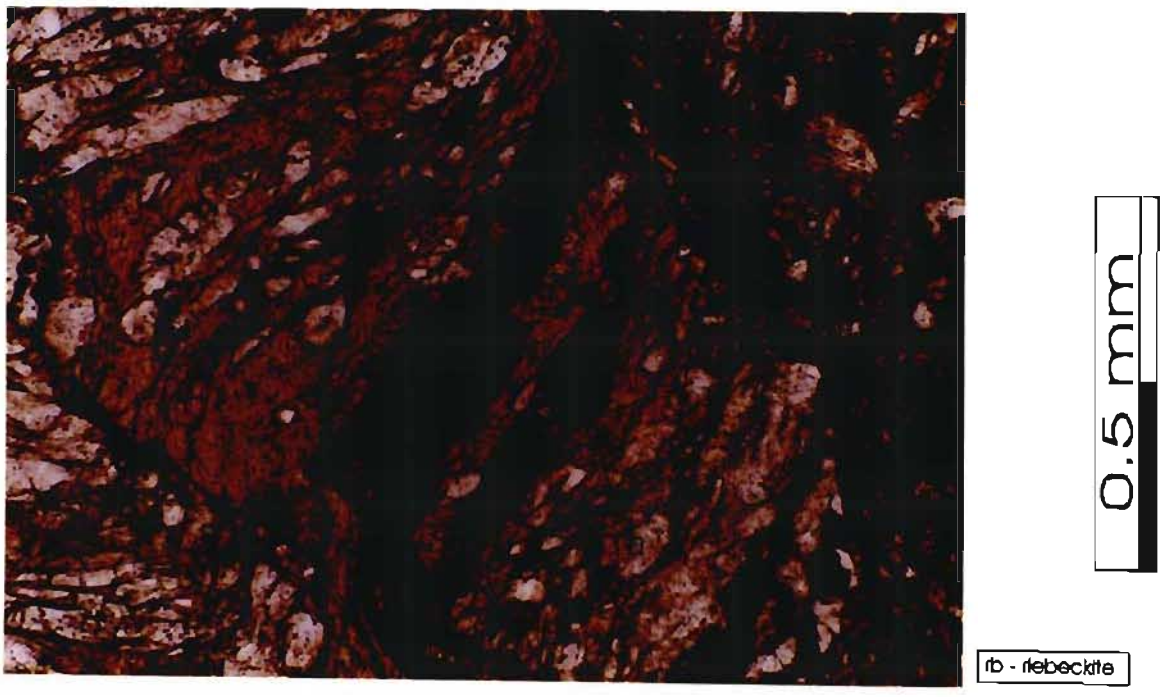

Figure 3.28 Relict riebeckite, highly altered to chlorite between two late brittle-ductile shears in the riebeckite-bearing phyllitic quartzite (***Slide PSFU 12b***). PPL.

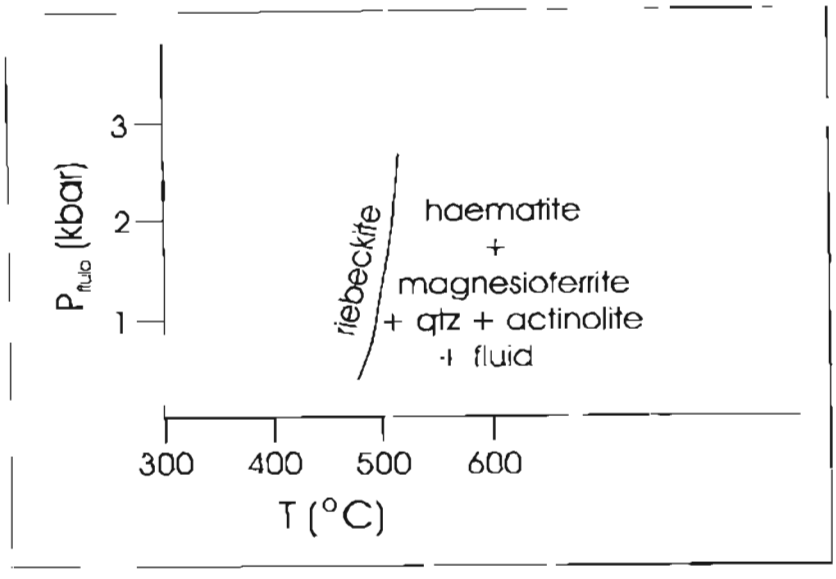

Figure 3.29 Stability curve of riebeckite; the control on riebeckite formation/breakdown is strongly temperature-dependant and the pressure control in negligible (Ernst, 1963 *in* Deer et al., 1992).

Riebeckite also occurs in columnar aggregates and deformed, segmented elongate laths. Epidote-actinolite facies ultracataclasite (***Slides PSFU-31 and 32***) indicates of temperature conditions below 500°C. This supports the conclusions of pre-cataclastic retrograde metamorphism as found in the Ngubevu area. The determination of protolith bulk assemblages and hence predictable metamorphic minerals, was not possible due to the extensive tectonic interleaving of adjacent lithologies. No thermal metamorphic overprinting of the dynamically metamorphosed lithologies is evident. Relic indicator minerals, such as epidote porphyroblasts and actinolite and riebeckite laths, are pre-cataclasis. Despite abundant calcite and/or siderite in the phyllitic quartzites and riebeckite-bearing phyllitic quartzite, no meta-calcsilicate minerals are present and thus the maximum grade reached prior to cataclasis is below the upper stability limit of riebeckite (Deer *et al.*, 1992). No inferences about the pressure conditions prevailing could be derived from the samples that were collected in this study, although Cain (1975) places the metamorphism of the Natal Thrust Front at 500-550°C and 12-16 kb, based on calc-silicate assemblages. The significance of late-tectonic calcite in the melange is equivalent to that of calcite found in a similar state in the Ngubevu area, that is, as a product of late-tectonic retrograde metasomatism. The ACF plots shown in Figure 3.30 are based on whole rock data (Appendix A3). The majority of data fall in the metabasite protolith field, showing a calcite enrichment\depletion trend while rocks from the eastern part of the field area fall in the montmorillonite/smectite-bearing protolith field.

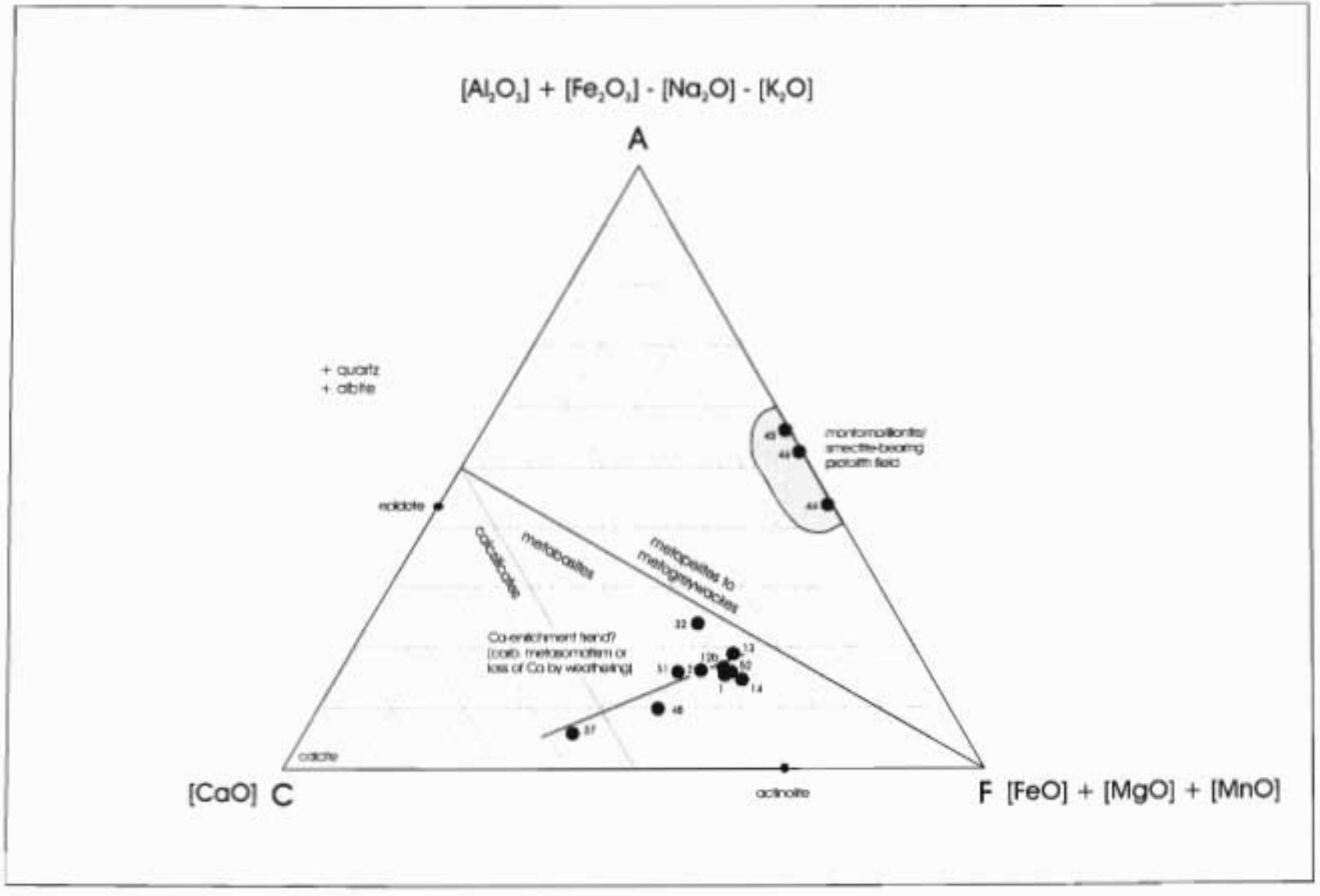

Figure 3.30 ACF plot of phyllitic quartzites, cataclastics and ultracataclastics of the northern Mforgosi Valley area. The lenses which host the majority of veining and the main workings appear to have had some component of pelitic or montmorillonite/smectite-bearing rock type in their protoliths. Data derived from whole rock major element oxide analyses (Appendix A2) and thin section examination

3.6) Discussion - Economic Potential

Modelling of a single rigid clast being rotated in a simple-shear system produces structural features which are similar to those observed in the northern Mfongosi Valley field area. The large-wavelength folds at 168→53° are akin to the large-wavelength folds observed by Bjornerud (1989) which formed at some distance from rotating clasts. Intrafolial or kink folds become apparent at $\gamma = 1.67$ to $\gamma = 1.99$ and are most evident near a rotating clast. The kink folds have two highs on contoured stereonet data, one at 235→42° and the other at 217→27°, which define the double hinge zones of intrafolial box folds although the poor outcrop often obscures a complete box fold form. It is significant that the peak concentrations of the large wavelength folds and the intrafolial folds are at obtuse angles to one another. Placing a two dimensional shear model, for example that at $\gamma = 2.72$ (Bjornerud, 1989), in the context of a displacement direction of 083/59° and assuming a clast with an infinite extent in the Z-axis of the model, a visual representation of the features around a single clast in the northern Mfongosi Valley area is obtained (Figure 3.31). Note that pure shear applied in the Y direction to this model will serve to further separate the two fold axes' concentrations in three dimensional space (Figure 3.31 - inset).

An apparent shear strain of 1.8 is derived from the semi-systematic arrangement of clast segments in the cataclastic matrix. A simple sequence of events, leading to the current vein segment configuration, may be derived:

1) formation of veins in fractures and shears which were imposed on the foreland Mfongosi Group rocks due to the emplacement of the Tugela Nappe/Natal Nappe Zone (Chapter 4)
2) formation of isoclinal folds in strata of the Mfongosi Group, with a progressive rotation of veins into near-parallelism with the S_0 or S_1 layering/fabric
3) the formation of the Mfongosi melange in post-epidote-actinolite metamorphic times (during retrograde metamorphism), cataclasis of the sequence and segmentation of veins which subsequently acted as competent clasts in an incompetent matrix, so approximating models of rigid particle rotation in matrix materials in simple shear systems. The total, apparent shear strain recorded is approximately 1.8, which is due to a contribution of simple and pure shear.

Gold grades derived from the veins and rocks in the Northern Mfongosi Valley area are low: whole rock samples usually assay at 10 ppb with the maximum being 35 ppb (sample PSFU-2; Appendix B2). Vein gold grades range from 10 to 93 ppb with a notable exception being sample PSFUV/43 b which assayed at 935 ppb. It is evident that a nugget effect is prevalent in the area as sample PSFUV/43 a, which is directly adjacent to sample b, assayed at <10 ppb.

Given the short strike extents of veins and their fairly inconsistent thicknesses and grades, it is not recommended that any further work be done in the northern Mfongosi Valley area or any areas exhibiting similar vein distributions. More about the fluid regime at the time of vein deposition is explained in Chapter 7.

3.7) Conclusion

The Northern Mfongosi Valley area is a large-scale analogue of clast rotation in an incompetent matrix, the matrix resulting from cataclasis of metagreywacke±volcanosedimentary Mfongosi Group rocks and the clasts resulting from segmentation of veining which intruded early in the deformation of foreland material.

Gold grades in the area are erratic and low while veining is of too an inconsistent thickness to mine. Sub-outcrop extents of veins, which may host supergenetically enriched copper and silver, are difficult to establish without drill tests.

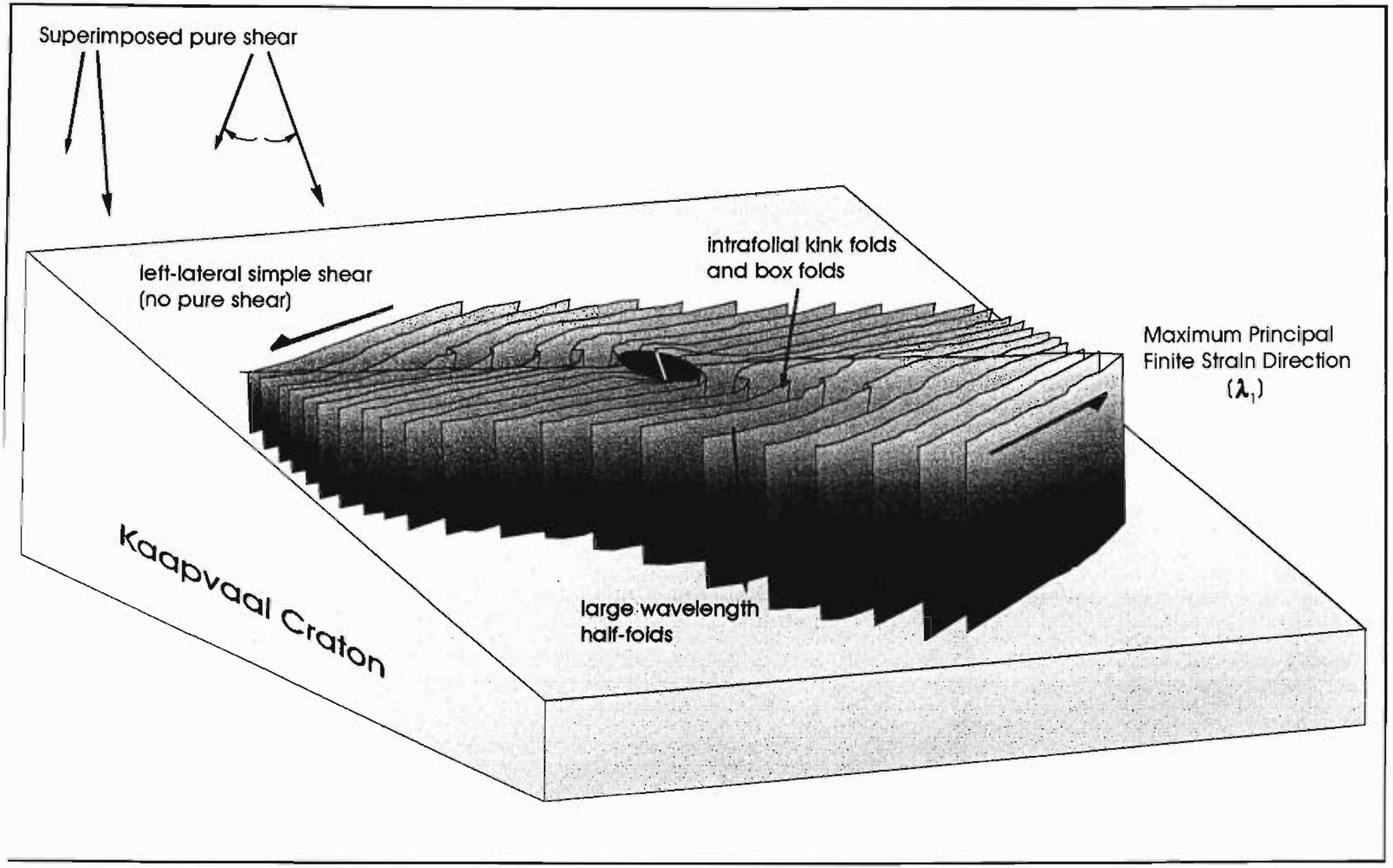

Figure 3.31 Model of the structural features observed in the northern Mfongosi Valley area. Rotation of rigid objects, in a matrix which is undergoing left-lateral simple shear, explains the banding discordancies, two types of folds with different orientations, and the distribution and segmentation of veins. Pure shear applied across the model will effectively serve to further separate each type of fold axis set in three-dimensional space

Chapter 4

Southern Mfongosi Valley Area

4.1) Economic History

The southern Mfongosi Valley area, at the confluence of the Mfongosi and Tugela Rivers, has been targeted for lead, silver, copper and gold exploration. This study area encompasses a portion of the Tugela Nappe in the south (the Manyane amphibolite) and tectonically conformable units of the Mfongosi Group schist to the north. The Manyane Thrust separates the Natal Nappe Zone in the south from the tectonostratigraphically lower Natal Thrust Front to the north (Figure 3.1) and seems to occur considerably further northwards than its position depicted in Harmer (1979) and Matthews and Charlesworth (1981).

The Manyane amphibolite hosts a shallow gold prospecting pit containing the Ayres Reef (Du Toit, 1931) or Mfongosi Gold Mine (Thomas *et al.*, 1990) which occurs 1 km east of the Mfongosi/Tugela River confluence on the northern bank of the Tugela River. The Ayres Reef is a set of vertical to steeply south-dipping quartz and quartzfeldspathic veins reminiscent of the Phoenix Mine veining, ranging in width from 40 cm to 1.2 m. Gray (1906) reported that as of 1905 only barren quartz had been extracted from the reef, until 1909 when a 1.1 m thick vein assayed 1325.3 g Au (Du Toit, 1931) and averaged 5.2 $g.t^{-1}$ Au (*op. cit.*) The term "ore body" is a little optimistic for the Ayres Reef which has a strike length of less than 50 m. Mfongosi Cu-Ag-Au occurrences are located about 1 km northwest of the confluence of the Mfongosi and Tugela Rivers in an area known as the Mfongosi Goldfield. Mineralization in deformed concordant granitoids which intrude chlorite schist, magnetite quartzite and limestone of the Mfongosi and Ntingwe Groups (Thomas *et al.*, 1990) was studied by Winfield (1979), Coldwell (1984), Becker (1986) and Pearman (1994). Mine shafts and adits are developed in quartz vein systems which cross-cut the volcanosedimentary Mfongosi Group layering. However, no Au grade information was published. The following sections describe the tectonostratigraphy of the Manyane amphibolite and the Mfongosi schist in the vicinity of the Manyane Thrust, and contain a structural analysis of both areas, leading to a mineralization model which relates Natal Nappe Zone and Natal Thrust Front rocks.

4.2) Manyane Amphibolite

a) Mineralogy

The Manyane amphibolite is a dusky green to pale blue rock of two main textural types (Harmer, 1979; this study), medium- to coarse-grained and fine-grained. Massive and veined types of each variety are separated by sharp contacts conformable to a S_{01} planar foliation. A dominance of plagioclase over hornblende results in a flecked appearance, however, a more melanocratic amphibolite is evident in the study area with a nematoblastic alignment of hornblende and stringers of quartz and plagioclase (Figure 4.1). Between slickensides the amphibolite is dominantly granoblastic although quartz and calcite vein margins host nematoblastic hornblende crystals. Foliation in the dominant plagioclase and epidote amphibolites, and the garnet amphibolites, is defined by narrow streaks and veins of granoblastic quartz which alternate with melanosomes of nematoblastic hornblende (Figure 4.2).

Figure 4.1 Typical Manyane amphibolite 28 metres to the south of the Manyane Thrust in the southern Mfongosi Valley area. Both textural types are shown. Note the alignment of nematoblastic hornblende crystals on the slickenside surface.

Harmer (1979) cites hornblende and plagioclase as essential constituents of this amphibolite (amphibolite- *sensu stricto*; over 40% amphibole content). Typical medium-grained amphibolite contains quartz and sphene ± epidote ± garnet ± diopside. Epidote and ore (opaques) are the most common accessories and a correlation between epidote and sphene content was

proposed by Harmer (1979) to imply a relationship between the conditions necessary for the reaction of hornblende and plagioclase to form epidote, and exsolution of Ti from the hornblende structure. A rock type similar to the Manyane amphibolite, in the Mfongosi schist, reveals idioblastic opaques contained within epidote glomeroporphyroblasts. Shearing of poikiloblasts and glomeroporphyroblasts distributed the opaque minerals which include magnetite, pyrite and ilmenite (the latter giving rise to halos of sphene) throughout the adjacent phyllitic quartzite.

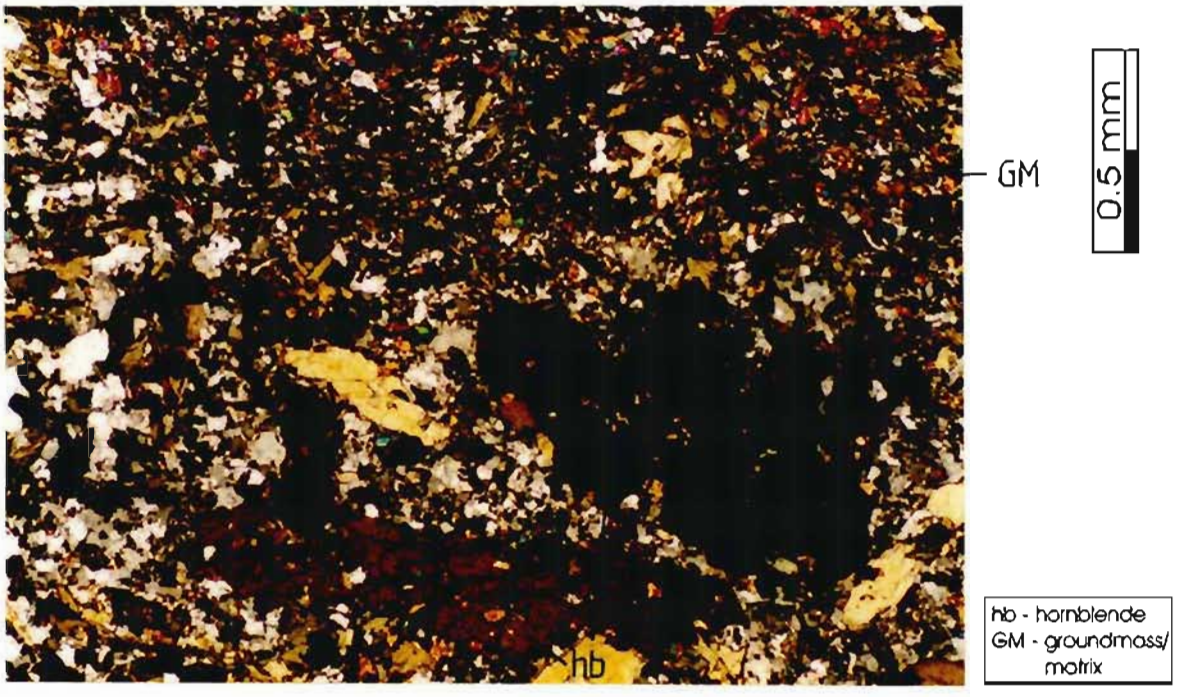

Figure 4.2 Coarse- and fine-grained Manyane amphibolite. Hornblende porphyroblasts/poikiloblasts are embedded in the groundmass which consists of quartz, epidote, albite, sphene and chlorite. (*Slide STA-1*). XP.

b) Structural Geology

I) Banding and Foliation

The Manyane amphibolite's well-developed planar foliation is parallel to numerous slickenside surfaces which contain aligned amphibole laths and is also evident at the contact between fine- and coarse-grained amphibolite or where feldspar proportions are highly variable. This foliation contains extensive down-dip linear features which are best displayed in a spatial sense (Figure 4.3). The best-fit great circle to S_{01} (Figure 4.4 a) has a pole which is parallel to the first-formed linear feature. This azimuth may therefore be considered as the axis of a boudinaging event.

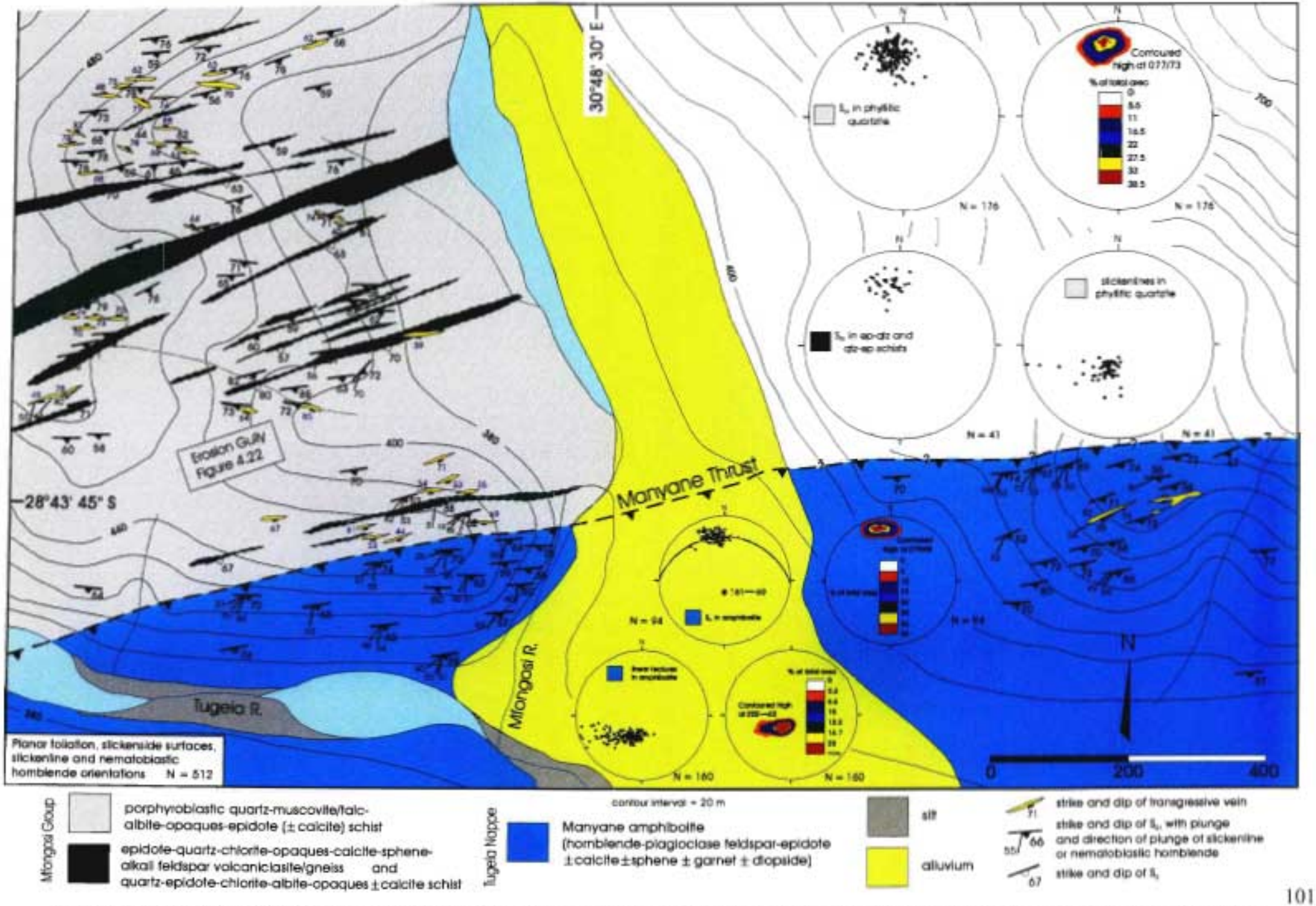

Figure 4.3 The southern Mfongosi Valley field area, encompassing a portion of the Manyane Thrust at the base of the Tugela Nappe (Manyane amphibolite) and the Natal Thrust Front (Mfongosi schist). There is a succession of linear features in the units; southerly-plunging lineations preceed southwest- and west-southwest-plunging lineations. Banding in the Mfongosi Group is simplified N = 512

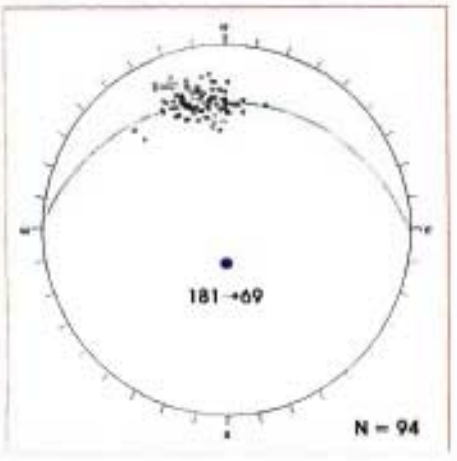

Figure 4.4 a) Equal angle plot of poles to planar foliation/slickenside surfaces in the Manyane amphibolite near the Manyane Thrust. An approximate great circle fit to data has a pole (possible boudinage axis) at 181→69° N = 94

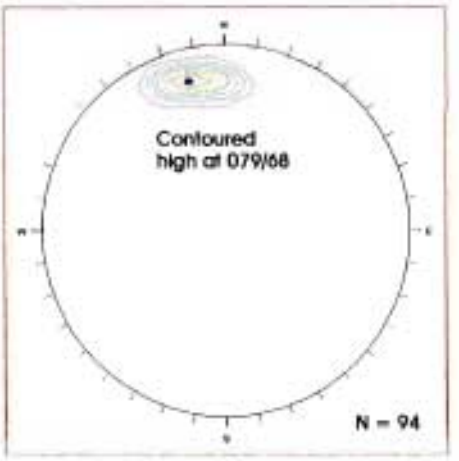

Figure 4.4 b) Contoured equal area plot of data in a). Contoured maximum is at 079/68° N = 94

ii) Linear Features

Three forms of linear features occur either between or on the S_{01} foliation or slickenside surfaces. The succession of lineation-forming events, in relation to the micro-textures and metamorphism in the amphibolite, provides the key to understanding the genesis of the veining in the Mfongosi Group to the north. Relative and average absolute orientations of the linear features are depicted in Figure 4.5.

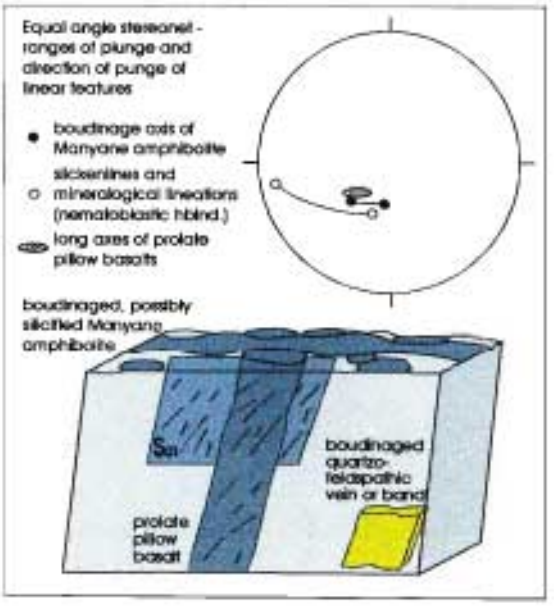

Figure 4.5 Relative and absolute average orientations of the three main types of linear elements occurring in the Manyane amphibolite near the Manyane Thrust.

① —— The first-formed linear feature is a stretching lineation, affecting palimpsest pillow basalts (Figure 4.6). The prolate ellipsoid produced by this event is generally flattened, and actual segments of ellipsoidal pillow basalt may be extracted from the outcrop due to the persistence of chill margins between adjacent pillows. The long axes of the pillow basalts tend to plunge moderately south-southwest.

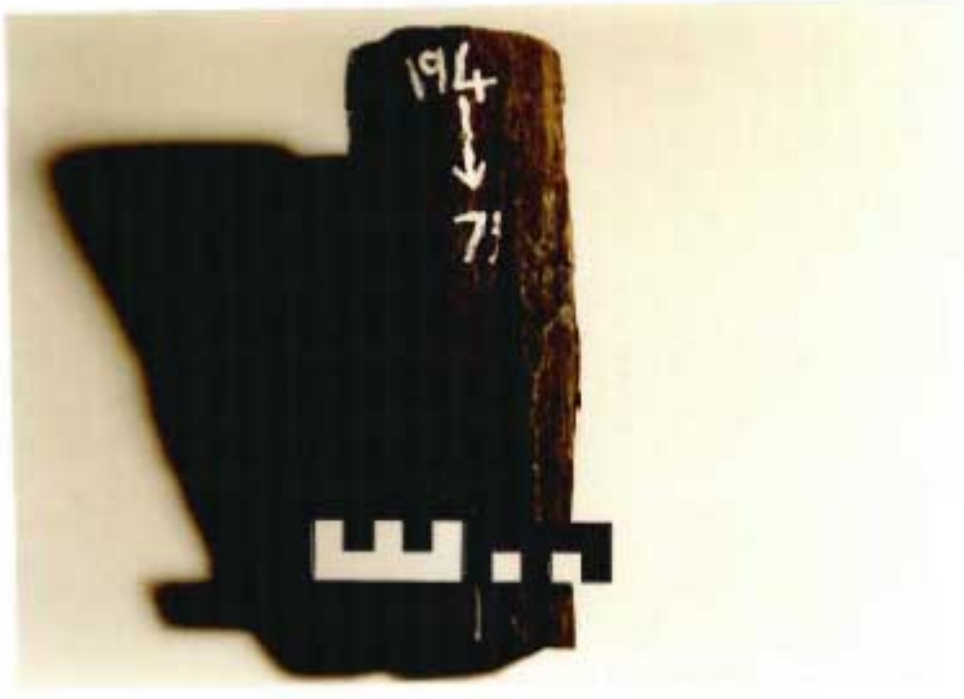

Figure 4.6 Elongate, prolate pillow basalts from the Manyanc amphibolite. In areas where there are concentrations of such features, a strong local down-plunge rodding texture is readily observed. Note the acutely transverse alignment of slickenlines and hornblende nematoblasts on the surface of the pillow.

② ——A succession of slickenlines are superimposed upon the planar foliation and margins of the prolate pillow basalts; slickenlines are not necessarily parallel to the amphibole laths forming the mineralogical lineation in ③. An extreme form of this lineation are "meso-boudins" of more competent strongly elongate segments of veined, silicified or albitized amphibolite (eg Figure 4.4). The slickenlines tend to plunge to the southwest.

③ ——A mineralogical lineation, superimposed upon the planar foliation or slickenside surfaces and strongly prevalent in the interior of prolate pillow basalts is defined by laths and megacrysts of hornblende and opaque phases. The hornblende lineation plunge ranges between the southwest and the west-southwest, often occurring in slickenlines.

All three linear features occur in the same outcrop although lineation types ② and ③ are invariably superimposed upon or wrapped around type ① which argues three different lineation-forming events. The first of these was a prolate-ellipsoid inducing/stretching event in a simple shear regime in the context of shearing along the Manyane Thrust with a consistent hangingwall-to-north movement (more accurately a reverse movement), followed by the second, and possibly third more brittle event(s) wherein strain was focussed along separate slickenside and pillow basalt surfaces (Figure 4.6). Three generations of amphibole laths on slickensides, each one successively more shallowly inclined to the west, imply that the amphibole laths grew on or in the slickenlines, so mimicking their orientations. The majority of the lineations are concentrated at 202→62° (Figure 4.7). The calcsilicate bands in the amphibolite preserve very little evidence of slickensiding, probably due to low-temperature carbonate mineral recrystallization.

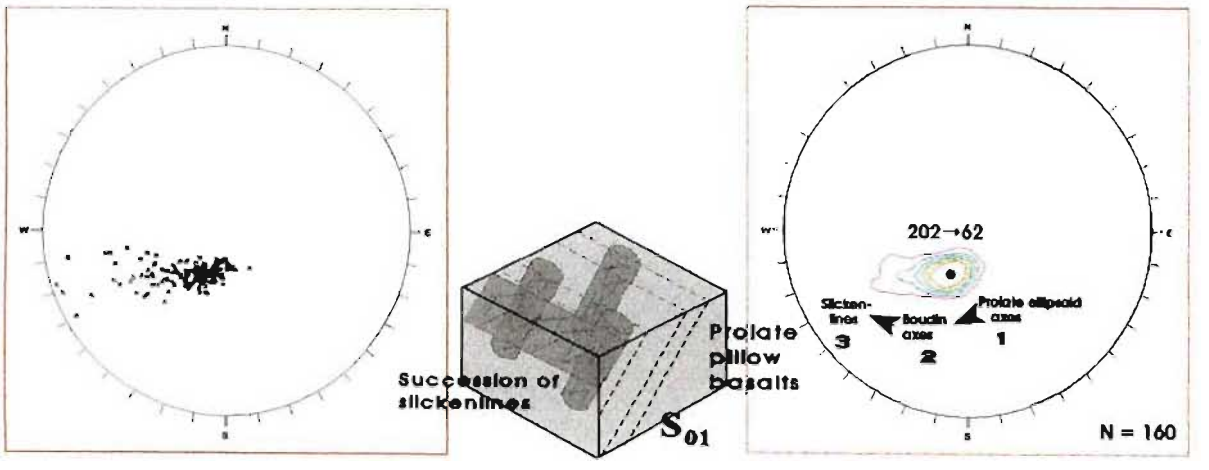

Figure 4.7 a) Equal angle stereonet plot of the plunge and direction of plunge of linear features in the Manyane amphibolite adjacent to the Manyane Thrust N = 160

Figure 4.7 b) Equal area contour plot of total lineations in the Manyane amphibolite to the south of the Manyane Thrust, southern Mfongosi Valley. The contour range is 0...20 and the contoured high is at 202→62°. Note the succession of lineation types N = 160.

Later lineations, at acute angles to the strong stretching lineation, were somewhat restricted by the latter during formation; local restraining and releasing features are evident on the southward-facing crests and east-west terminations of the boudins and ellipsoids, respectively. Narrow, pencil-like quartz rods may fill such features. A distinctive feature of the Manyane amphibolite in the field area is the absence of a second tectonically-induced foliation and the inference is that flattening and stretching at this locality were extreme and, although oblique

collision is still evident at the Manyane Thrust, later left-lateral movement was accommodated elsewhere in the Natal Thrust Front, for instance in the northern Mfongosi melange. A series of σ_1 orientations are derived from the combination of slickenlines and slickensides (Figure 4.7 c). The gross orientation of the stress axes is almost identical with that of the stress ellipsoid derived from slickenlines and slickensides at the Phoenix Mine, indicating a similarly-oriented stress field for the emplacement of the Tugela Nappe, and the tectonic movement post-dating vein formation at the Phoenix Mine.

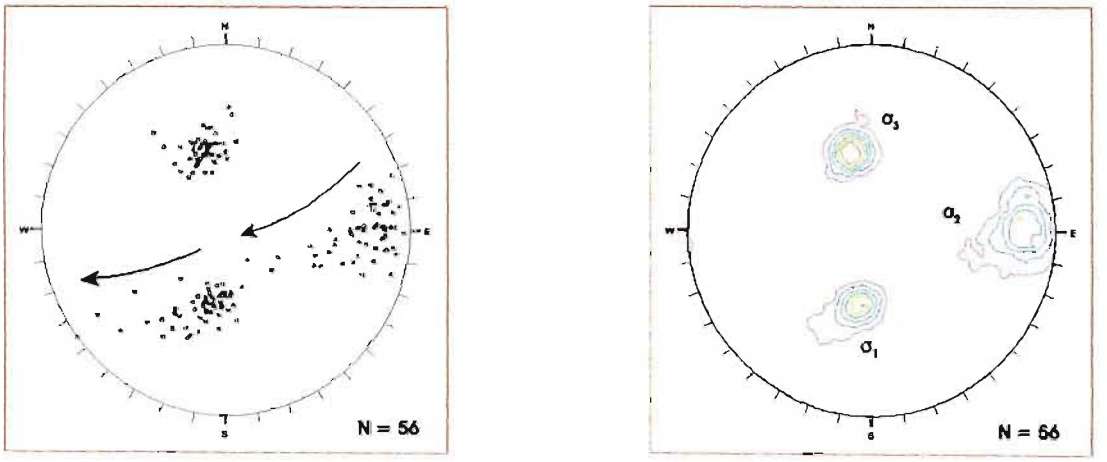

Figure 4.7 c The change in σ_1 orientation and stress ellipsoid axis orientation; data derived from a combination of slickenline and slickenside analysis. Contoured highs are as follows: $\sigma_1 = 186 \rightarrow 46°$, $\sigma_2 = 089 \rightarrow 12°$, $\sigma_3 = 344 \rightarrow 44°$. Contoured maximum is at 19% of total area. The rotation of the σ_1 and σ_2 axes in a clockwise sense indicates a progressively more southwest-oriented stress regime. In contrast, σ_3 remains constant. Note also that the orientations of σ_3 and σ_2 essentially switch in the transition to post thrust, east-west extension. N = 56

iii) Dilation

Evidence of purely brittle dilation is preserved in the Manyane amphibolite. Dilation cracks have widths of about 3-5 cm and extend down-dip for 90 cm (Figure 4.8). Crack infilling is usually euhedral quartz or secondary massive to anhedral calcite. The two main orientations of cracks usually have consistent cross-cutting relations. The first generation (**Dil-1**) has an approximate average strike and dip of 249/47° (Figure 4.9 a). The orientation of antitaxial, euhedral quartz crystals in Dil-1 implies consistent hangingwall-to-north movement during or after dilation as the quartz crystals occur at 70°-80° to the crack margins. Dil-1 is usually within 5° of being perpendicular to the nearby planar foliation (089/55°). The second generation of dilation cracks (**Dil-2**) are inclined to the west-southwest with an average strike and dip of 162/36° (Figure 4.9 b). Dil-2 usually restricts dilation in Dil-1 where the two crack generations occur together in outcrop although this cross-cutting relationship may be reversed.

Figure 4.8 Cross-cutting dilation cracks in the Manyane amphibolite about 30 metres south of the Manyane Thrust.

The intersection of Dil-1 and Dil-2 is at 286→32° (Figure 4.9 c). The gross contemporaneity of the dilation cracks may imply post-thrusting collapse after or during north-eastward movement and slickenline formation. It is during this period of post-thrust collapse that the veining in the Mfongosi Group was formed. Late-tectonic northeast movement subsequent to Ayres Reef and Phoenix Mine veining formation is discussed in the following section.

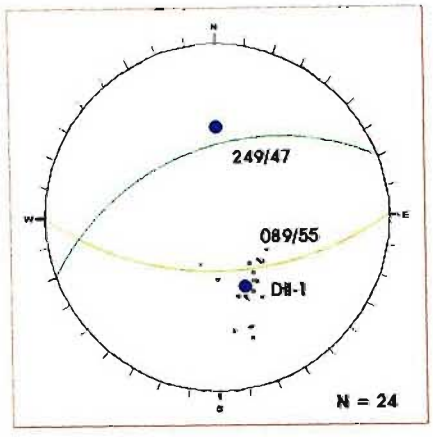

Figure 4.9 a Equal angle plot of poles to the dominantly first generation of dilation cracks (Dil-1) in the Manyane amphibolite to the south of the Manyane Thrust. An average strike and dip of 249/47° for Dil-1 is shown cross-cutting the nearby S_{01} planar foliation (089/55°) N = 24

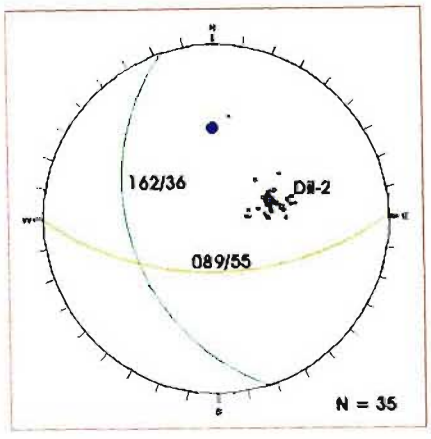

Figure 4.9 b Equal angle plot of poles to the second generation of dilation cracks (Dil-2) in the Manyane amphibolite to the south of the Manyane Thrust. An average strike and dip of 162/36° for Dil-2 is shown cross-cutting the nearby S_{01} planar foliation (089/55°) N = 35

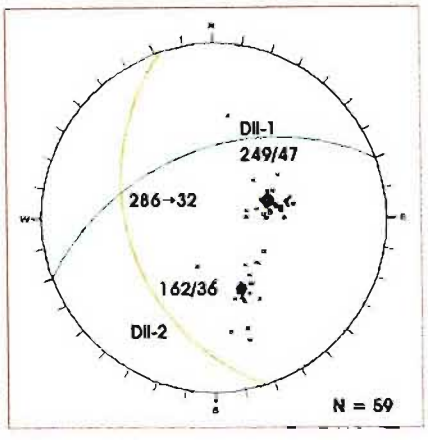

Figure 4.9 c Dil-1 and Dil-2 average planes, intersection at 286→32° N = 59

iv) Veining

Veining in the Manyane amphibolite is limited to 0.4 to 1.2 metre wide massive quartz and quartzofeldspathic veins which occur 1 km northeast of the Mfongosi River/Tugela River confluence. Three veins constitute the Ayres Reef and are subvertical to steeply south-dipping with limited strike extents of about 50 m and unknown down-dip extensions. The average orientation of veins comprising the Ayres Reef is 065/81° which is slightly discordant to the planar foliation in the host amphibolite which has a local orientation of 070/73° (Figure 4.10). No metallic mineralization was noted in the workings or veins. Slickenlines on the margins of the veins plunge towards the southwest (range in orientation of 250→59° to 255→23°) implying that vein formation predated the final strike-slip movement at the Manyane Thrust (Figure 4.11).

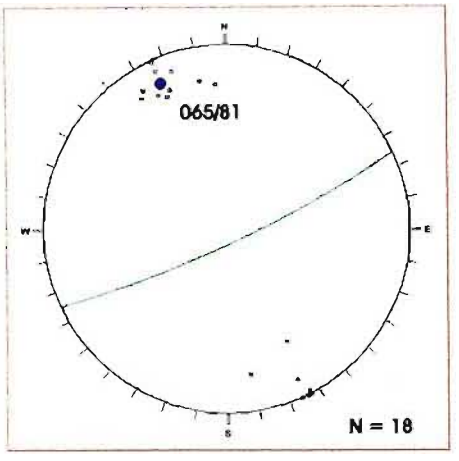

Figure 4.10 a Poles to margins of quartz veins in the Ayres Reef working. The average trend is 065° (sub-parallel to the trend of DIL-1) N = 18

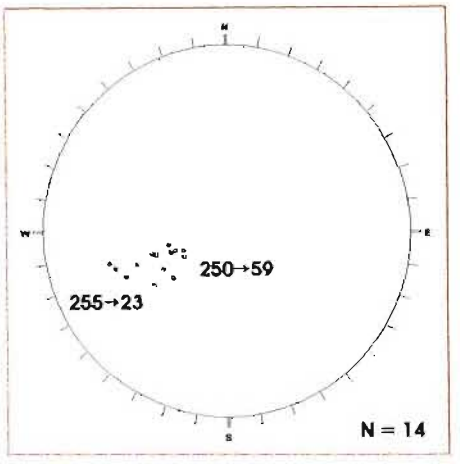

Figure 4.10 b Plunge and direction of plunge of slickenlines on the margins of veins at Ayres Reef. The orientations of the slickenlines are intermediate between those of the prolate ellipsoid axes (steeply south-plunging) and the slickenlines (shallowly WSW-plunging) N = 14

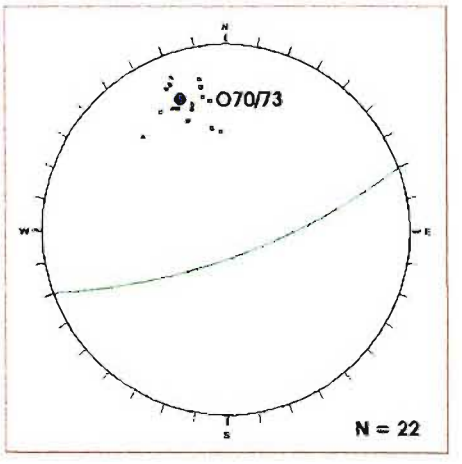

Figure 4.10 c Poles to S_{01} in the vicinity of the Ayres Reef working. The veins in the Ayres reef are slightly discordant to the host rock planar foliation which has an average strike and dip of 070/73° N = 22

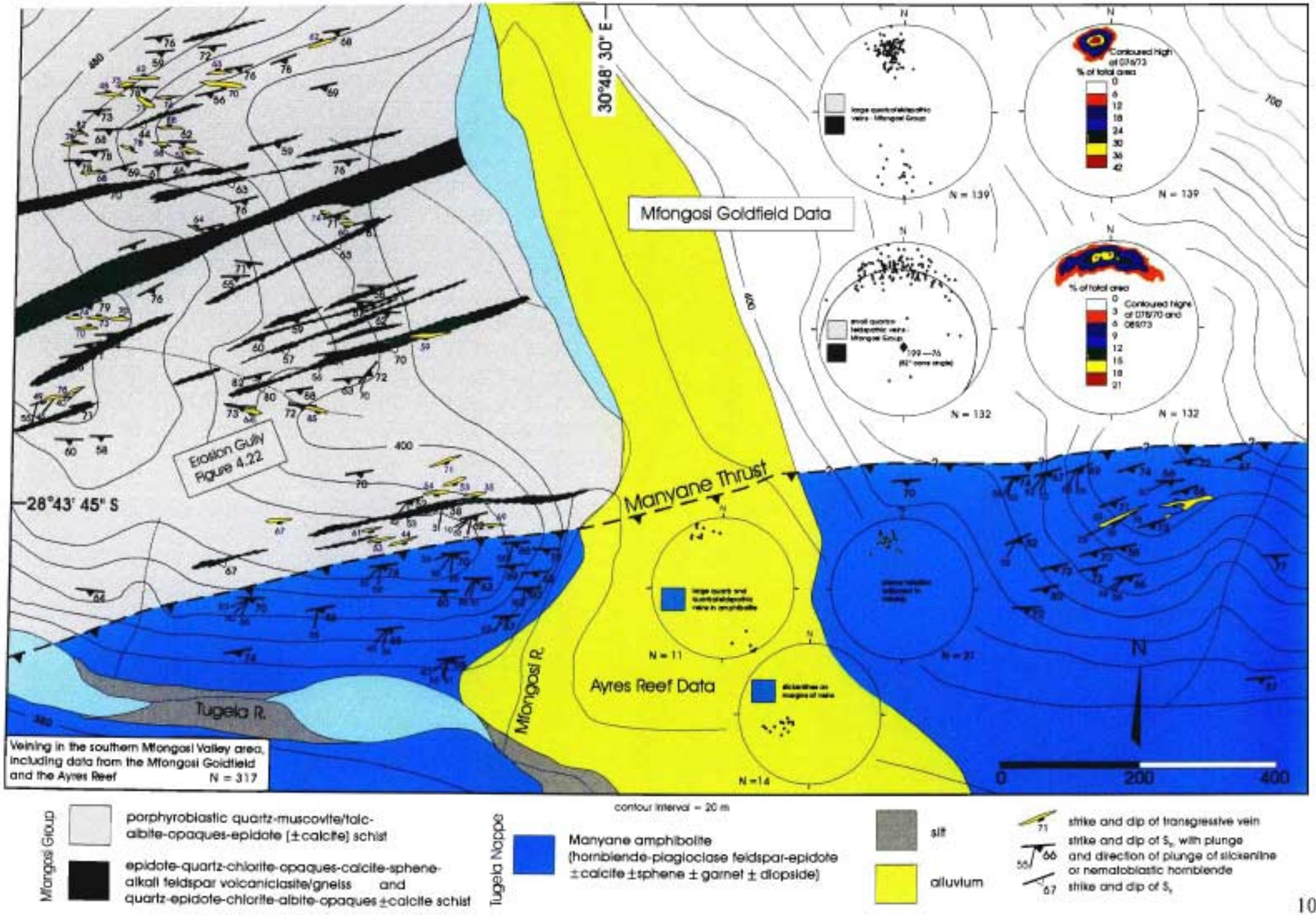

Figure 4.11 Veining in the southern Mfongosi Valley field area. In contrast to the copious veining in the Mfongosi Group, which displays a girdle distribution on stereonets, veining in the Manyane amphibolite is scarce and data was obtained only from the Ayres Reef working. Ayres Reef veining is similar to that of the Phoenix Mine, both in terms of timing and tectonic context. Banding in the Mfongosi Group is simplified N = 317

c) Metamorphism

It is necessary to summarize the succession of metamorphic events which the Manyane amphibolite has undergone and subsequently to consider the metamorphic textures and assemblages near the Manyane Thrust in the context of this evolution. This will be done to determine the effects of juxtaposition of the Tugela Nappe against the Mfongosi Group. Harmer (1979) encountered four main metamorphic assemblages in the Manyane amphibolite, distributed throughout the Tugela Nappe or "Manyane Slice" (Figures 4.12 a, b; Table 4.1).

Table 4.1 Summary of metamorphic facies prevalent in the Manyane amphibolite in the Tugela Nappe (summarized from Harmer, 1979).

Metamorphic Facies: Pressure/ Temperature Range	**Indicator Minerals**	**Position in Tugela Nappe**	**Assemblage**
upper amphibolite facies - above 625°C to below orthopyroxene-in isograd	appearance of diopside in metabasites	concentrated in the southern portions of the Tugela Nappe	**A** diopside + hornblende + Ca-plagioclase
amphibolite facies - 575°C to 625°C 3.5 to 4 kb	hornblende replaces diopside during falling temperatures	pervasive throughout the Tugela Nappe	**B** hornblende ± plagioclase ± epidote
upper greenschist facies - 400°C to 450°C	lower temperature limit set at the zoisite + actinolite-in isograd	shears, fractures and thrust planes	**C** epidote + actinolite ± chlorite
middle greenschist facies - about 405°C	prehnite in biotite flakes indicate low-grade overprinting of assemblage B and not retrogression due to shearing	limited distribution, not localised in shears	**D** prehnite in biotite

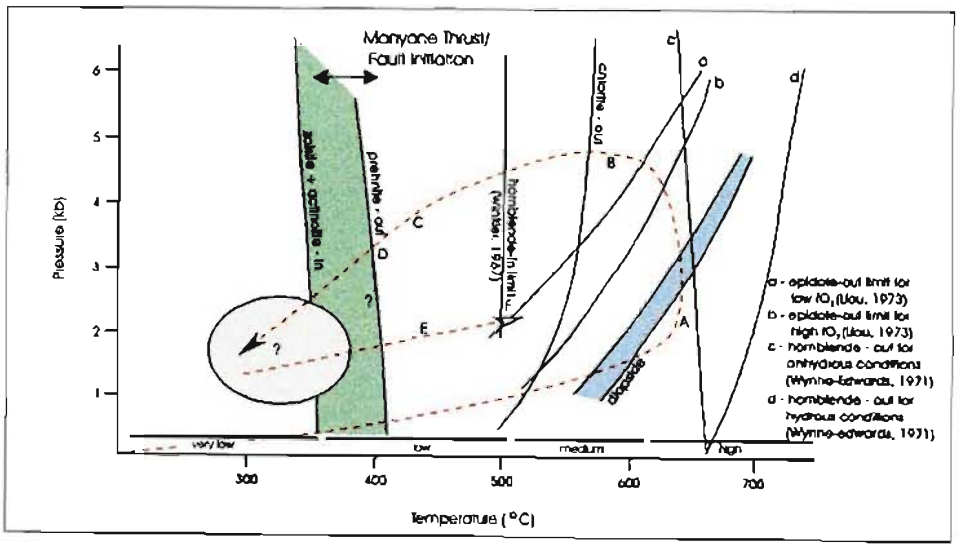

Figure 4.12 Position of the assemblages in the Manyane amphibolite in P-T space summarized from Harmer (1979). Assemblages E and F from this study. A late-metamorphic, post-cataclastic thermal pulse, co-incident with shear heating, is indicated at the base of the Tugela Nappe.

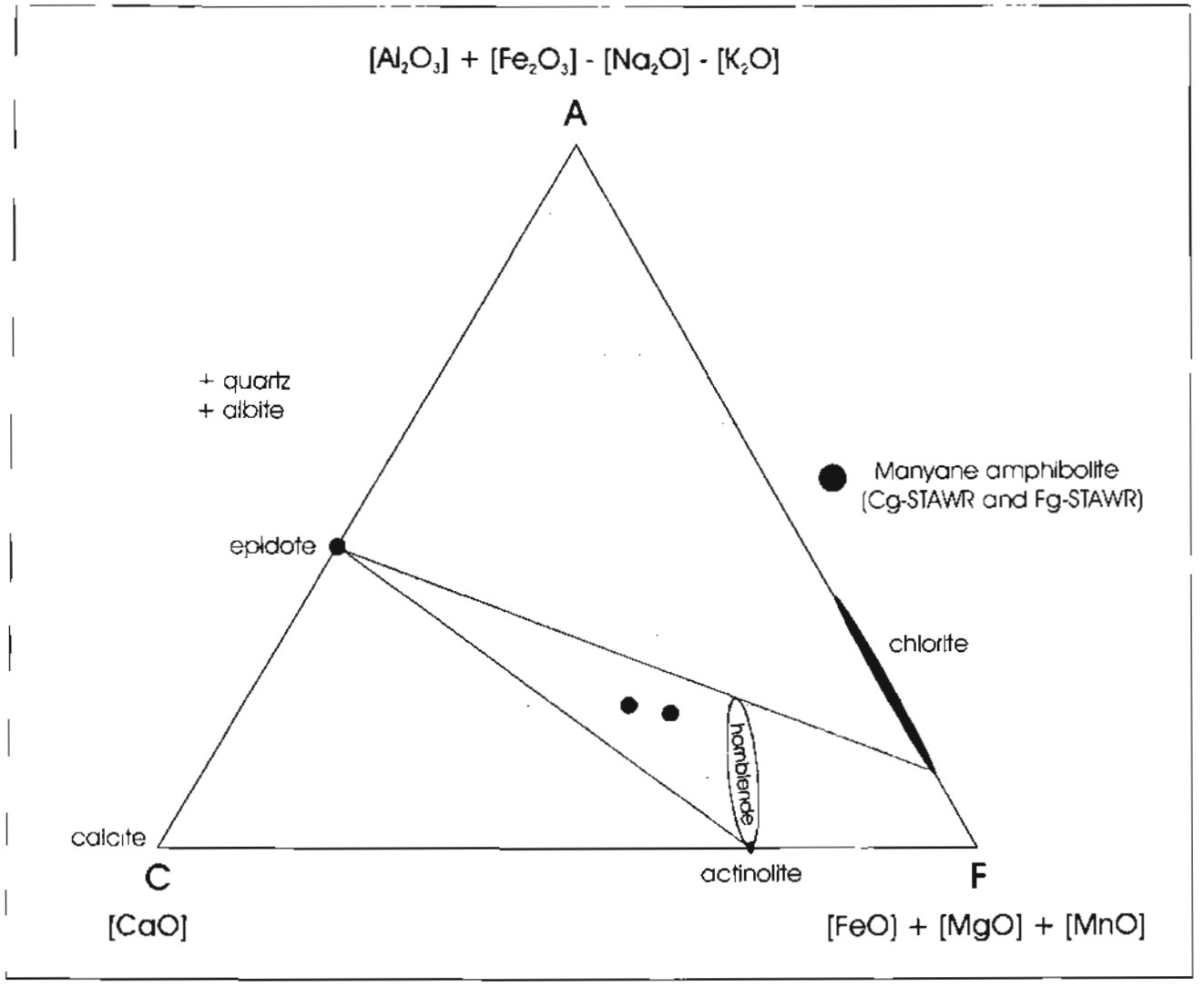

Figure 4.12 b ACF Parameters of the Manyane amphibolite in the southern Mfongosi Valley area, dervied from whole rock major element oxide analyses (Appendix A3) in conjunction with thin section studies

ACF parameters for the present metamorphic state of the Manyane amphibolite are derived from whole rock major element oxides (Appendix A3). Similarly, the Sundukazi Tectonic Unit (now classified as the eastern part of the Tugela Nappe), comprising interbedded tholeiitic meta-volcanics and pelitic and psammitic meta-sediments, has undergone an initial heating at 570°C - 600°C with pressures in excess of 5.5 kb which was overprinted by a retrograde, low-grade metamorphic event caused by overthrusting (Harmer 1979; Rigotti, 1977).

d) Conditions of Metamorphism Adjacent to the Manyane Thrust

Two main parageneses, often occurring in a single thin section, are present in the Manyane amphibolite near the Manyane Thrust. Furthermore, locally different parageneses may be encountered in layers/veins in the amphibolite. A combination of textural features and metamorphic assemblages near the Manyane Thrust, and metamorphic assemblages in the bulk of the Tugela Nappe, allows a simple sequence of late-tectonometamorphic P-T conditions to be inferred at the Tugela Nappe/Mfongosi Group contact and accordingly allows construction of a model for the veining in the Mfongosi Group.

I) Epidote - actinolite - opaques ± albite ± chlorite ± calcite schist

The majority of the Manyane amphibolite in the field area consists of a *porphyroblastic epidote - actinolite - opaques ± albite ± chlorite ± calcite schist* (Figure 4.13). The matrix consists of disseminated epidote and partially strained quartz and albite, largely with sutured and amoeboid grain boundaries. Anhedral opaque stringers of sphene are distributed along the planar foliation defined by actinolite and chlorite (after actinolite). Rotated and sheared porphyroblasts and glomeroporphyroblasts of epidote ± euhedral to subhedral opaques display a full range of movement indicators, from sheared-out polycrystalline epidote porphyroblasts to rotated glomeroporphyroblasts. Calcite occurs in the trails of the σ-structures defined by the epidote knots; a consistent hangingwall-to north shearing is evident in orientated thin sections from ellipsoidal pillow basalts (***eg Slide STP-1***). Rotated and aggregated actinolite forms very poor shear-sense indicators, presumably due to its length and a combination of simple shear and pure shear (Passchier and Simpson, 1986). A section perpendicular to the long axis of a stretched pillow basalt (eg ***Slide STP-2***) reveals no left-lateral movement indicators. Slickenlines on the

surface of the pillow basalts signifies that superimposed lateral movement in the form of discontinuous shear was focussed on pillow basalt surfaces in a more brittle regime. Layers of xenoblastic quartz-calcite-analcite display little deformation - calcite recrystallized at lower temperatures and also shielded larger quartz grains from cataclasasis and/or annealing.

Figure 4.13 Typical Manyane amphibolite in the vicinity of the Manyane Thrust. Note the abundant calcite bands and epidote stringers aligned in the plane of the shear zone (*Slide STP-1*). XP.

ii) Hornblende - Epidote ± Actinolite ± Plagioclase ± Opaques ± Chlorite

The other paragenesis prevalent in the Manyane amphibolite at this locality is *hornblende + epidote ± actinolite ± plagioclase ± opaques ± chlorite* (Figure 4.13). This assemblage is texturally varied as porphyroblastic and poikiloblastic hornblende occurs in a partially annealed, deformed, decussate matrix of chlorite, albite, oligoclase, actinolite and fine-grained epidote. Epidote is concentrated in linear arrays along the centre of hornblende poikiloblasts; these arrays result from hornblende replacing twinned actinolite. Poikiloblastic hornblende replaces and overgrows poikiloblastic twinned actinolite and annealed quartz, albite, oligoclase, and epidote. The hornblende poikiloblasts have no preferred orientation and transgress a very weak partially aligned generation of actinolite, chlorite and quartz stringers in the matrix (possibly constituting S_0). The matrix displays an annealed texture of post-cataclastic recrystallization of regionally metamorphosed quartz, oligoclase and albite (Spry, 1969).

Figure 4.14 Typical example of the prograde assemblage prevalent in the Manyane amphibolite in the vicinity of the Manyane Thrust. Note the large hornblende poikiloblasts/porphyroblasts overgrowing the partially annealed cataclastic matrix. In this plane, the poikiloblasts are not aligned and impinge upon one another. (***Slide STA-1***). XP.

iii) Metamorphic Reactions Near the Manyane Thrust

The metamorphic parageneses in the Manyane amphibolite in the study area indicate two main facies of metamorphism. Firstly assemblage **E** on Figure 4.12:

chlorite + clinozoisite/epidote ± actinolite ± quartz
(all being used in the formation of the higher temperature assemblage)

and imply the following reactions (Winkler, 1974) in the transition from low-grade assemblages, being either **C** or **D** as described by Harmer (1979 - Table 1):

$$\text{pumpellyite} + \text{chlorite} + \text{quartz} \rightarrow \text{clinozoisite/epidote} + \text{actinolite} + H_2O \qquad \mathbf{1}$$

or

$$\text{prehnite} + \text{chlorite} + \text{quartz} \rightarrow \text{clinozoisite/epidote} + \text{actinolite} + H_2O \qquad \mathbf{2}$$

The transition to a higher-grade paragenesis depends on a number of factors such as:

- the change from albite to plagioclase in the presence of hornblende (Miyashiro, 1973; Yardley, 1989)
- the change of amphibole from actinolite to hornblende (both of the "Calcic amphibole" group) across a miscibility gap (Miyashiro, 1973), implied by the ubiquitously sharp boundaries between actinolite and hornblende (this study)

- the change in colour of the Ca-amphibole, from pale blue-green actinolite (epidote-actinolite facies), to greenish-blue/bluish green (lower amphibolite facies), to green or green with a faint blue tinge (amphibolite facies), to brown (upper amphibolite facies) (Miyashiro, 1973).

The problem with this scheme is two-fold. Firstly, in greenschist facies conditions, where the P_{CO2} and P_{H2O} are high, the formation of actinolite is delayed with increasing temperature. Reaction **3** (Miyashiro, 1973) would be restricted from proceeding to the right due to the constant influx of reactants on the left. From the abundant calcite present in the Manyane amphibolite, this may have been the case. Note that this reaction does not involve epidote.

$$\text{antigorite/chlorite} + \text{calcite} + \text{quartz} \rightarrow \text{actinolite} + CO_2 + H_2O \qquad \mathbf{3}$$

Secondly, the change from purely albitic to plagioclase feldspar, with the onset of the amphibolite facies, may also not be valid as a metamorphic indicator. Although Fitz Gerald and Stünitz (1993) and Stünitz and Fitz Gerald (1993) cite an upper temperature limit of deformation of their amphibolitic granitoids of 400 - 450°C (based on an absence of actinolitic amphibole and oligoclase), Yardley (1989) takes the absence of albite and the appearance of plagioclase feldspar as the boundary between the greenschist and amphibolite facies. The key to this conundrum may be found in Fitz Gerald and Stünitz (1993); there is a tendency, with cataclasis and reduced grain size, for the feldspar to become more albitic and hence to change composition from andesine to oligoclase to albite. On the other hand, there is the tendency, with increasing temperature, for the feldspar to change from albitic to a plagioclase feldspar. These two processes evidently act against one another during regional metamorphism.

In the absence of any unambiguous upper limits to the greenschist facies, the assemblage *hornblende* + *epidote* ± *actinolite* ± *plagioclase* ± *albite* ± *opaques* ± *chlorite* must be taken as representing the maximum post-cataclastic grade in the Manyane amphibolite (**F** on Figure 4.12). This assemblage implies the reaction (Yardley, 1989):

$$\text{actinolite} + \text{chlorite} + \text{quartz} + \text{Al-epidote} \rightarrow \text{tschermakite hornblende} + \text{fluid} \qquad \mathbf{4}$$

A succession of metamorphic events at the Manyane Thrust may be surmised from porphyroblast-matrix relationships. Hornblende porphyroblasts, up to 1.8 mm in length, have been weakly cataclastically deformed and although the poikiloblastic inclusions in randomly-oriented hornblende are aligned. They are equant and reveal no indication of a pre-existing foliation or compositional layering. The inclusions are identical in size to crystals in the host quartz-albite-epidote-bearing matrix, although differing texturally in that they have scalloped and embayed grain margins indicating that they contributed to the reactants forming hornblende.

Any higher-temperature event is likely to obliterate or overgrow an earlier assemblage, especially if the pre-existing assemblage minerals have been reduced in size, either by cataclasis or by post-deformational annealing (Spry, 1969; Mason, 1990). The controversy over porphyroblast/matrix relationships is ongoing: Paterson *et al.* (1991) and Vernon *et al.* (1993 a, b) cite evidence for pre-foliation metamorphism in low pressure/high temperature (LPHT) terranes. Examination of the studies by Harmer (1979), Rigotti (1977) and Cain (1973, 1975) indicate that LPHT conditions may not be prevalent in the northern parts of the Tugela Nappe, however, the commencement of metamorphism in the very early stages of thrust emplacement and deformation is implicit. In the absence of evidence for the primary cause of LPHT metamorphism, namely mantle-derived, notably mafic magmas (Loosveld and Etheridge, 1990; Vernon *et al.*, 1993a), in the portion of the Manyane amphibolite under study, a model of strictly LPHT metamorphism is inappropriate. It is expected that such conditions applied in the contact aureole of the Tugela Rand Complex.

There is evidence for initiation of thermal (regional) metamorphism either before a foliation or fabric-forming event or during the earliest stages of deformation. The minerals comprising the epidote-actinolite grade of metamorphism are still evident, although cataclastically deformed, annealed and replaced by a higher-grade assemblage. Post-hornblende deformation was, however, limited; the poikiloblasts and porphyroblasts do not impact upon each other although they have been weakly aligned with the palimpsest S_{01} foliation in the annealed matrix. Banding may be preserved as variable linear concentrations of inclusions in the porphyroblasts but these inclusions are not elongate or aligned. The implication is that the porphyroblasts and poikiloblasts grew while the matrix was still very fine-grained, that is, before metamorphism had

induced appreciable grain regrowth in the matrix, and possibly also before a foliation had redeveloped. Such grain size reduction is common near a thrust plane, or in the basal sections of a thrust unit (Fitz Gerald and Stünitz, 1993; Stünitz and Fitz Gerald, 1993). The "exclusion" of a pre-existing fabric may occur in two ways (Vernon *et al.*, 1993a):

- the porphyroblast uses nearly all the matrix material and/or is able to eliminate partially included matrix as it grows, such that poikiloblastic inclusions are not abundant
- the porphyroblasts grow dendritically and so preserve matrix folia only in faster-growing, isolated segments which are spatially separated.

The absence of a foliation in the matrix negates these two options. These assemblages and textures indicate post-tectonic prograde metamorphism in this part of the Manyane amphibolite across the epidote-actinolite-in limit, and subsequently across the hornblende-in limit in contrast to the overall retrograde metamorphism in the remainder of the Tugela Nappe, (Figure 4.12). Recrystallization destroyed much of the weak fabric to form a granoblastic-polygonal network with disseminated epidote + opaques + chlorite. The maximum grade of metamorphism in the field area, based on indicator parageneses, is thus conservatively estimated at amphibolite facies. The paragenesis may constitute a "transitional assemblage" (Winkler, 1974; Yardley, 1989). Note that early calcite metasomatism, and epidotization after reaction **3**, is likely. A last point may be made about the notable presence of calcite in the amphibolite; metacalcsilicate assemblages are absent and introduction of the bulk of the calcite seems to have been late in the sequence of metamorphism (*c.f.* the widespread carbonate metasomatism of the Mfongosi schist - Bullen *et al.*, 1994; this study).

It therefore appears that the "hot iron effect" was operative in this portion of the Mfongosi Valley within the Manyane amphibolite, wherein CO_2-rich fluids, probably originating in the Ntingwe limestone to the north, moved towards the transitory high-temperature zone at the Manyane Thrust in late-cataclastic/late-thrusting times. This movement of CO_2-rich fluids *towards* the thrust plane explains the lack of notable skarn or any other metasomatism of the Ntingwe limestone.

4.3) Mfongosi Schist

The Mfongosi Group schist crops out in a 1-5 km wide tectonically conformable sequence with an east-west trend, occurring between the Kaapvaal Craton and the Natal Nappe Zone. Matthews (1959) proposed a stratigraphy for the Mfongosi schist, termed the "Upper Basement Complex", consisting of four broad subdivisions; the lower volcanic schists, the lower mica schists, the upper volcanic schists and the upper mica schists (Table 4.2). The mineralogies were described by Matthews (1959) and Matthews and Charlesworth (1981). This study concentrates on the veining and mineralogy of the schists.

Table 4.2 Subdivisions of the upper Basement Complex (Mfongosi Group schist). Overall metamorphism is in the greenschist facies (after Matthews, 1959)

Subdivision	Description/Composition
Upper Mica Schists	• phyllitic schists displaying two or more cleavages and kinking of micaceous layers • quartz - muscovite ± chlorite schists with abundant quartz secretion veins
Upper Volcanic Schists	• chlorite - epidote - (talc - carbonate - albite) schists and chlorite - epidote amphibolites with varying amounts of albite and clinozoisite • siliceous banded ironstone • chlorite - epidote schists and amphibolites (as for the Upper Mica Schists)
Lower Mica Schists	• laminated quartz - chlorite - epidote - sericite schists with intercalated quartz - carbonate- chlorite schists • fine-grained quartzite • laminated schists (as above), but without the calcsilicate bands, the higher-grade metamorphic equivalents are banded garnetiferous quartz-plagioclase-hornblende granulites
Lower Volcanic Schists	• coarse-grained, foliated or massive amphibolites showing metamorphosed amygdales and palimpsest volcanic textures

The Mfongosi schist has undergone extreme deformation including isoclinal folding, flattening of isoclinal folds, thrusting and reverse faulting. This study concentrates on a 0.7 km^2 area directly north of the Manyane amphibolite, which includes the "Mfongosi Goldfield", and seeks to provide a structural context to the veining and deformation of the host rock to veining (Figure 3.1; Hatch, 1910; Du Toit, 1931).

a) Mineralogy

Porphyroblastic quartz-muscovite/talc-albite-opaques-epidote±calcite schist

Host rock to the majority of the veining in the southern Mfongosi Valley area, this schist occurs in dark olive to light-brown, slightly pock-marked (due to negative weathering of magnetite and pyrite), discontinuous bands which host the other rock types of this volcaniclastic sequence (Figure 4.14) . Weak boudinaging of the more quartz-rich zones indicates that this is the most competent layer in this portion of the Mfongosi schist. The rock cleaves along a strong planar foliation developed either at concentrations of phyllosilicate minerals or at quartz stringer/matrix contacts. Well-defined, usually subvertical slickenlines are developed on regularly-spaced slickenside surfaces.

Figure 4.15 Field appearance of the porphyroblastic quartz-muscovite/talc-albite-opaques-epidote±calcite schist. Note the magnetite and pyrite crystals which have been entrained in slickenlines

In thin section this phyllitic quartzite displays evidence of deformation (portions of ***Slides FU2H-A, D, F, F', H, 15, 20***). The groundmass is composed of sutured to annealed saccharoidal quartz and albite, aligned muscovite and talc, and epidote and opaques between discontinuous bands of quartz. The matrix contains porphyroblasts of epidote ± quartz which are useful kinematic indicators. The average grain size in the matrix is 0.01 to 0.03 mm. The strained and sutured quartz bands are parallel to the planar foliation (S_{01}). Rare σ and δ structures

(Ramsay and Huber, 1983; Passchier and Simpson, 1986; Passchier, 1987) of porphyroblasts show consistent left-lateral movement parallel to the strike of slickensides (Figure 4.16 a) while sections parallel to the dip and perpendicular to the strike of the slickensides indicate a consistent hangingwall-to-north movement (Figure 4.16 b).

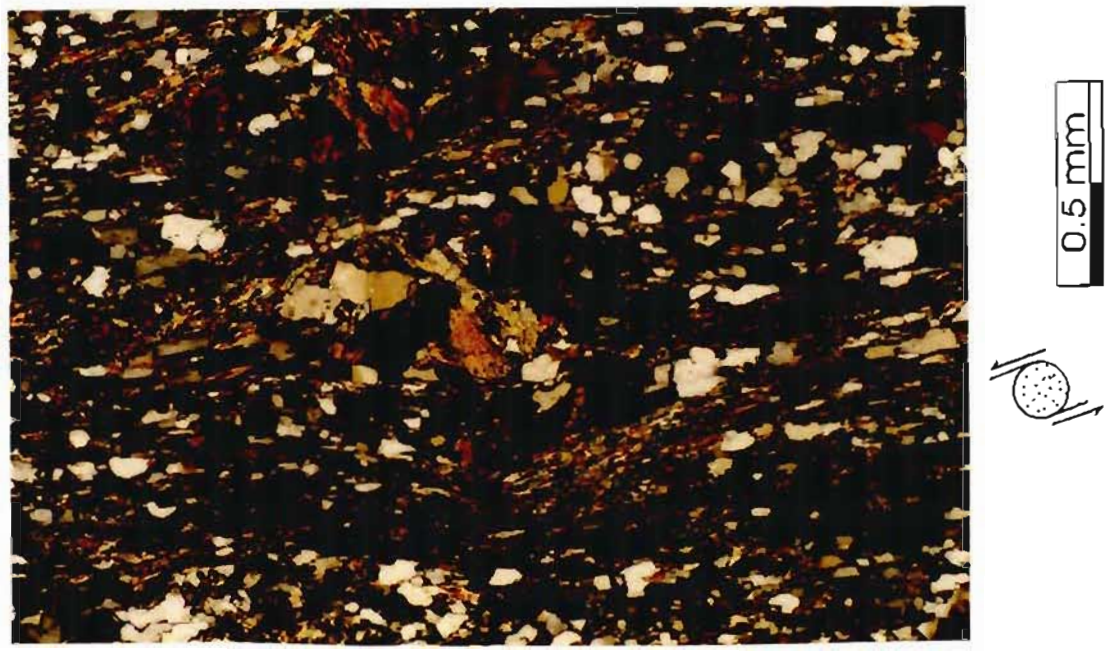

Figure 4.16 a Formed as a result of the oblique movement at the Manyane Thrust transmitted northwards to the Mfongosi schist, epidote glomeroporphyroblasts show left-lateral movement (σ-structure) in a section parallel to a nearby slickenside surface. The extent of left-lateral movement is limited given the azimuth of the nearby slickenlines (steeply south-southwest plunging). Porphyroblastic quartz-muscovite/talc-albite-opaques-epidote±calcite schist. (***Slide FU2H-H***). XP.

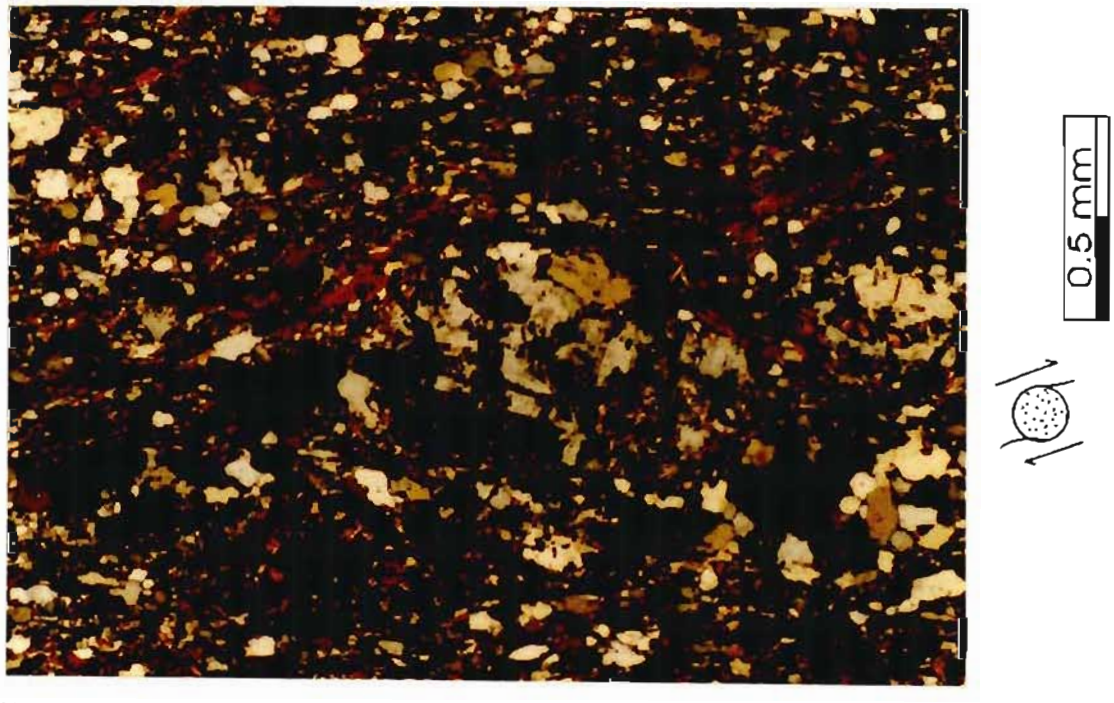

Figure 4.16 b A section parallel to the dip and perpendicular to the plane of nearby slickensides. A poorly-developed δ-structure indicating top-to-north shearing movement is evident within the disruption of the initial isoclinal folding in the phyllitic quartzite as a quartz-epidote glomeroporphyroblast has been rotated within the highly-sheared matrix. (***Slide FU2-20***). XP.

Where talc and/or muscovite become dominant over quartz in proportion, a dark-yellow to pinkish light brown rock is evident (Figure 4.17). Extreme carbonate metasomatism produces a light creamy yellow variety of this lithology. Carbonate metasomatism post-dated growth of euhedral magnetite and pyrite and flattening of opaques into the planar foliation as the calcite occurs in strain shadows of the competent opaques (*c.f.* late carbonate metasomatism as proposed by Bullen *et al.*, 1994; this study).

Figure 4.17 The dark yellow to pinkish light brown variant of the phyllitic quartzite (LBQ-3-VAR; the lateral variation of the phyllitic quartzite; wherein talc and/or muscovite are proportionally greater than quartz. Note that it is very difficult to distinguish movement indicators in this lithology (***Slide LBQ-3-VAR***). XP.

Quartz-epidote-chlorite-albite-opaques ± calcite schist

The phyllitic quartzite is interlayered with a *quartz-epidote-chlorite-albite-opaques ± calcite schist* (Figure 4.18, portions of ***Slides FU2H-B, E, 16***; Figure 4.19) which hosts phyllitic quartzite lenses and forms one of the dominant lithologies in this portion of the Mfongosi Group, but weathers far more readily than the adjacent layers due to its often high (up to 25 %) calcite and/or chlorite content. Its characteristic pale blue-green colour is imparted by epidote and chlorite. Evidence of deformation includes cataclastically-reduced quartz and albite, both annealed and often with 120° triple-point junctions. Other notable features are the abundance of opaque minerals, mainly magnetite and pyrite (collectively up to 5%), bands of decussate chlorite with quartz, albite and calcite. It is apparent that carbonate metasomatism was late in the

tectonometamorphic history of the rock as no high-temperature meta-calcsilicate minerals have formed despite the abundant reactants available. In other layers talc is the only evidence for possible metacalcsilicate reactions at low temperatures (Figure 4.17; Miyashiro, 1973; Yardley, 1989). Carbonate metasomatism was followed by epidotization. From grain relationships, carbonate metasomatism occurred after the annealing of quartz and albite, that is this post-peak carbonate metasomatism of the Mfongosi schists implies a late generation of carbonate-bearing fluids.

Figure 4.18 Field appearance of the quartz-epidote-chlorite-albite-opaques±calcite schist which is essentially similar to the epidote-quartz-chlorite schist which is described below.

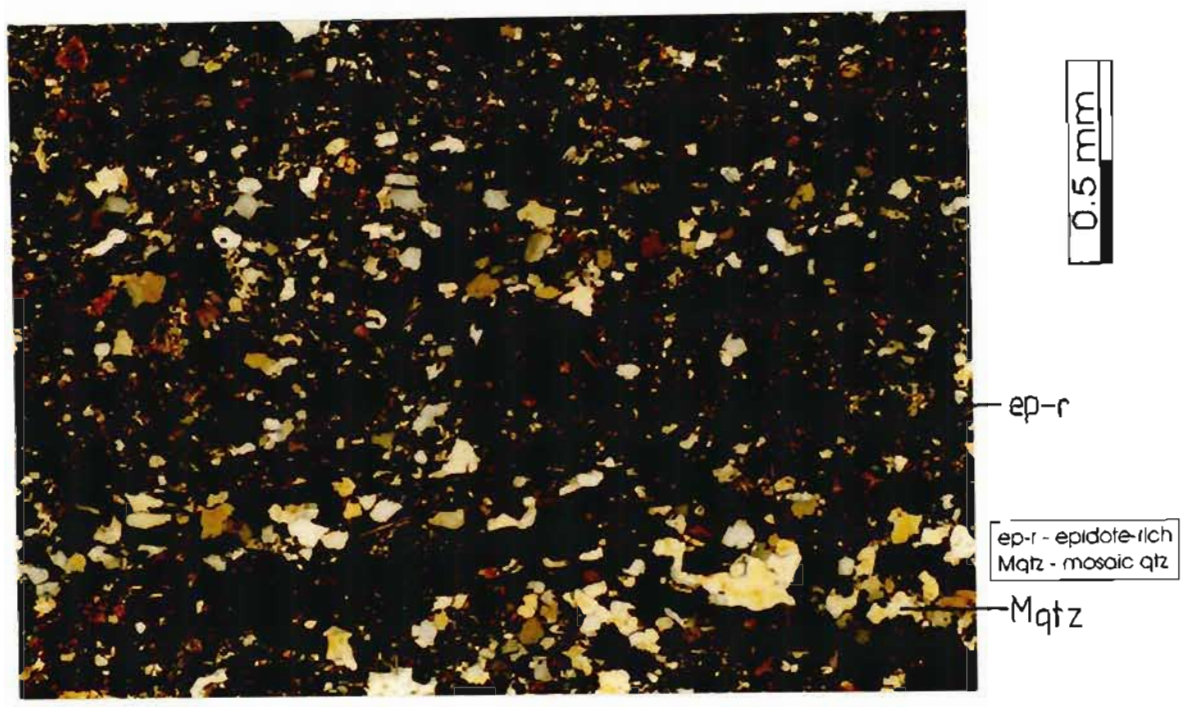

Figure 4.19 Quartz-epidote-chlorite-albite-opaques±calcite schist. Note the epidote-rich and mosaic-textured quartz-rich layers (***Slide FU2H-E***). XP.

Epidote-quartz-chlorite-opaques-calcite-sphene-alkali feldspar volcaniclastic/schist

The third rock type prevalent in the southern Mfongosi area contains the majority of the opaque phases (magnetite and pyrite) which may be up to 6% by volume. Epidote may comprise up to 50% by volume in this *epidote-quartz-chlorite-opaques-calcite-sphene-alkali feldspar volcaniclastic/schist* (portions of ***Slides FU2H- C, G, 17***, Figure 4.20). Flattened relic amygdales containing zeolites, epidote, K-feldspar (after, or reverted to zeolite), quartz and albite are common and occur in such volumes as to constitute a weak banding. Carbonate metasomatism was late in the sequence of fabric-forming events, producing calcite in augen strain shadows around pyrite and magnetite, indicating that flattening may have been prevalent during metasomatism (*cf.* late-tectonic flattening of isoclinal folds limbs in the Ngubevu area). Where this schist is silicified or albitized (thin section and field observations) early in the series of events affecting the Mfongosi Group, it exhibits weak pinch and swell structures as its competency must necessarily have increased with continued deformation.

This lithology is referred to as an "epidote-quartz-chlorite volcaniclastic". The complexity of the interlayering of the abovementioned rock types is depicted in Figure 4.22.

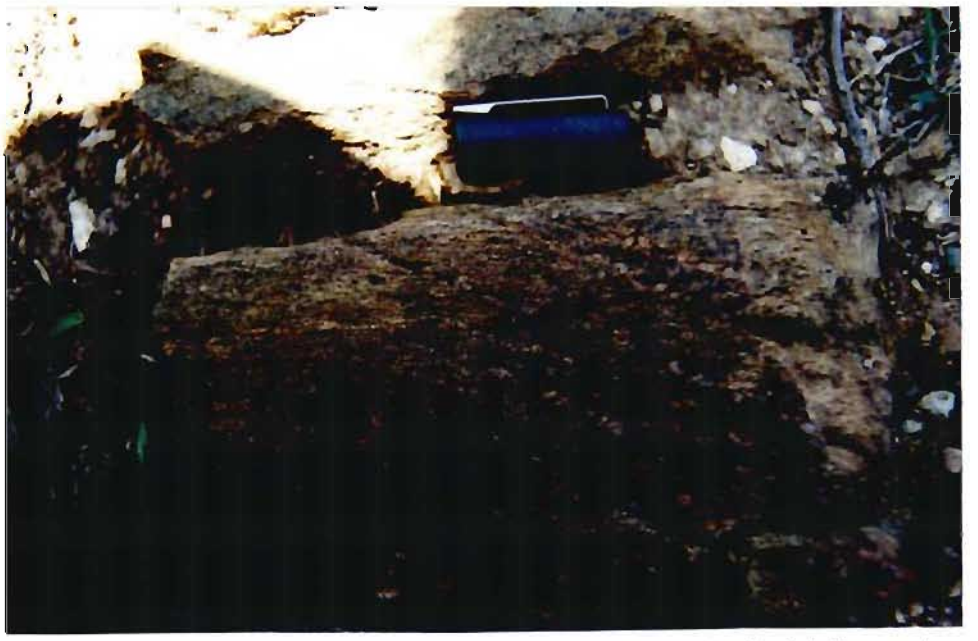

Figure 4.20 Light blue-green to grey epidote-quartz-chlorite-opaques-calcite-sphene-alkali feldspar volcaniclastic/schist, occurring as lenses and layers, which have undergone boudinaging, in the phyllitic quartzite

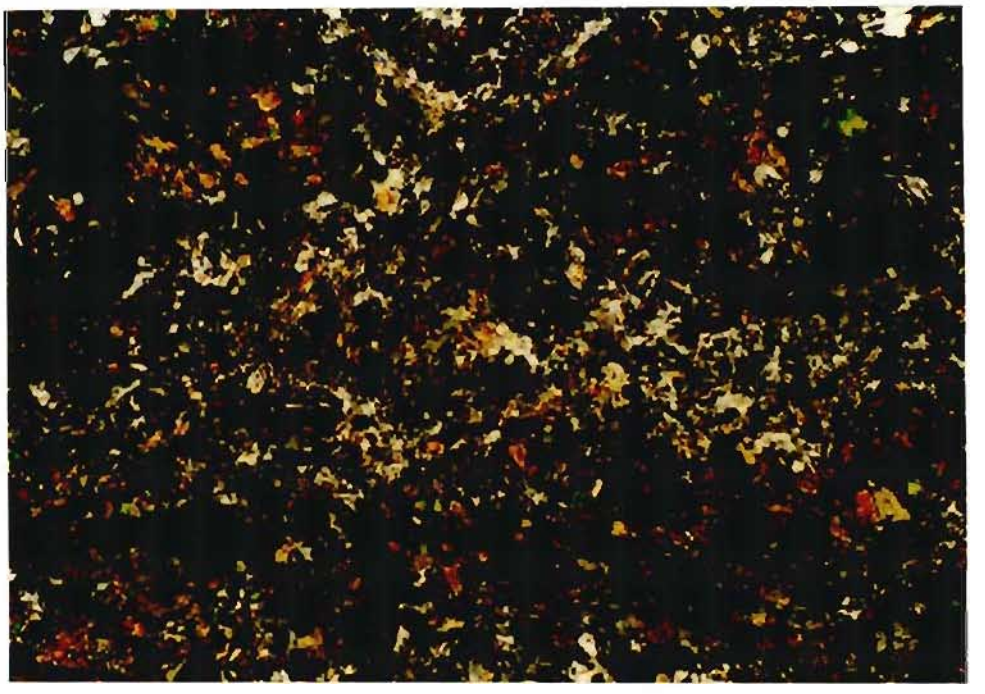

Figure 4.21 Epidote-quartz-chlorite-opaques-calcite-sphene-alkali feldspar volcaniclastic/schist. In this section, epidote and chlorite are dominant over quartz and alkali feldspar and layering is usually obscured due to the lack of alignment of epidote and the secondary nature of the chlorite *(Slide FU2H-C)*. XP.

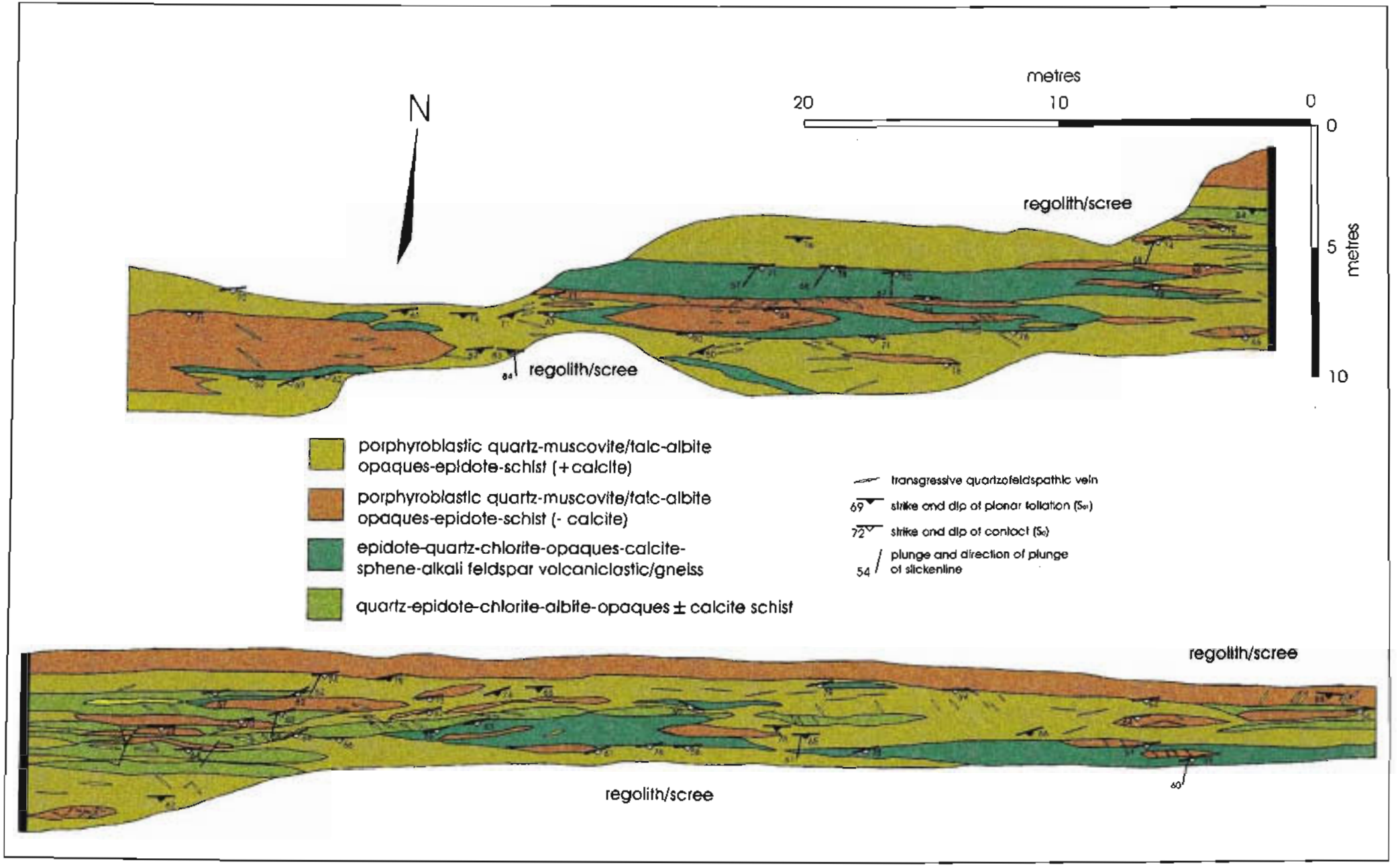

Figure 4.22 Map of a donga to the west of the Mfongosi River, which exposes relatively fresh Mfongosi Group rocks. The position of the donga is indicated on Figure 4.11. The layering and banding depicted in the Mfongosi Group in Figures 4.3 and 4.1 is simplified: the light brown phyllitic quartzites are grouped together, as are the epidote-quartz-chlorite schist and the quartz-epidote chlorite schist.

b) Structural Features

I) Banding/Separation of Units

In outcrop, local solution and redeposition of quartzofeldspathic and calcitic material may result in rather diffuse boundaries between lithologies which are usually separated by slickenside surfaces, often with the majority of shallowly southwest-plunging slickenlines such that the bulk of late left-lateral movement was accommodated on S_0 surfaces and the veins under study here do not transgress the slickensides developed on the S_0 plane. Slickensides may also cross-cut veining and are developed on the margins of suitably-oriented veins. A second, minor planar foliation (S_2) in the phyllitic quartzites is only observable in thin section.

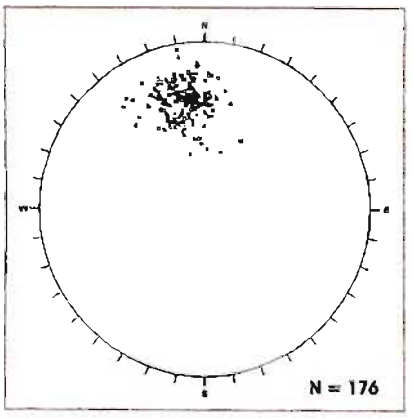

Figure 4.23 a Slickenside surfaces (S_{01}) in phyllitic quartzite of the Mfongosi Group in the southern Mfongosi Valley area. Note the greater variation in data spread when compared to that of the epidote-quartz-chlorite volcaniclastic N = 176

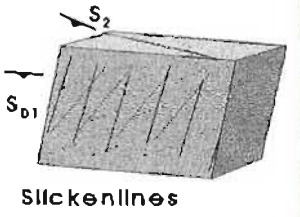

Figure 4.23 b Block diagram of the structural relationship between S_{01}, S_2 and slickenlines

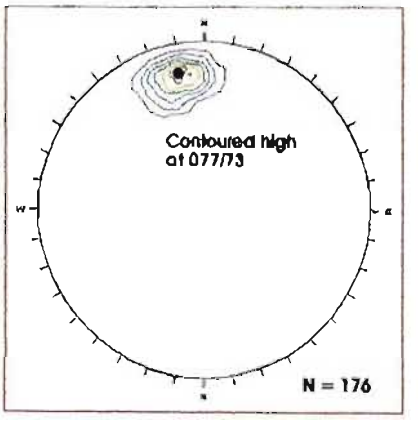

Figure 4.23 c Equal area, lower hemisphere stereonet plot of slickensides as shown at left. Contoured high is at 077/73°
N = 176

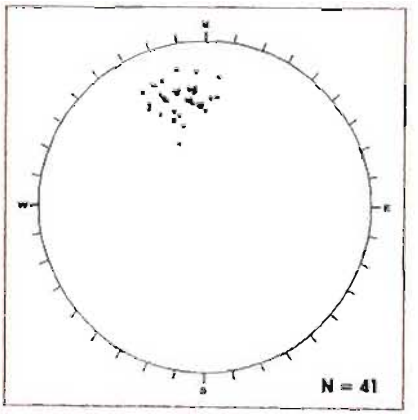

Figure 4.23 d Slickenside surfaces in epidote - quartz - chlorite - opaques - calcite - sphene - alkali feldspar volcaniclastic/schist in the southern Mfongosi Valley area. This lithology is largely conformable to, and hosted within, the phyllitic quartzite N = 41

The spatial distribution of slickensides in the epidote-quartz-calcite volcaniclastic display less variation possibly due to less boudinaging which only occurred after epidotization and/or silicification; the phyllitic quartzites were the most competent layers at the time of boudinaging. The angles between the S (S_2) and the C (S_{01}) cleavages, in individual lithologies, in the plane perpendicular to the S_{01} foliation and parallel to the strike, are as follows (Table 4.3):

Table 4.3 Range of angles and average angles between S (S_2)and C (S_{01}) cleavages in the dominant lithologies in the southern Mfongosi Valley area, measured from thin sections. The angle ϕ is shown on Figure 4.24.

Lithology	Range (ϕ)	Average (ϕ)
Porphyroblastic quartz-muscovite/talc-albite-opaques-epidote schist	18-28°	23° (n = 16)
Quartz-epidote-chlorite-albite-opaques ± calcite schist	5-24°	13° (n = 23)

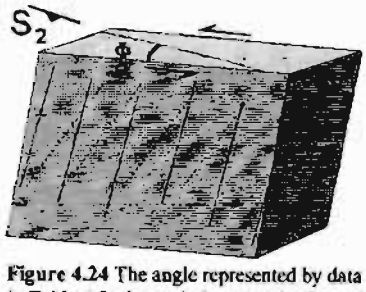

Figure 4.24 The angle represented by data in Table 4.3; the angle between the S_{01} and the S_2 foliations in the plane parallel to strike and perpendicular to the dip of S_{01} (termed Φ)

ii) Slickenlines

The nature and orientation of slickenlines in the dominant lithologies in the Mfongosi Group are similar to those in the Manyane amphibolite and the same succession of steeply south-plunging to shallowly southwest-plunging slickenlines are evident at the contact of each lithology (Figure 4.3; Figure 4.25). The variation in slickenline orientation may imply that initial thrust planes were being rotated, such that in the later stages of deformation, they become steep strike-slip to oblique-slip faults.

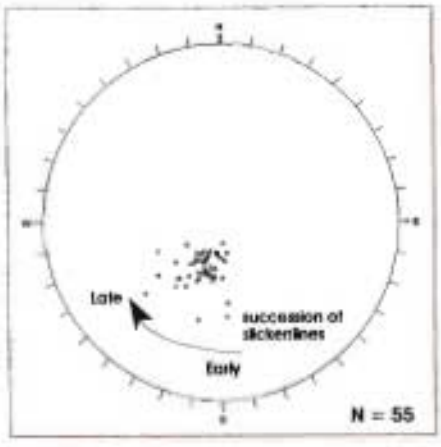

Figure 4.25 a Slickenlines on slickenside surfaces in the Mfongosi Group in the southern Mfongosi Field area. Plunge and direction of plunge of slickenlines vary from 176→34° to 231→32°, the southward-plunging slickenlines pre-dating the SW-plunging sets, the latter occurring primarily at S_0 contacts N = 55

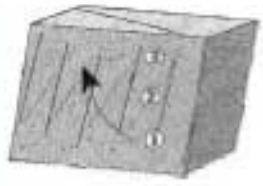

Figure 4.25 b Block diagram of the succession of slickenlines in the Mfongosi Group

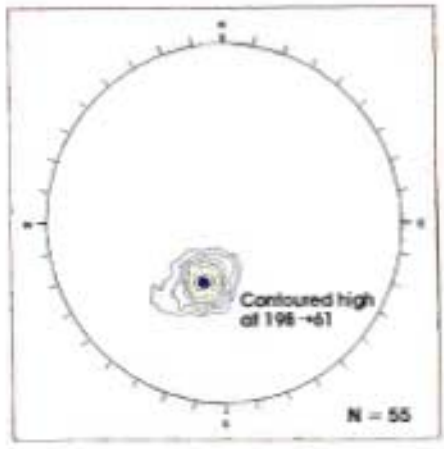

Figure 4.25 c Equal area, lower hemisphere contour plot of slickenlines as at left. Concentration of data is at 198→61° which coincides with the peak in linear features in the Manyane amphibolite, suggesting a synthesis of deformation N = 55

Steeply south-dipping slickenlines on the margins of the quartzofeldspathic veins suggest an early, pre-thrusting/pre-reverse faulting vein generation as explained below. The same succession of slickenlines (Figure 4.25) is frequently found on suitably oriented vein margins.

iii) Boudinaging

Both the phyllitic quartzite and the silicified/albitized epidote-quartz-chlorite volcaniclastic underwent boudinaging or pinching and swelling with the long axes of the pinch structures and boudin terminations at 184→66° parallel to the long axes of prolate pillow basalts in the amphibolite (Figure 4.26). Furthermore, large quartzofeldspathic veins also underwent a similarly-oriented attenuation, suggesting that they formed prior to thrusting and flattening of closed folds in the Mfongosi Group.

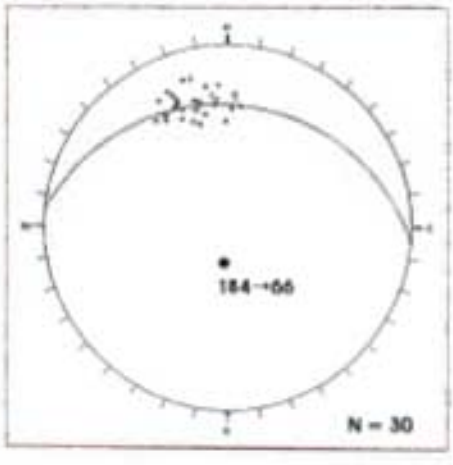

Figure 4.26 a Poles to margins of pinch and swell structures and boudins in phyllitic quartzites and silicified/albitized epidote-quartz-chlorite volcaniclastic in the Mfongosi Group. Long axes of pinch structures and boudin terminations, although not measured in the field, fall on the pole to a great circle approximation to data: 184→66° N = 30

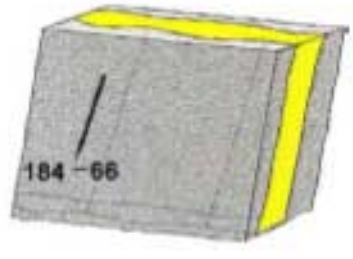

Figure 4.26 b Block diagram to illustrate the context of boudins in the host rock. Note that the veins are not parallel to the host rock planar foliation, but have been rotated towards it such that they are now sub-parallel to S_0.

iv) Veining - Fractures Related to Folding

The exact setting of veining in the deformation history and the orientation of the veining with respect to Natal Nappe Zone lithologies and the Kaapvaal Craton have formerly not been studied in any detail. Veining in the Mfongosi Group occurs in two main modes, both of which are offset by slickensides and lithological contacts. Both sets of veins are at acute angles to the host rock planar foliation and bear signs of boudinaging and slickenline formation on their margins:

- large white or grey quartzofeldspathic veins, which are up to 38 cm in thickness with maximum observed down-dip extensions of 7 m contain disseminated pyrite, magnetite, bornite and chalcopyrite, and host the bulk of the prospecting efforts in the Mfongosi Goldfield. The orientation of these veins is either steeply north-northwest dipping or steeply south-southeast dipping (Figure 4.27). Entrainment of the host phyllitic quartzite and epidote-quartz-chlorite volcaniclastic and slickensided margins are the most notable structural features. Larger veins form in correspondingly thicker units.

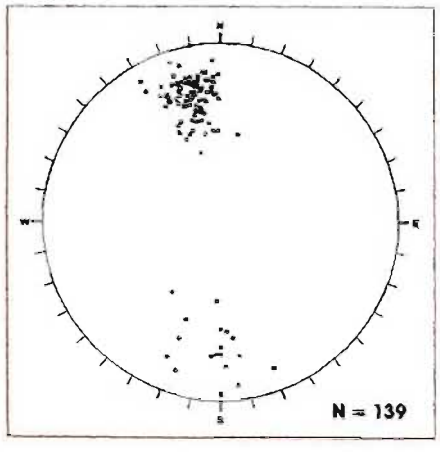

Figure 4.27 a Poles to large quartzofeldspathic veins in which the majority of the prospects of the Mfongosi Goldfield are hosted. Veins are steeply NNW- and steeply SSE-dipping N = 139

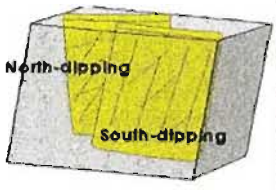

Figure 4.27 b Block diagram showing the situation of veins in the host rocks

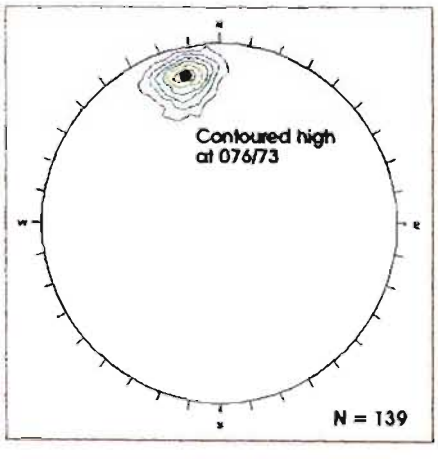

Figure 4.27 c Equal area, lower hemisphere projection of large quartzofelspathic veins in the Mfongosi Goldfield area as shown at left. Contoured high is at 076/73°, that is, almost identical to the S_0 maximum in phyllitic quartzites (077/73°) N = 139

- smaller, mutually cross-cutting veinlets up to 4 cm thick which have similar mineralogies to the larger veins but are more dusted with sulphides, making them opaque. These veins are at acute angles to the host planar foliation and are disrupted by the top-to-north movement along lithological contacts. The orientations of the veins appear somewhat random at first, but an equal angle stereonet plot shows a girdle distribution around

195→58° or a conical distribution around the point 199→76°: cone angle of 82° (direction of plunge and plunge). Either of these axes, which are spatially related, define the intersection between flattened and rotated, northeast-trending and northwest-trending veinlets. This vein set has slickensided margins, the orientations of which have been re-arranged by late oblique motion.

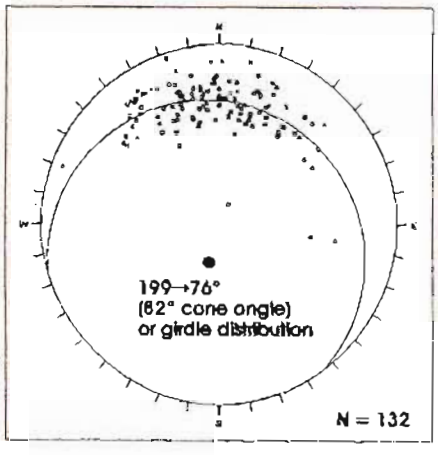

Figure 4.28 a Poles to margins of small quartzofeldspathic veins in the Mfongosi Goldfield. Veins trend between NE and NW, with dips similar to those of the host rock planar foliation N = 132

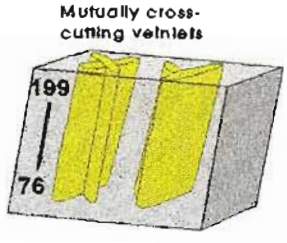

Figure 4.28 b Block diagram of the configuration of the smaller, mutually cross-cutting veinlets

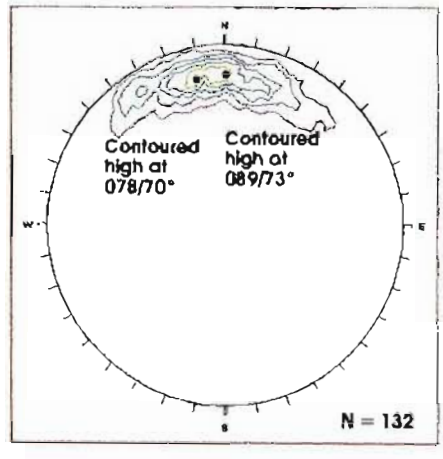

Figure 4.28 c Equal area, lower hemisphere projection of data at left, with two poorly-defined contoured highs at 078/70° and 089/73°, presumably representing the original separate sets of veins N = 132

Veining initiated at high angles to bedding but was subsequently rotated into near-parallelism to S_0 and S_1, segmented by S_{01} slickensides, and boudinaged due to the lateral extension of the Natal Nappe Zone (see Chapter 5). The exact mechanism of fracture genesis will be discussed.

c) Metamorphism

The three main rock types comprising the Mfongosi Group in the field area are often extensively intercalated, although an overall facies of metamorphism may be estimated. The laterally interlayered quartz - muscovite - albite - opaques - epidote schist and quartz - talc - albite - opaques - epidote schist are indistinguishable in hand specimen. Thin section work shows that each variant of the phyllitic quartzite displays a uniformly low-temperature greenschist facies assemblage, derived from the following mineral combinations:

- the low-temperature metamorphosed siliceous dolomitic limestone assemblage (talc - chlorite - epidote) with talc having been formed by the following reaction:

$$3 \text{ dolomite} + 4 \text{ quartz} + H_2O \rightarrow \text{talc} + (\text{calcite}) + 3\ CO_2$$
(Miyashiro, 1973)

- lower greenschist grade assemblage, from a partially pelitic protolith : muscovite + chlorite + albite (Yardley, 1989).

The dominant phyllitic quartzite samples (FU2H - A, D, F, F') and the talc-rich lateral variant (typified by sample LBQ-3-VAR, Figure 4.17), are plotted on an A'KF diagram (Winkler, 1974) due to the substantial K component. The ternary position is derived from combinations of major element oxides (Figure 4.29, Appendix A3) which correspond to those derived from mineral proportions despite the fact that talc and calcite may not be represented accurately on A'KF.

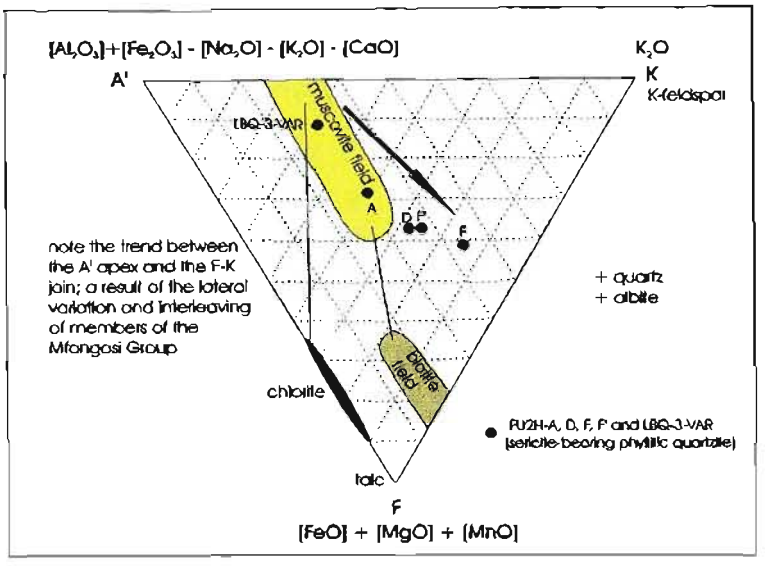

Figure 4.29 A'KF plot of the phyllitic quartzite (Samples FU2H - A, D, F, F' and LBQ-3-VAR)

The epidote-quartz-chlorite-calcite volcaniclastic (Samples FU2H - C and G) plot more readily on an ACF diagram although actinolite, characteristic of the epidote-amphibolite facies, is absent. Under a high P_{CO2} actinolite is decomposes to form calcite and chlorite: the higher the pressure of CO_2, the greater the extent of alteration; calcite and chlorite may be the only minerals remaining (Miyashiro, 1973), hence the indicator assemblage of epidote with chlorite and calcite (Figure 4.30).

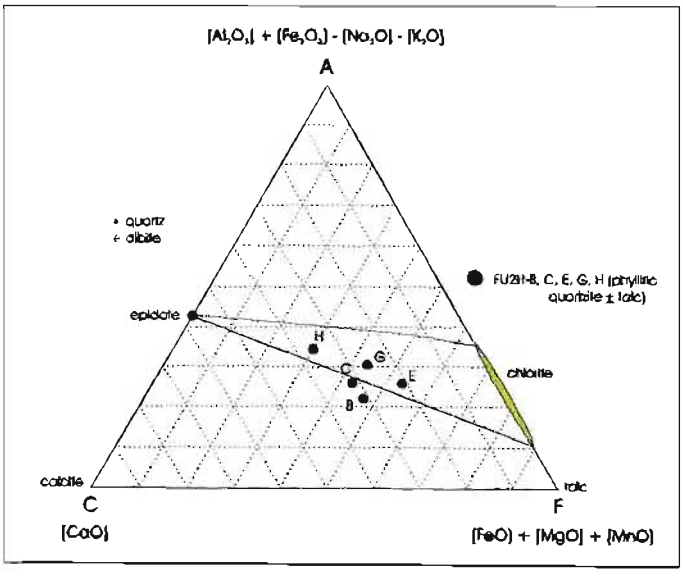

Figure 4.30 ACF plot of the epidote-quartz-chlorite volcaniclastic and the quartz-epidote-chlorite volcaniclastic (Samples FU2H - B, C, E, G, H)

The quartz - epidote - chlorite - albite - opaques ± calcite (Samples FU2H - B and E) ACF plot is essentially similar to that of the epidote-quartz-chlorite volcaniclastic although calcite is often confined to bands. As Miyashiro (1973) states, "rocks recrystallized at different P_{CO2} occur intermingled with a mineral zone of ordinary size, ie, on outcrop scale" allowing the adjacent assemblages to be attributed to the same metamorphic facies.

Stilbite, a Ca-zeolite, is found in glomeroporphyroblasts in the epidote-quartz-chlorite volcaniclastic. Stilbite is mainly of low-temperature igneous or metamorphic origin (Deer *et al.*, 1992) and the zeolite facies is that set of mineral assemblages which is characterized by the association of Ca-zeolite + chlorite + quartz in rocks of suitable composition. Zeolites may be transformed into feldspars (especially alkali feldspars) when subjected to thermal metamorphism. Due to the mineral assemblages, estimates of temperature only are possible and no conclusion about pressure may be attempted.

4.4) Tectonometamorphic Features

a) *Fracture patterns*

A model has to explain the following:

- formation of conduits to fluid movement in the Mfongosi Group, as well as the present configuration of veining in the Mfongosi schist
- the mechanism whereby temperatures were raised sufficiently in the Mfongosi schist so as to leach metallic and non-metallic components into pre-formed fractures
- the present inverted metamorphic sequence across the Manyane Thrust - lower-temperature greenschist facies in the Mfongosi Group near the Manyane Thrust to amphibolite facies in the Manyane amphibolite adjacent to the Manyane Thrust
- late- or post-tectonic recrystallization of the Manyane amphibolite above the Manyane Thrust
- the formation of a tectonic melange in the northern Mfongosi Valley area in post-veining/late-tectonic times

The relationships between fractures and minor and major folds prior to isoclinal fold formation and flattening must be ascertained. Past studies (eg Price, 1966; McQuillan, 1973) concentrated on minor fractures and shears in the limbs and hinge zones of major cylindrical buckle folds, which have consistent orientations with respect to bedding. Three major groups of fractures/shears are commonly developed during deformation of a foreland and the formation of buckle folds (Price, 1966; Price and Cosgrove, 1990):

- **Dilational fracture** patterns on fold limbs cut the fold axes at 90° and are perpendicular to the bedding while an orthogonal set trends parallel to fold axes while also being perpendicular to bedding (Figure 4.31). Dilational fracture type "D-a" is usually vertical while type "D-b" varies in dip (Price and Cosgrove, 1990). Type D-b dip variations becomes progressively less as the fold is flattened into a closed or isoclinal form (*op. cit*; this study). The intersection of D-a and D-b is initially sub-perpendicular to bedding. In the ideal system, there is no priority of formation, ie; nothing dictates that D-a develop before D-b. Alternating and repeated vein dilation may make for extremely complex opening sequences with abundant cross-cutting relationships. The maximum principal

extension direction (σ_3) for opening is different for D-a and D-b but is largely parallel to the bedding. Price and Cosgrove (1990) state that infilling by quartz or calcite is common, however, intuition dictates that the opening direction, coincident with σ_3, cannot be temporally identical in orientation for both dilation events.

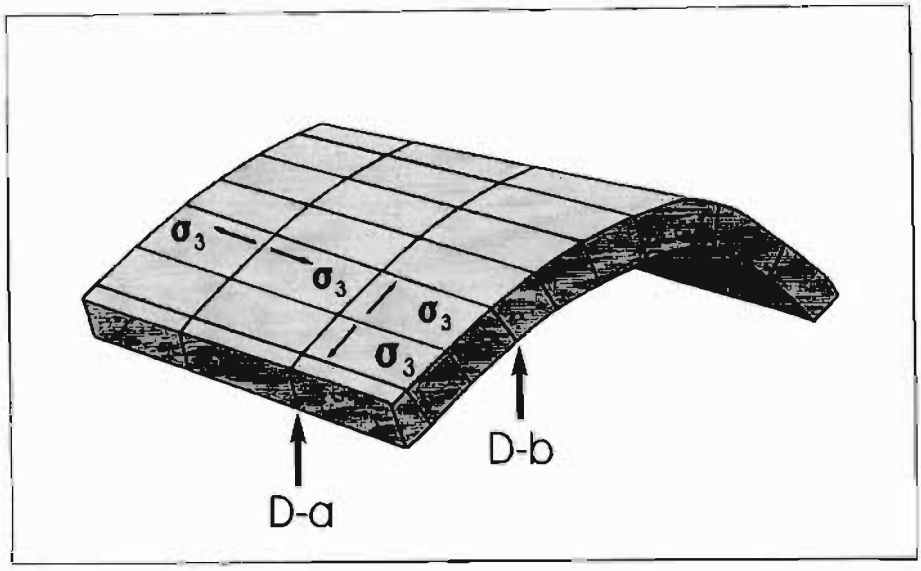

Figure 4.31 Ideal relationship of dilational fractures to a fold (after Figure 14.21a of Price and Cosgrove, 1990). D-a and D-b as in text. The orientation of the minimum principal *compressive* stress axis orientation = maximum principal *extension* direction (signifying dilation) for each are shown.

- **Shear fractures** are markedly more complex than dilational fractures. Price (1966) and Price and Cosgrove (1990) divide the shear fractures into four main systems (Figure 4.32 - S-a, S-b and S-c, S-d)
  - normal faults (S-a)
  - thrusts (S-b)
  - strike-slip faults (S-c)
  - oblique-slip faults (S-d)

If the intermediate principal compressive stress axis (σ_2) coincides with the intersection of conjugate faults or shear planes (Navier-Coulomb theory, Price and Cosgrove, 1990), generation of three different fault or shear types in the same layer must imply a variation in σ_2 orientation. The σ_3 orientation may vary too; in thrust faults σ_3 is perpendicular to the bedding whereas for other fault types, σ_3 is usually parallel to the bedding (Figure 4.32). Note the "rule of thumb"; the

frequency of occurrence of each type, for example, conjugate strike-slip faults usually occur most frequently, the intersections of which are initially at right angles to bedding. Intersections between conjugate veins, as for the intersections of D-a and D-b, will naturally be rotated towards the bedding plane as the fold limb is flattened. Extreme flattening may cause veins to be subparallel to the axial cleavage in fold limbs (*op. cit.*; this study). The vein distribution of Figure 4.27 a may be explained simply as infilling of the S-c and D-a shears/fractures by the larger quartzofeldspathic veins at deeper levels in the overburdened Mfongosi schist. These veins were subsequently rotated into parallelism with the S_{01} foliation (Figure 4.23). Note that both north-northwest and south-southeast-dipping veins are evident although the former are dominant in that the direction of dip of a large portion of the south-southeast dipping veins would have been reversed during tightening of the fold structures.

As a demonstration of the mechanisms of vein intrusion and deformation to produce the stereonet distributions on Figure 4.28 a, a hypothetical original fracture pattern (Figure 4.33) will be "deformed" to that of Figure 4.28 a. To begin with, fractures would have to define an essentially circular distribution on stereonets such that all relevant fracture and/or shear types would be represented. The centre of this distribution effectively describes an intersection lineation between conjugate vertical or subvertical fractures. This lineation would be sub-vertical (Figure 4.33 a) but, as the fractures, with or without veining, are rotated towards the axial surface of a progressively tightening fold, this lineation would also approach the fold axial plane. An extent of the deformation may be gauged in that such features (veining and foliation) are now broadly concordant (e.g. the poles to veins approach the S_{01} maxima - Figure 4.33 b). In the final stage a girdle distribution, that of Figure 4.28 a, is centred on a virtual lineation and may persist with the contoured high of poles to veinlets being similar to that of S_{01} (Compare S_{01} maximum at 077/73 with contoured maximum of Figure 4.28 c). Note also that in Figure 4.28 c there are two possible maxima which are the relics of the two shear directions and/or one dilational fracture orientations (S-c and D-a). Finally, the temporal trend of this virtual lineation will define a gross movement vector which, in this case, is not north-south, but trends at about 015°.

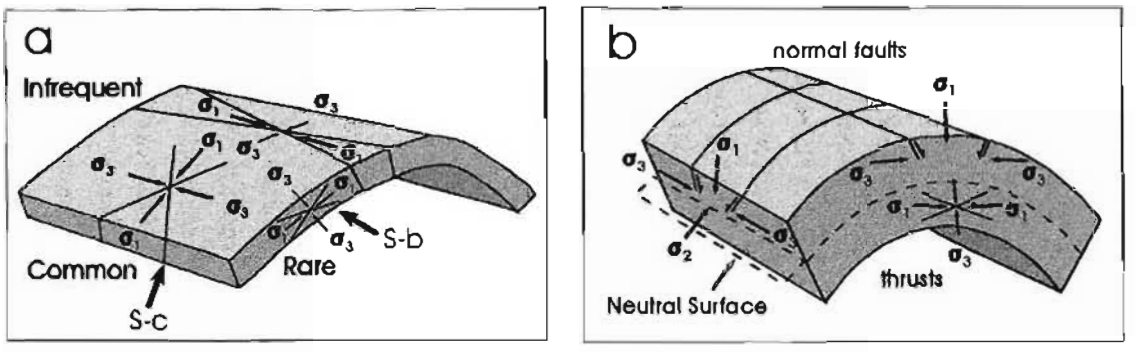

Figure 4.32 a) ideal orientations of shear fractures in a thin, bedded layer (after Figures 14.21b of Price and Cosgrove, 1990).
b) Typical orientation of normal faults and thrusts which develop in a thick, flexured unit. The emplacement of the Tugela Nappe or the Natal Nappe Zone was responsible for foreland deformation, fracture and shear initiation and dilation of these features, possibly due to overloading of the foreland by nappes.

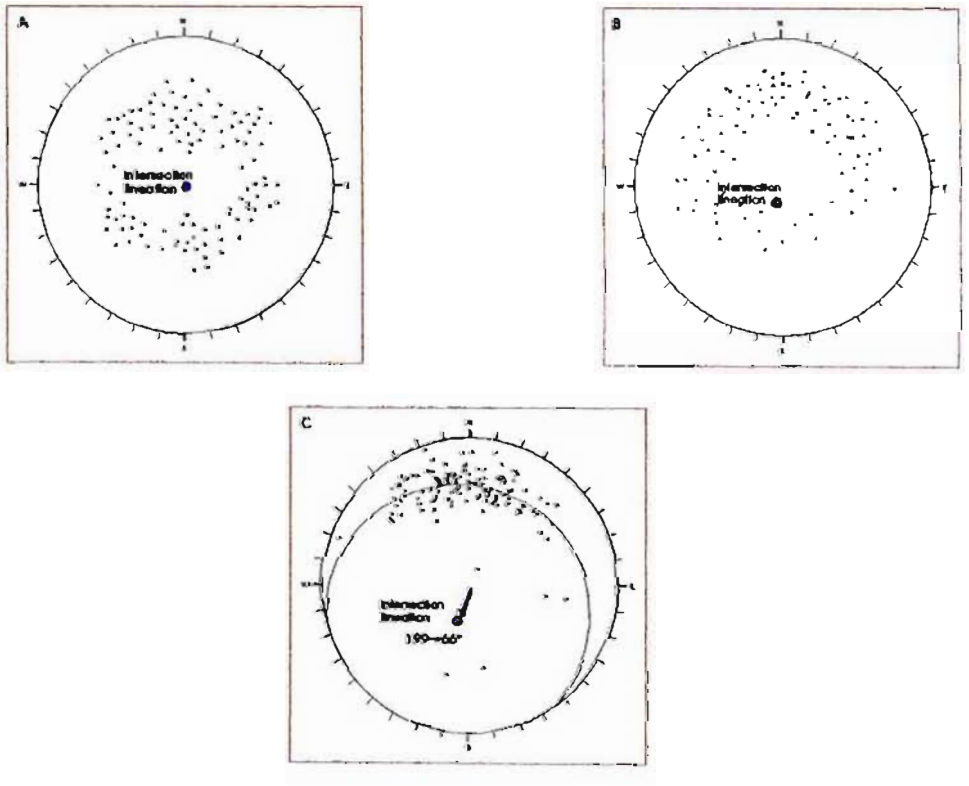

Figure 4.33 Evolution of the spatial distribution of small, cross-cutting veinlets in the Mfongosi Group. a) girdle distribution of poles to hypothetical fractures in a macrofold formed in foreland deformation b) with progressive tightening of the fold the poles to these fractures (possibly infilled by quartz etc) migrate towards the foreland "half" of the stereonet yet still maintain their girdle distribution c) with extreme deformation and closed folding the poles to the fractures or quartz veins approach the orientation of the dominant planar foliation. Note the movement vector of the intersection lineation, trending at approximately 015°.

Veining in the Mfongosi schists is due to the Manyane Thrust and the emplacement of the Tugela Nappe which was responsible for foreland margin/marginal volcaniclastic deformation, fracture initiation and infilling of these fractures due to overburdening of the Natal Nappe Zone. Structural evidence, especially orientations of linear features, indicates extensive reverse to thrusting movement along the Manyane Thrust, with the Tugela Nappe overriding the Mfongosi Group. The thermal evolution of the Tugela Nappe, the pressure-temperature-time () path during burial and exhumation (Figure 4.12), is compared to models developed by Richardson and England (1979), England and Thompson (1984), Thompson and England (1984) and Ridley (1989). Predictions of transient thermal regimes operating in thickened crust and at the margins of upward moving blocks provide a qualitative basis from which to interpret the metamorphic and orogenic evolution of the contact between the two above-mentioned structural domains. This understanding presumes a knowledge of likely paths of a rock volume in a given (modelled two-dimensional) tectonic environment and features of these paths and rock textures, such as porphyroblast/matrix relationships, which are diagnostic of a particular process (Ridley, 1989).

b) Temperature Increase at the Manyane Thrust due to Block Movement and/or Thrusting.
The emplacement of nappes or homogeneous horizontal shortening disturbs normal, pre-existing geothermal gradients and stable isotherms (Figure 4.34). In a cycle of thickening and erosion the metamorphic peak is reached later at progressively deeper levels in the crust (Richardson and England, 1979) such that a phase of deformation may post-date the metamorphic peak at relatively shallow levels but be pre-peak metamorphism in deeper buried rocks (England and Thompson, 1984). This case is exemplified when a thrust or steep fault cross-cuts rocks at intermediate depths and offers one option for renewed heating at the upthrown block (Manyane amphibolite) margins. In the upthrown/downthrown block scenario:

- if block movement takes place prior to the temperature maximum of the entire unit then the upthrown block undergoes continued heating after movement initiation (Ridley, 1989). Rocks near the edge of the downthrown block undergo renewed heating, producing a second post-deformational metamorphic peak which may obscure metamorphic features of the earlier thickening event (Thompson and England, 1984; Ridley, 1989).

- if block movement takes place near the metamorphic peak (the upper amphibolite facies in the Tugela Nappe - Harmer, 1979) the upthrown block will cool after deformation initiation. At the edge of the upthrown block, cooling starts after the first deformation increment and porphyroblast growth overlaps with the initial deformation as the time of cooling is progressively later towards the block centre (Ridley, 1989). This implies a second possibility for the porphyroblast/matrix relationship at the Manyane Thrust.

Houseman and England (1986), England (1987) and Ridley (1989) predict block movement in a path; strike-slip (and extensional) deformation of orogenic belts is likely when the crustal base reaches a critical temperature after thickening. The orogenic episode generally comprises a relatively rapid phase (<1 ma) of crustal thickening, with little temperature change, followed by a lengthier phase of erosion. The principal features are: thermal relaxation during which temperatures rise towards the level set by the higher geotherm supported by thickened crust, followed by a period of cooling as the rock approaches the cold land surface by exhumation (England and Thompson, 1984).

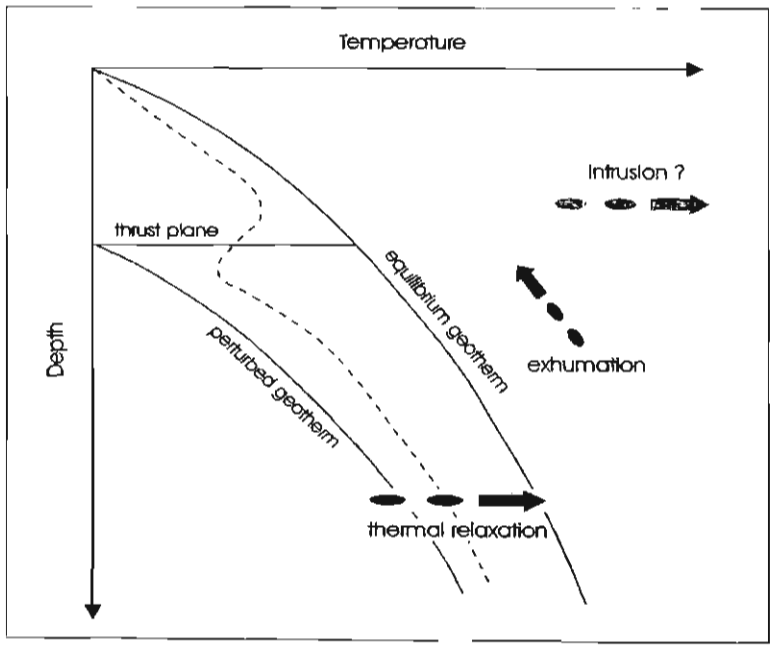

Figure 4.34 Overthrusting results in an instantaneous perturbation of a geotherm, followed by thermal relaxation - the basis of one-dimensional numerical P-T-t models. Exhumation accompanies thermal relaxation. Intrusion into any level of the overthrust pile will further perturb the geotherm (modified after Jamieson, 1991)

Crustal thickening by thrusting results in two zones of heat production, one starting at the surface and one immediately below the thrust whereas homogeneous thickening results in only one such zone (*op. cit.*). The average temperature perturbation is the same in both cases but the "steady state" geotherm is hotter and higher absolute temperatures are obtained for thrusting *(op. cit.*). The path of homogeneous thickening is similar to that of thrusting followed by erosion but assumes two volumes of rock at different initial pressures.

Thickening by thrusting

Thrusting establishes a heat supply distribution which supports a steady-state geothermal gradient higher than that of undisturbed crust (England and Thompson, 1984). Immediately after collision thermal gradients are considerably less than the undisturbed gradients; the difference between starting and equilibrium conditions is expressed as a regional perturbation of several hundred degrees (*op.cit.*; England, 1987; Ridley, 1989). Rocks below thrust sheets experience near-isothermal compression (Figure 4.35) unless a warm thrust sheet induces marked warming during loading or unless loading is slow compared with the thermal relaxation time (Thompson and England, 1984). Rocks above the thrust undergo near-isobaric cooling prior to a temperature increase and movement in P-T space to a steady-state geotherm. The features observed at the Manyane Thrust are placed into context in figure 4.35. As the post-cataclastic metamorphic grade above the Manyane Thrust is higher than that predicted by simple thrusting and erosion, and taking into account the comparatively small scale of the units involved, shear heating may have contributed to the post-deformation increase in metamorphism.

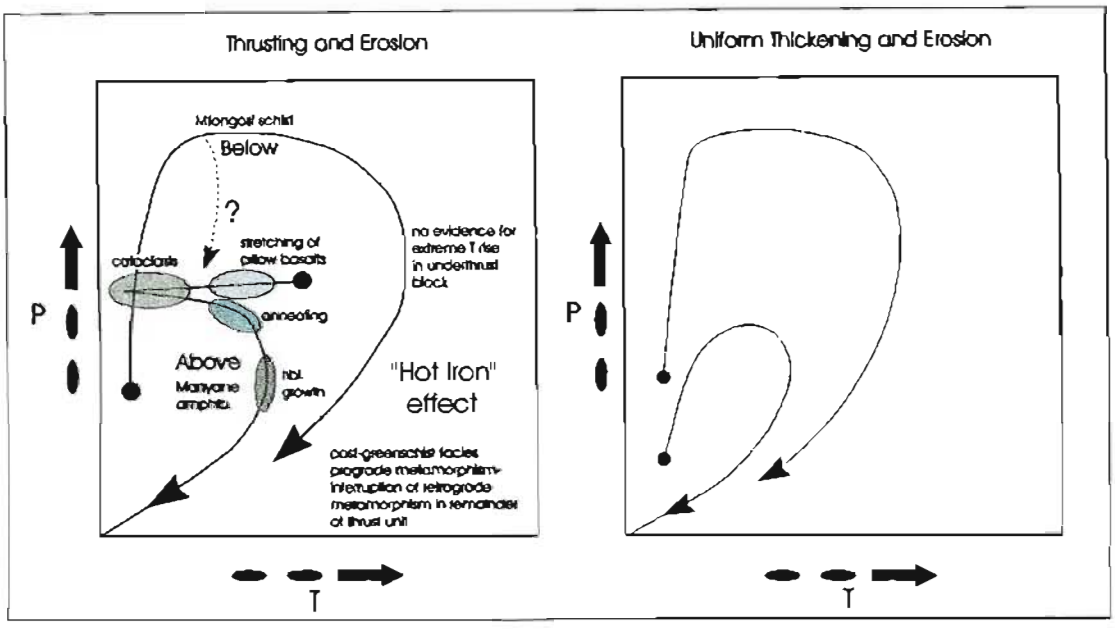

Figure 4.35 Schematic P-T-t diagrams of the forms of paths produced by two tectonic processes in continental collision. The paths for thrusting followed by erosion, and of uniform thickening followed by erosion, are very similar. The terms "above" and "below" refer to the thrust plane although a similar relationship has been proposed for uniform thickening, dependant upon the depth at which the effects are manifest. The features found in the Manyane amphibolite, near the Manyane Thrust, are placed into the context of a likely P-T-t path (modified after Thompson and England, 1984).

c) Increase in Temperature at the Manyane Thrust due to Shear Heating

Conductive heat redistribution accounts inadequately for temperature distributions which may often only be justified by shear heating in the region of faults resulting, in inverted metamorphic zonation beneath obducted ophiolites (Graham and England, 1975). Inverted metamorphic sequences result from downward conduction of heat after a hot slab overthrusts a cooler basement (Oxburgh and Turcotte, 1974; England and Thompson, 1984; Thompson and England, 1984; Rice *et al.*, 1989; Ridley, 1989) although shear heating may add significantly to the heating process (eg Graham and England, 1975). A sharply inverted metamorphic gradient in the footwall to a thrust is strong evidence for shear heating (Scholz, 1980), the effects of which may be indistinguishable from that of conduction due to overloading. Reitan (1968) was able to quantify heat generation and subsequent conduction over geologically short time intervals (eg. < 1 Ma) in blocks of restricted thicknesses (< 1 km). Significant temperature increases of up to 100°C in excess of steady state geothermal gradient-dictated temperatures are attributable to the conversion of mechanical energy to heat (*op. cit.*); heat from friction at shallow levels and from plastic deformation in ductile shear zones at deeper levels (Reitan, 1968).

A post-catacalstic temperature rise of 200°C has occurred at the base of the Tugela Nappe. Shear heating accompanying overthrusting produces both inverted thermal gradients and high temperatures (Bickle *et al.*,1975) causing a "transient thermal regime" (Graham and England, 1975). The longer the thrusting movement continues, the hotter any point on the base of the upper plate will become (*op. cit.*).

A comparison is made between metamorphism of the Pelona Schist of the Sierra Pelona (southern California) and metamorphism of the Mfongosi schist (Graham and England, 1975; this study). The displacement of transient thermal profiles in both terranes requires the displacement of large bodies of rock with contrasted thermal gradients, for example, the warmer, deeper parts of the Tugela Nappe interior juxtaposed against the cooler volcanosedimentary Mfongosi schist. Oxburgh and Turcotte (1974) and Graham and England (1975) provided a quantitative treatment of thermal profiles and regional metamorphism associated with overthrusting wherein conductive slow redistribution of heat results in underthrust masses of cold rock, such as the Pelona Schist, being subjected to high pressures with little increase in temperature. This thermal profile decays towards an equilibrium geothermal gradient: for thrust sheets of great thickness (> 15 km) thermal conduction continues for tens of millions of years after thrusting but the inverted thermal gradient across the thrust will be eliminated in less than 1 my by the locally large heat flux from the upper to lower plate. The heating event associated with these processes is consequently short and is usually termed a *thermal pulse* (*op. cit.*)

To be geologically recognizable, shear heating must result in temperature increases of several hundred degrees celsius, within several kilometres of the fault, which persist sufficiently long for metamorphic reactions to occur and which requires heat production on the fault of several times the ambient heat flow (Scholz, 1980). Scholz *et al.* (1979) and Scholz (1980) demonstrate that the prime control on shear heating must be pressure such that shear heating is greater along reverse or steep faults (*op. cit.*). For a time period comparable to the thermal time constant, about 10 my, either the fault must have moved at rates of tens of centimetres per year (an unrealistically high rate) or the shear stress was in the order of one kilobar or greater (*op. cit.*) Generally the greater the angle between the shear plane and the thrust movement vector, the greater will be the shear stress and thus the greater the heating for a given increment of movement

(*op. cit.*, Sibson *et al.*, 1975, Etheridge *et al.*, 1984; Sibson, 1987). In the case of the Manyane Thrust or reverse fault, with an average orientation parallel to the local S_{01} foliation and slickensides (079/69° to 077/73°), the thrust vector occurred at a high angle to the fault plane and shear stresses would have been high. Shear heating also results in thermal softening of the core of the shear zone, concentrating deformation and contributing to the stability of the shear zone. (Graham and England, 1975; Rice *et al.*, 1989).

4.5) Conclusion - Model for Mfongosi Schist Mineralization

The majority of the Tugela Nappe underwent an anticlockwise P-T-t path (Harmer, 1979; Figure 4.12) with the temperature maximum being reached prior to peak deformation. The P-T-t path matches that of a thrust unit which underwent intrusion early in its tectonometamorphic history (for example, due to the intrusion of Kotongweni tonalite). Adjustment of temperature and pressure towards a steady-state geotherm was disrupted by numerous thrusts and a normal decay of P and T may not have applied in the areas of the Tugela Nappe adjacent to the Tugela Rand Complex and the Natal Thrust Front. The Natal Thrust Front or Mfongosi schist, against which the Tugela Nappe is juxtaposed, would not have been at the same P-T state as rocks at depth in the Tugela Nappe at the onset of thrusting. The succession of assemblages **A-F** (Figure 4.12), although indicating an anticlockwise P-T-t loop, may not be used definitively for pressure calculations. Therefore, there is the possibility that a clockwise P-T-t path prevailed in this margin of the Tugela Nappe.

Combining separate structural features and metamorphic zones into a scenario of folding and thrusting (eg; Hafner, 1951; Graham and England, 1975; Jamieson, 1991; Rivers *et al.*, 1993) allows a model of progressive deformation and vein formation to be derived for the southern and northern Mfongosi Valley areas. The features described below are summarized in Figure 4.36:

1) *Early deformation of Mfongosi schist and Ntingwe limestone in the fold and thrust belt foreland; Initiation of the Manyane Thrust.*

Initial deformation includes movement of the leading edge of the Tugela Nappe along a thrust or reverse fault with a dip less than 66° to the south and infolding of fine-and coarse-grained amphibolite layers and segments of Kotongweni Tonalite. The southerly plunge of the long axes of prolate, ellipsoidal pillow basalts signifies an initial ductile movement from the southern hinterland. Estimates of the metamorphic grade in the amphibolite at thrust initiation are between lower amphibolite and lower greenschist facies (Harmer, 1979); the normal retrograde metamorphism of the Tugela Nappe was effectively interrupted by Manyane Thrust formation. The exact temperature reached at the thrust depends largely upon the extent of movement and the

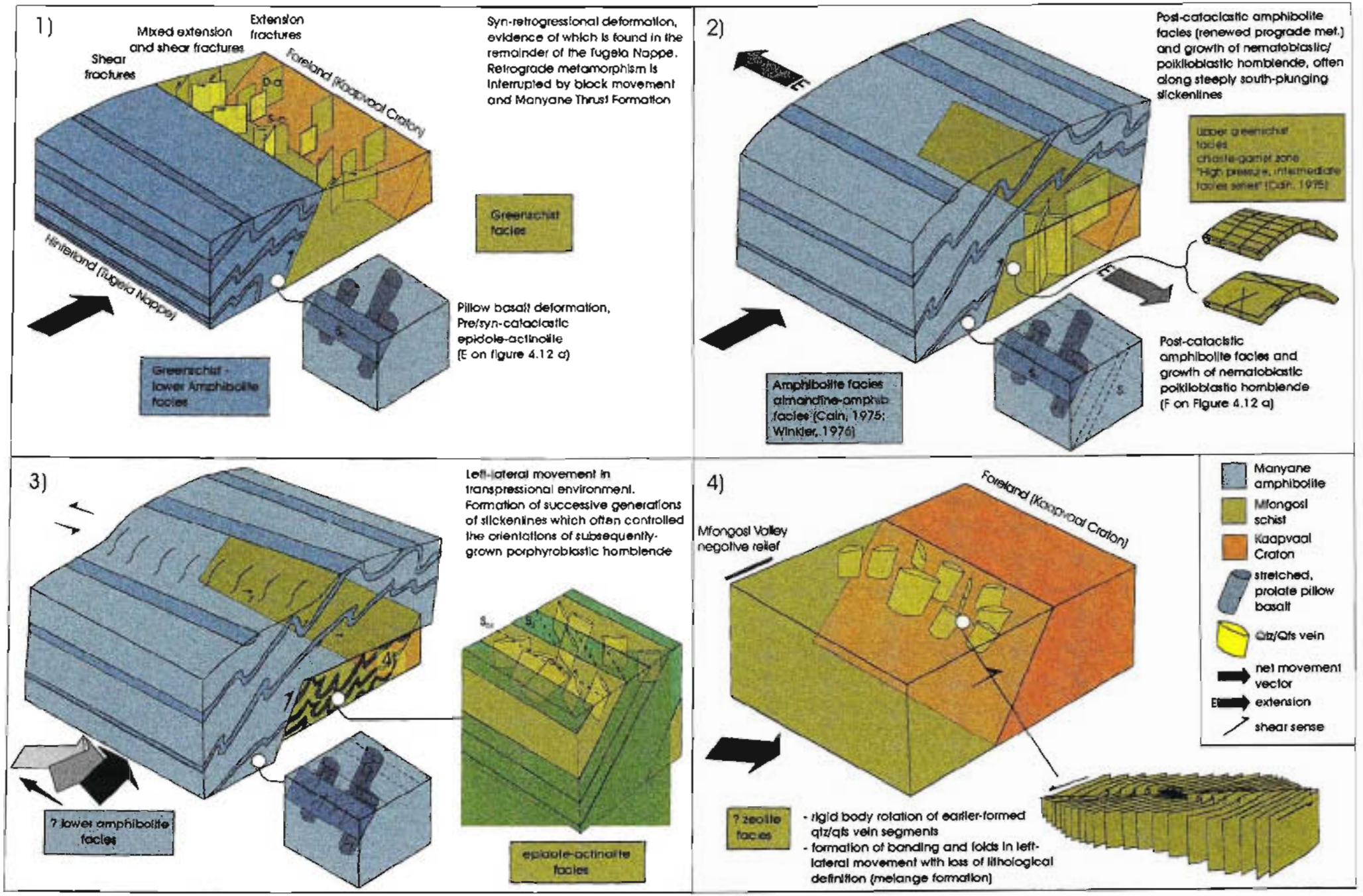

Figure 4.36 The tectono-metamorphic evolution of the Natal Thrust Front in the vicinity of the Manyane Thrust in the Mfongosi Valley. The formation of veining depends upon a combination of structural and metamorphic features, some of which are typically found in fold and thrust belts adjacent to foreland blocks.

angle of the maximum principal stress axis relative to the movement plane; the greater the translation along the thrust, the greater the temperature of amphibolite juxtaposed against the initially cooler Mfongosi schist. Shear heating, at these lower metamorphic grades, may also have contributed to the heat budget. The greenschist facies is the maximum grade which may have been reached in the Mfongosi schist at this stage, although Cain (1975) cites evidence for a later high-pressure facies.

Formation of two types of fractures during deformation of the foreland, in the various competent layers of the volcanosedimentary Mfongosi schist, also occurred at this stage. Fractures are of the vertical strike-slip type (S-c) and the vertical dilation type (D-a) (Figure 4.35).

2) *Dilation of pre-formed shears and fractures due to overloading of the Mfongosi schist by the Tugela Nappe and continued northward movement of the Tugela Nappe*

Translation of the direction of maximum principal stress from horizontal to near-vertical may have occurred with continued movement along the Manyane Thrust and overburdening (σ_L) of the Mfongosi schist by the leading part of the Tugela Nappe. Further minor fractures, according to theories of buckling of brittle/competent layers, would have formed in the Mfongosi schist near the Manyane Thrust. This may explain the predominance of larger quartzofeldspathic veins in the northern Mfongosi Valley area [ie: infilling of fractures formed in 1)] and the dominance of smaller quartzofeldspathic veins in the southern Mfongosi Valley field area (increased contribution to overall veining by minor fractures in small individually buckled layers). Widespread pressure solution of the host rocks is responsible for fracture and minor shear infilling.

The formation of boudins in the Manyane amphibolite occurred at this stage. In models of fold and thrust belts, folding and deformation of the hangingwall may precede that in the footwall to the thrust. Post-cataclastic overgrowth of epidote-actinolite facies minerals by hornblende poikiloblasts and porphyroblasts indicate raised temperatures along the thrust plane (due either to geotherm disturbance or to shear heating).

Leaching of fluids into pre-formed dilation fractures may be attributed to the "hot-iron" effect wherein fluids moved towards the higher temperature part of a block which has been overburdened. In this model, fluids move up the temperature gradient towards the Manyane Thrust. The spatial transition from shear to extension fractures in the central part of the Mfongosi Valley (Price and Cosgrove, 1990) is a probable explanation for the conspicuous negative weathering and lack of outcrop between the northern and southern Mfongosi Valley field areas.

3) *Initiation of lateral movement in the hangingwall, transmission of lateral movement into the thrust footwall and closed - isoclinal to sheath folding of the footwall Mfongosi schist*

Cessation of northward movement of the thrust unit was followed by lateral movement of the hangingwall, with slickenlines and σ_1 oriented progressively more westwards. Evidence of the lateral movement in the amphibolites includes slickenlines on the margins of the prolate ellipsoids and continued crystallization of nematoblastic hornblende along slickenlines.

Lateral movement of the Tugela Nappe was transmitted towards the northern foreland into the Mfongosi schist. Evidence of northward movement with superimposed lateral movement is preserved on quartzofeldspathic vein margins and at lithological contacts in the Mfongosi schist. Continued movement of the Manyane Thrust caused closed, then isoclinal, folding of the schist with sheath folding in top-to north/north-east shearing of this schist (Cobbold and Quinquis, 1980). Veins have been flattened into sub-parallelism with the S_{01} planar foliation, describing a girdle distribution on equal angle stereonet plots. The axial planar cleavage to the isoclinal folds served as slip surfaces. A second cleavage (S_2) observable in thin section indicates superimposed left-lateral movement. Pressure solution of the schist was responsible for hydrothermal fluid generation (see Chapter 7), with the overburdening and heating at the Manyane Thrust being responsible for the imposed temperature gradients and fluid movement.

4) *An added complication: formation of Mfongosi melange, loss of separate lithologies and rigid body rotation of veins in the melange with northward transport and lateral movement of the Mfongosi Group*

The features described in the first part of this chapter form the end-members of this deformation sequence. The structural features of highly deformed Mfongosi schist, wherein the loss of S_0 and microscopic S_2 observable in the southern Mfongosi Valley area has been affected, is attributable to rigid clast rotation in a left-lateral shear system. Flattening of the latter system produced a strong structural correlation between the various features. Post-thrust collapse of the Tugela Nappe is responsible for the formation of the east-west-trending fractures hosting the Ayres Reef in a similar mode to that of the Phoenix Mine. Ayres Reef veining formed prior to the final left-lateral movement.

The aureole of the Tugela Rand Complex is poorly defined although indications are that segments of the Complex have been transported northwards as lensoid bodies into the mass of Manyane amphibolite and Kotongweni tonalite (see Chapter 6). This feature would imply an early genesis of the Tugela Rand Complex with respect to the emplacement of the Tugela Nappe (*q.v.* Lambert, 1962).

4.7) Economic Potential

Deformation of the Mfongosi Group in a foreland fold and thrust belt was accompanied by early brittle fracturing. These fractures were subsequently infilled with the products of pressure solution with fluid movement being controlled by the transient thermal regime caused by the emplacement of the Tugela Nappe (the "hot iron effect"). The disturbance of existing geotherms, due to thrust initiation and nappe emplacement, served as an interruption to the retrograde metamorphism of the remainder of the Tugela Nappe. No high gold grades were encountered in the field area, whether in whole rocks or in veins. Gold grades for veins range from <10 to 38 ppb with one exception (FU2HV-22 a at 306 ppb; Appendix B3). A nugget effect is evident; sample FU2HV-22 b, a sample from the same vein which yielded the 306 ppb value, yielded only 12 ppb Au. Gold grades for host rocks are universally low: usually less than 10 ppb. More information about the fluid regime is gleaned from oxygen stable isotope studies (Chapter 7).

Chapter 5

Ngubevu Area

5.1) Economic History

The Ngubevu area, comprising that portion of the Mfongosi schist from the Ngubevu River to the Buffalo River, has been intensely prospected and explored since the 1800s. Three main mines are depicted on regional geological maps (Figure 5.1). These mines are: the Blue Spec Mine on the western bank of the "Ngobevu" (Ngubevu) River, the Golden Dove or Golden Eagle Mine on the eastern bank of the Ngubevu River and the Buffalo River Mine to the west of the junction between the Buffalo and Tugela Rivers (1 : 250 000 scale Geological Series, 2830-Dundee; Figure 5.1). The Champion Mine, apparently on the northern bank of a tributary to the Ngubevu River, could not be located. A number of reports on the economic potential of the area, concentrating on gold, lead, iron, copper and silver, have been produced. Gray (1899) refers to copper occurrences:

- as part of rich sulphides
- native copper in white quartz reefs (the most common occurrence of copper)
- pervasive stockwork-like veining in metamorphosed rocks
- impregnations and disseminations as sulphides and/or native copper in schist
- a native constituent of syenite

Galena ± silver occurred in pre-colonization Bantu workings in the vicinity of the Golden Eagle Mine (Gray, 1899). These pits contained quartz chips with galena (partly replaced by cerusite, and assaying at 3743 $g.t^{-1}$ Ag) adhering to them while copper, zinc, iron, lead and gold were found in the host Mfongosi schist in varying amounts. Prospecting continued in 1900 and 1901 (Gray, 1900; 1901) but no further reports on the Ngubevu River - Buffalo River area were produced until Gray (1906) documented small quartz veins accompanying diorite dykes and native copper adhering to syenite in the Buffalo River valley. Copper and cuprite, although often highly concentrated, were found to be irregularly distributed in quartz veins. Hall (1910 a, b) and Young (1910) documented the twenty claims pegged adjacent to the perennial Ngubevu stream.

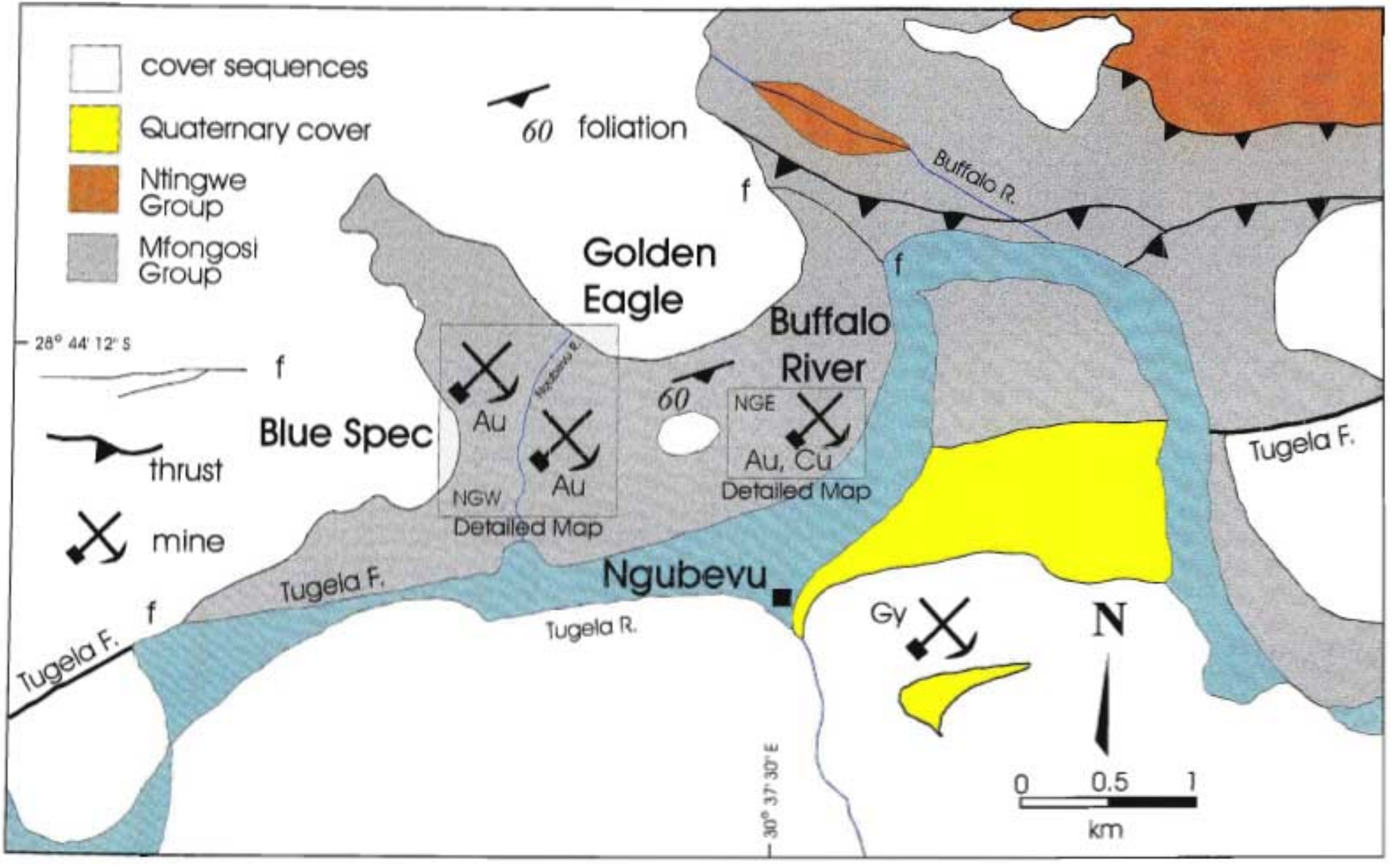

Figure 5.1 The Ngubevu area, depicting three mines: Blue Spec, Golden Eagle and Buffalo River. The names of these mines are based on the most recent company reports and private reports to the shareholders of mining consortiums extant in the early 1900s. These names will be used throughout this study. Base maps group the Blue Spec and Golden Eagle mines in the Ngubevu West area (NGW) and the Buffalo River Mine in the Ngubevu East (NGE) area.

The names given to the five square claims were as follows: the Champion Block, containing the Champion Reef; the Carter Block; Mick's Luck Block containing the majority of the Blue Spec Reef; the Blue Spec Block which supposedly contains the remainder of the Blue Spec Reef; and the Crompton Block (Figure 5.2). To the east of the Blue Speck Block is the unpegged Golden Dove claim. The southern Blue Spec Block or northern Crompton block contains what was termed the Golden Eagle Mine which was parallel to the Blue Spec Reef. A reef of limited extent in the extreme western portion of Mick's Luck Block is now encompassed by the Blue Spec Mine. This study therefore concentrates upon the mines in the Ngubevu area that are depicted on the 1:250 000 scale regional geological map (2803-Dundee).

Young (1910) recorded the ore bodies as being quartz veins with inclusions or intercalations of chloritic schist, Gibb (1911) observed pervasively veined, highly fissile zones in the Mfongosi schist which formed the focus of mining efforts in the vicinity of the Golden Eagle Mine. The adjoining Golden Dove prospect (Gibb, 1911) exhibited supergene enrichment; both shafts and adits rendered decreasing grades with increasing development into the interior of koppies or spurs on the northern bank of the Tugela River (Hall, 1910 a; Young, 1910; Table 5.1). Other targets included lenticular "bunches" and "blows" of quartz as opposed to parallel-sided veins which were termed "stringers".

In a private report to the Chairman of Champion Reef Development Syndicate, Hall (1910 b) disclosed information of a more sensitive nature and anticipated a regular thickness of 3 ft (0.97 m), a strike length of 1600 ft (487.7 m) and a down-dip extent of 1000 ft (304.8 m) for the Blue Spec Reef, totalling 180 000 tons of ore at 40% extraction. Quartzitic, lenticular ore bodies were found by Hall (1910 b) to strike between 060° and 120° and dip from 65° to 89° to the south. The walls of the quartz bodies were noted as being poorly defined; the gold was not only carried in the quartz but also in thin veins of red Fe-oxide which cross-cut the quartz lenses and veins at various angles. In 1910 various prospectors recognized the occurrence of the greater part of the gold in small but rich leaders parallel to sub-parallel to the average dip of the planar foliation of the host schist and distributed throughout the schistose host rock. The schist was noted as being markedly quartzitic in places, with numerous intercalated clear glassy to pyrite-rich, aplitic quartz bodies which formed the focus of mining efforts in the Blue Spec and Golden Eagle mines.

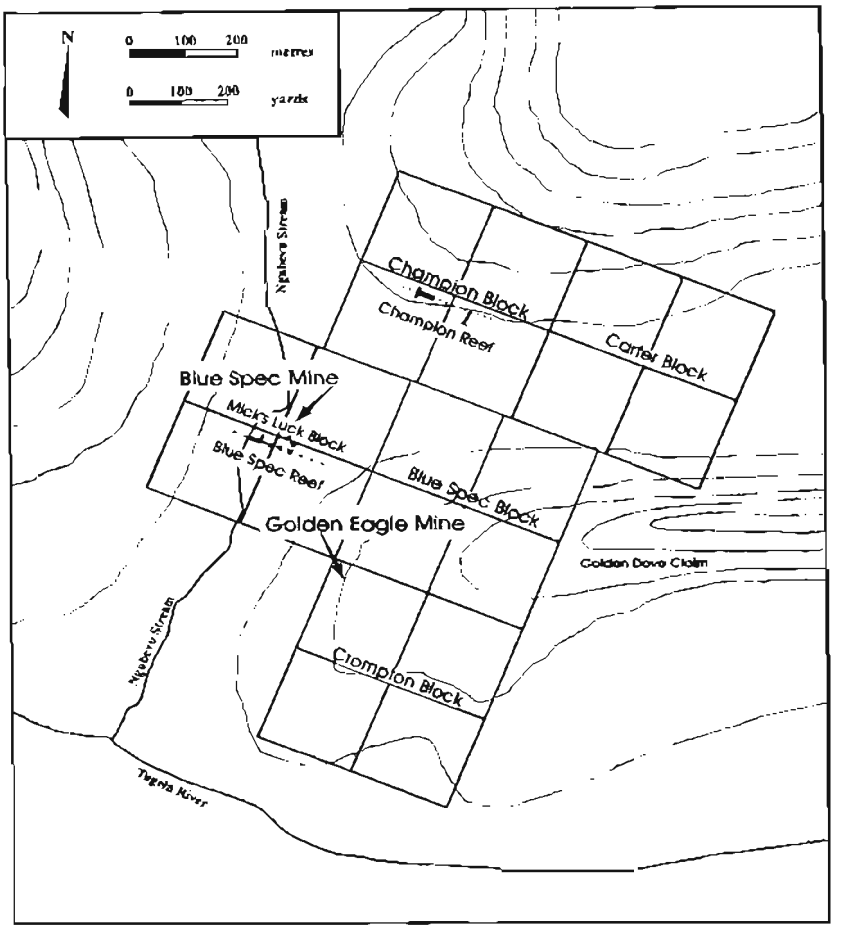

Figure 5.2 The positions of the five main claims adjacent to the perennial Ngubevu stream. Each claim consisted of four blocks; in total twenty blocks were claimed although very little trenching was undertaken. Each of the five claims covered an area of 300 square yards (250.8 m^2) and was equivalent to 250 Transvaal gold claims (Hall, 1910; Young, 1910).

Hall (1910b) also encountered cross-leads (cross-cutting veins or veinlets), consisting of glassy to opaque quartz, which were at high angles to the large quartz bodies contained in the planar foliation and enriched in pyrite and Au where they cross-cut the conformable bodies.

From these initial studies and as a first approximation gold implicitly occurs in four main modes: in lenticular bunches and blows of quartz; in highly fissile zones along strike from these bunches; in thin veins of Fe-oxide which cut the above-mentioned two modes, and in cross-leads - veins which cross-cut the other three structures at high angles.

Amongst more recent surveys Winfield (1979) concentrated on co-incident copper and zinc anomalies in the Mfongosi schist, particularly along the Tugela Fault which traverses almost the full length of the Natal Thrust Front. Co-incident copper, zinc or copper, zinc + nickel

anomalies were followed by with geophysical surveys which targeted high-grade metavolcanic rocks with abundant disseminated sulphides, the Tugela Fault and closures of major folds (*cf.* "saddle reefs"). Findings by Winfield (1979) were encouraging; copper values apparently showed a close correlation with regional and local lineations and were inferred to be fault-controlled; some copper anomalies were thought to be up to 2 km long (Winfield, 1979). Further findings were:

- sulphides associated with basic rocks, nickel defining or outlining mafic lithologies
- high zinc values associated with andesitic volcanic or volcaniclastic rock types
- a copper/zinc association
- copper anomalies associated with manganiferous quartz veins

A survey for precious and base metals by Anglo-American Prospecting Services and Mining Corporation targeted the Mfongosi schist between Ngubevu and Mfongosi (Coldwell, 1984) . Two main types of magnetic anomalies were noted; linear anomalies which were oriented obliquely to the general strike of the host schist; and numerous, small en-echelon anomalies. Minor anomalies were found to be associated with black shale and banded magnetite chert (Coldwell, 1984). The most important conclusions of this study were:

- interbanded carbonaceous shale, phyllite and pyritic carbonaceous shale have ubiquitously higher electromagnetic values than the volumetrically-dominant phyllite and chloritic schist
- gold occurs in thin quartz ± carbonate veinlets which cross-cut fissile, gossaniferous, black carbonaceous shale and sulphide-bearing (pyritic) tuff, however, carbonaceous black shale with pyrite usually has low base metal values
- en-echelon quartz-calcite veins, which are nearly conformable to the immediately adjacent planar foliation and which are limited in down-dip (and strike - this study) extent, contain the highest copper, nickel, lead and zinc values, but are not notably enriched in gold
- porphyroblastic epidote - chlorite schist shows the highest gold values

Gold grades from studies by mining consortiums in the latter part of the twentieth century are unavailable. However, the gold grades obtained from studies completed in the earlier part of this century are summarized in Table 5.1.

Table 5.1 Summary of gold grades obtained by various researchers and prospectors in the Ngubevu area. Grades are usually converted from dwt (pennyweights) over a certain thickness of reef (in inches) to grams over a distance in metres. Information is taken mainly from Young (1910). Names of reefs or mines used in this study are shown in *italics*. "Conformable" refers to the orientation of the ore body with respect to the dip and strike of the host schist.

Source	Gold Grade	Material Sampled	Reef/Block/Mine
Young (1910)	traces to 5.4 g over 1 m 17.3 g over 0.61 m	quartz vein	Mick's Luck Block (*Blue Spec Mine/Reef*)
Young (1910)	TRIAL PITS average 2.33 g over 1.08 m over a total strike length of 30.48 m	quartz vein	
	76.2 m long cross-cut 16.79 g over 0.1 m to 10.57 g over 0.48 m	quartz vein (cross-cutting strike of host rock)	
Young (1910)	25 g over 0.22 m to 42 g over 0.35 m	quartz vein, conformable (main adit)	Champion Block (Champion Reef)
Hall (1910 b)	42.45 g over 0.36 m to 38.9 g over 0.23 m	quartz vein, conformable (main adit)	
Gibb (1911)	trace over 0.92 m to 3.5 g over 0.23 m	schist (main adit - footwall)	
	0.77 g over 0.69 m to 13.2 g over 0.46 m	highly veined schist (main adit - hangingwall)	
Young (1910)	36.6 m long main drive average 9.67 g over 0.96 m	quartz vein, conformable (main adit)	
	15.5 g over 1.37 m to 12.44 g over 0.35 m	No. 1 Shaft ore	
Hall (1910 b)	26.7 g over 0.92 m to 37.32 g over 1.02 m	No. 2 Shaft ore	
	average grade expected; 12.44 g over 0.92 m over a strike length of 213.4 m	series of quartz stringers and lenses of quartz intercalated with chloritic schist	Blue Spec Block (*Golden Eagle Mine*)
Gibb (1911)	trace over 0.92 m to 1.55 g over 0.61 m	veined schist (main adit - hangingwall)	
	trace over 1.87 m to 0.78 g over 0.61 m	veined schist (main adit - footwall)	

The lithologies and structural features focussed upon in this study are: black, carbonaceous or graphitic shale, pale cream tuff, porphyroblastic epidote-actinolite schist (retrogressed to epidote-chlorite schist) and distinct generations of veining. The vein generations, of notably different compositions, cross-cut the shale, tuff and the epidote-actinolite schist. Due to an exhaustive description of the Mfongosi Group in the section on the northern and southern Mfongosi Valley, only cursory descriptions of the components of the Mfongosi Group will be made here and only basic estimates of the maximum metamorphic grade and rock protoliths will be presented.

5.2) Grouping of Units and Metamorphism

The Ngubevu Goldfield comprises two main lithological groups of distinctive field appearance and weathering relief. A third lithology, occurring at the contacts of narrow bands of the two main rock types, forms lenses aligned parallel to the east-southeast trend of regional structures (Figures 5.3 a, b). The terms "Banded Units" and Epidote - Actinolite schist are applied to the two main units, the former having a negative weathering relief and the latter having a positive weathering relief. No distinct shear zones or alteration haloes (*q.v.* De Klerk, 1991) could be located, even at the shafts and adits, as shearing has prevailed at each lithological contact and layers are tectonically intercalated. The Ngubevu West area (NGW) is concentrated on. As the layers are strongly intercalated and often finely banded units are distinguished according to their dominant mineralogy.

a) Lenses in epidote-actinolite schist - northern and southern limbs of regional F_1 fold

Banded Unit

These units crop out as 1-25 m thick bands enclosed in epidote-actinolite schist and, in the central portion of the western field area, are interlayered with a calcite-quartz-albite ± sericite ± talc ± chlorite schist (Table 5.2; Figures 5.3 a, b; 5.4). The bulk of the epidote-actinolite schist crops out in two broad bands in the north and south of the western Ngubevu field area (Figure 5.3) probably comprising the limbs of a regional F_1 fold. Indicators of a volcanosedimentary origin for the Mfongosi schist (*q.v.* Matthews, 1972; Cain, 1975) are common.

The central portion of the NGW field area consists predominantly of a very fine-grained calcite - quartz - albite ± sericite ± talc ± chlorite schist interlayered with the calcite-bearing lithologies in bands in the northern and southern limbs of a regional F_1 fold (Table 5.2), hence the marked negative relief of this narrow central band caused by extensive dissolution of the calcite. It is significant that this zone, like the Ca-rich, finely layered bands contained in the northern and southern limbs, is poorly veined presumably due to its low competency in comparison with the boudinaged bands of epidote-actinolite schist in the central zone.

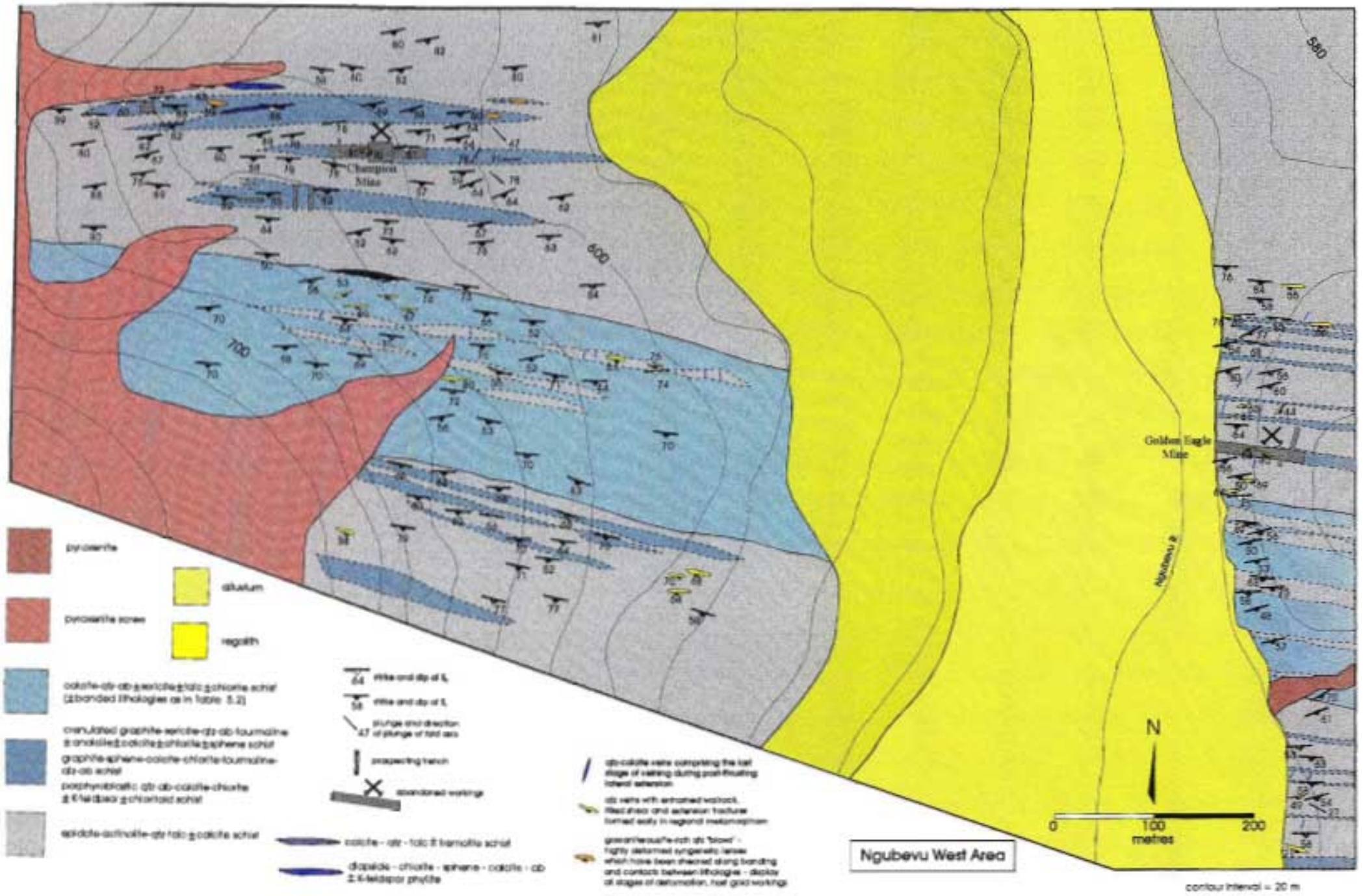

Figure 5.3 a The Ngubevu West area (NGW) wherein a regional F_2 fold is found. The Champion and Golden Eagle Mines are found within the NGW area. The general strike of the layering is east-southeast. Note that, due to the complexity of the area, the lithologies are distinguished on the strength of the dominant composite mineralogy

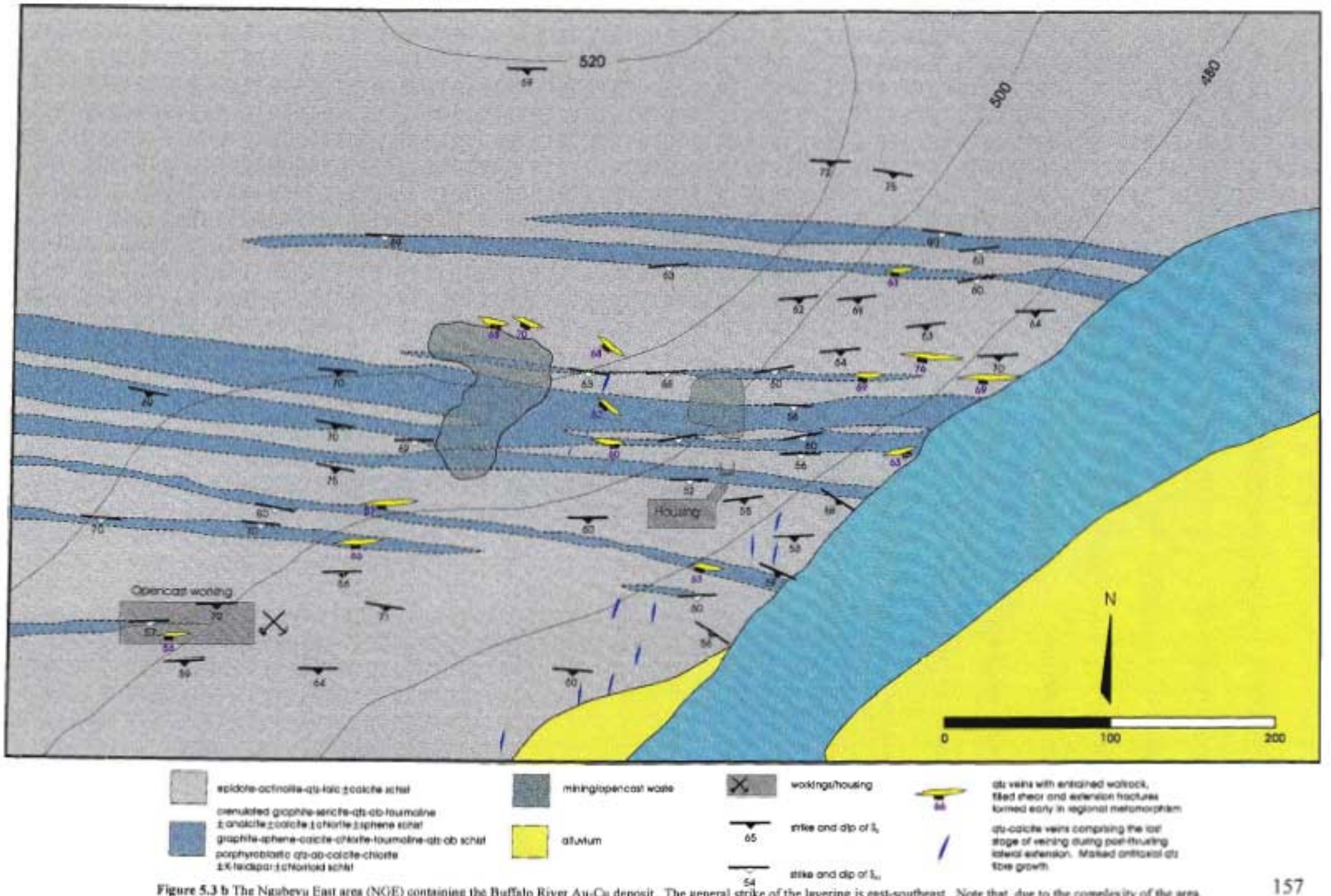

Figure 5.3 b The Ngubevu East area (NGE) containing the Buffalo River Au-Cu deposit. The general strike of the layering is east-southeast. Note that, due to the complexity of the area, the lithologies are separated on the strength of the dominant composite mineralogy

Figure 5.4 Field appearance of highly crenulated banded host rock to the Blue Spec Mine on the western bank of the Ngubevu stream. The axes of the kink folds comprise the F_2 fold generation in the structural scheme proposed in this study

Table 5.2 Lithological components of the banded units in the northern and southern limbs of the proposed regional F_1 fold. These layers also make up a large proportion of the central, negatively weathered zone and are interlayered with the calcite - quartz - albite ± sericite ± talc ± chlorite schist

Lithology	Description of salient features
Crenulated graphite - sericite - quartz - albite - tourmaline ± analcite ± calcite ± chlorite ± sphene schist ***(Slides NGW A1/HR Float, 2A-a, 2A-b, 6a, 6b,*** *NGW/A1/7 = chloritized sample)* Figure 5.5 a)	• dusky blue/black to light olive/white bands less than 2 mm thick, mainly of graphite, tourmaline and calcite • forms the host to gold workings in deformed quartz lenses in the Ngubevu area • highly crenulated - F_2 kink folding in outcrop and micro-folds, kinks defined by graphite, tourmaline or sericite • analcite as a relic of late-stage crystallization from hydrothermal solutions, occurring in clusters which represent deformed vesicles, usually in association with prehnite and zeolites: analcite + quartz → albite + H_2O • early generation and subsequent flattening/shearing of vein segments around which S_{01} is refracted; isoclinal folding of veinlets in a non-annealed matrix
Graphite - sphene - calcite - chlorite - tourmaline - quartz - albite schist ***(Slide NGW 2)*** Figure 5.5 b)	• dark yellow to light olive medium- to coarse-grained, partly gneissose rock interbanded with crenulated graphite schist as described above • psuedomorphing of equant, usually rectangular minerals (pyrite) by sphene and quartz, with subsequent infilling of strain shadows by calcite • poikiloblastic inclusions of sphene and quartz in calcite implying very late carbonate metasomatism • sphene and quartz pseudomorphs rotated in top-to-north shearing
Porphyroblastic quartz - albite - calcite -chlorite ± K-feldspar ± chloritoid schist ***(Slide NGW 1)*** Figure 5.5 c)	• introduction of calcite into fractures formed on the outer arcs of kinks • top-to-north shearing of calcite veinlets

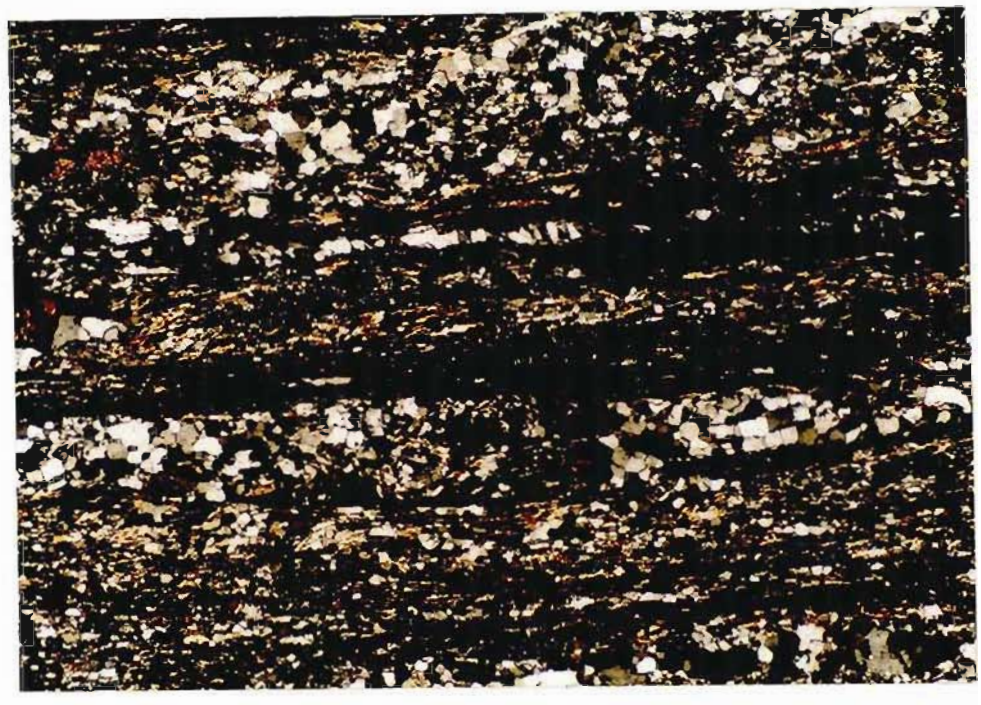

Figures 5.5 a) - An example of the constituents of the banded units in the NGW area: crenulated graphite-sericite-quartz-albite-tourmaline±analcite±calcite±chlorite±sphene schist (***Slide NGW-2A-a***). XP.

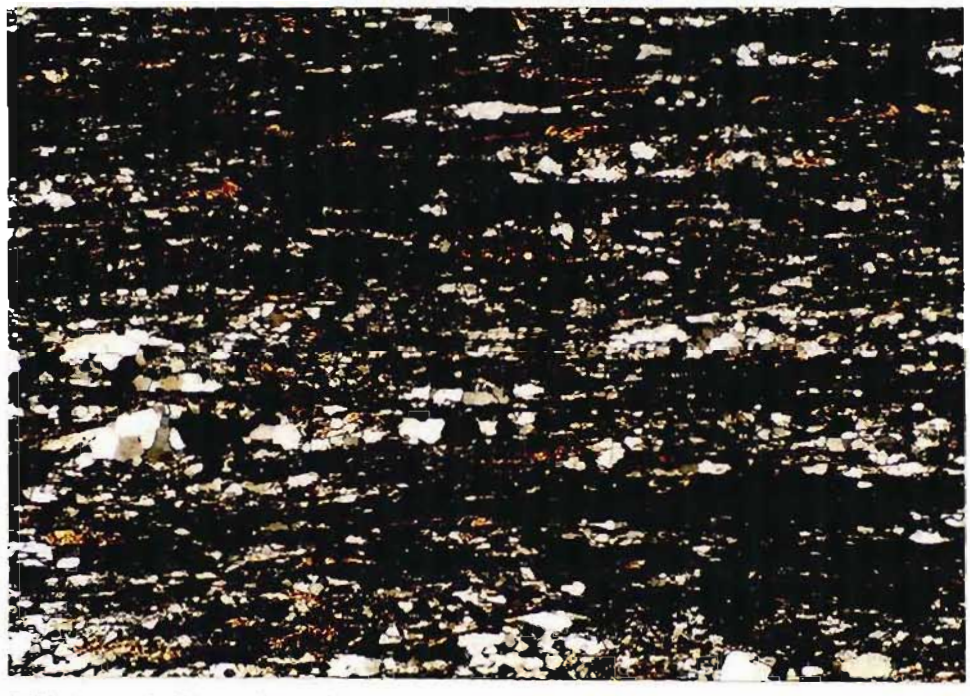

Figures 5.5 b) - An example of the constituents of the banded units in the NGW area: a graphite-sphene-calcite-chlorite-tourmaline-quartz-albite schist (***Slide NGW-2***). XP.

Figures 5.5 c) - An example of the constituents of the banded units in the NGW area; porphyroblastic quartz-albite-calcite-chlorite±K-feldspar±chloritoid schist (***Slide NGW-1***). XP.

Indications of the maximum metamorphic grade are found in a band of porphyroblastic chlorite - quartz - alkali feldspar - carpholite schist (Figure 5.6 a). Orthogonal thin sections of this rock type show the S_1 cleavage being deformed and crenulated to give an S_2 cleavage. The prismatic mineral carpholite is observed in its basal section, exhibiting bright first-order to second -order blue birefringence colours. Carpholite is characteristic, usually along with chloritoid, of argillaceous rocks which have undergone low temperature/high pressure metamorphism. No chloritoid was found in these rocks, but the medium-pressure blueschist facies (Goffe and Velde, 1984) may be tentatively inferred (Figure 5.6 c; Appendix A4).

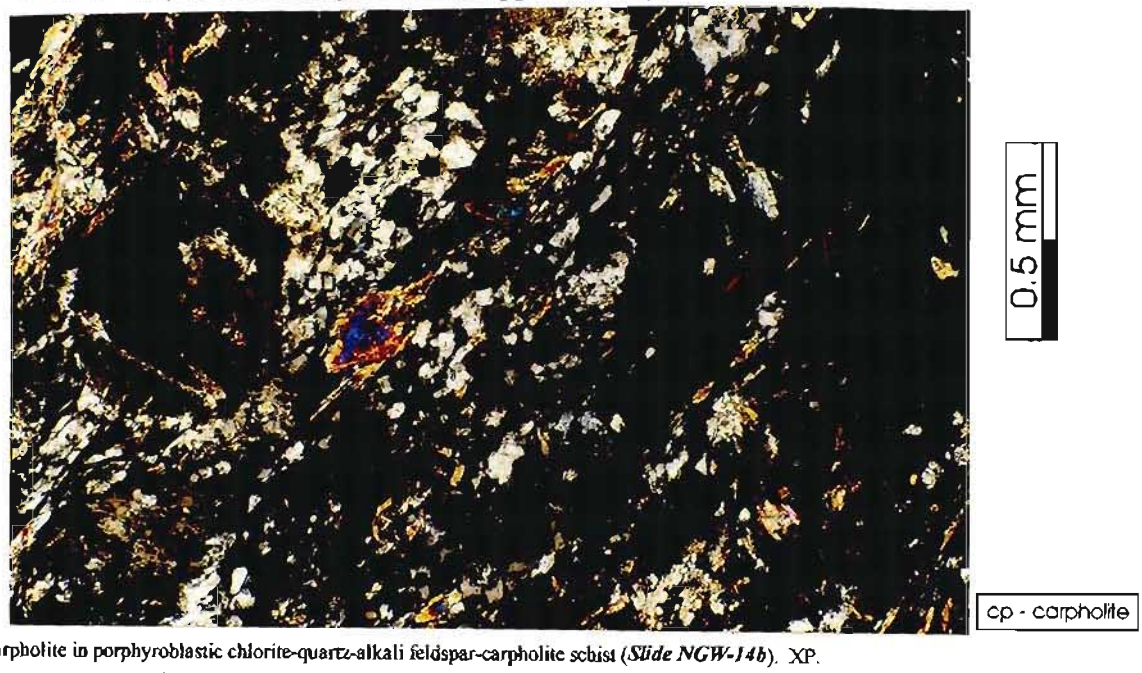

Figure 5.6 a Carpholite in porphyroblastic chlorite-quartz-alkali feldspar-carpholite schist (***Slide NGW-14b***). XP.

b) Dominant lithology of northern and southern limbs of regional F_1 fold

Epidote - actinolite - quartz - talc ± calcite schist

The epidote - actinolite - quartz - talc ± calcite schist (***Slide NGW 28 a, b***) forms the largest competent layers in the NGW and NGE field areas and comprises the northern and southern limbs of the regional F_1 fold in the NGW area (Figure 5.3 a). The schist is compositionally homogeneous except where quartzofeldspathic veins, quartz-calcite-talc bands and mortar-textured quartz-calcite-sphene bands are developed. It is an indication of the high competency of the epidote-actinolite schist that several vein generations are prevalent, having formed throughout the tectonometamorphic history. The numerous quartz-calcite-talc layers have resulted from syn- to late-tectonic shearing of infilled early tectonic shears or late-tectonic extension gashes which both have subsequently become mineralized. As for the majority of the Mfongosi Group, no subsequent growth of metacalcsilicate minerals has occurred indicating either that post-emplacement temperatures were not sufficient to form minerals such as diopside (late-tectonic carbonate metasomatism), or that minerals produced by low-grade calcsilicate metamorphism have been lost in subsequent pressure solution. Temperatures of about 250°C to 350°C are estimated for ensuing vein shearing (quartz plasticity at 300°C - Scholz, 1988) wherein ductile features may be observed resulting in an annealed mortar/mosaic texture. The textural and compositional variations in the epidote-actinolite schist may be a result of vein resorption.

Figure 5.7 a Typical field appearance of the epidote-actinolite and chloritic schists, eastern bank of the Ngubevu stream

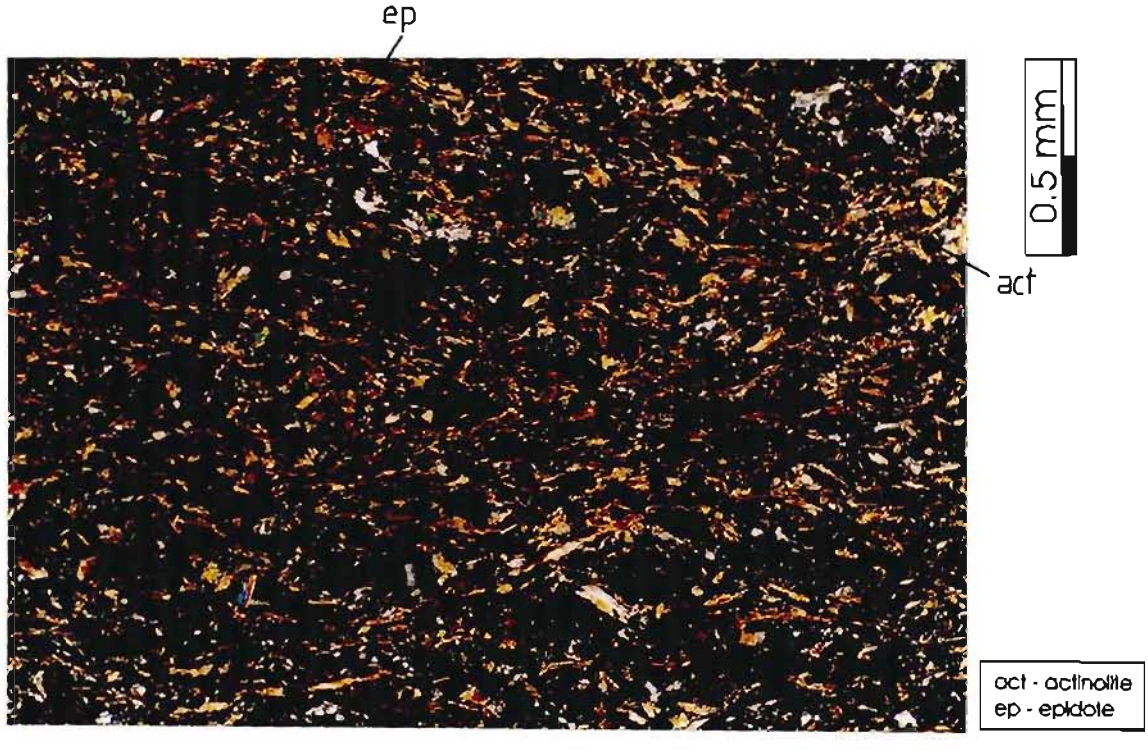

Figure 5.7 a Typical thin section view of the epidote-actinolite schists, eastern bank of the Ngubevu stream (***Slide NGW-27b***). XP.

c) Lenses of limited strike length and width

Diopside - chlorite - sphene - calcite - albite ± K-feldspar phyllite and calcite - quartz - talc ± tremolite schist

These rock types are remarkable for their limited extents as three separate lenses about 2-3 m wide and about 60 m long, confined between the dominant lithologies. The *diopside - chlorite - sphene - calcite - albite ± K-feldspar phyllite* (***Slide NGW 7***) consists of 25% diopside. Evenly distributed sphene comprises about 18% of the rock and forms haloes around the opaques and chlorite and develops predominantly in strain shadows around sericitized orthoclase porphyroclasts. Calcite is present in a mosaic form containing local open clusters of various minerals. Cataclastic deformation of this lithology is not obvious; post-deformational metamorphism has removed traces of initial regional deformation while late-stage deformation has been accommodated in adjacent lithologies as described below. The clinopyroxene may have formed from volcanosedimentary-derived quartz and calcite or a very early quartz-calcite vein generation (although diopside is particularly characteristic of contact-metamorphosed Ca-rich metasediments), but is commonly preceded in the metamorphic sequence by tremolite or forsterite (Miyashiro, 1973). Diopside occurs early in the mineral sequence during increased metamorphism of siliceous dolomites (*op. cit.*) but may occur in basic igneous rocks in the higher grades of the amphibolite facies (Yardley, 1989) according to the reaction:

$$\text{hornblende} + \text{calcite} + \text{quartz} \rightarrow \text{diopside} + \text{anorthite} + CO_2 + H_2O \text{ (Yardley, 1989)}$$

Furthermore:

$$\text{tremolite} + \text{calcite} + \text{quartz} \rightarrow \text{diopside} + 3CO_2 + H_2O \text{ (Winkler, 1974)}$$

for which the equilibrium paragenesis of diopside + tremolite + calcite + quartz is significant. Admittedly, the temperature of metamorphism implied by the above assemblages is difficult to reconcile with the medium-pressure blueschist grade implied by the presence of carpholite. The reason for the lack of tremolite may be disequilibrium or the reaction :

$$\text{dolomite} + \text{quartz} \rightarrow \text{diopside} + CO_2 \text{ (Miyashiro, 1973)}$$

The fact that there is no epidote or zoisite in these samples implies a constant early influx of H_2O-rich fluid as zoisite and quartz are not stable in the presence of CO_2 - at higher grades even small amounts of CO_2 will cause the following reaction to proceed to the right:

$$\text{zoisite} + CO_2 \rightarrow \text{Ca-plagioclase} + \text{calcite} + H_2O$$

The release of CO_2 that accompanies the prograde metamorphism of these rocks should, if the fluid composition were internally buffered, lead to a CO_2-rich phase and preclude the possibility of zoisite being present in higher-grade zones. The composition of the fluid is thus interpreted to have changed from early CO_2-poor during prograde metamorphism to CO_2-rich during post-thrusting metasomatism, lateral extension and infilling of the late high angle extension fractures mentioned in the section on economic history and structural geology.

The *calcite - quartz - talc ± tremolite schist* (***Slide NGW 8***) consists of randomly oriented talc laths surrounded, along with feldspar and minor tremolite, by poikiloblastic calcite. Opaque minerals are surrounded by cataclastically reduced quartz and feldspar which implies that the opaque minerals are syngenetic with respect to volcanic sedimentation or were introduced early in the tectonometamorphic sequence by veining. The assemblage of calcite + talc + tremolite has little petrographic significance, save that if the reaction

$$\text{talc} + \text{calcite} + \text{quartz} \rightarrow \text{tremolite (altered to chlorite)} + CO_2 + H_2O \text{ (Winkler, 1974)}$$

results in talc + calcite + tremolite + quartz, then equilibrium metamorphic conditions have applied in the early stages of deformation and metamorphism. An oxygen stable isotope study on this area reveals more about the fluid regime.

5.3) Structural Geology

a) D_1 -Primary banding : S_{01} and F_1

Primary banding is preserved in the banded lithologies described in Table 5.2 . Bands of talc, graphite, sericite and tourmaline of the order of 2 mm thick are the only indications of syngenetic, formational layering (S_0). There is no evidence of the first fold generation, F_1, affecting these layers (i.e. folding is present, but cryptic) although F_1 is evident in the adjacent epidote-actinolite and chloritic schist and S_0 is only obviously deformed and crenulated in F_2. This would imply that this banding is in fact S_1 and thus may be included in S_{01}. S_1 in the epidote-actinolite schist is marked by actinolite (retrogressed to chlorite), bands of mosaic-textured graphite, quartz and albite. S_{01} is marked by the highly-sheared but lineation-poor margins of individual lithologies. The lensoid shape, extent and often abrupt terminations of the incompetent banded layers hosted in competent epidote-actinolite schist (Figure 5.3 a) is suggestive of sheath folding (eg. Cobbold and Quinquis, 1980) in top-to-north shearing. The proposal of a regional F_1 fold is not unreasonable given the repetition of layers in the NGW area. Unfortunately the axial planar cleavages of the F_1 fold generation were not discernable and possible primary banding, lithology margins and S_1 showed a close correlation on stereonets; again, an indication of the extreme deformation and flattening strain which this area has undergone.

The pole to a great circle fit to total S_{01} data, 115→36°, (Figures 5.8 a, b) corresponds closely to the orientation of F_1 fold axes derived for each sub-area on the base maps. The F_1 axis derived from the total S_{01} data matches the actual F_1 fold axes orientations measured in the field (Figures 5.9 a, b; 5.10; 5.11). Local stereonet plots for individual outcrops and a summation plot of regional data displays refolding about small circles, the axes of which are classified as F_3 in this scheme. No F_3 axes were directly observed but their presence may be confidently inferred and the spread of S_{01} data towards the margins of equal-angled stereonets is a further indication of non-cylindrical folding (eg Figure 5.8 a).

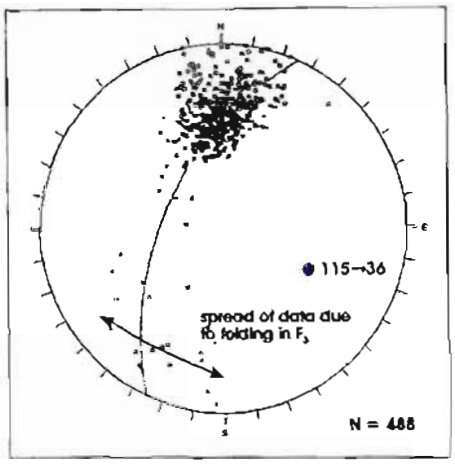

Figure 5.8 a Poles to S_{01} in epidote-actinolite and chloritic schist. Data is from the Ngubevu West and Ngubevu East areas and show significant spread toward the margins of the stereonet indicating a component of non-cylindrical folding in F_3. The approximate best circle fit to data has a pole with a plunge and direction of plunge of 115→36° defining an approximate F_1 axis which is evident on the outcrop scale N = 488

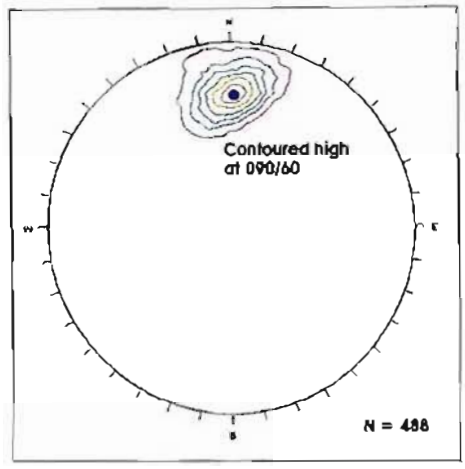

Figure 5.8 b Contoured equal area, lower hemisphere stereonet projection of poles to S_{01} in epidote-actinolite and chloritic schist in the NGW and NGE areas. Contoured high is at 090/60° at 28% of total area concentration N = 488

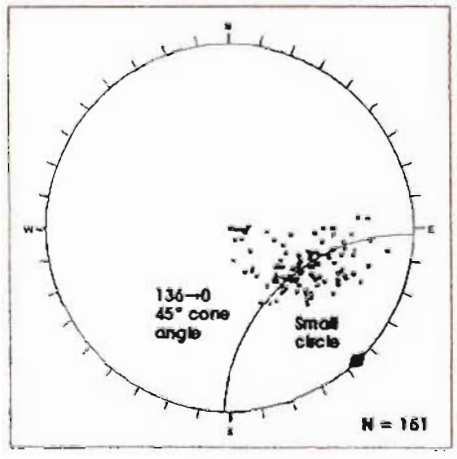

Figure 5.9 a Plunge and direction of plunge of minor F_1 fold axes in epidote-actinolite and chloritic schist in the NGW and NGE areas. Although not entirely clear on this compilation of data, individual outcrops show well-defined small circle distributions of F_1 axes indicating non-cylindrical refolding in F_3. The F_1 axes are thus refolded about the axis of a small circle (F_3' ?) which plunges at 0° towards 136°, the cone apical angle being 45° N = 151

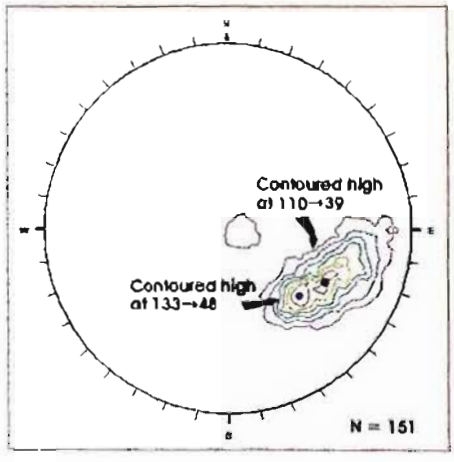

Figure 5.9 b Contoured equal area, lower hemisphere stereonet plot of minor F_1 axes, measured in the field and derived from stereonet great circle fits to data. Although a small circle distribution is not apparent from this summation plot, individual outcrops give a better depiction of this refolding (see maps). Two highs are defined at approximately 18% concentration as a percentage of total net area: 110→39° and 133→48° N = 151

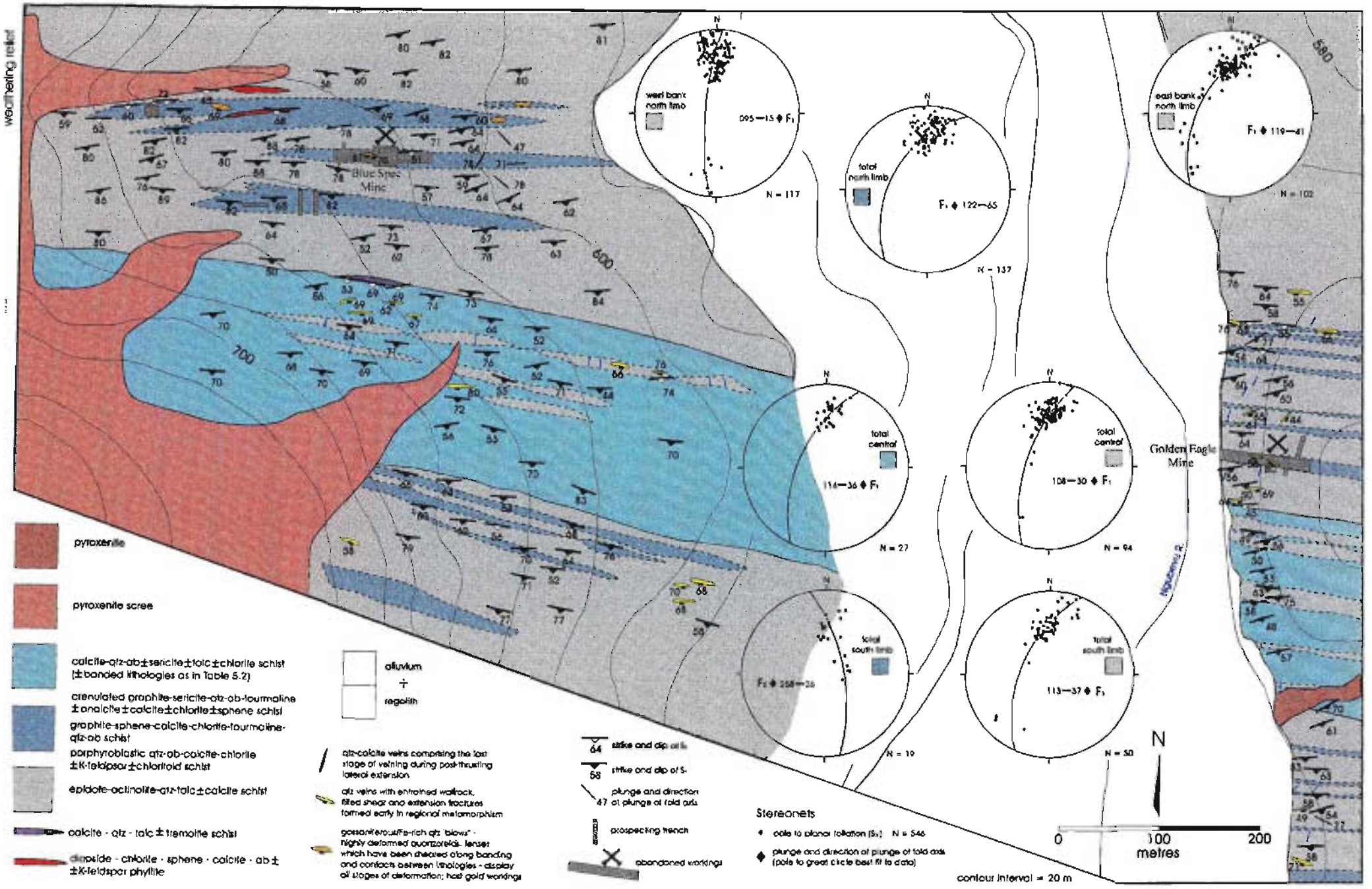

Figure 5.10 a The Ngubevu West area, showing the distribution of poles to S_{01}; great circle fits to data indicate a moderately-plunging, east-southeast-trending fold axis which is termed F_1 in the scheme adopted here. F_1 is refolded about a small circle with a near-horizontal, southeast-trending non-cylindrical axis, as for the Ngubevu East area. A steeply-plunging, southwest-trending fold axis is termed F_2 and is only prevelant in the incompetent, finely-banded units

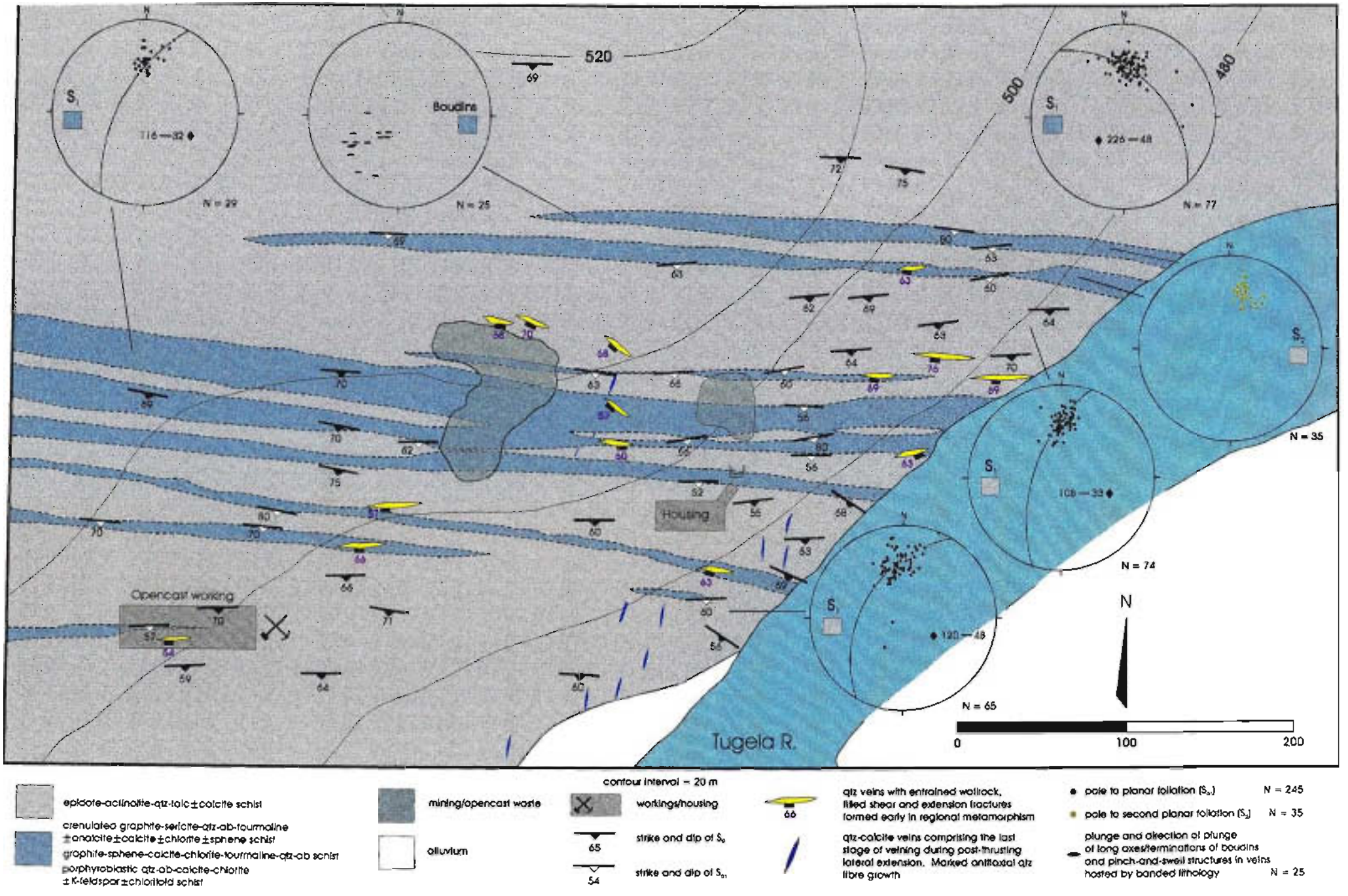

Figure 5.10 b The Ngubevu East area, showing the distribution of poles to S_{01} and S_2; great circle fits to data indicate a moderately-plunging, east-southeast-trending fold axis which is termed F_1 in the scheme proposed here. F_1 is, in turn, folded about a small circle with a near-horizontal, southeast-trending non-cylindrical fold axis (F_2). A steeply-plunging, southwest-trending fold axis is termed F_3, the orientation of which is similar to the plunge and direction of plunge of the terminations of boudinaged quartzofeldspathic veins

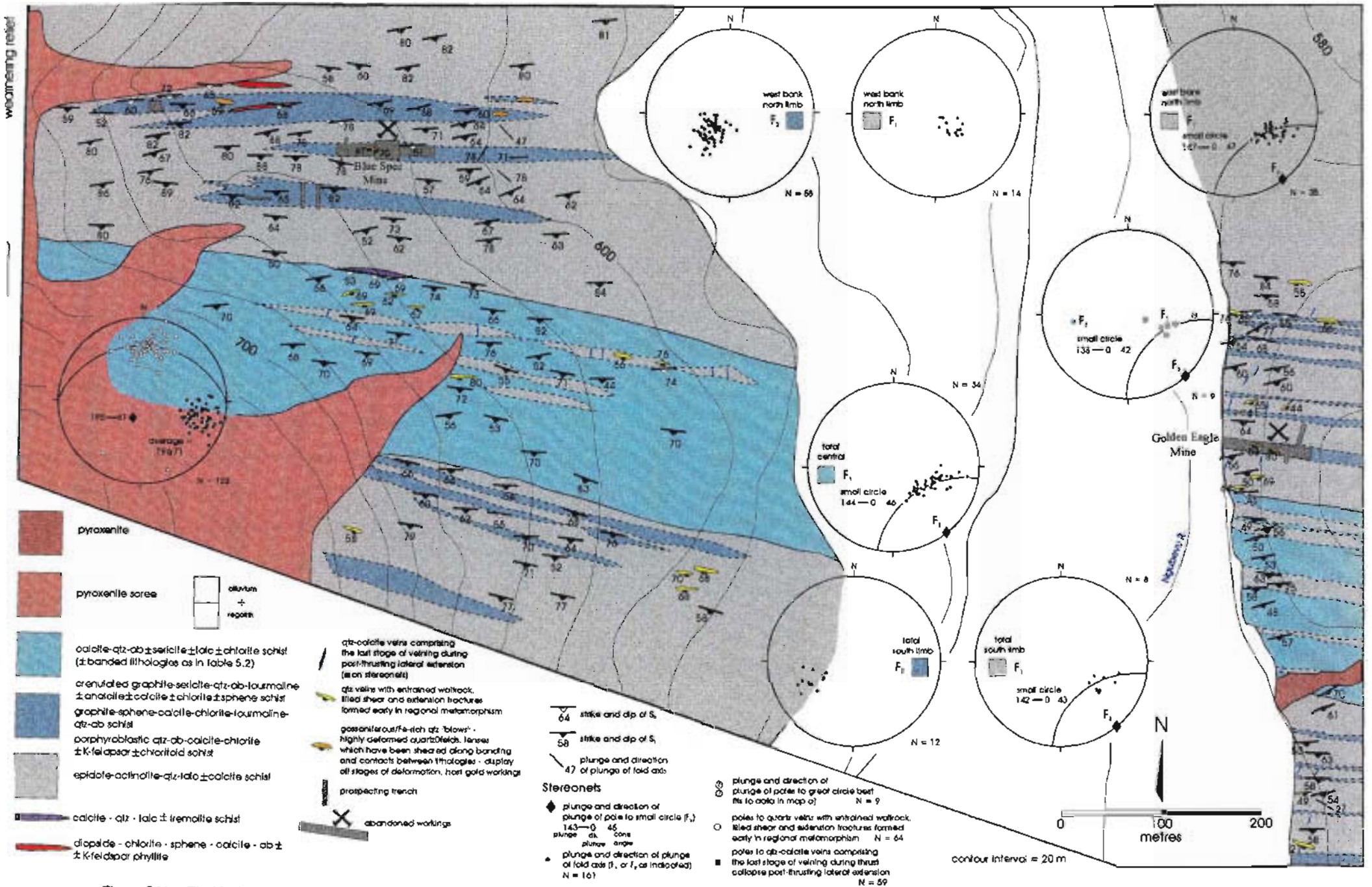

Figure 5.11 a The Ngubevu West area, showing the distribution of F_1 fold axes about small circles, implying refolding about non-cylindrical folds with sub-horizontal axes trending southeast-northwest. Also depicted are the plunge and direction of plunge of the the F_2 fold axes in the finely-banded units hosted within the epidote-actinolite schist, and the poles to late-tectonic tension gashes and early-tectonic quartzofeldspathic veining

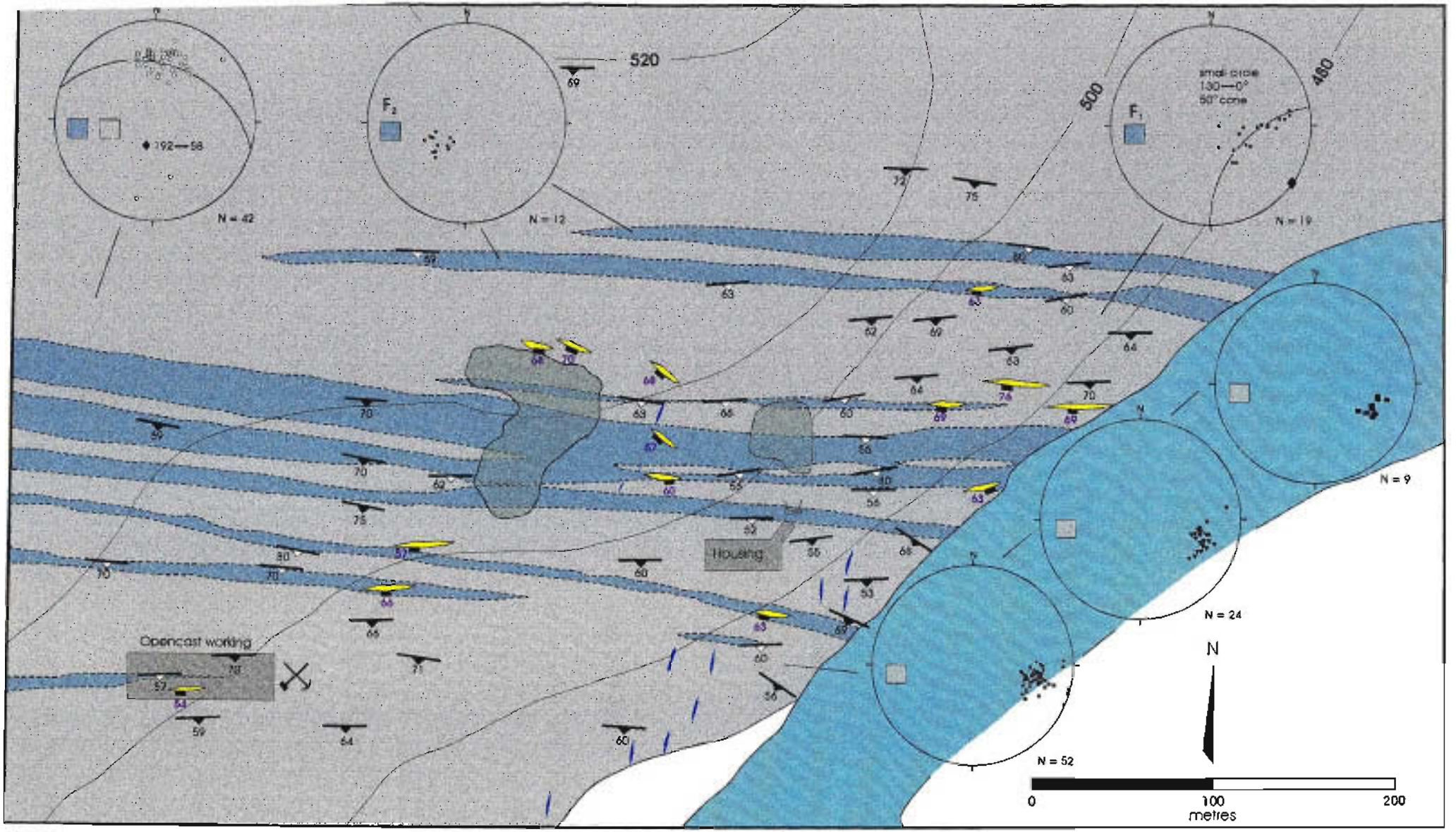

Figure 5.11 b The Ngubevu East area; F_1 is refolded by a non-cylindrical fold with a sub-horizontal, southeast-northwest-trending axis, such that the Minor F_1 axes have small circle distributions. Included in this map are the poles to late-tectonic, antitaxially-filled quartz-calcite veins, the plunge and direction of plunge of the long axes of antitaxial quartz crystals, poles to early-tectonic segregated quartzofeldsthatic/hornblende veining and the plunge and idrection of plunge of F_2 fold axes in the finely-banded lithologies. The orientation of F_1 and F_2, and the early quartzofeldspathic veining and late-tectonic quartz-calciteveining are essentially similar to those of the Ntuli

The median line of the long dimension of contours to data displays a curvature in an opposite sense to that derived from small-circle fits to data from outcrop sub-areas at NGW and NGE (Figure 5.9 b). This characteristic may imply that the F_3 flexural slip fold has been flattened, such that the small circle has been "deformed" (Ramsay, 1967).

The F_1 fold axes measured in the field were well-preserved, the folds usually having moderately- to gently-plunging fold axes and approximations of axial planes which are steeply inclined (Fleuty, 1964; Figure 5.12).

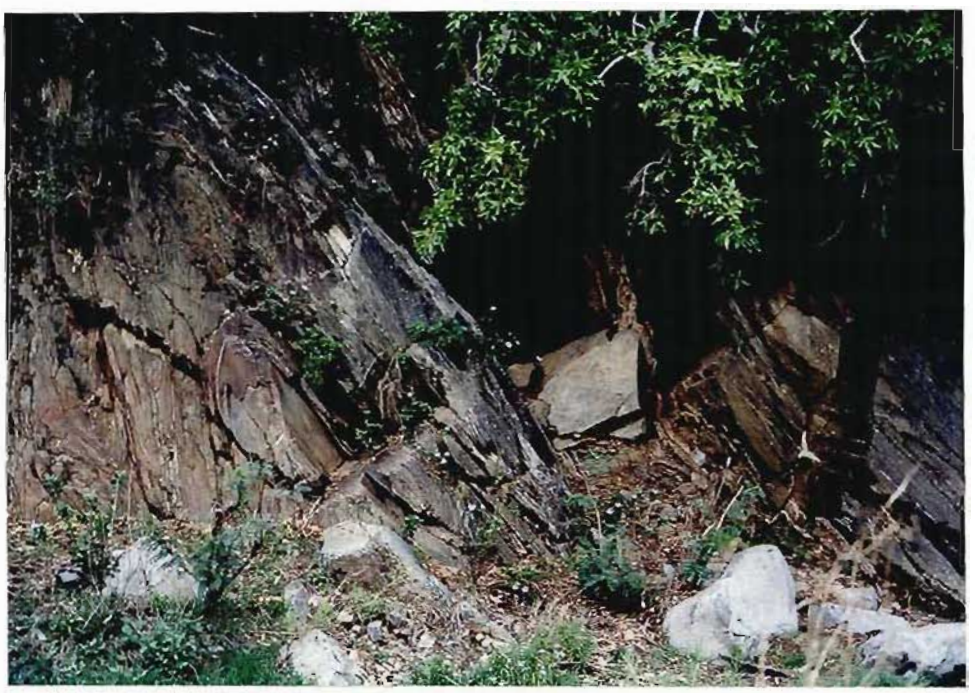

Figure 5.12 A typical example of the F_1 fold generation in epidote-actinolite schist (locality - eastern bank of the Ngubevu Stream, NGW area)

Dip isogon characteristics and t_α vs α plots of fold profiles in the epidote-actinolite and chloritic schist (Ramsay, 1967; Ramsay and Huber, 1987 - page 348) divide these folds almost entirely into two types according to the material which underwent folding:

a) Class 1A and Class 1B - parallel to ptygmatic folds in early and syn-tectonic quartzofeldspathic veins. These veins are, in places, indistinguishable in orientation from the host S_{01} planar foliation but usually exhibit disharmonic folding with respect to F_1 folds in the host schist (Figure 5.13). The veins are the result of very early infilling of shear and dilation fractures as described in the section on the southern Mfongosi Valley area. Sparse examples of similar folds in quartz-rich epidote-actinolite schist are also found.

Figure 5.13 Disharmonic, partially ptygmatically-folded, early-tectonic quartzofeldspathic veins in the epidote-actinolite and chloritic schists

b) Class 1C (rare), Class 2 and Class 3 folds - similar folds with flattened limbs in the epidote-actinolite and chlorite schist (Figure 5.12). No accentuation of shearing or flattening of fold limbs was encountered in the hangingwalls or footwalls of the mined-out deposits relative to the remainder of the field area. Characteristically the hinge zones of such folds may display parallel fold patterns but strain on the limbs is evident from transgression of the Class 1C/Class 3 divider line on $t_{\alpha'}$ vs α plots, with increasing distance away from the hinge zone. In Figure 5.14, selected corrected profiles from oriented photographs are plotted on $t_{\alpha'}$ vs α plots with fairly consistent results. A representative sample of fold profiles is also shown in Figure 5.14. Strain recorded on the fold limbs, according to the method of Ramsay (1967), ranges from 1 to >10 with the higher values on fold limb segments which are furthest away from the fold hinge.

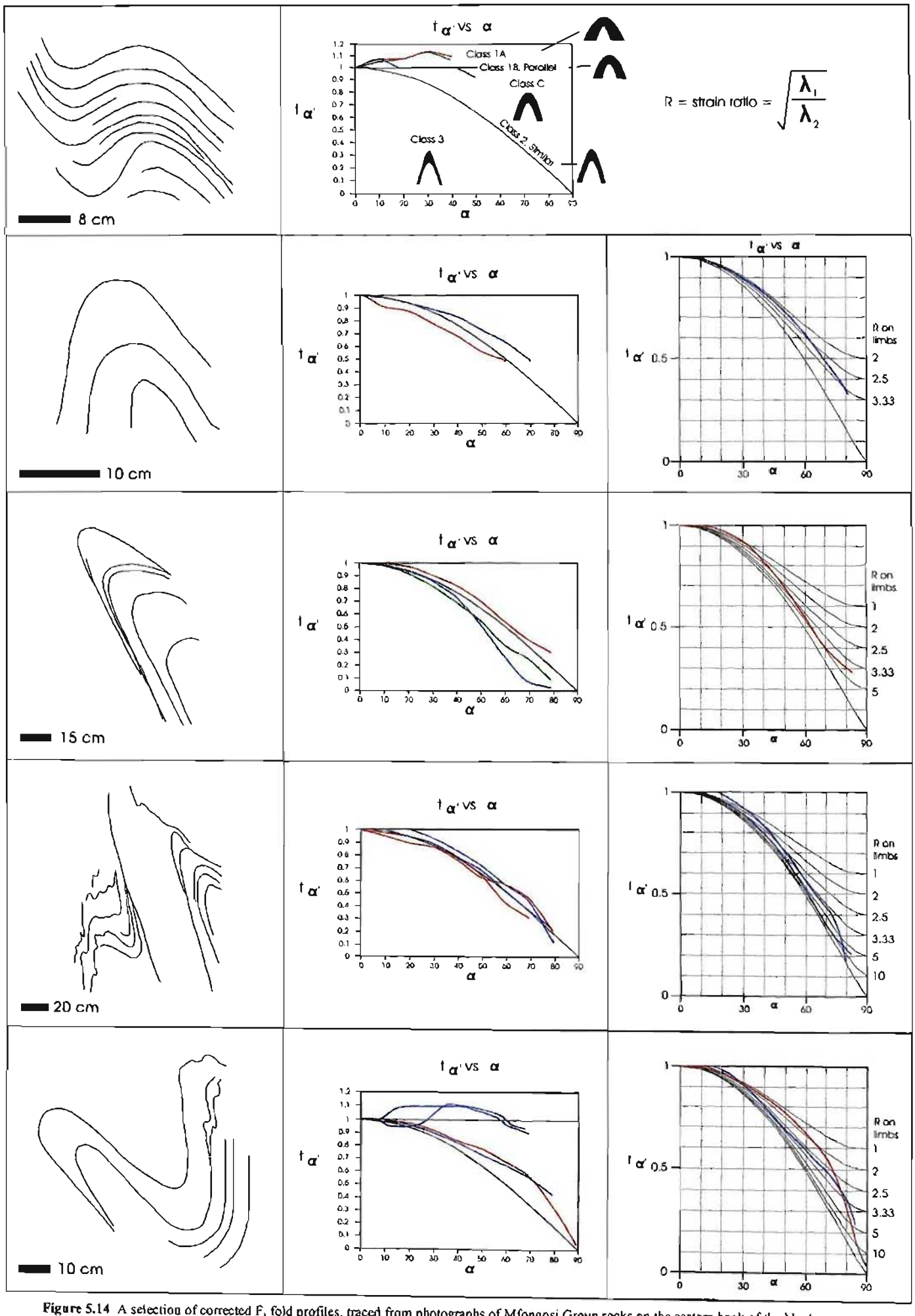

Figure 5.14 A selection of corrected F_1 fold profiles, traced from photographs of Mfongosi Group rocks on the eastern bank of the Ngubevu stream. Fold profiles are corrected according to Figure 18.5, page 368 of Ramsay and Huber (1987). Strain ratios (R) on fold limbs, from t vs alpha plots, are predicted by equations in Ramsay (1967) although the results are extremely sensitive to small changes in the variables of the equations and the graphical method is therefore preferred in this study

b) D_2 - S_2 and F_2

Syn- to late-tectonic lateral movement is incorporated in the Mfongosi Group in two main ways in the second deformation event:

- in the more competent units such as the epidote-actinolite schist, D_2 is expressed by a second planar foliation, in addition to S_{01} (Figure 5.15). S_2 does not obliterate S_{01} but rather forms a synthetic plane in a left-lateral system, with S_2 stepping up across epidote glomeroporphyroblasts and actinolite crystals (Figure 5.15).

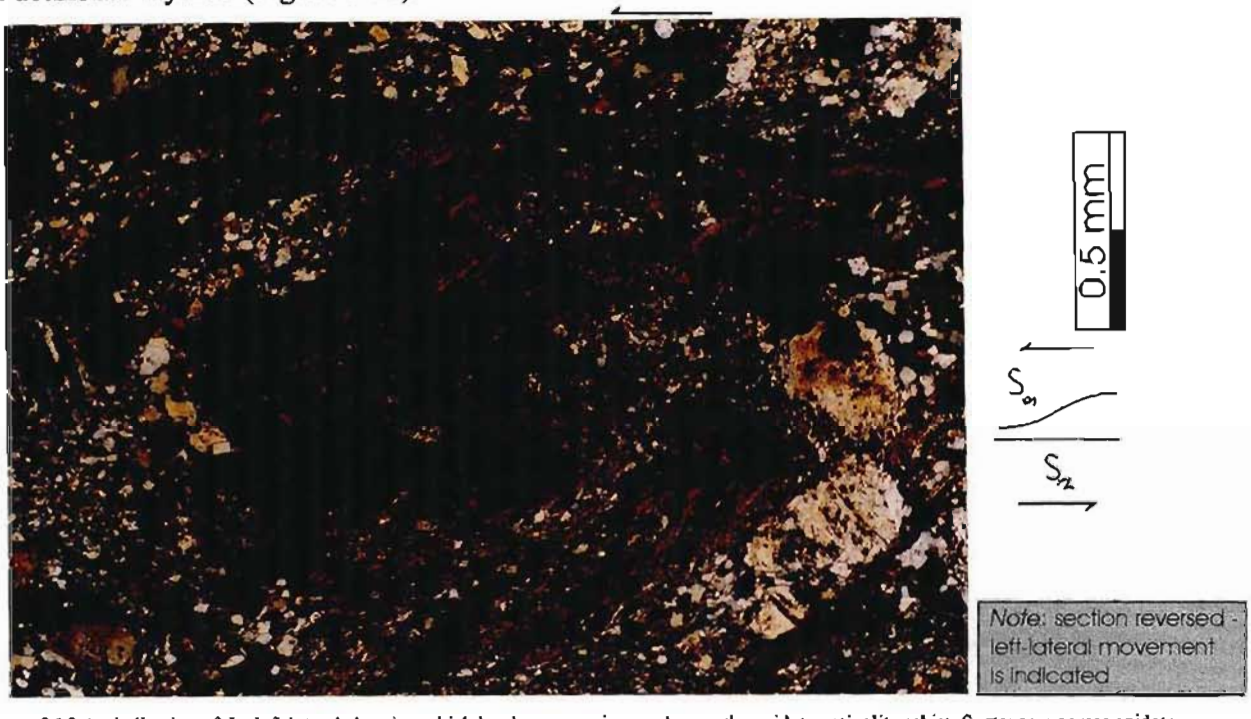

Figure 5.15 An indication of the left-lateral shearing which has been superimposed upon the epidote-actinolite schist; S_2 steps up across epidote glomeroporphyroblasts in a synthetic sense in a left-lateral shear system. There is an acute angle between S_{01} and S_2 in the phyllosilicates, examples of which are given in Table 5.3

Thin section studies of the Mfongosi schist show the S_{01} ∧ S_2 acute angles to vary in the left-lateral system, in the plane parallel to strike and perpendicular to S_{01} and also in the plane at right angles to this (Table 5.3) wherein S_2 cleavage exhibits an invariable top-to-north shear sense in the schistose rocks (although S_2 in many places is merely transposed S_1 in the plane at right angles to that already mentioned). Summation of S_2 data across both the NGW and NGE areas gives the distribution in Table 5.3 and Figure 5.16. An indication of the high strain in these rocks is given by the orientation of the F_1' fold axis, the pole to the great circle fit to S_2 data (Figure 5.16); F_1' at 103/63 is similar in orientation to F_1 for the total data set. It is apparent that the stress causing F_1 similar and ptygmatic folds has continued, or has indeed been causative, in the formation and folding of S_2. In the classic shear models, these continuous mechanisms of

progressive deformation are the norm. A component of non-cylindrical folding, with data spreading at the margins of an equal-angle stereonet, may be inferred for S_2 (Figure 5.16). There is the further possibility that the plane to the S_2 contoured high defines the axial surface of the F_1 fold generation.

Table 5.3 Compilation of measurements of acute angles (angle in the direction of shear) between the S_{01} and S_2 cleavages in the epidote-actinolite and chloritic schists.

Thin Section	Plane parallel to strike, perpendicular to dip	Plane parallel to dip, perpendicular to strike	Intersection azimuth in field (where noted)
NGW 14 a	13-16 (av. = 14)	21-39 (av. = 27)	101→45
NGW 15		21-27 (av. = 25)	-
NGW 16	10-19 (Av. = 17)	9-19 (av. = 17)	-
NGW 26a		15-25 (av. = 19)	135→45
NGW 30b		14-26 (av. = 21)	114→38
NGW 37a+b	6-16 (av. = 12)	15-29 (av. = 19)	126→49
NGW 43b		21-32 (av. = 27)	101→24
NGW 52		21-27 (av. = 24)	183→56

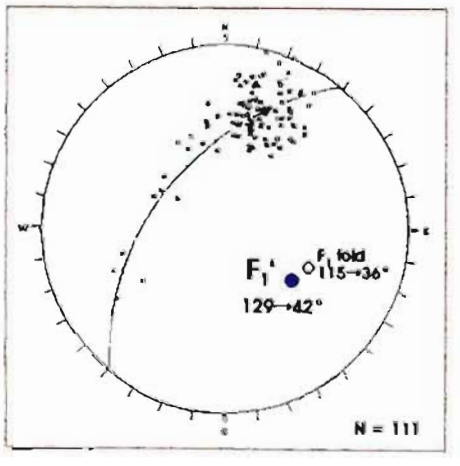

Figure 5.16 a Poles to the S_2 planar foliation in the epidote-actinolite and chloritic schist. The poles to great circle fits to S_{01} (115→36) and S_1 data are spatially very close, indicating a similarly-oriented, progressive causative stress. S_2 is folded about 129→42°. The sense of movement implied by the acute angle between S_{01} and S_2 is sinistral and indications of this movement may be found across the width of the Mfongosi Group N = 111

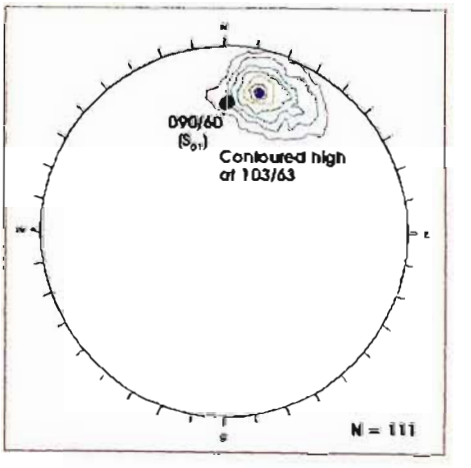

Figure 5.16 b Contoured equal area, lower hemisphere projection of poles to S_2 in epidote-actinolite and chloritic schist. Contoured high at 27% of total area is at 103/63 which, when combined with the contoured high of S_{01} data (090/60), signifies a late-tectonic left-lateral shear system for the Mfongosi Group N = 111

● The banded lithologies accommodate D_2 by kink folding and crenulations with axes at high angles to F_1 (Figure 5.17). F_2 fold axes plunge steeply towards the southwest and show slight further distortion (i.e. D_3/F_3) about small circles on equal angle stereonets. The average plunge and direction of plunge of F_2 axes, found using the WINDOW function of DIPS (Appendix E) which averages the orientation data inside a defined polygon, is 230→52°. F_1 refolding in F_2 in an epidote-actinolite schist, was encountered in the field and thus the present classification is adopted. Note that F_2 fold axes cluster about the inferred axial surface of F_1', originating from the plane to the contoured maximum of S_2 data. F_2 is therefore best described as "intrafolial" in nature. This feature is a result of F_2 tending towards, or being controlled by, a pre-existing surface. The distribution of S_2 over the Ngubevu West area is shown in Figure 5.18.

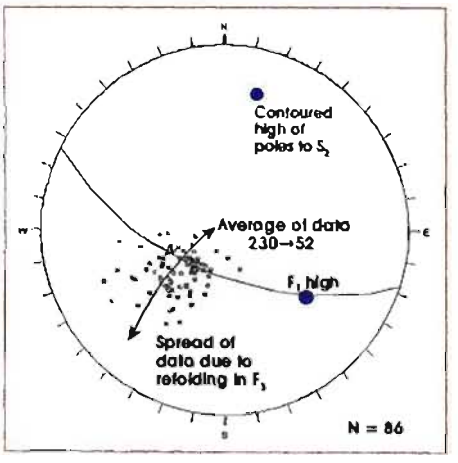

Figure 5.17 a Plunge and direction of plunge of F_2 fold axes, measured in the field and derived from best-fit great circles to fold limb orientation data on stereonet plots, in the banded lithologies. An average of the data, calculated from data enclosed in a four-sided polygon, is 230→52°. Note the spread in F_2 data due to refolding about F_1 N = 86

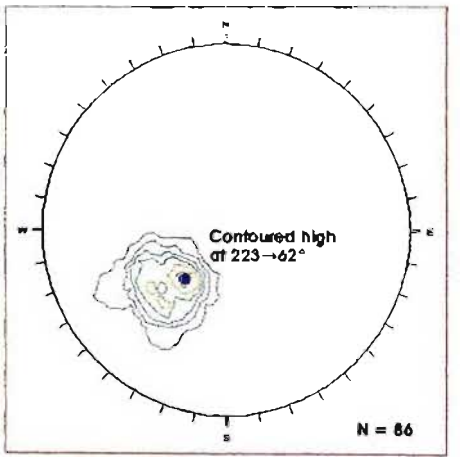

Figure 5.17 b Contoured equal area, lower hemisphere stereonet projection of F_2 azimuths in the banded lithologies. F_2 folds are crenulation or kink folds in the finely banded rocks. Contoured high at 28% concentration is at 223→62° N = 86

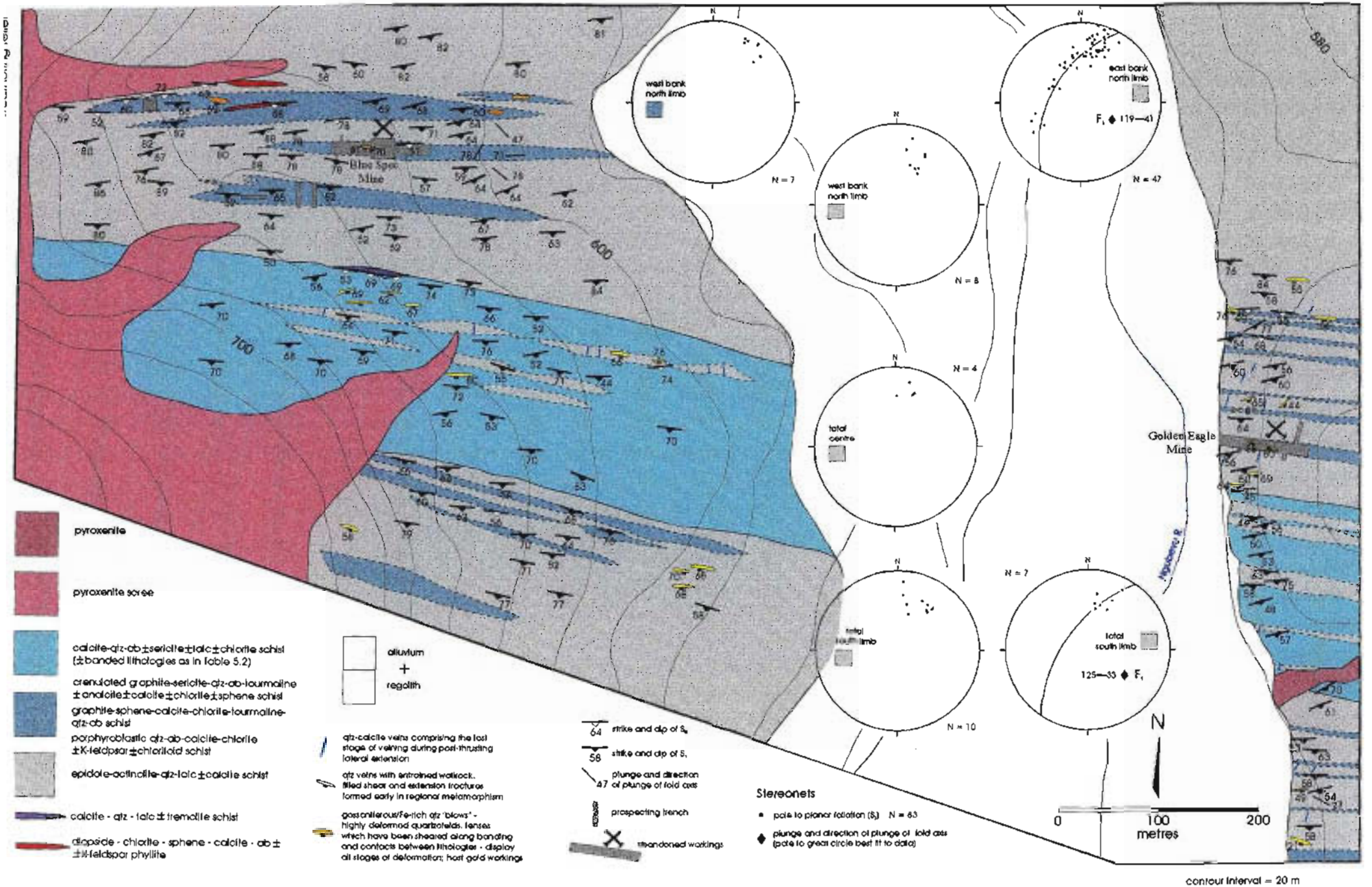

Figure 5.18 the distribution of the S_2 planar foliation over the Ngubevu West area. Note that the S_2 fabric is found primarily in the epidote-actinolite schist in the northern and southern limbs of regional F_1 folds and is only weakly developed in the banded lithologies and in the core of the regional F_1 fold. D_2 is expressed in the banded lithologies by the formation of F_2

c) D_3 - F_3

As discussed in section 4.3 a, F_1 is refolded non-cylindrically about a small circle. The cone axis producing this small circle is approximately subhorizontal and trends at 143° with a cone angle of 45° (Figure 5.19). Refolding of F_1 is an expression of the continued left-lateral movement across the Mfongosi schist.

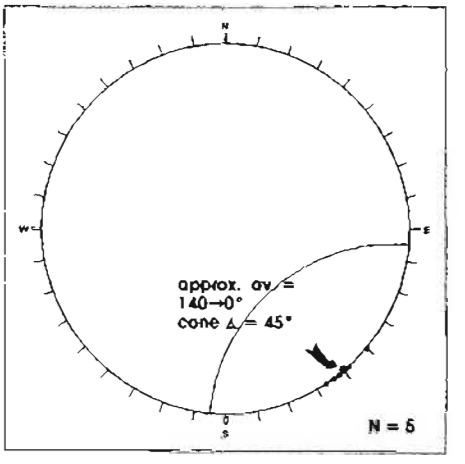

Figure 5.19 Compilation of F_3 small circle (cone) axes (F_3 minor folds - small-circle fits to F_1 axes) from individual outcrops in the NGW and NGE areas. Cone apical angles vary from 42° to 50° while an acceptable average for F_3, based on these data, is 140→0°, with a cone angle of 45°
N = 5

d) Veining - Characterization of different modes of deposit

The pattern of vein intrusion and the subsequent modification of this pattern must account for the different modes of deposit as described by Gray (1900, 1901, 1906), Hall (1910 a, b), Young (1910), Gibb (1911), Winfield (1979) and Coldwell (1984) amongst others. Field mapping has located and matched the lithotypes found by many of these authors who studied mineralization in narrow bands and veins (*op.cit.*; De Klerk, 1991), particularly the lithologies containing finely-banded graphite, calcite and tourmaline which are laterally continuous with the black shales and tufaceous horizons mentioned in these reports. What remains to be accomplished is an adequate explanation for the targets of exploration and mining: quartz veins with inclusions of chloritic schist, lenticular "bunches" and "blows" of quartz, highly fissile zones along strike from these bunches, thin veins of Fe-oxide which cross-cut the latter and veins cross-cutting the other deposit types at high angles.

A unifying theory, based on careful structural orientation data interpretation, may account for all of these features accurately (except the Fe-oxide veins, which were not encountered in the field) and signifies a simple repetition of mechanisms which have operated from the micro- to the macro-scale, probably for the duration of tectonism. Veins will be described in a chronological order, according to their timing of emplacement and cross-cutting characteristics.

1) Early veins in shear and tension fractures formed during the first folding increment - V_1

The first veining episode is similar to that of the southern Mfongosi Valley area. Veins formed by infilling and subsequent deformation and rotation of early-tectonic/syn-folding (early F_1) shear and tension gashes, initially forming regular patterns according to Figure 14.21 a)-d) of Price and Cosgrove (1990). Vein material is commonly mineralogically indistinguishable to that of the host schist, that is, quartz, feldspar and massive actinolite with chloritic and sericitic margins (Figure 5.20). The vein mineralogy is indicative of the process of pressure solution and re-deposition of (often) segregated more mafic (OH-bearing) and more felsic components of the host schist. The orientation of this vein generation closely matches that of the host S_{01} planar foliation and the margins of lithological lenses in the Mfongosi Group (Figure 5.1 a). The contoured maxima is at 089/64° although this distribution is distorted by refolding in F_3 (Figure 5.21).

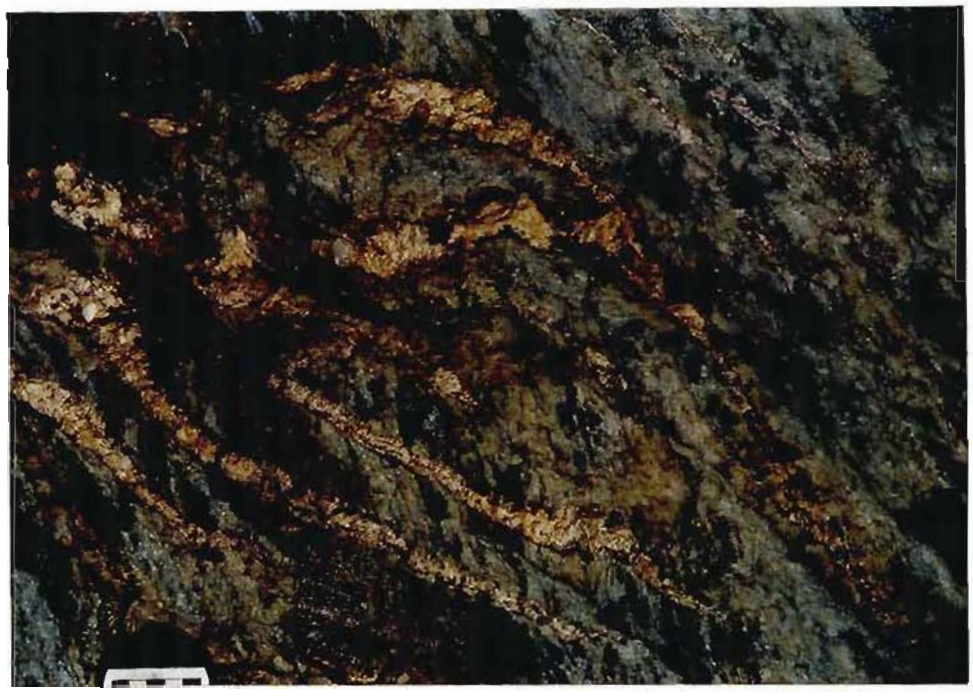

Figure 5.20 Early-tectonic quartzofeldspathic veining in the epidote-actinolite schist on the eastern bank of the Ngubevu R.(NGW field area). Note that this generation of veining has undergone all of the deformation events and has been ptygmatically folded and sheared

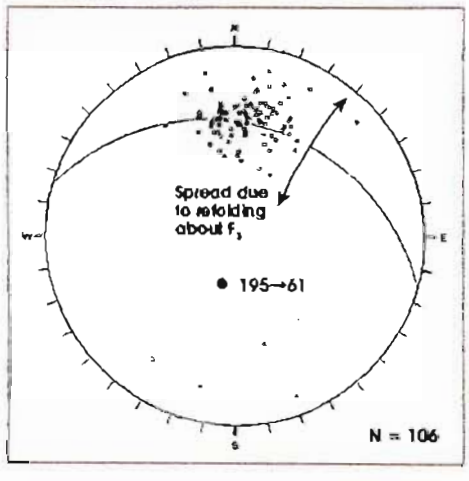

Figure 5.21 a Poles to quartzofeldspathic veins in the NGW and NGE areas which were intruded into shear and tension fractures early in the folding event. Ensuing deformation has altered the initial pattern such that veins have approached the orientation of the host planar foliation. Veins are distributed about a great circle with a pole at 195→61° which corresponds to the remnant of the virtual intersection axis between the sets of contemporaneously-formed veins. This weakly-defined pole agrees well with that found for similar veins in the southern Mfongosi Valley area (ie 195→58°, girdle axis) although a girdle may not be inferred here. The spatial variation in the data may be due to refolding about the non-cylindrical F_3 axis
N = 106

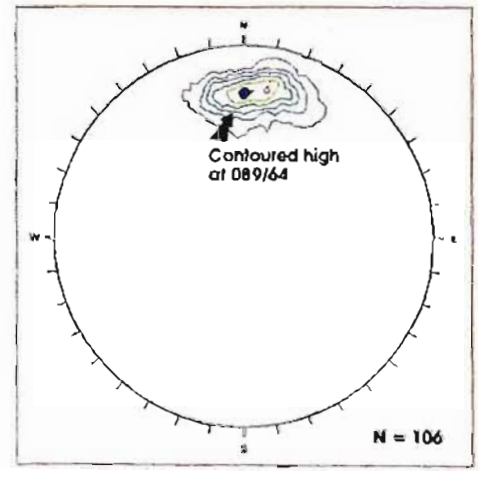

Figure 5.21 b Contoured equal area, lower hemisphere stereonet projection of poles to early quartzofeldspathic veins. Contoured high is at 089/64° which is very similar to the contoured high of S_{01} data (Figure 5.8 - 090/60°). A better indication of the implied fit of a girdle or great circle is seen in this figure and was used in the generation of the great circle fit in Figure 5.21 a
N = 106

2) Syn-tectonic to late-tectonic Tension Gashes

a) Ptygmatically folded syn- to late-tectonic microveinlets - V_2

The second vein generation is remarkable for two reasons. I exhibits a notable variation in scale, from ptygmatically folded veins 0.5 mm thick (Figure 5.22) to 2-4 cm thick straight-sided veins with antitaxial quartz fibre growth (Figure 5.23) to relics of initially larger veins emplaced in an identical fashion to smaller scale analogue. Secondly, this vein generation has a large temporal range with respect to deformation, that is veins formed from early to late-tectonic times. The characteristics of these veins therefore may overlap, in terms of characteristics and timing, with those described in 1) above. Veins in this category are divided into two groups:

Figure 5.22 Ptygmatic fold hinge of originally en-echelon quartzofeldspathic micro-veinlets in the epidote-actinolite schist (*Slide NGW/40a*). PPL.

Figure 5.23 Late-tectonic, post-thrusting tension gashes with antitaxial quartz fibre growth. The massive, interstitial calcite had been weathered away.

I) Vein characteristics observed on a variety of scales in the Ngubevu area

Asymmetric foldlets in micro-veinlets form fish-hook and rootless folds in the limbs of similar to near-similar folds (Figure 5.24) after the fashion of Sorby (1879) *in* Ramsay and Huber (1983). Thinned or sheared limbs lie parallel to S_{01} while thickened limbs are more varied in orientation with respect to the host foliation. Often the foliation of the host schist is superimposed on the thickened parts of fish-hook folds.

A number of generations of co-folded veins or initially en-echelon veins is evident (eg **Slide NGW/40b**). Such folding results in the thinned limbs being within 5° of each other. Further deformation of these initially subvertical to vertical veinlets has resulted in isolated, lenticular pods of vein material, free of opaque minerals, consisting of quartz, albite, sericite and minor chlorite, the chlorite being concentrated at the margins of the veinlets. Extreme flattening on the limbs of similar folds results in obliteration of the thinned limbs leaving only the thickened pods of mosaic textured quartz, albite and minor minerals, completely surrounded by the host schist matrix (Figures 5.24, 5.25). Transcurrent shearing distributed throughout the schist, and accommodated in a more discontinuous fashion at lithological contacts (eg Hobbs *et al.*, 1976 - page 238; Figure 5.26), distributed vein material into S_{01} parallelism. Although difficult to measure in the field the fold axes of these fish-hook folds, here termed F_4, are almost vertical to being parallel to the dip of the host rock.

The product of these processes acting together is an en-echelon distribution of mineralogically and structurally similar pods of quartz and albite with phyllosilicate-rich margins and with quartz/albite stringers originating at the strike-parallel pod terminations (Figures 5.24, 5.25). These vein arrays are similar to those described by Winfield (1979) and Coldwell (1984) and to those found in this study, in that quartzofeldspathic material, whether gold-bearing or not, is recrystallized in foliation-parallel, discontinuous, anastomosing and en-echelon veinlets and pods which cross-cut the banded lithologies at acute angles. Pressure solution of the north and south asperities of the lenses must also be considered as the mosaic-textured felsic material is often recrystallized into massive amorphous quartz or feldspar.

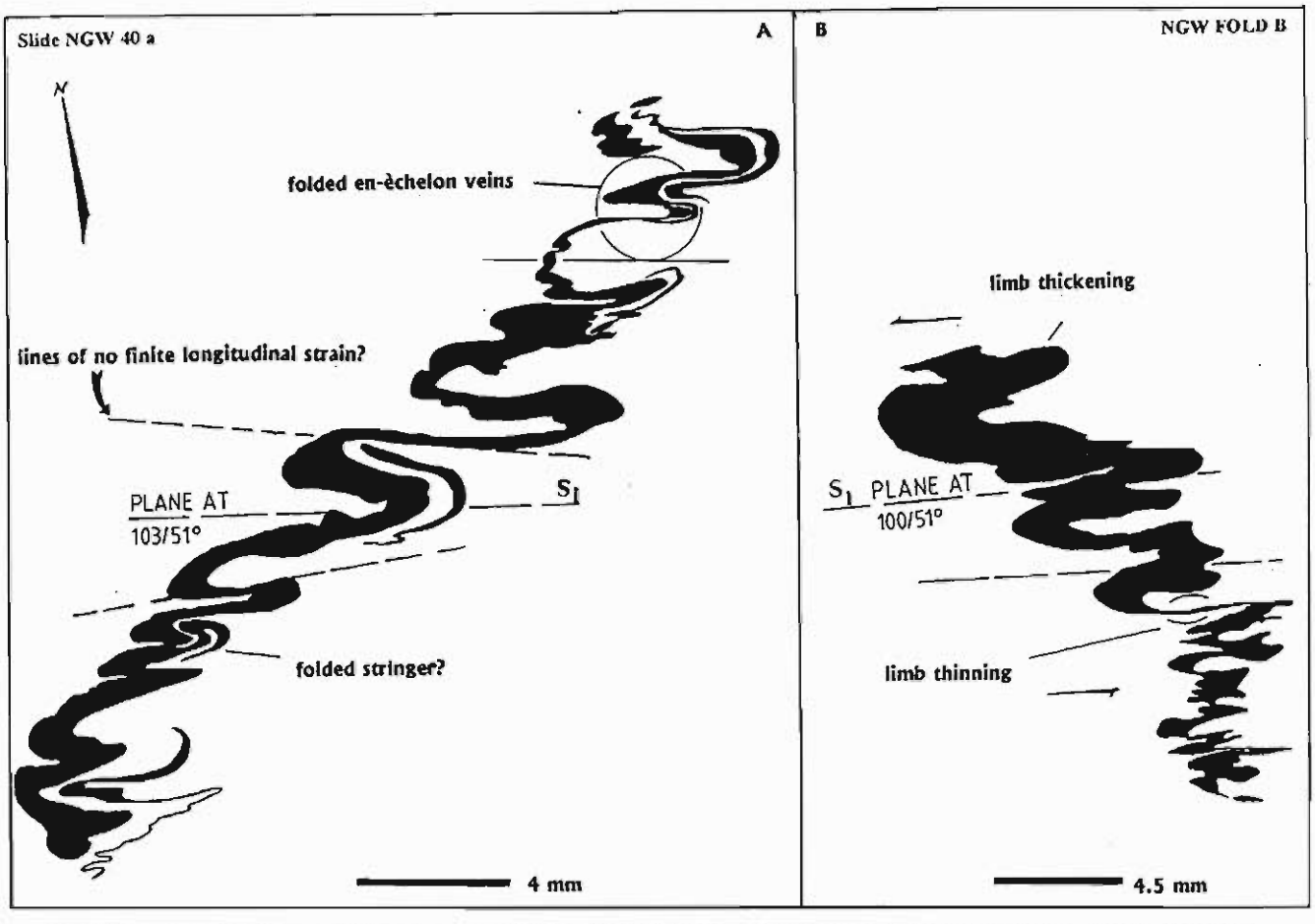

Figure 5.25 **a** and **b** Continuous folds of originally en-èchelon felsic/quartzofeldspathic veinlets. Drastically thickened or thinned fold limbs, are the expression of combined simple and pure shear, depending upon the orientation of the respective fold limbs relative to the first increment of straining. Left-lateral shear is not apparent, nor is a loss of vein continuity, as the thin limbs are re-adsorbed into the host matrix

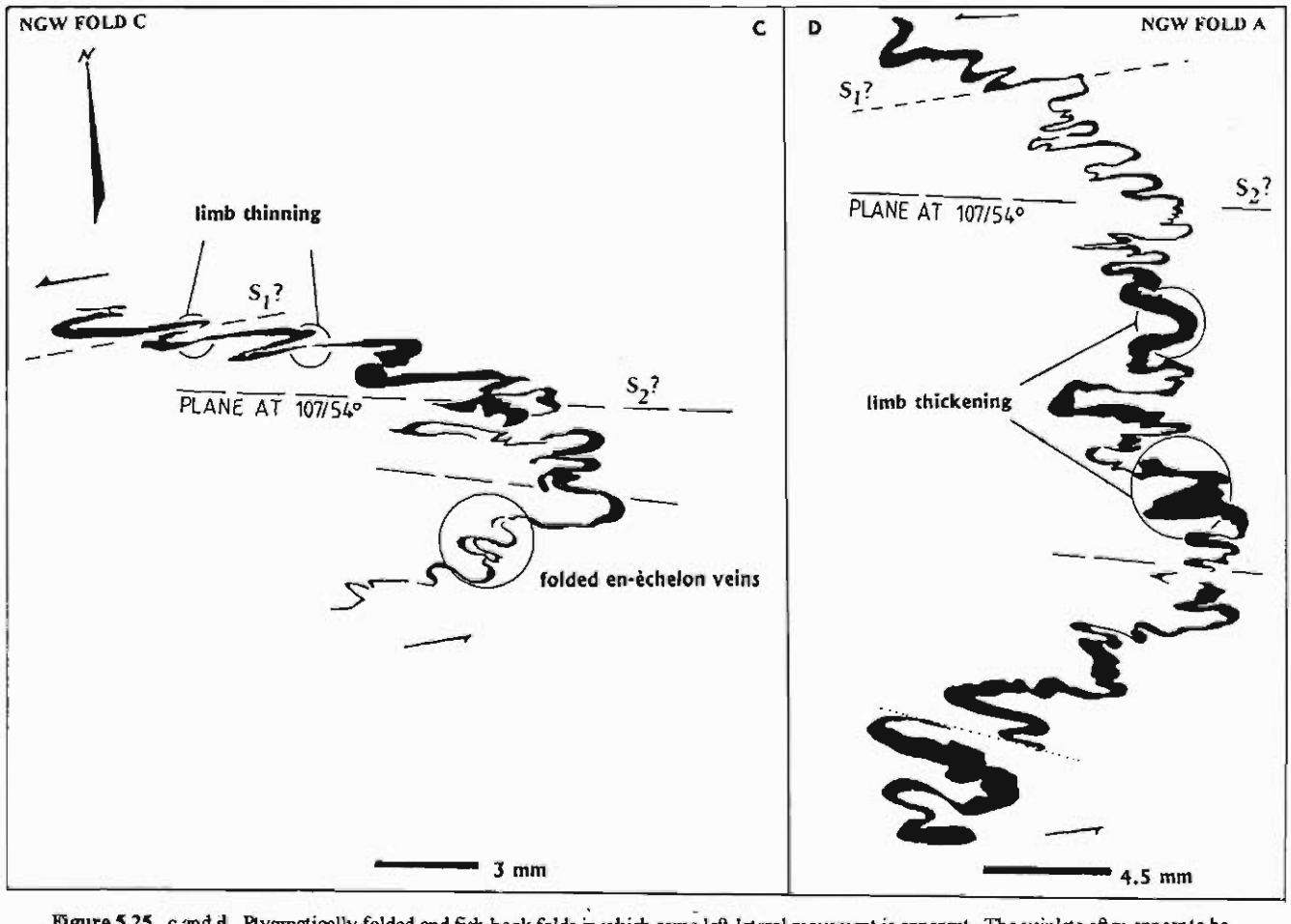

Figure 5.25 **c** and **d** Ptygmatically-folded and fish-hook folds in which some left-lateral movement is apparent. The veinlets often appear to be refolded. Unfortunately, an inaccurate estimate of inhomogeneous simple shear will result from attempting to find the offset of an initial vein orientation as pure shear has greatly affected these rocks

Figure 5.25 Photomicrograph showing the isolation of a quartzofeldspathic lense or "blow" in epidote-actinolite schist. Joining the blows are the thinned limbs of fish-hook folds. These limbs may become totally re-absorbed into the matrix due to pressure solution and hence the proposal of the recycling of felsic material during the tectonic history. Alternatively, the thinned limbs may form along-strike "stringers" at the terminations of the quartzofeldspathic blows (***Slide Fold-B***). PPL.

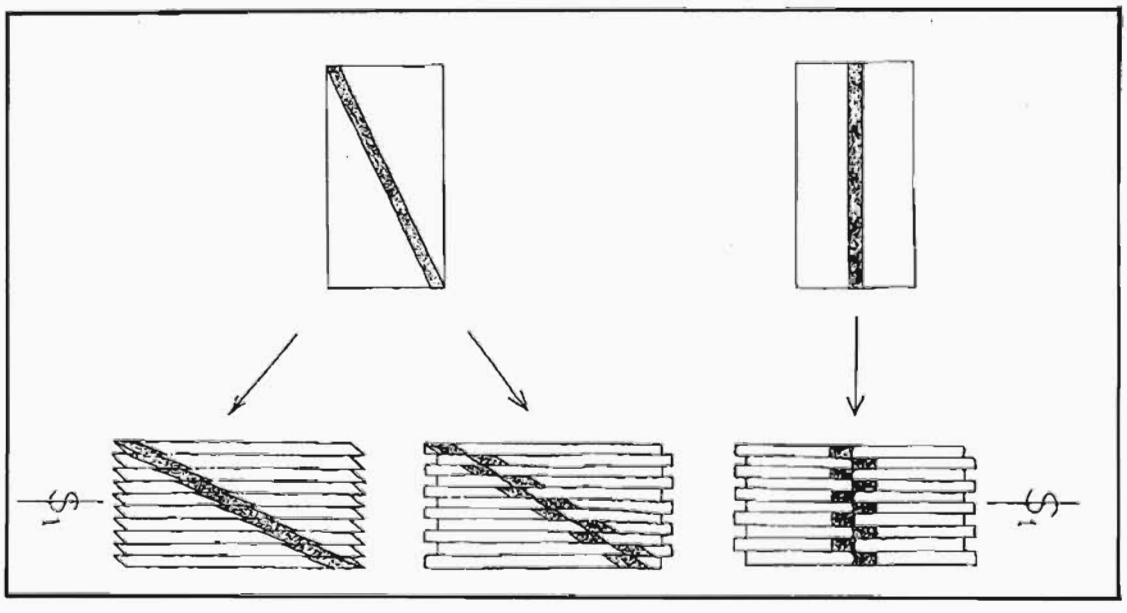

Figure 5.26 The possibility of discontinuous deformation mechanisms; offset vein segments due to discontinuous pure shear (Hobbs et al., 1976)

ii) Modelling of vein pattern formation in a unit circle during homogeneous straining

As a conceptual tool, the processes of continuous pure shear and continuous left-lateral simple shear in the Mfongosi Group are applied to a unit square which contains a unit circle (Figures 5.27 a and b). The unit circle contains an early tectonic tension gash intruded at a bearing of about 230° and folded during F_1 and F_2 which have affected the epidote-actinolite and chloritic schist. Strain due to pure and simple shear were calculated according to the equations in Appendix C1.

In the following scheme a number of assumptions are made:

- ψ_{xz} is negative (left-lateral shear)
- there is no area change ($\Delta A = 0$) in simple shear while area change in pure shear is naturally noticeable and will be the cause of pressure solution
- only continuous shear mechanisms are exhibited, no discontinuous simple or pure shear acts on the unit circle and unit square
- there is no competency contrast between the vein and the host rock. Certainly, this may be valid when the vein assumes a saccharoidal or mosaic-textured crystal form and thus does not strictly constitute a competent layer in an incompetent matrix although the initial ptygmatic form is symptomatic of such an initial contrast
- the processes of pressure solution cannot be simulated

In Figure 5.27 a) the development of the felsic bunches, blows and stringers is demonstrated in a scenario of simple shear with values of $\gamma = 0.2$, 0.4 and 0.6 superimposed on pure shear with R_p (strain ratio of pure shear) = 2, 5, 7 and 10. Similar features were observed by other researchers and found in this study, With a shear strain of $\gamma = 0.6$ superimposed upon a pure shear ellipse of R = 10, five effects are immediately evident:

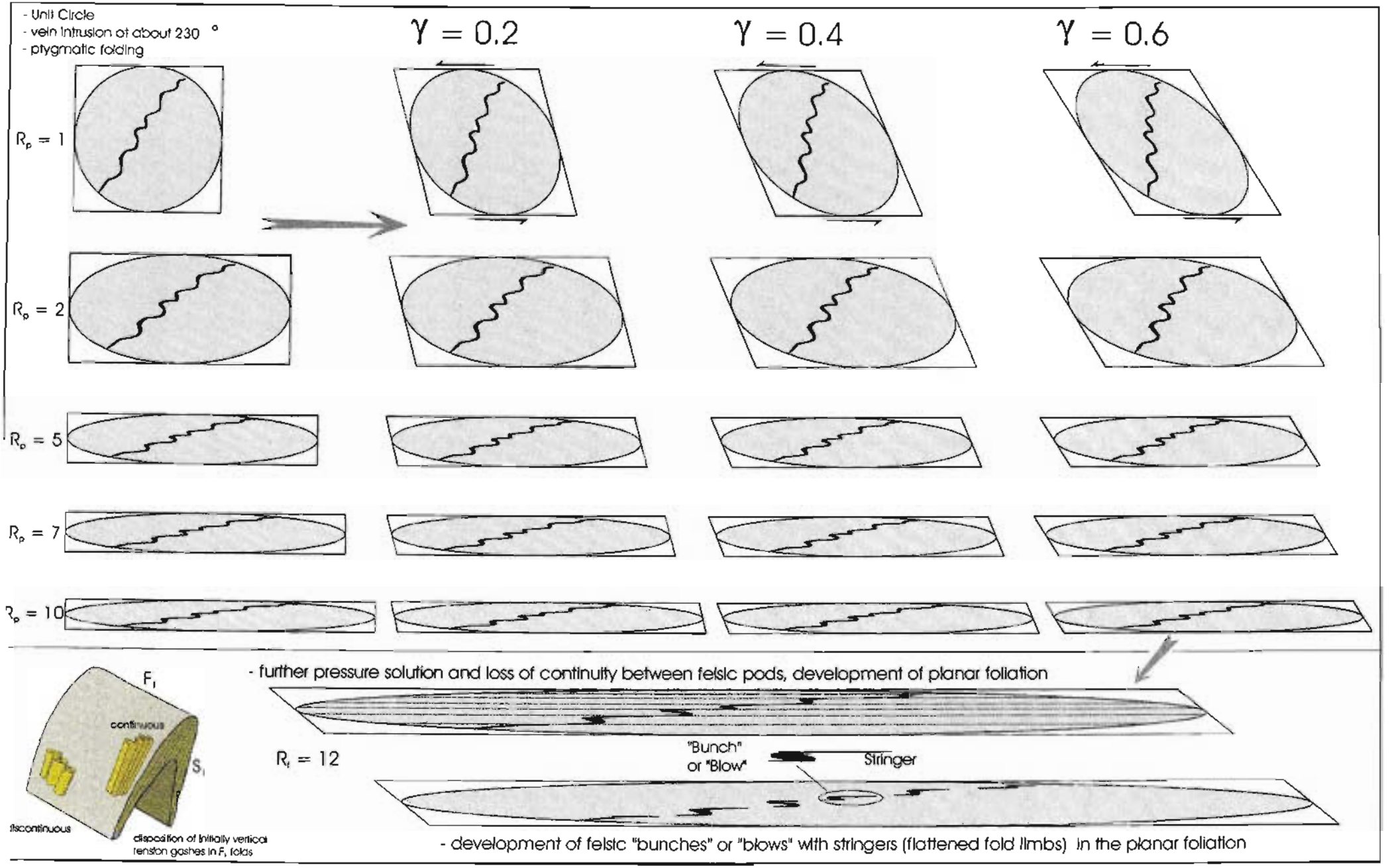

Figure 5.27 a Possible mode of development of discontinuous felsic bunches, blows and stringers during deformation of an early-tectonic tension gash intruded, at about 230 degrees bearing, into the epidote-actinolite and chloritic schists. In this scheme simple shear strains of $\gamma = 0.2$, 0.4 and 0.6 are superimposed upon pure-sheared (coaxially-deformed) unit circles, producing finite strains (R_s) approximately equal to those produced by continuous pure shear. For these variations in γ, and the strain ratios reasonably inferred from t_α vs α plots, the "vergence" of veining remains constant; ie, veins remain in the same sector of extension.

- the finite strain ratios (R_f) produced in this succession of possible strain events are similar to R_p (ellipse ratio due to pure shear alone)
- pressure solution acting on the thinned limbs of the deformed veins may result in discontinuous, en-echelon sets of felsic bunches and stringers in an apparent right-lateral shear situation
- discontinuous pure shear may also account for an en-echelon format of veining.
- a portion of the felsic stringers will be parallel to the planar foliation inherent in the finite strain ellipse
- the Ptygmatically-folded veinlet passes from a sector of compression to one of extension in incremental straining

In Figure 5.27 b) a more probable mode of felsic bunch and stringer development is displayed. As a variation on Figure 5.27 a), pure shear with values of $R_p = 2, 5, 7, 10$ and 12 is superimposed on simple shear with $\gamma = 0.8$ and 0.9. With a combination of $R_p = 12$ superimposed on simple shear $\gamma = 0.9$, a finite strain ratio of $R_f = 24.3$ is produced which, from estimates of finite strain ratios of about 12 on $t_{\alpha'}$ vs α plots, is unrealistically high. From micro-veinlet observations a more realistic strain combination results in a finite strain ratio (R_f) of *c.* 12 (approximated here by $R_f = 11.6$) and could result from a pure shear ratio of 7 superimposed on a simple shear of $\gamma = 0.8$. The features evident from this scheme are:

- finite strain ratios (R_f) are produced which are far greater than those of R_p alone
- pressure solution or discontinuous strain may separate the bunches and result in stringers or "ghost" (palimpsest) flattened folds and stringers (eg Figure 5.25)
- the ptygmatically-folded veinlet enters a sector of compression
- the ptygmatically-folded veinlets are refolded in this scheme as any asperity of the initial veinlet is exaggerated by deformation
- the finite strain ellipse $1 + e_2$ axis orientation is notably at an angle to the pure shear $1 + e_2$ axis orientation in accordance with the anticipated left-lateral simple shear found in other field areas and in agreement with the initial sense of vein intrusion and antitaxial quartz fibre growth found in the Ngubevu area.

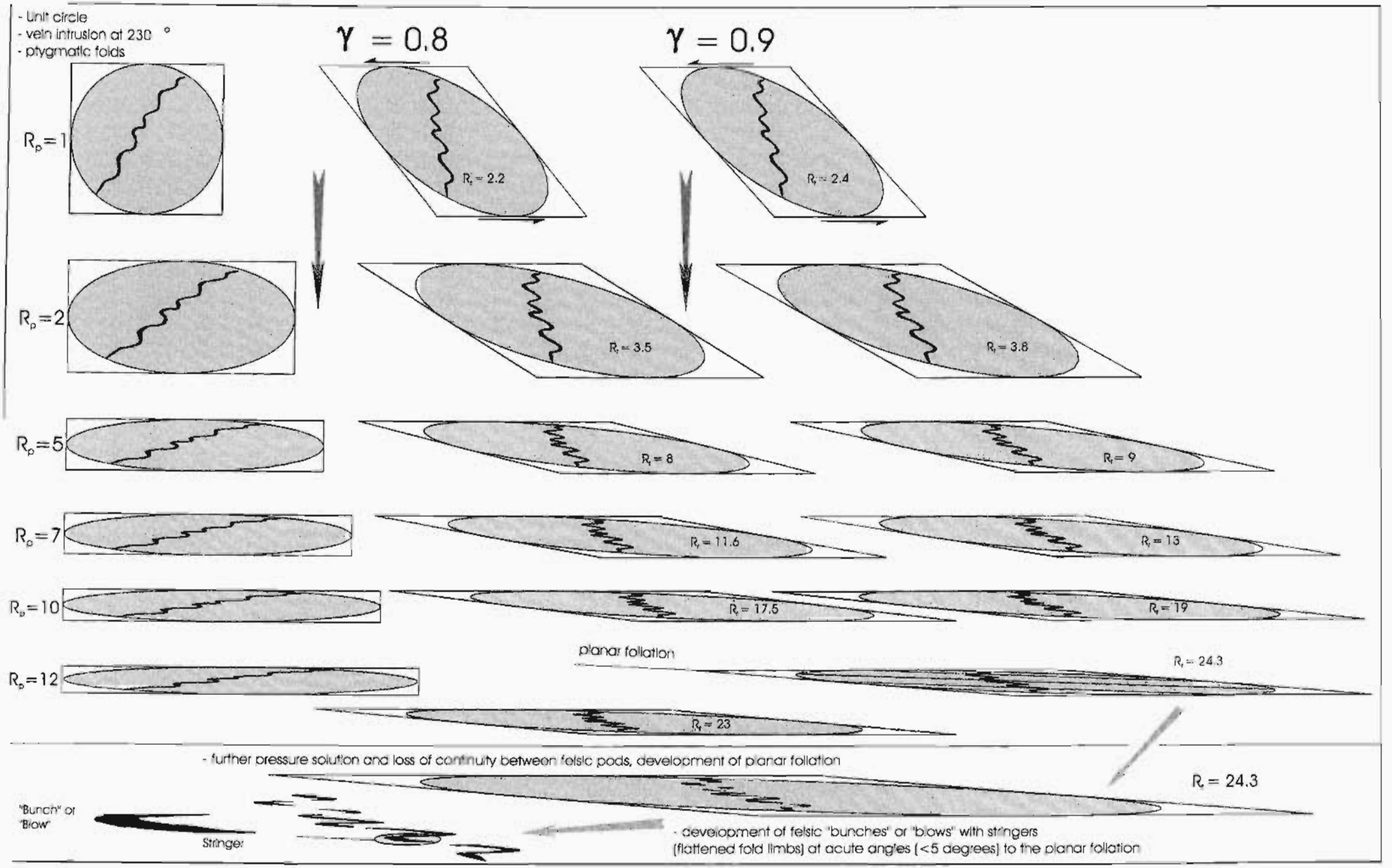

Figure 5.27 h Probable mode of development of discontinuous felsic bunches, blows and stringers during deformation of an early-tectonic tension gash intruded, at a bearing of about 230 degrees, into the epidote-actinolite and chloritic schist. In this scheme, pure shear with coaxial flattening with R_p = 2, 5, 7, 10 and 12 is superimposed upon simple-shearing (non-coaxial) with γ = 0.8 and 0.9 resulting in Rf (finite strain ratio) much higher than those imposed in pure shear. Furthermore, the $R_f(1+e_1)$ axis is notably at an angle to the $(1+e_1)$ axis of superimposed pure shear. An apparent left-lateral movement is evident in the ptygmaticaly-folded vein, that is, veins have entered the sector of compression. Refolding of the ptygmatic folds may also occur. As an approximation, a shear strain of γ = 0.8-0.9 with a superimposed R_p of 5 matches the vein patterns found in the schists.

b) Late-tectonic vertical to sub-vertical antitaxially-filled tension gashes -V_3

These subvertical to vertical undeformed analogous of the microveinlets vary in thickness from about 0.5 to 4 cm and display readily measurable antitaxial quartz fibre growth (Figure 5.23). Veins of this generation cross-cut the F_1, F_2 and F_3 and are affected by lateral displacements at the lithological contacts and intra-lithological shears. Often the only indication of the existence of these veins, well-displayed on the eastern bank of the Ngubevu stream, are planar fractures, often with herringbone surface patterns with relict quartz crystals (Figure 5.28) indicating brittle failure of the rock. The vertical and horizontal dimensions of vein walls vary from 1 m to 8 m and 2 m to 8 m, respectively. The opening directions, from quartz fibre measurement, are consistently perpendicular to the vein margins and coincide with the poles to the veins in 2-dimensional stereonet space at 192→66° (Figures 5.30 a-d). The veins are interpreted as true dilation structures which accommodated lateral extension and post-thrusting collapse. Tensional vein characteristics are summarised in Table 5.4.

Table 5.4 A summary of the series of tension gashes which have formed over the duration of deformation in the Ngubevu area

	← Vein emplacement continuum →	
	Early tectonic/early folding	Late-tectonic/late-thrusting
Present form	fish-hook to rootless ptygmatic folds, en-echelon lenses with S_{01}-parallel vein material distribution	vertical to sub-vertical, parallel-sided veins offset at lithological contacts and banding
Mineralogy	qtz-ab-sericite ± chlorite	qtz-calcite
Orientation w.r.t. host rock	parallel to sub-parallel to S_{01}	at obtuse angles to S_{01}
Absolute orientation	contoured high at 089/64° parallel to S_{01}	contoured high at 196/67°
Opening azimuth	none discernable	106→23°

Figure 5.28 Surface ripples in the herringbone format on a weathered vein margin. Pure brittle dilation and fracture initiation is suggested.

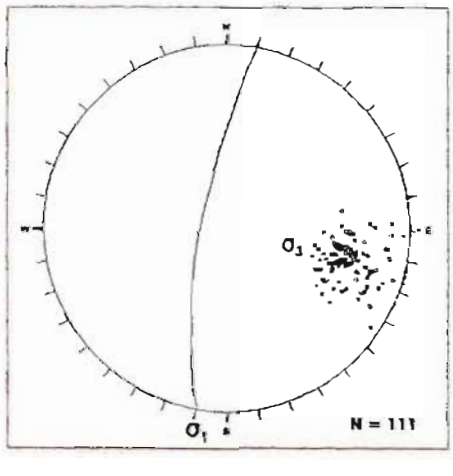

Figure 5.29 a Poles to late-tectonic tension gashes with antitaxial quartz and massive, anhedral calcite infilling. This vein generation cross-cuts all known generations of folding and is thus attributed to the post-thrusting lateral extension stage. A good estimate of the positions of the maximum extension direction (σ_3), the maximum principal stress axis (σ_1) and the intermediate principal stress axis (σ_2) may be made (Fig. 5.29b) N = 111

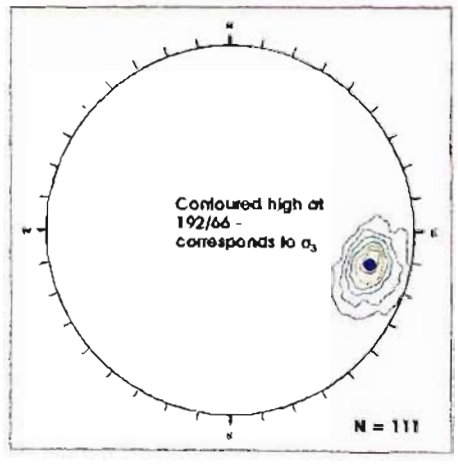

Figure 5.29 b Contoured equal area, lower hemisphere stereonet plot of poles to late-tectonic tension gashes in the epidote-actinolite and chloritic schist. Contoured high, at 28% of total concentration, is at 196/66° and corresponds to the main extension direction (σ_3) for the Ngubevu area N = 111

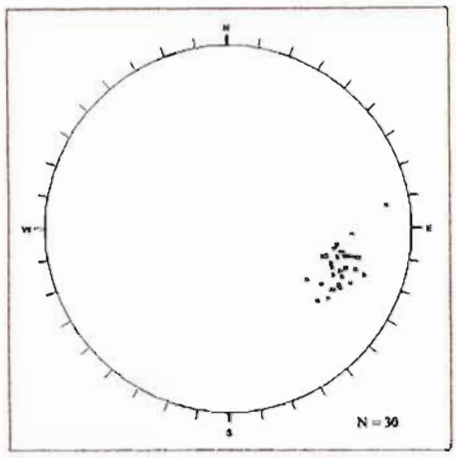

Figure 5.29 c Plunge and direction of plunge of long axes of antitaxial quartz crystals in the late-tectonic tension cracks. The average opening direction, inferred from the field and the WINDOWS function of DIPS is 106→23° which is within 4° and 1° of the plunge and direction of plunge of the pole to vein margins' contoured high indicating that vein dilation was at right angles to vein margins and parallel to the σ_3 axis derived from the poles to the late-tectonic tension gashes N = 30

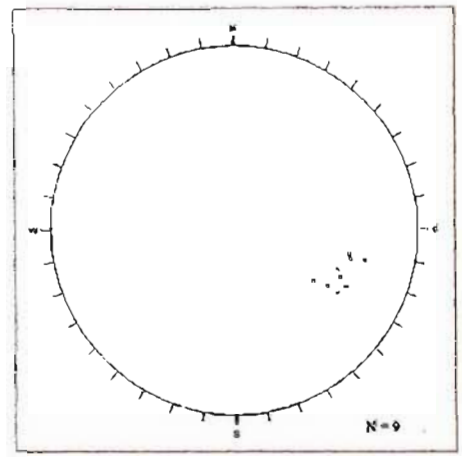

Figure 5.29 d Plunge and direction of plunge of long axes of stretched porphyroblasts and relic amygdales in the epidote-actinolite schist at NGE. Late-tectonic lateral extension was therefore not only limited to discrete fractures, ie the tension gashes, but was pervasive throughout many parts of the host schist and may therefore be assumed to have been a continuous mechanism in the earlier stage of deformation which later became brittle N = 9

5.4) Conclusion - Context of Mineralization in a Tectonometamorphic Model

The enigma of isolated and en-echelon pods, with lengths of up to 4 m parallel to strike, and widths of up to 1.5 m in the banded layers is explained by deformation of early- to syn-tectonic veins which intruded the competent epidote-actinolite and chloritic schist and cross cut the lenses which contain finely-banded calcite, graphite and tourmaline. Quartz and felsic stringers along strike from these bunches or blows are products of S_{01}-parallel shearing and redistribution of vein material of the blows into the foliation and strain shadows around the quartzofeldspathic lenses. Pressure solution on the northern and southern extremities of the saccharoidal- or mosaic-textured lenses has resulted in massive quartz and/or feldspar in strain shadows along strike from the quartz lenses (effectively thickened limbs of formerly ptygmatically-folded veins which have been transformed into fish-hook folds). Such features are best observed in the Blue Spec Mine on the western bank of the Ngubevu Stream in the NGW. Here the focus of the mining efforts has been a felsic lens in a highly weathered graphite-calcite-sphene ± chlorite ± albite ± pyrite schist host which forms a layer of limited extent in the surrounding epidote-actinolite/chloritic schist. After intrusion of this large, early-tectonic vein, loss of vein continuity at the boundary contact of the banded lithologies was followed by flattening and ptygmatic folding.

An examination of geochemical soil surveys performed by various mining companies demonstrates the unpredictability of the position of these bunches and blows. Base metal and/or gold anomalies are distributed in such a way as to imply a constant repetition of the processes described above (Figure 5.30). For instance, an early-tectonic tension gash, which has been transformed into a fish-hook fold, may be cross-cut by a syn- or late-tectonic tension gash, either at the lensoid or stringer part of the first vein. Ptygmatic and/or fish-hook folding may be repeated in the second vein and therefore quartzofeldspathic material ± Au may be recycled in a feedback system. A combination of these processes, and the fact that mineralization occurs at the intersection of veining and the banded lithologies, makes for a complicated final pattern of mineralization, and hence the apparent en-echelon and/or along-strike anomalies encountered by former researchers.

Late-tectonic tension gashes, filled with antitaxial quartz and amorphous, massive calcite, are apparently enriched in mineralization and occur at high angles to the bunches and blows, cross-cutting the quartzofeldspathic stringers. These veins occur at a consistent orientation of about 192/66° and are often sub-vertical, displaying opening directions which are at right angles to the planar vein margins, i.e., towards 106→23° which may be tentatively inferred as the vector of late-tectonic lateral extension/post-thrusting collapse. Fracture initiation in the latest stages of tectonism was brittle, as inferred from the herringbone vein wall patterns. It is anticipated that earlier veining, formed in the initial increments of folding in the Mfongosi Group (early D_1 or 'D_0'), as at the southern Mfongosi Valley area, formed in a similar orientation although the modelling in Figure 5.27 is applied to a tension gash which started at a bearing of 230° simply to emphasize the processes involved.

The small-scale, ptygmatically-folded and fish-hook veinlets occurred and were similarly deformed on a number of scales. Larger analogues of this vein generation cross-cut the banded lithologies enriched in pyrite and stibnite (associated with graphite), and were favourable sites of Au deposition, but not necessarily for base metals. It is pertinent that Winfield (1979) and Coldwell (1984) considered the epidote-actinolite/chlorite schist as the units which contained the highest Au values; the concentrations of Au found in this study were often low (*cf.* 10 ppb). A concentrating mechanism is necessary, such as pressure solution followed by mineral deposition in veins which cross-cut the banded units. The banded lithologies are variably enriched in base metals but unpredictably so.

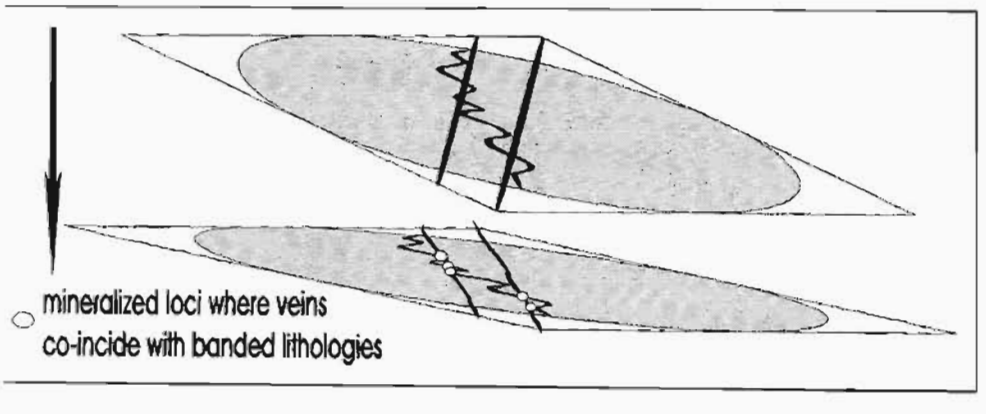

Figure 5.30 The simple repetition of tension gash formation, followed by ptygmatic, then fish-hook folding makes for a complex final distribution of potential mineralization sites. This is further complicated by the limited and unpredictable extent of the banded lithologies which host the mineralization

Evolution of the NGW and NGE areas is summarized in Figure 5.31 and in Table 5.5, with the terminology of the episodes of deformation and accompanying foliation and fold development adopted from this study. This model is not in agreement with that proposed by De Klerk (1991) who proposes an alteration-zone model for mineralization. There are chloritic borders to some of the felsic bunches and blows in the schist but they are not the norm and are not attributable to "syn-thrusting" alteration. They are better assigned to wallrock alteration and chloritization adjacent to tension gashes which formed at trends of 190°- 230°. The variation in certain elements, plotted by De Klerk (1991) over the "ore-zone"-wallrock contact, is expected from such a contrast in mineralogy between felsic vein and more mafic host rock.

Deformation and mineralization initiated at the same point as the first-formed fractures described for the southern Mfongosi Valley area. The larger-scale initiation of fractures in a foreland is accompanied, nearer the thrust plane, by the initiation of dilational fractures and shears on a smaller scale in individual layers of the protoliths of the epidote-actinolite and chloritic schist. Infilling of these fractures by the segregated mafic and felsic material, formed during initial pressure solution and the "hot-iron" effect, as described for the Mfongosi Valley area.

Veins were rotated into parallelism with the S_0 and embryonic S_1 layering and foliation while the first set of tension gashes were initiated in the progressively more flattened fold limbs of closed F_1 folds. The intersection of these tension gashes, containing the products of pressure solution of the epidote-actinolite and chloritic schist, with the banded lithologies was responsible for the first set of mineralised loci. As D_1 continued and the F_1 fold limbs were progressively flattened, the tension gashes assumed ptygmatic and fish-hook forms. The final stages of D_1 and the start of D_2 were responsible for the loss of continuity between the hinge zones and limbs of the fish-hook folds and the production of the quartzofeldspathic bunches, blows and stringers; bunches and blows forming discordant, enigmatic lensoid features while the stringers becoming essentially indistinguishable in orientation from the host S_{01} fabric.

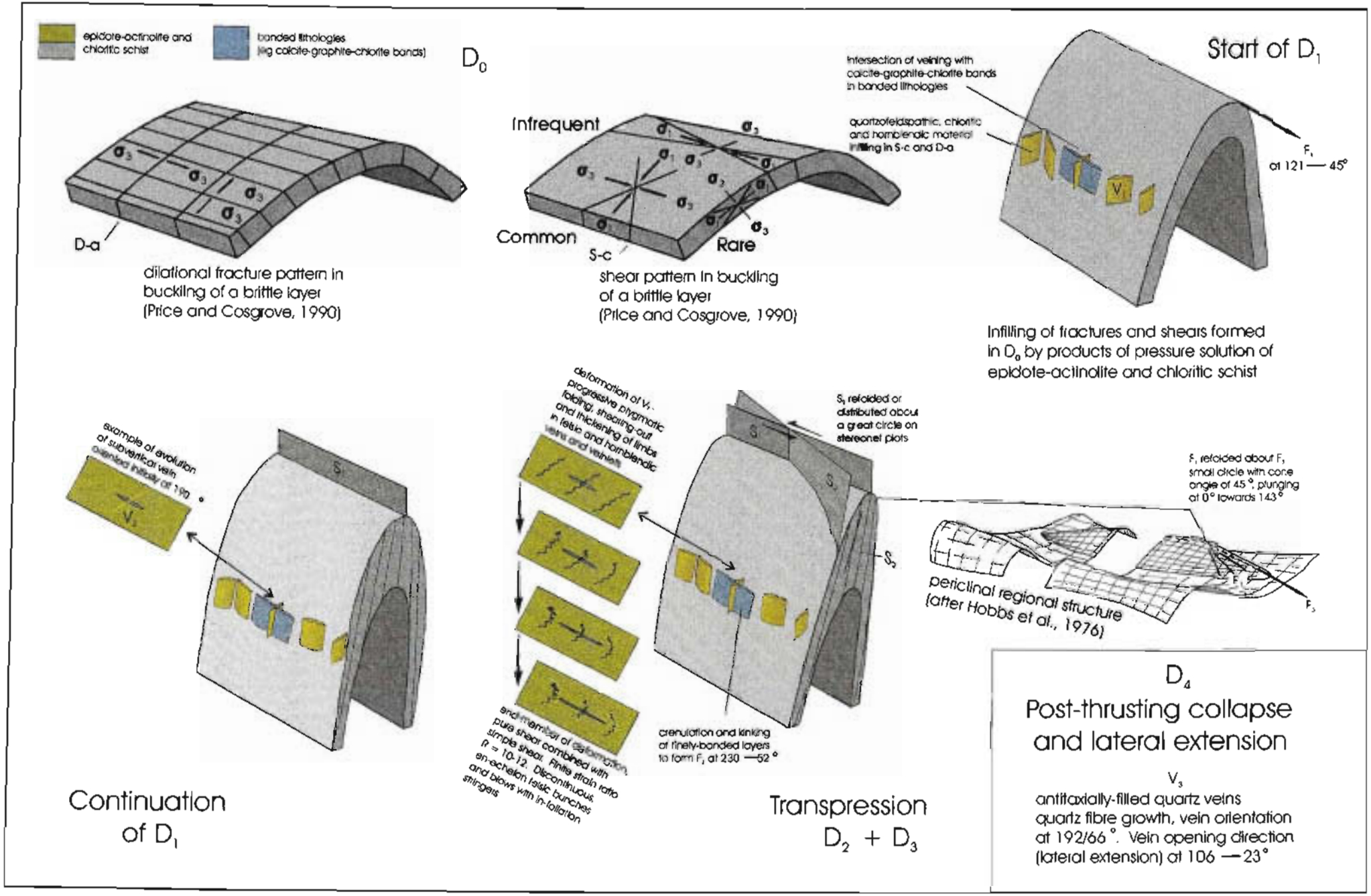

Figure 5.31 Model for the tectonometamorphic evolution of the Ngubevu area, showing the configuration and mode of development of the mineralised loci. The terminology of the structural features is that described in Table 5.5 and in the text

Left-lateral movement, active in D_2, continued in D_3 with the kinking of the finely-banded lithologies (eg the graphite - sphene - calcite - chlorite - tourmaline - quartz - albite schist) to form the steeply southwest-plunging F_2 fold set. In D_3, F_1 was refolded about a non cylindrical fold axis plunging 45° toward 143°.

The final stage of deformation, D_4, comprised lateral extension. D_4 tension gashes were intruded at an average orientation of 196/67° at an oblique angle to the planar foliation and consisting of anitaxial quartz and interstitial calcite, indicating and extension azimuth or σ_3 to 106→23°. An indication of the negative dilation or transpression across the Mfongosi Group in the Ngubevu area may be obtained from a combination of vein and foliation orientations. Given that the dominant shear plane is parallel to the 090/60° and that the σ_1 trend is parallel to the strike of late-tectonic tension gashes (V_3) at 192/66°, 90° minus the angle between σ_3 (dilation direction according to vein orientation) and S_{01} in a plane perpendicular to the vein margins, gives an angle termed θ' (Figure 5.33; θ'= 12°). As an example, plotting θ' = 12° and γ = 0.8 (Figure 5.27) gives a definite negative dilation of just under 0.5 (<-0.5) and a final strain ratio of approximately 3.75. This is in contradiction with the strain ratio found from a visual analysis of ptygmatically-folded veins. However, the main point to be noted is that this area of the Mfongosi Group is a zone of transpression with a potential negative dilation of less than 0.5 (Figure 5.33). Features such as high-angle en-echelon vein arrays, pressure solution seams/stripes and stylolites are common in such transpressional shear systems and, with the marked negative dilation, the potential for pressure-solution generated fluids is great.

These features comprise the essential elements of a fold and thrust belt which has undergone transpression, pressure solution and the intrusion of veins and veinlets throughout the history of deformation. Oxygen stable isotope studies add further weight to the argument of pressure solution and proximal redeposition.

Gold grades, as for the other field areas under study, are usually low and range from 10 ppb to 129 ppb (Appendix B4). Samples NGW-10 at 3826 ppb and sample NGW/A1/3 at 1953 ppb in the NGW field area are exceptions. Both samples are from gossaniferous/iron-rich veins in a layer of the highly banded lithology hosted within the epidote-actinolite/chloritic schist. Sample NGW-10 occurs in highly crenulated graphite and calcite-bearing schist which displays the F_2 fold generation. The structure of this 1 m long quartz pod and its D_2 deformation indicate an early formation with respect to the peak of deformation. The pod generally conforms to a "blow" as described in previous sections (Figure 5.32). The across-strike continuity of an early tension gash is not evident due to shearing at lithological contacts. The Blue Spec Mines' main shaft occurs on a larger blow of this nature. Sample NGW/A1/3 conforms to the along-strike "stringer" classification, that is, continued deformation and redeposition of felsic material along strike from the quartzofeldspathic blows accounts for the presence of these thin veins (1-4 cm thick) in the highly banded units. The presence of mineralization may thus be attributed to the co-incidence or intersection of a lithological layer and a regularly-oriented structural feature i.e. early tectonic veining, whether of the 190°-trending tension gash or the veins formed by the infilling of fractures formed during the initial buckling of the foreland (Chapter 3).

Figure 5.32 Photograph of the main lode, in the form of a doubly-terminating quartzofeldspathic pod, at the Champion Mine. The sheared-out limbs of this large deformed tension gash form the along-strike stringer veins in the metamorphosed sapropelite/metacalcsilicate which miners followed

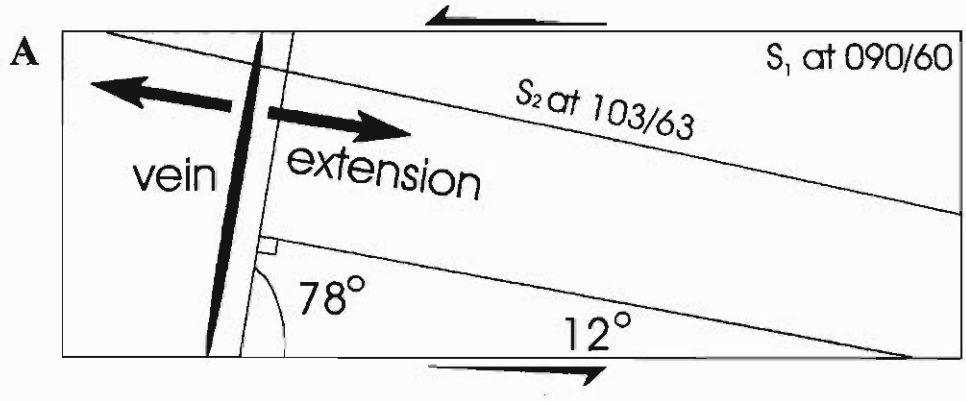

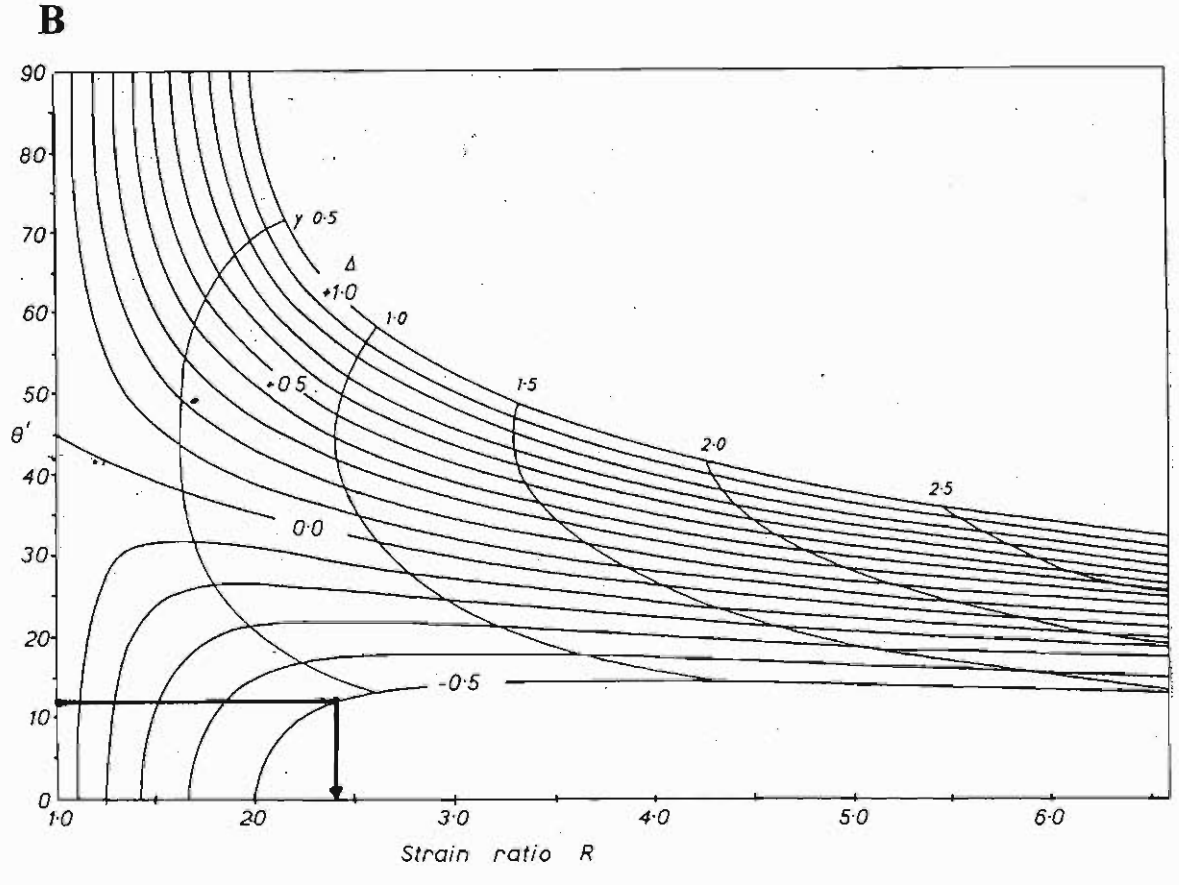

Figure 5.32 a Framework of estimation of the negative dilation across the Mfongosi Group. The orientations given are explained in the text and are averages derived from contouring of stereonet data. b Curves of variations in ellipse orientation (θ') and ellipticity (R) for differing simple shears (γ) and dilations (Δ) accross a sheared zone such as the Mfongosi Group. A negative dilation of less than 0.5 is implied by the structural data (Figure 3.20 of Ramsay and Huber, 1983)

Table 5.5 Summary of the deformation events and resulting structural features in the Ngubevu field areas. D_0 is not necessarily distinguishable from D_1, but is included for the sake of clarity.

Deformation Event	Description of Event	Planar Foliation	Folding	Veining	Other Linear Features	Metamorphic Conditions
'D_0'	**buckling** of competent volcaniclastic succession, formation of S-c and D-a brittle shears and fractures in buckle folds. Orientation of S-c at about 45° to σ_1, D-a parallel to σ_1. $\sigma_1$at about 190° to 200° trend			**V_1** infilling of S-c and D-a brittle shears and fractures by segregated quartzo-feldspathic, chloritic and hornblendic material		zeolite facies?
D_1	**pressure solution** and low-grade metamorphism. formation of S_1 which becomes indistinguishable in orientation from S_0	**S_1** axial planar foliation to F_1, orientation 090/60°	**F_1** Class 1B-Class C folds in epidote-actinolite schist, axes at 121→45°	vein rotation towards S_{01} plane, great-circle/girdle distribution of poles to S-c and D-a veins, defining pole at 195→61° average vein orientation at 089/64° (*cf.* S_{01} at 090/60°)		
D_2	**transpression** causing tightening of F_1, kink folding in finely-banded calcite-graphite-chlorite (etc) bands synthetic S-cleavage in epidote-actinolite indicating left-lateral movement	**S_2** S_2 at 103/63° (ie. at 10° from S_{01})	**F_2** asymmetrical kink folding and crenulation in banded layers, F_2 at about 230→52° tightening of F_1 (limb flattening) **F_1 in S_2** Fold axis at 129→42° (*cf.* F_1 at 115→36°)	**V_2** tension gashes filled with felsic material, parallel to σ_1, during tightening of F_1 vertical dilation cracks trending between 190° and 200° **deformation of V_2** range of vein morphologies - fish-hook folds in (V_1/V_2) - discontinuous felsic bunches and blows - felsic stringers		start of high-pressure metamorphism? possible isograd folding chlorite grade on vein margins
D_3						
D_4	**continued transpression** causing tightening and refolding of F_1 in epidote-actinolite and chloritic schist. Non-cylindrical folding of S_2 strain ratio R = 12 in flattened F_1 fold limbs **late-tectonic lateral extension**	intensification of S_2?	**F_3** non-cylindrical folding small circle with cone angle of 45°, axis plunging 0° towards 143° Class-C/Class-2 (Similar) to Class-3 folds in F_1	**V_3** antitaxially-filled veins, qtz fibre growth. Veins contain amorphous calcite. Sub-vertical vein orientation at 196/67°	long axes of quartz crystals at 106→23° (vein opening direction) stretching lineation (long axes of epidote glomero-porphyroblasts) 106→23°	**epidote-actinolite facies** ↕ carbonate metasomatism

5.5) Economic Potential

The Ngubevu area mineralization is hosted in equant blows and multiple along-strike quartzofeldspathic stringers in highly banded lithologies which contain dominant amounts of finely-banded tourmaline, calcite and graphite. These banded layers are erratic in distribution and are hosted within epidote-actinolite and chloritic schist. The spatial location of mineralization resulted from the intersection of a structural feature (veining) with a lithological feature (finely-banded units). Throughout the deformation and metamorphism, recycling of vein material due to pressure solution and/or metamorphic heating resulted in the high-angle vein mineralization comprising the 190°-trending late-tectonic quartz-calcite tension gashes; an indication of late-tectonic lateral extension.

In the NGE area, in the vicinity of the Buffalo River copper mine, two samples yielded anomalous gold grades: NGW-48 at 3840 ppb and NGW-50 at 2242 ppb. The former is a quartzofeldspathic vein hosted within the banded lithology as described above while the latter is a quartzofeldspathic vein occurring in epidote-actinolite schist. Both veins display boudinaging and their attitude implies that they intruded early in the sequence of metamorphism and deformation.

As it is difficult to distinguish the banded lithology from the epidote-actinolite schist, due to extensive weathering in the vicinity, and given the multiple deformation causing veining and the recycling of this vein material it would be extremely difficult to predict the position and grade of further mineralization in the Ngubevu area.

Chapter 6

Phoenix Mine

6.1) Economic History

The Phoenix Gold Mine to the east of the eastern lobe of the Samungu loop, a 12 kilometre-long meander in the Tugela River (Figure 1.3), is hosted within amphibolitic to meta-gabbroidal/meta-noritic rock. Numerous south-dipping, east-west trending quartz veins have been mined with the majority of the gold being extracted from quartz veins near the footwall to this vein set. The main adit is 25 metres above the level of the Tugela River on the eastern bank (Figure 6.1). Initially worked by 27 miners in 1906, at which time only 100 tons of quartz had been extracted and stockpiled, three main adits are constructed along the strike of the veins at 27, 42 and 58 m above river level (Gray, 1906). The total length of the tunnelling was 74 m. A fourth tunnel at 121 metres above river level and 600 metres from the river's edge was partly opened in 1909 (Hatch, 1910). It appears that the quartz veining may be up to half a kilometre in strike length (Theart, 1986; 1987; this study). In 1907, it was reported that 90 tonnes of ore were milled at Phoenix Mine, from which an average 8.4 $g.t^{-1}$ Au was recovered by amalgamation (Hatch, 1910; Theart, 1987). Assay results by Hatch (1910), Theart (1987) and Smith (1986, 1987) are summarized in Table 6.1.

Table 6.1 Summary of grades obtained and materials sampled by various researchers. Original pennyweights were converted to grams by multiplying by 1.555

Study	Au Grades Obtained	Material Sampled
Hatch (1910)	3.6 $g.t^{-1}$ over 0.81 metres to 47.31 $g.t^{-1}$ over 1.22 metres Highest assay result - 122 $g.t^{-1}$	vein quartz
Theart (1987) Survey by P. Becker and H.F.J. Theart	Channel sample at Adit 1 = 6.0 $g.t^{-1}$ over 0.7 metres	gossaniferous vein quartz (with entrained mafic stringers)
	Grab sample (one of three) - 3.7 $g.t^{-1}$	as above
	Slimes dump material = 2.1 $g.t^{-1}$	vein quartz + amphibolitic and pyroxenitic host rock powders
Smith (1987) Follow-up survey to Theart (1986, 1987) by G.L. Smith and G. Brown	0.02 to 6.1 ppm averaging 0.66 ppm	gossaniferous vein quartz, with iron staining and mafic mineral entrainment

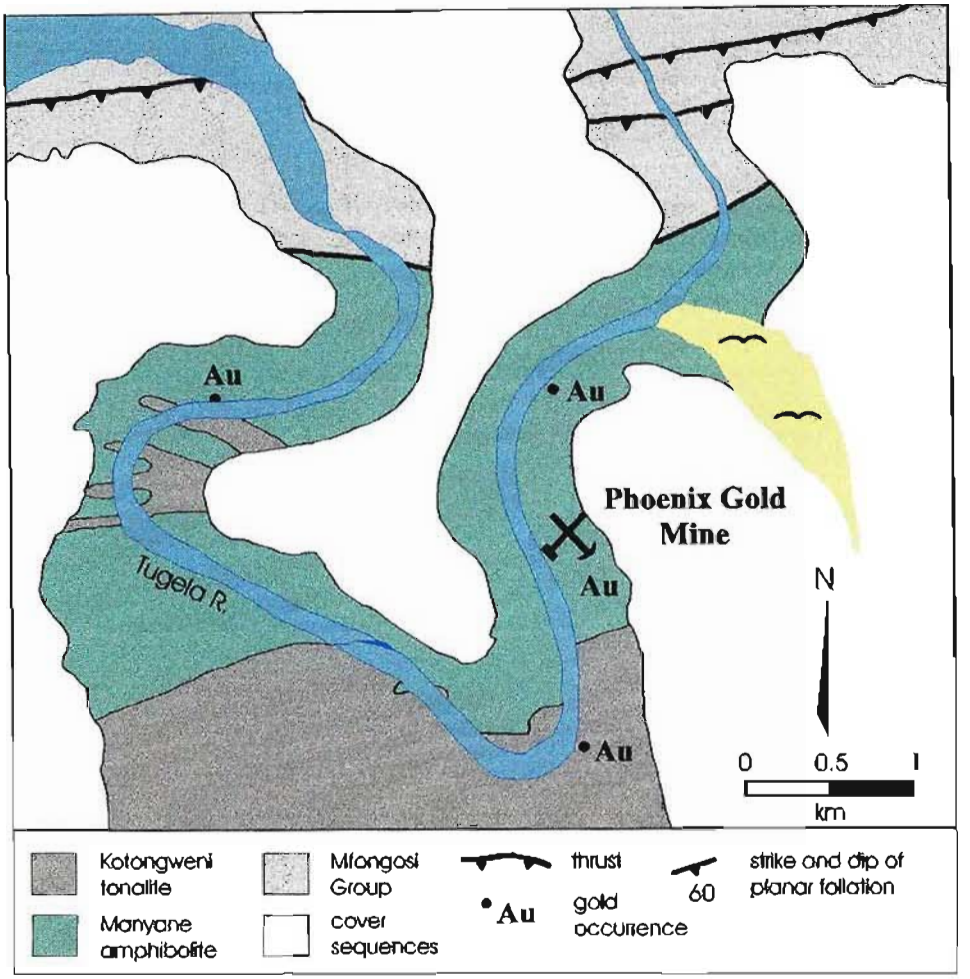

Figure 6.1 Situation of the Phoenix Mine on the eastern lobe of the Samungu Loop of the Tugela River course

6.2) Host Rocks to Veining

The "Manyane amphibolite" in the hangingwall and footwall to veining of the Phoenix Mine is different than Manyane amphibolite of the southern Mfongosi Valley area (Harmer, 1979; Matthews and Charlesworth, 1981). The hangingwall to the adits is a weakly metamorphosed meta-gabbro or meta-norite (Gray, 1906; Theart, 1986, 1987; Becker, 1986; this study) which displays notable palimpsest igneous textures. The footwall grades into a medium-grained meta-pyroxenite to retrogressed amphibolite. Veining resulted from leaching and silica metasomatism before late-tectonic lateral movement.

The hangingwall assemblage is as follows: ortho- and clinopyroxene (relic igneous) - plagioclase feldspar (relic igneous?) - actinolite - chlorite - opaques, and is interpreted as an amphibolitized meta-gabbro or meta-norite with a relic poikilitic texture. No preferred orientation of amphiboles (nematoblastic texture) or quartz stringer alignment is present; this host rock is homogenous, granoblastic and usually medium- to coarse-grained. Plagioclase and pyroxene crystals are observed in the field, with the pyroxenes being volumetrically dominant (Figure 6.2 a, b). In thin section, actinolite and rare hornblende occurs as decussate grain clusters (Harmer, 1979; this study) and as poikiloblasts with embayed and scalloped margins. The actinolite commonly replaces the pyroxene or the limited amount of early hornblende, leaving discrete blebs of quartz at the replacement boundary (Figure 6.2 c). The pyroxenes and the amphiboles are peripherally retrogressed to chlorite; plagioclase feldspar (An_{38} to An_{56} - Harmer, 1979) is pervasively altered to epidote and felted masses of sericite indicating post-cooling retrogression of mafic and felsic minerals accompanied by weak deformation. The retrogressed footwall amphibolite is dominated by hornblende. A variant of the hangingwall material occurring to the south of the main shear zone (Figure 6.8) consists of decussate, fine-grained clinopyroxene, relic actinolite, garnet, epidote and chlorite with elongate minerals and deformed epidote defining the weak planar foliation. This fine-grained amphibolite is infolded with coarser-grained amphibolite about a fold axis plunging at 58° towards 120°. Formerly transgressive quartz-epidote-opaque veins (defining an agmatic macro-texture) have been flattened into the weak planar foliation. Ductile, chlorite-filled shear zones are deformed around the fold hinge zone indicating folding by discontinuous flexural shear (Ramsay and Huber, 1987).

a) Dynamic Metamorphism on the Crystal Scale

Evidence of dynamic metamorphism is rare; twin planes in the pyroxenes are slightly deformed; polycrystalline and mosaic-textured quartz is annealed and slightly strained, and chlorite laths are tangential to the margins of relic plagioclase crystals and do not constitute augen structures. Sieve-textured quartz is common along the median line of actinolite crystals. Brittle deformation planes containing cataclastic material transect igneous and metamorphic minerals.

Figure 6.2 a General host rock in the field: meta-gabbro to meta-norite. In areas outside of the main zone of alteration, a faint green hue is visible, indicating weak montmorillonitic ("green argillic") alteration

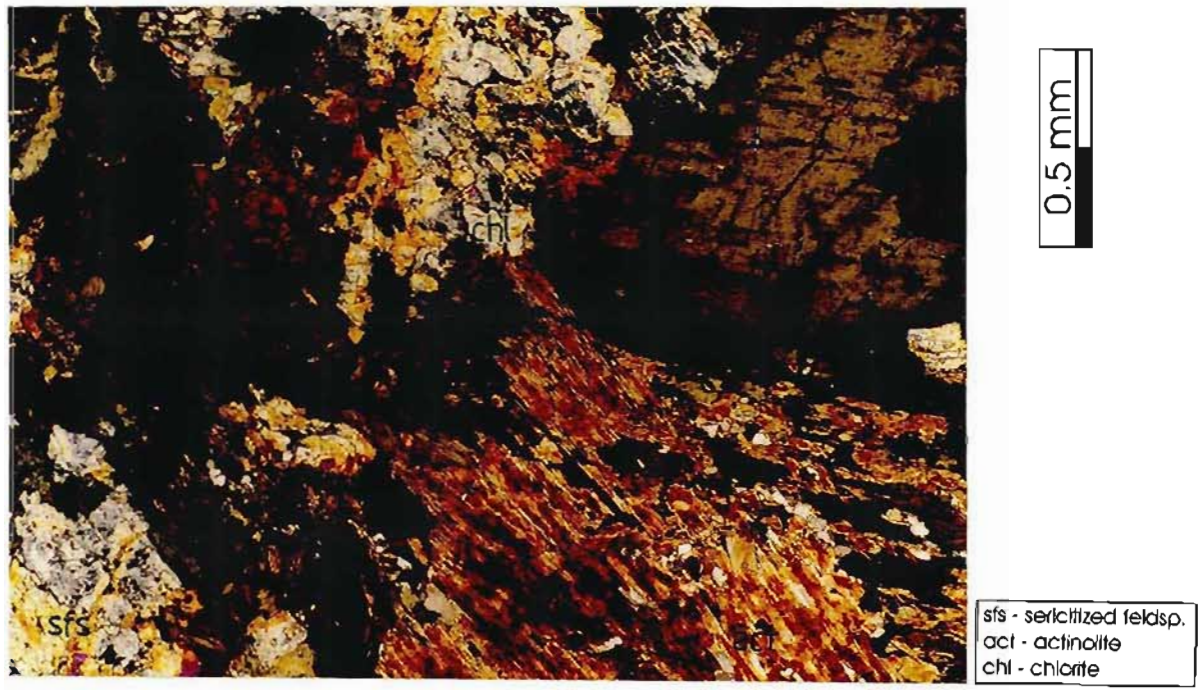

Figure 6.2 b General host rock - meta-gabbro or meta-norite in thin section showing pyroxene, sericitized feldspar and actinolite and chlorite replacing ferromagnesian minerals (***Slide PH-10***). XP.

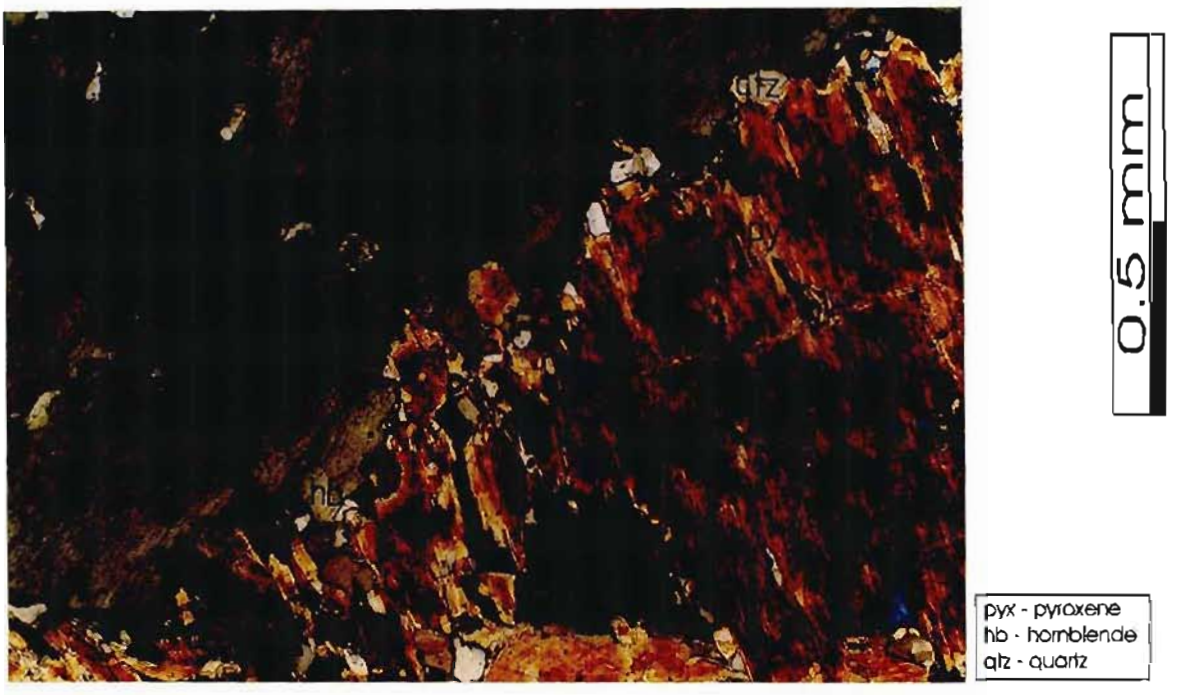

Figure 6.2 c Quartz blebs at the replacement boundary between pyroxene and hornblende (***Slide PH-10'***). XP.

b) Opaque Phases

Slides PH-1a and PH-1b contain linear arrangements of opaques that follow three preferred orientations within a glomeroporphyroblast of hornblende and actinolite (Figure 6.3 a). The angle between adjacent lines of opaques is 60° to 90° depending upon the section. Linear arrays of opaques transgress individual grain boundaries, twin planes and contacts between masses of hornblende, actinolite and chlorite which are in turn interstitial to large, altered plagioclase crystals. Harmer (1979) states that post-peak metamorphic conditions caused hornblende to replace clinopyroxene in the Manyane amphibolite which may be the case here where undeformed to brittly-deformed augite/diopside with exsolution lamellae is replaced by a mass of amphibole and chlorite. This is consistent with the common 120° triple-point junction angles between amphiboles and relic clinopyroxene crystals. Elongate crystals with a strong lattice anisotropy, such as hornblende and actinolite, do not readily form 120° triple-point junctions even in an equilibrium metamorphic texture - triple point junctions with angles of about 120° are more common in pyroxenes in an igneous texture (Spry, 1969; Mason, 1990). Grain contacts and exsolution lamellae are parallel to the dominant lattice orientations or dominant cleavages. The majority of the opaques may have been exsolved from the pyroxenes prior to replacement, the triple-point junction angle having persisted. The opaques also concentrate in the interstices between the relic feldspar crystals and at plagioclase/pyroxene contacts (Figure 6.3 b) although

both embayed cubic opaques, and anhedral, interstitial opaques with halos of sphene occur in the hangingwall meta-gabbro/meta-norite. Retrogression of the clinopyroxenes to actinolite and/or hornblende, retrogression of actinolite, hornblende and clinopyroxene to chlorite, and alteration of plagioclase feldspar to epidote and sericite, is pervasive adjacent to veins and minor fractures.

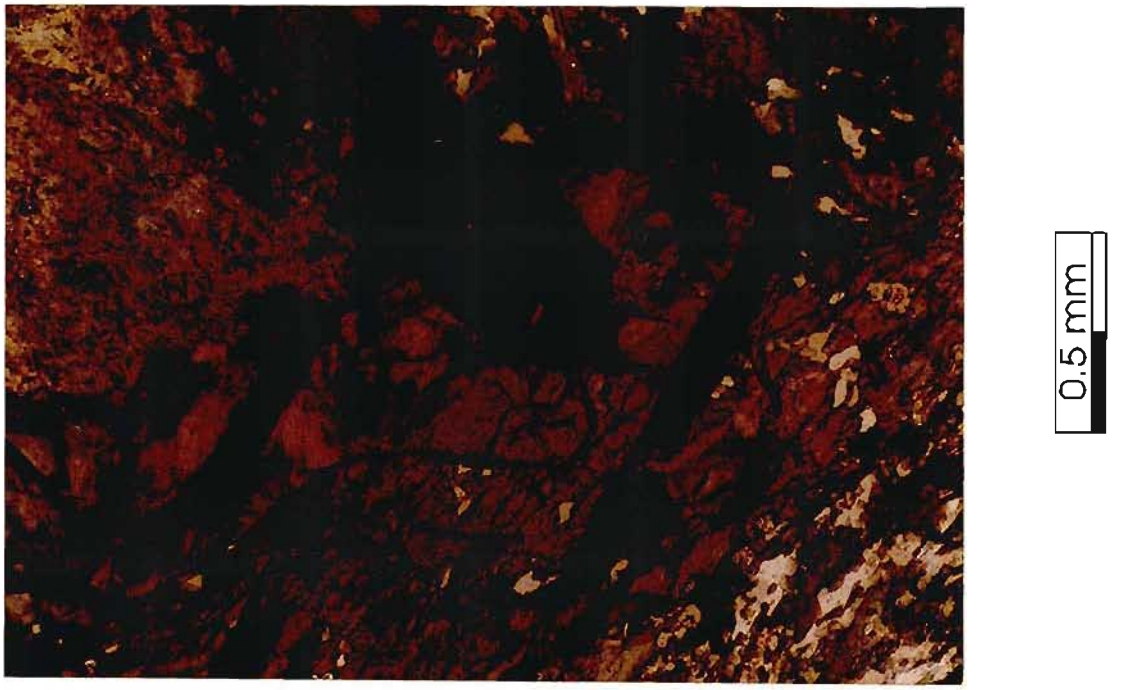

Figure 6.3 a Linear, trellis-type arrangement of opaque phases in highly altered/ retrogressed meta-gabbro/meta-norite (***Slide PH-1B***). PPL

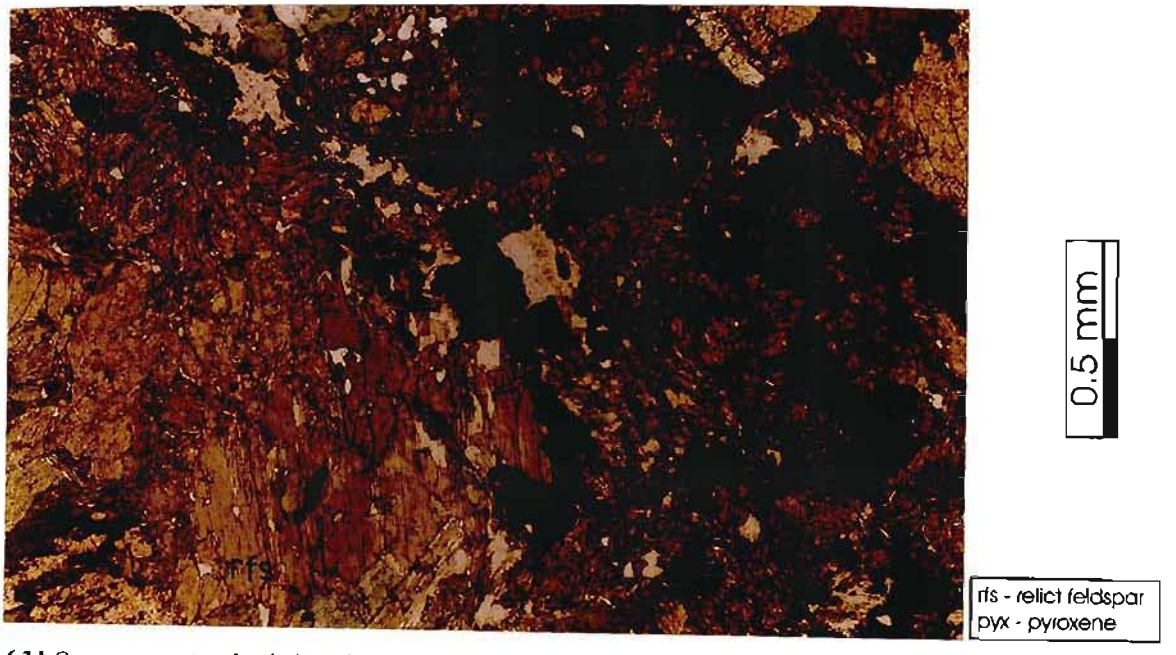

Figure 6.3 b Opaques concentrated at the interstices between relic feldspar crystals and at plagioclase/pyroxene contacts (***Slide PH-11***). PPL.

c) Silica Metasomatism

Although quartz is evident in the amphibolite of the southern Mfongosi Valley area, there are indications of silica metasomatism of the other rock types in the Phoenix Mine area. In fine- to medium-grained heteroblastic quartz-feldspar-talc-chlorite-garnet aplite/gneiss quartz is strained, sutured and porphyroclastic alkali feldspar grains have cataclastically-reduced margins defining a flaser structure (Figure 6.4). Aplites cross-cut all the lithologies of the "Dimane" Tectonic Unit (Lambert, 1962) and are leucocratic, white to pale pink with saccaroblastic (sugary) textures of quartz, feldspar and biotite (Harmer, 1979). The aplite veins are 0.5 to 2 metres wide. The effects and presence of Si-metasomatism may be gauged from the following features:

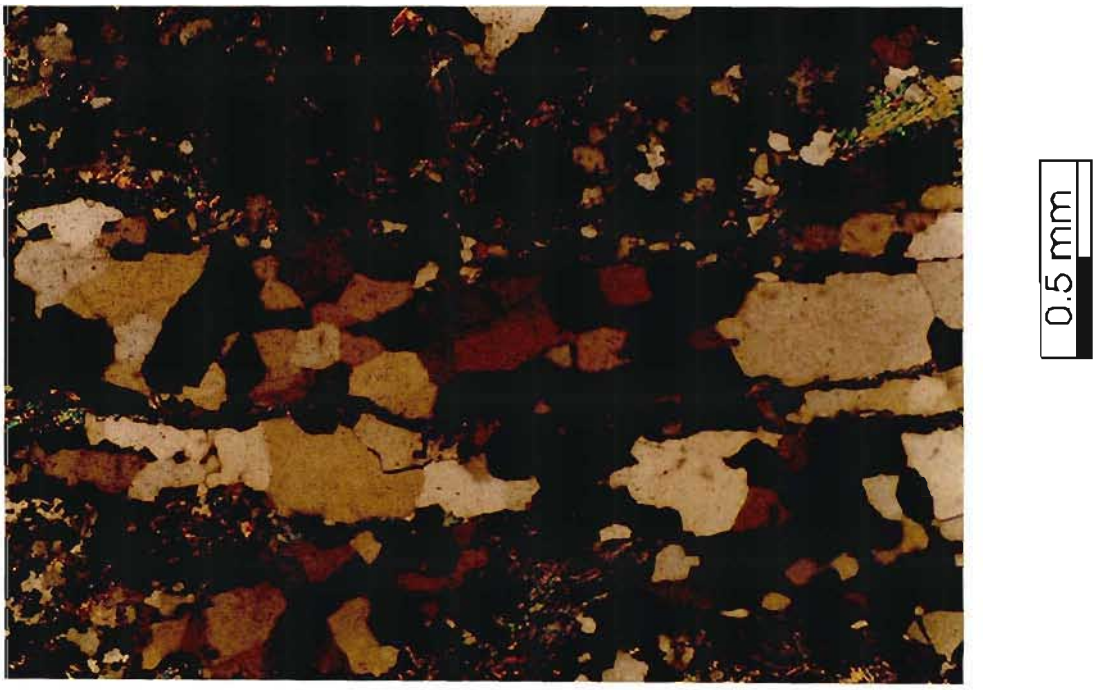

Figure 6.4 Non-annealed saccharoblastic or sugary texture of the aplite/schist which is commonly interfolded with the meta-gabbro/meta-norite adjacent to the Phoenix Mine (*Slide PH-3a*). XP.

- the presence of talc; metasomatism with a high Si activity promotes the formation of talc. The Mg necessary for talc formation may have been derived from the margins of amphiboles, pyroxenes or garnets
- palimpsest alkali feldspar and plagioclase feldspar porphyroclast margins may be observed despite pervasive alteration (epidotization and sericitization). The feldspar grains have embayed and scalloped margins and exhibit island and atoll structures which are completely enclosed in quartz

- opaques and chlorite are closely associated with quartz-epidote concentrations. This implies that SiO_2-rich solutions were the transporting medium for metals which concentrated where the epidotization of feldspar and quartz metasomatism was most intense. A leaching/replacement effect is therefore implied. No calcite was observed in any of the sections.
- feldspars are replaced from the edges inward by dendritic and skeletal sphene and fine-grained quartz

These effects were observed in the quartz-feldspar-talc-chlorite-garnet gneiss up to 170 metres away from the veined zone of the Phoenix Mine in samples PH- 4, 6 and 8 (Appendix B5). Evidence of metasomatism and alteration may also be observed in footwall amphibolite. Retrogression of clinopyroxene (and possibly also orthopyroxene) to actinolite with copious blebs of quartz is common and results in a dominant, overprinted greenschist facies assemblage, rather than consistent retrogression to hornblende. In ***Slides PH-9Ca and 9Cb*** (Figure 6.5) pervasive alteration has resulted in a retrogressed palimpsest igneous texture wherein actinolite is poikiloblastic and sieve-textured and contains opaque phases.

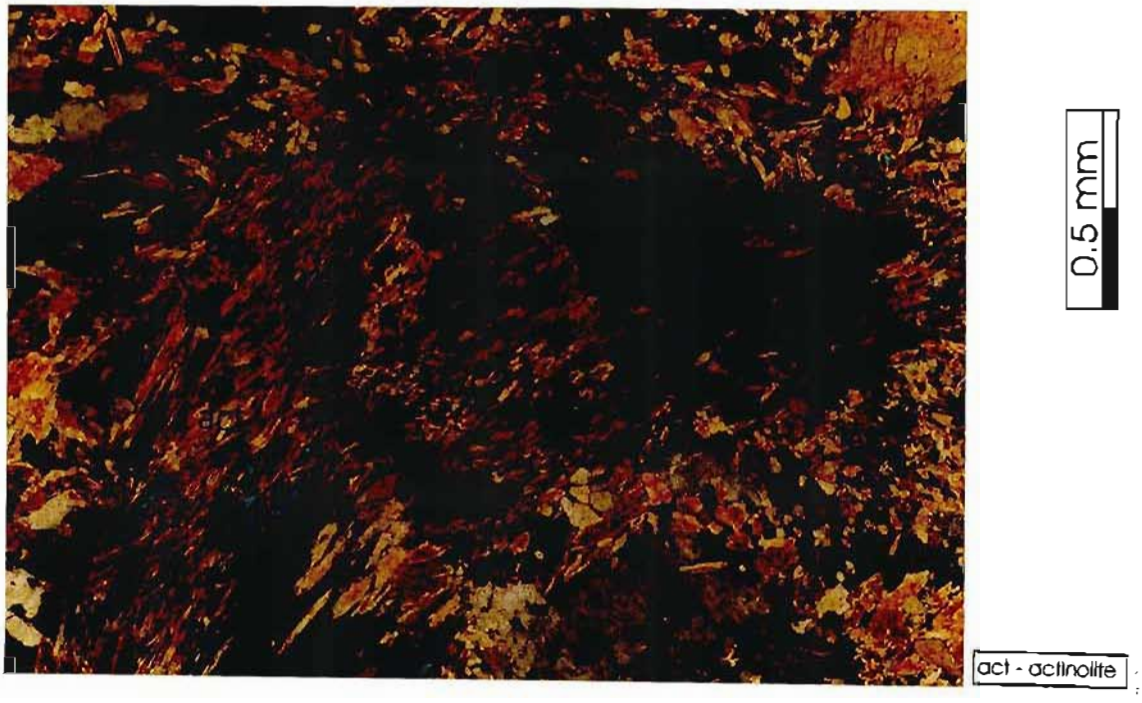

Figure 6.5 Actinolite with poikiloblastic opaques (***Slide PH-9c***). XP.

d) An Igneous Origin?

Convincing evidence of an igneous origin of the host rocks to the shear zone, besides the linear arrays of magnetite and Ti-magnetite, are reaction rims on megacrysts of twinned pyroxene (Figure 6.6). This corona texture is marked by a concentration of fine- to medium-grained, recrystallized opaques, which is in turn surrounded by a fibrous reaction rim of chlorite ± actinolite. Islands of the original, relatively unaltered pyroxene remain in the megacryst. Medium- to coarse-grained (igneous?) opaques are dominant in the chloritic matrix which displays a blocky, palimpsest igneous texture. Concentrations and linear arrangements of opaques and quartz grains are evident along megacryst contacts.

Figure 6.6 Reaction rims on relic pyroxene megacryst margins (*Slide PH-9c*)

Widespread relic igneous textures of the chloritized amphibolite include the following:

- ❖ possible intercumulus pyroxenes with mutually intergrown grain boundaries and 120° triple-point junctions. Remnant (sub-ophitic?) orth- and clinopyroxenes also occur
- ❖ relic corona textures of weakly-coloured pyroxene around a single pyroxene crystal
- ❖ triangular trellis arrangement of opaque phases with consistent orientations, indicating the former presence of a strong cleavage, and also the possible presence of clinopyroxene

- ❖ relic triple-point junctions and "blocky" textures of the majority of metamorphic minerals, similar to textures of equilibrium crystallization in an igneous rock
- ❖ rounded masses of chlorite and serpentine, possible replacing olivine
- ❖ corona texture of fine-grained and medium-grained recrystallized opaques, surrounded by fibrous reaction rims of chlorite and actinolite, around pyroxene megacrysts

6.3) Host Rocks - Regional Overview

The relic mineralogy of the hangingwall rock is at variance with that of the Manyane amphibolite, in which the Phoenix Mine is proposed to occur, as indicated on the regional geological map of Matthews and Charlesworth (1981). In the vicinity of the Phoenix Mine, there is an east-west trending contact between the Manyane amphibolite to the north and the Kotongweni tonalite to the south. No gabbroidal or noritic lenses have been depicted at the contact, or indeed nearby, on regional geological maps. Examination of Map 1 of Harmer (1979), however, shows that the Manyane amphibolite interfingers with the Kotongweni tonalite to the south of the mine; there is a meta-gabbro/meta-pyroxenite sliver at the amphibolite-tonalite contact; aplitic sheets, meta-gabbro, meta-pyroxenite and anorthosite lenticular bodies are common in the meander to the south of Jamesons Drift.

This study proposes that there is a lens of medium- to coarse-grained meta-gabbro/meta-norite, possibly with a pyroxenite layer on its northern margin, in contact with the Manyane amphibolite to the north. The veining at Phoenix Mine occurs near this contact which trends from 078° to 085° which is similar to the trend of the southern margin of the Kaapvaal Craton and that of the dominant foliation developed at the northern extremity of the Natal Nappe Zone and the Natal Thrust Front. Shearing along vein margins may explain the folding of aplitic sheets to the south of the mine. According to Lambert (1962) and Harmer (1979), the aplitic sheets were the last products of intrusion of the Tugela Rand Complex, 11 kilometres south-east of the Phoenix Mine.

The Tugela Rand Complex contains an initially-emplaced ultramafic suite, subsequently invaded by gabbroic components of the mafic suite which consists of hypersthene-gabbro,

pyroxenite and olivine-gabbro (Lambert, 1962; Matthews, 1959 and Harmer, 1979). Matthews and Charlesworth (1981) cite norite, bronzite, gabbro, troctolite and websterite as the main constituents of the mafic suite. The gabbro is melanocratic, medium-grained and displays intergranular (intercumulate - Lambert, 1962) textures of pyroxenes and cumulate textures of interlocking plagioclase feldspar (*op. cit.*). The mafic suite was subsequently intruded by a felsic suite (the Mkondene Diorite and the Dambe Granite - Harmer, 1979). The final sign of igneous activity was the intrusion of aplitic sheets similar to those observed to the south of the veining at the Phoenix Mine. In summary, vein intrusion, accompanying brittle host rock deformation, Si-metasomatism in surrounding lithologies and mild retrogression of igneous protoliths, post-dated the intrusion of the Tugela Rand Complex. This may be inferred as the aplitic sheets also underwent this Si-metasomatism. Mobilization of ore minerals accompanying the metasomatism is also evident on a variety of scales.

6.4) Structural Geology

a) Phoenix Mine area

Mining activity is confined to seven distinct sheared quartz veins, varying in width from 10 to 37 cm (Figure 6.7). The veins are boudinaged and discontinuous along their lengths although they appear to be more uniform in width down-dip (Figure 6.8). Between veins is a cataclastically-deformed meta-gabbro/meta-norite to amphibolite similar to that of the hangingwall. Rocks of this zone are, however, pervasively retrogressed to actinolite and chlorite and are not readily recognisable as igneous in origin. Partitioning of mafic and felsic constituents has occurred; the footwall pyroxenite and the hangingwall materials only have about 4% quartz. The quartz veins display a full range of Fe-enrichment features, from Fe-staining to gossaniferous surface crusts. Malachite, pyrite, magnetite and siderite are the most common minerals on quartz vein surfaces and in slickenlines on vein margins. Some metallic minerals are sheared and elongated along slickenlines implying a period of quartz vein formation, and hence possibly ore mineral remobilisation, before or during lateral movement.

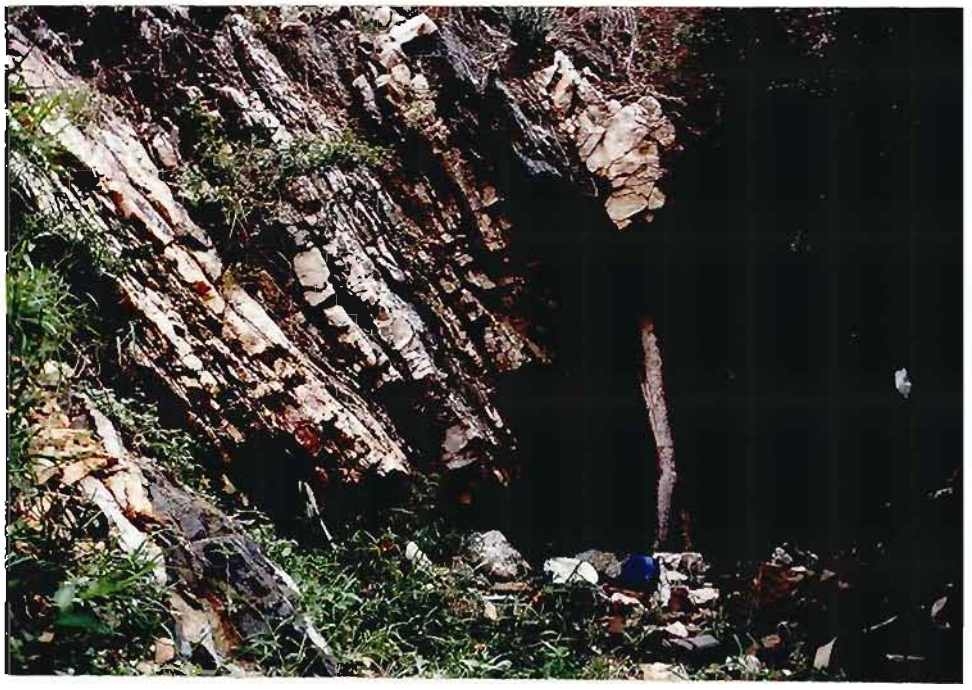

Figure 6.7 The veining at the Phoenix Mine. There is a highly retrogressed amphibolite separating the veins which dip at about 53° to the south-southwest

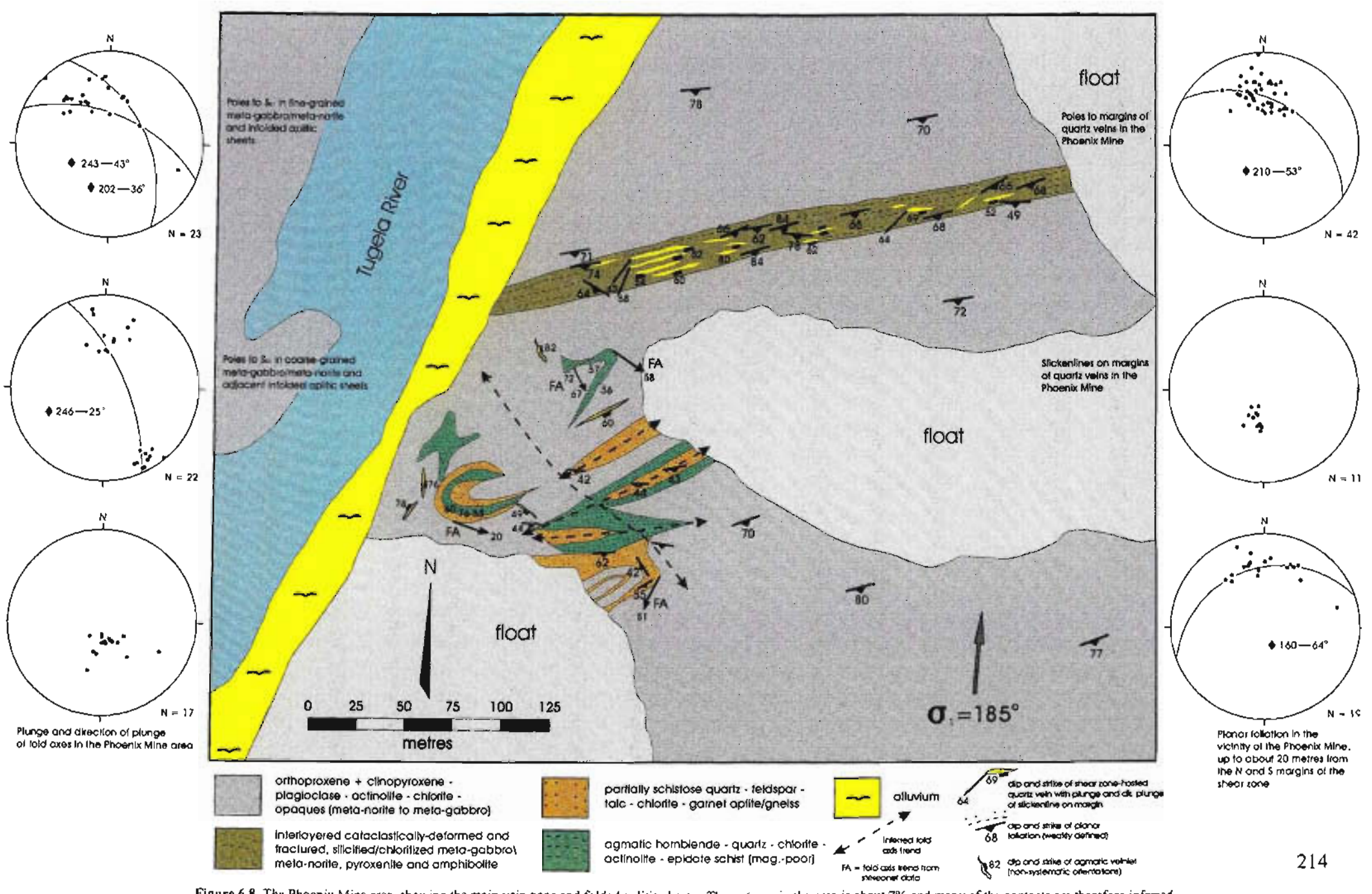

Figure 6.8 The Phoenix Mine area, showing the main vein zone and folded aplitic sheets. The outcrop in the area is about 7% and many of the contacts are therefore inferred

b) Veining and Slickenlines

The trends of individual quartz veins are variable but in surface outcrop their long axes strike between 078° and 085° (Figure 6.8, 6.9 a). Measurements on the margins of boudinaged quartz veins produce more variable results. Forty-two measurements on the margins of the quartz veins define boudin long axes at 210→53°, matching the orientation of the margins of boudinaged, silicified/albitized quartz-epidote-chlorite schist hosted within phyllitic quartzite layers of the Mfongosi Group, and the linear features in the Manyane amphibolite of the southern Mfongosi Valley area. The meta-gabbro/meta-norite in the majority of the area has undergone partial cataclastic deformation but little retrogression, except adjacent to quartz veining. The orientations of slickenlines on the margins of quartz veins are summarized in Figure 6.9 b and define an average of 196→54°, similar to the orientation of slickenlines in the units of the Mfongosi Group in the southern Mfongosi Valley area. The maximum principal stress axis orientation after vein formation may be calculated from an analysis of the slickensided vein margins and accompanying slickenlines, the results of which are shown in Figure 6.9 c.

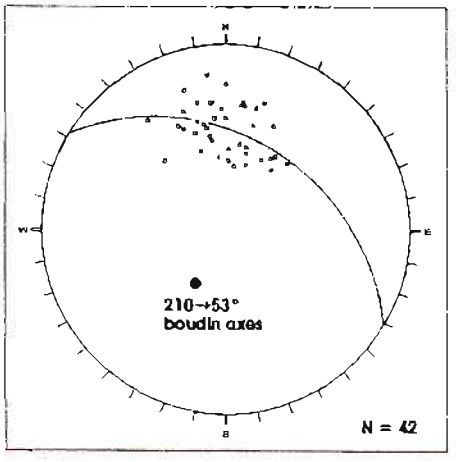

Figure 6.9 a Poles to margins of boudinaged quartz veins hosted in the anastomosing veining at Phoenix Mine. A great circle fit to data gives a boudin long axes at 210→53°. This azimuth is very similar to that of boudin axes in the Mfongosi schist and linear features in the Manyane amphibolite of the southern Mfongosi Valley area. This azimuth is furthermore sub-parallel to the slickenlines on the margins of the fracture-hosted veins in the Ayres Reef and Phoenix Mine N = 42

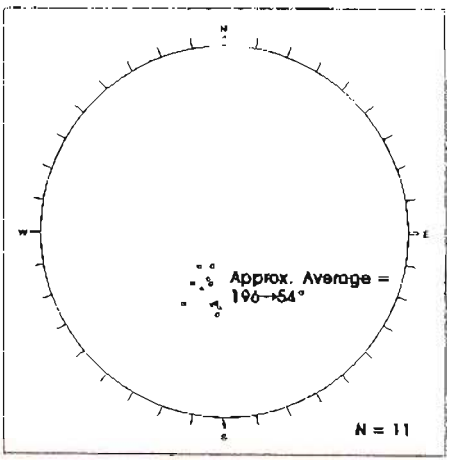

Figure 6.9 b Plunge and direction of plunge of slickenlines on the margins of quartz veins in the anastomosing veining at Phoenix Mine. An approximate average is 196→54° (sub-parallel to the boudin axis)
N = 11

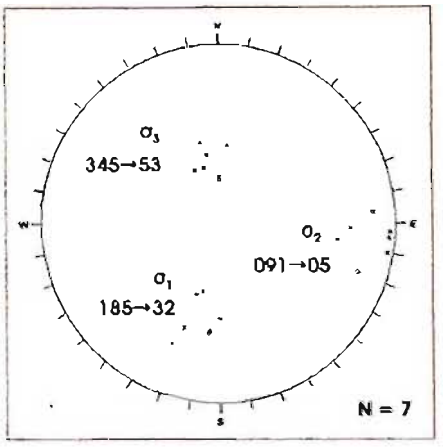

Figure 6. 9 c Orientations of the principal axes of the stress ellipsoid derived from analysis of slickenlines and slickensides on vein margins. Approximate averages for each axis are shown in the figure N = 7

c) Foliation

Although deformation of the contact between the hangingwall and footwall meta-gabbro/meta-norite took place by cataclasis, there is a strong foliation, defined by chlorite as the retrograde product of pyroxene and actinolite, directly adjacent to and between the lowermost quartz veins (Figure 6.8, 6.10). The orientations of these planar foliations are sub-parallel to the strike of quartz veins. A great circle fit to the data yields a fold axis at 160→64°. This fold axes orientation is similar to F_1 axes observed in the Ngubevu area, implying cohesion between the strain and/or causative stress orientation at Ngubevu, Phoenix Mine and Ayres Reef (Figure 6.10) and therefore a possible continued superimposed left-lateral movement. There is no accentuation of the weak host rock planar foliation as one moves from the host rock to the veining, suggesting that shearing at the margins of the veins was brittle.

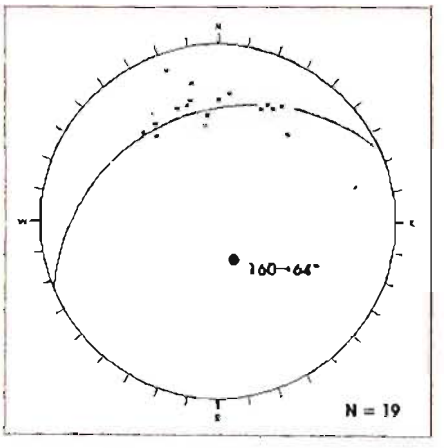

Figure 6.10 Planar foliation in the immediate vicinity (up to 15 metres on either side of the veining) of the Phoenix Mine. Readings are taken from the hangingwall and footwall meta-gabbro/meta-norite. The planar foliation is defined by chlorite as the retrograde product of pyroxene and actinolite. Only one great circle may confidently be fitted to the data, defining a fold axis at 160→64° N = 19

d) Folding

Folding in the vicinity of Phoenix Mine is observed in finer-grained meta-gabbro/meta-norite and in the aplitic sheets to the south of the veined zone (Figure 6.8). In the field, two stereonets were constructed; one of S_{01} in medium-grained meta-gabbro/meta-norite, combined with the adjacent weak foliation in the aplitic sheets (Figure 6.11 a); and the other of S_{01} in coarse-grained meta-gabbro/meta-norite and the adjacent aplitic sheets (Figure 6.11 b). The orientation of fold axes, from great circle approximations to the data, correspond to those observed in the Mfongosi schist in the Ngubevu area. Fold axes are 243→43° and 202→36° (Figure 6.11 a - *q.v.* F_2 in the Mfongosi schist, northern Mfongosi Valley area), and 246→25°(Figure 6.11 b).

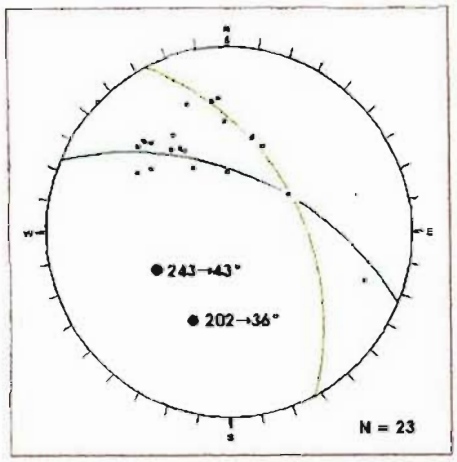

Figure 6.11 a Poles to S_{01} in medium-grained meta-gabbro/meta-norite, combined with an adjacent weak foliation in the infolded aplitic sheets N = 23

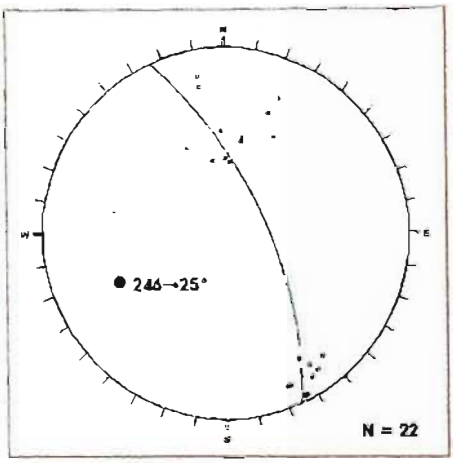

Figure 6.11 b Poles to S_{01} in coarse-grained meta-gabbro/meta-norite and infolded aplitic sheets. A probable fold axis, defined by a great circle fit to the data, falls on 246→25° N = 22

6.5) Discussion - Economic Potential

It appears that the quartz veins in the Phoenix Mine were sufficiently competent to have become boudinaged within the host meta-gabbro/meta-norite. Furthermore, it seems that vein emplacement was early enough in the tectonic evolution of the area to exhibit late-tectonic left-lateral movement, evidence of which is found in the south-southwest-plunging slickenlines on the quartz vein margins. A further indication of left-lateral movement developed in the immediate footwall and hangingwall to the veining, the south-southeast-plunging fold axes in the field area (Figure 6.10). Poles to great circle best-fits to S_{01} data are similar to the F_1 and F_2 fold axis orientations in the Mfongosi Group in the Ngubevu Area. The Phoenix Mine veining may be considered as being primarily shear- or fracture-zone hosted. Vein intrusion appears to be in a

similar mode to that of the Ayres Reef in the Manyane amphibolite in the southern Mfongosi Valley area. Veins have formed in a set of approximately east-west trending fractures in the gabbroic/noritic host rock in post-Tugela Rand Complex intrusion times, prior to left-lateral movement of the Tugela Nappe and Natal Thrust Front.

The rocks to the south of the vein set exhibits evidence of deformation similar to left-lateral shearing in the Ngubevu area. The rocks to the north of the mine is virtually undeformed. Boudinaging of the veins may have occurred at this stage. Following vein emplacement and Si-metasomatism of the rocks to the south of the vein set, left-lateral transpressive motion occurred as indicated by slickenlines on vein margins. Slickensiding also sheared pre-existing ore minerals such as pyrite and magnetite. Stable isotope studies (Chapter 7) indicate high-temperature (*c.* 400°C), extensive wallrock:fluid interaction. The gold grades at the Phoenix Mine for vein and whole rock values range from 10 to 52 ppb with no consistent relation between the material sampled and the gold grade. A single exception to this is the 1079 ppb value of sample PH-19 (Appendix B5), a sulphide-rich vein with an orientation of 084/52°. The weathered sulphides, forming a gossaniferous weathering feature, comprise up to 15% of the quartzofeldspathic vein. Samples PH-15 and 16 in the adit yielded insignificant gold values of 53 and 11 ppb, respectively. Although the relative timing of the veining at the Phoenix Mine has now been resolved, it seems that prediction of mineralization grade and siting is impossible with the existing data. However, such large-scale features, which do not necessitate a lithological contrast for formation, may be widespread, whether vein-infilled or not.

The enrichment and depletion of elements within the sheared zone/alteration zone may be assessed using Hildreth plots (Appendix G2). Schistose samples, PH11, 13 and 14 normalized to sample PH20 (relatively unaltered metagabbro/metanorite) indicate that with the exception of vein chemistry, the main zone of alteration is enriched in Fe, Mg, K, Na, Pb, Zn, Ni and As (±Au). Depletions of Si, Al, Ca and Cu, possibly due to the compounding effect of weathering and later leaching of silica. The wallrock to the alteration zone (Sample PH1) shows an enrichment in Fe, Mg, K, Pb, Cu, Zn and As but a depletion in Si, Al, Ca, Na and Ni. Similarly, a sample 25 metres away from the alteration zone (*sensu stricto*) shows similar enrichments and depletions. The schistose quartz-feldspar-talc-chlorite-garnet aplite/gneiss shows the converse of the

enrichment/depletion trend in the meta-gabbro/meta-norite. Sample PH6 (within 20 metres of the alteration zone), normalized to sample PH8 (130 metres south of the alteration zone), exhibits marked depletions in Al, Fe, Mn, Ca, Pb, Cu, Zn, Ni and As, and an enrichment in Si, K and Na. This simple observation implies that the source of metallic elements in the veining/alteration zone, is linked, spatially and temporally, to the intrusion of the aplite/gneiss protolith. Phyllitic alteration, with the formation of chlorite, pyrite, magnetite, haematite and siderite is indicated. It is important to note that montmorillonitic ("green argillic") alteration is often visible in the host metagabbro/meta-norite at >50 metres from the alteration zone. A Cordilleran vein-type deposit is strongly indicated. (The reader is referred to page 466 of Guilbert and Park, 1986, for the striking similarity between Phoenix Mine and Ayres reef veining and several economical Cordilleran-type veins).

6.6) Conclusion

The host rocks to veining comprise meta-gabbro and meta-norites which have been variably altered due to a narrow zone of contact metamorphism adjacent to the vein zone, and in the slivers between individual veins. Subsequent movement of the Tugela Nappe served to impart a foliation in the chloritized and silicified slivers between the veins and in the immediate host rock to the set. Vein formation thus post-dated the intrusion of the last stage of the Tugela Rand Complex (the intrusion of aplitic sheets) but pre-dated any indication of left-lateral movement such as that manifest at competent/incompetent rock boundaries like the Phoenix Mine. The expression of this movement was slickensiding of the vein margins after boudinaging. The Phoenix Mine veining, alteration, dip and tectonic timing strongly indicate that it, and the Ayres Reef, fall in the Cordilleran Vein-type category. As the extent of the veining has not been fully investigated, the potential for extensive veining is large.

Chapter 7

Oxygen Stable Isotope Study

7.1) Introduction

In order to qualitatively determine the origin of veining and the possible influence of any igneous-generated fluids an isotopic study of veins and host rocks was undertaken. There are a number of applications of oxygen isotope studies in geology, the full potentials of which are explained in Appendix D1. Sample preparation was done at the University of Natal (Durban) while oxygen extraction and isotopic measurement was performed at the University of Cape Town (South Africa) by the Chlorine Triflouride (ClF_3) method (Vennemann and Smith, 1990; Appendix D2). The final $\delta^{18}O$ value was calculated according to set formulas in which values are compared or normalized to a sequence of widely-used standards (Appendix D3).

A total of 105 whole rock and vein samples were analysed for $\delta^{18}O$. The distribution of whole rock and vein samples is even (Table 7.1 and Appendix D4). No statistical conclusions may be made in any one area, given that the analyses encompass five field areas in different tectonic units and/or settings, However, comparisons may be made between Natal Thrust Front values and Natal Nappe Zone values. Matching of whole rock and vein pairs was made on the strength of field relationships of the entire area; directly adjacent veins and fresh wallrock were not available for $\delta^{18}O$(vein) vs $\delta^{18}O$ (whole rock) plots and the isotopic values of identical rock types have been substituted.

The five field areas will be grouped and described under: the influence of mineralogy on $\delta^{18}O$ values, general observations of ranges of data, wall rock:vein fractionation, $\delta^{18}O$(vein) vs $\delta^{18}O$ (whole rock) plots and transport mechanisms - advection and diffusion, culminating in a general model for fluid movement in each area.

Table 7.1 Distribution of 105 oxygen isotope samples between the five field areas under consideration. It is pertinent to divide the samples into those from Natal Thrust Front areas (N and S Mfongosi Valley and Ngubevu) and Natal Nappe Zone areas (Mbongolwane Flats and Phoenix Mine).

Field Area	Whole Rock Analyses	Vein Analyses
Northern Mfongosi Valley	7	12
Southern Mfongosi Valley	8	16
Ngubevu West and East	8	23
Mbongolwane Flats	8	11
Phoenix Mine	8	4
Totals	**39**	**66**

7.2) General Considerations of Processes in Oxygen Isotope Alteration and Equilibration

Each of the five field areas has undergone a unique sequence of metamorphic, alteration and fluid-generating events producing distinctive vein and rock $\delta^{18}O$ distributions which may be used with structural and metamorphic information to define a general model for fluid movement. Expanding on Appendix D1, combined vein and whole rock $\delta^{18}O$ data may be interpreted in various ways:

a) The range in $\delta^{18}O$ values of whole rocks and veins may be assessed as separate data sets; that is, $\delta^{18}O$ values may be compared with relevant ranges in $\delta^{18}O$ derived from the literature. This exercise serves only as an approximation and only gross qualitative estimates of the extent of alteration may be obtained but it is useful in determining any influence of igneous-derived fluids given the protolith geochemistry and mineralogy. It is beneficial to observe a correspondence with $\delta^{18}O$ values obtained in lithologies from similar tectonostratigraphic environments (eg Wickham and Taylor, 1985).

b) Whole rock and vein data in one area may be compared to that of another area within the Natal Metamorphic Province. There is a distinct difference in ranges of vein and whole rock data between components of the Natal Nappe Zone and those of the Natal Thrust Front such that ranges of each occupy distinct zones on the entire $\delta^{18}O$ spectrum.

c) In the Ngubevu area two generations of quartz-bearing veins are recognized. The temporal evolution of the fluid phase, variations in fluid:rock interaction and the degree of fractionation between the host rock and vein may be qualitatively evaluated. A similar study cannot be employed in other areas where different vein generations are not recognised.

d) Perhaps the most useful application is vein $\delta^{18}O$ vs whole rock $\delta^{18}O$ plots which give an indication of the contribution of an igneous-derived fluid in the process of vein formation according to the degree of fractionation between host rock and vein. Data histograms give a similar relationship and show the degree of overlap between whole rock $\delta^{18}O$ and vein $\delta^{18}O$ values. Histograms also give a crude estimate of the concentration of values, that is, the $\delta^{18}O$ values which the fluids approached over time (e.g. the convergence of isotope oxygen values in late-tectonic quartz-calcite veins in the Ngubevu area).

In the following sections, the various methods of data interpretation will be described for the Ngubevu area first as this locality has been structurally well-constrained in addition to it having the largest data set (31 analyses). The methodology used in the Ngubevu study is then applied to the remaining field areas. The sampling localities of veins and host rocks are shown in Appendix B4.

7.3) Results and Interpretation of Results

a) Ngubevu West and East Areas

The Mfongosi Group was deformed under a transpressional regime from which external fluids would have been excluded. Only internal, possibly pressure solution-derived fluids would have been available for vein deposition (negative dilation - Section 5.4)

The Influence of Mineralogy on $\delta^{18}O$ Values

Variations in isotopic ratios may be regarded partially as a result of the variation in rock type; from calcite-rich crenulated calcite-graphite-sericite-quartz-albite schist to calcite-poor epidote-actinolite schist; and partially as a result of the variation in mineral proportions within several specimens of the same rock type. These variations stem from the different tendencies of minerals to concentrate the heavier oxygen isotope (^{18}O) during equilibrium isotope exchange. For example, quartz concentrates ^{18}O preferentially relative to alkali feldspar and albite. The order of the ability to concentrate ^{18}O, and a succession of $\delta^{18}O$ values from lower to higher, is from Hoefs (1980).

low $\delta^{18}O$ high $\delta^{18}O$

magnetite < chlorite < pyroxenes < plagioclase < albite < K-feldspar < dolomite < quartz

A rock with a larger proportion of quartz or dolomite will tend to be richer in ^{18}O than a rock with a lower quartz content and higher concentrations of chlorite or magnetite (compare the phyllitic quartzite of the northern Mfongosi Valley area with the meta-gabbro/meta-norite of the Phoenix Mine area - Figure 7.4). When comparing $\delta^{18}O$ values of rocks in a sedimentary or volcanosedimentary layer the proportions of constituent minerals must be taken into account as must the possibility of micro-veining and post-depositional alteration (eg Kerrich *et al.*, 1984; Hoy, 1993). One of the objectives of this study is to determine the validity of rock-buffering and ^{18}O and ^{16}O contribution from a range of host lithologies. Refining of $\delta^{18}O$ values attributable to specific minerals is beyond the scope of this study. Decarbonation, as has occurred in late-tectonometamorphic times in this area, is capable of whole rock ^{18}O-depletion (Peters and Wickham, 1995).

General Observations of Ranges of Data

Whole rock $\delta^{18}O$ values vary from 9.34 $^{o}/_{oo}$ to 14.23 $^{o}/_{oo}$ while the first-formed vein generation (veins occupying the S-c and D-a shears and fractures) have a greater overall range in values than the whole rocks with the majority of the data clustering between 13 $^{o}/_{oo}$ and 16 $^{o}/_{oo}$ (Figure 7.1). Cross-cutting, late-tectonic quartz-calcite tension gashes (quartz fraction) yield restricted $\delta^{18}O$ values, between 13.28 $^{o}/_{oo}$ and 13.64 $^{o}/_{oo}$.

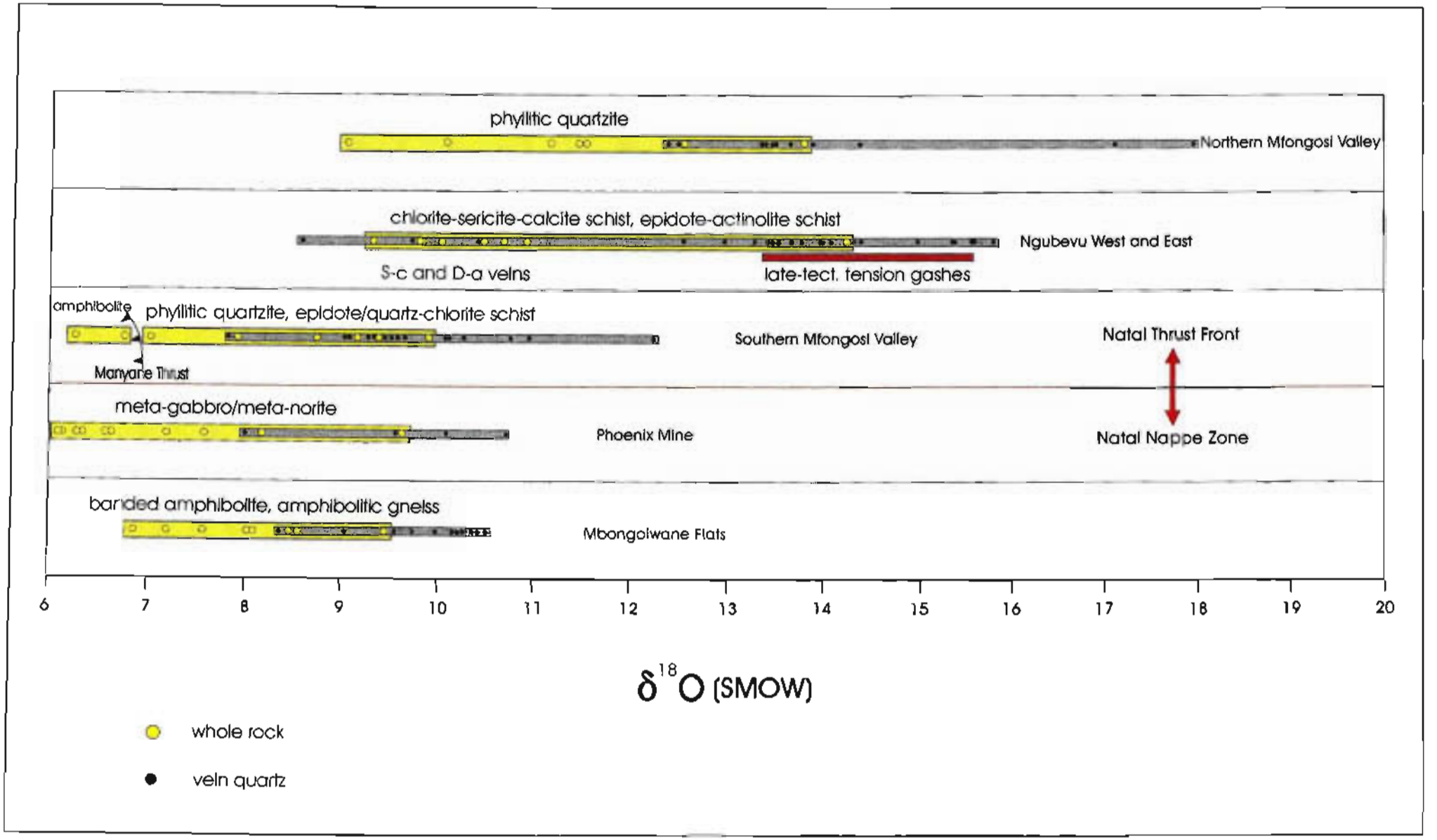

Figure 7.1 Linear plot of oxygen isotope data (whole rock and vein) in parts per thousand (ppt) relative to Standard Mean Ocean Water (SMOW) for the five field areas. Note that the $\delta^{18}O$ of the veins is usually displaced towards higher values than the accompanying host rocks due to the fact that only the quartz fraction is analysed for the veins. Note also the degree of overlap between the fields. It is also possible that the accompanying host rocks have been depleted in $\delta^{18}O$, relative to their unmetamorphosed protoliths. The pertinent comments for each area are explained in the text. The rectangles delineate ranges of data which may be directly compared between areas. Note that the similarity of the southern Mfongosi Valley area to areas in the Natal Nappe zone is due to its proximity to the Tugela Nappe and the Manyane Thrust. Refer to Appendix D4. (N = 105)

The range in $\delta^{18}O$ values of the host rocks encompasses a portion of the first vein generation range while the values of the second vein generation are entirely contained within the ranges of the whole rock and the first-formed veins (Figure 7.1). There is a convergence of vein $\delta^{18}O$ values over time. The range of the majority of $\delta^{18}O$ values of vein quartz is displaced to higher $\delta^{18}O$ values relative to the host rocks although some $\delta^{18}O$ values are lower than the accompanying host rocks (Figure 7.1 and 7.2).

The variation in $\delta^{18}O$ values amongst the veins stems from the composition of the quartz. In early-tectonic S-c and D-a veins, the products of pressure solution are evident; veins comprise recrystallized host rock and vein quartz is massive although polished section studies show variable amounts of "dusted" magnetite. The greater spread in S-c and D-a vein values is due to the magnetite fraction and the veins being constrained to a single layer. This reflects a dominant (proximal) host rock isotopic control. The late-tectonic antitaxial quartz is free of inclusions and better reflects the $\delta^{18}O$ value of the fluid during late-tectonometamorphic times.

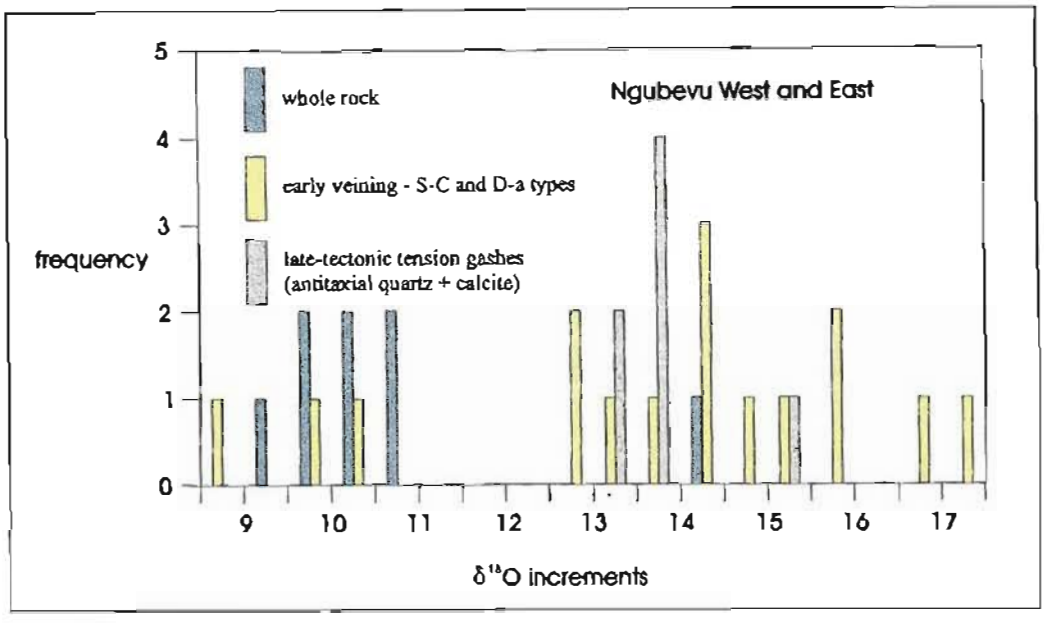

Figure 7.2 Histogram plot of $\delta^{18}O$ values (vein and wall rock) in the Ngubevu area. Of importance are the displacement of $\delta^{18}O$ (vein) towards the higher end of the scale relative to the host rocks, and the convergence of vein ratios towards approximately 13.6 $^{o}/_{oo}$.

Wall-Rock:Vein Fractionation

The tendency of the range of vein $\delta^{18}O$ values to be displaced towards the heavier end of the isotopic scale (dominance of ^{18}O), is a relic of the fractionation between vein quartz and host rock (Figure 7.1). Assuming, *a priori*, equilibrium, rock-buffered conditions, the $\delta^{18}O$ value of the host rock equals that of the vein quartz $\delta^{18}O$ value minus an intercept term which consists of the bulk $\Delta^{18}O$ value minus the $\Delta^{18}O_{(quartz\text{-}water)}$ between rock and fluid (Grey *et al.*, 1991). For isothermal exchange between rock and fluid by dissolution and later re-precipitation, the ^{18}O content of the vein quartz is normally expected to be high relative to the whole rock because $\Delta^{18}O_{(quartz\text{-}water)}$ is generally the largest fractionation factor. Although this effect may be assumed to have been dominant here one cannot yet rule out igneous-derived fluids which may have lowered the whole rock $\delta^{18}O$ value; the original $\delta^{18}O$ value of the unaltered protoliths of the Ngubevu rocks are not well known. It is possible that an unseen intrusion has lowered the $\delta^{18}O$ value of the rocks. However this effect may not be distinguishable from the complementary action of producing apparently higher vein $\delta^{18}O$ values. Certainly, subsurface fluids evolve towards more ^{18}O-rich compositions as the fluid reacts with rocks (Grey *et al.*, 1991; Sheppard, 1986). In many fluid movement systems, the altered rock $\delta^{18}O$ values evolve from low to high with time (Hoy, 1993), hence the markedly higher $\delta^{18}O$ (vein) values at Ngubevu compared to

other areas and hence a possible reason for the higher gold grades in the Ngubevu area. Hoy (1993), studying the Noranda District, found a positive correlation between the size of the ore deposit and the $\delta^{18}O$ value. The greater the $\delta^{18}O$ value, the greater the extent of the plumbing system, the longer the period of fluid flow and the equilibration of the fluid phase with the host rock, and the greater the size of the deposit. In the absence of any proof of contact metamorphism or syn-deformational intrusions the theories of equilibrium and rock-buffering may be tested via vein $\delta^{18}O$ vs whole rock $\delta^{18}O$ plots.

Vein $\delta^{18}O$ vs Whole Rock $\delta^{18}O$ Plots

Vein $\delta^{18}O$ vs whole rock $\delta^{18}O$ plots are useful tools in assessing the behaviour of co-existing veins and host rocks although the conditions of equilibrium and rock-buffering are always assumed initially. The transpressional environment derived for the Mfongosi Group during the period of vein formation implies a closed system (stress analysis - maximum principal stress directions related to planar foliations, S-C cleavages) wherein fluid was generated by pressure solution of deformed lithologies. A fluid phase existed which would have been rock-buffered throughout the evolution of the area. The enrichment of the veins in ^{18}O, relative to the host rocks has been discussed. The ranges in vein/host rock pairs for the five field areas are shown in Figure 7.3 and will be compared to typical arrays found in the literature.

Three main types of behaviour are displayed by vein/host rock pairs (Grey *et al.*, 1991; Figure 7.4). The trend the arrays in two-dimensional space have implications for the origin of the veining; each scenario is explained in Figure 7.4 and the three main cases described below:

- **Case 1)** in contact aureoles, where the $\delta^{18}O$ values of co-existing vein and host rock pairs cross the zero fractionation line (Figure 7.4 b and d)
- **Case 2)** the steep, near-vertical to vertical arrays where the isotopic composition of the vein is independent of the local host rock and where the $\delta^{18}O$ of the veins are greater than the $\delta^{18}O$ values of the host rocks (Figure 7.4 c - the most common array in this study)
- **Case 3)** where the $\delta^{18}O$ values of the veins are variable and independent of the host-rocks, in inclined arrays (Figure 7.4 d). A component of an array such as 1) in Figure 7.4 d is also found in some areas.

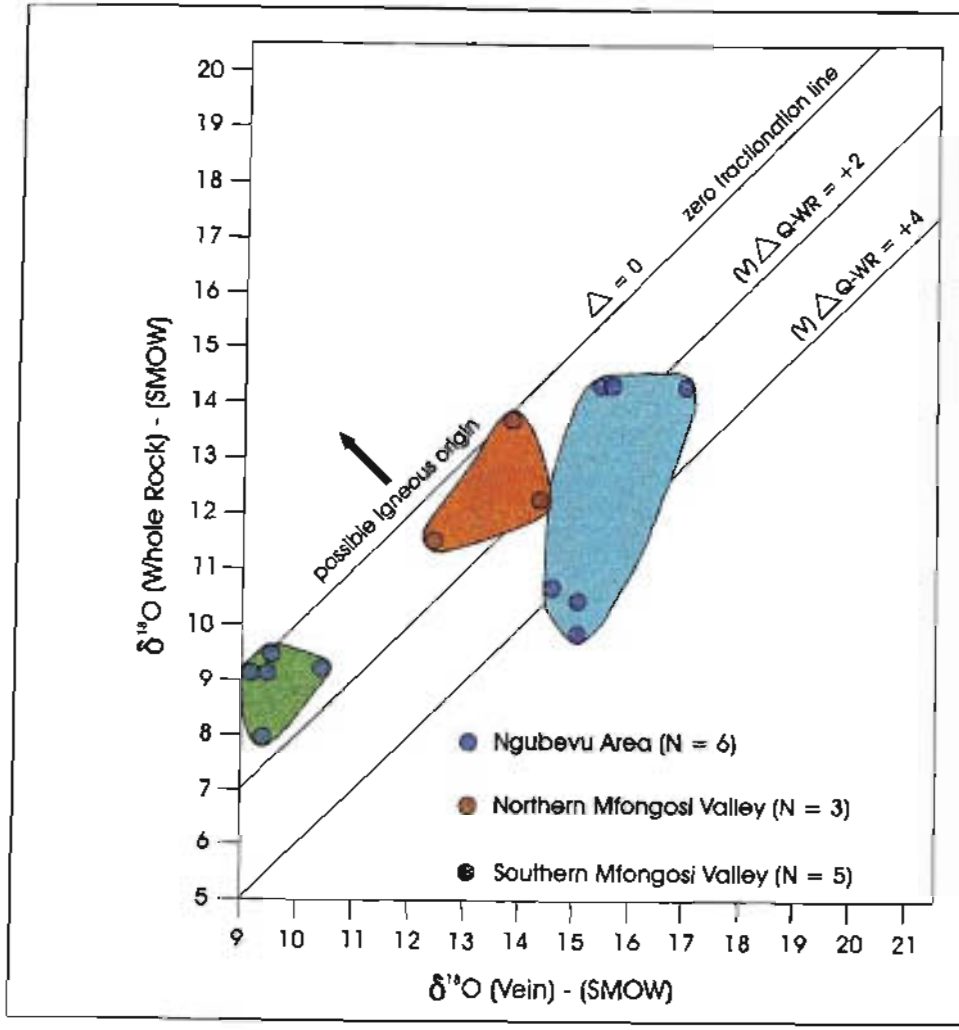

Figure 7.3 a $\delta^{18}O$ (Vein) vs $\delta^{18}O$ (Whole Rock) for related rocks and veins in the Natal Thrust Front. There is a spread in data for areas in the Natal Thrust Front such that each set forms a distinct field. Within the Mfongosi Valley area, there is a distinct difference in the position of vein/whole rock pairs. As for the Natal Nappe Zone, a vertical distribution of data is present, being most pronounced in the Ngubevu area. The variation of data parallel to the $\delta^{18}O$ (Vein) axis is also prevalent, especially in the Ngubevu area. Data do not span the zero fractionation line, indicating that there has been no influence of igneous-derived fluids during vein formation. (graph from Grey *et al.*, 1991)

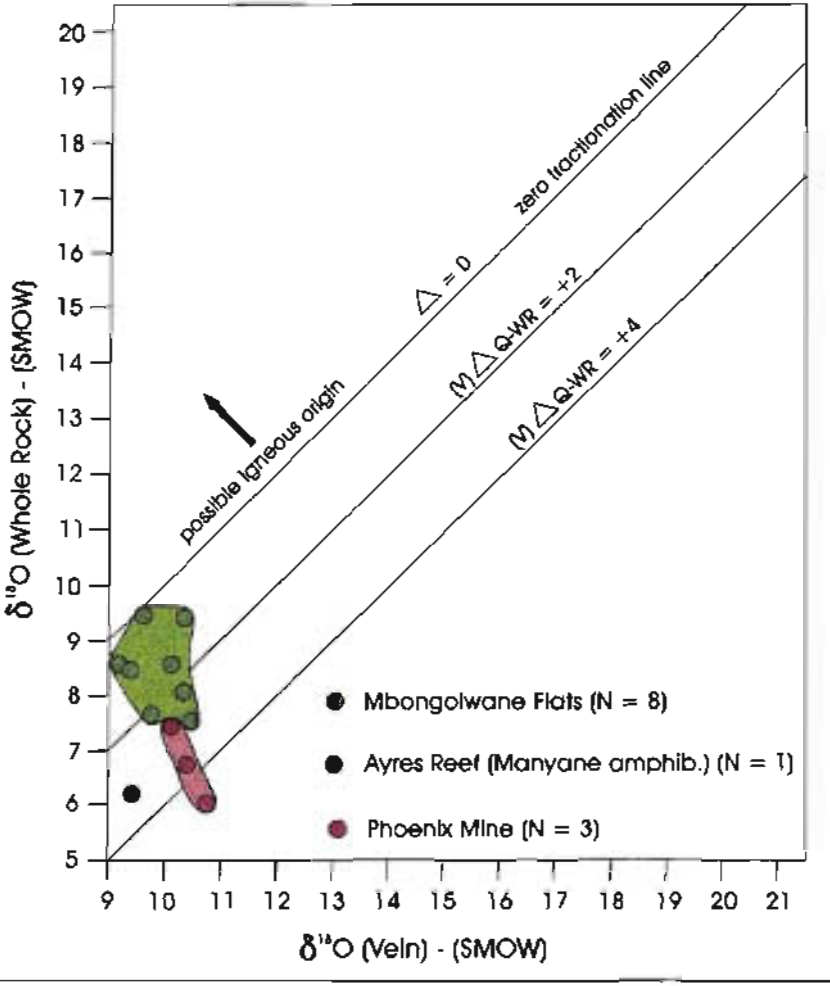

Figure 7.3 b $\delta^{18}O$ (Vein) vs $\delta^{18}O$ (Whole Rock) for related rocks and veins in the Natal Nappe Zone. In the case of the Mbongolwane and the Phoenix Mine areas, weak vertical arrays are observed, with variations in the $\delta^{18}O$ (Vein) also being present. Data from the Natal Nappe Zone cluster within a particular region and note also that none of the data fields straddle the zero fractionation line, which would indicate a lack of igneous-derived fluids in vein formation although see the comments on the Mbongolwane Flats area (graph from Grey *et al.*, 1991)

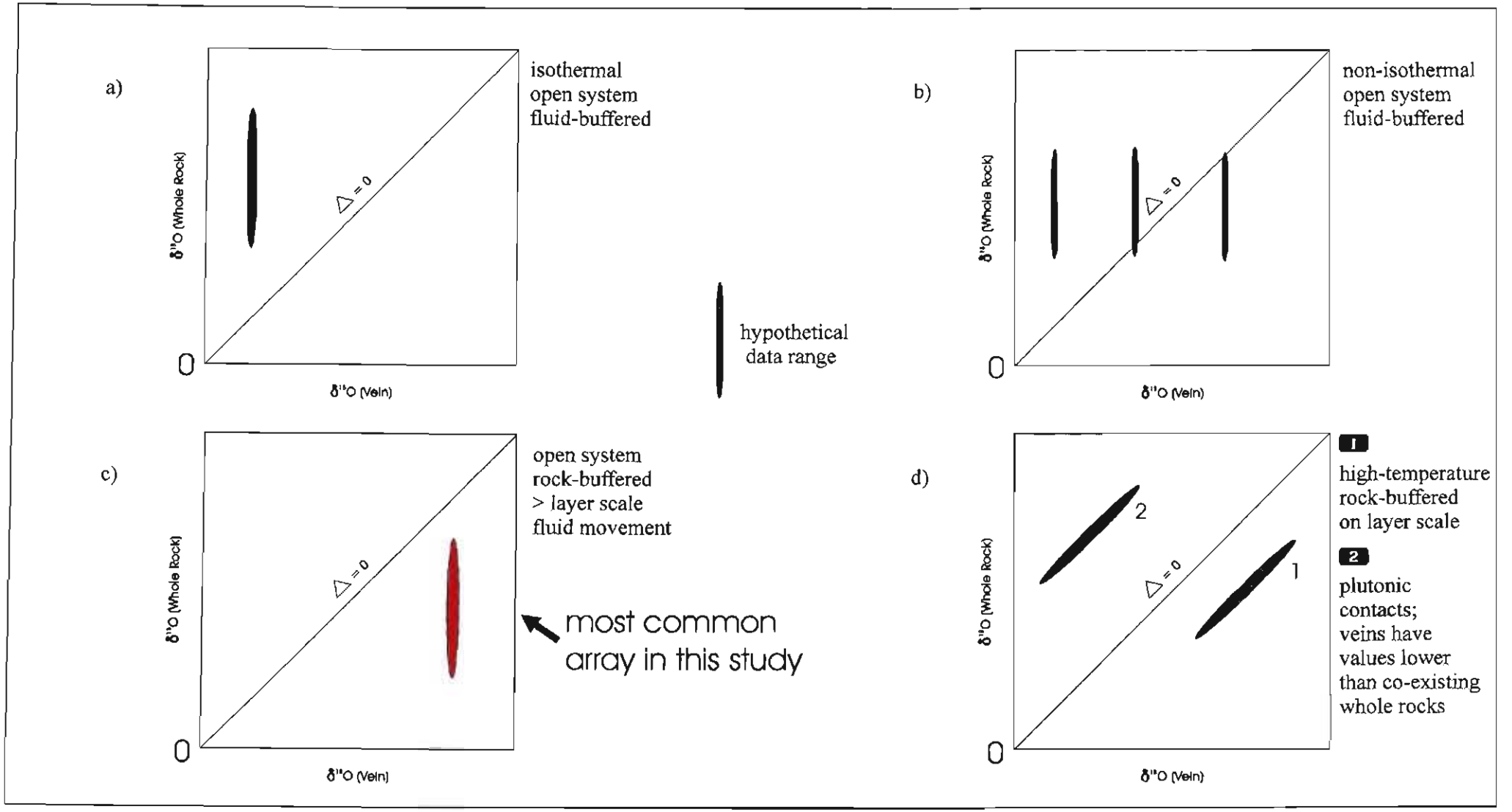

Figure 7.4 Possible vein deposition scenarios, using the example of a deformed interbedded sandstone-shale sequence - Vein $\delta^{18}O$ vs Whole Rock $\delta^{18}O$ plots (Grey *et al.*, 1991)

a) a fluid-buffered, open system, under isothermal conditions
b) a fluid-buffered, open system, with non-isothermal conditions, veins formed over a range in temperatures
c) a rock-buffered, open system with fluid movement greater than layer scale
d) 1 - a high-temperature, rock-buffered system where the fluid is buffered on the layer scale
2 - veins with lower values than co-existing whole rocks, fluid flows up-temperature towards plutonic contacts - vein-whole rock pairs define a group parallel to and above the zero fractionation line

The most common behaviour is the Case 2 where the veins are homogeneous and possess $\delta^{18}O$ values which are largely independent of the immediate host rock $\delta^{18}O$ values. This last point is important because 190°-trending cross-cutting tension gashes have sampled a number of lithologies during their formation. Although initiated in the more competent epidote-actinolite schist, these late veins transect crenulated, calcite-rich layers (banded lithologies) hosted within the epidote-actinolite schist, resulting in a contribution of $\delta^{18}O$ values from each different lithology. Henry *et al.* (1996), in a transect through the Western Alps, cite evidence of contribution of vein material from the dominant lithologies. In the example of the Alps, isotopic homogenization with the most abundant lithology of each zone in a rock-buffered system occurred such that the vein quartz isotopic ratios are homogeneous regardless of the rock type in which the vein is situated. The late stage tension gashes exhibit similar characteristics.

Where late tension gashes transect an earlier generation of veins (S-c and D-a types, as above) re-incorporation of previously deposited vein material into the fluid system would have occurred. Vein minerals resulting from pressure solution during deformation have been recycled due to a repetition of tension gash formation throughout the later stages of deformation. This partly accounts for the complexity and unpredictability of vein-hosted gold deposits in the area. Grey *et al.* (1991) state that recycling of fluid in such a system would yield rock-buffered, equilibrium vein isotopic values stemming from low fluid:rock ratios which average the host rock inputs at the scale of a stratigraphic layer hence the greater spread of $\delta^{18}O$ (vein) values of early S-c and D-a vein quartz values (Figure 7.1). The larger spread in early vein $\delta^{18}O$ values may be partly attributed to rock-buffering on the sub-layer scale. However, the isotopic ratios of the final generation of brittle antitaxially-filled (quartz-calcite) tension gashes fall within a very narrow range. This implies that the system was a greater than layer-scale one during late-tectonism/late-metamorphism (*cf.* the convergence of values which is mentioned in a previous section).

For Cases 1 and 3 (and the vertical array in Figure 7.4 a), the behaviour of coexisting veins and host rocks departs from the predictions of a rock-buffered system (Grey *et al.*, 1991; Figure 7.4). In Case 1 (contact aureoles) quartz veins with lower $\delta^{18}O$ values than the co-existing host rocks imply fluid flow up temperature towards plutonic contacts and vein-whole rock pairs may define a grouping aligned parallel to and above the zero fractionation line (Figure 7.4 d),

indicating non-equilibrium conditions. For Case 3 the large spread in vein $\delta^{18}O$ values is consistent with a fluid-buffered system and this vein heterogeneity is similar to that observed in short-lived fluid-movement systems (eg Larson and Taylor, 1987; Figure 7.4 b). In a rock-buffered regime, the $\delta^{18}O$ values of the quartz veins are insensitive to temperature change during vein formation. This is in contrast to a fluid-dominated system where the $\delta^{18}O$ values of the veins would reflect the temperature evolution of the system and perhaps also the change in the source of the fluid with time (Grey *et al.*, 1991).

Transport Mechanisms - Advection and Diffusion

A prevalent method of fluid movement, *advection* occurs where there is mass transfer of material into a fracture by hydrothermal/metamorphic solutions in an open system by physical motion of the fluid which is controlled by hydraulic gradients (Etheridge *et al.*, 1983; Yardley, 1989). Advection depends on rapid changes in silica solution chemistry and requires large fluid fluxes and changes in temperature and/or pressure at scales much greater than bed or layer scale. These fluid regimes are likely to exhibit open-system behaviour and high fluid:rock ratios.

Diffusional mass transfer of locally-derived material and fluid from the country rock into a fracture in an essentially closed system within a static or spatially confined fluid phase is influenced by the chemical potential gradient (eg Beach, 1974; Ramsay, 1980). Diffusion may operate with extremely small fluid:rock ratios as long as a suitable driving force (eg non-hydrostatic stress - emplacement of the Natal Nappe Zone, oblique collision/transpression etc) is maintained over long periods. This process is spatially restricted at scales generally less than 10 cm (Grey *et al.*, 1991). The isotopic signatures of the veins would then reflect rock buffering in a closed system at a scale limited by the length of the vein fractures. It is pertinent that the S-c and D-a fractures are characteristically limited to a single layer while late-tectonic tension gashes may be up to 20 m in length and transgress lithology boundaries. Diffusional mass transfer appears to have been dominant in the infilling of S-c and D-a fractures in the Ngubevu area (and probably similar fractures in the northern and southern Mfongosi Valley areas), particularly since vein-hosted re-constituted or recrystallized adjacent wall rock is considered by many authors to be the result of metamorphic-derived fluids depositing material in a closed, rock-buffered system (eg Grey *et al.*, 1991; Henry *et al.*, 1996). Certainly, in the Ngubevu and Mfongosi Valley areas, veins are primarily composed of the coarse-grained recrystallized material of the host rocks.

Homogenization across widely varying lithologies, as for late-tectonic tension gashes, is either attributable to abundant convection or single pass fluid flow (Wickham and Taylor, 1985). If a terrain preserves its pre-metamorphic isotope heterogeneity, the process of diffusive, fluid-poor metamorphism and exchange has operated; alternatively, fluid flow has been highly channelized (Ganor *et al.*, 1989; Cartwright and Valley, 1991). The effects of previous metamorphic events must be considered; these cause extensive fluid loss and depletion or expulsion of pore fluids thereby limiting further potential fluid sources (Wickham and Peters, 1992). Subsequent fluid regimes may consequently comply to the condition of low fluid:rock ratio.

Conclusion - Ngubevu West and East Areas

The evolution of the fluid system and vein deposition in the Ngubevu area may be summarized:

- infilling of S-c and D-a shears and fractures in a short-lived fluid-flow system, with emplacement of recrystallized wall rock material in a closed, non-advective fluid system. The S-c and D-a fractures and veins are more or less restricted to the extent of an individual layer hence the initial variability of $\delta^{18}O$ (vein) values corresponding to the initial variability in isotope ratios of the host rocks; a diffusional fluid flow is proposed. Evidence of a rock-buffered system is found in that the majority of $\delta^{18}O$ (vein quartz) values are greater (isotopically heavier) than the accompanying host rocks. The origin of the short-lived fluid system would have been emplacement of a large thickness of ophiolitic material (the Natal Nappe Zone - the Tugela Nappe and succeeding nappes), above the Natal Thrust Front, resulting in the disturbance or inversion of pre-existing geotherms and hence a change in temperature of the Mfongosi Group.

- a change in the characteristics of the fluid phase to a more open rock-buffered system with a convergence of $\delta^{18}O$ (vein quartz) values to approximately 13.6 $^{o}/_{oo}$ in the late-stage quartz-calcite tension gashes. Contributions of material from pressure solution of a variety of lithologies in the limbs of isoclinal folds became more dominant over time. The later stages of fluid movement were probably controlled by advection rather than diffusion in a pervasive fluid phase under low fluid:rock ratios. Again, the $\delta^{18}O$ (vein) values are greater than the $\delta^{18}O$ (whole rock) values implying a fractionation-type relation in the absence of igneous-derived fluids. Although the final isotopic signatures of veins in the

Natal Thrust Front differ from one area to the next, there may have been no significant difference in the thermal characteristics of the discharging fluids, although the period of fluid movement may have been longer in the Ngubevu area (*cf.* Hoy, 1993). A generalization may be made concerning the tectonic situation; in extension accompanied by thinning and the input of magmas, a high thermal gradient operates which promotes convective recirculation, whereas in compression and the creation of low geothermal gradients (eg England and Thompson, 1984) in the absence of syn-metamorphic intrusions (eg Patino Douce *et al.*, 1990) no convective circulation is likely. Rather, there is a strong possibility of single pass fluid flow and evolution of the fluid system towards being completely rock-buffered.

b) Northern and Southern Mfongosi Valley Areas

Two thermal regimes have acted in tandem or in opposition:

- a normal geothermal gradient in the tectonostratigraphically higher northern Mfongosi Valley area.
- an inverted geothermal gradient caused by the juxtaposition of a higher-temperature portion of the Natal Nappe Zone (Tugela Nappe) against a cooler foreland basin (the Natal Thrust Front). In this case, the "hot iron effect" is implicit in that fluids in the Mfongosi Group would have moved up-temperature towards the Manyane Thrust which was at amphibolite facies temperatures.

General Observations of Ranges of Data

The northern Mfongosi Valley area vein quartz $\delta^{18}O$ values range from 12.39 $^{o}/_{oo}$ to 17.94 $^{o}/_{oo}$, while that of the wall rock melange ranges from 9.07 $^{o}/_{oo}$ to 13.28 $^{o}/_{oo}$ (Figure 7.1). In comparison, the southern Mfongosi Valley area exhibits lower $\delta^{18}O$ (vein quartz) and $\delta^{18}O$ (whole rock) values than the northern Mfongosi Valley area; vein $\delta^{18}O$ values vary from 7.81 $^{o}/_{oo}$ to 12.21 $^{o}/_{oo}$ while whole rock $\delta^{18}O$ values are consistently lower overall, at 7.02 $^{o}/_{oo}$ to 9.90 $^{o}/_{oo}$ (Figure 7.1). As no succession of veining events may be determined in the Mfongosi Valley, no inferences about the temporal evolution of the composition of the fluid phase is possible.

The Influence of Mineralogy on $\delta^{18}O$ Values

The dominance of the homogeneous, calcite-rich, phyllitic quartzite/Fe-stained quartzite in the northern Mfongosi Valley is the cause of the generally high $\delta^{18}O$ (whole rock) values. Vein quartz derived from this melange shows concomitantly higher $\delta^{18}O$ values. In contrast, the southern Mfongosi Valley displays whole rock $\delta^{18}O$ values consistent with a phyllitic quartzite/epidote-actinolite-chlorite schist layering.

Wall Rock : Vein Fractionation

As for many of the other field areas, vein $\delta^{18}O$ values are consistently higher than those of co-existing whole rocks (Figures 7.1 and 7.5). On the strength of the known relationships between whole rock and vein, the transpressional environment of the Mfongosi schist and the emplacement of veins with bulk compositions almost identical to the immediate host rock, a scenario of vein formation which is similar to that in the early evolution of the Ngubevu area is proposed. The variability of the vein quartz $\delta^{18}O$ values may be a relic of a short-lived, layer-scale, rock-buffered, closed fluid movement system which was initiated by the emplacement of the Natal Nappe Zone. The evolution of the system to a more open rock-buffered one as at Ngubevu cannot be fully assessed in the absence of late-stage tension gashes whilst only one set of contemporaneously-formed S-c and D-a veins are recognized.

Vein $\delta^{18}O$ vs Whole Rock $\delta^{18}O$ Plots

The northern and southern Mfongosi Valley areas form distinct groupings on vein $\delta^{18}O$ vs whole rock $\delta^{18}O$ plots and both describe arrays which have variations in the vertical and the horizontal planes (whole rock and vein axes, respectively) (Figure 7.3 a). This indicates a combination of two processes. Firstly, the vertical extent of data indicates that the isotopic composition of the veins is partly independent of the local host rock composition and the dispersion parallel to the X-axis is consistent with high-temperature rock-buffering on a layer-scale. Fluid flow in relation to a contact aureole is not indicated as the (data does not cross the zero fractionation line.

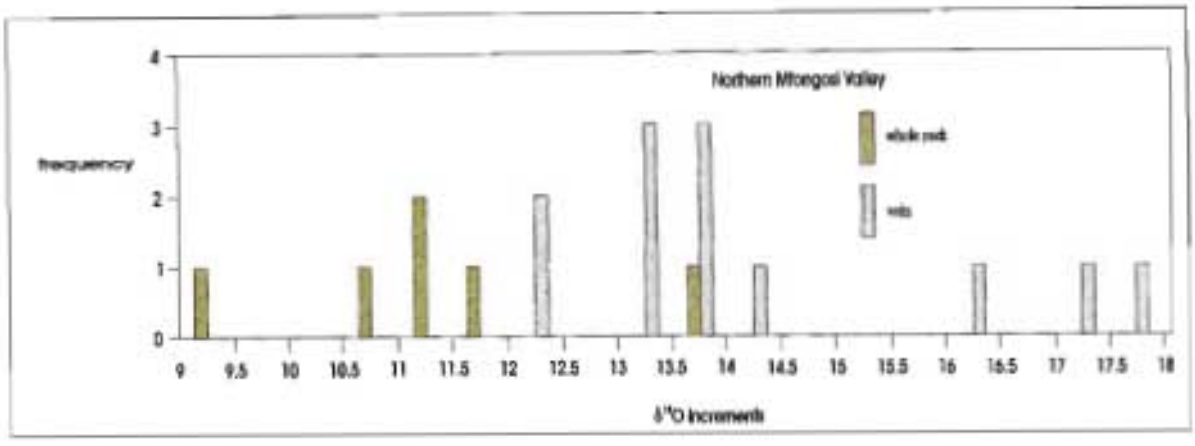

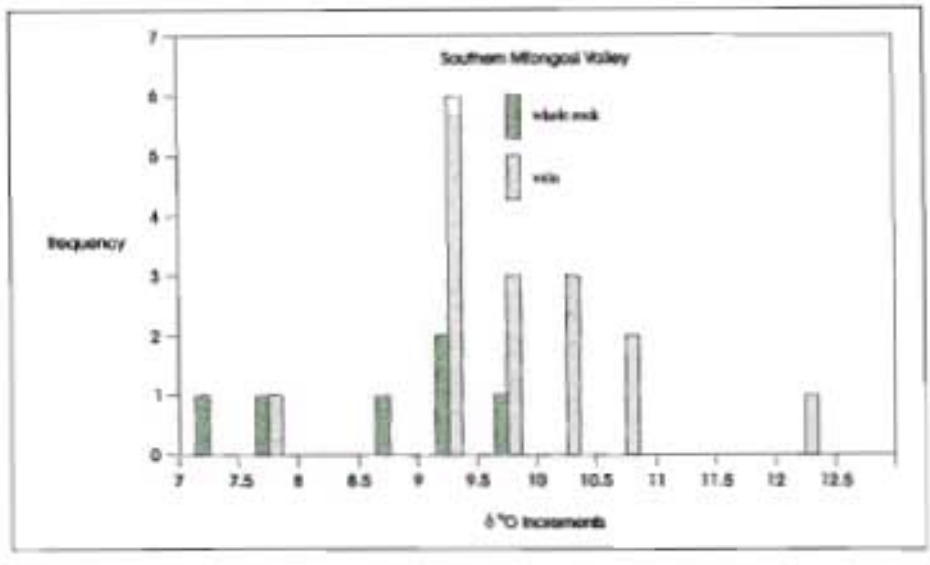

Figure 7.5 Histogram plot of $\delta^{18}O$ values (vein and wall rock) in the northern (a) and southern (b) Mfongosi Valley areas. Of importance are the displacement of $\delta^{18}O$ towards consistently higher values relative to the host rocks and the difference in vein ratios between the two areas within the Mfongosi Group.

Transport Mechanisms - Advection and Diffusion

The permeability of the Mfongosi schist would have been increased by the initiation of S-c and D-a fractures. The short-lived fluid movement system would be facilitated by these pervasive fractures. The fractures occur at all scales and a channelized flow (*sensu stricto*) may not have operated.

Conclusion - Northern and Southern Mfongosi Valley areas

Veins of the northern Mfongosi Valley area display $\delta^{18}O$ values which are suggestive of fractionation of ^{18}O with quartz-rich host rocks, with $\delta^{18}O$ values between 11.13 $^{o}/_{oo}$ and 13.78 $^{o}/_{oo}$, possibly under the influence of a short-lived, mainly rock-buffered, layer-scale fluid-movement system. The southern Mfongosi Valley yields lower overall $\delta^{18}O$ (vein) and $\delta^{18}O$ (whole rock) values due to the influence of a larger volume of epidote-, actinolite- and chlorite-bearing rocks during the deformation of the succession. However, the mechanisms of vein formation and deposition would have been identical to that of the S-c and D-a fracture infilling in the Ngubevu area. The thermal budget in each area was influenced by two factors: steepening of the geotherms (and heating at depth) due to the emplacement of the Tugela Nappe

c) Mbongolwane Flats Area

The Mbongolwane Flats area displays consistent whole rock and vein $\delta^{18}O$ values despite the widespread distribution of sampling points and the different rock types sampled. The whole rock data set, which includes amphibolitic gneiss, banded amphibolite and granite-gneiss, is only 0.7 $^{o}/_{oo}$ less restricted than that of the Phoenix Mine area wherein a fairly homogeneous, spatially limited set of rocks was analysed.

General Observations of Ranges of Data

Whole rock values vary from 6.85 $^{o}/_{oo}$ to 9.41 $^{o}/_{oo}$ while vein values vary from 8.39 $^{o}/_{oo}$ to 10.48 $^{o}/_{oo}$ (Figure 7.1). Compared to the other field areas, the Mbongolwane Flats displays the best distinction between ranges of veins and ranges of whole rock $\delta^{18}O$ values. Overall values are amongst the lowest in the entire data set and are very similar to those of the Phoenix Mine area. As for most of the other field areas, no deductions may be made about the evolution of the fluid system given that late-stage veining in this area is primarily of albitic composition and cannot be directly compared isotopically to quartz veining. What needs to be stressed is the extensive, greater than layer-scale fluid system which covered a 42 km^2 area containing such varied rocks.

The Influence of Mineralogy on $\delta^{18}O$ Values

The narrow range in $\delta^{18}O$ attests to the pervasiveness of the fluid phase and to widespread, probably advective fluid circulation. Under the influence of an igneous-derived fluid, absolute values of whole rock $\delta^{18}O$ will be displaced towards the isotopically lighter end of the scale (lower $\delta^{18}O$) while each rock maintains its approximate isotopic position in relation to its neighbour (eg Peters and Wickham, 1995; Figure 7.6).

Wall Rock : Vein Fractionation

The characteristically greater $\delta^{18}O$ (vein) ratios relative to the accompanying wallrock indicates that fractionation occurred (Figure 7.6).

Vein $\delta^{18}O$ vs Whole Rock $\delta^{18}O$ Plots

The Mbongolwane Flats data array is similar to the southern Mfongosi Valley array although the mechanisms behind such a similarity are different for each area (Figure 7.3 a, b). The vertical variation of data parallel to the Y-axis implies some isotopic independence from the host rocks (see Figure 7.4-d). As for the other field areas the array does not cross the zero fractionation line. This is effect is a consequence of the sustained metamorphism which has succeeded the intrusion of the Thaweni granite-gneiss and the Zidoni amphibolitic gneiss into the Silambo banded amphibolite. The variety of lithologies, the scale involved and the relatively restricted range in vein and whole rock isotopic ratios in the Mbongolwane area implies an open, fluid-buffered or fluid-dominated system which was probably non-isothermal and which occurred on a scale greater than that of individual layers.

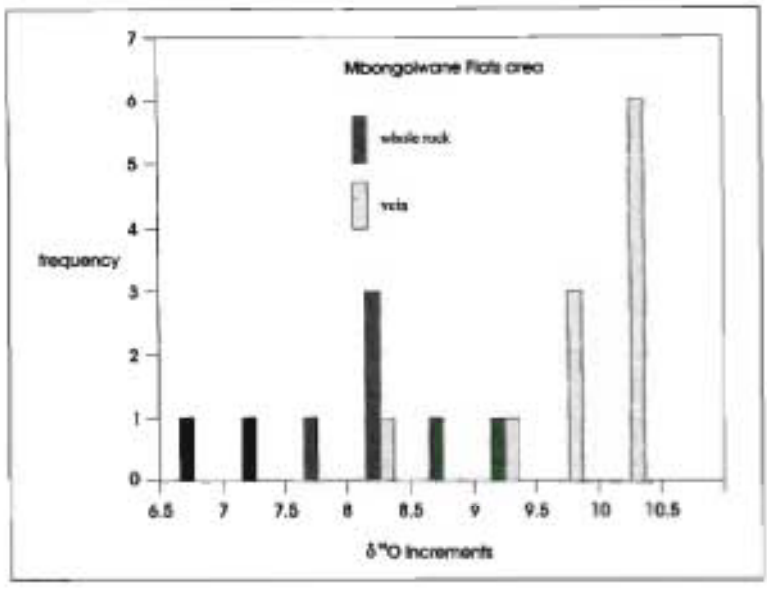

Figure 7.6 Histogram plot of vein and whole rock $\delta^{18}O$ values in the Mbongolwane flats area. Note the higher $\delta^{18}O$ values of the veins compared to those of the host rocks (note: veining is mainly albitic)

Transport Mechanisms - Advection and Diffusion

The structural interpretation of the Mbongolwane Flats area provides for a large-scale, possibly advective fluid system. In the absence of pressure solution or any evidence of large-scale metasomatism, the source of the fluids may be attributed to one of the igneous elements in the area; either the Thaweni Granite-gneiss or the Zidoni amphibolitic gneiss. The overall low $\delta^{18}O$ value of the host rocks to veining is attributable to ^{18}O-depletion due to fractionation with characteristically low-^{18}O igneous-derived fluids such that the range in $\delta^{18}O$ (whole rock) values are very similar to that of the meta-gabbro/meta-norite in the Phoenix Mine area. Even a quartz and feldspar-rich rock, such as the Thaweni Granite gneiss, has undergone this depletion, such that it has a similar $\delta^{18}O$ value to rocks with abundant chlorite and actinolite.

The homogenization of vein $\delta^{18}O$ values across widely varying lithologies commonly results from abundant convection or single-pass fluid flow (eg Wickham and Taylor, 1985). The long-lived metamorphism is consistent with a model of advective circulation.

Conclusion - Mbongolwane Flats area.

A large, kilometre-scale, open advective system, providing fluid-mediated exchange between co-existing rocks (ie mainly fluid-buffered), and driven by early- to syn-deformational intrusions, is indicated for the Mbongolwane area. The characteristic fractionation between wall rock and veins has occurred although the $\delta^{18}O$ values of the host rocks has probably been lowered due to the influence of intrusion-derived fluids. Syn-intrusive deformation of the host rocks is evident in the field but the extent of the influence of intrusion-derived fluids during the initiation of the late-tectonic NNE- and ENE-trending left-lateral shears is not known. Modification of the isotopic patterns by metamorphism would have followed intrusion.

d) Ayres Reef (Manyane amphibolite) and Phoenix Mine

The Ayres Reef and the Phoenix mine are grouped together on the basis of their similarities in position on the $\delta^{18}O$ (vein) vs $\delta^{18}O$ (whole rock) plot below the zero fractionation line (Figure 7.3 b), and since both deposits are situated in the Tugela Nappe. No deformation mechanisms during the emplacement of the veining are evident although both vein sets display slickensides and slickenlines attributable to late-tectonic superimposed left-lateral movement.

General Observations of Ranges of Data

The host rock to the Phoenix Mine (meta-gabbro/meta-norite) and the host rock to the Ayres Reef (Manyane amphibolite) all possess $\delta^{18}O$ values below 9.75 $^{o}/_{oo}$. Veins in the Ayres Reef area are relatively uniform in isotopic ratio, with a variation from 9.27-9.64 $^{o}/_{oo}$; the Phoenix Mine veins have a rather greater spread in values, from 7.99 $^{o}/_{oo}$ to 10.70 $^{o}/_{oo}$ (Figure 7.1).

The Influence of Mineralogy on $\delta^{18}O$ values

The host rocks display low $\delta^{18}O$ values as they are quartz-poor, magnetite + chlorite-rich mafic and amphibolitic rocks. The isotopic ratios of the veins is also low although it is inconceivable that pressure solution generated these large, highly-veined zones.

Wall Rock : Vein Fractionation

The characteristic enrichment of veins in ^{18}O is present for both areas, as for the other field areas, although vein and whole rock values are amongst the lowest in the entire data set (Figure 7.7).

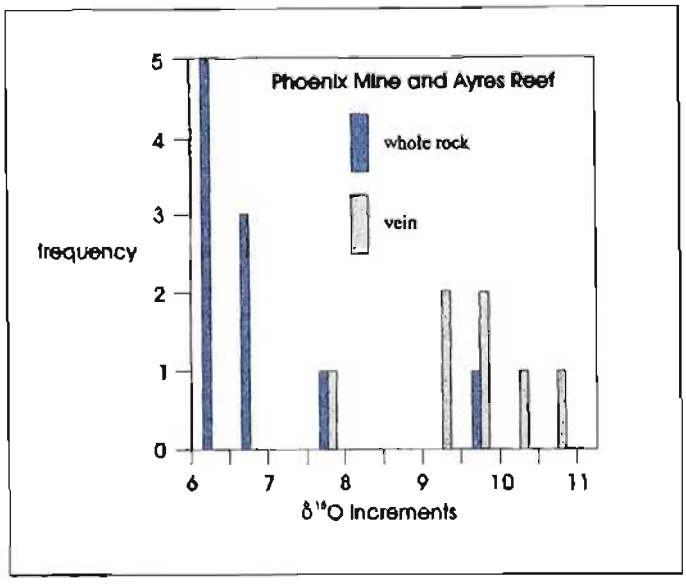

Figure 7.7 Histogram plots for the Ayres Reef and the Phoenix Mine. Note the overall similarity in vein and whole rock values

Vein $\delta^{18}O$ vs Whole Rock $\delta^{18}O$ Plots

One data point could be extracted from the Ayres Reef area and no deductions about the conditions of vein formation may be made. The spread in vein $\delta^{18}O$ values for the Phoenix Mine display a small variation in adjacent wall rock type, consistent with a fluid buffered system. The heterogeneity of the vein data suggests a short-lived fluid-movement system. The data field does not cross the zero fractionation line which implies that the fluids were not of an igneous origin.

Transport Mechanisms - Advection and Diffusion

The formation of these thick veins resulted from tapping of a metamorphic fluid reservoir during post-thrusting collapse and the channelling of these fluids into east-west and north-northeast-trending brittle fractures formed by the north-south extension of the Tugela Nappe.

A halo of isotopically altered country rock may surround an intrusion. However, intrusion of earlier igneous rocks by igneous rocks, originating from the same magma chamber may yield a similar effect. Study of the wall rocks to the Phoenix Mine indicates that there has been extensive silica metasomatism accompanying brittle fracturing of the meta-gabbro/meta-norite.

The mineralogical changes which accompanied the lowering of $\delta^{18}O$ values in the wallrock to veining are as follows and include some of the effects observed in rocks of the Phoenix Mine area:

- cloudiness of alkali feldspars
- alteration of pyroxenes and olivines to uralitic amphibole, chlorite, Fe-Ti oxides and/or epidote
- granophyric (micrographic) intergrowths of turbid alkali feldspar and quartz
- miarolitic cavities and veins with quartz, alkali feldspar, epidote, chlorite or sulphide minerals

A large-scale fracture system during post-cooling deformation of the meta-gabbro/meta-norite would have enhanced these effects considerably. It is proposed that an advective fluid system, which carried mainly silica and sulphides, was responsible for leaching and redeposition of material in fractures in the host rocks to the Phoenix Mine. Wall rock alteration in the Ayres Reef host rocks has been overprinted by the amphibolite-grade thermal pulse at the Manyane Thrust. In contrast, the Phoenix Mine wall rocks have undergone only brittle deformation and fairly pervasive silica metasomatism succeeded by left-lateral movement.

Conclusion - Ayres Reef and Phoenix Mine

The unusually thick quartz veins at these deposits results from late- to post-Tugela Rand Complex fluids or the tapping of late-tectonic metamorphic fluid reservoirs which caused metasomatism and leaching with redeposition of material in brittle fractures. Abundant, but variable metasomatism in the wall rocks resulted from the extensive or widespread fracture systems id recently intruded and as yet unmetamorphosed mafic rock. A highly channelized, single-pass fluid system is proposed. As there is no indication of igneous-derived fluids involved in vein formation (vein $\delta^{18}O$ vs whole rock $\delta^{18}O$ plots) the origin of the fluids is likely to be from late-tectonic metamorphically-generated fluid reservoirs similar to those in the Mbongolwane Flats area.

Chapter 8

Geochemistry

8.1) Introduction

Geochemical data assists in determining the protoliths and provenance of the host rocks to veining and allows indirect assessment of the alteration of each lithology. Geochemical provenance or tectonic discrimination diagrams are used to develop a model for the pre- to syn-collisional tectonic setting of the Natal Nappe Zone and Natal Thrust Front. Sparsely-sampled meta-sedimentary rocks interbedded with the meta-volcanic rocks, aid in refining the overall model. Geochemical features of all rock types are compared to geochemical signatures of similar rocks in terrains worldwide.

a) Methodology

i) The geochemical data from each rock type is discussed first in terms the ranges of concentrations of major and other elements, for example SiO_2, Al_2O_3, Zr. Ranges and averages will be compared to those of similar rock suites from elsewhere.

ii) Classification diagrams, for example SiO_2 vs Total Alkalis, and other more complex bivariate function plots are used to classify each rock type. Analogous plots for sedimentary rock diagrams will also be used.

iii) A range of element plots, such as Zr vs Ti, Zr vs Y and Zr vs Nb, are used to classify possible processes in the rock suites. The internal coherence of geochemical data is assessed by establishing significant correlations (the Pearson Product-moment Co-efficient of linear Correlation: PCC - "r"). Correlation is defined as a measure of the strength of association between two variables, measured on a number of individuals within a population. The principle of ignoring outliers in an analyzed population of samples is accomplished on the strength of basic chemical characteristics and field appearance.

Geologically important, common major element oxides such as SiO_2, Fe_2O_3, CaO, K_2O and TiO_2 are correlated with SiO_2 and CaO, as the latter two elements are strongly related to the effects of silica and carbonate metasomatism prevalent in the five field areas (e.g. late-tectonic carbonate metasomatism in the Ngubevu area).

iv) Once the validity of using certain immobile-incompatible elements as discriminants of tectonic setting has been established, a range of geochemical discrimination diagrams are plotted for each area's metavolcanics and the Zidoni amphibolitic gneiss in the Mbongolwane flats area. Mobile-compatible elements are checked against other plots for internal consistency. These diagrams contribute towards a pre-collisional structural model of the Natal Thrust Front and Natal Nappe Zone.

b) Discussions

i) As all the considered lithologies fall within a metamorphic or mobile belt the direct use of tectonic discrimination diagrams is practiced. Obducted material is likely to have undergone low-temperature seafloor weathering or halmyrosis, lower greenschist facies hydrothermal alteration and possibly subsequent regional metamorphism. Because ophiolites are commonly located adjacent to tectonic terranes, and because low-temperature alteration and metamorphism are ubiquitous, caution must be exercised in geochemical data interpretation; structural relationships and major element geochemistry may not be definitive of rock origin. Trace elements which are relatively immobile during metamorphism, and which have been successfully used as discriminants of ophiolite petrogenesis (e.g. Pearce, 1975, 1979; Pearce and Cann, 1971, 1973; Pearce and Norry, 1982; Shervais, 1982), are focused on in this study.

Lithogeochemical characterization has traditionally made use of well-established diagnostic parameters such as Mg # and Harker Alkali vs SiO_2 diagrams (e.g. Peccerillo and Taylor, 1976). These discrimination diagrams, designed primarily to classify pristine igneous rocks, employ elements which are for the most part igneous compatible and mobile under hydrothermal conditions. This inherent mobility is useful in indicating hydrothermal alteration but these elements are not suited to precursor rock type and petrochemical identification.

ii) Interpretation involves the discussion of each rock type in terms of its most likely tectonic setting. As stated above, combining the results of metasedimentary rock data analysis with the results from metabasite analysis, allows for a more complete model.

c) Conclusions

The final section combines the results an areas' study into a final model, essentially a broad geochemical scenario. Any irregularities/contradictions are highlighted, as are the potential areas for further work.

d) Analytical techniques

Sample Preparation for X-ray analysis

Major and minor elements were analyzed using the lithium tetraborate fusion method of Norrish and Hutton (1969). Relatively unweathered whole rock samples of between 10 and 20 kg were selected for analysis. Each sample was trimmed to remove weathered crusts, cut into fist-sized segments and then placed in an ultrasound cleaner bath for 30 minutes. Samples were then thoroughly rinsed in distilled water and placed in a drying oven at 110°C for 24 hours. Whole rock and vein samples were then reduced using a jaw crusher and two stages of cone-and-quartering to obtain a representative sample. The crushed aggregate was then milled to a fine powder, part of which was used for the preparation of fusion discs and powder pellets, and part kept for future use. Internationally accepted standard values are from Abbey (1989). Prof. A.H. Wilson of the Department of Geology, University of Natal, Durban, compiled the computer programs for reduction of count data and calculation of mass absorption co-efficients. X-ray fluorescence analysis determined total iron. A standard ratio of $Fe^{2+}/Fe^{3+} = 9$ was used for comparison of oxide values with analyses from other sources.

e) Geologically important elements and groups of elements

Elements are divided into major elements, expressed as weight percent (wt%) of the oxide, comprising Si, Ti, Al, Fe, Mn, Mg, Ca, Na, K and P while trace elements are defined as those elements which are present at less than the 0.1% level. This division is usually adhered to by the data with the exception of S in the Ngubevu area which is over 6000 ppm in one sample. The element K is highly mobile and is problematic in that it could be viewed as a trace element in this data set (e.g. some of the metabasites). Geologically significant trace elements are depicted in Figure 8.1 in red. The trace elements are subdivided on the strength of their ionic ratio versus ionic charge into a number of groups each displaying distinct behavior under normal igneous or metamorphic processes. Saunders *et al.* (1979) proposed a division of magmatophile elements into two groups based on the ionic character. Elements with large ionic radii, low charges and low charge-to-size

ratios are termed low field strength elements (LFSE) and are analogous to large ion lithophile (LIL) elements (Schilling, 1973). Such elements tend to be mobile during low temperature alteration. Elements of a small ionic radii and high charge-to-size ratio are termed high field strength elements (HFSE). HFSE are generally strongly incompatible, have very small partition coefficients in most situations (except in monazite, zircon or apatite, where the partition coefficients may be very high) and are considered immobile during low-temperature alteration (*op. cit*; Figure 8.1; Rollinson, 1993; Cattalani and Bambic, 1994). Element mobility/immobility differs from element compatibility/incompatibility:-

- Compatible trace elements whose preference is the mineral phase in a magmatic system and have partition coefficients >1 (defined as "D" = concentration in mineral/concentration in melt). Some elements are initially incompatible but are accommodated later in crystallization or fractionation, indicating the onset of crystallization of a particular mineral phase.
- Examples of elements which are incompatible over a broad compositional range are the LIL elements (K, Rb, Sr, Ba, Zr and Y and light REE). HFSE such as Zr, Nb, Y and some REE are highly incompatible in most basaltic and some tholeiitic rock suites. Of these, Zr and Y represent igneous fractionation trends in tholeiitic magmas.
- Mobile elements tend to form aqueous complexes and enter into solution during metasomatic, metamorphic or hydrothermal processes. Since hydrothermal alteration mainly involves mass loss/removal of mobile components, immobile elements may be residually concentrated in the rock (Cattalani and Bambic, 1994).

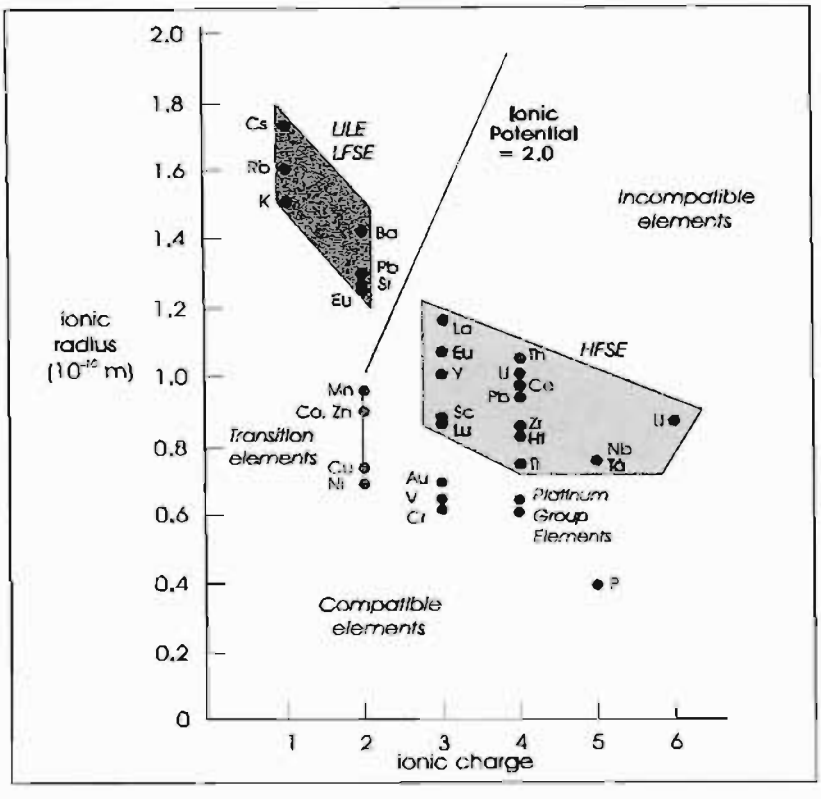

Figure 8.1 Division of the geologically significant major and trace elements into groups, based on the elements' charge-to-ionic size ratio. The general mobilities of these elements are described in the text. The elements in red are used in this study, along with other major and trace elements, to determine the protolith and provenance of the rock samples and alteration effects/mass changes (modified after 1982 and Rollinson, 1993)

In each of the five field areas the relevant elements in each rock type are tested for immobility by bivariate diagrams which use immobile elements or components. There may be a high degree of correlation PCC > 0.80) in the data array, the respective correlation coefficients resulting from enrichment or dilution of immobile elements. Mass losses (chloritization and/or sericitization) and gains (silicification, carbonitization and/or pyritization) may also be presented by these correlations and a Zr ppm vs TiO_2 (wt%) plot. A coherent and consistent behaviour of data over a variety of binary diagrams confirms the immobility of an element. If a sample plots in the basaltic field on one discrimination diagram, it must consistently plot as a basalt in all diagrams consulted. This condition of "internal consistency" will be the basis of the geochemical treatment of this study.

8.2) The Mbongolwane Flats

a) Introduction

The Mbongolwane Flats area consists of three main rock types, the Silambo banded amphibolite (SBA) into which the Zidonj amphibolitic gneiss precursor (ZAG) intruded, and the sheet-like Thaweni granite-gneiss (Chapter 2) which intruded both the SBA and the ZAG. Difficulties were encountered in sampling in the Mbongolwane Flats which contains only 2% outcrop and samples in the surrounding mountainous areas are clustered. As this geochemical survey is more of a regional one, the elucidation of the chemical variation between, rather than within, terranes is the object of this study. Each rock type is considered separately but, due to only four examples of the Thaweni granite-gneiss having been sampled because of a lack of outcrop, no significant statistical conclusion are made for this suite. Sampling of the banded amphibiolite was limited to 7 samples.

b) Silambo Banded Amphibolite (SBA)

Samples of SBA were taken only from the Lauwrie outcrop, in a 6 metre thick vertical section adjacent to the abandoned gold mine in the northeastern part of the field area (Appendix B1, F1). A total of 7 samples were analysed (Appendix F1). The Madidima Nappe is interpreted as being the lowest in a series of nappes which comprise the Natal Nappe Zone. It is proposed in this study that the nappe complex constitutes a hinterland-dipping duplex and that the higher, more westwards nappes are more allochthonous in nature than the Madidima Nappe at the base. The lowest nappe is also relatively allochthonous given the other mobile belt inlier to the east, nearer Empangeni (Figure 1.2, Chapter 1). The determination of the provenance of the nappes' constituent rocks is a significant contribution modelling Natal Nappe Zone and Natal Thrust Front tectonics.

i) Chemical Characterisation - Basic Survey of Data

The SBA fall into the high-Ti metabasalt group of Naidoo *et al.* (1991), having TiO_2 wt% values well above 0.95, at 1.55 to 2.53 wt%. SiO_2 is between 50.14 and 54.21 wt% which is notably higher than that of the metabasites at Ngubevu. High-Ti metabasites have clustered V concentrations (394 to 544 ppm) and high Cr contents, between 28 and 59 ppm (*c.f.* Bloomer, 1987) with the exception of sample BOAFS-3 which has Cr = 3.4 ppm. Metabasites have Ti/Zr ratios, is another measure of "high-Ti" affinity (Naidoo *et al.*, 1991) of 89 to 117. The SBA is provisionally proposed to be almost identical to the seamount/spreading ridge volcanic products or rifted continental margin sequences near the southern portion of the Bou-Azzer-El Grara ophiolite in Morocco (Naidoo *et al.*, 1991).

Table 8.1 Ranges of major element oxides of the Mbongolwane Flats metabasites. The numbers in brackets are means of the data (SBA: N = 7)

	SiO_2	Al_2O_3	Na_2O	K_2O	CaO	MgO	MnO	FeO
SBA	50.14-54.25 (52.65)	12.68-13.79 (12.97)	2.23-3.34 (2.68)	0.34-0.88 (0.54)	6.72-8.15 (7.45)	3.82-5.41 (4.52)	0.20-0.30 (0.24)	11.52-14.34 (13.37)

The magnesium number (Mg #) is particularly useful as an index of crystal fractionation in basaltic liquids (e.g. Wilkinson, 1982). The inverse of this ratio is a measure of iron enrichment. The Mg#, defined as (MgO/40.32)/[(MgO/40.32+FeO/71.85], ranges from 33.38 to 45.56, which is low relative to the Mg# of basaltic rock compositions associated with cumulates (*cf.* Sivell and Foden, 1988). The relatively low CaO concentration (CaO<10 wt%), low Mg# and regular concentrations of elements implies basalt fractionation from liquids of reasonable or regular compositions, i.e.: not in contact with cumulate material.

ii) Major Element Data Analysis

There are a number of ways in which major element data, particularly the elements Si, Ti, Al, Fe, Mn, Mg, Ca, Na, K and P, are used. Firstly, in rudimentary sedimentary and igneous rock classification, secondly in variation diagrams which may show the interrelationship between elements in a data set which leads to conclusions on geochemical processes and, thirdly, the plotting of chemical compositions on phase diagrams. The first category of diagrams will be emphasized in this section.

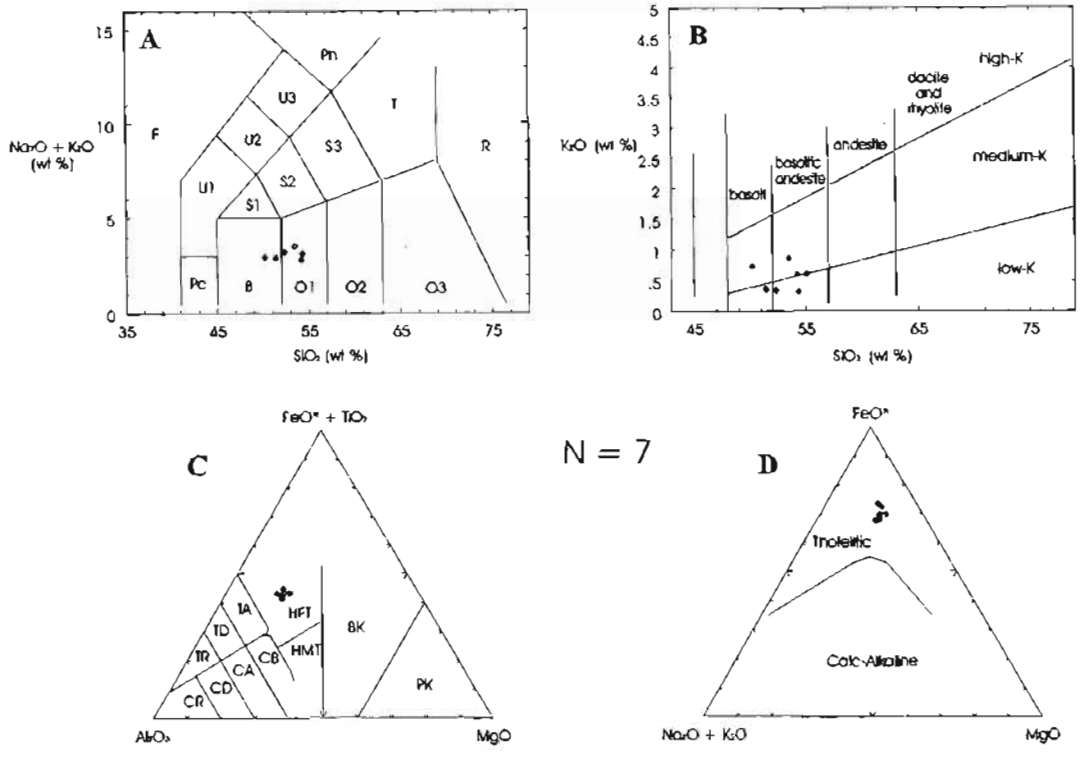

Figure 8.2 Major element oxide classification diagrams **a)** After Le Maitre (1987, Figure B.14), the SBA plot as basalts and basaltic andesites **b)** After Le Maitre (1987, Figure B.15), the SBA plot as basalts and basaltic andesites **c)** After Jensen (1976), the SBA plots as High Iron Tholeiites (HFT) on this major element cationic plot and **d)** Tholeiitic vs Calk-Alkaline plot of Irvine and Baragar (1971) showing the SBA to be markedly tholeiitic in nature in contrast to data from the Ngubevu area which fall on the Fe-enrichment side of the Fe-saturation apex or point N = 7

Major element classification diagrams (Figure 8.2) classify the Silambo banded amphibolite and a medium- to low-potassium basalt to basaltic andesite (le Maitre, 1987), with a strong iron tholeiitic signature (Jensen, 1976; Irvine and Baragar, 1971).

iii) Correlations between Critical Elements - Original Igneous Fractionation Patterns

The remnant magmatic or petrochemical affinity of discriminants is given by the degree of correlation between two incompatible elements (e.g. the High Field Strength Elements - HFSE), and involves the testing of incompatibility of the elements in one rock type on bivariate plots such as Y-Zr and La-Yb (Cattalani and Bambic, 1994; Barrett and Maclean, 1991, 1993). For example, the Zr/Y ratio for tholeiitic rocks is 2-5; Zr-Y usually shows linear trends, indicating incompatible element enrichment from basalt to rhyolite compositions (*op. cit.*; Watson and Harrison, 1983 - Figure 3).

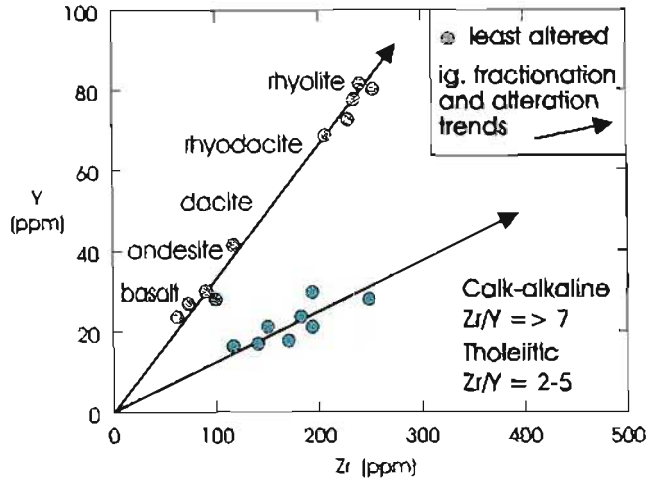

Figure 8.3 A typical bivariate immobile-incompatible Zr vs Y plot (after Watson and Harrison, 1983; Cattalani and Bambic, 1994) showing the basalt-rhyolite fractionation trend (Zr/Y = 2-5) and the calk-alkaline trend (Zr/Y = 7 - may be up to 30).

Ratios which are useful for the determination of magmatic affinity include La/Yb, Zr/Yb and Zr/Yb, although Yb concentrations were not determined in this study. A Zr/Y ratio of 1.9 to 3.4 is defined by the Mbongolwane metabasites (Figure 8.4a) and a Pearson's product-moment correlation coefficient (PCC - quoted at the 95% confidence level) of +0.85 is applicable to 73% of the population. A significant PCC of +0.95, applicable to 87% of the population, is calculated for Zr/Nb (Figure 8.4b). These rocks define tholeiitic trends on the ternary FeO^*-(Na_2O+K_2O)-MgO plot of Irvine and Baragar which uses potentially mobile, compatible elements as discriminants.

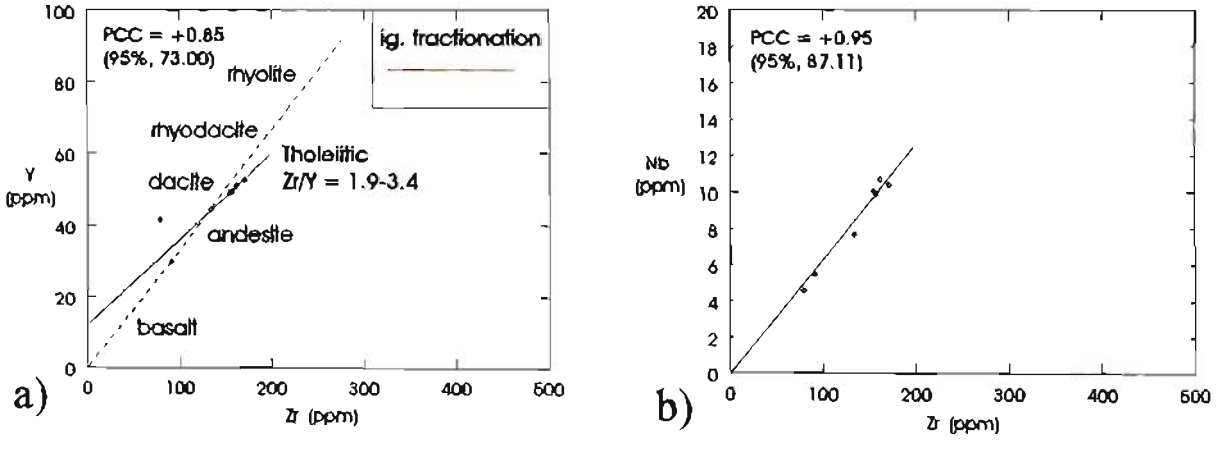

Figure 8.4a Silambo banded amphibolite bivariate immobile-incompatible element plots - a) Zr vs Y and b) Zr vs Nb (both plots after Cattalani and Bambic, 1994). Plots a) and b) show that magmatic fractionation trends are still evident in the geochemical data which implies that at least the immobile-incompatible elements may be used in tectonic discrimination diagrams in the next section

The fractionation trend for tholeiitic to transitional rock series on a Zr vs TiO_2 diagram generally describes a concave, depletion-style curve which is quantified by a complex second-order polynomial equation (Cattalani and Bambic, 1994). Because TiO_2 mimics the behaviour of FeO during fractionation, the fractionation trend described here is analogous to the Fe-enrichment trend on the Irvine-Barager AFM diagram. In Zr-TiO_2 space the steep positive slope at low Zr values corresponds to the trend from the MgO apex to the FeO* apex on the AFM diagram (Figure 8.5). The data yield a positive slope on the Zr-TiO_2 plot relating to the fractionation of silicate minerals such as olivine, pyroxene or plagioclase, and residual Fe-enrichment. The inflection point or apex marks the point where Ti becomes saturated in the liquid. This point is analogous to the apex in the AFM diagram after which Fe becomes saturated in the liquid fraction. Continued evolution of the melt causes continuous enrichment in Ti and Fe and a residual enrichment in silica and the alkalis, reflecting the ongoing crystallization of pyroxene, hornblende, biotite and eventually alkali feldspar and quartz (*op. cit.*). The last part of the process translates as a negative slope in Zr-TiO_2 space and is analogous to the trend towards the alkali apex in AFM space. By virtue of its high incompatibility (*cf.* FeO which is compatible), Ti is continuously enriched over the compositional range. Ti and Fe have not become saturated in the melt.

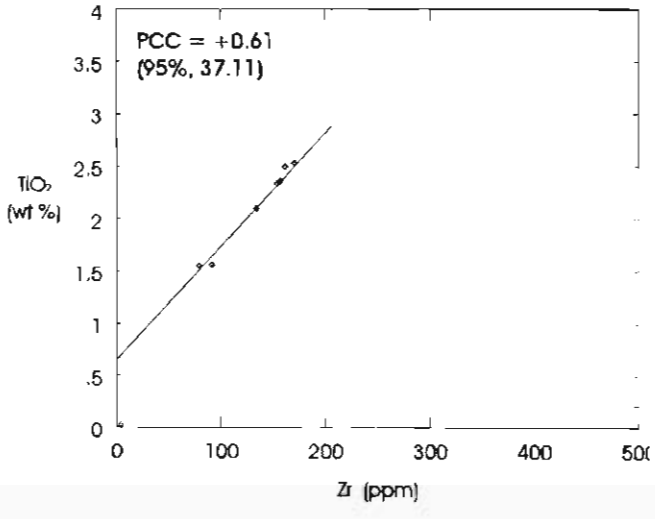

Figure 8.5 Immobile-incompatible element (Zr ppm) vs compatible-mobile (TiO_2 wt%) plot showing a typical tholeiitic trend on similar to that on the the positive side of a of a basalt-rhyolite igneous evolution curve. Mass gain and mass loss, according to the effects of alteration, cannot be quantified here because essential higher silica portions of the rock suite are not present and the entire curve may not be defined (e.g. in Cattalani and Bambic, 1994)

The preservation of fractionation trends of initial magmas permits the use of immobile-incompatible elements in tectonic discrimination diagrams. The Zr vs TiO_2 plot does not define the chemical alteration of the SBA metabasite. The original composition of the SBA is inferred to be a low- to medium-K, high-Fe tholeiitic basalt to andesite.

iv) Classification and Tectonic Discrimination Diagrams

The probable tectonic setting of the SBA, in the context of mobile belt formation, can be progressively refined and quickly plotted using the Fortran-based Shareware program "NewPet". There is agreement within the geochemical plots applied to the SBA. The SBA can initially be defined as a low-K tholeiite/ocean floor basalt on the ternary (Ti/100) - (Y*3) - Zr plot of Pearce and Cann (1973) and the Ti vs Cr plot of Pearce (1975; Figures 8.6a and b). This classification is confirmed by applying the ternary (Ti/100) - (Zr) - (Sr) plot of Pearce and Cann (1973) and the V vs Ti/1000 bivariate plot of Shervais (1982; Figures 8.6c and d).

The Ti/1000 vs V plot of Shervais (1982) depends upon the change in ionic characteristics of V such that V is a sensitive indicator of both partial melting and fractional crystallization. The effects of seawater/basalt interaction at low and high temperatures have been studied in the Deep Sea Drilling Program (DSDP) (e.g. Alt and Hannorez, 1984; Alt *et al.*, 1986) which reveals that Ti and V are stable over a wide range of temperatures and water:rock ratios, even in samples which have been entirely converted to chlorite and quartz. Ti and V show coherent behaviour during alteration so that their ratio remains the same as that of the fresh rock, but are affected by mass change of the rock (Shervias, 1982). During the regional metamorphism of ophiolites or obducted terranes, at either the intermediate or high grade (amphibolite to granulite facies) Ti and V are sufficiently immobile to use in provenance discrimination (Nicollet and Andrianbololona, 1980; Weaver and Tarney, 1981).

The SBA is defined as an N-MORB/Mid-Ocean-Ridge-Basalt (Normal MORB) by the ternary (Nb*2) - Y - (Zr/4) plot of Meschede (1986; Figure 8.6e) and a mid-ocean ridge basalt on a bivariate Zr vs Zr/Y plot (Pearce and Norry, 1979; Figure 8.6f). Wood (1980) uses a ternary (Zr/117) - (Nb/16) - Th plot which classifies the SBA as a destructive plate margin basalt or differentiate (Figure 8.6g). The log Zr vs log Ti plot of Pearce (1982) classes the SBA samples as within-plate basalts but also as MORBs (Figure 8.6h).

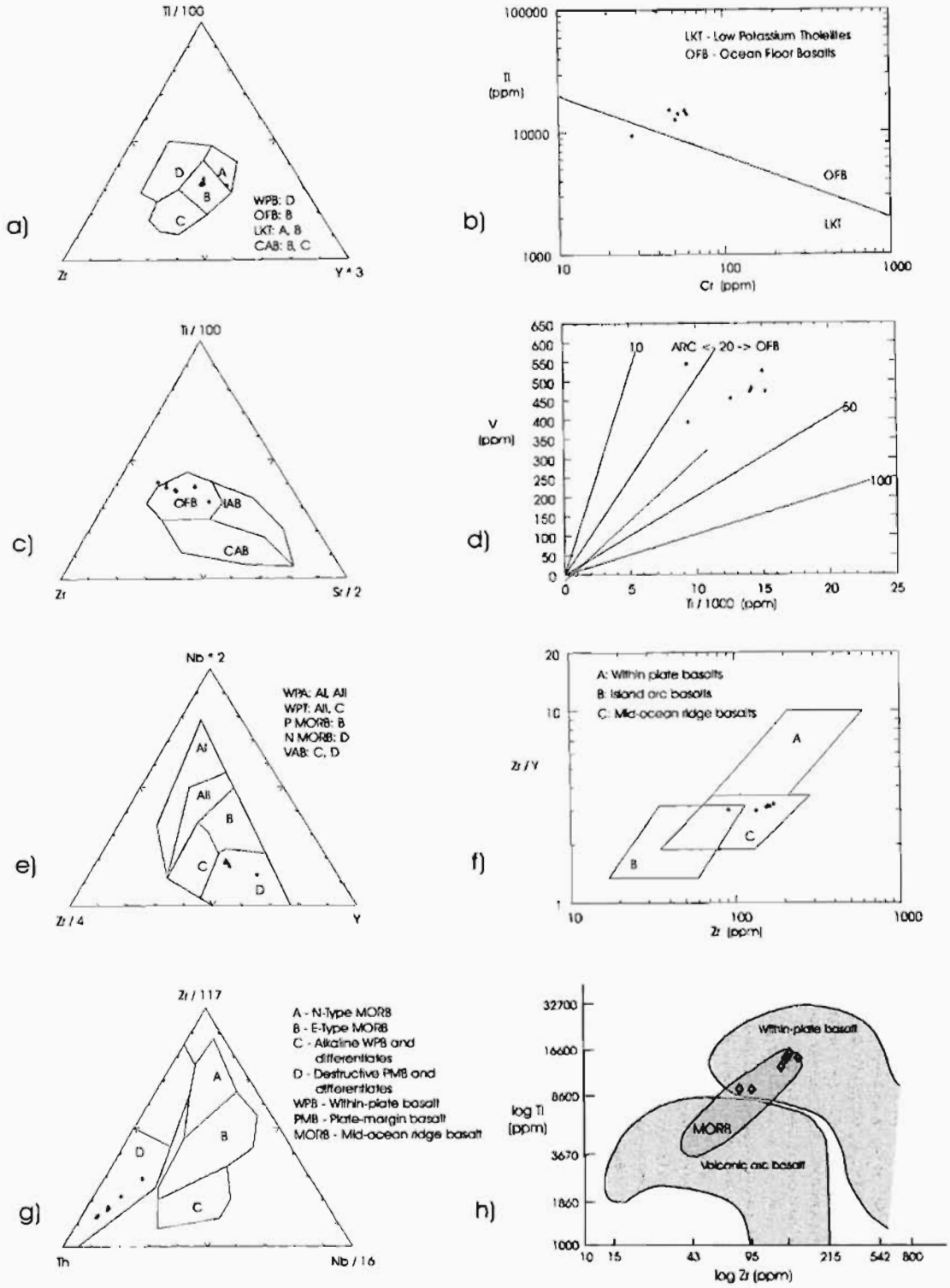

Figure 8.6 - Tectonic Discrimination Diagrams

a) Ternary plot of Pearce and Cann (1973): (Ti/100)-(Y*3)-(Zr): Conclusion : **Ocean floor basalt**

b) Bivariate log Ti vs log Cr (Pearce, 1975): Conclusion : **Ocean floor basalt**

c) Ternary plot of (Ti/100)-(Sr/2)-Zr (after Pearce and Cann, 1973): Conclusion: **Ocean floor basalt**

d) Simple, effective bivariate plot of Shervais (1982) which essentially uses the basic ratio between these two elements: Conclusion: **Ocean floor basalt.** This diagram was designed for the efficient discrimination between arc-related tholeiites, MORB and alkali basalts

e) Ternary plot of Meschede (1986) which classes the SBA as a **Volcanic Arc Basalt (VAB)** or **Mid Ocean Ridge Basalt (MORB)** in (Nb*2)-Y-(Zr/4) space

f) Bivariate plot of Pearce and Norry (1979) which classes the SBA protolith as a **Mid-Ocean Ridge to Island Arc Basalt**

g) Ternary complex discriminant plot of Wood (1980) which places the SBA data into the **"Destructive plate margin basalt and differentiates"** class, using the discriminants of (Zr/117)-(Nb/16)-(Th)

h) Log Ti vs log Zr plot showing a **Within-Plate Basalt and MORB** affinity (after Pearce, 1982)

v) Conclusion

The Silambo banded amphibolite may be classified using mainly incompatible-immobile elements which are inferred to have been largely unaffected by sea-floor alteration and regional metamorphism. The SBA have many features in common with the "high-Ti" metavolcanics of the Bou-Azzer-El Grara ophiolite complex in Morocco (Naidoo *et al.*, 1991), which originated in a rifted continental margin to seamount setting prior to the obduction of the ophiolite complex. Upon eruption, compositions were on the Fe and Ti peaks of typical fractionation trends, beyond the Fe and Ti-depletion stage of the melt (prior to Fe and Ti-saturation). This implies the emplacement of the basalts after the fractionation of olivine. Tectonic discrimination diagrams classify the SBA as a tholeiitic/sub-alkaline basalt to andesite which originated in a within-plate/MORB/ocean floor setting. The protoliths of the metabasalts may further be classified as N-MORB. The possibility that segments of the Natal Nappe Zone are obducted ophiolites must therefore be seriously considered.

c) Zidoni Amphibolitic Gneiss

As this geochemical study concentrates on the metabasites and/or metasedimentary rocks which potentially host mineralization, a cursory study will be made of the Zidoni amphibolitic gneiss (ZAG). A total of 18 samples of the ZAG were analyzed (Appendix F2) although it was found that four of these, SBA-BACK, MANDRB-ZAG, MANDRB-ZAG2 and SMMS-5 are geochemically distinct from the majority of samples.

i) Chemical Characterization - Basic Survey of Data

The ZAG samples are generally higher in SiO_2, Al_2O_3, Na_2O and K_2O, but significantly lower in FeO and MnO than the Silambo banded amphibolite (Table 8.2, Figure 8.6). As the ZAG is actinolite-rich (i.e. contains sufficient Ca, Mg and Mn to form amphiboles) the use of the magnesium number (Mg#) is credible. The Mg# of the ZAG samples varies from 47.61 to 60.07, higher than that of the SBA samples.

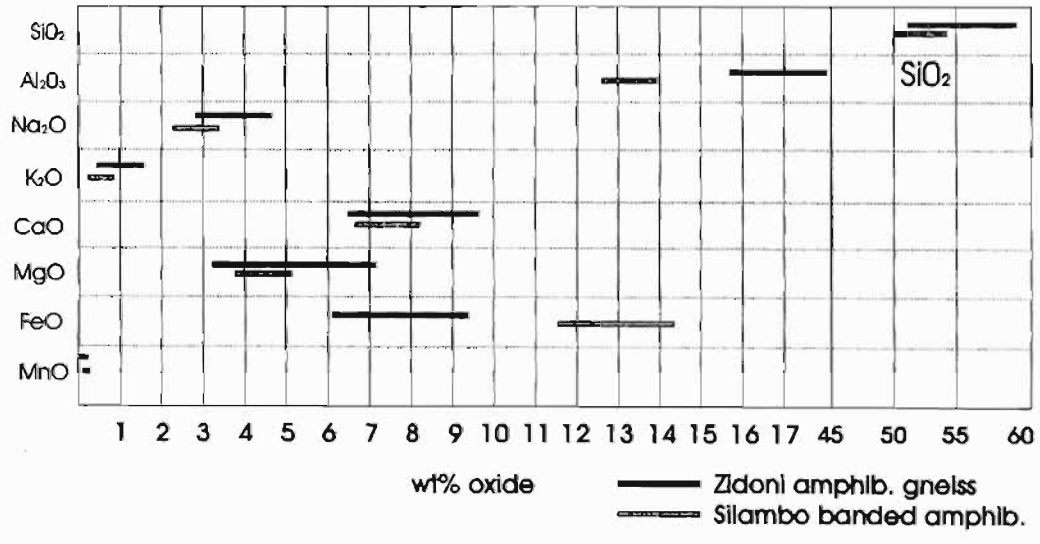

Figure 8.6 Ranges of geochemically significant major element oxides in the Silambo banded amphibolite (SBA) and the Zidoni amphibolitic gneiss (ZAG). See text for discussion

Table 8.2 Ranges of major element oxides for the Zidoni amphibolitic gneiss. Numbers in brackets are means (SBA: N = 7, ZAG: N = 14)

	SiO_2	Al_2O_3	Na_2O	K_2O	CaO	MgO	MnO	FeO
SBA	50.14-54.25 (52.65)	12.68-13.79 (12.97)	2.23-3.34 (2.68)	0.34-0.88 (0.54)	6.72-8.15 (7.45)	3.82-5.41 (4.52)	0.20-0.30 (0.24)	11.52-14.34 (13.37)
ZAG	51.06-59.84 (54.52)	15.74-17.95 (16.85)	2.92-4.60 (3.50)	0.47-1.59 (0.93)	6.48-6.69 (8.16)	3.23-7.18 (5.09)	0.11-0.24 (0.17)	6.10-9.41 (7.97)

The higher CaO and Mg# compared to the SBA indicates that the gneissic precursors may have crystallized from less compositionally regular or cumulate-enriched melts (Wilkinson, 1982) than the metabasites. It will be shown later that the ZAG and SBA were formed from very similar magmas. Auto-intrusion of the ZAG has been recorded in studies of the Madidima Nappe (Schulze-Hulbe, 1977). This conclusion is reached by the construction of spidergrams or normative element plots (*op. cit.*). It is possible to use the bivariate immobile-incompatible and immobile-compatible elements which are used for the SBA as the maximum metamorphic conditions have been similar.

ii) Major Element Data Analysis

In view of the fact that the ZAG is described as an amphibolite-bearing meta-granitoid and that a large range of silica values are present (51.06-59.84 wt%), this rock type is plotted on a variety of major element oxide diagrams (Figures 8.7 a-e). The protolith of the ZAG is defined as a quartz-monzodiorite to quartz-diorite on the Total Alkalis vs SiO_2 plot of Middlemost (1985; Figure 8.7a) and as tonalite/quartz diorite/gabbro in the complex discrimination diagram of Debon and Le Fort (1983) (Figure 8.7b).

The geochemistry of the ZAG can be further defined; a metaluminous rock is indicated by the Al-(K+Na+2Ca) vs (Fe+Mg+Ti) plot of Debon and Le Fort (1983). The characteristic mineralogy of their Group IV granitoids is hornblende+biotite with orthopyroxene and clinopyroxene, primary epidote and sphene (Figure 8.7 c). This mineralogy is very similar to that of a protolith which was metamorphosed to the mineralogical composition described by Schulze-Hulbe (1977). Lastly, the ZAG shows sub-alkaline to calc-alkaline characteristics (Figures 8.7 d, e). It may be noted that the ZAG samples which were excluded from this main study show strong gabbroic tendencies in these

plots. The ZAG suite is therefore not as homogenous as was previously supposed (e.g. Schulze-Hulbe, 1977).

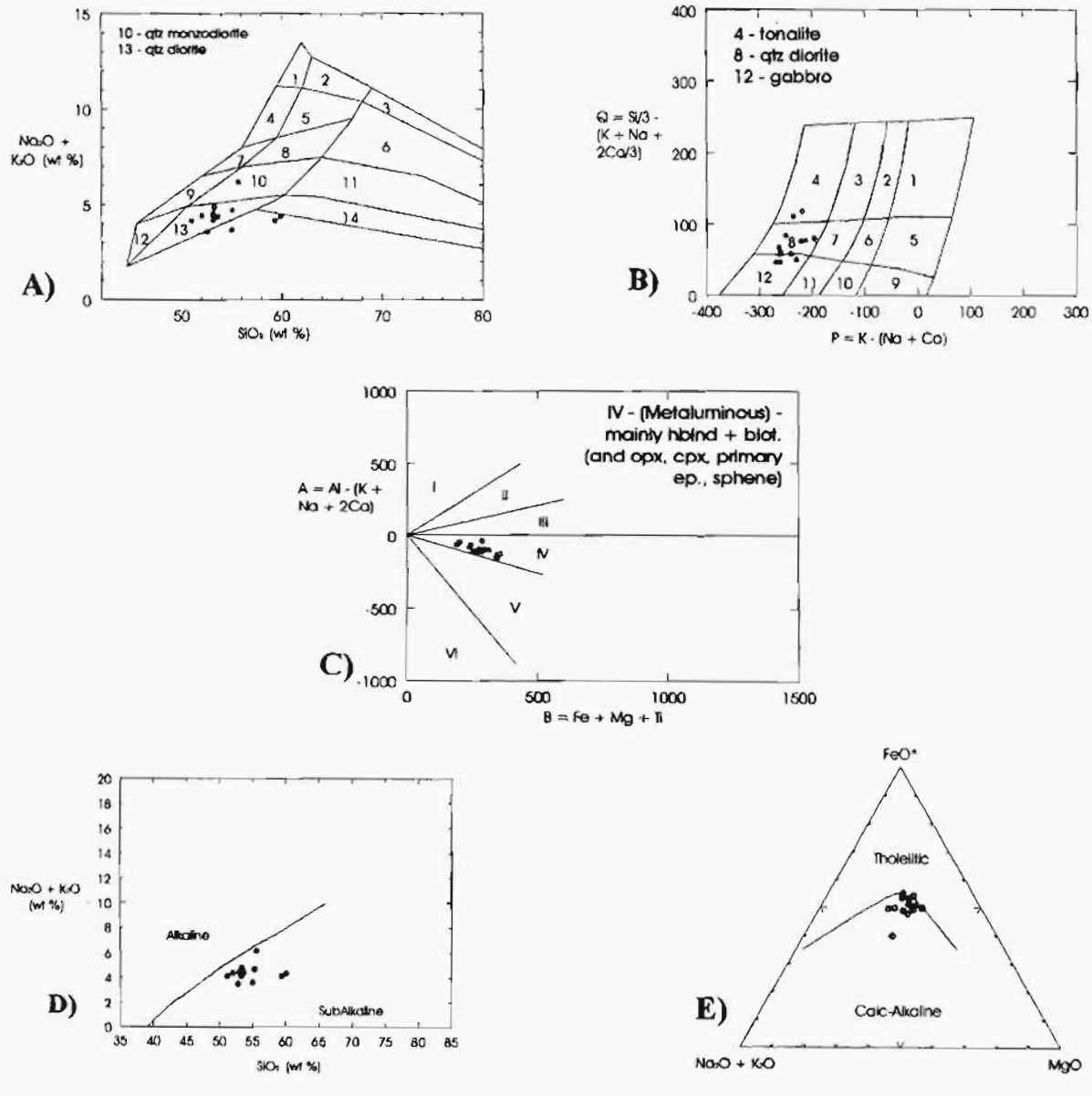

Figure 8.7 a) Total Alkalis vs SiO_2 plot of Middlemost (1985); ZAG samples plot as qtz-monzodiorites to qtz-diorites
b) A similar result is obtained by the complex discrimination plot of Debone and Le Fort (1983) where the ZAG samples are classified as tonalites, quartz-diorites and gabbros **c)** Complex discrimination diagram for the ZAG samples (Debone and Le Fort, 1983) which are classified as metaluminous granitoids, characteristically consisting of hornblende, biotite, orthopyroxene, clinopyroxene, primary epidote and sphene **d) + e)** Plots from Irvine and Baragar (1971) show the ZAG to be sub-alkaline to calk-alkaline in nature.

The Zidoni amphibolitic gneiss suite is heterogeneous and is classified as a sub-alkaline to calk-alkaline metamorphosed quartz monzodiorite, quartz diorite, tonalite to gabbro. The meta-granitoids are classed primarily as metaluminous with hornblende and biotite being the characteristic minerals typical of such a suite, along with orthopyroxene, clinopyroxene, primary epidote and sphene.

iii) Correlations between Critical Elements - Original Igneous Fractionation Patterns

A magmatic affinity can be determined in the ZAG via the methods used for the SBA as proposed by Cattalani and Bambic (1994). The Zr/Y ratio is still broadly in the 2-5 range for tholeiitic rocks (Cattalani and Bambic, 1994) at 2.03 to 5.55 and shows a significant PCC of +0.86 at the 95% confidence level, applicable to 73.12% of the data population (Figure 8.8a). Good correlation is found for other plots: Zr/Nb show an almost perfect correlation at +0.99, at the 95% confidence level, applicable to 97% of the population (Figure 8.8 b). Zr (ppm) vs TiO_2 (wt%) shows a +0.99 correlation coefficient at the 95% level, relevant to 98% of the total theoretical population (not plotted).

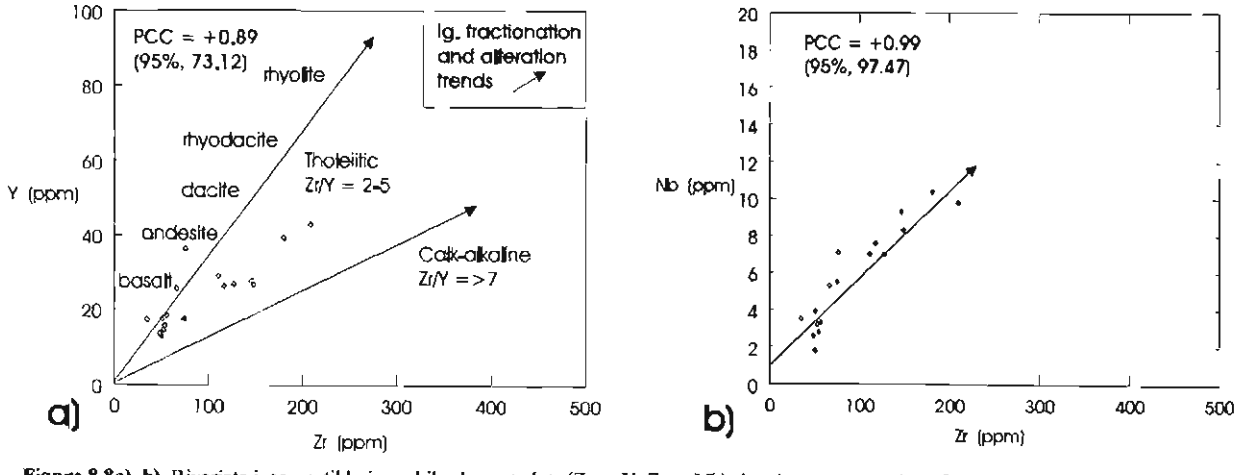

Figure 8.8a), b) Bivariate incompatible-immobile element plots (Zr vs Y, Zr vs Nb) showing a preservation of magmatic fractionation trends.

Given that the magmatic fractionation trends can still be discerned after metamorphism, the use of tectonic discrimination diagrams as below is considered justified and valid.

iv) Classification and Tectonic Discrimination Diagrams

The tectonic setting of the ZAG, prior to nappe emplacement, is defined by using immobile-incompatible and mobile-incompatible elements. Batchelor and Bowden (1985) found that multicationic ("complex discrimination") diagrams classify granitoids formed during mobile belt development or orogenic uplift (Figure 8.9). Like the "discriminant function" or "discrimination function" diagrams of Roser and Korsch (1988), used for classifying sandstone-mudstone suites, these diagrams are difficult to analyse critically. However, they do take into consideration a substantial number of elements and are more definitive than simple compatible-mobile element diagrams. On Figure 8.9, the ZAG samples plot in the pre-plate collision granitoid field.

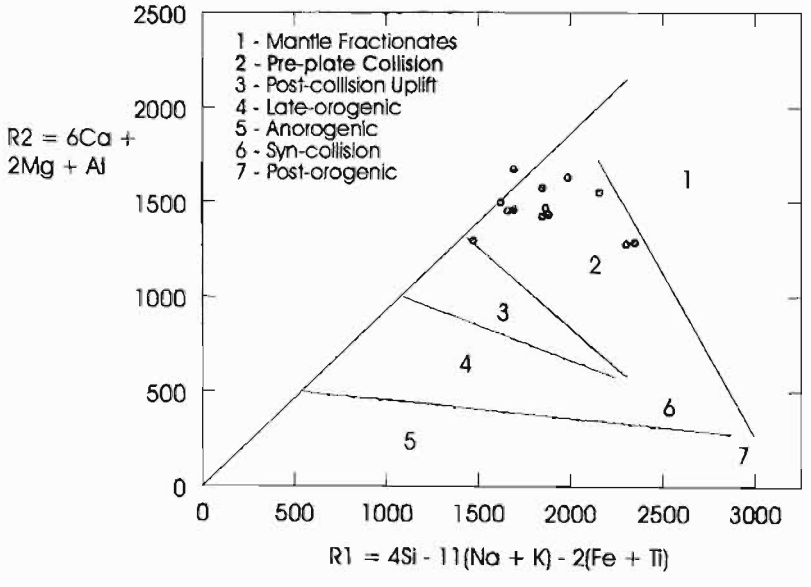

Figure 8.9 Multicationic/Complex Discrimination plot of Batchelor and Bowden (1985) showing the ZAG samples to be pre-plate collision in origin. The unusually high Ca and Mg values in some samples displaces the data from Field 2 and is probably due to the assimilation of SBA with fine dolomite or calcite bands, corresponding to a mass gain.

The (Zr+Nb+Ce+Y) vs FeO*/MgO plot of Whalen *et al.* (1987; Figure 8.10 a) effectively separates orogenic granitoid types (OGT - unfractionated M, S and I types) from fractionated felsic granites (FG - A-type "anorogenic" granites as for intracratonic granitic intrusions). Figure 8.10 shows the ZAG to show orogenic characteristics, most likely from a pre-plate collision setting (*qv.* Batchelor and Bowden, 1985). The refinement of the tectonic setting is given in Figures 8.10 b and c (after Pearce *et al.*, 1984). The Nb vs Y plot (Figure 8.11b) shows the granitoids to be either of the volcanic-arc or syn-collision type whereas the addition of Rb as another discriminant removes the

linear format of Y vs Nb, as on Figure 8.11b, but separates syn-collision granitoids from volcanic arc granitoids (Figure 8.11c).

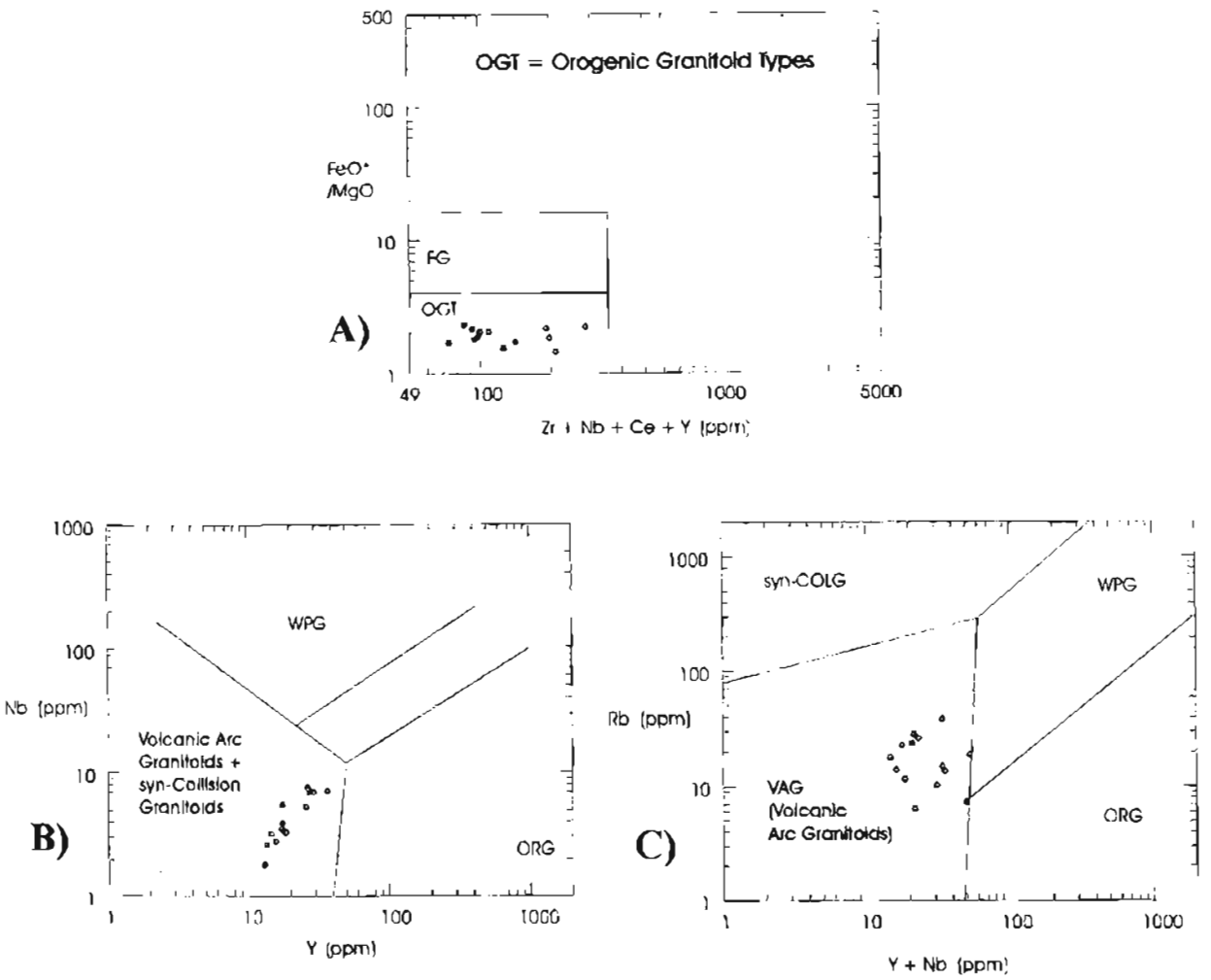

Figure 8.11 a) Separation of granitoids into fractionated felsic granites (= A-type granites) and orogenic granitoid types (OGT) (after Whalen *et al.*, 1987). The ZAG plots in the OGT field.
b) and **c)** classify the ZAG as volcanic arc granitoids using Y-Nb and (Y+Nb) - Rb (after Pearce *et al.*, 1984)

v) Conclusion

The Silambo banded amphibolite was intruded by the Zidoni amphibolitic granitoid/diorite/gabbro prior to the emplacement of the Madidima Nappe. The ZAG is a metaluminous tonalite/quartz/diorite/quartz-monzodiorite/gabbro with typical protolith minerals including hornblende, biotite, orthopyroxene, clinopyroxene, primary epidote and sphene. Unusually high Ca and Mg values in some samples may be due to the assimilation of SBA which contains thin bands of

calcite or dolomite. Given the complete fractionation curve of the suite, it might be possible to infer a mass gain from a Zr vs TiO_2 plot, however, the data is limited in this compositional space and only the positive, pre-Fe and Ti-saturation side of the fractionation curve is defined. The ZAG is consistently classified, using pertinent immobile-incompatible trace elements, as showing orogenic (unfractionated M-, I- and S-type) granitoid characteristics typical of emplacement into a volcanic arc. A similar relationship is proposed for the banded metabasites/intrusives in other nappes, with the exception of the Tugela Nappe which hosts the mafic/ultramafic Tugela Rand Complex.

8.3) Southern Mfongosi Valley Area

a) Introduction

The southern Mfongosi valley area within the Mfongosi Group contains up to 40% basic rocks which are metamorphosed to quartz-epidote-actinolite and epidote-quartz-actinolite schist. The original nature of the contacts with the thicker associated metasedimentary layers is obscured by slickensiding and boudinaging of silicified metabasites. Tectonic juxtaposition may have caused unusually high heat and fluid fluxes. Due to the high proportion of epidote in the rocks (*c.f.* Naidoo *et al.*, 1991) the geochemical compositions of the metabasites may not be definitive of their protolith compositions.

b) Metabasites

i) Chemical Characterization - Basic Survey of Data

The small number of samples from the southern Mfongosi Valley field area does not allow any statistical treatment of data. However, basic assumptions regarding the suitability of an extended interpretation of these samples are made (Appendix F3). The Manyane amphibolite, comprising a coarse-grained and fine-grained variety, contains 53 and 51.28 wt% SiO_2 which are similar proportions to Ngubevu area metabasites, while the Mfongosi Group metabasites contain between 54.52 and 73.34 wt% SiO_2, possibly due to the effects of silicification prior to boudinaging. V is characteristically high in Natal Thrust Front and Natal Nappe Zone rocks; 276 and 343 ppm for the Manyane amphibolite and 81 to 312 ppm for the Mfongosi Group. Cr and Ni values are unusually low for both rock suites, and indicate substantial hydrothermal alteration (*c.f.* Naidoo *et al.*, 1991). The Ti/Zr ratio is variable, from 22 to 106 ppm for Mfongosi Group rocks and 92-126 for the Manyane amphibolite. The Mg# of the Mfongosi Group rocks is between 44.15 and 55.59, while that of the Manyane amphibolite is 40.62 to 51.50. The total alkali value of the Manyane amphibolite is greater than 1, at 2.18 to 2.80 (*c.f.* Naidoo *et al.*, 1991) and the CaO/MgO ratio is well under 5 for these rocks (2.64 and 1.61), implying that these samples are suitable for interpretation using igneous-rock-derived plots. The Mfongosi Group samples are also suitable for such chemical interpretation; total alkali values are 3.11 to 4.4 and the CaO/MgO ratios are 1.02 to 2.48.

ii) Validity of Data and Major Element Data Analysis

Significant correlation between immobile-incompatible element pairs is not possible as only two samples of Manyane amphibolite and four samples of Mfongosi Group metabasites were analyzed. The small number of samples potentially show a large range in possible protolith rock types, with the Manyane amphibolite having basaltic compositions (Figures 8.12 a) and the southern Mfongosi amphibolites andesitic to dacitic protoliths. The (Nb*2)-(Zr/4)-Y plot of Meschede (1986) classifies the metabasites in the southern Mfongosi Valley as N-Type MORBs to Volcanic Arc Basalts (Figure 8.12b).

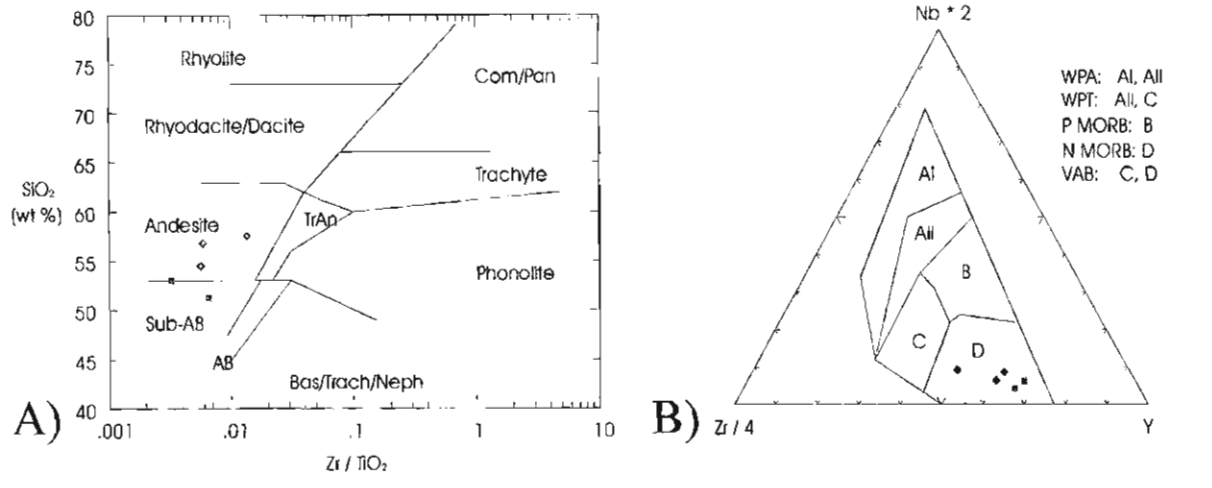

Figure 8.12 a) SiO_2 vs Zr/TiO_2 plot of Winchester and Floyd (1977) applied to the southern Mfongosi Valley area samples (green squares = Manyane Amphibolite, red squares = Mfongosi Group rocks).
8.12 b) (Nb*2)-(Zr/4)-Y ternary plot of Meschede (1986), classifying the metabasites as N-Type MORBS to Volcanic Arc Basalts

iii) Conclusion

No confident assessment of the provenance of the metabasic rocks of the southern Mfongosi Valley may be made as the data imply extensive movement of the mobile-compatible and immobile-compatible elements. Furthermore, limited sampling does not allow for testing for igneous fractionation trends. The use of immobile-incompatible elements is also questionable. The metabasites may be N-MORBs to VAB/andesites. A possible mass gain may be attributed to carbonitization of the metabasites, as deduced from thin section studies. Other studies have shown ankerite to be abundant in the Ngubevu area (Gold Fields of South Africa - internal company reports). The carbonitization may, in turn, be a direct effect of the juxtaposition of the hotter, deeper parts of the Tugela Nappe against the cooler, shallower Mfongosi Group rocks. Tectonic movement resulted

in a short-lived thermal pulse with the fluids moving towards the higher temperature zone and caused hornblende porphyroblasts to overgrow a cataclastic texture in the Manyane amphibolites. Metamorphism was accompanied by the movement of carbonate-rich fluids through the Mfongosi Group metabasites and metagreywackes. The fluids probably originated in the Ntingwe limestone to the north of this study area. Major and trace element proportions are likely to have been changed and even simple rock discrimination diagrams must be viewed with caution.

The movement of carbonate-rich fluids explains the lack of Carlin-type mineralization in the Ntingwe limestone and the absence of the metasomatism of fluids from potentially gold-enriched portions of Mfongosi Group rocks into Ntingwe limestone.

c) Metasediments

The metabasites in the southern Mfongosi Valley field area are interlayered with light grey to brown phyllitic quartzites. Field observations and literature surveys indicate a sedimentary origin with the deposition of sedimentary rocks being interrupted by the extrusion of basalts in the pre-collisional setting of the Mfongosi Group. The nature of the pre-collisional contact between sedimentary and volcanic rocks is unclear; deformation has resulted in slickensiding of these contacts. As the metasediments display little lateral variation in terms of texture or colour and since individual bands are traceable along-strike for up to 50 m, representative samples are readily available.

i) Chemical Characterization - Basic Survey of Data

The chemical composition of sediments is a result of their provenance and tectonic setting of deposition. Sediments are particularly important in characterizing and constraining tectonic settings and crustal composition during the Precambrian (e.g. Wronkiewicz and Condie, 1987, 1989; Condie and Wronkiewicz, 1990) although such studies are also applicable to the Proterozoic (e.g. Bhatia, 1983; Taylor and McLennan, 1985).

In general, the metasediments are broadly "acidic" in composition with 67.5 to 73.3 wt% SiO_2. Large ion lithophile (LIL) element concentrations are fairly inconsistent with, for example, K_2O between 0.99 to 2.72 wt% (Appendix F4). LIL ratios are uniform with, for example, K/Rb between 548-584. High Na_2O values (*c.f.* Floyd *et al.*, 1989 - Na_2O above 2.00 wt%) of 3.49 to 4.55 wt% are present. Cr values are extremely low, between 0 and 14.1 ppm while Cr/Th ratios are between 1.04 and 9. Ni values range from 10 to 38 ppm and FeO concentrations range from 2.32 to 3.32 wt%.

ii) Classification Diagrams and Provenance Geochemistry

The K/Rb ratio of the metasediments in this study is similar to the magmatic trend defined by Shaw (1968), unmetamorphosed arkosic sands (Van De Kamp *et al.*, 1976) and typical low-grade metagreywackes (Caby *et al.*, 1977; Figure 8.13). The protoliths of the phyllitic quartzites in the southern Mfongosi area had mainly intermediate to acidic source rocks although the K_2O concentration is high for any given Rb concentration relative to typical metagreywackes (Figure 8.13; Caby *et al.*, 1977).

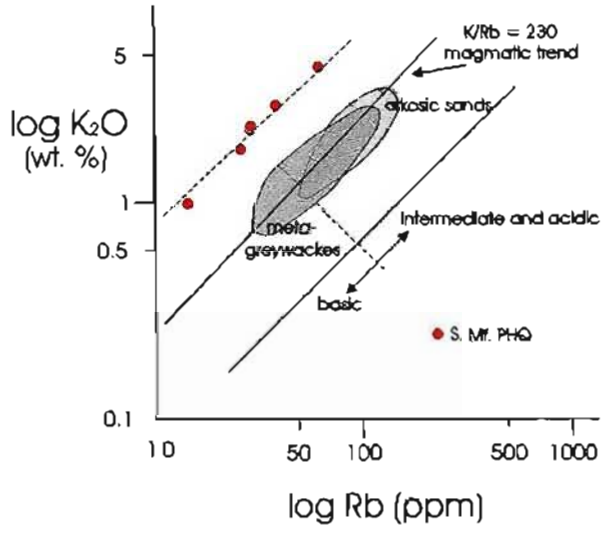

Figure 8.13 Log K_2O vs log Rb for southern Mfongosi Valley area phyllitic quartzite, compared to the fields of unmetamorphosed arkosic sands (van de Kamp *et al.*, 1976), low grade metagreywackes (Cabie *et al*, 1977) and the magmatic trend of Shaw (1968). The crustal K/Rb ratio of 230 defines the magmatic trend which has been divided into a basic and intermediate+acidic portion.

Condie *et al.* (1991) use the concentration of Cr and Ni as indications of a mafic source rock influence in greywacke sedimentation. They consider Cr values of 100 to 152 ppm and Ni values of 10 to 38 ppm to be low and to differ from the Cr and Ni values of most Archaean greywackes and pelites (Taylor and McLennan, 1985; Wronkiewicz and Condie, 1989). They cite these low values as evidence of felsic granitoids being dominant in the source rock area and for the influence of weathering products from mafic and ultramafic rocks to have been negligible. The extremely low Cr values (0 to 14.1) and Ni values (0 for all samples) strongly implies an affinity with rocks derived from almost a mafic/ultramafic-free hinterland. Further support for this is given by calculating the Cr/Th ratio. Condie *et al.* (1991) consider ratios below or equal to 75 to be indicative of a hinterland dominated by felsic granitoids or felsic volcanics. The Cr/Th ratio for the phyllitic quartzites from

this study area is between 1.04 and 9 indicating an overwhelming predominance of felsic source rocks. A good measure of the degree of chemical weathering can be obtained from the chemical index of alteration (CIA: Nesbitt and Young, 1982). The CIA values of the phyllitic quartzites range from 61.56 to 65.27. The CIA of the garnet paragneiss studied by Condie *et al.* (1991) ranges from 53 to 60 and indicates that no significant K loss has occurred, thereby raising the CIA value. A Ti versus Ni plot establishes the original sediment protolith and separates these immature sediments, derived from magmatic/magmatogenic precursors, from normal mature sediments (Figure 8.14, 8.15). The phyllitic quartzite samples plot in the magmatogenic greywacke field (*q.v.* Shaw, 1968; Figure 8.14) and exhibit a poorly defined magmatic trend, possibly with a component of a sedimentary (sandstone) trend although more samples would be needed to confirm this.

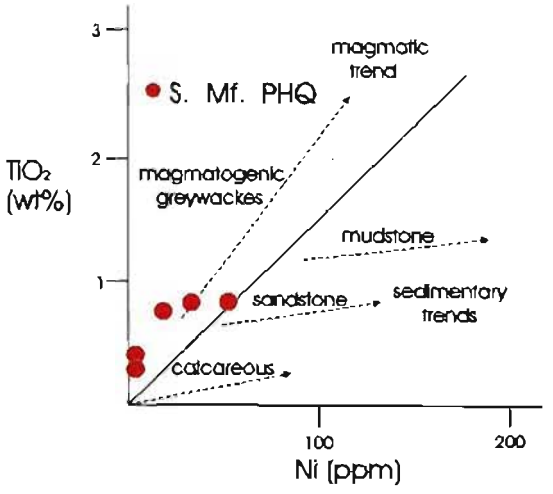

Figure 8.14 TiO_2 vs Ni plot of the southern Mfongosi samples showing the weak magmatogenic greywacke trend/magmatic trend with the possible influence of a sedimentary (sandstone) trend. This plot indicates the immaturity of the metasedimentary protolith (after Floyd *et al.*, 1989)

The results of Figure 8.14 match those of the K-Rb plot, the classification of phyllitic quartzites by more conventional ternary and bivariate plots using major element oxides (e.g. Pettijohn *et al.*, 1973 and Blatt *et al.*, 1980; Figure 8.15). Figure 8.15 reveals that on major element plots and on a Log Sr vs Log Ba plot, the phyllitic quartzites have mostly immature sedimentary rock/greywackes as protoliths although one sample (Sample LBQ-3-VAR) plots in the mature sediment/arkose field. The K_2O/Na_2O vs SiO_2/Al_2O_3 plot from Condie *et al.* (1991) shows the phyllitic quartzites to have a greywacke protolith (Figure 8.15b).

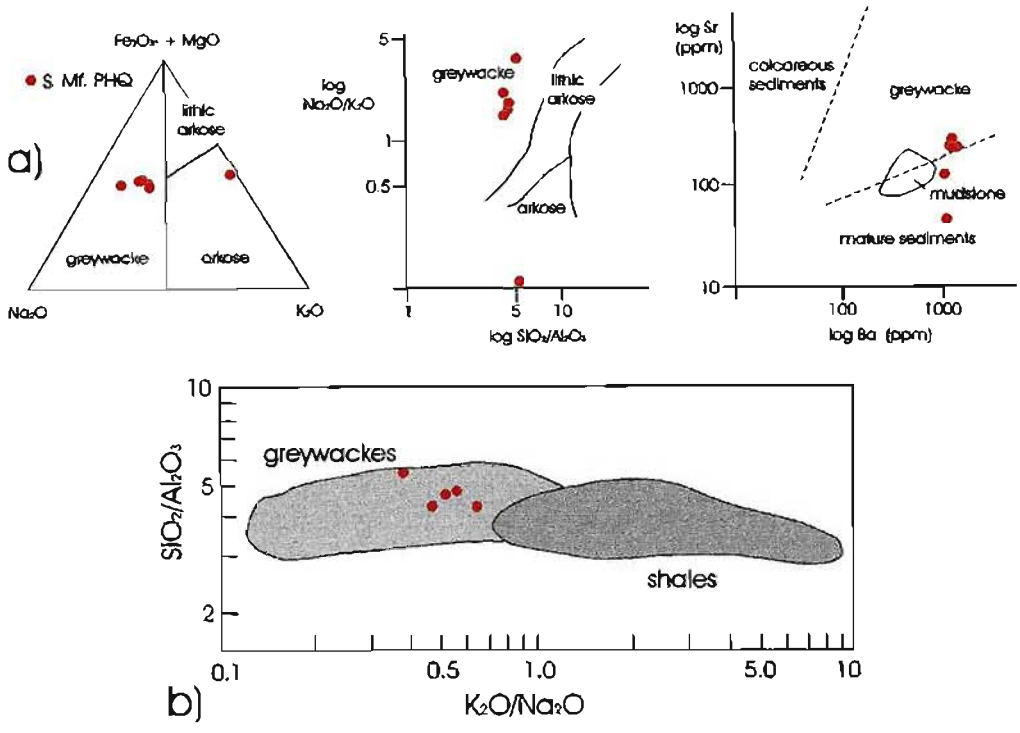

Figure 8.15a) Chemical classification of the Southern Mfongosi phyllitic quartzites as predominantly greywackes (immature sediments) with weak mature or arkosic tendencies. Major element plots from Blatt *et al.* (1980) and Pettijohn *et al.* (1973).
3b) SiO_2/Al_2O_3 vs K_2O/Na_2O plot showing the fields of greywackes and shales (after Wronkiewicz and Condie, 1987 and Condie *et al.*, 1991)

iii) Possible Tectonic Setting

Some basic assumptions may be made regarding the pre-collision setting of the rocks at southern Mfongosi and Ngubevu. The alternating sequence of metagreywackes and metabasites of the southern Mfongosi valley were derived from a predominantly intermediate to acid hinterland with volcanism subordinate or far less prevalent than at the Ngubevu area where only 2-5% of the surface exposure of rocks consists of thin, mainly metapelitic bands. It is likely that the metagreywackes comprise material derived from the Kaapvaal Craton, while the interlayered metabasites may have originated in the south (African azimuths) from proximal volcanic sources.

A further indication of the pre-collisional configuration of the two field areas is the intense deformation of the Ngubevu rocks, with strain ratios up to 12. This implies that the southern and northern Mfongosi rocks were deformed almost in situ on the margin of the Kaapvaal Craton and comprise autochthonous to parautochthonous terranes. The highly-deformed Ngubevu area rocks

constitute part of an allochthonous terrane, originating from the south, and less affected by direct/proximal continental margin sedimentation. It is proposed that a major tectonic discontinuity or unconformity exists within the Mfongosi Group, separating the sediment-poor Ngubevu-type sequence from the sediment-dominated Mfongosi-type sequence. This discontinuity is likely to trend east-southeast and is an excellent topic for further study.

A two-day survey of rocks at the Nkandlha area, in the eastern portion of the Natal Thrust Front, revealed that metabasic units are absent from the Mfongosi Group. This apparent gradation, from a greater proportion of metabasites in the Ngubevu area, to a metabasite-poor/free Mfongosi Group at Nkandlha, implies one of two things: either sedimentary zoning or distribution was obliquely aligned along the Kaapvaal Craton margin, or deformation and flattening has imposed this apparent oblique zoning on the Mfongosi Group. The latter explanation is preferable. The "Ngubevu Terrane" was accreted onto the southern portion of the sediment-dominated Mfongosi Group. This relationship may negate the proposition that the vector of initial collision was more orthogonal to the margin of the Kaapvaal Craton than later tectonic movements and most of the tectonic movement is proposed to be north-easterly.

Provenance diagrams, based on immobile/incompatible elements such as Th, La, Sc and Zr (Bhatia and Crook, 1986) yield somewhat different results than those plots based on "discrimination function" diagrams which primarily utilize major elements. In addition, plotting metagreywacke data on graphs designed for more mature sediments like sandstones, must be approached with caution.

Bhatia and Crook (1986) distinguished between sandstone and greywacke suites on the strength of basic observations of geochemical data and preferred immobile element ternary diagrams for greywacke and metagreywacke discrimination. These researchers were able to distinguish between oceanic island arc-, continental island arc-, active continental margin- and passive margin-derived greywackes. The southern Mfongosi Valley samples correspond to two of these groups on the ternary La-Sc-Th plot where they are classified as ocean island arc and continental island arc metagreywackes (Figure 8.16). The La, Sc, Th and Zr concentrations of the metagreywackes are

inconsistent which may make them undependable discriminatory elements. The ternary Th-Sc-Zr/10 plot (Figure 8.16 b; Bhatia and Crook, 1986) is not as definitive: samples fall on the boundary of, and outside of, the continental island-arc field. Ironically, plots based on major element oxides give a consistent result (Figures 8.17 and 8.18; Bhatia, 1983), possibly due to their lack of dependency on minerals such as sericite or chlorite which could carry spurious trace element or trace element values Figures 8.17a and b and Figure 8.18 indicate that the phyllitic quartzite/metagreywackes are components of an active continental margin or continental arc.

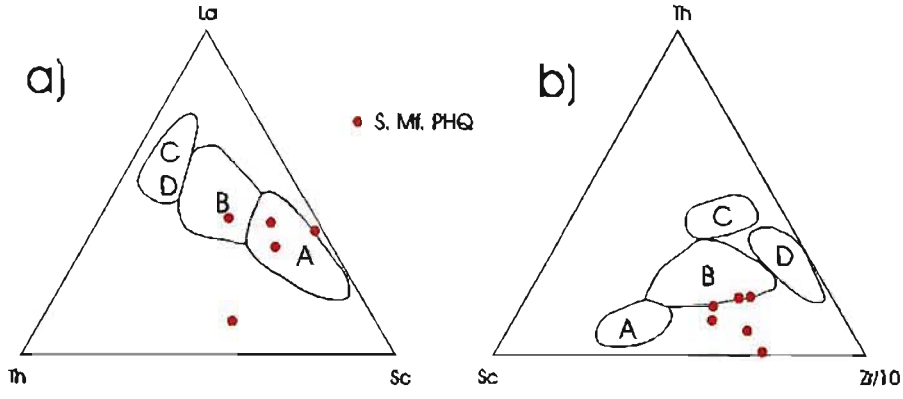

Figure 8.16a) La-Th-Sc discrimination diagram for greywackes b) Th-Sc-Zr/10 discrimination diagram for greywackes (a and b after Bhatia and Crook, 1986). Note that due to inconsistent Th, Sc, La and Zr concentrations in the metagreywackes the results from these plots may not be dependable (refer to previous discrimination diagrams which utilize major element oxides) A - Ocean Island Arc, B - Continental Island Arc, C - Active Continental Margin, D - Passive continental margin

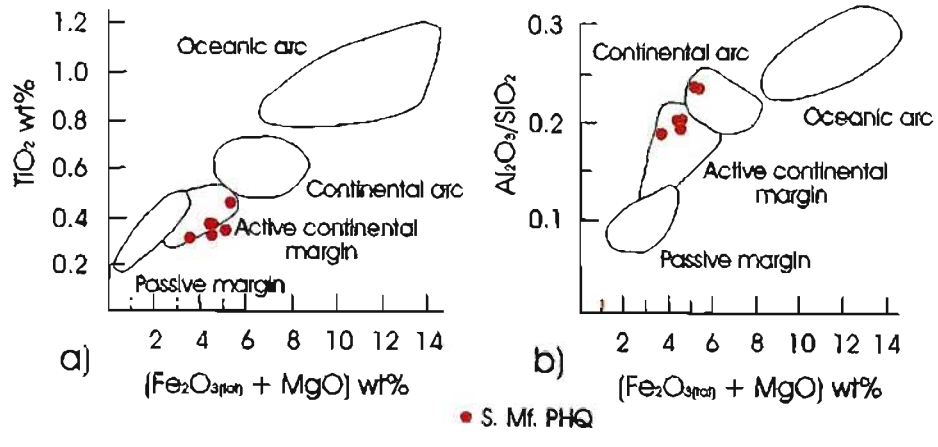

Figure 8.17a) and **b)** discrimination diagrams for sandstones (note: not greywackes) based on bivariate combinations of the less mobile major element oxides. It is apparent the samples fall mainly within the active continental margin field, but also overlap into the continental arc field. Plots after Bhatia (1983)

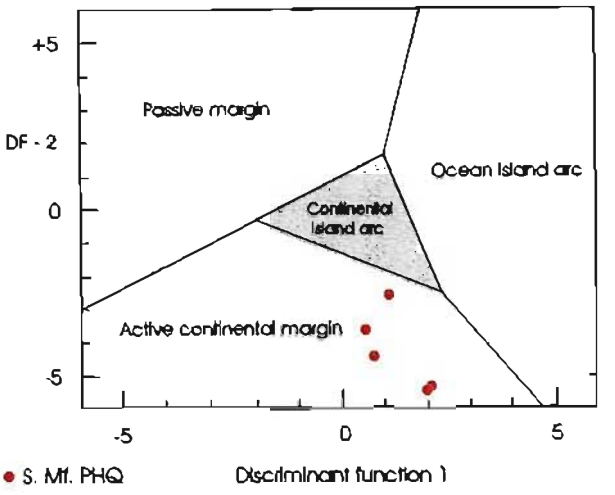

Figure 8.18 Discrimination diagram based on a bivariate combination of first and second discriminant functions of major element oxides (after Bhatia, 1983). This plot produces the same result as the plots in Figure 8.17 a and b, classifying the metagreywackes as being of active continental margin origin. The discriminant functions are as follows:

Discriminant function 1 = -0.0447 SiO_2 - 0.972 TiO_2 + 0.008 Al_2O_3 - 0.267 Fe_2O_3 + 0.208 FeO - 3.082 MnO + 0.140 MgO + 0.195 CaO + 0.719 Na_2O - 0.032 K_2O + 7.510 P_2O_5 + 0.303

Discriminant function 2 = -0.421 SiO_2 + 1.988 TiO_2 - 0.526 Al_2O_3 - 0.551 Fe_2O_3 - 1.610 FeO + 2.720 MnO + 0.881 MgO - 0.907 CaO - 0.177 Na_2O - 1.840 K_2O + 7.244 P_2O_5 + 43.57

iv) Discussion

Comparison with representative analyses of arkose and subarkose confirm the immaturity of the phyllitic quartzite protoliths. FeO concentrations, 2.32 - 3.32 wt%, are markedly higher than those of typical arkosic and subarkosic rocks (usually less than 0.7 wt% - Pettijohn, 1975). MgO concentrations in the phyllitic quartzites are also greater, sometimes by an order of magnitude, than typical arkosic and subarkosic values. The higher MgO and FeO possibly reflect the chloritic fraction of the metagreywackes. The chemistry of the phyllitic quartzites in this study correspond well with the "representative chemical analyses of greywackes" (Table 7.9 - Pettijohn, 1975) in almost every major element oxide, with the exception of MgO which is low in the samples of this study. the Mg deficiency may result from a dominantly sericitic matrix between the widespread polycrystalline or mosaic-textured quartz grains. The metagreywackes in the southern Mfongosi Valley area are poorer in CaO and MgO than Clontibret (Ireland) greywackes (Table II - Steed and Morris, 1986). Due to the deformation and metamorphism at Mfongosi, the usually recognizable characteristics of greywackes are largely absent (e.g. dark grey appearance, marked induration and a lack of normal pore-filling cement). Instead, the matrix consists of a fine-grained intergrowth of sericite and chlorite,

and silt-sized quartz and feldspar. The high Na_2O values (*c.f.* Floyd *et al.*, 1989 - Na_2O above 2.00 wt%) of 3.49 to 4.55 indicate phyllitic quartzite protolith derivation from immature sediments although the possibility of alkali metasomatism and the influence sericitization must be considered.

Greywackes are both mineralogically and texturally immature sandstones derived from many different types of source rock and so no one fragment type may be said to be dominant in the rock suite (Blatt *et al*, 1980). Blatt *et al.* (1980) uses the term greywacke for aerially extensive and similar-looking field occurrences of synorogenic "dirty" sandstones. Greywackes form in tectonically active or orogenic environments, most are of Palaeozoic age or older and most are found in a flysch-like sequence (Pettijohn, 1975; Caby *et al*, 1977; Bhatia, 1983, 1985) and may show a gradation from distal greywackes (distal with respect to a volcanic center) rich in feldspar, into "volcanic wackes" (*op. cit*). Reading (1978) cites greywackes as typical components of melanges, along with radiolarian cherts and dark mudstones. He mentions that many ancient turbidites have a "greywacke texture" with 15% to 40% matrix, so using the term greywacke in a textural sense rather than a genetic. Reading (1978) recognizes the significance of turbidites and greywackes in "geosynclinal" basins and in the near-margin "eugeosynclinal" trough in the "catastrophic eugeosynclinal sediment zone" where turbidity currents prevail. The use of the term "geosyncline" in the literature has since declined but the combination of greywackes and metabasites is unique in an overall tectonostratigraphy. It is apparent that there are at least two contrasting palaeo-depositional environments within the Natal Thrust Front. The NTF is by no means as homogeneous as was previously thought and division into upper and lower portions (Matthews, 1959) may be a relic of the juxtaposition of two different terranes. Alternatively, there could have been lateral variation in sediment deposition modes.

Archaean and Proterozoic sedimentary rocks are fundamentally distinct. Most Archaean sedimentary rocks are characterized by high mineralogical and geochemical immaturity, high concentrations of transition metals and low concentrations of rare-earth elements (REEs) without a pronounced Eu anomaly (Taylor and McLennan, 1985; McLennan and Taylor, 1988). Proterozoic sedimentary rocks are generally more mature and characterized by high REE abundances, with pronounced light REE enrichment and strong depletion in Eu (Taylor and McLennan, 1985).

Condie *et al.* (1991) studied garnet paragneisses which form part of the Precambrian Hapschan Series of Siberia and classified these rocks as metagreywackes on the basis of an SiO_2/Al_2O_3 vs K_2O/Na_2O plot, despite granulite grade metamorphism between 850-950°C and 10-11 kbar. Pan *et al.* (1991) in their study of the late Archaean Hemlo-Heron Bay Greenstone belt of the Superior Province, Ontario, used K_2O, Na_2O and Al_2O_3 as discriminants, even though their type area near the Hemlo Gold Deposit had been intruded by the massive Cedar Lake Pluton. Another measure of the maturity of a sediment is an Al_2O_3/Na_2O ratio (Naqvi *et al.*, 1988) of 3.32 to 3.82 for greywackes from the Hemlo-Heron bay Greenstone Belt, values considered typical of immature sedimentary rocks. The Al_2O_3/Na_2O ratio in the metagreywackes of the southern Mfongosi area is between 3.56 and 4.17. As Mg, Fe, Mn and all the transition trace elements (except for Cu) show concentrations a small proportion of phyllosilicates in the schists, representing the clay component of the original sediments, is implied. As the chemical classification of sediments often depends on the LIL elements, such as K and Na, which may become highly mobile during metamorphism, it is fortunate that the abundance and ratios of LIL elements show an overall coherence even though the sample population is small. If lots of TiO_2 vs Ni, Zr/Nb vs TiO_2 and Cr vs V can be correlated with the phyllites' position on plots using SiO_2, Al_2O_2, Ba, Sr, Fe, Mg and Na as discriminants, then it is probable that the geochemical classification is valid (Rollinson, 1993). Even allowing for internal mobility, most LIL elements would be trapped in the micaceous fraction of the phyllites upon metamorphism and it is acceptable to use both major and/or trace LIL elements to chemically classify the metasediment.

v) Conclusion

The phyllitic quartzite of the southern Mfongosi Valley area is termed a metagreywacke on the strength of the SiO_2/Al_2O_3 vs K_2O/Na_2O plot of Wronkiewicz and Condie (1987). Discriminant plots using the alkali oxides, FeO, MgO, Ba and Sr also confirm the greywacke protolith of the phyllitic quartzite. A positive correlation between K and Rb is parallel to the K/Rb = 230 magmatic trend of Shaw (1968) and data fall into the intermediate and acidic portion of the K-Rb plot. The phyllitic quartzites are classed as magmatogenic metagreywackes, on the strength of the data position in a TiO_2 vs Ni plot.

The high Na_2O values, above the 2.00 wt% limit of Floyd *et al.* (1989), strongly indicates material derivation from immature sediments or source rock. Moreover, the Al_2O_3/Na_2O ratio (Naqvi *et al.*, 1988) is high for greywackes and indicates a predominance of felsic material in the weathering hinterland. The influence of felsic, possibly volcanic rock in the source area is determined by the Cr and Ni concentration (Condie *et al.*, 1991) which are 0-14 ppm and 0, respectively. The Cr/Th ratio of between 1.04 and 9 also indicates an overwhelming predominance of felsic source rocks.

The provenance or situation of the metagreywackes is poorly defined on ternary La-Sc-Th and Th-Zr/10-Sc plots (Bhatia and Crook, 1986), presumably because of the very low Th concentrations. The metagreywackes are cautiously defined as having formed in an ocean island arc or continental island arc setting. The metagreywackes are more consistently defined in terms of their provenance on ($Fe_2O_{3(TOT)}$ + MgO) vs TiO_2 or Al_2O_3/SiO_2 plots and on complex discrimination diagrams which make use of the total range of major element oxides (e.g. Bhatia, 1983), as being of active continental margin or continental arc origin. The phyllitic quartzites formed on the slope of a continental margin, with material derived from the Kaapvaal Craton which comprised predominantly felsic granitoids or volcanics. The minor interbanded metabasites, the origins of which are poorly constrained in this study, indicate a distal volcanic source, probably existing in the south. Metabasites are absent from the sequence in the Nkandlha area and the dominant rock type closely resembles that of the northern Mfongosi Valley area (pers. comm. C. Pearman).

The change in metabasite proportion, from a metabasite-free/poor Mfongosi Group in the Nkandlha area, to 40% in the southern Mfongosi Valley area, may be attributed to the initial pre-deformational sedimentary zoning of a continental margin and adjacent island arc. The southern Mfongosi Valley area sequence represents a mixture of sedimentation from mainly felsic/granitic sources, most likely from the Kaapvaal Craton (north - African azimuths), and distal volcanic basalt extrusion/reworking from the south to south west.

8.4) Ngubevu Area

a) Introduction

The Ngubevu area holds the best prospect for interpreting the type and mode of economic/sub-economic mineralization. Of the 41 samples, five have metasedimentary protoliths and are finely interbedded with the volumetrically dominant metavolcanic epidote-actinolite and chloritic schists (Appendix F5). At Ngubevu, metagreywacke is absent and sedimentation is minor, although it seems to have played an important role in the mode of mineralization. In testing the suitability of the use of incompatible-immobile elements such as Zr, Y and Nb in discrimination plots the correlation co-efficients between elements, obtained by the statistical analysis of 29 samples, are proposed to be significant and representative. The pre- to syn-collisional context of the metasedimentary layers is consistent with the tectonic setting deduced for the associated metabasite layers.

b) Metabasites

Samples of the epidote-actinolite and chloritic schist were taken in three main areas. The first group of samples was taken in the vicinity of the Champion Mine and includes samples with a significant metasediment fraction. The second group of samples originate from the east bank of the Ngubevu river and display largely metabasic geochemical characteristics. Included in this group are samples from near the Golden Eagle Mine which show similar, but very minor metasediment-type anomalies as for the samples from the Champion Mine area. Samples NGE-1 to 7 were taken from the host rock to a small open pit Au and Cu mine in the NGE area.

i) Chemical Characterization - Basic Survey of Data

The Ngubevu area metabasites (NGB) are geochemically distinct from the metabasites of the Mbongolwane Flats area (Table 8.2). The NGB display lower SiO_2, CaO and FeO, but higher Al_2O_3, Na_2O, K_2O, MgO and MnO than the SBA (Table 8.3, Figure 8.19). Lower CaO may be attributed to the paucity of calcite and dolomite banding, compared to the SBA. Careful sampling served to separate the metasediments from the metabasites and only those samples which display no visible metasedimentary characteristics are included in the 29 metabasites in this section.

Table 8.3 Ranges of major element oxides of the Ngubevu metabasites. The numbers in brackets are arithmetic means of the data (NGB = Ngubevu area metabasites, N=29: SBA = Silambo banded amphibolites, N=7)

	SiO_2	Al_2O_3	Na_2O	K_2O	CaO	MgO	MnO	FeO
NGB	46.59-51.92 (48.93)	15.22-18.57 (17.00)	4.2-9.95 (7.09)	3.9-4.15 (2.75)	3.90-10.78 (9.26)	10.82-14.66 (12.59)	1.08-1.47 (1.25)	7.89-10.68 (9.10)
SBA	50.14-54.25 (52.65)	12.68-13.79 (12.97)	2.23-3.34 (2.68)	0.34-0.88 (0.54)	6.72-8.15 (7.45)	3.82-5.41 (4.52)	0.20-0.30 (0.24)	11.52-14.33 (13.37)

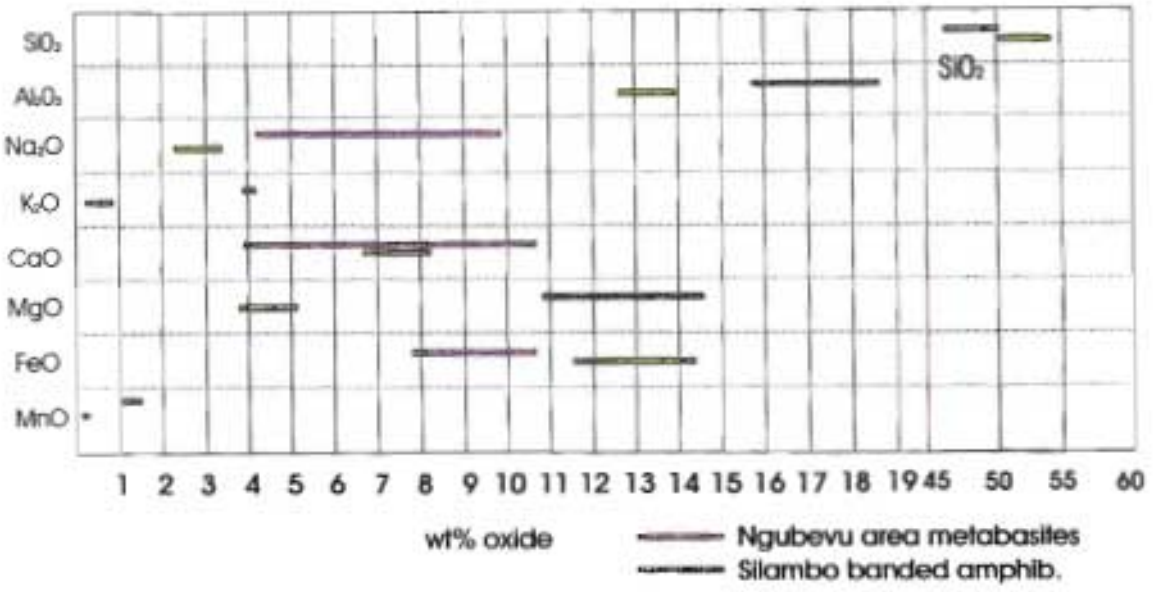

Figure 8.19 Ranges of geologically important major element oxides in the Ngubevu area metabasites (N=29) compared to the Silambo banded amphibolite from the Mbongolwane Flats area (N=7)

The Ngubevu samples fall into the high-Ti metabasite group of Naidoo *et al.* (1991) with TiO_2 concentrations between 1.20 and 2.05 wt%, slightly lower than those of the Mbongolwane metabasites but higher than the upper limit of the "low-Ti" metabasite class (*op. cit.*, 0.95 wt%). SiO_2 concentrations are between 46.59 and 51.92 wt%, lower than the SiO_2 concentration of the bulk of the Mbongolwane samples. The Ngubevu high-Ti metabasites have clustered V values, mostly between 201 and 329 ppm, excluding anomalous samples in the vicinity of the abandoned mines. High Cr values are evident, between 117 and 260 ppm. The samples in this study have *Ti/Zr* ratios of 79.15 to 95.79 (*c.f.* Naidoo *et al.*, 1991), indicating a high-Ti character. The Mbongolwane and Ngubevu metabasites are similar to the ophiolite complex studied by Naidoo *et al.* (1991), implying that the Ngubevu metabasites are similar to seamount/spreading ridge volcanics or rifted continental margin sequences.

The Magnesium Number (Mg#) of these rocks ranges from 42.39 to 63.99 which is consistently higher than the 33.38 to 45.56 range of Mbongolwane metabasites, indicating a tendency towards cumulate enrichment. The higher CaO wt% (3.96 to 11.31) and higher Mg# suggests basalt fractionation in equilibrium with cumulates, although the high CaO is more likely a result of the pervasive carbonate metasomatism. Carbonate metasomatism may also have had the effect of changing the Sr, Ba, Ti and Zr concentrations of the basalts and consequently only samples which contain the least visible calcite were selected for analyses from the field area.

Naidoo *et al.* (1991) consider samples with CaO/MgO ratios ≥5 and/or samples with (Na_2O + K_2O) <1 as yielding genetically in correct element interpretations as these ratios indicate almost total recrystallization to epidote. Although the samples studied here may consist of up to 25% epidote (visual analyses), they are by no means monominerallic and have CaO/MgO ratios of 0.45 to 2.36 wt% and total alkalis well above 1 wt%, ranging from 2.30 to 4.36 wt %. They are suitable for discrimination diagrams provided that significant correlations between incompatible-immobile elements hold. Later sections demonstrate that immobile elements have remained immobile during sea-floor alteration and subsequent metamorphism and still reflect the igneous processes which partitioned them. Samples do not show the significant and often unsystematic variations in concentration indicative of monominerallic zones (*c.f.* Hynes, 1980; Frimmel *et al.*, 1996).

ii) Major Element Data Analysis

The Ngubevu metabasites are plotted on the Total Alkali vs SiO_2 plots of Le Maitre (1989 - Figure 8.20 a and b). Both diagrams yield consistent results which are further confirmed by rock type discrimination diagrams using Zr/TiO_2 vs Nb/Y (Figure 8.20 c) and SiO_2 vs Zr/TiO_2 (Figure 8.20 d). The Ngubevu metabasites are classified as sub-alkaline or tholeiitic basalts.

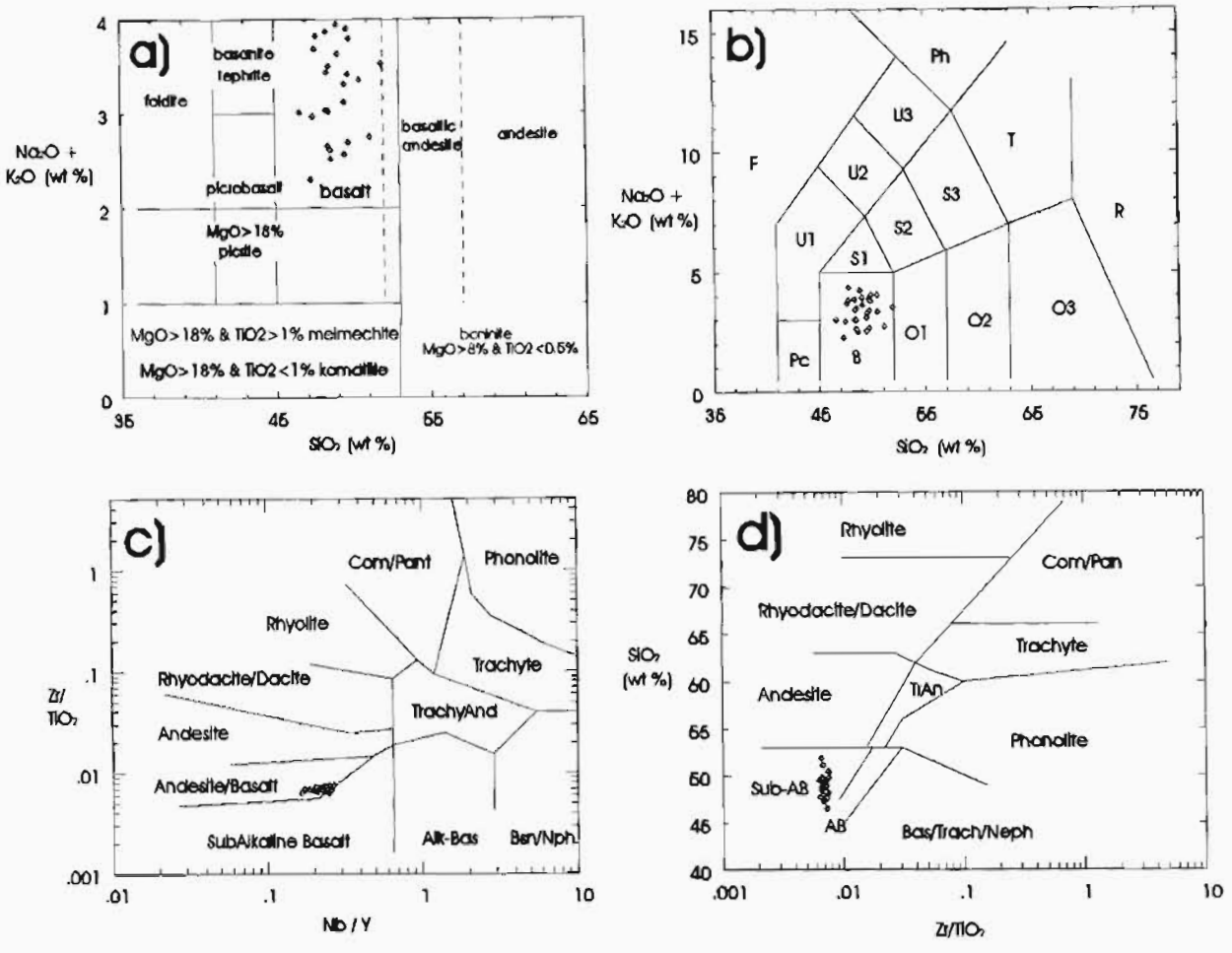

Figure 8.20 a)+b) Total Alkalis ($Na_2O + K_2O$) vs SiO_2 plot for Ngubevu samples show the rocks to be typical (meta)basalts, while the SiO_2 - K_2O plot shows the samples to be medium- to low-K (meta)basalts (a and b after Le Maitre, 1989)
c) Ratio-Ratio (Zr/TiO_2 vs Nb/Y) plot after Winchester and Floyd (1977) giving the rock type as andesite/basalt while d) includes SiO_2 in the discriminants and yields a result consistent with other plots; sub-alkali basalt. This also may imply that little or no Si-metasomatism has occurred (plot after Winchester and Floyd, 1977)

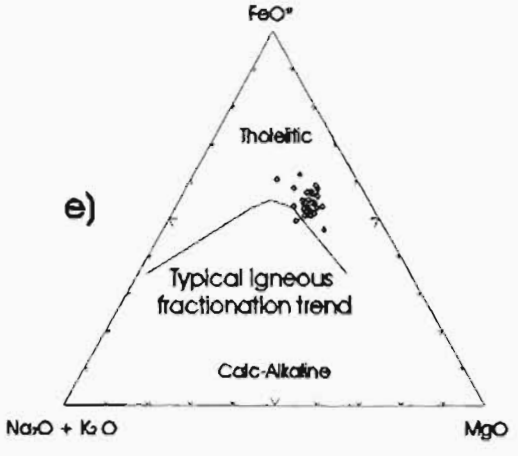

e) Ternary FeO^*-(Na_2O+K_2O)-MgO plot of Irvine and Baragar (1971). Data conform to the Fe-enrichment trend in the tholeiitic portion of the curve. The rocks at Ngubevu also plot further towards the basalt portion (as opposed to the ferro-basalt portion) of the fractionation curve and away from the apex where Fe becomes incompatible, compared to the Mbongolwane Flats data

iii) Correlations between Critical Elements - Original Igneous Fractionation Patterns

The criteria used by Cattalani and Bambic (1994) to determine the immobility of certain elements in a rock suite involves the plotting of bivariate diagrams (Cattalani and Bambic, 1994; Barret and Maclean, 1991, 1993). The Zr/Y ratio of the Ngubevu rocks are between 2 and 5 (3.25 to 3.94), implying that the samples adhere to the incompatible element enrichment trend from basalt to rhyolite compositions (Figure 8.21 a; Watson and Harrison, 1983). A Zr vs Nb plot (Figure 8.21 b) exhibits the original igneous correlation between elements. The Pearsons Product-moment co-efficient of correlation (PCC), at the 95% level (at which all correlations are stated) is +0.81, applicable to 65% of the population.

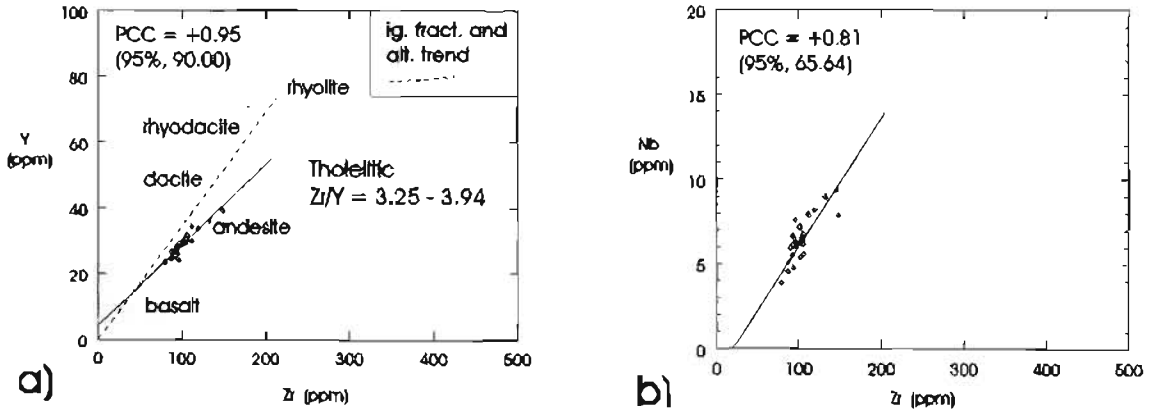

Figure 8.21 a) Bivariate incompatible-immobile element Y vs Zr plot (after Watson and Harrison, 1983; Cattalani and Bambic, 1994). A definite basalt-rhyolite fractionation trend is evident with Zr/Y between 3.25 and 3.94. PCC = +0.95, applicable to 90% of the population. Note that the trend of the data passes very near to the origin of the plot.
b) Plot of Nb vs Zr (Nb is similar to Y in geochemical behavior) showing the strong correlation of data and the preservation of igneous fractionation trends and element ratios

As there are strong correlations between geologically (and magmatically) important elements (PCC>+0.80), the use of Zr, Y, Nb but not necessarily Ti, in tectonic discrimination diagrams is possible and should yield good results.

iv) Classification and Tectonic Discrimination Diagrams

The low- to medium-K tholeiite/sub-alkali basalts of the Ngubevu area are geochemically classified in terms of their pre-collisional tectonic setting. Plots utilizing Ti, Zr, Y and Sr in bivariate and ternary form, show the Ngubevu metabasites to be ocean floor basalts (OFB) (Figure 8.22 a, b and c; Pearce and Cann, 1973).

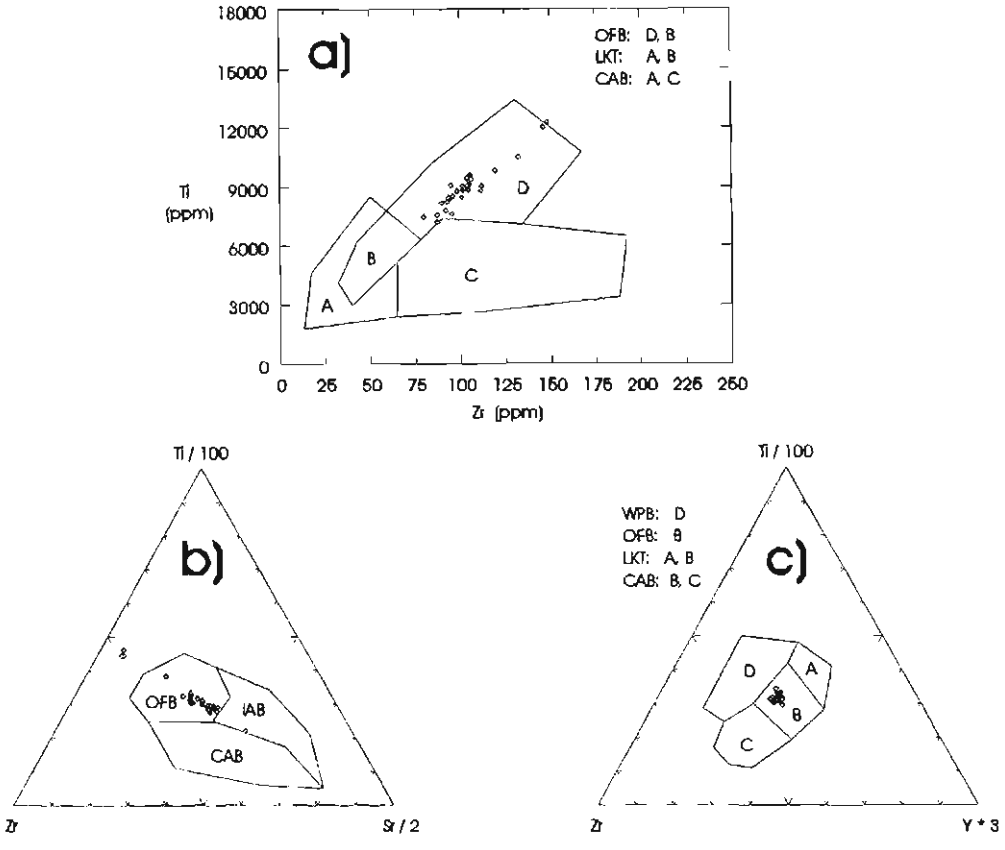

Figure 8.22 a), b) and c) Tectonic discrimination diagrams of Pearce and Cann (1973). The Ngubevu basalts plot in the Ocean Floor Basalt (OFB) field on the Ti vs Zr plot, the (Ti/100)-(Sr/2)-Zr plot and the (Ti/100)-(Y*3)-Zr plot.

The metabasites also plot in the OFB field in discrimination diagrams from more recent studies - the Ti vs Cr and Ti/1000 vs V plot of Pearce (1976) and Shervias (1982), respectively (not shown). The basalts may be better defined as Mid-Ocean Ridge Basalts (MORB) and Within-Plate Basalts (with minor Volcanic Arc Basalts- VAB) on the log-Zr vs log Ti plot of Pearce (1982 - Figure 8.23).

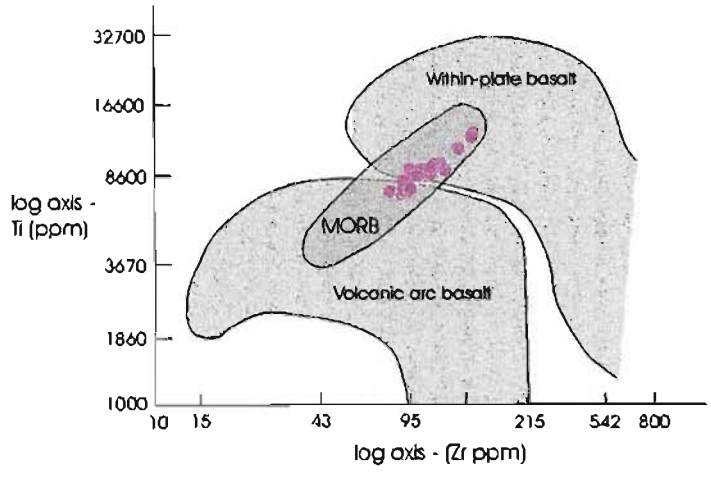

Figure 8.23 Log Ti vs Log Zr (ppm) plot of Pearce (1982). Ngubevu samples plot in the MORB field but overlap between the volcanic arc and within-plate basalt fields

Refinement of the classification of these basalts relies on Th, Zr, Nb and Y ternary plots (Figures 8.24 a and b) which impart the greatest amount of information about the type of MORB at Ngubevu. A tectonic juxtaposition of MORB types may have occured in the Ngubevu area. Samples NGW-27, 42 and NGE 1,3,4,5 plot as E-Type ("enriched") MORB on the ternary (Zr/117)-(Nb/16)-Th plot of Wood (1980). The remainder of the samples plot as Destructive Plate Margin Basalts and Differentiates. There may be a MORB type transition from the NGW to NGE areas, with E-Type MORBs being more notable in the NGE area of the Mfongosi Group.

The "E-Type MORB" samples do not display the overall low Ti and Y values and higher Nb values (e.g. Rollinson, 1993) but are identical in their major and minor element geochemistry to the remainder of the metabasite samples. Ce concentrations are notably higher and Th concentrations lower, compared to the majority of metabasite samples. It may be tentatively concluded that the difference in MORB-type is very subtle and hinges on the Th and Nb concentrations. The separation is false and is forced by Th and Nb. The discrimination of basalt types (Figure 8.24 b) shows the samples to plot almost exclusively in the N-MORB ("Normal") type field. The variable Th concentrations, particularly due to unnoticed minor intercalations of metasediment in the samples, has confused the issue and therefore Th is not considered to be a good discriminant. A discrimination diagram which does not use Th, for instance the (Y/15)-(Nb/8)-(La/10) ternary plot of Cabanis and Lecolle (1989 - Figure 8.24 c), classifies a subset of the metabasites as E-Type MORBs. The very low

or absent La values, and low Nb values, may interfere with reaching a conclusion regarding the type of MORB. La is known to be mobile under hydrothermal conditions and so highly altered basalts may show some distortion or peculiar placement, relative to the La apex. Lastly, Nb is high and variable in the metasediment; again, caution must be exercised and only samples from NGW-15 onwards must be considered and even then some samples within this group may show metapelitic anomalies due to their association with metasedimentary layers.

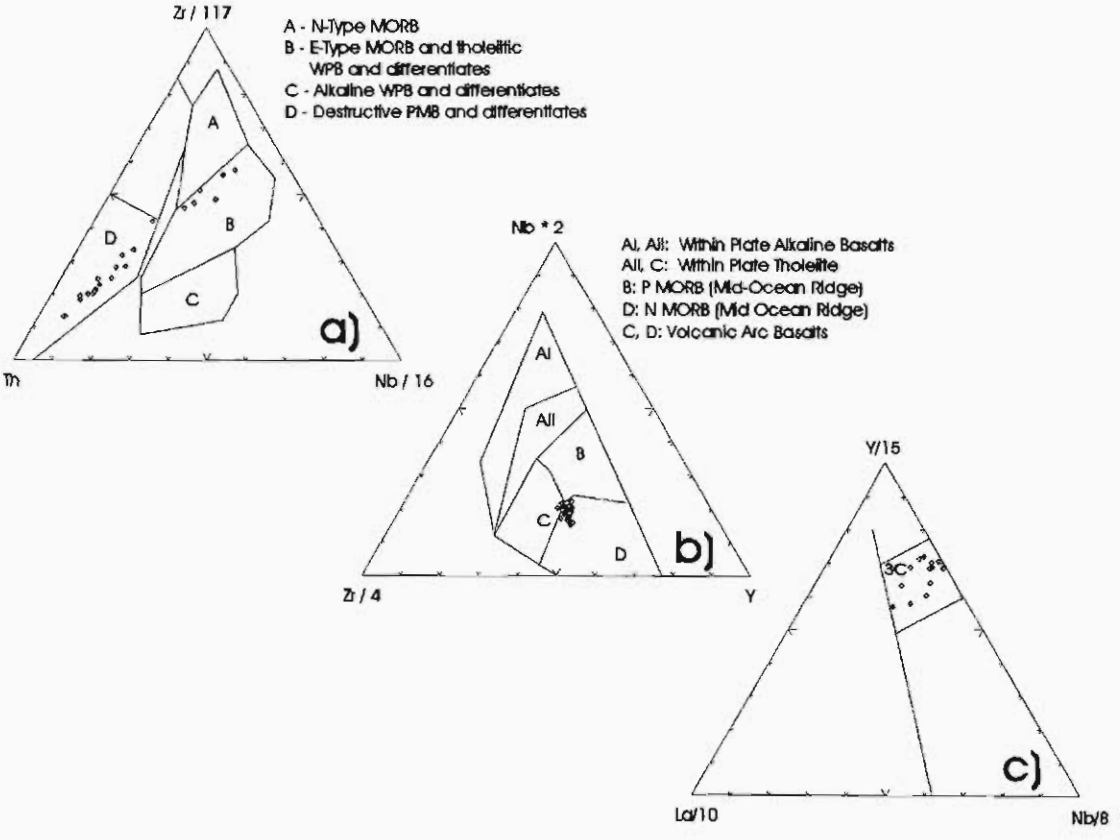

Figure 8.24a) Plot of Wood (1980) apparently distinguishing between Destructive Plate Margin Basalts and Differentiates, and E-Type MORBs. Samples NGW 27, 42 and NGE 1,3,4,5 plot in the E-Type MORB field
b) Plot from Meschede (1986) which shows the bulk of the Ngubevu metabasites to be N-MORBS. This is perhaps the most reliable plot as it does not depend on or use highly variable (i.t.o. concentration) parameters such as Th and La, which are also known to be unusually enriched or depleted in the associated metasediment
c) samples plot in the E-Type MORB field of Cabanis and Lecolle (1989). Samples NGW 15,25,28,29B,39B,40,42,42,44,52A,52B show unusual element chemistry indicate an unremarked metasediment fraction.

Th and La are not useful discriminants. Minor intercalations of the metasediment are very likely responsible for the disruption and linear format of data towards the "problem" apex (Figures 8.24 a and c). The (Nb*2)-Y-(Zr/4) plot of Meschede (1986) provides for a suitable cluster of data and classifies the Ngubevu metabasites as N-MORBs.

v) Conclusion

Metabasite samples which were relatively free of metapelitic/sapropelitic fractions were taken in order to obtain significant correlations between geologically important elements. The Ngubevu data plot coherently on bivariate incompatible-immobile plots and yield feasible results for precursor composition, despite metamorphism and metasomatism. Zr, Y and Nb (and possibly Ti) are found to be useful discriminants as their original precursor ratios have been preserved.

The Ngubevu metabasites are geochemically distinct from the metabasites of the Mbongolwane Flats area, in terms of major element oxides. Ngubevu metasediments had "high-Ti" basalt protoliths and, based on the Mg#, indicate melts in contact with cumulates. The metabasites are classified as Ocean Floor Basalts or Within Plate Basalts originating in a mid-ocean ridge setting, and / or as N(Normal)-Type MORBs on the (Nb*2)-Y-(Zr/4) plot of Meschede (1986) which obviates the need to use Th or La as discriminants.

c) Metasediments

i) Chemical Characterization - Basic Survey of Data

Mineralized, often massive quartz lenses and pods occur at the intersection of a structural feature (190°-trending antitaxial quartz-calcite veins, deformed according to the mechanisms described in Chapter 5, Section 5.3) and a finely-layered rock type, previously termed "banded", a metasediment consisting of a laterally variable series of fine bands.

The bands comprise graphite-sericite-quartz-albite-tourmaline±analcite±calcite±sphene schist; graphite-sphene-calcite-chlorite-tourmaline-quartz-albite schist and minor, thinner porphyroblastic quartz-albite-calcite-chlorite K-feldspar chloritoid schist.

Anomalous samples (NGW-A1/HR, 2A, 6, 9 and 14 - Appendix F6, which highlights some of the discriminant element concentrations or ratios which distinguish the banded rocks from the enclosing metabasites) are distinctive firstly from a lithological point of view in that they consist of finely-banded light grey graphite, white calcite-quartz and darker tourmaline bands, with or without pyrite. The graphitic component is distinguishable by its streak and the fact that it weathers negatively compared to the calcite-quartz layers.

The banded layers weather negatively compared to the enclosing epidote-actinolite schist. Potentially mineralized bands may be traced along strike with relative ease. The banded lithology exhibits a markedly higher S content than the associated schist (up to 6211 ppm S), and higher Si and K (Appendix F6, Table 8.4). Elements such as Al, Fe, Mn, Mg, Ca, Ti and P are all relatively much lower in concentration than the enclosing metabasite/schist (Appendix F6). A further distinction may be made between the mineralized banded units and non-mineralized enclosing schist in that the former have higher Pb, Th, U, Zr and Nd (Appendix F6). Other elements such as Na, Au, Sc, Co, Nb, Y, La, As, Ga and Ce do not serve as useful discriminants.

Table 8.4 Ranges of major element oxides in wt% and minor elements in ppm, which may be used for a first-order separation of metasedimentary units. The values are listed in order of most notable distinction. The numbers in brackets are means of the data (BANDED = Ngubevu area metabasediments, N=5: NGB = Ngubevu area metabasites, N=29). Average values of each set are in brackets. Elements in red denote notably higher values in the banded units while blue indicates a markedly lower value. Na_2O may not be used as a first-order discriminant.

	Banded	NGB		Banded	NGB
S	10-6211 (2771)	0-124 (36.14)	Al_2O_3	12.06-17.11 (2.87)	15.22-18.57 (17.00)
SiO_2	46.59-51.92 (48.93)	46.59-51.92 (48.93)	FeO	0.62-3.24 (1.9)	7.89-10.68 (9.10)
K_2O	1.66-4.36 (2.87)	3.9-4.15 (2.75)	MnO	0.0065-0.00637 (0.02)	1.08-1.47 (1.25)
Pb	10.3-44.2 (28.40)	0.1-21.1 (9.92)	MgO	0.68-1.3 (1.08)	10.82-14.66 (12.59)
Th	3.8-16.2 (7.9)	0-6.1 (1.9)	CaO	0-0.48 (0.2)	3.9-10.78 (9.26)
U	6.1-28.7 (15.08)	0-3.9 (0.83)	TiO_2	0.42-1.75 (1.04)	1.20-2.05 (1.50)
Zr	164-302 (212.9)	79.4-148.2 (103.7)	P_2O_5	0.03-0.17 (0.09)	0.11-0.26 (0.17)
Nd	3.2-26.5 (12.4)	0-7.3 (1.02)	Na_2O	2.56-4.99 (3.46)	4.2-9.95 (7.09)

Geochemical differences between metabasite and metasediment may be considered esoteric in the light of one being able to distinguish the lithologies from one another in favourable outcrops. However, due to the often limited thickness of the bands (2 mm) and their often very limited strike lengths (apparently only up to 10 m at Golden Dove Mine), and due to the extreme deformation of the area, careless sampling could incorporate a significant proportion of unwanted host epidote-actinolite or chloritic schist. Examination of anomalous metabasites from the Golden Eagle and Buffalo River Copper Mines reveal only slight differences in useful discriminatory element concentrations but these anomalies are identical to those for the well-recognized banded units, even though discrete banded units were not observed at the Golden Eagle and Buffalo River mines. The relative or semi-quantitative approach of rock classification, on the grounds of geochemical data has been applied. An unfortunate consequence of the inclusion of minor amounts of schistose host material is an "opaqueness" or scatter on geochemical plots however, the volume of banded material is still sufficient for the purposes of geochemical discrimination.

ii) Key Element Data Analysis - Possible Protoliths

The anomalous S, Th, U and Pb values of the mineralized rocks at the Champion Mine led the author to studies on calc-silicate/argillaceous layers interlayered with basalts and thereby to the metallogeny of black shales (e.g. Pasova, 1996) and to the importance of associated tourmaline and graphite (e.g. Karpeta, 1997). Metal-rich black shales are characterized by anomalous Zn, V, Ni, Cr, Cu, Al, Mo, Au, Pb and Pt and are ubiquitously closely associated with submarine mafic volcanic rocks in semi-isolated basins (Pasova, 1996). An example of such a relation is given by Loukola-Ruskeeniemi and Heino (1996) who describe a Ni-Cu-Zn deposit hosted in Early Proterozoic black shales in association with mafic volcanogenic rocks at Talvivaara (Finland). The ore deposit resulted from submarine volcanogenic hydrothermal activity in an anoxic basin, associated with sea-floor spreading. It must be mentioned that the presence of tourmaline in the banded lithologies at Ngubevu (De Klerk, 1995; this study) and the magmatogenic greywackes in the southern Mfongosi Valley area (Section 4.3) are indicative of the conditions that were prevalent between extrusion of volcanic material. Lateral extensions of these metasedimentary intercalations potentially host tourmaline-bearing stratabound gold deposits in unmapped portions of the Mfongosi Group to the west.

The importance of black shales has recently come to the fore in that:

- indurated black shales are essentially organic-matter rich metasediments, commonly interbanded with carbonates, which can become accumulators of trace metals as well as pyrite and sulphur (Anderson *et al.*, 1985)
- these shales may represent important sources of metals such as U, Mo, Ni, Mn, V, Hg, Sb and W
- shales of this type can serve as sources of metals and sulphur for diagenetic ores (e.g. the Kupferschiefer type - Oszczepalski, 1989) or as sources of metals for metamorphogenic deposits or even magmatic deposits
- black shales also provide a source of carbon for carbonates in siderite-sulphide vein deposits
- black shales are pivotal during deformation and metamorphism in that they are less permeable and more ductile in relation to other strata and are instrumental in trapping hydrothermal mineralization (e.g. Zentilli and Groves, 1990)

- the formation of native Fe and sulphides during interaction with tholeiitic magma or volcaniclastic layers during the deformation of the entire sequence (Pederson, 1977) may be induced by black shales

The possibility of mineralization associated with black shales (also termed "sapropelites") is discussed. The samples from this study will be compared to those of other studies via element concentration comparison. The recognition of residual fractionation trends of the associated metavolcanic samples, on bivariate immobile-incompatible element plots is an indication that element ratios have been preserved in the metasediments. The superposition of a relatively hot basaltic layer on a thin pelitic layer is likely to have caused substantial changes in the concentrations of some elements due to leaching (e.g. Haack *et al.*, 1984).

iii) Chemical Environment of Deposition

In an attempt to geochemically distinguish between groups of shales, Quinby-Hunt and Wilde (1996) utilized Ca-Mn ratios of modern black shales in known environments of deposition. As economic potential cannot be simply determined from its field lithological description or its C/S ratio, a relatively simple chemical test which serves as a guide to the environmental conditions of shale formation is needed (Berner and Raiswell, 1983). Because ambient redox (Eh) and pH conditions determine thermodynamic stability fields during deposition and early diagenesis, the geochemical characteristics of black shales may provide evidence of the chemical composition of their depositional environment (Berner, 1981). Compaction produces low porosity and permeability so that the basic chemical signature is preserved although metamorphism. Metasomatism will modify this to some degree, causing the loss of most metals (Haack *et al.*, 1984). One could infer that the metal content of the shales in the Ngubevu area was initially much higher than it is now, particularly since mapping shows the movement of metal sulphides into cross-cutting quartz-calcite veins and veinlets.

Quinby-Hunt *et al.* (1991) found four distinct groups of shales, separated on their Mn, Fe and V concentrations (Table 8.5), which were related to four particular thermodynamic zones of Eh-pH conditions. It has been established by Quinby-Hunt *et al.* (1991) that variations in Mn and Fe concentrations in low-calcic shales can be used as indicators of Eh-pH

conditions during deposition and early diagenesis. These ratios may persist through low-grade metamorphism despite the loss of other metals. Whether or not these metals retain their initial ratios is a matter of debate (*op. cit.*).

As the maximum Ca concentration is 0.34% in NGW 14 (average of 1380 ppm for the data set), the banded units at Ngubevu are low-calcic black shales, particularly since thin quartz-calcite bands in the analyzed samples would contribute to the total Ca concentration of the final, composite analysis. Quinby-Hunt and Wilde (1996) consider a shale with <4000 ppm Ca to be a low Ca-shale while Loukola-Ruskeeniemi and Heino (1996) state that metasediments in the Proterozoic of eastern Finland are defined as black shales if they contain more than 1% graphitic carbon and more than 1% sulphur. Refining the classification further, using Table 8.5, Mn<750 ppm, Fe < 37500 ppm and V is variable, being either greater than or less than 320 ppm (Quinby-Hunt and Wilde, 1993; Table 1). It is clear that the Ngubevu sapropelites fall into either Group 3 or Group 4 of Quinby-Hunt and Wilde (1996). The average concentrations of the samples in this study are given in Table 8.4 and also imply a classification into either Group 3 or Group 4.

Group 3 low-calcic shales contain reduced Fe and Mn which are relatively stable. This reflects anoxic, but apparently non-sulphate-reducing Eh and intermediate to low pH during deposition. The solubility of Mn^{2+} and Fe^{2+} and the Mn and Fe mineral stability is reflected in the low average Mn and Fe concentrations (170 and 3000 ppm, respectively) of Group 3. Group 3 samples compare to the IIb field in Figure 8.25. Note that rhodochrosite formation is possible within the Eh-pH conditions of Group 3 (Quinby-Hunt and Wilde, 1993; 1996).

Group 4 samples are low-calcic black shales also have low Mn and Fe concentrations; Mn<260 ppm (average of 80 ppm) and Fe is 36000 ppm (average of 19000 ppm). Group 4 black shales have V>300 ppm. The high V and low Mn and Fe concentrations suggest low Eh and low pH during deposition (Quinby-Hunt and Wilde, 1993; 1996). Group 4 samples correspond to field IV in Figure 8.25 (Quinby-Hunt and Wilde, 1993). It is therefore not impossible that pyrite was formed during sedimentation, as the initial Eh-pH conditions would have allowed for its formation.

Another indicator of the pelitic character of the banded units is the significant positive correlation between MnO and CaO (Pearsons product-moment correlation coefficient of +0.67, applicable to 45.08% of the sample population) which is high, given the number of samples (5). There is a far weaker positive correlation between MnO and CaO for the enclosing metabasites (PCC = +0.23 applicable to 5.25% of the population). This simple correlation may prove useful in regional sampling studies.

The Mn concentration ranges from 100 to 500 ppm and averages 200 ppm (Table 8.4). It has been mentioned that there are often abundant conformable bright red "iron-oxide" layers and veinlets crosscutting the banded units (De Klerk, 1995). Although no such veinlets were recorded, rhodochrosite, rather than Fe-oxide is likely to have been present. The occurrence of rhodochrosite is possible in view of the rhodochrosite fields of Figure 8.25 (in purple) overlapping with fields IIb and IV. Furthermore, Calvert and Pederson (1996) found that rhodochrosite and another Mn carbonate - kutnorite - in ancient organic-rich shales, limestones and marl sequences and in many Mn deposits, indicates that the sediments originally accumulated in oxygenated bottom waters. This may be the case for the layers at Ngubevu, especially since they contain fine quartz-carbonate bands indicative of at least some biogenic activity in oxygenated waters. It is unlikely that there was a rapid change in Eh-pH conditions to produce an "anoxic" shale directly over a graphite or calc-silicate layer.

Table 8.5 - Average concentrations of redox indicators in low-calcic shales (concentrations in ppm - after Quinby-Hunt and Wilde, 1993)

	Group 1 oxic	**Group 2** Mn soluble	**Group 3** Mn, Fe soluble	**Group 4** High V	This study, banded units (averages)
General characteristics	Mn>800 Fe>37500 V<320	Mn<750 Fe>37500 V<320	Mn<750 Fe<37500 V<320	Mn<750 Fe<37500 V>320	Mn=200 Fe=14769 V=352
Averages: **Mn** **Fe** **V**	1300 56000 130	310 52000 140	170 23000 170	76 19000 1500	**Conclusion: Group 3 or 4**

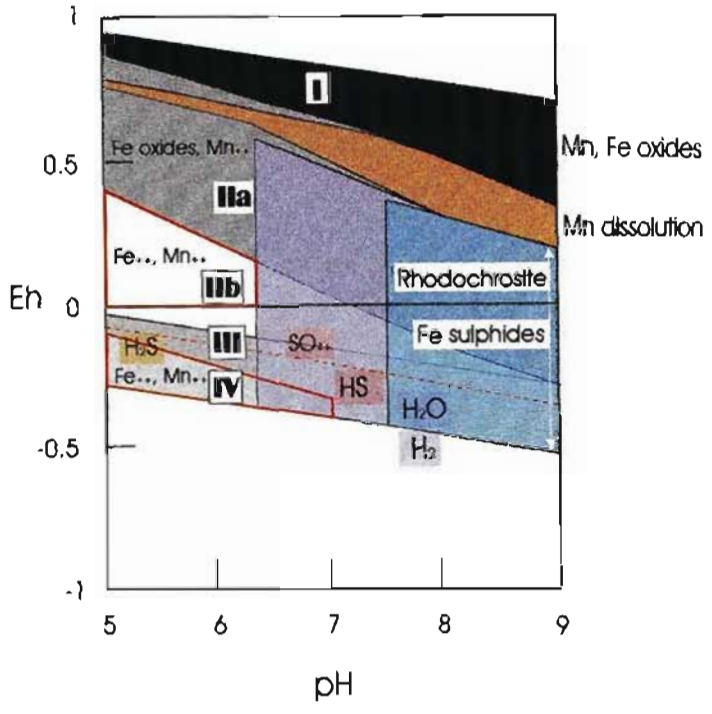

Figure 8.25 A combination of Figures 2 and 4 of Quinby-Hunt and Wilde (1996) which shows the redox zonation of black shales based on mineral dissolution, from concentrations of minerals observed in oxic seawater. The base of the "Mn-Fe oxides" field marks the reduction of NO^{3-} to N^{3} and is usually considered as the boundary between oxic and anoxic conditions. Reduction of SO_4^{2-} to H_2S and HS^- (red, dashed line) indicates the boundary between oxic and sulphide species. Note that the correspondence is not exact as pyrite can appear within the sulphate stability zone. Also shown are the Eh-pH fields for Mn in seawater. Black area = Mn oxide phase stable under oxic conditions of dissolved Mn. The area marked "Mn dissolution" which is the region in which Mn oxides dissolve until concentrations observed under anoxic conditions are reached. The rhodochrosite stability fields are shown under two conditions: the purple area where total dissolved carbonate species is that of modern oceans and the blue field where the total dissolved carbonate species is 18x its normal concentration. The areas outlined in red conform to the conditions proposed for the formation of the Ngubevu banded units.

In a study of Phanerozoic analogues for carbonaceous matter in Witwatersrand deposits, Parnell (1996) places emphasis on the colour of black shales or "bitumens". In Early- and Late-Proterozoic siliclastic sequences, uraniferous bitumens are red bands whereas predominantly thoriferous bitumens occur in white-grey beds, a feature which reflects the preferential mobility of U and Th in high and low Eh conditions, respectively. Given the white-grey colour of the banded layers at Ngubevu and the inferred low Eh value of about -0.25 (Figure 8.25), it is likely that some component of the thoriferous bitumen of Parnell (1996) is present at Ngubevu.

Loukola-Ruskeeniemi and Heino (1996) classify black schists or shales on the basis of Ni and Mn contents: the classification scheme places Ngubevu samples into the low-Ni-Mn (Ni<0.1%, Mn<0.8%) class. In their study, graphite typically occurs as small flakes, often with pyrite and chalcopyrite; graphite flakes are coarser in strongly deformed zones, for

example near quartz veins, as is found at Ngubevu. The banded units cannot, however, be classified as black "calc-silicates" (typically Ca>= 3.5%) which are more abundant in association with Ni- and Mn- rich black schists. As expected, Al and Zr correlate negatively as in black schists which are geochemically restricted (Loukola-Ruskeeniemi and Heino, 1996). This geochemical restriction points to a basin of limited size or a "restricted basin" such as one that would occur behind a volcanic island arc in proximity to a continental margin or another island arc.

iv) Possible Tectonic Environment of Deposition

Two possible fields of Eh-Ph conditions could have applied in the formation of the black shales at Ngubevu (Figure 8.25). Zone A where field IIb overlaps with the rhodochrosite field or the entire field IV (Zone B) wherein the formation of pyrite-rich layers is made possible. The scarcity of layered rhodochrosite (De Klerk; 1995, this study) may be explained simply by the very low concentrations of Mn in the banded units. Maynard (1982) and Tiebing *et al.* (1996) state that black pelites with a high total organic carbon content and diagnostic pyrite represent a relatively deep-water, low energy, reducing, even euxinic environment. In such a depositional environment, manganese is concentrated in oxygen-deficient seawater. Conversely, the banded units at Ngubevu display low Mn and pyrite concentrations and suggest an environment of deposition at variance to that mentioned above, that is, possibly oxic and in shallow water.

The thickness of the carbonate-quartz bands and the entire thickness of the banded lithology at the Champion Mine, imply very short-lived periods of sapropelite/shale deposition. Although the Champion and Golden Eagle mines occur along a horizon which represents a period of significant sedimentation of black shales, such sedimentary activity was erratic, indeed, there has been insubstantial development of black shale layers at the Golden Eagle Au and Buffalo River Cu mines. This difference in sedimentation, may be a consequence of palaeotopography - it is unlikely that there was any great differential downwarping between the mined areas over a distance of 150 m. An alternative hypothesis could be syn-depositional folding of the stratigraphy, prior to renewed volcanism, which would in turn imply a complex interaction between tectonism and sedimentation. Carbonate formation seems to have been

more prevalent to the north of this accreted terrane, the highly deformed Ntingwe limestone (Matthews, 1959).

Calvert and Pederson (1996) conclude that the presence of carbon/graphite seams is a direct result of a high supply of organic matter to sediments deposited under oxygenated bottom waters, probably in continental margin settings, the upper margins of continental slopes or in nearshore basins. These settings are considered as having high productivities of organic-rich sediments (*q.v.* Pederson and Price, 1982; Shimmield and Price, 1986). A useful feature of the graphite-bearing horizons is that they may be distinguished from other quartz-rich metasediments by their strong electrical conductivity, however, this contrast may not be as well-defined for graphite-bearing layers interbanded with metabasites on such a scale as that at Ngubevu. Resort should be made to the anomalous Th, U and S values or Mn:Ca ratios of the black shales in prospecting, rather than those of base metals or gold.

v) Significance of Tourmaline-Graphite Association

De Klerk (1995) located substantial occurrences of black tourmaline (thin section studies), in the same finely-banded format as the black shale/graphite/calcite/quartz layers, along strike from the abandoned workings in the Ngubevu area. Tourmaline-related mineralization is well known and seems to naturally fall into two main groups distinguishable on the basis of their origin. The first type is classified as "syndepositional exhalative" which encompasses an origin in boron-rich hydrothermal fluids exhaled onto the seafloor, precipitating boron-rich sediments with anomalous gold (Karpeta, 1997).

The second style of mineralization involves hydrothermal boron-rich fluids, derived from granitoid intrusions, migrating up major fractures to react with chemically responsive rocks such as carbonaceous shales, particularly in domes beneath impermeable caprocks (*op. cit.*). Table 8.6 includes a description of very thin bands (10 cm thick) which have host rocks not dissimilar to those at Ngubevu (i.e. pelites, mafic volcanics/volcaniclastics/tuffs, graphitic pelites and carbonaceous schists). These deposits are classed mainly as exhalitives and occur in greenstone to gneissic terranes, of widely varying ages, which have undergone greenschist to amphibolite facies metamorphism. Even though B could not be analyzed for in the

Ngubevu samples, the similarities in terms of age, country rocks, metamorphism and regional tectonic setting, to Brazillian stratabound tourmalinites summarized by Karpeta (1997), are striking.

Tourmaline-hosted mineralization is most often found in relation to some of the well-known gold and base-metal schists in other parts of the world. One of the most well-known of these deposits is the Athabasca Ni-As (Co, Fe) deposit which comprises mainly pitchblende with subordinate coffinite and envelopes of chloritization, silicification, tourmalinization and calcite-dolomite vein impregnation (Guilbert and Park, 1986). The key elements in the formation of Athabasca were the co-mingling of reducing, graphite-buffered, methane-bearing fluids from below (basement gneiss and interlayered/infolded metapelite) with oxidizing heamatite-buffered U^{6+}-bearing fluids from along the unconformity with the overlying Athabasca Formation sandstone (*op. cit.*). Welty (1980) considers metamorphosed marine or volcanic sediments, typically pelitic or calcic shale protoliths (locally with graphite), as being the prime ingredient in Athabasca-type mineralization.

In considering deposits related to submarine volcanism and sedimentation, it is profitable to consider the overall tectonic context of black shales. It is an oversimplification to apply the terms "proximal" and "distal" to volcanic centers without knowledge of the exact location of the volcanic epicenter or the point of venting of volcanically-derived fluids into marine basins.

Table 8.6 Summary of well-known Brazillian tourmaline-hosted/related gold deposits (after Karpeta, 1997), after Da Silva (1991) and Texeixeira and Kuyamjian (1991). GS = Greenschist, AM = Amphibolite

Locality (Brazillian State)	Stratigraphic Unit	Thickness (m)	Country Rocks	Metamorphic Facies	Possible Tourmailine Precursors	Possible origin of Tourmaline	Setting
Passegem De Mariane	Minas Group	0.1-0.3	pelites, carbonates, BIFs, mafic volcanics	GS	-	exhalative	forearc
Rio Oliveira/Itapema	Brusque Complex	0.1-1.0	calc-silicates, mafic tuffs, pelites, coticule	GS/AM	boron-rich (tourmaline) chemically-precipitated sediments	sedimentary/ exhalitive	gneiss belt
Serra Do Itaberaba	Serra Do Itaberaba Group	-	metabasalts, mafic tuffs, pelites, calc-silicates, BIFs	AM	-	exhalative	greenstone belt
Pilar Do Sul	Setuva Group	-	mafic schists, quartzites, gondites, graphitic pelites	GS	-	exhalative	greenstone belt
Pitangui/Mateus Leme	Pitangui Greenstone Belt	-	BIFs, graphitic cherts, mafic and ultramafic schists	-	-	exhalative	greenstone belt
Ivaporunduva	Setuva Group	0.1-4.0	pelites (locally graphitic), felsic tuffs	GS	boron-rich (tourmaline) chemically-precipitated sediments	exhalative	greenstone belt
Anapolis Sheet	Silvania Sequence	0.1	pelites (locally graphitic)	GS/AM	boron-rich (tourmaline) chemically-precipitated sediments	exhalative	greenstone belt
Chapdao	Porongos Complex	0.1 -0.3	pelites with carbonaceous schist	GS	boron-rich (tourmaline) chemically-precipitated sediments	exhalative	gneiss belt
Guarinos	Guarinos Greenstone Belt	0.1-4.0	graphitic pelites and mafic schists	GS	-	exhalative	greenstone belt
Sao Caetano	Embu Complex	0.1-0.3	pelites and mafic schists	AM	boron-rich (tourmaline) chemically-precipitated sediments	exhalative	gneiss belt

It is, however, appealing to think in terms of a progressive shift from proximal to distal as involving the progressive dilution of volcanic components by terrestrial, terrigenous sediments as one moves from the volcanic arc side to the continental side of an oceanic back-arc basin (Guilbert and Park, 1986). These concepts necessitate the movement of metals and S for up to 200 km - an unlikely scenario. A more likely origin for metallization are altered, mineralized conduits in the immediate footwall to the black shales. What few of these deposit models consider is the subsequent deformation (over and above alteration during diagenisis) of the volcanic/volcaniclastic-shale sequence and the emplacement of veins under constrictive or transpressional settings. This may approximate a syn-depositional fluid system; pressure solution and greenschist facies metamorphism which could supply the medium for fluid movement and mineralization of fine sapropelitic/black-shale layers.

A ternary plot of Al_2O_3-(FeO+MgO)-CaO is instructive; the relatively higher Al_2O_3 concentration in samples of interest indicating a significant shale fraction (Figure 8.26). The trend found on Figure 8.26 approximates the situation of advanced argillic or phyllic alteration (Meyer and Hemley, 1967; Guilbert and Park, 1986). This feature, along with high U, Th and V values, a correlation between Ca and Mn and a potentially high electrical conductivity in areas where graphite bands may be thicker, could be useful in exploration.

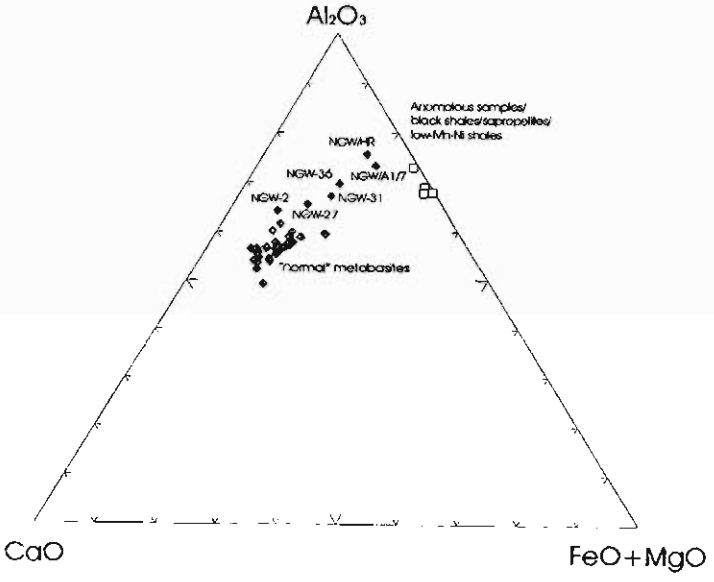

Figure 8.26 Ternary Al_2O_3-CaO-(FeO+MgO) plot of Guilbert and Park (1986). "Anomalous" shale samples plot closer to the Al_2O_3-(FeO+MgO) join than the metabasite samples. Samples from the Champion Mine (blue squares) plot almost directly on this join while samples with fine metapelite bands or sapropelitic affinities (black squares), plot between the bulk of the metatholeiite data (green squares) and the Champion Mine data. It is significant that these "intermediate" samples were taken from or very near the adit at the Golden Eagle Mine.

vi) Conclusion

In the Champion Mine area, a distinct, finely-banded metapelite/sapropelite layer is present. The banded units essentially consist of finely-interbanded (on the scale of 2-5 mm) layers of calcite+quartz, graphite and metapelite with or without tourmaline. The banded layers are chemically distinguishable by having significantly higher S, Th, U, V, Pb, Nd and Al concentrations than the associated metabasites. Higher concentrations of Si and K, but lower concentration of major elements such as Fe, Mn, Mg, Ca, Ti and P are recorded for the banded layers. Elements such as Au (positive correlation with S), Sc, Co, Nb, Y, La, As, Ge and Ce are not useful parameters in lithological separation. The banded layers display positive correlation between MnO and CaO, an indication of a pelitic character.

The sapropelitic fraction of the banded units, which is dominant in the samples studied here, fall into Group 3 and/or Group 4 of the low-calcic shales of Quinby-Hunt and Wilde (1996), based on their Mn, Fe and V concentrations. The metapelite may be classed as a low-calcic shale as it contains less than 4000 ppm Ca. Comments by de Klerk (1995) regarding bright red oxide layers could be taken to imply the presence of primary rhodochrosite, the scarcity of which is probably due to the very low Mn content of these samples (average of 200 ppm Mn). A consideration of major element concentrations leads to the conclusion that the metapelites formed in the pH range of 5 to 7 and an Eh range of -0.4 to -0.1 or 0 to 0.4 (*c.f.* Quinby-Hunt and Wilde, 1996). Pyrite formation is possible in these Eh-pH conditions although it must not be assumed that anoxic environments prevailed during the deposition of the pelites. The low Mn and pyrite concentrations in the pelites indicate an oxic, shallow-water environment of deposition, by the reasoning of Maynard (1982) and Tiebing *et al.* (1996). This conclusion is supported by the finely-interbanded quartz-calcite and graphite (ex-carbon) layers which are also indicative of shallow water, oxidizing conditions. A chemically restricted basin of deposition allows high productivities of organic-rich sediments (*q.v.* Pederson and Price, 1982; Shimmield and Price, 1986).

The tectonic setting of the banded layers was a continental margin, the upper margin of a continental slope or a nearshore basin. The depostition of the metapelites and associated calcite-quartz and graphite layers was interrupted by the extensive outpouring of the basalts

which constitute the bulk of the Ngubevu and adjacent areas. It is also evident that periods of sedimentation were much shorter-lived than at the southern Mfongosi Valley area. This may be a relic of the change in dip of the underlying Kaapvaal continental margin, from steep in the west to shallow in the east, or an indication of entirely different pre-collisional settings of volcanism and sedimentation from east to west or, a "false" distribution produced by accretion.

Tourmaline layers, interbanded with graphitic pelites and minor calcsilicates, both interbanded with mafic schists is a strong indication of a statabound tourmalinite-like genesis (*c.f.* Da Silva, 1991; Teixeira and Kuyumtian, 1991).

Chapter 9

Synthesis of Relevant Structural Features in the Natal Thrust Front and Natal Nappe Zone

The Natal Thrust Front exhibits different deformational features to the Natal Nappe Zone (Figure 9.1). Deformation of the leading edge of collision, the Natal Thrust Front, formed S-c and D-a fractures in the initial increment of folding. The first stages of fluid-flow filled these fractures with quartzitic and segregated mafic material. Subsequent deformation and tightening of folds caused veins to be rotated into parallelism with an embryonic S_1, producing a girdle distribution on stereonets. Following this, a left-lateral shearing regime persisted or became dominant in the Mfongosi Group. Slickenlines on S_{01} and on the margins of veins define a consistent north- to north-easterly convergence of folds.

With continued transpression, veins in the areas directly adjacent to the Kaapvaal Craton became segmented and were incorporated as clasts in a large-scale matrix:porphyroblast system. Vein segment rotation indicates a minimum shear strain of γ=1.8. The cataclastic matrix in these areas developed a discordant foliation, S_2, and steeply southwest-plunging kink folds in the Northen Mfongosi Valley. Such features are absent towards the southern margin of the Mfongosi Group towards the extensive base of the nappe zone. In these areas slickenlines indicate a temporal clockwise rotation of σ_1 and σ_2 within the thrust front (Figure 9.1).

The base of the Tugela Nappe exhibits consistent top-to-north shearing and boudinaging of veins and relic pillow basalts. Superimposed on these steeply south-plunging, prolate pillow basalt segments are slickenlines indicating left-lateral movement during continued northeasterly convergence. Slickenlines, along which syn-thrusting hornblende has crystallized, indicate the same clockwise rotation of σ_1 and σ_2 as found in the Natal Thrust Front (Figure 9.1).

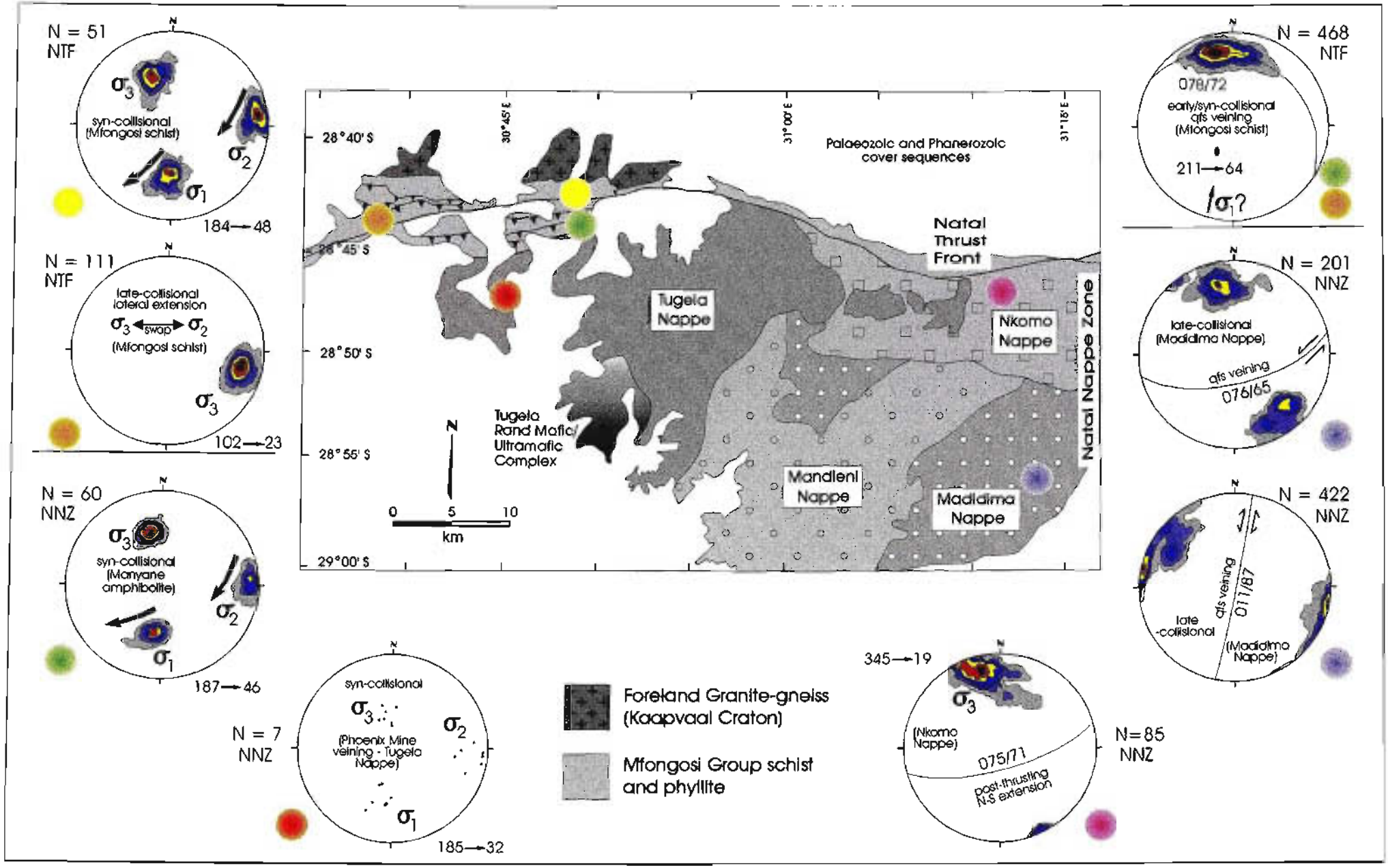

Figure 9.1 Summary of the salient structural features of the Natal Thrust Front and Natal Nappe Zone. Structural data indicate that 1) the western areas of the thrust front underwent greater strain than the eastern areas 2) left-lateral transpressional motion was not limited to the south of the Lilani-Matigulu Shear Zone 3) exploration for vein-type deposits must take into account this left-lateral motion and its effects on vein morphology. Data of post-thrusting N-S extensional veins from the Nkomo Nappe is added for the sake of completeness

The Ngubevu area has undergone extreme strain: early-formed veins filling S-c and D-a fractures display flattening and shearing into parallelism with S_{01} and S_2 (Figure 9.1). Early-tectonic tension gashes formed parallel to the ambient σ_1 (190°) are highly deformed and crenulated into fish-hook and ptygmatic folds. Thickened limbs of fish-hook folds are transformed into sub-economic mineralized blows where they intersect metabasite/metacalcsilicate bands. Thinned fold limbs formed stringers parallel to the host planar foliation. Syn- to late-thrusting lateral extension is implied by dilation of tension gashes (parallel to σ_3 at 102°→23°), and the deformation of epidote glomeroporphyroblasts in the metabasite. Combined pure and simple shear strain in the Ngubevu area produced finite strain ratios as high as R=12. Negative dilation (pure shear component) across the area is approximately 0.5. There is a marked increase in strain from the center (Mfongosi Valley area) to the westernmost extremity of the thrust front (Ngubevu Area).

The Mbongolwane Flats area exhibits evidence of strain mechanisms at variance to those of the thrust front. The dominant shear orientation and location is controlled by an F_2 fold in competent Thaweni granite-gneiss which intruded relatively incompetent amphibolite and amphibolitic gneiss. The competent southern margin of this regional F_2 fold altered the dominant fold orientation within the metabasites. A discontinuous left-lateral shear system incorporating block rotation is evident. North-northeast to north-east-trending veins are hosted on the margins of kilometer-scale blocks which contain complex folding.

The Tugela Nappe displays signs of transpressional motion: slickenlines on veining in the Phoenix Mine indicate a σ_1 orientation of 185°→32° (Figure 9.1). This orientation is intermediate between that indicated by the 190°-trending tension gashes in the Ngubevu area and the 180°-trending prolate pillow basalts in the Manyane amphibolite. The author concludes that "late-tectonic"shearing in the Mzumbe and Margate terrains, was not limited to the southern unexposed margin of the Kaapvaal Craton, coincident with the left-lateral Lilani-Matigulu Shear Zone. Left-lateral movement, north-easterly emplacement of the nappe zone in hinterland-dipping complex, and deformation of the para-autochthonous thrust front in mainly north-easterly vengeance is indicated.

Fluid-Flow Regimes in the Natal Thrust Front and Natal Nappe Zone

Oxygen isotope studies from both the Natal Thrust Front and the Natal Nappe Zone allow a qualitative assessment of fluid-flow regimes during vein formation (Figure 9.2). Infilling of S-c and D-a fractures occurred during early tectonism. These fractures formed by early buckling of the Mfongosi Group in a short-lived, non-advective, rock-buffered fluid flow system which initiated the emplacement of recrystallized wall rock material (segregated quartzofeldspathic and mafic fractions). The initial variability of $\delta^{18}O$ (vein) corresponds to the initial variability in host rock composition and isotopic signature. Veins in the metagreywacke-dominated Northern Mfongosi Valley exhibit $\delta^{18}O$ values suggestive of ^{18}O fractionation with mainly quartz-rich host rocks. An increasing metabasite component is conversely associated with a lower $\delta^{18}O$ value (e.g. the Southern Mfongosi Valley and Ngubevu areas). The fluid flow was implicitly initially layer-scale and seems to have been longer-lived in the Ngubevu area compared to other areas - a fact which probably corresponds to the comparatively higher strain ratios encountered at Ngubevu.

The emplacement of the Natal Nappe Zone above the Natal Thrust Front contributed to a short-lived fluid-flow system in the Mfongosi area. This resulted in a short-lived thermal pulse which caused fluid movement towards the extensive basal thrust of the nappe zone in a local convective fluid system. The movement of fluids *towards* the 80 km long basal thrust plane of the nappe zone partly accounts for the lack of Carlin-type mineralization or extensive metasomatism of the Ntingwe limestone. Late-tectonic carbonate metasomatism of the Mfongosi Group and the adjacent Manyane amphibolite was caused by carbonate-rich fluids derived from the Ntingwe limestone.

Continued deformation caused the fluid phase to became more rock-buffered and open with the convergence of $\delta^{18}O$ (vein) values of progressively later-tectonic quartz-calcite tension gashes. The latter stages of fluid movement were probably controlled by advection rather than diffusion in a pervasive fluid phase under low fluid:rock ratios. A greater-than layer-scale, CO_2-rich fluid movement system is proposed for late-tectonic times. No influence of a magmatic fluid source is evident; a fact strongly supported by $\delta^{18}O$ (vein) vs $\delta^{18}O$ (whole rock) plots.

The Mbongolwane Flats area exhibits evidence of a kilometre-scale, open advective system which provided fluid-mediated/fluid-buffered exchange between co-existing rocks. The fluid regime would have been driven by residual heat from early- to syn-deformational intrusions. The $\delta^{18}O$ (vein) vs $\delta^{18}O$ (whole rock) plots indicate a paucity of intrusion-derived fluids, as is the case for the Natal Thrust Front.

Veining in the Ayres Reef (hosted in the Manyane amphibolite) and the Phoenix Mine (hosted in the metagabbro/metanorite of the Tugela Rand Complex), resulted from the tapping of late-tectonic metamorphic fluid reservoirs. The fluids caused extensive metasomatism and leaching of wall rocks. A highly channelized, single-pass fluid system is suggested for both sets of veining. The salient features of veining in this study are summarized in Table 9.1.

Table 9.1 Summary of the characteristics of veining encountered in the Natal Thrust Front and Natal Nappe Zone.

Area	Tectonic Unit	Host Lithology	Composition	Timing	Fluid Flow Regime	Type / Model
N+S Mfongosi Valley	*Natal Thrust Front*	Mfongosi schist (metagreywacke, metabasite)	quartz, hornblende, chlorite, galena, argentite	early- / syn-collisional	short-lived, non-advective, rock-buffered, layer-scale	metamorphic
Ngubevu East + West	*Natal Thrust Front*	Mfongosi schist (metapelite/ metacalcsilicate, metabasite)	1) quartz, hornblende, chlorite, serpentine 2) quartz, calcite, actinolite, chlorite	1) early- / syn-collisional 2) late-collisional	1) short-lived, non-advective, rock-buffered, layer-scale 2) open, rock-buffered, advective, pervasive; low fluid:rock ratio, greater-than layer-scale	metamorphic (related to black shale / tourmalinite-type mineralization and remobilization)
Mbongolwane Flats	*Madidima Nappe*	Metabasite, amphibolitic gneiss /metaluminous granitoids	quartz, pyrite, chalcopyrite, calcite, chlorite	late-collisional	km-scale, open, advective, fluid-mediated / fluid-buffered exchange between rock types; (driven by residual heat from early- to syn-tectonic intrusions)	metamorphic, possibly Cordilleran-type
Phoenix Mine	*Tugela Nappe*	meta-gabbro / meta-norite	quartz, malachite, pyrite, magnetite, siderite	syn- / late-collisional	tapping of syn- to late-tectonic metamorphic fluid reservoirs, highly channelized, single-pass fluid-flow system	metamorphic, Cordilleran-type

The Natal Thrust Front exhibits both a lateral and an across-strike (N-S) variation in lithologies (Figure 9.3). In the easternmost portion of this inlier, metasediments dominate and basaltic components are absent. The Nkandlha area exhibits rocks similar to the northern Mfongosi Valley area, that is, melanged metagreywackes in which veins are fragmented and assume the morphology of a macro-scale left-lateral clast/matrix system.

The Mfongosi Valley and Ngubevu areas reveal two important features. The first of these is a north-south change in metabasite/metasediment proportion between the northern and southern Mfongosi Valley areas. To the north, within about 1.5 km of the exposed southern margin of the Kaapvaal Craton, no metabasite units are distinguishable and the area is simply a melange of veined metagreywacke of various description. The Mfongosi Group in the southern Mfongosi Valley area contains minor metamorphosed sub-alkaline basalts to andesites of normal (N) mid-ocean ridge affiliation, which are interlayered with very immature meta-greywackes. The greywackes were derived from predominantly felsic source rocks set in a hinterland free of mafic or ultramafic rocks (i.e. the southern margin of the Kaapvaal Craton). In terms of tectonic provenance, the meta-greywackes formed on an active continental margin or in a continental arc setting. The minor interbanded metabasites indicate a distal volcanic source and this terrain may be regarded as being relatively (*c.f.* Ngubevu terrain) in situ or para-autochthonous.

The Ngubevu area contains a predominance of metabasites hosting thin intercalations of metasediment. The metabasites are classified as ocean floor basalts or within plate basalts which originated in a mid-ocean ridge (volcanic arc?) setting, as N (Normal)-type MORBs. The finely-layered metasedimentary units comprise metamorphosed sapropelites, pelites, calcsilicates and tourmalinites. The metapelite protolith was a low-calcic shale which formed in a pH range of 5 to 7 and an Eh range of -0.4 to -0.1 or 0 to 0.4. An oxic, shallow water environment of deposition prevailed during sediment deposition. Tourmaline bands within the graphitic schist member of the metasedimentary layers may allow the application of the stratabound tourmaline model. The area just to the west of the Ngubevu area would be particularly revealing as regards ore deposit modeling, although Palaeozoic and Phanerozoic cover hampers exploration efforts there.

The Ngubevu area exhibits very high finite strain ratios (approximately R =10-12) which are at variance to those evident in the Mfongosi Valley area. The reason for this may be that the Ngubevu terrain is fully allochthonous and/or oblique transpression has imposed a more extensive period of early ductile deformation in the westernmost portions of the Natal Thrust Front.

It is proposed that the Ngubevu area accreted onto the southern margin of the Mfongosi "low-metabasite" terrain and that a tectonic contact may lie between the Mfongosi Valley and the Ngubevu area. Alternatively, there may have been a lateral gradation of sediment proportion and types between the two areas (Figure 9.3) although this gradation is likely to have been highly disturbed. A survey with Gold Fields' geologists showed that the melange zone persists laterally across the northern edge of the Mfongosi Group although the melange becomes darker as the metabasite content increases.

A north-east / southwest distribution of zones within the Natal Thrust Front, albeit deformed and transposed, is implied by the data. The main point in this study is that the Ngubevu terrain may comprise the slopes of a distinct island arc in addition to those island arcs incorporated in the Mzumbe and Margate terrains (Thomas, 1989 b). The southern presence of an island arc would have provided a shallow water, oxic sedimentary environment in the west, in which metapelites and sapropelites formed. The basin would have deepened eastwards into the marginal sea between the island arc and the craton margin. The curvilinear form of the southern margin of the craton suggests the northern, northwestern and western limit of such a basin (ref. Figure 1.1). Oblique, transtensional motion of an island arc, progressively more deformed and truncated on its western side, caused a progressively more restricted shallow basin, but in the western portions of the Natal Thrust Front.

Clastic sedimentation rates in the central and eastern portions of the craton margin would have increased with the uplift caused by collision. Basalt extrusion from the island arc would have been more pronounced in the west but diluted by clastic sedimentation to the east, aided by the increase in dip of the Mfongosi Thrust and the overlying thrust front from west to east (Matthews, 1972). In the west (shallower parts of an asymmetrical, trough-shaped basin) these features are recorded as

being gently-dipping, whilst further eastwards the dips of the Mfongosi Thrust and the thrust front increase to a steepness more characteristic of a continental margin, implying a concomitantly higher craton-derived sediment input during the mid-Proterozoic.

The author proposes that the rock types in the largely bimodal Mfongosi Group were initially distributed in a NE-SW manner, prior to the completion of collision and that the current configuration is merely a transposition of this distribution with simple shear having largely obliterated signs of pure shear strain. It is postulated that left-lateral movement in the western parts of the Mfongosi Group was prevalent throughout collision. This contrasts with the Mfongosi area where the orientation of prolate pillows in the Manyane amphibolite indicate predominantly northwards vengeance with a minor component of late-tectonic, left-lateral motion. This implies an anticlockwise motion of the entire island arc, accompanied by a converse clockwise rotation of slickenlines and stress axes orientation as the left-lateral motion propagated eastwards, becoming dominant at progressively later stages of collision. It is proposed that left-lateral motion would be dissipated and minimized towards the easternmost portions of the inlier but that this motion is by no means limited to areas to the south of the Lilani-Matigulu Shear Zone. Exploration programs which target vein hosted gold and base metal mineralization should take the tectonic evolution of this highly complex area into account.

Acknowledgements

The author wishes to express his gratitude to the following companies, institutions and persons for their assistance in the completion of this study:

Gold Fields of South Africa, Gold Fields Mining and Development, Gold Fields Training Services for their generous sponsorship of study fees, field vehicle and fuel, caravan, subsistence, the cost of geochemical analyses and gold assays, thesis printing costs, photograph development costs and for prompt logistical support in many other areas including the payment of a full salary during the last four months of the project. In particular, the following persons are thanked: Dr R. P. Viljoen, P. Vickers, S. Hill, R. Osborn, C. Pearman and P. Lambert.

The Staff of the University of Natal (Durban), Department of Geology and Applied Geology in which is included the main supervisor of the project, Prof. M. K. Watkeys and the secondary supervisor, Prof. A. H. Wilson. Prof. M. Watkeys was pivotal in productive discussions on the project, review of written material and general encouragement towards the final stages of completion. Other members of staff which provided stimulating discussion or encouragement were: Prof F. G. Bell, Prof. J. Krynauw, R. Uken and J. McCarthy. Prof. Bell earned my gratitude and respect by being a constant source of support and encouragement, even though he did not directly supervise the thesis. C. Jermy is thanked profusely for his unfailing assistance in computing problems. The staff of Africa Geological Services, including R. Seyambu, M. Seyambu and P. Suthan, are thanked for their assistance in the analysis of whole rocks and veins. The technical staff, I. Houston, V. Pakiri and G. Chetty are thanked for their slide preparation and assistance in various technical matters.

The Foundation for Research development (FRD) for a two-year research grant which assisted greatly in establishing a home-from-home in the field.

The University of Cape Town, Department of Geological Sciences, and in particular Dr C. Harris, for excellent supervision in oxygen isotope analyses, and for use of an in-line reaction/extraction facility and mass spectrometer. The University of Cape Town Department of Geological Sciences is also thanked for accommodation during the author's stay.

Reviewers: S.T. Johnstone (School of Earth and Ocean Sciences, University of Victoria), D.L. Reid (Department of Geological Sciences, University of Cape Town) and J. Reinhardt (School of Geological and Computer Science, University of Natal, Durban) are thanked for their diligent review of the manuscript, and for comments and suggestions which improved the final product immeasurably.

The authors friends, in particular A. H. Bellengére, D. Spurrett, M. Jelbert, S. Masters, R. Stenhouse, N. Crankshaw, N. Klug, A. Cooper, C. Haycock, W. Ambrose, J. Ambrose, D. Meth, W. Miller, I. Wright, P. Ramsay, D. Walker and E. Hingston are thanked for equal proportions of chastisement and encouragement. The author expresses his thanks to D. A. Barrowman for his patience with late-night studying and early morning arrivals. My landlady, Joy Ross and her wonderful family are thanked for their concern and her excellent meals during studying ("..to keep my strength up...."). The author expresses his gratitude to Natalie, for her unwavering fortitude in the face of so much part-time studying. Lastly, the greatest debt of gratitude needs to be expressed: to God who created me and made all this possible and so very rewarding - thank you.

References

Abbey, S. (1989). The evaluation of reference materials for rock analysis. *In:* Ahmedali, S.T. (Ed.), *X-Ray Fluorescence Analysis in the Geological Sciences: Advances in Methodology*. Geol. Assoc. Canada: Short Course 7, 38pp.

Alt, J.C. and Honnores, J. (1984). Alteration of the upper oceanic crust. Deep Sea Drilling Project (DSDP), Site 417: Mineralogy and Chemistry. *Contrib. Mineral. Petrol.*, **87**, 149-169.

Alt, J.C., Honnorez, J., Laverne, C. and Emmerman, R. (1986). Hydrothermal alteration of a 1 km section through the upper oceanic crust, Deep Sea Drilling Project (DSDP), Hole 504B: Mineralogy, chemistry and evolution of seawater-basalt interactions. *J. Geophys. Res.*, **91**, 10309-10335.

Anderson, A., Dahlman, B., Gee, D. and Snell, S. (1985). The Scandinavian alum shales. *Sverige Geologisca Unders. Ser. Ca.*, **56**, 86pp.

Apotria, T.G., Snedden, W.T., Spang, J.M. and Wiltschenko, D.V. (1993). Kinematic models of deformation at an oblique ramp. *In:* McClay, K.R. (Ed.), *Thrust Tectonics*. Chapman and Hall, Great Britain, 141-154.

Barkhuizen, J.G. and Matthews, P.E. (1990). Gravity modelling of the Natal Thrust Front: A mid-Proterozoic crustal suture in southeastern Africa. *Abstr. Geocongr. Geol. Soc. S. Afr.*, 32-35.

Barret, T.J. and MacLean, W.H. (1991). Chemical mass and oxygen isotope changes during extreme hydrothermal alteration of an Archaean rhyolite, Nornada, Quebec. *Econ. Geol.*, **86**, 406-414.

Barret, T.J. and MacLean, W.H. (1993). Lithogeochemistry of a metamorphosed VMS alteration zone at Montauban, Grenville Province, Quebec. *Explor. and Min. Geol.*, **2(4)**, 367-386.

Batchelor, R.A. and Bowden, P. (1985). Petrogenetic interpretation of granitoid rock series using multicationic parameters. *Chem. Geol.*, **48**, 43-55.

Beach, A. (1974). A geochemical investigation of pressure solution and the formation of veins in a deformed greywacke. *Contrib. Mineral. Petrol.*, **46**, 61-68.

Becker, P.G. van G (1986). Tugela Valley Gold, Kwazulu: Final Research Report. South African Development Trust Corporation Ltd, Report No. RD/PGB/2289.

Berner, R.A. (1981). A new geochemical classification of sedimentary environments. *J. Sed. Petrol.*, **51**, 359-365.

Berner, R.A. and Raiswell, R. (1983). Burial of organic carbon and pyrite sulphur in sediments over Phanerozoic time: an new theory. *Geochimica et Cosmochemica Acta*, **47**, 855-862.

Berthé, D., Choukroune, P. and Jegouzo, P. (1979). Orthogneiss, mylonite and non-coaxial deformation of granites: the example of the South Armorican Shear Zone. *J. Struc. Geol.*, **1(1)**, 31-42.

Bhatia, M.R. (1983). Plate tectonics and geochemical compositions of sandstones. *J. Geol.*, **91**, 611-627.

Bhatia, M.R. (1985). Composition and classification of Palaeozoic flysch mudrocks of eastern Australia: implications in provenance and tectonic setting interpretation. *Sediment. Geol.*, **41**, 249-268.

Bhatia, M.R. and Crook, R.A.W. (1986). Trace element characteristics of greywackes and tectonic discrimination of sedimentary basins. *Contrib. Min. Petrol.*, **92**, 181-193.

Bickle, M.J., Hawksworth, C.J., England, P.C. and Athey, D.R. (1975). A preliminary thermal model for regional metamorphism on the Eastern Alps. *Earth Plan. Sci. Lett.*, **26**, 13.

Bjornerud, M. (1989). Mathematical model for folding of layering near rigid objects in shear deformation. *J. Struc. Geol.*, **11(3)**, 245-254.

Blatt, H., Middleton, G. and Murray, R. (1980). *Origin of Sedimentary Rocks - 2nd Edition.* Prentice-Hall Publishers, New Jersey, 634 pp.

Bloomer, S.H. (1987). Geochemical characteristics of boninite- and tholeiitic-series volcanic rocks from the Mariana Forearc and the role of an incompatible-enriched fluid in arc petrogenesis. *Geol. Soc. Spec. Pap.*, **125**, 151-164.

Bowen, R. (1988). *Isotopes in the Earth Sciences.* Elsevier, Cambridge, 550pp.

Boyer, S.E. (1986). Styles of folding within thrust sheets: examples from the Appalachians and Rockey mountains of the USA and Canada. *J. Struc. Geol.*, **8(3/4)**, 325-339.

Boyer, S.E. and Elliot, D. (1982). Thrust systems. *Bull. Am. Ass. Petrol. Geol.*, **66**, 1196-1230.

Bullen, W.D., Thomas, R.J. and Mckenzie, A. (1994). Gold mineralization in Natal, South Africa. *J. Afr. Earth Sci.*, **18(2)**, 99-109.

Bullen, W.D., Thomas, R.J. and Jordaan, L.T. (in prep.) Towards a new exploration model for gold and base metal mineralization in the Natal Thrust Belt, Zululand, South Africa.

Burger, A.J. and Coertze, F.J. (1973). Radiometric age measurements on rocks from southern Africa to the end of 1971. *Bull. Geol. Surv. S. Afr.*, **58**, 46pp.

Cabanis, B. and Lecolle, M. (1989). Le diagramme La/10-Y/15-Nb/8: un outil por la discrimination des series volcaniques et la mise en evidence des processus de melange et/ou de contamination crustale. *C.R. Acad. Sci. Ser. II*, **309**, 2023-2029.

Caby, R., Dostal, J. and Dupuy, C. (1977). Upper Proterozoic volcanic greywackes from northwestern Hoggar (Algeria). *Precamb. Res.*, **5**, 283-297.

Cain, A.C. (1973). Aspects of the geology and regional metamorphism in the Namaqua-Natal Belt north of Durban. *Petros*, 27-42.

Cain, A.C. (1975). A preliminary review of the stratigraphic relationships and distribution of metamorphism in the northern part of the Natal-Namaquarides, South Africa. *Geol. Rundsch.*, **64**, 192-215.

Calvert, S.E. and Pederson, T.F. (1996). Sedimentary geochemistry of Mn: Implications for the environment of formation of manganiferous black shales. *Econ. Geol.*, **91**, 36-47.

Camiré, G.E., Lafléche, M.R. and Ludden, J.N. (1993). Archaean metasediments from the northwestern Pontiac Subprovince of the Canadian Shield: chemical characterization, weathering and modeling of the source areas. *Precamb. Res.*, **62**, 285-305.

Cartwright, I. and Valley, J.W. (1991). Steep oxygen isotope gradients at marble-metagranite contacts in the northwestern Adirondacks Mountains, New York, USA: Products of fluid-hosted diffusion. *Earth Plan. Sci. Lett.*, **107**, 148-163.

Cattalani, S. and Bambic, P. (1996). Lithogeochemistry and mass changes: applications to mineral exploration. Short course, l'association professionelle des les Géologues at Géophysiciens du Quebec, April, 1994, Val d'Or, Quebec, 38 pp.

Chapple, W.M. (1978). Mechanics of thin-skinned fold-and-thrust belts. *Geol. Soc. Am. Bull.*, **89**, 1189-1198.

Charles worth, E.G. (1981). *Tectonics and Metamorphism of the Northern Margin of the Namaqua-Natal Mobile Belt, Near Eshowe, Natal.* Unpub. Ph.D. Thesis, University of Natal (Durban), 433pp.

Clayton, R.N. and Mayeda, T.K. (1963). The use of bromine pentaflouride in the extraction of oxygen from oxides and silicates for isotopic analysis. *Geochim. Cosmochim. Acta*, **27**, 43-52.

Cloos, M. (1984). Landward-dipping reflectors in accretionary wedges: active dewatering conduits? *Geology*, **12**, 519-522.

Cobbold, P.R. and Quinquis, H. (1980). Development of sheath folds in shear regimes. *J. Struc. Geol.*, **2 (½)**, 119-126.

Coldwell, A. P. C. (1984). *Ngubevu Project for South African Development Trust Corporation.* Anglo American Prospecting Services Pty. Ltd. Final Report for period April 1982 - March 1984, Lease No. R1/2/NZ/97.

Condie, K.C. and Wronkiewicz, D.J. (1990). Evolution of the Kaapvaal Craton: the Cr/The ratio in pelites as an index of craton maturation. *Earth. Plan. Sci Lett.*, **97**, 256-267.

Condie, K.C., Wilks, M., Rosen, D.M. and Zlobin, V.L. (1991). Geochemistry of metasediments from the Precambrian Hapschan Series, eastern Anabar Shield, Siberia. *Precamb. Res.*, **50**, 37-47.

Coplen, T.B., Kendall, C. and Hopple, J. (1983). Comparison of stable isotope reference samples. *Nature*, **307**, 236-238.

Coward, M.P. (1983). Thrust tectonics, thin skinned or thick skinned, and the continuation of thrusts to deep in the crust. *J. Struc. Geol.*, **5(2)**, 113-123.

Craig, H. (1963). Standard for reporting concentrations of deuterium and oxygen-18 in natural waters. *Science*, **133**, 1833.

Da Silva, L.C. (1991). A preliminary evaluation of the Brazilian Archaean and Proterozoic stratabound tourmalinites and their significance as potential gold deposits. *In:* Ladeira, E.A. (Ed.) *Ext. Abstr. Brazil Gold '91*, 241-245.

De Beer, J.H., Van Zijl, J.S.V. and Gough, D.I. (1982). The Southern Cape Conductive Belt: its composition, origin and tectonic significance. *Techtonophysics*, **83**, 205-225.

De Beer, J.H. and Meyer, R. (1984). Geophysical characteristics of the Namaqua-Natal Mobile Belt and its boundaries. *S. Afr. J. Geodyn.*, **1**, 473-493.

Debon, F. and Le Fort, P. (1983). A chemical-mineralogical classification of common plutonic rocks and associations. *Trans. R. Soc. Edinburgh Earth Sci.*, **73**, 135-149.

Deer, W.A., Howie, R.A. and Zussman, J. (1992). *An Introduction to the Rock-Forming Minerals - Second Edition.* Longman Scientific and Technical, New York, 696pp.

De Klerk, I. D. (1991). *The Nature and Origin of Gold Mineralization in the Tugela Valley: Natal Structural and Metamorphic Province.* Unpub. M.Sc. Dissertation, Rhodes University, Grahamstown, 113pp.

Du Toit, A.L. (1931). The geology of the area surrounding Nkandla, Natal. *Expl. Sheet 109, Geol. Surv. S. Afr.*, 111pp.

Eglington, B.M., Harmer, R.E. and Kerr, A. (1986). Petrographic, Rb-Sr, isotopic and geochemical charactersitics of intrusive granitoids from the Port Edward - Port Shepstone area, Natal. *Trans. Geol. Soc. S. Afr.*, **89**, 199-213.

Eglington, B.M., Harmer, R.E. and Kerr, A. (1989). Isotope and geochemical constraints on Proterozoic crustal evolution in south-eastern Africa. *Precamb. Res.*, **45**, 159-174.

England, P.C. (1987). Diffuse continental deformation: length scales, rates and metamorphic evolution. *In*: Oxburgh, E.R., Yardley, B.W.D. and England, P.C. (Eds), *Tectonic Settings of Regional Metamorphism.* Philosophical Transactions of the Royal Society, London, **134**, 201-214.

England, P.C. and Thompson, A.B. (1984). Pressure-temperature-time paths of regional metamorphism I. Heat transfer during the evolution of regions of thickened continental crust. *J. Petrol.*, **25(4)**, 895-928.

Etheridge, M.A., Wall, V.J. and Vernon, R.H. (1983). The role of the fluid phase during regional metamorphism and deformation. *J. Met. Geol.*, **1**, 205-226.

Etheridge, M.A., Wall, V.J. and Cox, S.F. (1984). High fluid pressures during regional metamorphism and deformation: implications for mass transport and deformation mechanisms. *J. Geophys. Res.*, **89 (B6)**, 4344-4358.

Faure, G. (1986). *Principals of Isotope Geology (2nd Ed.).* John Wiley and Sons, New York, 490pp.

Fernandez, A. (1987). Preferred orientation developed by rigid markers in two-dimensional simple shear strain: a theoretical and experimental study. *Tectonophysics*, **136**, 151-158.

Fitz Gerald , J.D. and Stünitz, H. (1993). Deformation of granitoids at low metamorphic grade I: Reactions and grain size reduction. *Techtonophysics*, **221**, 269-297.

Fleuty, M.J. (1964). The description of folds. *Proc. Geol. Assoc. Lond.*, 75, 461-492.

Floyd, P.A., Winchester, J.A. and Park, R.G. (1989). Geochemistry and tectonic setting of Lewisian clastic metasediments from the Early Proterozoic Loch Maree Group of Gairloch, NW Scotland. *Precamb. Res.*, **45**, 203-214.

Friedman, I. and O'Neil, J.R. (1977). Compilation of stable isotope fractionation factors of geochemical interest. *In*: Data Geochem (6th Ed.). *Geol Surv. Prof. Paper 440KK.*

Frimmel, H.E., Hartnady, C.J.H. and Koller, F. (1996). Geochemistry and Tectonic Setting of Magmatic Units in the Pan-African Gariep Belt, Namibia. *Dept. Geological Sciences - Information Circular No. 15, University of Cape Town.*

Fyfe, W.S. and Kerrich, W.S. (1985). Fluids and thrusting. *Chemical Geology*, **49**, 353-362.

Ganor, J., Matthews, A. and Paldov, N. (1989). Constraints on effective diffusivity during oxygen isotope excange at a marble-schist contact, Sifnos (Cyclades), Greece. *Earth Plan. Sci. Lett., **94**, 208-216.*

Garlick, G.D. (1969). The stable isotopes of oxygen. *In*: Wedepohl, K.H. (Ed.), *Handbook of Geochemistry, Chapter VIII/B.* Springer, Berlin.

Gibb, J. A. P. (1911). *Report - Champion Reef Mine.* The Anglo-French Exploration Co. Pty. Ltd., Johannesburg.

Gibb, R.A. and Thomas, M.D. (1976). Gravity signature of fossil plate boundaries in the Canadian Shield. *Nature*, **262**, 199-200.

Goffe, B. and Velde, B. (1984). Contrasted metamorphic evolutions in thrusted cover units of the Briançonnais Zone (French Alps): a model for the conservation of HP-LT metamorphic mineral assemblages. *Earth Plan. Sci. Lett.*, **68**, 351-360.

Graham, C.M. and England, P.C. (1975). Thermal regimes and regional metamorphism in the vicinity of overthrust faults: and example of shear heating and inverted metamorphic zonation from southern California. *Earth and Plan. Sci. Lett.*, **31**, 142-152.

Gray, C.J. (1899). *Colony of Natal - Report on the Mining Industry of Natal in the Year 1899.* Times Printing and Publishing Co. Ltd., Pietermaritzburg.

Gray, C.J. (1900). *Colony of Natal - Report on the Mining Industry of Natal in the Year 1900.* Times Printing and Publishing Co. Ltd., Pietermaritzburg.

Gray, C.J. (1901). *Colony of Natal - Report on the Mining Industry of Natal in the Year 1901.* Times Printing and Publishing Co. Ltd., Pietermaritzburg

Gray, C.J. (1902). *Colony of Natal - Report on the Mining Industry of Natal in the Year 1902.* Times Printing and Publishing Co. Ltd. Pietermaritzburg.

Gray, C.J. (1906). *Colony of Natal - Report on the Mining Industry of Natal in the Year 1906.* Times Printing and Publishing Co. Ltd., Pietermaritzburg.

Gray, C.J. (1907). *Colony of Natal - Report on the Mining Industry of Natal in the Year 1907.* Times Printing and Publishing Co. Ltd., Pietermaritzburg.

Grey, D.R. and Willman, C.E. (1991). Thrust-related strain gradients and thrusting mechanisms in a chevron-folded sequence, southeast Australia. *J. Struc. Geol.*, 13(6), 691-710.

Grey, D.R., Gregory, R.T. and Durney, D.W. (1991). Rock-buffered fluid-rock interaction in deformed quartz-rich turbidite sequences, Eastern Australia. *J. Geophys. Res.*, **96 (B12),** 19681-19704.

Groenewald, P.B., Grantham, G.H. and Watkeys, M.K. (1991). Geological evidence for a Proterozoic to Mesozoic link between southeastern Africa and Dronning Maud Land, Antarctica. *J. Geol. Soc. Lon.*, 148, 1115-1123.

Groves, D.I., Phillips, G.N., Ho, S.E. and Houston, S.M. (1985). The nature, genesis and regional controls on gold mineralization in Archaean greenstone belts of the Western Australian shield: a brief review. *Trans. Geol. Soc. S. Afr.*, **88**, 135-148.

Haack, U., Heinrichs, H., Baress, M. and Schneider, A. (1984). Loss of metals from pelites during regional metamorphism. *Contrib. Min. Petrol.*, **85**, 103-115.

Hafner, W. (1951). Stress distributions and faulting. *Geol. Soc. Am. Bull.*, 62, 373-398.

Hall, C. (1910 a). *Formal Report - Ground East of the Blue Speck Block.* Champion Reef Development Syndicate, Greytown

Hall, C. (1910 b). *Informal Report on the Ngubevu District, Natal.* Champion Reef Development Syndicate, Greytown.

Harmer, R.E. (1979). *Pre-Cape Geology of the Tugela Valley North of Kranskop, Natal.* Unpub. M.Sc. Thesis, Univ. Natal (Durban), 235pp.

Harmer, R.E. (1981). The stratigraphy and metamorphic history of the Tugela Nappe, northern Natal. *Abstr. S. Afr. Geodyn. Symp. - Geocongress '81. Geol. Soc. S. Afr.*, Pretoria, 1981.

Hatch, F.H. (1910). *Report on the Mines and Mineral Resources of Natal (other than coal).* Clay and Sons, London, 155pp.

Hedges, J.S. (1909). Ann. Rep. Comm. of Mines for Natal - 1909.

Henderson, J.B. (1972). Sedimentology of Archaean turbidites at Yellowknife, Northwest Territories. *Can. J. Earth. Sci.*, **9**, 882-902.

Henry, C., Burkhard, M. and Goffe, B. (1996). Evolution of synmetamorphic veins and their wallrocks through a Western Alps transect: no evidence for large-scale fluid flow. Stable isotope, major- and trace-element systematics. *Chem. Geol.*, **127**, 81-109.

Hobbs, B. E., Means, W. D. and Williams, P.F. (1976). *An Outline of Structural Geology*. John Wily and Sons, Inc. United States, First Edition, 571 pp.

Hoefs, J. (1980). *Stable Isotope Geochemistry (2nd Ed.)*. Springer-Verlag, Berlin/Heidelberg, 208pp.

Hopwood, T. (1975). Conformable elongate orebodies and intrafolial folds parallel to a mineral streaking lineation. *Geocongress - 1975, Stellenbosch, S. Afr.*

Houseman, G. and England, P. (1986). A dynamic model of lithosphere extension and sedimentary basin formation. *J. Geophys. Res.*, **91**, 719-729.

Hoy, L.D. (1993). Regional evolution of hydrothermal fluids in the Noranda District, Quebec: Evidence from $\delta^{18}O$ values from volcanogenic massive sulphide deposits. *Econ. Geol.*, **88**, 1526-1541.

Hutchinson, C.S. (1983). Economic Deposits and their Tectonic Setting. Macmillan, London, 365pp.

Hynes, A. (1980). Carbonitization and mobility of Ti, Y and Zr in Ascot Formation Metabasalts, SE Quebec. *Contr. Min. Petrol.*, **75**, 79-87.

Ildefonse, B. and Fernandez, A. (1988). Influence of the concentration of rigid markers in a viscous medium on the production of preferred orientations. An experimental contribution - I. Non-coaxial strain. *In*: Talbot, C.J. (Ed.). *Geological Kinematics and Dynamics (in honour of the 70th birthday of Hans Ramberg). Bull. Geol. Inst. Univ. Uppsala.*, **14**, 55-60.

Ildefonse, B. and Mancktelow, N.S. (1993). Deformation around rigid particles: the influence of slip at the particle/ matrix interface. *Tectonophysics*, **221**, 345-359.

Ildefonse, B., Sokoutis, D. and Mancktelow, N.S. (1992). Mechanical interactions between rigid particles in a deforming ductile matrix. Analogue experiments in simple shear flow. *J. Struc. Geol.*, **14(10)**, 1253-1266.

Irvine, T.N. and Baragar, W.R.A. (1971). A guide to the chemical classification of the common rocks. *Can. J. Earth. Sci.*, **8**, 523-548.

Jackson, C. and Harris, R.W. (1997). Microstructural evidence for extensional reactivation of the Hartbees River Thrust Belt, northeastern Namaqua Tectonic Province. *Abstr. XIII Anniversary Conf., Tectonics Division, Geological Society of South Africa.*

Jacobs, J. and Thomas, R.J. (1994). Oblique collision at about 1.1 Ga along the southern margin of the Kaapvaal continent, south-east Africa. *Geol. Rundsch.*, **83**, 322-333.

Jacobs, J., Thomas, R.J. and Weber, K. (1993). Accretion and indentation tectonics at the southern edge of the Kaapvaal craton during the Kibaran (Grenville) Orogeny. *Geology*, **21**, 203-206.

Jamieson, R.A. (1991). P-T-t paths of collisional orogens. *Geologische Rundschau*, **80 (2)**, 321-323.

Karpeta, W.P. (1997). Clastic-hosted, tourmaline-bearing stratabound gold deposits. *Gold Fields of South Africa Int. Rep.*, 19pp.

Kerrich, R, Beckinsdale, R. and Durham, J. (1977). The transition between deformation regimes dominated by intercrystalline diffusion and intracrystalline creep evaluated by oxygen isotope thermometry. *Tectonophysics*, **38**, 241-257.

Kerrich, R., La Tour, T.E.A. and Willmore, L. (1984). Fluid participation in deep fault zones: evidence from geological, geochemical and $^{18}O/^{16}O$ relations. *J. Geophys. Res.*, **89**, 4331-4343.

Knoper, M., Andreoli, M.A.G. and Ashwal, L.D. (1997). The geology of Steenkampskraal, Namaqualand, South Africa. *Abstr. XIII Anniversary Conf., Tectonics Division, Geological Society of South Africa.*

Lambert, J.F. (1962). *The Petrology of the Ultrabasic Rocks of the Tugela Valley, Natal.* Unpub. Ph.D. Thesis, Univ. Natal (Durban), 109pp.

Langmuir, S.H. and Bender, J.F. (1984). The geochemistry of oceanic basalts in the vicinity of transform faults: observations and implications. *Earth. Plan. Sci. Lett.*, **69**, 107-127.

Lapidus, D.F. and Winstanley, I. (1987). *Dictionary of Geology*. Collins, Glascow, 565.

Larson, P.B. and Taylor, H.P. (1986). An oxygen isotope study of hydrothermal alteration in the Lake City Caldera, San Juan Mountains, Colorado. *J. Volcanology and Geothermal Res.*, **30**, 47-82.

Larson, P.B. and Taylor, H.P. (1987). Solfataric alteration in the San Juan Mountains, Colorado: oxygen isotope variations in a boiling hydrothermal environment, *Econ. Geol.*, **82**, 1019-1036.

Larson, P.B. and Geist, D.J. (1995). On the origin of low-^{18}O magmas: evidence from the Casto Pluton, Idaho. *Geology*, **23**, 209-212.

Le Maitre (Ed.) (1989). *A Classification of Igneous Rocks and Glossary of Terms.* Blackwell, Oxford, 193pp.

Liou, J.G. (1973). Synthesis and stability relations of epidote - $Ca_2Al_2FeSi_3O_{12}(OH)$. *J. Petrol.*, **14**, 381-413.

Liou, J.G., Maruyama, S. and Cho, M. (1985). Phase equilibria and mineral parageneses of metabasites in low-grade metamorphism. *Min. Mag.*, **49**, 321-333.

Looseveld, R.J.H. and Etheridge, M.A. (1990). A model for low-pressure facies metamorphism during crustal thickening. *J. Met. Geol.*, **8**, 257-267.

Loukola-Ruskeeniemi, K. and Heino, T. (1996). Geochemistry and genesis of the black-shale hosted Ni-Cu-Zn deposit at Talvivaara, Finland. *Econ. Geol.*, **91**, 80-110.

Mancktelow, N.S. (1992). Neogene lateral extension during convergence in the Central Alps: evidence from interrelated faulting and backfolding around the Simplonpass (Switzerland). *Tectonophysics*, **215**, 295-317.

Mandl, G. (1988). Mechanics of tectonic faulting: Models and basic concepts. *In*: Zwart, H.J. (Ed), *Developments in Structural Geology - I*, Elsevier, Netherlands, 135-156.

Martin, A.K. and Hartnady, C.J.H. (1986). Plate tectonic development of the south west Indian Ocean: a revised reconstruction of east Antarctica and Africa. *J. Geophys. Res.*, **91(B5)**, 4767-4786.

Mason, R (1990). *Petrology of the Metamorphic Rocks - Second Edition.* Cambridge University Press, Great Britain, 230pp.

Matthews, P.E. (1959). The metamorphism and tectonics of the pre-Cape formations in the Post- Ntingwe Thrust Belt, S.W. Zululand, Natal. *Trans. Geol. Soc. S. Afr.*, **62**, 257-322.

Matthews, P.E. (1972). Possible Precambrian obduction and plate tectonics in southeastern Africa. *Nature*, **240**, 37-39.

Matthews, P.E. (1981a). A new tectonic model for the northern region of the Namaqua-Natal Belt in Natal. *Proc. Geol. Soc. S. Afr. 1981*, 150-151.

Matthews, P.E. (1981b). Eastern or Natal sector of the Namaqua-Natal Mobile Belt in Southern Africa, *In*:- Hunter, D.R. (Ed.), *Precambrian of the Southern Hemisphere, Developments in Precambrian Geology*, **2**, 705-795, Elsevier Publishers.

Matthews, P.E. (1985). Archaean post-Pongola granites in the southeastern Kaapvaal Craton. *S. Afr. J. Sci.*, **81**, 479-484.

Matthews, P.E. (1987). Tectonic evolution of a late Archaean Pongola Aulacogen and deformed epicratonic basin in SE Africa. *Abstr. Ann. Geol. Surv. S. Afr.*, **21**, 95-106.

Matthews, P.E. (1988). Regional geology of the Melmouth Area, northern Natal. *Melmouth Centenary Volume, 1988*, 9-14.

Matthews, P.E. (1991). A transpressional tectonic model for regional deformation and emplacement of granites within the late Archaean Pongola Aulacogen in Southeastern Africa. *Ext. Abstr. Conf. Precamb. Sed. Basins of S.A. 1991, Terra-Abstr, sup 3 to Terra Nova*, **3**, 21-22.

Matthews, P.E. and Charlesworth, E.G. (1981). Geological map of the northern margin of the Natal Mobile Belt in northern Natal. *Univ. Natal (Durban), S. Afr., 1:140 000.*

Maynard, J.B. (1982). Extension of Berner's "New geochemical classification of sedimentary environments" to ancient sediments. *J. Sed. Petrol.*, **52**, 1325-1331

McLennan, S.M. and Taylor, S.R. (1988). Crustal Evolution: Comments on "The Archaean-Proterozoic transition: Evidence from the geochemistry of metasedimentary rocks from Guyana and Montana" by A.K. Gibbs, C.W. Montgomery, P.A. O'Day and E.A. Erslev. *Geochim. Cosmochim. Acta.*, **52**, 785-787.

Mc Quillan, H. (1973). Small-scale fracture density in the Asmari Formation of SW Iran and its relation to bed thickness and structural setting. *Am. Assoc. Petrol. Geol. Bull.*, **57 (12)**, 2367-2385.

Meschede, M. (1986). A method of discriminating between different types of mid-ocean ridge basalts and continental tholeiites with the Nb-Zr-Y diagram. *Chem. Geol.*, **56**, 207-218.

Meyer, C. and Hemley, J.J. (1967). Wall rock alteration. *In:* Barnes, H.L. (Ed.) *Geochemistry of Hydrothermal Ore Deposits*. Holt, Rinehart and Winston, New York, 166-235.

Middlemost, E.A.K. (1985). *Magmas and Magmatic Rocks*. Longman, London.

Mitra, S. (1986). Duplex structures and imbricate thrust systems: geometry, structural position and hydrocarbon potential. *Bull. Am. Ass. Petrol. Geol.*, **70(9)**, 1087-1112.

Miyashiro, A. (1973). *Metamorphism and Metamorphic Belts*, William Clowes and Sons, Great Britain, 491pp.

Naidoo, D.D., Bloomer, S.H., Saquaque, A and Hefferan, R. (1991). Geochemistry and significance of metavolcanics from the Bou-Azzer-El Grara Ophiolite (Morocco). *In*: Stern, R.J. and Van Schmus, W.R. (Eds), *Crustal Evolution in the Late Proterozoic*, Precamb. Res., **53**, 79-97.

Naqvi, S.M., Sawkar, R.H., Subba Rao, D.V., Govil, P.K. and Gnaneswar Rao, T. (1988). Geology, geochemistry and tectonic setting of Archaean greywackes from Karnataka nucleus, India. *Precamb. Res.*, **39**, 193-216.

Nesbitt, H.W. and Young, G.M. (1982). Early Proterozoic climates and plate motions inferred from the major element chemistry of lutites. *Nature*, **299**, 715-717.

Nicolaysen, L.O. and Burger, A.J. (1965). Note on an extensive zone of 1000 million year old metamorphic and igneous rocks in southern Africa. *Sci. Terra.*, **10**, 497-516.

Nicollet, C. and Andrianbololona, D.R. (1980). Distribution of transition elements in crustal metabasic igneous rocks. *Chem. Geol.*, **28**, 79-90.

Norris, R.J. and Henley, R.W. (1976). Dewatering of a metamorphic pile. *Geology*, **4**, 333-336.

Norrish, K. and Hutton, J.T. (1969). An accurate X-ray spectrographic method for the analysis of a wide range of geological samples. *Geochim. Cosmochim. Acta.*, **33**, 431-435.

Nur, A., Ron, H. and Scotti, O. (1989). Kinematics and mechanics of tectonic block rotations. *In* : Cohen, S.C. and Vanicek, P. (Eds). *Slow Deformation and Transmission of Stress in the Earth.* Geophysical Monograph 49, IUGG Volume 4, 31-46.

Oszczepalski, S. (1989). Kupferschiefer in southwestern Poland: Sedimentary environments, metal zoning and ore controls. *Can. Geol. Surv. Spec. Pap.* **36**, 571-600.

Oxburgh, E.R. and Turcotte, D.L. (1974) Thermal gradients and regional metamorphism in overthrust terranes with special reference to the Eastern Alps. *Schweizerische Mineralogische und Petrographische Mitteilungen*, **54**, 641-662.

Pan, Y., Fleet, M.E. and Stoe, W.E. (1991). Geochemistry of metasedimentary rocks in the late Archaean Hemlo-Heron Bay Greenstone Belt, Superior Province, Ontario: Implications for provenance and tectonic setting. *Precamb. Res.*, **52**, 53-69.

Pasova, J. (1996). Preface - A group of papers devoted to the metallogeny of black shales. *Econ. Geol.* and *Bull. Soc. Econ. Geol* , Jan-Feb, **91(1)**, 1-3.

Passchier, C.W. (1987). Stable positions of rigid objects in non-coaxial flow - A study in vorticity analysis. *J. Struc.Geol.*, **9**, 679 - 690.

Passchier, C. W. and Simpson, C. (1986). Porphyroclast systems as kinematic indicators. *J. Struc. Geol.*, **8(8)**, 831-843.

Passchier, C.W., Myers, J.S. and Kröner, A. (1990). *Metamorphism of high grade terranes.* Springer-Verlag, Berlin, 150pp.

Parnell, J. (1996). Phanerozoic analogues for carboniferous matter in Witwatersrand ore deposits. *Econ. Geol.*, **91**, 55-62.

Paterson, S.R., Tobisch, O.T. and Vernon, R.H. (1991). Emplacement and deformation of granitoids during volcanic arc construction in the Foothills terrane, central Sierra Nevada, California. *Tectonophysics*, **191**, 89-110.

Patino Douce, A.E., Humphreys, F.D. and Johnston, A.D. (1990). Anatexis and metamorphism in tectonically thickened continental crust exemplified by the Sevier Hinterland, western North America. *Earth. Plan. Sci. Lett.*, **97**, 290-315.

Pearce, J.A. (1975). Basalt geochemistry used to investigate past tectonic environments on Cyprus. *Tectonophysics*, **25**, 41-67.

Pearce, J.A. (1979). Geochemical evidence for the genesis and eruptive setting of lavas from Tethys Ophiolites. *Proc. Int. Ophiolite. Symp., Cyprus*, 261-272.

Pearce, J.A. (1982). Trace element characteristics of lavas from destructive plate boundaries. *In*: Thorpe, R.S. (Ed.), *Andesites*. Wiley, Chichester, 525-548.

Pearce, J.A. and Cann, J.R. (1971). Ophiolite origin investigated by discriminant analysis using Ti, Zr and Y. *Earth. Plan. Sci. Lett.*, **19**, 290-300.

Pearce, J.A. and Cann, J.R. (1973). Tectonic setting of basic rocks determined using trace element analysis. *Earth Plan. Sci. Lett.*, **19**, 290-300.

Pearce, J.A. and Norry, M.J. (1979). Petrogenetic implications of Ti, Zr, Y and Nb variations in volcanic rocks. *Contrib. Min. Petrol.*, **69**, 33-47

Pearce, J.A., Harris, N.B.W. and Tindle, A.G. (1984). Trace element discrimination diagrams for the tectonic interpretation of granitic rocks. *J. Petrol.*, **25**, 956-983.

Pearman, C. (1994). *Gold Potential of the Natal Thrust Front*. Gold Fields of South Africa - Internal Company Report, 20pp.

Peccerillo, A. and Taylor, S.R. (1976). Geochemistry of Eocene calc-alkaline volcanic rocks from the Rostomanu area, Northern Turkey. *Contrib. Min. Petrol.*, **58**, 63 - 81.

Pederson, A.K. (1977). Iron-bearing and related volcanic rocks in the area between Gieseckes Dol and Hommes Dol, Northwest Disco. *Rapport Gronlands Geol. Unders.*, **81**, 5-14.

Pederson, T.F. and Price, N.B. (1982). The geochemistry of manganese carbonates in Panama Basin sediments. *Geochimica et Cosmochimica Acta*, **46**, 59-68.

Peters, M.T. and Wickham, S.M. (1995). On the causes of ^{18}O-depletion and $^{18}O/^{16}O$ homogenization during regional metamorphism; the East Humboldt Range core complex, Nevada. *Contrib. Mineral. Petrol.*, **119**, 68-82.

Pettijohn, E.J., Patter, P.E. and Siever, R. (1973). *Sand and Sandstone*. Wiley, New York, 618pp.

Pettijohn, E.J. (1975). *Sedimentary Rocks - 3rd Edition*. Harper and Row, Singapore, 628pp.

Price, N.J. (1966). *Fault and joint development in brittle and semi-brittle rocks*. Oxford, Pergamon, 176pp.

Price, N. J. and Cosgrove, J. W. (1990). *Analysis of Geological Structures*. Cambridge University Press, Cambridge, Second Edition, 502pp.

Quinby-Hunt, M.S., Wilde, P. and Berry, W.B.N. (1991). The provenance of low-calcic black shales. *Mineralium Deposita*, **26**, 113-121.

Quinby-Hunt, M.S. and Wilde, P. (1996). Thermodynamic zonation in the black shale facies based on iron-manganese-vanadium content. *Chem. Geol.*, **113**, 297-317.

Quinby-Hunt, M.S. and Wilde, P. (1996). Chemical depositional environment of calcic marine black shales. *Econ. Geol.*, **91**, 4-13.

Ramsay, J.G. (1967). *Folding and Fracturing of Rocks.* McGraw-Hill, New-York, 568pp.

Ramsay, J.G. (1980a). Shear zone geometry: a review. *J. Struc. Geol.*, **2(1,2)**, 83-99.

Ramsay, J.G. (1980b). The crack-seal mechanism of rock deformation. *Nature*, **284**, 135-139.

Ramsay, J.G. and Graham, R.H. (1970). Strain variation in shear belts. *Can. J. Earth. Sci.*, 7, 786-813.

Ramsay, J.G. and Huber, M.I. (1983). *The Techniques of Modern Structural Geology - Vol I: Strain Analysis.* Academic Press, Oxford, 307pp.

Ramsay, J.G. and Huber, M.I. (1987). *The Techniques of Modern Structural Geology - Vol II: Folds and Fractures.* Academic Press, Oxford, 393pp.

Reading, H.G. (Ed.) (1978). *Sedimentary Environments and Facies.* Blackwell Scientific Publications, Great Britain, 557pp.

Reed, J.J. (1957). Petrology of the Lower Mesozoic rocks of the Wellington District. *Bull. New Zealand. Geol. Surv.*, **52**, 60pp.

Reitan, P.H. (1968). Frictional heating during metamorphism: quantitative evaluation of concentration of heat generation in time. *Lithos*, **1**, 151-163.

Rice, A.H.N., Bevins, R.E., Robinson, D. and Roberts, D. (1989). Thrust-related metamorphic inversion in the Caladonides of Finnmark, north Norway. *In:* Daly, J.S., Cliff, R.A. and Yardley, B.W.D. (Eds), *Evolution of Metamorphic Belts,* Geological Society Special Publication No. **43**, 413-421.

Richardson, S.W. and England, P.C. (1979). Metamorphic consequences of eclogite production in overthrust orogenic zones. *Earth Plan. Sci. Lett.*, **42**, 183-190.

Ridley, J. (1989). Vertical movement in orogenic belts and the timing of metamorphism relative to deformation. *In:* Daly, J.S., Cliff, R.A. and Yardley, B.W.D. (Eds), *Evolution of Metamorphic Belts,* Geological Society Special Publication No. **43**, 103-115.

Rigotti, S.O. (1977). *The Geology of the Tugela Group in the Middledrift Area, Natal.* Unpub. M.Sc. Thesis, University of Natal (Durban), 153pp.

Ring, U. (1993). Aspects of the kinematic history and mechanism of superposition of the Proterozoic mobile belts of eastern Central Africa (northern Malawi and southern Tanzania). *Precamb. Res.* **62**, 207-226.

Rivers, T., van Gool, J.A.M. and Connelly, J.N. (1993). Contrasting tectonic styles in the northern Grenville province: implications for the dynamics of orogenic fronts. *Geology*, **21**, 1127-1130.

Rollinson, H.R. (1993). *Using Geochemical data: Evaluation, Presentation, Interpretation.* Longman, Singapore, 352pp.

Roser, B.P. and Korsch, R.J. (1988). Provenance signatures of sandstone-mudstone suites using SiO_2 content and K_2O/Na_2O ratio. *J. Geol.*, **94**, 635-650.

Saggerson, E.P. (1973). Metamorphic facies series in Africa: a contrast. *Spec. Publ. Geol. Soc. S. Afr.*, **3**, 227-234.

Saggerson, E.P. and Turner, L.M. (1980). Distribution of regional metamorphism in Africa. *Geol. Rundsch.*, **69 (3)**, 745-756.

Saunders, A.D., Tarney, S., Marsh, N.G. and Wood, D.A. (1979). Ophiolites as ocean crust or marginal basin crust: a geochemical approach. *Proc. Int. Ophiolite. Symp., Cyprus*, 193-204.

Schiffman, P. and Liou, J.G. (1980). Synthesis and stability relations of Mg-Al pumpellyite, $Ca_4Al_5MgSi_6O_{21}(OH)_7$. *J. Petrol.*, **21**, 441-474.

Schilling, J.G. (1973). Iceland mantle plume: geochemical evidence along the Reykjais Ridge. Nature, 242, 565-571.

Scholz, C.H. (1980). Shear heating and the state of stress on faults. *J. Geophys. Res.* **85 (B11)**, 6174-6184.

Scholz, C.H. (1988). The brittle-plastic transition and the depth of seismic faulting. *Geol. Rund.*, **77/1**, 319-328.

Scholz, C.H., Beavan, J. and Hanks, T.C. (1979). Frictional metamorphism, argon depletion, and tectonic stress on the Alpine fault, New Zealand. *J. Geophys. Res.* **84**, 6770-6782.

Schulze-Hulbe, A. (1977). *A study of the Structure and Metamorphism of the Rocks of the Tugela Group Exposed in the Mambula-Mbongolwane Area, Natal.* Unpub. M.Sc. Thesis, University of Natal (Durban), 229pp.

Schurink, H. (1986). Rebellion Reef Gold - Mbongolwane Flats. Report for the South African Development Trust Corporation, Ltd. (STK), Mining Department, 15pp.

Scogings, A.J. (1986). Peralkaline gneissic granite in the Ngoye Granite-gneiss Formation, Natal. *Trans. geol. Soc. S. Afr.*, **92(4)**, 339-351.

Scogings, A.J. (1989). Peralkaline granitoid and associated alkaline mafic gneisses northwest of Eshowe, Natal. *Geol. Soc. S. Afr.*, **89**, 361-365.

Shaw, D.M. (1968). A review of K-Rb fractionation trends by covariance analysis. *Geochim. Cosmochim. Acta.*, **32**, 537-602.

Sheppard, S.M.F. (1986). Characterization and isotopic variations in natural waters, *In*: (Valley, J.W.; Taylor, H.P. and O'Neill, J.R., Eds). *Stable Isotopes in High Temperature Geological Processes. Rev. Mineral.*, **16**, 165-185.

Shervais, J.W. (1982). Ti-V plots and the petrogenesis of modern and ophiolitic lavas. *Earth Plan. Sci. Lett.*, **59**, 101-118.

Shimmield, G.B. and Price, N.B. (1986). The behavior of molybdenum and manganese during early sediment diagenesis - offshore Baja California, Mexico. *Marine Chemistry*, **19**, 261-280.

Sibson, R.H. (1977). Fault rocks and fault mechanisms. *J. Geol. Soc. Lon.*, **133**, 191-213.

Sibson, R.H. (1980). Transient discontinuities in ductile shear zones. *J. Struc. Geol.*, **2**, 165-171.

Sibson, R.H. (1987). Earthquake rupturing as a mineralizing agent in hydrothermal systems. *Geology*, **25**, 701-704.

Sibson, R.H., McM. Moore, J. and Rankin, A.H. (1975). Seismic pumping - a hydrothermal fluid transport mechanism. *J. Geol. Soc. Lond*, **131**, 653-659.

Sivell, W.J. and Foden, J.D. (1988). Amphibolites from the Entia Gneiss Complex, eastern Arunta Inlier: Geochemical evidence for a Proterozoic transition from extensional to compressional tectonics. *Precamb. Res.*, **38**, 235-255.

Smalley, T.J. (1980). *Structure and Metamorphism of the Tugela Group within the Northern Zone of the Natal Mobile Belt*. Unpub Ph.D. Thesis, University of Natal (Durban), 220pp.

Smith, G.A. and Hallam, A. (1970). The fit of the southern continents. *Nature*, **225**, 139-144.

Smith, G.L. (1986). Update on Tugela Mapping Project, South African Development Trust Corporation (STK) Ltd.

Smith, G.L. (1987). Report on Tugela mapping project. South African Development Trust Corporation (STK) Ltd.

South African Committee for Stratigraphy (SACS) (1980). Stratigraphy of South Africa, Part 1: Lithostratigraphy of the Republic of South Africa/South West Africa/Namibia and the Republics of Boputhatswana, Transkei and Venda. *Handbook Geol. Surv. S. Afr.*, **8**.

Spry, A. (1969). *Metamorphic Textures*. Pergamon, Oxford. 350pp.

Steed, G.M. and Morris, J.H. (1986). Gold mineralization in Ordovician greywackes at Clontibret, Ireland. *In*: (Keppie, J.D., Boyle, R.W. and Haynes, S.J. - Eds) *Turbidite-Hosted Gold Deposits*. Geol. Soc. Canada. Spec. Paper 32, 67-86.

Stel, H. (1986). The effect of cyclic operation of brittle and ductile deformation on the metamorphic assemblages in cataclasites and mylonites. *PAGEOPH*, **124 (1/2)**, 289-307.

Stünitz, H. and Fitz Gerald, J.D. (1993). Deformation of granitoids at low metamorphic grade II: Granular flow in albite-rich mylonites. *Techtonophysics*, **221**, 299-324.

Tankard, A.J., Jackson, M.P.A., Eriksson, K.A., Hobday, D.K., Hunter, D.R. and Minter, W.E.L. (1982). *Crustal Evolution of Southern Africa - 3.8 Billion Years of Earth History*. Springer-Verlag, Cape Town, 532pp.

Taylor, S.R. and McLennan, S.M. (1985). *The Continental Crust: its Composition and Evolution*. Blackwell, Oxford, 312pp.

Texeixeira, N.A. and Kuyamjian, R.M. (1991). The Mateus Leme - Pitangui hydrothermal zone: do they represent a fossil hot spring system in the Rio das Velhas greenstone belt, Central Brazil? *In:* Ladeira, E.A. (Ed.) *Ext. Abstr. Brazil Gold '91*, 171-177.

Theart, H.F.J. (1986). Phoenix Gold Mine, Tugela : Kwazulu. Report for Evaluation Committee. South African Development Trust Corporation (STK) Ltd.

Theart, H.F.J. (1987). Phoenix Gold Mine, Kwazulu - Research Communication. South African Development Trust Corporation (STK) Ltd.

Thomas, R.J. (1988a). The geology of the Port Shepstone area. Expl. Sheet 3030 - Port Shepstone. Geol. Surv. S. Afr., 136pp.

Thomas, R.J. (1988b). Late Proterozoic granitoids of the Natal Structural and Metamorphic Province in the Port Shepstone area. *Ext. Abstr., Geocongr. '88, Geol. Soc. S. Afr.*

Thomas, R.J. (1988c). The petrology of the Oribi Gorge Suite: Kibaran charnokitic granitoids from southern Natal. *S. Afr. J. Geol.*, **91**, 275-291.

Thomas, R.J. (1989a). Preface to the special issue on the Proterozoic rocks of the Natal Structural and Metamorphic Province. *S. Afr. J. Geol.*, **92(4)**, 339-351.

Thomas, R.J. (1989b). A tale of two tectonic terrains. *S. Afr. J. Geol,*, **92(4)**, 306-321.

Thomas, R.J., Bullen, W.D., de Klerk, I. and Scogings, A.J. (1990). The distribution and genesis of precious and base metal mineralization in the Natal Metamorphic Province, South Africa. *S. Afr. J. Geol.*, **93(4)**, 683-695.

Thomas, R.J. and Eglington, B.M. (1990). A Rb-Sr, Sm-Nd and U-Pb zircon isotopic study of the Mzumbe Suite, the oldest intrusive granitoid in southern Natal, South Africa. *S. Afr. J. Geol.*, **93(5)**, 761-765.

Thomas, R.J., Eglington, B.M., Bowring, S.A. Retief, E.A. and Walraven, F. (1993). New isotope data from a Neoproterozoic porphyritic granitoid-charnockite suite from Natal, South Africa. *Precamb. Res.*, **62**, 83-101.

Thompson, A.B. and England, P.C. (1984). Pressure-temperature time paths of regional metamorphism II. Their influence and interpretation using mineral assemblages in metamorphic rocks. *J. Petrol.*, **25 (4)** 929-955.

Tiebing, L., Delian, F. and Jie, Y. (1996). Origin of the black shale-hosted Chadian Phosphorus-Manganese Deposit, Shoonxi Province, China. *Econ. Geol.*, **91**, 48-54.

Tullis, J.T. (1982). The brittle-ductile transition in feldspathic rocks. *EOS*, **44**, 1464.

van de Kamp, P.C., Leake, B.E. and Senior, A. (1976). The petrography of some Californian arkoses with application to identifying gneisses of metasedimentary origin. *J. Geol.*, **84**, 195-212.

Van Den Driessche, J. and Brun, J-P. (1987). Rolling structures at large shear strain. *J. Struc. Geol.*, **9(5/6)**, 691-704.

Vennemann, T.W. and Smith, H.S. (1990). The rate and temperature of reaction of ClF3 with silicate minerals, and their relevance to oxygen isotope analysis. *Chemical. Geol. (Isotope Geoscience)*, **86**, 83-88.

Vernon, R.H., Collins, W.J. and Paterson, S.R. (1993a). Pre-foliation metamorphism in low-pressure/high temperature terranes. *Techtonophysics*, **219**, 241-256.

Vernon, R.H., Paterson, S.R. and Foster, D. (1993b). Growth and deformation of porphyroblasts in the Foothills Terrane, Central Sierra Nevada, California: negotiating a microstructural minefield. *J. Met. Petrol.*, **2**, 203-222.

Von Veh, M.W. and Anderson, N.J.B. (1990). Normal-slip faulting in the coastal areas of northern Natal and Zululand, South Africa. *S. Afr. J. Geol.*, **93**, 574-582.

Vrolik, P., Myers, G. and Casey, J. (1988). Warm fluid migration along tectonic melanges in the Kodiak Accretionary Complex, Alaska. *J. Geophys. Res.*, **93 (B9)**, 10313-10324.

Watson, E.B. and Harrison, T.M. (1983). Zirconium saturation revisited: temperature and composition effects in a variety of crustal magma types. *Earth Plan. Sci. Lett.*, **64**, 295-304.

Weaver, B.L. and Tarney, J. (1981). Chemical changes during dyke metamorphism in high-grade basement terranes. *Nature*, **289**, 47-49.

Wells, P.R.A. (1980). Thermal models for the magmatic accretion and subsequent metamorphism of continental crust. *Earth Plan. Sci. Lett.*, **46**, 253-265.

Welty, S.W. (1980). Red Creek Canyon, Utah - a Precambrian unconformity-type pitchblende deposit. *Unpub. B.A. (Hons) Dissertation*, Williams College, 78pp.

Whalen, J.B., Currie, K.L. and Chappell, (1987). A-Type granites: geochemical characteristics, discrimination and petrogenesis. *Contrib, Min, Petrol.*, **95**, 407-419.

Wickham, S.M. and Taylor, H.P. (1985). Stable isotopic evidence for large-scale seawater infiltration in a regional metamorphic terrane: the Trois Seigneurs Massif, Pyrenees, France. *Contrib. Mineral. Petrol.*, **91**, 122-137.

Wickham, S.M. and Peters, M.T. (1992). An oxygen isotope discontinuity in high-grade rocks of the East Humboldt Range, Nevada. *Nature*, **345**, 150-153.

Wilkinson, J.F.G. (1982). The genesis of mid-ocean ridge basalt. *Earth. Sci. Rev.*, **18**, 1-57.

Wilson, M. (1989). *Igneous Petrogenesis*, Unwin-Hyman Inc., London, 466 pp.

Winchester, J.A. and Floyd, P.A. (1977). Geochemical discrimination of different magma series and their differentiation products using immobile elements. *Chem. Geol.*, **20**, 325-343.

Wood, D.A. (1980). The application of a Th-Hf-Ta diagram to problems of tectonomagmatic classification and to establishing the nature of crustal contamination of basaltic lavas of the British Tertiary volcanic province. *Earth. Plan. Sci. Lett.*, **50**, 11-30.

White, S. (1975). Tectonic deformation and recrystallization of oligoclase, *Contr. Min. Petr.*, **50**, 287-304.

Wilcox, R.E., Harding, T.P. and Seely, D.R. (1973). Basic wrench tectonics. *Bull. Am. Ass. Petrol. Geol.*, **57**, 74-96.

Winfield, O. (1979). *The Tugela Fault Area, Kwazulu.* Mining Corporation Limited, Report No. RD/OW/1059.

Winkler, H.G.F. (1967). *Petrogenesis of Metamorphic Rocks - Second Edition.* Springer-Verlag, New York, 342pp.

Winkler, H.G.F. (1974). *Petrogenesis of Metamorphic Rocks - Fifth Edition.* Springer-Verlag, New York, 348pp.

Wronkiewicz, D.J. and Condie, K.C. (1987). Geochemistry of Archaean shales from the Witwatersrand Supergroup, South Africa: Source-area weathering and provenance. *Geochim. Cosmochim. Acta.*, **51**, 2401-2416.

Wronkiewicz, D.J. and Condie, K.C. (1989). Geochemistry of sediments from the Pongola Supergroup, South Africa: evidence for a 3-Ga-old evolved continental craton. *Geochim. Cosmochim. Acta.*, **53**, 1537-1549.

Wynne-Edwards, H.R. (1971). Plutonites, gneisses and granulites of the Granulite Facies. *Freiberger Forschungshefte.*

Yardley, B.W.D. (1989). *An Introduction to Metamorphic Petrology.* Longman, Singapore, 248pp.

Young, M. (1910). *Memo on "Champion Reef", Natal Proposition.* Champion Reef Development Syndicate, Greytown.

Zentilli, M. and Groves, M.C. (1990). Carbon compounds and ore deposit models. *Abstr. 8th IAGOD Quadrennial Symposium*, A110-111.

Appendix A

Calculation of ACF and AKF parameters from whole rock major element oxide data (Appendices A1 to A5)

ACF and AKF diagrams are ternary plots on which whole rock major element oxide data, or petrographic data, may be plotted. Fields in these ternary plots encompass likely protoliths to the plotted metamorphic rocks. The three parameters for each ternary plot are calculated from the ratios of certain groups of elements, the abundances of which are normalized to their molecular weights. For instance, the 'C' apex of the ACF diagram is calculated as follows:

CaO (relative abundance, reduced to a percentage, in whole rock analyses) divided by the molecular weight of CaO. Similarly, the other apices are calculated as follows

ACF

A - $Al_2O_3 + Fe_2O_3 - (Na_2O + K_2O)$
F - $FeO + MgO + MnO$

AKF

A' - $Al_2O_3 + Fe_2O_3 - (Na_2O + K_2O + CaO)$
K - K_2O
F - $FeO + MgO + MnO$

Once the values of the apices are calculated each is reduced to a percentage of the sum of the values of the three apices. These percentages become the three parameters of the ternary plot. Examples of the protolith fields in which data commonly fall, are shown in the figure below. Note that certain minerals, because of their major element ratios, may be plotted at apices and along joins between apices, or they may occupy 2-d fields in the ternary plot.

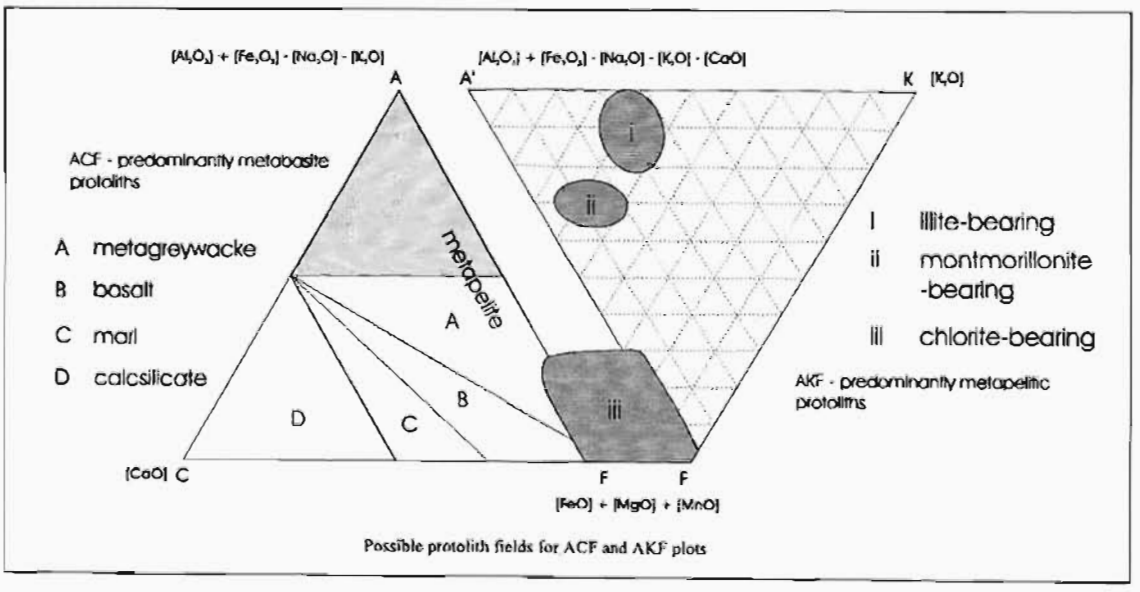

Possible protolith fields for ACF and AKF plots

Appendix A1 Major oxide values of the main whole rock components of the Madidima Nappe in the Mbongolwane Flats area
ACF parameters calculated as per Winkler (1967), Miyashiro (1973) and Mason and Moore (1982)

			90%Fe2O3 (T)	10%Fe2O3 (T)	(T)															
Molecular weight	60.07	101.82	71.84	159.68		70.930	40.31	56.07	61.97	94.20	79.89	141.92								
	SiO2	**Al2O3**	**FeO**	**Fe2O3**	**Fe2O3**	**MnO**	**MgO**	**CaO**	**Na2O**	**K2O**	**TiO2**	**P2O5**	**TOTAL**	**A**	**C**	**F**	**A+C+F**	**A%**	**C%**	**F%**	**Check**
SBAQ	53.16	17.01	8.63	1.07	10.66	0.212	4.73	8.33	3.90	0.62	1.04	0.33	99.99	0.12	0.15	0.24	0.51	23.18	29.33	47.49	100
SBA-BACK	45.99	17.69	10.75	1.33	13.27	0.217	6.05	10.90	3.15	0.67	1.07	0.98	99.98	0.14	0.19	0,30	0.64	21.77	30.59	47.64	100
QNPWR	52.08	16.74	9.41	1.16	11.62	0.210	4.80	8.30	3.48	0.93	1.43	0.45	100.05	0.13	0.15	0.25	0.53	23.82	28.12	48.06	100
MANDRB-ZAG1	47.15	17.82	9.77	1.21	12.06	0.190	6.51	9.85	3.65	0.80	1.42	0.49	99.95	0.13	0.18	0.30	0.61	21.74	28.89	49.37	100
MANDRB-ZAG2	46.85	17.78	9.98	1.23	12.32	0.192	6.76	9.99	3.24	0.81	1.44	0.53	99.91	0.14	0.18	0.31	0.63	22.14	28.46	49.40	100
ZAGQWR	55.66	17.59	6.12	0.76	7.56	0.109	5.17	6.48	4.60	1.59	0.94	0.29	99.98	0.12	0.12	0.22	0.45	26.65	25.64	47.71	100
SMMWR-$AG	52.85	17.95	8.36	1.03	10.32	0.148	5.47	7.41	2.92	1.48	0.63	0.30	99.48	0.15	0.13	0.25	0.54	28.15	24.58	47.27	100
SMMWRAG-1	58.95	17.02	6.22	0.77	7.68	0.122	3.54	7.18	3.31	0.83	0.51	0.22	99.36	0.13	0.13	0.18	0.43	29.51	29.67	40.81	100
BOAFSS1	51.36	12.89	14.33	1.77	17.69	0.259	4.34	7.65	2.55	0.37	2.53	0.31	99.95	0.10	0.14	0.31	0.55	18.34	24.91	56.75	100
BOAFSS2	54.21	12.68	12.77	1.58	15.77	0.242	4.34	7.09	2.84	0.34	2.10	0.23	99.86	0.09	0.13	0.29	0.51	18.16	24.91	56.92	100
BOAFSS3	50.14	12.96	14.34	1.77	17.70	0.295	4.96	8.15	2.23	0.74	2.50	0.27	99.93	0.11	0.15	0.33	0.58	18.93	24.96	56.11	100
BOAFSS4	52.21	12.79	13.78	1.70	17.01	0.247	4.43	7.32	2.88	0.35	2.36	0.27	99.87	0.09	0.13	0.31	0.53	17.67	24.67	57.66	100
BOAFS2	53.39	12.91	13.13	1.62	16.21	0.241	4.30	6.72	2.66	0.88	2.34	0.28	99.93	0.10	0.12	0.29	0.52	20.03	23.22	56.75	100
BOAFS3	54.25	12.76	13.76	1.70	16.99	0.219	3.87	7.48	2.24	0.61	1.55	0.17	100.15	0.11	0.13	0.29	0.53	20.04	25.15	54.80	100
BOAFS4	53.00	13.79	11.52	1.42	14.22	0.200	5.41	7.77	3.34	0.51	1.56	0.15	99.95	0.10	0.21	0.30	0.60	15.88	34.87	49.26	100
SMMS1	55.08	16.38	7.73	0.95	9.54	0.157	5.57	7.82	3.39	1.31	0.54	0.27	100.07	0.13	0.12	0.25	0.49	25.50	24.33	50.17	100
SMMS2	53.71	15.74	8.81	1.09	10.88	0.182	6.27	7.95	3.07	1.30	0.69	0.33	100.12	0.13	0.14	0.28	0.55	22.95	25.76	51.29	100
SMMS3	52.59	17.24	8.56	1.06	10.57	0.205	5.13	9.69	3.09	0.47	0.70	0.33	100.01	0.13	0.15	0.25	0.53	24.70	28.30	46.99	100
SMMS4	51.06	15.84	9.10	1.12	11.23	0.236	7.18	9.42	3.39	0.75	0.77	0.22	100.08	0.12	0.16	0.31	0.58	19.99	26.86	53.15	100
SMMS5	69.77	15.08	3.39	0.42	4.19	0.095	0.93	3.06	4.84	1.28	0.52	0.20	99.97	0.09	0.04	0.07	0.20	42.62	21.96	35.42	100
SMMS6	53.25	17.22	7.82	0.97	9.65	0.185	5.16	8.44	4.14	0.72	0.89	0.31	99.96	0.12	0.13	0.24	0.49	23.65	27.52	48.82	100
SMMS7	53.14	16.92	7.91	0.98	9.76	0.184	5.78	8.93	3.54	0.63	0.78	0.28	99.96	0.12	0.14	0.26	0.51	23.67	26.59	49.74	100
SMMS8	59.84	16.69	6.10	0.75	7.53	0.114	3.23	7.36	3.68	0.69	0.48	0.24	99.86	0.12	0.10	0.17	0.38	30.34	26.30	43.36	100
SMMS9	55.08	16.79	7.76	0.96	9.58	0.175	4.64	9.27	3.05	0.62	0.62	0.29	100.12	0.13	0.13	0.23	0.49	26.36	27.29	46.35	100
SMMS10	56.88	16.74	6.85	0.85	8.46	0.153	4.63	7.65	3.51	1.10	0.59	0.27	99.99	0.12	0.11	0.21	0.45	27.98	24.39	47.63	100

Appendix A2 Major oxide values of the main components of the Northern Mfongosi Valley area
ACF parameters as per Winkler (1967), Miyashiro (1973) and Mason and Moore (1982)

			90%Fe2O3(T)	10%Fe2O3(T)	(T)															
Molecular wehight	60.07	101.82	71.84	159.68		70.93	40.31	56.07	61.97	94.2	79.9	141.92								
	SiO2	**Al2O3**	**FeO**	**Fe2O3**	**Fe2O3**	**MnO**	**MgO**	**CaO**	**Na2O**	**K2O**	**TiO2**	**P2O5**	**TOTAL**	**A**	**C**	**F**	**A+C+F**	**A%**	**C%**	**F%**	Check
PSFU/1	53.13	14.61	10.97	1.35	13.54	0.199	4.07	8.13	4.33	0.4	1.48	0.21	100.09	0.08	0.14	0.26	0.48	16.24	30.25	53.50	100
PSFU/2	53.92	14.27	10.23	1.26	12.63	0.202	4.18	9.27	3.74	0.41	1.26	0.17	100.06	0.08	0.17	0.25	0.50	16.75	33.22	50.03	100
PSFU/12B	59.78	14.15	7.82	0.97	9.66	0.157	3.51	6.26	5.02	0.23	1.07	0.18	100.02	0.06	0.11	0.20	0.37	16.58	30.06	53.36	100
PSFU/13	45	16.4	12.25	1.51	15.12	0.2	6.97	10.23	2.7	0.08	2.91	0.33	99.95	0.13	0.18	0.35	0.65	19.26	27.86	52.87	100
PSFU/14	48.62	12.95	10.97	1.35	13.54	0.194	9.01	11.12	2.26	0.09	2.01	0.22	100.01	0.10	0.20	0.38	0.68	14.54	29.36	56.10	100
PSFU/32	53.21	19.44	6.94	0.86	8.57	0.136	5.83	9.13	3.03	1.22	0.22	0.04	100.82	0.13	0.16	0.24	0.54	24.88	30.13	44.99	100
PSFU/37	97.88	0.29	0.53	0.07	0.65	0.031	0.04	0.81	0.07	0.06	0.01	0.01	99.84	0.00	0.01	0.01	0.02	6.03	58.51	35.46	100
PSFU/44	60.87	19.42	8.51	1.05	10.51	0.059	1.64	0.04	0.19	5.59	1.33	0.18	99.83	0.13	0.00	0.16	0.30	45.63	0.24	54.13	100
PSFU/45	63.04	21.57	4.62	0.57	5.7	0.022	1.1	0.04	0.98	6.13	1.18	0.16	99.92	0.13	0.00	0.09	0.23	59.24	0.31	40.45	100
PSFU/46	63.85	20.08	5.20	0.64	6.42	0.021	1.49	0.05	0.26	6.05	0.96	0.11	99.29	0.13	0.00	0.11	0.24	54.58	0.37	45.06	100
PSFU/51	58.13	14.2	7.84	0.97	9.68	0.202	2.59	8.19	4.62	1.09	1.06	0.19	99.95	0.06	0.15	0.18	0.38	15.56	38.27	46.17	100
PSFU/52	63.94	14.56	5.49	0.68	6.78	0.122	2.86	4.6	5.8	0.49	0.72	0.1	99.99	0.05	0.08	0.15	0.28	17.33	29.34	53.33	100

Appendix A3 Major oxide values of the main components of the Northern Mfongosi Valley area
ACF parameters and A'KF parameters (highlighted) as per Winkler (1967), Miyashiro (1973) and Mason and Moore (1982)

			90%Fe2O3 (T)	10%Fe2O3 (T)	(T)								A	C	F	A+C+F	A%	C%	F%	
Molecular weight	60.07	101.82	71.84	159.68		70.930	40.31	56.07	61.97	94.20	79.89	141.92								
	SiO2	Al2O3	FeO	Fe2O3	Fe2O3	MnO	MgO	CaO	Na2O	K2O	TiO2	P2O5	TOTAL	A'	K	F	A'+K+F	A'%	K%	F%	Check
Cg-STAWR	53.00	14.29	11.31	1.40	13.96	0.220	4.34	10.66	1.97	0.21	1.17	0.14	99.96	0.12	0.19	0.27	0.57	20.07	33.16	46.77	100
Fg-STAWR	51.28	15.57	10.47	1.29	12.93	0.205	6.24	10.03	2.61	0.19	0.86	0.11	100.02	0.12	0.18	0.30	0.60	19.50	29.85	50.64	100
FU2H-A	71.42	14.83	3.13	0.39	3.87	0.122	0.62	2.29	3.57	2.03	0.38	0.08	99.22	0.03	0.02	0.02	0.07	40.60	31.17	28.23	100
FU2H-B	54.52	17.00	7.99	0.99	9.86	0.185	5.05	9.06	3.06	0.05	0.84	0.33	99.94	0.12	0.16	0.24	0.52	23.52	30.84	45.63	100
FU2H-C	57.44	17.32	7.40	0.91	9.13	0.169	3.28	8.15	3.12	0.20	0.77	0.16	99.75	0.12	0.15	0.19	0.46	27.09	31.92	41.00	100
FU2H-D	70.59	14.77	3.09	0.38	3.82	0.300	0.56	3.15	3.54	1.80	0.39	0.10	99.01	0.02	0.02	0.02	0.05	27.52	34.96	37.53	100
FU2H-E	56.72	17.56	7.98	0.99	9.85	0.186	5.57	5.68	2.98	0.13	0.84	0.31	99.81	0.13	0.10	0.25	0.48	26.78	21.00	52.22	100
FU2H-F	67.51	16.13	3.32	0.41	4.10	0.075	0.98	2.96	4.29	2.72	0.36	0.11	99.24	0.01	0.03	0.03	0.07	15.09	43.16	41.75	100
FU2H-F	68.20	16.22	3.80	0.47	4.69	0.128	0.69	2.90	4.55	2.09	0.46	0.11	100.03	0.01	0.02	0.02	0.06	25.29	37.64	37.07	100
FU2H-G	73.34	13.29	2.76	0.34	3.41	0.120	1.94	2.92	4.17	0.24	0.41	0.21	100.05	0.06	0.05	0.09	0.20	30.92	25.63	43.44	100
FU2H-H	73.32	13.66	2.28	0.28	2.82	0.088	0.84	4.05	3.49	0.99	0.31	0.09	99.66	0.07	0.07	0.05	0.20	35.40	37.00	27.60	100
LBQ/3/VAR	75.64	14.51	3.12	0.39	3.85	0.012	0.60	0.03	0.34	4.38	0.32	0.03	99.72	0.09	0.05	0.02	0.16	59.09	29.74	11.17	100

Appendix A4 Major oxide values of the host rocks in the Ngubevu West and Ngubevu East areas

ACF parameters and AKF parameters (highlighted) as per Winkler (1967), Miyashiro (1973) and Mason and Moore (1982)

			90% Fe2O3 (T)	10% Fe2O3 (T)	(T)														
Molecular Weight	60.07	101.82	71.84	159.68		70.930	40.31	56.07	61.97	94.20	79.89	141.92							
	SiO2	Al2O3	FeO	Fe2O3	Fe2O3	MnO	MgO	CaO	Na2O	K2O	TiO2	P2O5	TOTAL	A A'	C K	F F	A+C+F A'+K+F	A% A'%	C% K%	F% F%	Check
NGW-A1-HR	70.77	16.72	3.24	0.40	4.00	0.017	1.30	0.22	2.88	3.07	1.08	0.08	100.15	0.08	0.03	0.08	0.19	43.18	16.81	40.01	100
NGW 2	50.96	18.01	10.57	1.31	13.05	0.195	6.00	7.80	2.18	0.05	1.63	0.20	100.08	0.15	0.14	0.30	0.59	25.43	23.69	50.88	100
NGW 2A	79.80	12.06	0.62	0.08	0.77	0.008	0.68	0.20	3.57	1.66	1.09	0.17	100.01	0.04	0.02	0.03	0.08	48.10	21.12	30.77	100
NGW 4	49.35	16.46	9.45	1.17	11.67	0.201	7.44	9.63	2.81	0.76	1.48	0.15	99.95	0.12	0.17	0.32	0.61	19.06	28.33	52.61	100
NGW 6	71.42	15.70	1.86	0.23	2.30	0.007	1.27	0.09	4.99	2.37	1.75	0.07	99.96	0.05	0.03	0.06	0.13	36.90	19.20	43.90	100
NGW 7	48.58	17.49	10.10	1.25	12.47	0.161	6.67	6.54	4.47	0.82	2.23	0.27	99.69	0.10	0.12	0.31	0.52	18.85	22.27	58.87	100
NGW/A1/7	52.57	17.93	11.55	1.43	14.26	0.143	6.30	1.72	3.49	1.30	2.07	0.22	100.01	0.11	0.03	0.32	0.46	24.73	6.60	68.67	100
NGW 8	49.23	17.00	10.04	1.24	12.39	0.225	7.24	9.21	1.70	1.47	1.43	0.16	100.05	0.13	0.16	0.32	0.62	21.29	26.56	52.15	100
NGW 9	76.54	14.33	1.35	0.17	1.67	0.020	0.90	0.00	2.56	2.90	0.85	0.03	99.81	0.07	0.03	0.04	0.14	49.11	21.69	29.20	100
NGW$FLOAT	63.50	12.87	7.97	0.98	9.84	0.254	3.57	4.80	2.99	0.96	1.05	0.26	100.09	0.07	0.09	0.20	0.36	20.43	23.60	55.98	100
NGW/HR	53.24	17.47	11.88	1.47	14.67	0.169	6.96	1.68	3.31	0.63	1.80	0.22	100.16	0.12	0.03	0.34	0.49	24.57	6.10	69.33	100
NGW 14	69.54	17.11	2.45	0.30	3.02	0.064	1.26	0.48	3.31	4.36	0.42	0.08	99.64	0.06	0.05	0.07	0.17	35.41	26.57	38.01	100
NGW 15	50.41	17.19	9.59	1.18	11.84	0.182	6.16	8.47	3.97	0.09	1.47	0.18	99.97	0.11	0.15	0.29	0.55	20.18	27.41	52.41	100
NGW 20	48.25	16.32	10.28	1.27	12.69	0.189	6.47	11.11	2.96	0.07	1.75	0.20	100.00	0.12	0.20	0.31	0.62	19.18	31.75	49.07	100
NGW 25	48.20	16.61	9.70	1.20	11.97	0.180	7.75	10.59	2.50	0.14	1.47	0.16	99.58	0.13	0.19	0.33	0.65	19.89	29.17	50.93	100
NGW 26	50.32	16.13	9.36	1.16	11.55	0.185	6.42	10.06	2.91	0.44	1.51	0.22	99.74	0.11	0.18	0.29	0.59	19.47	30.64	49.89	100
NGW 27	49.57	17.73	10.75	1.33	13.27	0.178	8.40	6.02	0.29	3.03	1.52	0.16	100.16	0.15	0.11	0.36	0.61	23.73	17.50	58.77	100
NGW 27A	47.32	17.03	9.95	1.23	12.29	0.199	7.28	11.05	2.64	0.32	1.47	0.17	99.78	0.13	0.20	0.32	0.65	19.90	30.41	49.69	100
NGW 28	49.68	15.78	9.57	1.18	11.82	0.182	7.53	10.02	2.93	0.49	1.39	0.15	99.99	0.11	0.18	0.32	0.61	17.98	29.24	52.78	100
NGW 29A	47.26	17.71	10.30	1.27	12.72	0.190	6.84	11.31	2.13	0.17	1.50	0.16	99.99	0.15	0.20	0.32	0.66	21.97	30.41	47.61	100
NGW 29B	48.46	17.35	9.86	1.22	12.17	0.176	7.26	9.49	2.88	0.62	1.41	0.15	99.97	0.12	0.17	0.32	0.61	20.35	27.56	52.08	100
NGW 30	47.73	16.38	8.76	1.08	10.82	0.183	6.61	12.54	4.15	0.21	1.24	0.14	100.01	0.10	0.22	0.29	0.61	16.12	36.62	47.25	100
NGW 31	48.76	18.57	10.89	1.35	13.45	0.175	8.08	4.85	2.18	2.06	1.60	0.18	99.91	0.13	0.09	0.35	0.57	23.27	15.05	61.68	100
NGW 35	58.18	12.53	6.65	0.82	8.21	0.137	4.24	13.93	1.77	0.03	0.82	0.09	99.95	0.10	0.25	0.20	0.55	18.14	45.38	36.47	100
NGW 36	49.82	18.31	10.74	1.33	13.26	0.180	8.66	3.90	1.91	2.15	1.58	0.18	99.94	0.13	0.07	0.37	0.57	23.56	12.18	64.26	100
NGW 39A	48.37	16.60	11.06	1.37	13.65	0.194	7.22	8.47	2.98	0.90	1.56	0.17	100.12	0.11	0.15	0.34	0.60	18.97	25.15	55.89	100
NGW 39B	47.58	17.46	10.42	1.29	12.86	0.195	8.09	8.45	2.93	0.76	1.52	0.18	100.02	0.12	0.15	0.35	0.62	19.92	24.18	55.90	100
NGW 40	48.64	15.22	11.45	1.41	14.14	0.213	7.27	10.38	2.21	0.31	1.57	0.18	100.14	0.12	0.19	0.34	0.65	18.44	28.60	52.96	100

Appendix A4 (continued) Major oxide values of the host rocks in the Ngubevu West and Ngubevu East areas
ACF parameters and AKF parameters (highlighted) as per Winkler (1967), Miyashiro (1973) and Mason and Moore (1982)

				10% Fe2O3 (T)	(T)															
Molecular Weight	60.07	101.82		159.68		70.930	40.31	56.07	61.97	94.20	79.89	141.92								
	SiO2	**Al2O3**	**FeO**	**Fe2O3**	**Fe2O3**	**MnO**	**MgO**	**CaO**	**Na2O**	**K2O**	**TiO2**	**P2O5**	**TOTAL**	**A**	**C**	**F**	**A+C+F**	**A%**	**C%**	**F%**	**Check**
NGW 41	49.63	17.74	10.17	1.26	12.56	0.175	4.20	9.90	3.78	0.12	1.64	0.22	99.96	0.12	0.18	0.25	0.54	22.00	32.42	45.58	100
NGW 42	47.71	16.99	11.29	1.39	13.94	0.232	6.11	9.01	3.61	0.22	2.01	0.26	100.10	0.12	0.16	0.31	0.59	19.57	27.34	53.09	100
NGW 43	46.59	17.17	11.87	1.47	14.66	0.233	5.94	10.13	2.61	0.40	2.05	0.26	100.04	0.13	0.18	0.32	0.63	20.93	28.77	50.30	100
NGW 44	49.45	15.67	9.82	1.21	12.12	0.192	6.68	11.14	2.77	0.35	1.51	0.16	100.04	0.11	0.20	0.31	0.62	18.33	32.21	49.46	100
NGW 45	51.92	17.04	9.27	1.14	11.44	0.159	6.61	7.86	2.99	0.55	1.37	0.16	100.10	0.12	0.14	0.30	0.56	21.67	25.22	53.11	100
NGW 52A	49.80	15.53	9.98	1.23	12.32	0.175	9.95	7.02	3.31	0.49	1.27	0.16	100.03	0.10	0.13	0.39	0.62	16.52	20.36	63.12	100
NGW 52B	48.56	16.45	10.32	1.27	12.74	0.206	7.33	10.39	2.42	0.19	1.57	0.18	100.03	0.13	0.19	0.33	0.64	20.01	28.86	51.14	100
NGW 59	34.59	1.88	1.04	0.13	1.28	0.249	2.85	58.70	0.00	0.08	0.10	0.05	99.78	0.02	1.05	0.09	1.15	1.60	90.72	7.68	100
NGE/1	49.54	17.38	9.69	1.20	11.96	0.158	6.26	10.78	2.03	0.54	1.41	0.16	100.22	0.14	0.19	0.29	0.62	22.38	30.79	46.83	100
NGE/2	51.10	17.49	9.91	1.22	12.23	0.174	6.59	8.14	2.27	0.48	1.37	0.16	100.01	0.14	0.15	0.30	0.59	23.47	24.74	51.79	100
NGE/3	49.67	17.69	10.03	1.24	12.38	0.166	6.70	9.01	2.19	0.50	1.46	0.17	99.95	0.14	0.16	0.31	0.61	23.10	26.36	50.54	100
NGE/4	48.44	17.52	9.72	1.20	12.00	0.177	6.97	10.29	2.39	0.63	1.42	0.17	100.00	0.13	0.18	0.31	0.63	21.37	29.20	49.43	100
NGE/5	47.97	16.89	9.74	1.20	12.02	0.175	7.82	9.56	3.07	0.34	1.29	0.11	99.25	0.12	0.17	0.33	0.62	19.31	27.38	53.31	100
NGE/6	49.12	17.49	9.37	1.16	11.57	0.175	7.03	9.75	3.06	0.58	1.27	0.13	100.16	0.12	0.17	0.31	0.60	20.42	28.76	50.82	100
NGE/7	49.05	17.57	9.55	1.18	11.79	0.172	7.33	8.94	3.61	0.34	1.20	0.13	100.13	0.12	0.16	0.32	0.59	19.85	26.81	53.34	100

Appendix A5 Whole rock major element oxides for the Phoenix area

			90%Fe2O3 (T)	10%Fe2O3 (T)	(T)							
Molecular weight	60.07	101.82	71.84	159.68		70.93	40.31	56.07	61.97	94.2	79.89	141.92	
	SiO2	**Al2O3**	**FeO**	**Fe2O3**	**Fe2O3(T)**	**MnO**	**MgO**	**CaO**	**Na2O**	**K2O**	**TiO2**	**P2O5**	**TOTAL**
PH 1	42.77	16.72	14.39	1.78	17.76	0.22	8.27	12.85	0.47	0.11	0.64	0.01	99.81
PH 3	77.86	13.91	0.92	0.11	1.13	0.03	0.14	0.96	4.14	1.73	0.03	0.02	99.94
PH 4	77.76	13.87	0.81	0.10	1.00	0.01	0.37	0.77	4.44	1.65	0.06	0.02	99.94
PH 6	77.18	12.61	1.50	0.19	1.85	0.03	0.51	3.56	3.09	0.98	0.15	0.03	99.98
PH 7	41.07	15.52	15.96	1.97	19.70	0.21	7.89	13.73	0.37	0.19	1.02	0.01	99.72
PH 8	40.62	15.45	17.22	2.13	21.26	0.19	7.95	12.41	0.68	0.16	0.89	0.18	99.78
PH 8B	78.97	12.05	1.26	0.16	1.56	0.03	0.44	3.15	3.17	0.68	0.12	0.02	100.17
PH 9C	45.71	6.53	14.80	1.83	18.27	0.24	18.64	9.05	0.36	0.03	0.25	0.01	99.10
PH 10	44.82	17.66	11.27	1.39	13.91	0.20	8.46	13.42	0.66	0.23	0.59	0.01	99.96
PH 10B	46.53	16.82	9.86	1.22	12.17	0.21	8.83	14.01	0.86	0.19	0.36	0.02	100.01
PH 11	42.00	16.33	15.05	1.86	18.58	0.19	8.33	13.10	0.61	0.15	0.65	0.01	99.95
PH 13	44.98	15.90	14.39	1.78	17.77	0.21	13.63	6.30	0.57	0.24	0.44	0.11	100.14
PH 14	50.44	10.32	10.27	1.27	12.68	0.23	14.55	10.46	0.70	0.27	0.30	0.07	100.03
PH 20	43.64	17.18	12.71	1.57	15.69	0.19	7.53	14.34	0.52	0.11	0.69	0.01	99.90
PH 21	46.69	22.53	5.65	0.70	6.98	0.13	6.61	14.59	1.38	0.33	0.13	0.01	99.39

Appendix B1 - Sampling localities and gold values in parts per billion (fire assay) in the Mbongolwane flats area (samples in yellow are veins)

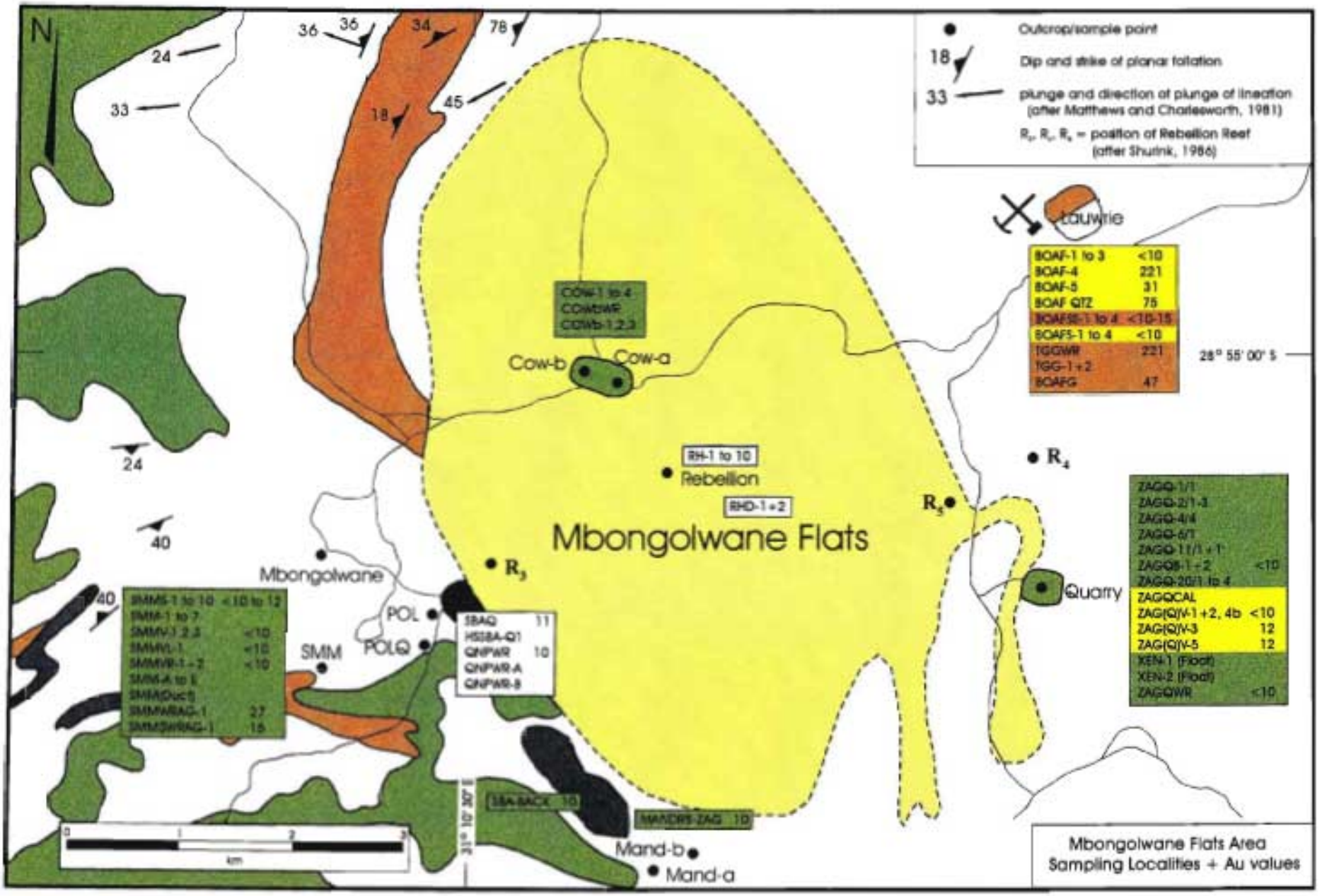

Appendix B2 Sampling localities and gold values in parts per billion (fire assay) in the Northern Mfongosi Valley area (samples in yellow are veins)

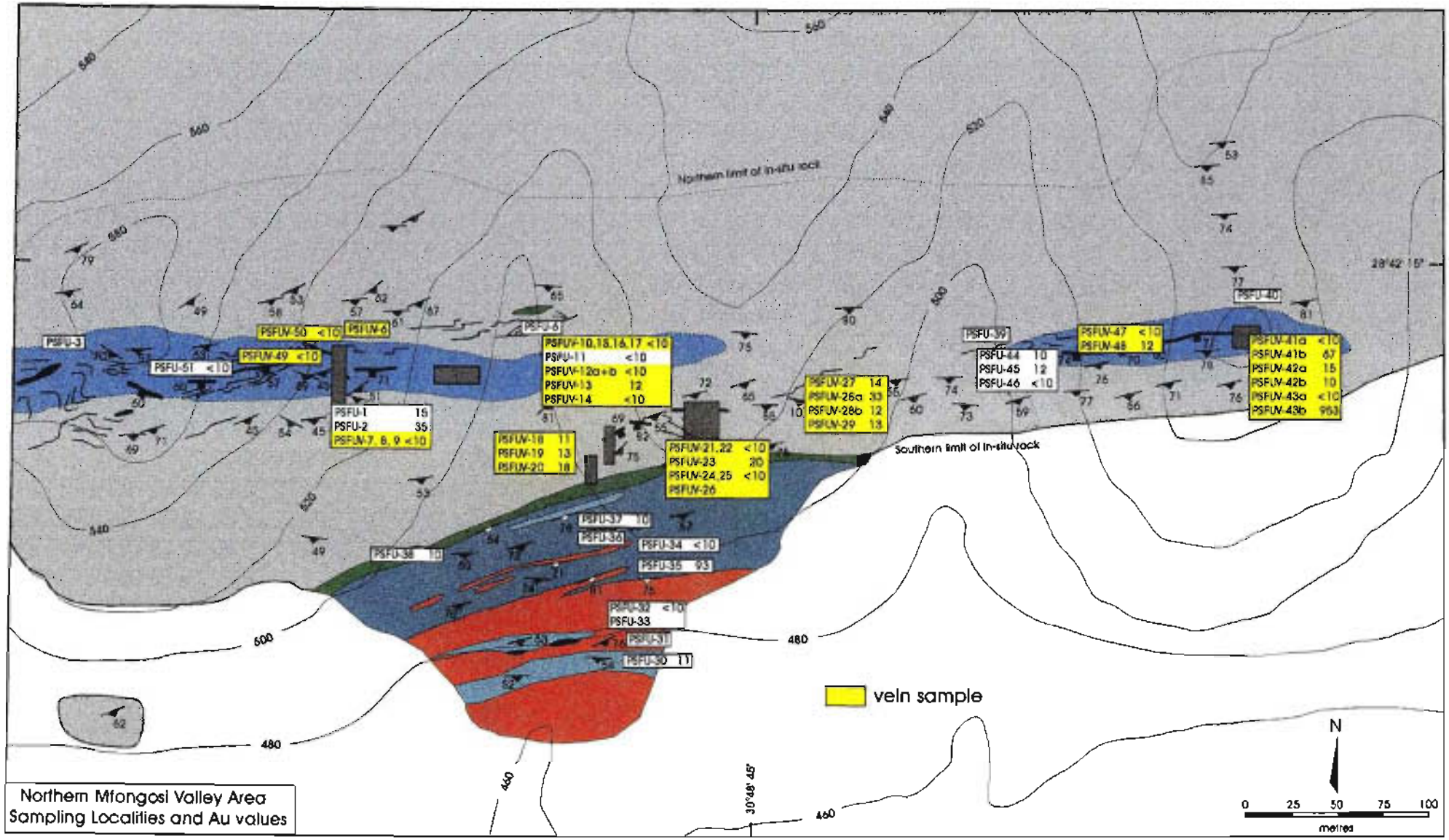

Appendix B3 Sampling localities and gold values in parts per billion (fire assay) in the Southern Mfongosi Valley area (samples in yellow are veins)

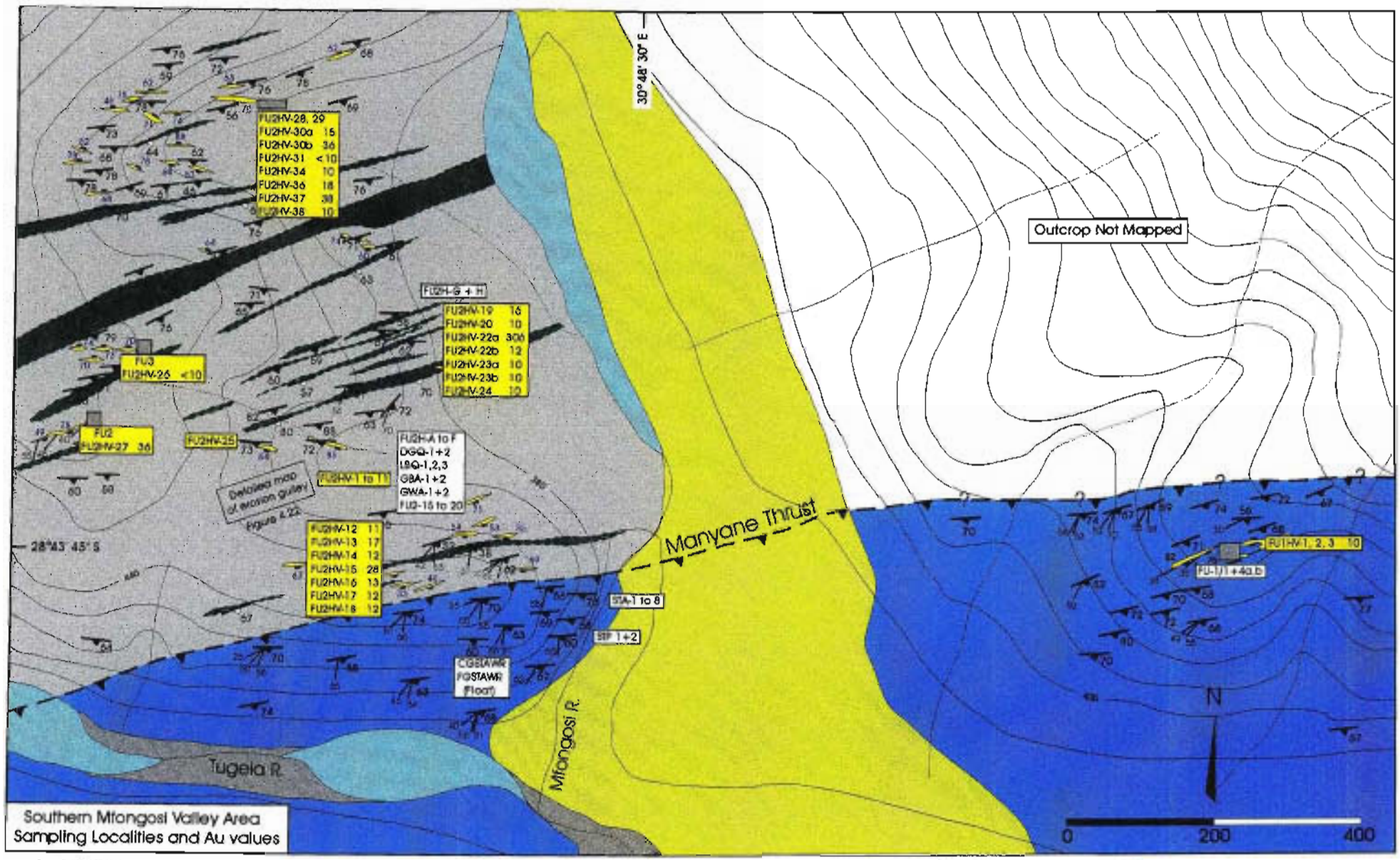

Appendix B3 Sampling localities and gold values in parts per billion (fire assay) in the erosion donga in the Southern Mfongosi Valley area (samples in yellow are veins)

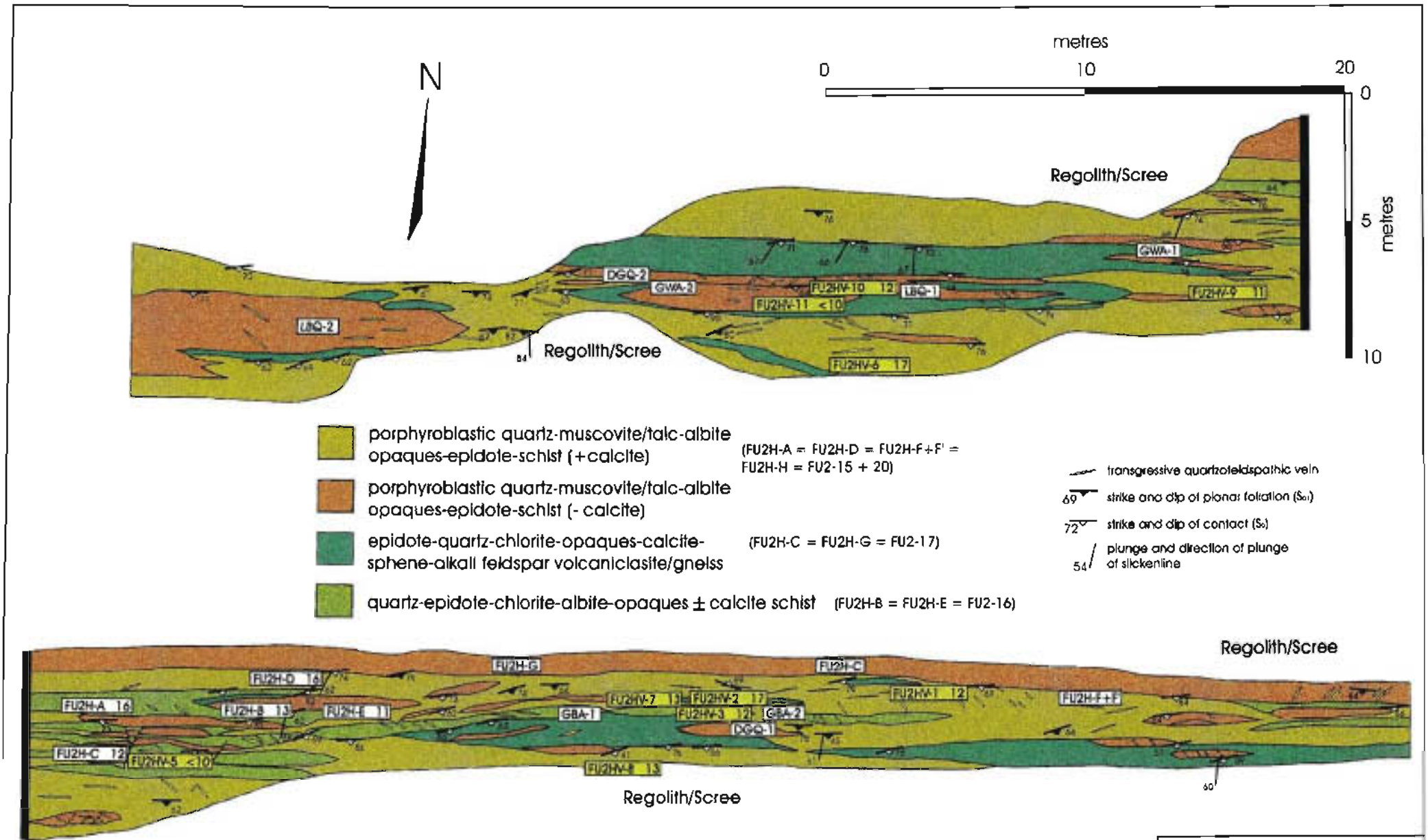

Detailed Map of Erosion Donga in Southern Mfongosi Valley Sampling Localities and Au values

Appendix B4 Sampling localities and gold values in parts per billion (fire assay) in the Ngubevu West area (samples in yellow are veins)

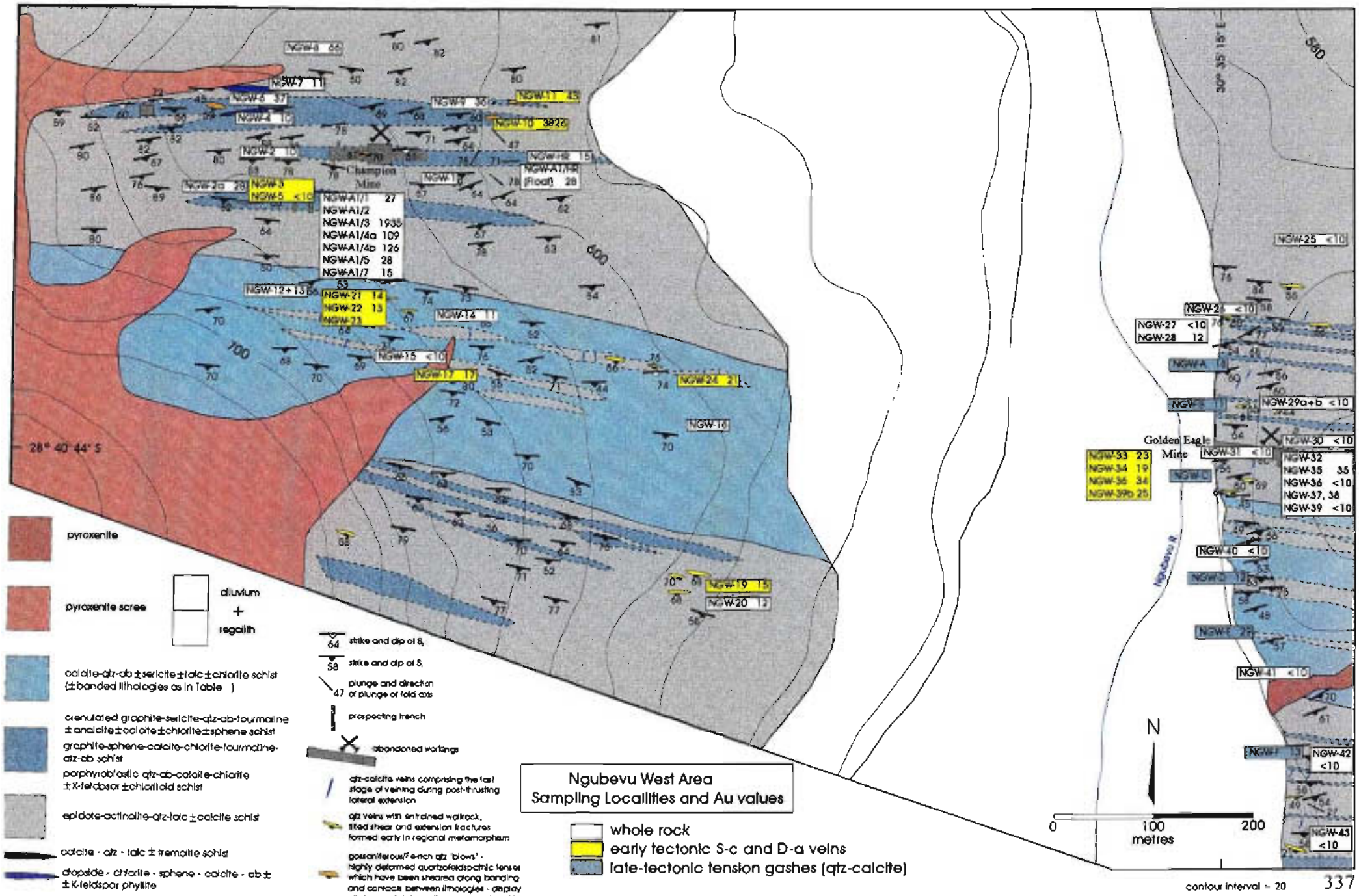

Appendix B4 Sampling localities and gold values in parts per billion (fire assay) in the Ngubevu East area (samples in yellow are veins)

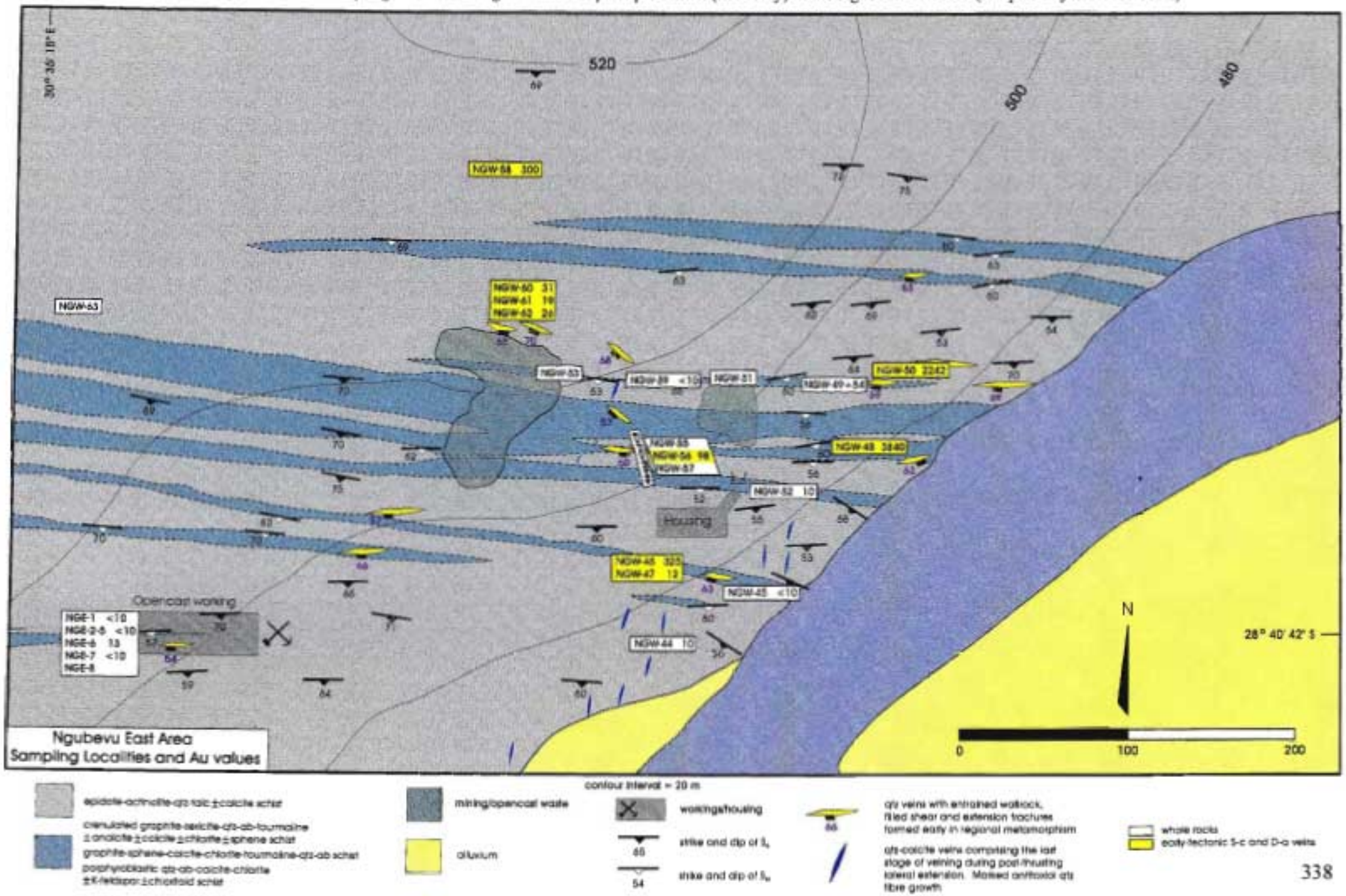

Appendix B5 Sampling localities and gold values in parts per billion (fire assay) in the Phoenix Mine area (samples in yellow are veins)

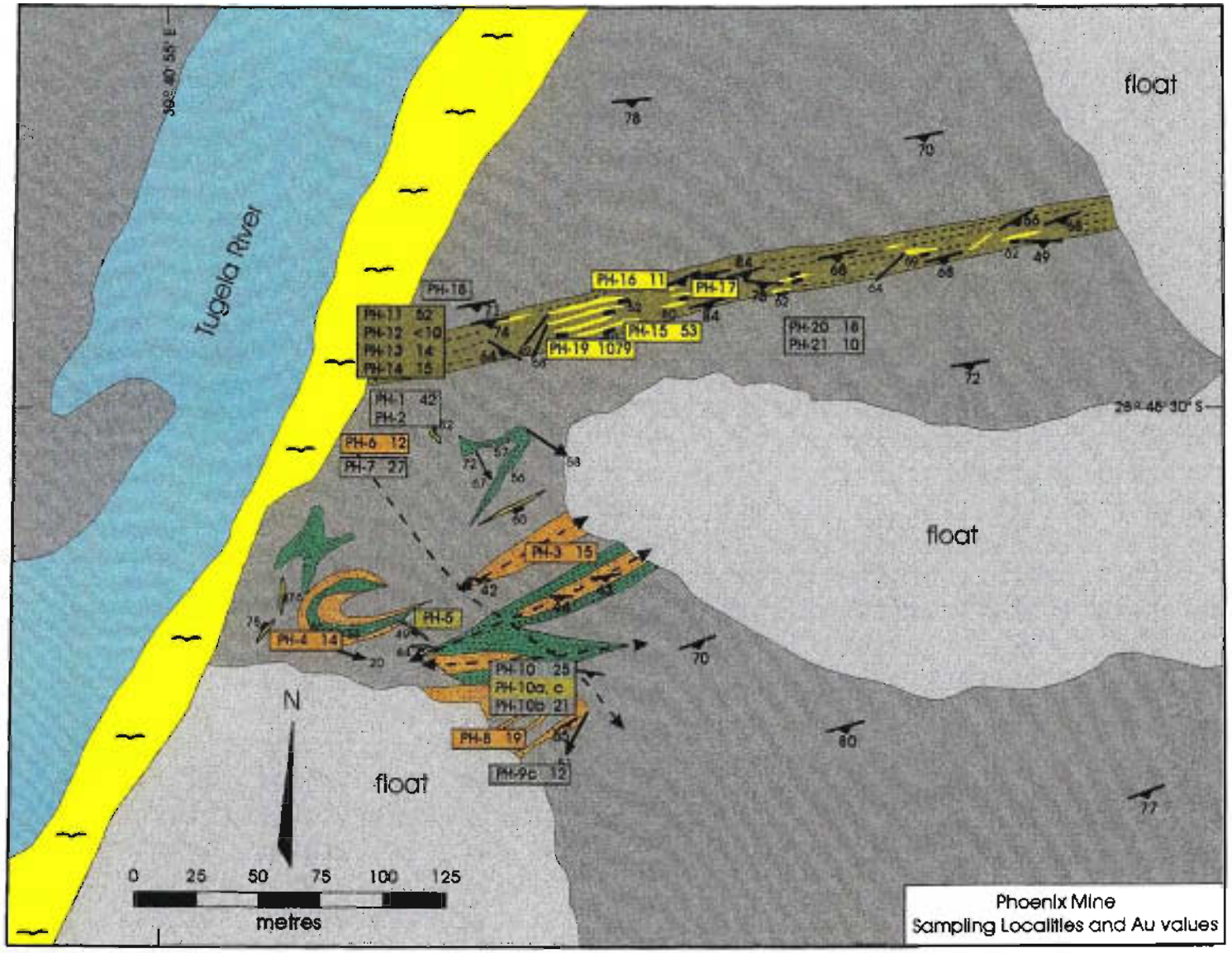

Appendix C1

Relationship between angles and shear strain (Ramsay, 1967; Ramsay and Huber, 1983)

Shear strain across a zone of homogeneous or continuous simple shear may be expressed as a function of the angle made by a linear marker in the shear zone. Assuming that the shear zone has parallel sides and that the linear marker was initially perpendicular to the margins of the shear zone, the angle between the initial 90° and the final orientation of the marker may be termed ψ (see figure below). The amount of shear strain induced in the shear zone is expressed in terms of the shear strain (γ) parallel to the walls of the shear zone:

$$\gamma = \tan \psi$$

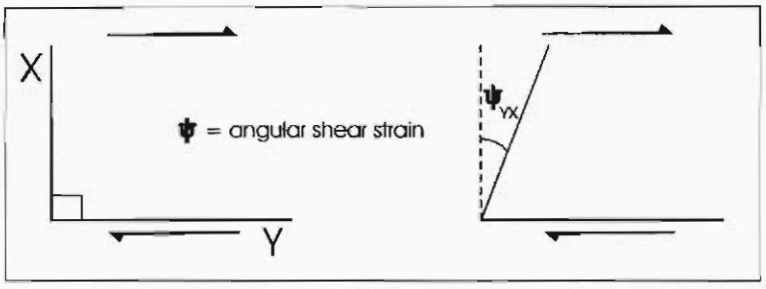

In the event that there be no initially perpendicular marker, but other markers are present, the initial orientation of which is known, then the change in angle of the marker may also be used for strain estimation (Figure 3.25) and the reader is referred to Sessions 1 and 2 of Ramsay and Huber (1983) as a fuller description here is not warranted.

Calculation of pure shear in homogeneous straining (Price and Cosgrove, 1990)

The most commonly used method for measuring the change in length of a line is that of extension (e) which is defined as follows and shown in the figure below:

$$e = (l_1 - l_0)/l_0 = dl/l_0$$

where l_0 and l_1 are the original and final length of a line. This formula may be applied in two dimensions, that is, to a square deforming to a rectangle. If the square initially contains a unit circle, the strain ratio (ratio of the long axis to the short axis of a pure shear ellipse) may be calculated for the ellipse which results from flattening of the square. Extension may be checked by applying the parameter of quadratic extension or elongation:

$$\lambda = (1 + e)^2$$

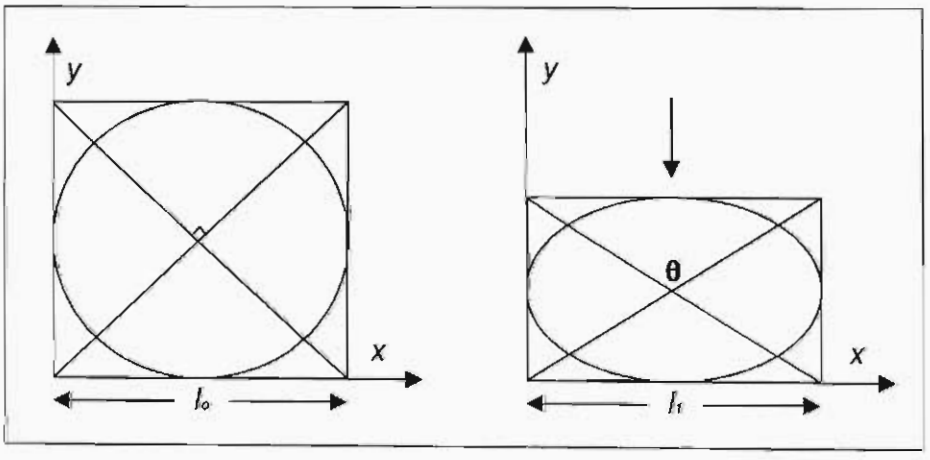

Appendix C2

Mathematical solution of Fernandez (1987) for calculation of the simple shear ratio from the final orientations of a number of initially randomly-orientated rigid objects in an incompetent matrix undergoing simple shear. Note that the θ of Ramsay and Huber (1983) is akin to the ω used here

$$\cot \theta' = \cot \theta + \gamma \quad \text{Ramsay (1967)} \qquad (1)$$

If no dilation takes place during strain, $\lambda_1.\lambda_2 = 1$ (λ = conventional quadratic extension, the strain ellipsoid has the same area as the initial unit circle prior to shearing) then an element of a sector of the initial unit circle with an element angle $d\theta$ is transformed by strain to an element of sector of the deformation ellipse (angle element $d\theta'$), the areas of both being the same. The ratio between $d\theta$ and $d\theta'$ can be obtained directly from the ratio of the area of both element sectors.

If the Area of the sector of circle $Ac = d\theta.r^2/2$ and...
The area of the sector of the ellipse $Ae = d\theta'.r'^2/2$ and r' is given in multiples of r (where r is the unit radius of the unit circle prior to shearing) then the ratio

$$d\theta/d\theta' = r'^2 \qquad (2)$$

At the same time, as the fraction of markers at the initial state oriented between ω and $(\theta + d\theta)$ is the same as the fraction of markers that lies between θ' and $\theta' + d\theta'$ after strain, the *relative orientation density* D in the θ' direction in the strained state is given by:

$$D = d\theta/d\theta' = r'^2 \qquad (3)$$

The ratio of particles as opposed to a ratio of angles is inferred to be the inverse of this value. Hence, if there are 101 particles angularly distributed evenly over 180° then $d\theta = 0.56$ and for a ten degree interval $d\theta = 5.6$.

Now, r' has a maximum value in the direction of the major axis of the strain ellipse, the density distribution function also has a maximum, D_m, in the *same direction*. As the vector radius r' has a unit length in K and K' directions, the relative orientation density along both of these directions is equal to 1.

Differentiating (2) and taking into account (3):

$$D = \sin^2\theta/\sin^2\theta' \qquad (4)$$

Rearranging (1) gives

$$\sin^2\theta'/\sin^2\theta = (\cos\theta' - \gamma\sin\theta) + \sin^2\theta' \qquad (5)$$

Taking (4) into account and combining it with (5) gives:

$$D = [(\cos\theta' - \gamma\sin\theta') + \sin^2\theta']^{-1} \qquad (6)$$

which is a function that gives the relative orientation density distribution of perfectly linear markers in a two-dimensional simple shear system (the density is "normalized" or given in multiples of the uniform distribution), the angles being referred to the strained state.

The numerical value of D_m can be obtained from (7) which gives the principal quadratic extension λ_1 of the strain ellipse (Nadai, 1931 *in* Fernandez, 1987):

$$\lambda_1 = 1 + \gamma/2[\gamma + (4 + \gamma^2)^{0.5}] \qquad (7)$$

But, as strain without area change implies that $D_m = \lambda_1$, (7) also gives the *value* of the density maximum as a function of the amount of shear.

Appendix D1

Applications of Oxygen Isotope Studies

Stable isotope studies encompass an extremely broad range of applications such that the examination of an individual isotope (eg C, O or S) is regarded as a specialized field. The uses of stable isotopes in applied geology, mineralogy and exploration are well established. Some of the various techniques used, as well as the results obtained from them, are outlined below. Special reference is made to oxygen isotope studies:

1) *Estimates of the provenance or protoliths of unmetamorphosed and metamorphosed rocks* - the three basic groups of rocks; igneous, metamorphic and sedimentary, occupy fairly distinct ranges in the total possible $\delta^{18}O$ spectrum (eg Faure, 1986; Bowen, 1988)

2) *Calculation of the temperature of equilibration and crystallization between co-existing coevally-formed minerals in the absence of post-crystallization re-equilibration* - the difference in the $^{18}O/^{16}O$ ratios between co-existing minerals varies systematically with temperature (Appendix D3). Examples of mineral pairs used for these purposes are: quartz-calcite, anorthite-magnetite, albite-magnetite and quartz-magnetite (from Table 25.2 in Faure, 1986).

3) *Estimation of the composition of the fluid phase/water co-existing with a particular mineral during mineral formation* - the oxygen isotope fractionation between mineral and fluid is a function of temperature (eg Friedman and O'Neil, 1977). This technique may also be used paired, co-formed minerals equilibrated oxygen with the same reservoir at the same temperature.

4) *Estimation of $^{18}O/^{16}O$ homogenization during regional and dynamic metamorphism* - the extent or degree of isotope homogenization in terms of area, volume, position relative to intrusions etc, may be calculated. The scale and degree of homogeneity of $\delta^{18}O$ in different lithologies from a metamorphic terrain are useful for assessing the importance of fluid flow (eg Wickham and Taylor, 1985). Stemming from this, the isotopic evolution of a regionally and dynamically metamorphosed terrain may be defined (eg Kerrich *et al.*, 1984; Peters and Wickham, 1995). This aspect has greater implications; the thermochemical conditions of an ore-forming fluid may be derived from the oxygen isotope alteration of wall rocks (eg Hoy, 1993).

5) *The degree of mixing of two pre-existing or proposed hypothetical fluids to form a single more complex fluid* - This process also applies in the semi-solid or molten state wherein mixing magmas and contact aureoles of intrusions may be examined for isotopic homogenization or ^{18}O depletion/enrichment (eg Larson and Taylor, 1986; Larson and Geist, 1995).

6) *The determination of fluid-rock interaction* is perhaps the most widely-used application of oxygen isotope geochemistry, particularly in the case of economic mineral-enriched veins or massive orebodies have formed (eg Gray *et al.*, 1991). Constraints on the thermal system, using isotopic studies in combination with other areas of geology such as structural geology and metamorphism, include the following:

- estimates of water fluid:rock ratios
- indications as to the system being fluid- or rock-buffered
- the degree of fluid circulation, convection or diffusion in relation to the scale of mineralization and the degree of openness of the system, that is, the scale of the fluid system

Appendix D2

Sample Preparation and Oxygen Isotope Extraction

All samples were initially selected on the basis of their state of weathering, position in the field and significance in relation to the problem of mineralization. Only whole rock samples which are unveined, or veins which are composed of massive quartz and/or monominerallic portions of the veins, are considered for analysis. The entire preparation procedure was done by the author at the University of Natal (Durban). Whole rock samples which were not entirely fresh had their weathered portions removed by diamond sawing. Fresh portions of the material were then washed in distilled water, placed in an ultrasound cleaner filled with distilled water and dried thoroughly in a furnace at 110°C for 24 hours. The samples were then crushed in a jaw crusher and milled in a flat tungsten mill to provide a powder-like specimen which was then used for analysis.

Sample analysis was performed by the author at the University of Cape Town Geological Sciences Department (South Africa), under the guidance of Dr C. Harris. Oxygen was liberated from the silicate minerals by the Chlorine Triflouride (ClF_3) method of Vennemann and Taylor (1990), by reaction of 10 mg of sample with BrF_5 in sealed nickel tubes. The liberated oxygen was then converted in-line to CO_2 by reaction with a hot carbon/graphite rod so as to produce a more manageable and less volatile product for mass spectrometry. The samples were then transferred to break-seal glass tubes which were inserted into the MAT 252 Mass Spectrometer in the Department of Archaeology at the University of Cape Town. Two NBS-28 standards were included in each set of ten samples so as to provide a good standard control and as indicators of the analytical precision of the machine. Mass spectrometer results are presented relative to a standard CO_2 gas which is let into the spectrometer with each sample (Appendix D4 - δ^{46}). These results are converted to values relative to SMOW, in parts per thousand, by the formula presented in Appendix D3 (Craig 1963). Note that the average of the two NBS-28 standards are used in the calculation of the final results (Appendix D4 - Av. NBS-28).

Appendix D3

Standards, Comparison of Standards, Fractionation

Oxygen is the most abundant element on Earth, occurring in most compounds (gaseous, liquid and solid) and forms an important constituent of most rock-forming minerals including the silicates, oxides, carbonates and phosphates. There is a large amount of literature on the naturally occurring variations of oxygen isotope ratios but the isotopes usually utilized in geology are those of ^{16}O and ^{18}O, the two most abundant isotopes, compared to the third isotope (^{17}O) which makes up only 0.0375% of the total isotopic budget (Garlick, 1969). The isotopes ^{16}O and ^{18}O constitute 99.763% and 0.1995%, respectively, of the total volume of oxygen in existence (Garlick, 1969).

As small changes in isotopic ratios are measured, the isotopic ratios in a sample must be measured relative to a standard. The most commonly used standard in the past was the PDB standard (Craig, 1963), a Cretaceous belemnite from the Peedee Formation, which has now been exhausted.. As the total carbonate of the PDB standard may be related to the value of the Standard Mean Ocean Water (SMOW) standard (Craig 1963), which is in widespread use today, by the following equation:

$$\delta^{18}O_{(SMOW)} = 1.03086\ (\delta_{(PDB)}) + 30.86$$

Conversion of older data to be compared with newer results is possible (see below; Coplen *et al.*, 1983). Another way of expressing the relationship between sample and standard is as follows:

$$\delta \text{ in } {}^{o}/_{oo} = [R_{(Sample)} - R_{(Standard)}]/R_{(Standard)} \times 1000$$

where R is the isotopic ratio and the accepted unit of isotope ratio measurement being given as parts per thousand, denoted as $^{o}/_{oo}$ (Hoefs, 1980). This terminology stems from the fact that the ratio of the numbers of any two isotopes in one chemical compound A, divided by the corresponding ratio for another chemical compound B, is termed the fractionation factor and is written as follows:

$$\alpha_{A\text{-}B} = R_A/R_B$$

where R_A is the isotopic ratio in sample A. If the isotopic ratios of two samples are compared in relation to the same standard and if $\delta_A > \delta_B$ then sample A is isotopically heavier than sample B. As the isotopes are randomly distributed over all possible positions in the compounds A and B, α is related to the equilibrium constant K by:

$$\alpha = K^{1/n}$$

where n is the number of atoms exchanged (Hoefs, 1980). For simplicity isotope exchange reactions are written such that only one atom is exchanged during equilibration at a particular temperature. The equilibrium constant is identical to the fractionation factor in this case and $K = \alpha$. Values of α are usually near to unity, typically 1.00X where X is between 0 and 9 and rarely greater than 4 (Faure, 1986; see below), therefore the introduction of the representation of isotopic fractionation in terms of Δ-values, the value of X above being in per mil ($^{o}/_{oo}$) (Hoefs, 1980; Faure, 1986). The relation between temperature and fractionation is set out below.

The standard used in this study is NBS-28, obtained from the National Bureau of Standards. The value of this standard, relative to the SMOW standard which is used worldwide, is well known. The SMOW water standard is simply a hypothetical water sample originally defined by Craig (1961). Two further samples exist, including the V-SMOW standard which is identical to the originally-defined SMOW within the limits of analytical uncertainty (Hoefs, 1980). All data in this study are therefore reported relative to the SMOW standard (Appendix D4).

Appendix D3 (continued)

Comparison of Existing Standards and Conversion of Data

Unfortunately not all the δ-values cited in the literature are given relative to a single universal standard, so often several standards for one element are presently in use. To convert δ-values from one standard to another the following equation may be applied (in addition to those quoted above):

$$\delta_{X\text{-}A} = \{[(\delta_{B\text{-}A}/10^3) +1][(\delta_{X\text{-}B}/10^3)-1]\}^{1000} \quad \text{(Hoefs, 1980)}$$

where X represents the sample; A and B are standards. Thus, although all values reported in the literature are relative to a universal standard such as SMOW and V-SMOW, a working standard, in this case NBS-28, is used on a daily basis in the laboratory. The conversion of data from the δ^{46} values (relative CO_2 standard in used in the mass spectrometer) to $\delta^{18}O$ via the SMOW standard, derives from the simultaneous solution of two equations as written above. The final solution is:

$$[(1000 \times P) + 1009640]/[(Q + 1000)-1000]$$

where P = δ^{46} value (Mat 252 MS CO_2 standard) and Q = average NBS-28 value from the average of the two standards analysed with each batch of eight unknowns (whole rock or vein).

Fractionation of Rock-Forming Minerals
(Experimental equilibration of oxygen between minerals and water at elevated temperatures)

Although the absolute values of isotopic fractionation factors in systems containing liquids and solids cannot be calculated directly from theory, one may assume temperature dependance of the form:

$$\ln \alpha \propto 1/T^2 \quad \text{(Faure, 1986)}$$

Where α is the isotopic fractionation factor and T is the absolute temperature. Although this relationship is usually true only at temperatures greater than 1000°K, when the frequencies of vibration of the constituent molecules are not too high, this proportionality may be valid at lower temperatures (eg a few hundred Kelvin). The proportionality expressed above is useful for extrapolation of results throughout the temperature range of geological interest (0-1200°C). As mentioned above, the fractionation factors for the exchange of oxygen isotopes between two phases under equilibrium conditions have numerical values of the order of $\alpha = 1.00X$ where X is rarely greater than 4. As the natural logarithm of 1.004 is 0.00398, the following approximation is justified:

$$1000 \ln 1.00X = X$$

and the representation of the relationship between α and T is made easier:

$$1000 \ln \alpha = A(10^6T^{-2}) + B$$

in co-ordinates (or on a plot) of 1000 ln α *vs* 10^6T^{-2}, where A and B are constants.

Appendix D4

δ^{46} (value of standard CO_2 gas in MAT 252 MS), NBS-28 (relative to SMOW) and average NBS-28 (relative to SMOW); $\delta^{18}O$ values of mainly co-evally formed whole rock and vein samples from the five field areas.

Note: $\delta^{18}O(SMOW) = ((1000*\delta^{46} + 1009640)/(Av.\ NBS\text{-}28\ value\ for\ run\ of\ 8 + 1000) - 1000)$

Mbongolwane Flats samples - Rebellion Reef

Whole Rocks

Sample	*δ^{46}*	*NBS-28 (SMOW)*	*Av. NBS-28*	*$\delta^{18}O$ (SMOW)*
TGGWR	?	?		8.63
SBA-BACK	-8.22	-6.70		8.47
BOAFSS-1	-8.63	-6.94	-6.99	8.06
BOAFSS-3	-9.66	-6.70		6.85
QNPWR	-7.11	-6.94	-6.82	9.41
SMMS-1	?	?		7.54
MANDRB-ZAG	?	?		7.20
SBA-Q	?	?		8.19

Total Range = **6.85-9.41** **N = 8**

Veins

	Sample	*δ^{46}*	*NBS-28 (SMOW)*	*Av. NBS-28*	*$\delta^{18}O$ (SMOW)*
	BOAF-5	-7.23	-6.52		9.04
	BOAF-3	-6.11	-6.62	-6.57	10.17
	BOAFQTZ	-5.935			10.34
(Ab)	ZAG(Q)B	-7.871			8.39
(Ab)	ZAG(Q)V-2	-6.307			9.97
(Ab)	ZAG(Q)V-1	-6.727			9.55
	SMMVR-1	-6.551			9.72
	SMMVR-2	-6.36	-7.07		10.42
	SMMV-1	-6.31	-7.07	-7.07	10.48
	SMMV-2	-6.59			10.19
	SMMV-3	-6.55			10.23

Range (QTZ) = 9.04-10.48
Range (Ab) = 8.39-9.97
Total Range = **8.39-10.48** **N = 11**

$\delta^{18}O$ (Vein) vs δ^{18}(Whole Rock) plots - matched pairs

Whole Rock	Vein
TGGWR	BOAF-5
TGGWR	BOAF-3
BOAFSS-1	BOAFQTZ
SBA-BACK	(av.) ZAG(Q)V
QNPWR	(av.) SMMV (1,2,3)
QNPWR	SMMVR-1
SMMS-1	SMMVR-1
SMMS-1	SMMVR-2

Appendix D4 (continued)
Northern Mfongosi Valley Area Samples

Whole Rocks

Sample	δ^{46}	*NBS-28 (SMOW)*	*Av. NBS-28*	$\delta^{18}O$ *(SMOW)*
PSFU-1	-5.08	-6.70		11.46
PSFU-2	?	?		11.51
PSFU-11	-2.78	-6.94	-6.82	13.78
PSFU-12b	?	?		12.55
PSFU-30	?	?		10.50
PSFU-32	?	?		9.07
PSFU-34	-5.40	-6.94		11.13

Total Range = **9.07-13.78** **N = 7**

Veins

Sample	δ^{46}	*NBS-28 (SMOW)*	*Av. NBS-28*	$\delta^{18}O$ *(SMOW)*
PSFUV-5	-2.450	-6.16		13.65
PSFUV-22	-2.293	-6.58	-6.37	13.80
PSFUV-23	-2.257			13.84
PSFUV-24	-2.626			13.47
PSFUV-27	-2.623			13.47
PSFUV-28b	-2.707			13.39
PSFUV-29	0.248			16.36
PSFUV-41	1.029			17.15
PSFUV-42	-3.74	-6.50		12.48
PSFUV-48	-1.88	-6.50	-6.50	14.35
PSFUV-49	-3.83			12.39
PSFUV-50	1.68			17.94

Total Range = **12.39-16.36** **N = 12**

$\delta^{18}O$ (Vein) vs δ^{18}(Whole Rock) plots - matched pairs

Whole Rock	Vein
PSFU-1	PSFUV-49
PSFU-11	PSFU-23
(av.) Whole Rock = 12.12	(av.) Vein = 14.36
PSFU-2	PSFUV-49
PSFU-12	PSFUV-24

Appendix D4 (continued)

Southern Mfongosi Valley Area samples

Whole Rocks

Sample	δ^{46}	*NBS-28 (SMOW)*	*Av. NBS-28*	$\delta^{18}O$ *(SMOW)*
FU2H-A	-7.58	-6.74		9.12
FU2H-B	-8.79	-6.94	-6.99	7.90
FU2H-C	-7.32			9.38
FU2H-C'	-6.31	-6.50		9.90
FU2H-C"	-9.49	-6.82		7.02
LBQ-3-VAR	?	?		8.74
CGSTAWR]	Ayres Reef			6.73
FGSTAWR]	Ayres Reef			6.24

Total Range = **6.24-9.9** **N = 8**

Veins

Sample	δ^{46}	*NBS-28 (SMOW)*	*Av. NBS-28*	$\delta^{18}O$ *(SMOW)*
FUIH-1(Ayres R.)	-7.39	-7.07		9.39
FUIH-2(Ayres R.)	-7.14	-7.07	-7.07	9.64
FUIH-3(Ayres R.)	-7.50			9.27
FU2HV-3	-7.41			9.37
FU2HV-6	-6.95	-6.63		9.50
FU2HV-8	-7.379	-6.86	-6.74	9.07
FU2HV-9	-7.418			9.03
FU2HV-13	-8.482			7.81
FU2HV-15	-6.978			9.47
FU2HV-17	-6.944			9.51
FU2HV-26	-5.525			10.94
FU2HV-27	-6.358			10.10
FU2HV-31	-6.067	-6.82		10.26
FU2HV-34	-6.241	-6.43	-6.62	10.09
FU2HV-36	-4.129			12.21
FU2HV-37	-5.614			10.72

Total Range = **7.81-12.21** (bimodal distribution - cut-off at about 9.8?) **N = 16**

$\delta^{18}O$ (Vein) vs δ^{18}(Whole Rock) plots - matched pairs

Whole Rock	Vein
FU2H-A	FU2HV-15
FU2H-A	FU2HV-31
FU2H-C	FU2HV-3
FU2H-A	FU2HV-9
Ayres Reef Whole Rock	Ayres Reef Vein
(av.) FG and CGSTAWR	(av.) FU1H-1,2,3

Appendix D4 (continued)

Ngubevu West and East Area samples (includes Champion, Golden Eagle and Buffalo River deposits)

Whole Rocks

Sample	δ^{46}	*NBS-28 (SMOW)*	*Av.NBS-28*	$\delta^{18}O$ *(SMOW)*
NGW-6	-2.00	6.5	6.52	14.23
NGW-7	-5.81	-6.84		10.67
NGW-31	?	?		10.90
NGW-36	-6.00	-6.70	-6.77	10.48
NGW-39A	-6.46	?		10.02
NGW-39B	-6.75	?		9.73
NGE-2	?	?		9.82
NGE-5	?	?		9.34

Total Range = **9.34-19.28** **N = 8**

Veins (S-c and D-a - early-tectonic vein generation)

Sample	δ^{46}	*NBS-28 (SMOW)*	*Av.NBS-28*	$\delta^{18}O$ *(SMOW)*
NGW/A1/1	-0.79	-6.82		15.58
NGW/A1/4A	-0.46	-6.43	-6.62	15.56
NGW/A1/4B	0.40			16.77
NGW/10	-6.51	-6.50		9.70
NGW/11	-0.98	-6.60		15.37
NGW/17	-2.37	-6.60	-6.60	13.97
NGW/19	0.688			17.04
NGW/22	-1.967			14.37
NGW/33	-7.52	-6.77		8.95
NGW/36	-1.385			14.96
NGW/36'	-6.00	-6.77		10.48
NGW/47	-3.93			12.62
NGW/48	-3.94			12.96
NGW/60	-2.47			14.03
NGW/61	-2.21			14.29

Total Range = **8.95-17.04** **N = 15**

NGE/8	-2.795			13.28

Veins (late-tectonic quartz-calcite tension gashes)

NGW/A	-2.566			13.51
NGW/A'	-2.226			13.78
NGW/B	-2.116			13.97
NGW/C	-2.674	-6.335		13.40
NGW/D	-2.541	-6.371	-6.35	13.46
NGW/E	-2.438			13.64
NGW/F	-0.727			15.36

Total Range = **13.28-13.97** **N = 8**

Appendix D4 (continued)
Ngubevu area (contd) $\delta^{18}O$ (Vein) vs δ^{18}(Whole Rock) plots - matched pairs

Whole Rock	Vein
NGW-6	NGW/A1/4A
NGW-6	NGW/A1/4A
NGW-6	NGW/A1/1
NGW-7	NGW-22
(av.) NGW-39 A and B	NGW-36
NGW-36	NGW-36

Phoenix Mine Samples

Whole Rocks

Sample	*δ^{46}*	*NBS-28 (SMOW)*	*Av.NBS-28*	*$\delta^{18}O$ (SMOW)*
PH-7	?	?		6.03
PH-9C	-10.11	-6.74		6.57
PH-11	-9.9		-6.82	6.60
PH-12	-10.37	-7.26	-6.99	6.31
PH-13	-9.15			7.54
PH-14	?	?		6.30
PH-15	?	?		9.59
PH-20	?	?		6.08

Total Range = **6.08-9.59** **N = 8**

Veins

Sample	*δ^{46}*	*NBS-28 (SMOW)*	*Av.NBS-28*	*$\delta^{18}O$ (SMOW)*
PH-5	-6.458	-6.349		9.52
PH-10c	-7.982	-6.212	-6.28	7.99
PH-16	-5.927			10.06
PH-19	-5.287			10.70

Total Range = **7.99-18.2** **N = 4**

$\delta^{18}O$ (Vein) vs δ^{18}(Whole Rock) plots - matched pairs

Whole Rock	Vein
(av.) PH-11,12,13	(av.) PH-16,19
PH-12	PH-19
PH-13	PH-16

Appendix E

DIPS® - Stereonet Analysis

Structural data were first plotted manually on basic stereonets and then analyzed to find the optimal representation of the structural feature in question. Once a suitable scheme or strategy had been established for regional data presentation, data were entered into a standard template in WordPerfect 5.1. Each file was then exported as an ASCII Text file and subsequently imported into DIPS® - Version 3.0 (Advanced Version). DIPS® is a stereonet plotting program designed by the Rock Engineering Group, Department of Civil Engineering, at the University of Toronto (1989) and, although specifically catering for engineering, many of the functions therein are applicable to Geology and lower hemisphere plotting is permitted.

The basic stereonet plot (points or poles) is an equal angle, lower hemisphere Schmidt Net. If enough data are present then it is enlightening to construct an equal area, lower hemisphere contoured stereonet. In the latter plot the data is contoured by calculating the concentrations as a percentage of the total, by area - per 1% area. The contoured stereonets in this thesis show the data displaced towards the edge of the stereonet: this is a relict of the plotting method and cannot be avoided. In all cases, the contoured maxima on the equal area plots correspond (within two degrees) to the contoured equal angle stereonet defined maxima although it is not correct to present a contoured equal angle stereonet in scientific literature. Linear features (e.g. preferred elongate mineral alignment, slickenline orientations) are plotted as plunge (angle below the horizontal) and direction of plunge - compass bearing at which this angle is measured. Planar features are plotted as strike and dip (right-hand rule).

Slightly more advanced features of the DIPS® program include the Plane function wherein a great circle may be fitted to the data to define folding, the pole to the plane defining the fold axis. In the case of non-cylindrical folding it is better to fit small circles to the data although this must be done on a trial and error basis. The WINDOW function of DIPS® allows the user to demarcate a particular data set to find the average (compared to the contoured high) of the data. This result is useful in the cases where data is limited.

Field Techniques - measurement of data

The standard SILVA compass-clinometer was used to obtain structural and other data from the field areas. Lineations were measured and plotted as defined above and dips and strike was measured using the right-hand rule. This method is preferred as the strike of the data allow a more comprehensive visualization of the structure of the area, compared to a distribution of dips and dip directions, for instance. In the Mbongolwane Flats area, simple areal photographs combined with triangulation served the author well in the mapping stage however, the outcrop localities were subsequently very well fixed using a MAGELLAN Global Positioning System hand-unit, on loan from the Antarctic Research Unit, using the WGS 84 spheroid.

Appendix F1 - Major (wt%) and Trace Element (ppm) data for the Mbongolwane Flats

Silambo banded amphibolite

	BOAFSS1	BOAFSS2	BOAFSS3	BOAFSS4	BOAFS2	BOAFS3	BOAFS4
SiO_2	51.36	54.21	50.14	52.21	53.39	54.25	53.00
Al_2O_3	12.89	12.68	12.96	12.79	12.91	12.76	13.79
FeO	14.33	12.77	14.34	13.78	13.13	13.76	11.52
Fe_2O_3	1.77	1.58	1.77	1.70	1.62	1.70	1.42
$Fe_2O_3(T)$	17.69	15.77	17.70	17.01	16.21	16.99	14.22
MnO	0.26	0.24	0.30	0.25	0.24	0.22	0.20
MgO	4.34	4.34	4.96	4.43	4.30	3.87	5.41
CaO	7.65	7.09	8.15	7.32	6.72	7.48	7.77
Na_2O	2.55	2.84	2.23	2.88	2.66	2.24	3.34
K_2O	0.37	0.34	0.74	0.35	0.88	0.61	0.51
TiO_2	2.53	2.10	2.50	2.36	2.34	1.55	1.56
P_2O_5	0.31	0.23	0.27	0.27	0.28	0.17	0.15
TOTAL	*99.95*	*99.86*	*99.93*	*99.87*	*99.93*	*100.15*	*99.95*
Cr	46.90	50.70	57.90	52.80	59.50	3.40	27.80
V	474.10	454.50	526.00	481.40	473.10	544.90	394.10
Au	15.00	0.00	0.00	0.00	0.00	0.00	0.00
Sc	60.50	57.40	57.80	59.00	62.10	66.30	51.80
Co	56.40	58.90	57.30	58.80	58.80	67.80	62.40
Zn	136.20	140.40	159.30	137.40	171.80	135.00	114.70
Cu	77.50	71.30	52.60	47.10	39.60	60.40	44.10
Ni	23.50	25.10	36.80	26.30	27.60	11.90	20.30
Rb	6.30	3.40	17.00	3.40	16.20	9.00	5.80
K	3071.00	2822.00	6142.00	2905.00	7304.00	5063.00	4233.00
Ba	121.30	119.60	227.80	115.40	224.90	107.60	122.20
Pb	14.70	5.80	10.90	14.30	12.20	7.70	17.20
Sr	143.10	107.70	173.50	99.30	168.70	133.70	208.30
Th	4.70	7.40	6.70	2.70	6.10	4.10	3.50
U	1.00	2.40	0.00	0.00	0.80	0.10	1.40
Zr	170.30	133.40	161.10	156.80	154.10	79.20	90.90
Ti	15167.95	12566.72	14964.72	14133.21	14015.11	9300.04	9343.81
Nb	10.40	7.70	10.70	9.90	10.10	4.60	5.50
Y	52.50	44.50	51.00	49.40	49.10	41.70	30.00
La	0.00	0.00	0.00	0.00	0.00	0.00	0.00
S	33.00	54.00	76.00	44.00	98.00	84.00	46.00
As	4.00	3.00	3.00	3.00	5.00	4.00	4.00
Ga	20.50	21.00	24.70	22.70	20.10	20.60	20.50
Nd	0.00	0.00	0.00	0.00	0.00	0.00	0.00
Ce	3.40	0.00	1.60	0.00	0.00	0.00	0.00
CaO/MgO	1.76	1.63	1.64	1.65	1.56	1.93	1.44
Na_2O+K_2O	2.92	3.18	2.97	3.23	3.54	2.85	3.85
Mg#	35.05	37.71	38.14	36.43	36.85	33.38	45.56
Ti/Zr	89.07	94.20	92.89	90.14	90.95	117.42	102.79
Zr/Y	3.24	3.00	3.16	3.17	3.14	1.90	3.03
Zr/Nb	16.38	17.32	15.06	15.84	15.26	17.22	16.53

metallic elements
transition elements
low field strength elements/LIL
high field strength elements

Appendix F2 - Major (wt%) and Trace Element (ppm) data for Mbongolwane Flats

Zidoni amphibolitic gneiss

	SBAQ	SBA BACK	QNPWR	MANDRB -ZAG1	MANDRB -ZAG2	ZAGQWR	SMMWR -$AG	SMMWR -AG1
SiO_2	53.16	45.99	52.08	47.15	46.85	55.66	52.85	58.95
Al_2O_3	17.01	17.69	16.74	17.82	17.78	17.59	17.95	17.02
FeO	8.63	10.75	9.41	9.77	9.98	6.12	8.36	6.22
Fe_2O_3	1.07	1.33	1.16	1.21	1.23	0.76	1.03	0.77
Fe_2O_3(T)	10.66	13.27	11.62	12.06	12.32	7.56	10.32	7.68
MnO	0.21	0.22	0.21	0.19	0.19	0.11	0.15	0.12
MgO	4.73	6.05	4.80	6.51	6.76	5.17	5.47	3.54
CaO	8.33	10.90	8.30	9.85	9.99	6.48	7.41	7.18
Na_2O	3.90	3.15	3.48	3.65	3.24	4.60	2.92	3.31
K_2O	0.62	0.67	0.93	0.80	0.81	1.59	1.48	0.83
TiO_2	1.04	1.07	1.43	1.42	1.44	0.94	0.63	0.51
P_2O_5	0.33	0.98	0.45	0.49	0.53	0.29	0.30	0.22
TOTAL	*99.99*	*99.98*	*100.05*	*99.95*	*99.91*	*99.98*	*99.48*	*99.36*
Cr	49.70	31.60	54.20	146.60	156.30	171.10	85.50	31.70
V	207.30	321.70	217.50	253.30	253.00	152.40	225.60	166.80
Au	11.00	10.00	10.00	10.00	10.00	12.00	0.00	0.00
Sc	38.20	33.70	37.50	36.00	35.30	20.20	35.40	26.20
Co	77.80	58.60	65.30	65.00	58.00	47.70	38.20	63.60
Zn	120.10	103.90	123.80	122.30	125.70	84.10	76.90	69.30
Cu	62.60	144.50	98.50	152.70	125.60	28.00	49.50	108.00
Ni	39.50	9.40	39.40	67.80	70.80	96.50	21.70	6.50
Rb	7.30	8.70	18.90	13.70	14.50	38.60	28.20	17.70
K	5146.00	5561.00	7719.00	6640.00	6723.00	13197.00	12284.00	6889.00
Ba	648.30	287.00	691.10	436.90	423.40	1155.40	712.90	649.20
Pb	20.20	5.80	19.00	7.30	16.30	15.50	14.80	9.10
Sr	484.00	760.00	490.20	755.30	726.20	1026.60	568.00	705.60
Th	0.80	1.20	1.80	0.80	2.00	0.50	0.00	0.00
U	0.30	1.90	2.80	1.70	1.10	1.80	0.00	1.80
Zr	180.60	76.20	209.30	148.10	146.30	127.20	50.70	50.00
Ti	6222.81	6404.46	8586.04	8518.90	8645.99	5608.92	3775.65	3029.27
Nb	10.40	7.10	9.80	8.30	9.30	7.00	3.90	1.80
Y	39.30	36.20	42.90	26.70	27.60	26.80	17.40	12.80
La	27.90	14.90	24.80	14.50	17.60	9.00	13.10	21.20
S	194.00	3332.00	298.00	576.00	480.00	40.00	932.00	416.00
As	4.00	3.00	6.00	4.00	4.00	3.00	3.00	3.00
Ga	17.80	22.80	20.80	21.40	21.40	20.60	15.50	17.10
Nd	29.70	53.90	42.60	30.80	34.50	24.70	10.00	2.10
Ce	48.60	70.80	69.00	43.10	55.90	47.00	24.60	27.20
CaO/MgO	1.76	1.80	1.73	1.51	1.48	1.25	1.35	2.03
Na_2O+K_2O	4.52	3.82	4.41	4.45	4.05	6.19	4.40	4.14
Mg#	49.40	50.08	47.61	54.29	54.89	60.07	53.83	50.35
Ti/Zr	34.46	84.05	41.02	57.52	59.10	44.10	74.47	60.59
Zr/Y	4.60	2.10	4.88	5.55	5.30	4.75	2.91	3.91
Zr/Nb	17.37	10.73	21.36	17.84	15.73	18.17	13.00	27.78

metallic elements

transition elements

low field strength elements/LIL

high field strength elements

Appendix F2 - Major (wt%) and Trace Element (ppm) data for Mbongolwane Flats

Zidoni amphibolitic gneiss

	SMMS1	SMMS2	SMMS3	SMMS4	SMMS5	SMMS6	SMMS7	SMMS8	SMMS9	SMMS10
SiO_2	55.08	53.71	52.59	51.06	69.77	53.25	53.14	59.84	55.08	56.88
Al_2O_3	16.38	15.74	17.24	15.84	15.08	17.22	16.92	16.69	16.79	16.74
FeO	7.73	8.81	8.56	9.10	3.39	7.82	7.91	6.10	7.76	6.85
Fe_2O_3	0.95	1.09	1.06	1.12	0.42	0.97	0.98	0.75	0.96	0.85
Fe_2O_3(T)	9.54	10.88	10.57	11.23	4.19	9.65	9.76	7.53	9.58	8.46
MnO	0.16	0.18	0.20	0.24	0.09	0.19	0.18	0.11	0.17	0.15
MgO	5.57	6.27	5.13	7.18	0.93	5.16	5.78	3.23	4.64	4.63
CaO	7.82	7.95	9.69	9.42	3.06	8.44	8.93	7.36	9.27	7.65
Na_2O	3.39	3.07	3.09	3.39	4.84	4.14	3.54	3.68	3.05	3.51
K_2O	1.31	1.30	0.47	0.75	1.28	0.72	0.63	0.69	0.62	1.10
TiO_2	0.54	0.69	0.70	0.77	0.52	0.89	0.78	0.48	0.62	0.59
P_2O_5	0.27	0.33	0.33	0.22	0.20	0.31	0.28	0.24	0.29	0.27
TOTAL	*100.07*	*100.12*	*100.01*	*100.08*	*99.97*	*99.96*	*99.96*	*99.86*	*100.12*	*99.99*
Cr	98.50	171.50	36.00	126.70	6.00	92.30	112.20	18.40	33.90	43.20
V	217.00	247.10	223.50	219.00	69.40	185.10	189.60	158.50	203.60	186.10
Au	11.00	0.00	0.00	0.00	0.00	0.00	0.00	12.00	0.00	0.00
Sc	34.10	36.10	33.90	37.60	23.10	31.20	33.10	25.80	30.10	28.90
Co	27.30	63.10	56.70	79.00	68.40	90.10	65.70	69.20	78.90	69.00
Zn	70.30	91.00	89.00	145.80	82.10	103.60	94.90	59.30	79.70	71.50
Cu	3.60	36.00	27.80	16.30	0.00	68.40	76.70	28.20	4.10	28.10
Ni	20.30	61.30	9.40	125.60	7.70	74.30	99.80	3.60	10.40	9.30
Rb	23.70	26.30	6.40	10.20	40.40	15.00	14.70	14.00	11.60	22.90
K	10873.00	10790.00	3901.00	6225.00	10624.00	5976.00	5229.00	5727.00	5146.00	9130.00
Ba	579.20	493.20	252.00	216.30	1714.20	385.30	410.60	517.30	471.80	565.80
Pb	14.60	11.30	6.30	17.30	22.10	15.00	13.90	5.50	17.50	12.30
Sr	486.50	471.60	671.00	387.90	406.80	515.50	444.00	757.90	724.30	627.40
Th	2.00	1.10	5.60	4.10	7.00	1.90	6.60	2.50	7.30	0.00
U	1.60	0.00	3.00	0.00	1.00	1.40	1.40	2.10	3.20	0.50
Zr	35.20	75.00	56.20	66.80	215.60	117.30	111.10	48.60	54.40	52.80
Ti	3236.70	4122.16	4213.29	4599.96	3115.60	5309.17	4680.90	2899.18	3738.48	3510.67
Nb	3.50	5.50	3.30	5.30	13.10	7.60	7.00	2.60	2.80	3.20
Y	17.30	17.50	18.40	25.60	37.50	26.30	29.00	13.50	12.00	14.50
La	1.40	0.00	0.00	0.00	33.20	0.60	1.60	0.00	6.20	3.00
S	821.00	182.00	118.00	46.00	132.00	63.00	215.00	174.00	110.00	1868.00
As	3.00	4.00	5.00	3.00	5.00	5.00	5.00	4.00	5.00	6.00
Ga	19.50	16.40	19.20	18.30	18.10	20.70	18.50	17.20	18.50	16.90
Nd	4.10	7.60	17.70	11.70	43.20	24.40	19.20	3.60	12.70	9.80
Ce	17.20	43.10	30.30	27.40	122.00	44.40	44.70	20.40	26.40	23.80
CaO/MgO	1.40	1.27	1.89	1.31	3.29	1.64	1.54	2.28	2.00	1.65
Na_2O+K_2O	4.70	4.37	3.56	4.14	6.12	4.86	4.17	4.37	3.67	4.61
Mg#	56.23	55.90	51.64	58.45	32.81	54.05	56.58	48.55	51.59	54.63
Ti/Zr	91.95	54.96	74.97	68.86	14.45	45.26	42.13	59.65	68.72	66.49
Zr/Y	2.03	4.29	3.05	2.61	5.75	4.46	3.83	3.60	4.53	3.64
Zr/Nb	10.06	13.64	17.03	12.60	16.46	15.43	15.87	18.69	19.43	16.50

metallic elements
transition elements
low field strength elements/LIL
high field strength elements

Appendix F3 - Major (wt%) and Trace Element (ppm) data for S. Mfongosi valley area

Mfongosi Group metabasites

	(Manyane Amphibolite)					
	Cg-STAWR	Fg-STAWR	FU2H-B	FU2H-C	FU2H-E	FU2H-G
SiO_2	53.00	51.28	54.52	57.44	56.72	73.34
Al_2O_3	14.29	15.57	17.00	17.32	17.56	13.29
FeO	11.31	10.47	7.99	7.40	7.98	2.76
Fe_2O_3	1.40	1.29	0.99	0.91	0.99	0.34
$Fe_2O_3(T)$	13.96	12.93	9.86	9.13	9.85	3.41
MnO	0.22	0.21	0.18	0.17	0.19	0.12
MgO	4.34	6.24	5.05	3.28	5.57	1.94
CaO	10.66	10.03	9.06	8.15	5.68	2.92
Na_2O	1.97	2.61	3.06	3.12	2.98	4.17
K_2O	0.21	0.19	0.05	0.20	0.13	0.24
TiO_2	1.17	0.86	0.84	0.77	0.84	0.41
P_2O_5	0.14	0.11	0.33	0.16	0.31	0.21
TOTAL	*99.96*	*100.02*	*99.94*	*99.75*	*99.81*	*100.05*
Cr	23.10	20.10	36.30	43.60	134.30	14.00
V	276.70	343.10	297.60	140.10	312.50	81.20
Au	0.00	0.00	0.00	0.00	0.00	0.00
Sc	36.70	34.40	26.60	16.80	32.20	14.50
Co	76.00	90.50	44.30	67.90	57.70	125.50
Zn	97.30	86.90	80.00	117.80	99.50	54.40
Cu	77.10	42.60	80.90	77.20	43.40	7.80
Ni	25.90	20.00	32.40	19.10	52.20	3.30
Rb	3.5	2.7	0.5	3.3	1.4	5.2
K	1743.00	1577.00	415.00	1660.00	1079.00	1992.00
Ba	70.70	90.30	67.70	88.80	109.60	161.80
Pb	9.50	8.80	13.60	20.80	2.80	13.00
Sr	221.7	236.8	299.9	449.6	306.1	189.6
Th	0.1	0.0	0.0	1.1	0.0	3.7
U	1.8	0.0	1.6	1.1	0.0	0.8
Zr	37.60	55.80	47.40	104.00	49.20	110.60
Ti	7002.76	5135.32	5041.20	4632.34	5011.22	2464.54
Nb	1.10	1.00	1.70	3.00	1.20	4.80
Y	23.30	30.20	23.70	30.80	22.00	23.00
La	0.00	0.00	9.20	0.00	0.50	3.50
S	49.00	641.00	36.00	37.00	69.00	195.00
As	4.00	4.00	3.00	4.00	2.00	3.00
Ga	16.60	16.50	16.30	16.70	14.30	9.00
Nd	0.00	0.00	0.00	5.50	0.00	8.00
Ce	0.00	0.00	3.70	13.10	0.00	11.00
CaO/MgO	2.46	1.61	1.79	2.48	1.02	1.51
Na_2O+K_2O	2.18	2.80	3.11	3.32	3.11	4.41
Mg#	40.62	51.50	52.98	44.15	55.44	55.59
Ti/Zr	186.24	92.03	106.35	44.54	101.85	22.28
Zr/Y	1.61	1.85	2.00	3.38	2.24	4.81
Zr/Nb	34.18	55.80	27.88	34.67	41.00	23.04

metallic elements
transition elements
low field strength elements/LIL
high field strength elements

Appendix F4 - Major (wt%) and Trace Element (ppm) data for S. Mfongosi valley area

Mfongosi Group phyllitic quartzites

Samples 21 and 12 from Steed and Morris (1986),
Samples 1031B and 1030A from Camire et al. (1993)
Samples 96-11 and 56-3 from Floyd et al. (1989)
Sample B from Pettijohn (1975) and Sample M from Reed (1957)

	FU2H-A	FU2H-D	FU2H-F	FU2H-F	FU2H-H	LBQ/ 3/VAR	21	12	1031B	1030A	96-11	56-3	B	M
SiO_2	71.42	70.59	67.51	68.20	73.32	75.84	61.28	59.26	67.50	66.30	63.18	68.15	66.24	71.10
Al_2O_3	14.83	14.77	16.13	16.22	13.66	14.51	14.65	13.70	15.82	16.30	13.50	13.67	15.28	13.9
FeO	3.13	3.09	3.32	3.80	2.28	3.12	3.38	4.02	4.77	5.15	6.41	4.60	4.53	2.70
Fe_2O_3	0.39	0.38	0.41	0.47	0.28	0.39	0.38	0.45	0.53	0.57	0.71	0.51	0.70	0.20
$Fe_2O_3(T)$	3.87	3.82	4.10	4.69	2.82	3.85	3.76	4.47	5.30	5.72	7.12	5.11	5.23	2.90
MnO	0.12	0.30	0.07	0.13	0.09	0.01	0.08	0.07	0.07	0.06	0.03	0.07	0.06	0.05
MgO	0.62	0.56	0.98	0.69	0.64	0.60	2.94	2.92	3.01	2.81	4.44	0.85	2.74	1.30
CaO	2.29	3.15	2.96	2.90	4.05	0.03	3.44	3.39	2.08	1.68	2.34	2.04	1.70	1.80
Na_2O	3.57	3.54	4.29	4.55	3.49	0.34	2.57	0.24	2.98	5.04	1.72	3.84	3.12	3.70
K_2O	2.03	1.80	2.72	2.09	0.99	4.38	2.84	3.04	3.51	1.52	3.38	2.99	1.91	2.30
TiO_2	0.38	0.39	0.36	0.46	0.31	0.32	0.75	0.76	0.57	0.58	0.83	0.59	0.64	0.50
P_2O_5	0.08	0.10	0.11	0.11	0.09	0.03	0.15	0.08	0.17	0.16	0.19	0.13	0.12	0.10
TOTAL	*99.22*	*99.01*	*99.24*	*100.03*	*99.66*	*99.72*	*100.36*	*94.64*	*101.00*	*100.10*	*98.60*	*99.21*	*100.24*	*99.80*
Cr	0.00	2.70	6.60	7.10	14.10	16.60	147.00	190.00	213.00	215.00	300.00	10.00	-	-
V	18.40	12.20	23.10	10.60	27.70	58.80	118.00	128.00	-	-	150.00	34.00	-	-
Au	-	-	-	-	-	-	-	-	-	-	-	-	-	-
Sc	9.50	8.10	12.90	10.70	7.20	12.20	-	-	-	-	150.00	95.00	-	-
Co	80.90	93.20	62.90	81.30	117.80	85.00	-	-	-	-	-	-	-	-
Zn	24.90	35.60	29.80	52.00	21.50	5.60	-	-	-	-	-	-	-	-
Cu	40.80	125.80	6.30	1.50	6.80	0.00	-	-	-	-	-	-	-	-
Ni	0.00	0.00	0.00	0.00	0.00	0.00	90.00	131.00	73.00	39.00	76.00	2.00	-	-
Rb	29.70	26.10	39.70	29.70	15.00	60.40	79.00	85.00	118.00	52.00	131.00	106.00	-	-
K	16849.00	14940.00	22576.00	17347.00	8217.00	36354.00	23572.00	25232.00	29133.00	12616.00	28054.00	24817.00	15853.00	19090.00
Ba	1239.40	1324.60	1069.90	1494.50	1351.40	1087.20	635.00	482.00	820.00	318.00	413.00	1012.00	-	-
Pb	11.30	10.70	5.40	10.00	7.70	10.70	-	-	-	-	-	-	-	-
Sr	227.9	293.6	126.5	227.5	238.5	44.2	214.00	173.00	309.00	226.00	121.00	230.00	-	-
Th	2.30	0.30	3.70	6.80	5.30	5.10	-	-	-	-	8.60	14.50	-	-
U	0.0	0.0	0.1	1.2	0.0	2.8	-	-	-	-	3.07	3.85	-	-
Zr	191.80	192.80	178.80	222.60	171.80	170.00	176.00	135.00	159.00	135.00	186.00	308.00	-	-
Ti	2299.08	2315.87	2128.82	2778.06	1880.03	1934.59	4496.25	4556.20	3417.15	3477.10	4875.85	3537.05	3836.80	2997.50
Nb	6.5	6.7	5.9	7.9	6.8	6.7	15.00	7.00	7.00	7.00	10.00	14.00	-	-
Y	38.0	42.1	31.4	46.1	31.8	43.4	-	-	-	-	-	-	-	-
La	8.40	5.40	8.60	13.20	1.60	0.00	-	-	-	-	30.00	47.00	-	-
S	14.00	15.00	20.00	0.00	4.00	388.00	-	-	-	-	-	-	-	-
As	4.00	3.00	2.00	5.00	2.00	8.00	-	-	-	-	-	-	-	-
Ga	12.90	15.20	14.00	15.50	10.00	7.40	-	-	-	-	-	-	-	-
Nd	15.90	11.80	7.70	9.10	11.10	10.80	-	-	-	-	-	-	-	-
Ce	21.40	26.90	26.70	29.30	19.90	25.90	-	-	-	-	-	-	-	-
							-	-	-	-	-	-		
SiO_2/Al_2O_3	4.82	4.78	4.19	4.20	5.37	5.21	4.18	4.33	4.27	4.07	4.68	4.99	4.34	5.12
K_2O/Na_2O	0.57	0.51	0.63	0.46	0.28	12.88	1.11	12.67	1.18	0.30	1.97	0.78	0.61	0.62
Al_2O_3/Na_2O	4.15	4.17	3.76	3.56	3.91	42.68	5.70	57.08	5.31	3.23	7.85	3.56	4.90	3.76
K/Rb	567.31	572.41	568.66	584.07	547.80	601.89	298.38	298.85	246.89	242.62	214.15	234.12	-	-
Zr/Nb	29.51	28.78	30.31	28.18	25.26	25.37	11.73	19.29	22.71	19.29	18.60	22.00	-	-
Cr/Th	0.00	9.00	1.78	1.04	2.66	3.25	-	-	-	-	34.88	0.69	-	-

metallic elements
transition elements
low field strength elements/LIL
high field strength elements

Appendix F5 - Major (wt%) and Trace Element (ppm) data for Ngubevu area

Mfongosi Group metabasites

	NGW 15	NGW 20	NGW 25	NGW 26	NGW 27	NGW 27A	NGV 28	NGW 29A	NGW 29B	NGW 30
SiO_2	50.41	48.25	48.20	50.32	49.57	47.32	49.68	47.26	48.46	47.73
Al_2O_3	17.19	16.32	16.61	16.13	17.73	17.03	15.78	17.71	17.35	16.38
FeO	9.59	10.28	9.70	9.36	10.75	9.95	9.57	10.30	9.86	8.76
Fe_2O_3	1.18	1.27	1.20	1.16	1.33	1.23	1.18	1.27	1.22	1.08
$Fe_2O_3(T)$	11.84	12.69	11.97	11.55	13.27	12.29	11.82	12.72	12.17	10.82
MnO	0.18	0.19	0.18	0.18	0.18	0.20	0.18	0.19	0.18	0.18
MgO	6.16	6.47	7.75	6.42	8.40	7.28	7.53	6.84	7.26	6.61
CaO	8.47	11.11	10.59	10.06	6.02	11.05	10.02	11.31	9.49	12.54
Na_2O	3.97	2.96	2.50	2.91	0.29	2.64	2.93	2.13	2.88	4.15
K_2O	0.09	0.07	0.14	0.44	3.03	0.32	0.49	0.17	0.62	0.21
TiO_2	1.47	1.75	1.47	1.51	1.52	1.47	1.39	1.50	1.41	1.24
P_2O_5	0.18	0.20	0.16	0.22	0.16	0.17	0.15	0.16	0.15	0.14
TOTAL	*99.97*	*100.00*	*99.58*	*99.74*	*100.16*	*99.78*	*99.99*	*99.99*	*99.97*	*100.01*
Cr	226.60	219.30	235.60	204.40	98.10	150.00	246.00	237.30	196.20	164.90
V	218.20	261.30	239.80	232.80	304.90	217.80	224.80	262.10	239.60	233.10
Au	<10	12.00	<10	<10	<10	<10	12.00	<10	<10	<10
Sc	38.70	37.30	32.90	30.00	51.80	32.50	33.40	37.60	35.40	30.10
Co	45.20	47.70	59.70	50.80	45.70	52.30	59.30	54.90	61.20	35.90
Zn	95.40	100.00	85.90	92.50	92.50	97.60	88.40	98.00	92.70	72.80
Cu	34.80	80.90	65.80	73.80	36.50	45.90	4.70	45.40	58.80	43.70
Ni	49.70	68.60	91.20	68.40	76.90	94.80	111.90	87.00	81.80	62.70
Rb	2.30	1.20	3.60	12.90	68.70	7.50	12.10	3.80	16.80	4.10
K	747	581	1162	3652	25149	2656	4067	1411	5146	1743
Ba	35.00	38.60	54.30	128.20	644.90	135.60	165.40	71.60	190.90	34.30
Pb	10.50	21.10	0.10	15.00	15.20	6.80	5.00	13.20	10.00	13.40
Sr	398.9	220.7	228.2	190.9	24.3	221.8	171.6	248.1	197.7	82.6
Th	3.20	3.60	0.00	1.90	0.20	0.00	0.00	2.90	3.00	0.70
U	0.90	0.00	0.00	2.90	0.00	2.00	0.00	0.00	0.40	0.50
Zr	111.3	132.1	101.2	111.6	95	104.2	93.4	102.5	100.8	79.4
Ti	8809.7	10516.4	8830.6	9030.3	9100.4	8827.6	8340.8	8966.1	8478.7	7461.4
Nb	8.00	9.00	5.40	7.90	6.50	6.60	4.80	7.20	7.20	3.90
Y	29.90	36.20	28.90	34.30	26.20	30.80	28.20	30.50	29.60	23.60
La	3.10	0.00	4.30	0.00	0.00	0.00	2.50	31.00	2.00	0.00
S	54.00	57.00	24.00	51.00	41.00	20.00	29.00	124.00	11.00	44.00
As	12.00	5.00	3.00	3.00	16.00	4.00	3.00	6.00	3.00	9.00
Ga	20.30	18.80	18.40	16.30	19.70	17.70	17.10	21.30	18.20	14.30
Nd	1.20	3.80	0.00	2.10	0.00	0.00	0.00	0.00	1.10	0.00
Ce	3.10	9.40	0.00	11.80	6.80	2.90	0.00	8.90	12.50	0.00
CaO/MgO	1.38	1.72	1.37	1.57	0.72	1.52	1.33	1.65	1.31	1.90
Na_2O+K_2O	4.06	3.03	2.64	3.35	3.32	2.96	3.42	2.30	3.50	4.36
Mg#	53.37	52.87	58.75	55.01	58.20	56.58	58.36	54.19	56.75	57.34
Ti/Zr	79.15	79.61	87.26	80.92	95.79	84.72	89.30	87.47	84.11	93.97
Zr/Y	3.72	3.65	3.50	3.25	3.63	3.38	3.31	3.36	3.41	3.36
Zr/Nb	13.91	14.68	18.74	14.13	14.62	15.79	19.46	14.24	14.00	20.36

metallic elements

transition elements

low field strength elements/LIL

high field strength elements

Appendix F5 - Major (wt%) and Trace Element (ppm) data for Ngubevu area

Mfongosi Group metabasites

	NGW 31	NGW 36	NGW 39A	NGW 39B	NGW 40	NGW 41	NGW 42	NGW 43	NGW 44
SiO_2	48.76	49.82	48.37	47.58	48.64	49.63	47.71	46.59	49.45
Al_2O_3	18.57	18.31	16.60	17.46	15.22	17.74	16.99	17.17	15.67
FeO	10.89	10.74	11.06	10.42	11.45	10.17	11.29	11.87	9.82
Fe_2O_3	1.35	1.33	1.37	1.29	1.41	1.26	1.39	1.47	1.21
$Fe_2O_3(T)$	13.45	13.26	13.65	12.86	14.14	12.56	13.94	14.66	12.12
MnO	0.17	0.18	0.19	0.19	0.21	0.18	0.23	0.23	0.19
MgO	8.08	8.66	7.22	8.09	7.27	4.20	6.11	5.94	6.68
CaO	4.85	3.90	8.47	8.45	10.38	9.90	9.01	10.13	11.14
Na_2O	2.18	1.91	2.98	2.93	2.21	3.78	3.61	2.61	2.77
K_2O	2.06	2.15	0.90	0.76	0.31	0.12	0.22	0.40	0.35
TiO_2	1.60	1.58	1.56	1.52	1.57	1.64	2.01	2.05	1.51
P_2O_5	0.18	0.18	0.17	0.18	0.18	0.22	0.26	0.26	0.16
TOTAL	*99.91*	*99.94*	*100.12*	*100.02*	*100.14*	*99.96*	*100.10*	*100.04*	*100.04*
Cr	205.10	215.90	156.50	155.10	77.20	39.80	111.90	149.20	235.90
V	329.00	324.60	252.70	230.90	262.20	227.00	281.80	279.50	235.40
Au	<10	<10	<10	<10	<10	<10	<10	<10	10.00
Sc	48.60	52.80	38.90	30.50	31.80	29.20	34.50	34.00	37.40
Co	41.90	57.20	40.60	65.60	62.00	50.40	53.90	55.90	51.90
Zn	93.00	99.60	107.90	102.90	110.40	99.60	123.00	113.80	90.30
Cu	62.60	59.90	84.10	68.60	12.70	110.00	81.40	74.70	80.30
Ni	74.20	80.80	84.40	97.50	74.30	48.10	58.40	60.80	102.90
Rb	48.10	52.60	21.30	19.20	6.60	2.40	2.20	10.30	10.20
K	17098	17845	7470	6308	2573	996	1826	3320	2905
Ba	455.20	441.10	273.10	237.90	122.60	47.00	95.90	143.80	165.10
Pb	8.40	10.20	9.30	13.00	6.90	14.80	19.90	11.70	17.00
Sr	30.8	27.4	192.2	172.8	170.7	258.8	212.2	245.5	233.9
Th	0.00	1.90	1.40	2.60	3.60	6.10	0.40	3.40	4.40
U	0.00	0.00	0.10	1.30	1.20	2.40	0.30	0.90	3.90
Zr	105.3	105.1	105	105	103.6	119.3	146.1	148.2	101.4
Ti	9598.6	9474.5	9338.4	9134.0	9440.3	9819.8	12036.8	12270.6	9043.5
Nb	6.80	6.40	6.20	6.80	6.40	8.20	9.40	7.90	6.5
Y	29.60	30.10	31.10	31.90	30.50	33.70	39.80	39.10	30.00
La	0.00	0.00	0.00	1.10	1.30	0.00	0.40	1.10	6.90
S	32.00	39.00	38.00	18.00	20.00	2.00	34.00	10.00	69.00
As	9.00	14.00	6.00	3.00	2.00	5.00	3.00	2.00	4.00
Ga	18.00	20.60	15.60	18.40	19.40	22.80	20.20	24.00	17.20
Nd	1.20	2.30	0.00	0.00	2.70	3.20	7.30	0.00	0.00
Ce	0.00	21.20	0.00	0.00	3.70	6.80	17.20	7.10	0.50
CaO/MgO	0.60	0.45	1.17	1.04	1.43	2.36	1.47	1.71	1.67
Na_2O+K_2O	4.24	4.06	3.88	3.69	2.52	3.90	3.83	3.01	3.12
Mg#	56.93	58.96	53.78	58.05	53.08	42.39	49.09	47.13	54.80
Ti/Zr	91.15	90.15	88.94	86.99	91.12	82.31	82.39	82.80	89.19
Zr/Y	3.56	3.49	3.38	3.29	3.40	3.54	3.67	3.79	3.38
Zr/Nb	15.49	16.42	16.94	15.44	16.19	14.55	15.54	18.76	15.60

metallic elements
transition elements
low field strength elements/LIL
high field strength elements

Appendix F5 - Major (wt%) and Trace Element (ppm) data for Ngubevu area

Mfongosi Group metabasites

	NGW 45	NGW 52A	NGW 52B	NGE/1	NGE/2	NGE/3	NGE/4	NGE/5	NGE/6	NGE/7
SiO_2	51.92	49.80	48.56	49.54	51.10	49.67	48.44	47.97	49.12	49.05
Al_2O_3	17.04	15.53	16.45	17.38	17.49	17.69	17.52	16.89	17.49	17.57
FeO	9.27	9.98	10.32	9.69	9.91	10.03	9.72	9.74	9.37	9.55
Fe_2O_3	1.14	1.23	1.27	1.20	1.22	1.24	1.20	1.20	1.16	1.18
Fe_2O_3(T)	11.44	12.32	12.74	11.96	12.23	12.38	12.00	12.02	11.57	11.79
MnO	0.16	0.17	0.21	0.16	0.17	0.17	0.18	0.18	0.18	0.17
MgO	6.61	9.95	7.33	6.26	6.59	6.70	6.97	7.82	7.03	7.33
CaO	7.86	7.02	10.39	10.78	8.14	9.01	10.29	9.56	9.75	8.94
Na_2O	2.99	3.31	2.42	2.03	2.27	2.19	2.39	3.07	3.06	3.61
K_2O	0.55	0.49	0.19	0.54	0.48	0.50	0.63	0.34	0.58	0.34
TiO_2	1.37	1.27	1.57	1.41	1.37	1.46	1.42	1.29	1.27	1.20
P_2O_5	0.16	0.16	0.18	0.16	0.16	0.17	0.17	0.11	0.13	0.13
TOTAL	*100.10*	*100.03*	*100.03*	*100.22*	*100.01*	*99.95*	*100.00*	*99.25*	*100.16*	*100.13*
Cr	114.30	452.80	260.40	131.40	130.80	117.80	117.10	246.80	135.30	167.70
V	288.80	239.60	249.80	211.20	230.60	232.20	208.80	240.00	201.10	212.70
Au	<10	<10	<10	<10	<10	<10	<10	<10	13.00	<10
Sc	18.20	35.50	36.70	29.00	27.70	31.30	27.80	31.90	28.90	27.30
Co	61.30	53.70	60.30	49.20	56.40	53.20	55.70	65.80	55.60	56.40
Zn	89.40	98.00	96.40	89.20	98.10	91.90	91.70	92.50	81.90	87.90
Cu	19.40	4.40	74.80	52.50	43.30	79.90	52.70	50.40	46.50	27.30
Ni	75.30	108.40	99.70	81.90	87.10	78.60	83.00	91.90	78.10	86.60
Rb	15.10	13.20	5.10	11.80	12.50	10.60	14.70	8.40	14.10	9.50
K	4565	4067	1577	4482	3984	4150	5229	2822	4814	2882
Ba	126.10	154.10	87.40	143.40	138.30	144.60	186.70	103.70	173.10	121.30
Pb	2.60	7.00	7.50	13.30	12.80	7.40	1.80	0.30	8.70	4.80
Sr	222.8	211.5	195	219	185.8	194.5	213.6	221.1	186.7	141.5
Th	4.70	2.90	1.60	0.50	2.00	0.60	0.40	0.40	2.80	0.00
U	2.70	1.80	0.00	0.00	1.00	0.00	0.00	0.00	1.40	0.40
Zr	89.7	95.4	106	93.7	92.8	98.2	95.9	91.1	87.3	87.1
Ti	8189.2	7627.4	9407.4	8465.5	8242.5	8782.1	8527.9	7721.0	7589.1	7200.0
Nb	6.00	6.10	5.60	6.20	6.70	6.20	7.60	5.50	4.60	5.10
Y	26.00	24.20	31.80	27.50	27.30	29.00	29.30	25.30	26.70	24.60
La	0.00	4.10	1.20	0.00	0.00	0.30	0.00	0.00	1.40	0.00
S	0.00	33.00	54.00	20.00	25.00	31.00	46.00	53.00	38.00	31.00
As	3.00	4.00	3.00	4.00	3.00	3.00	3.00	2.00	4.00	3.00
Ga	15.00	17.00	19.00	16.60	19.30	16.60	17.30	16.40	18.00	18.60
Nd	0.00	0.00	0.00	4.70	0.00	0.00	0.00	0.00	0.00	0.00
Ce	0.00	0.00	0.00	17.20	9.40	0.00	2.10	14.60	0.00	0.00
CaO/MgO	1.19	0.71	1.42	1.72	1.24	1.34	1.48	1.22	1.39	1.22
Na_2O+K_2O	3.54	3.80	2.61	2.57	2.75	2.69	3.02	3.41	3.64	3.95
Mg#	55.97	63.99	55.86	53.52	54.24	54.35	56.10	58.87	57.21	57.77
Ti/Zr	91.30	79.95	88.75	90.35	88.82	89.43	88.92	84.75	86.93	82.66
Zr/Y	3.45	3.94	3.33	3.41	3.40	3.39	3.27	3.60	3.27	3.54
Zr/Nb	14.95	15.64	18.93	15.11	13.85	15.84	12.62	16.56	18.98	17.08

metallic elements
transition elements
low field strength elements/LIL
high field strength elements

Appendix F8 - Major (wt%) and Trace Element (ppm) data for Ngubevu area
Mfongosi Group pelites/sapropelites (highlighted) with the associated metabasites, included for comparison only and not used in the metabasite study

	NGW-A1/HR	NGW 2	NGW 2A	NGW 4	NGW 6	NGW 7	NGW-A1/7	NGW 8	NGW 9	NGW$-FLOAT	NGW/HR	NGW 14	NGW 35
SiO_2	70.77	50.96	79.60	49.35	71.42	48.58	52.57	49.23	76.54	63.50	53.24	69.54	58.18
Al_2O_3	16.72	18.01	12.06	16.46	15.70	17.49	17.93	17.00	14.33	12.87	17.47	17.11	12.53
FeO	3.24	10.57	0.62	9.45	1.86	10.10	11.55	10.04	1.35	7.97	11.88	2.45	8.65
Fe_2O_3	0.40	1.31	0.08	1.17	0.23	1.25	1.43	1.24	0.17	0.98	1.47	0.30	0.82
Fe_2O_3(T)	4.00	13.05	0.77	11.67	2.30	12.47	14.26	12.39	1.67	9.84	14.67	3.02	8.21
MnO	0.02	0.20	0.01	0.20	0.01	0.18	0.14	0.22	0.02	0.25	0.17	0.06	0.14
MgO	1.30	6.00	0.68	7.44	1.27	6.67	6.30	7.24	0.90	3.57	6.96	1.26	4.24
CaO	0.22	7.80	0.20	9.63	0.09	6.54	1.72	9.21	0.00	4.80	1.68	0.48	13.93
Na_2O	2.88	2.18	3.57	2.81	4.99	4.47	3.49	1.70	2.56	2.99	3.31	3.31	1.77
K_2O	3.07	0.05	1.66	0.76	2.37	0.82	1.30	1.47	2.90	0.96	0.63	4.36	0.03
TiO_2	1.08	1.63	1.09	1.48	1.75	2.23	2.07	1.43	0.85	1.05	1.80	0.42	0.82
P_2O_5	0.08	0.20	0.17	0.15	0.07	0.27	0.22	0.16	0.03	0.26	0.22	0.08	0.09
TOTAL	*100.15*	*100.08*	*100.01*	*99.95*	*99.96*	*99.69*	*100.01*	*100.05*	*99.81*	*100.09*	*100.16*	*99.64*	*99.95*
Cr	158.30	111.20	106.80	181.20	76.90	198.00	109.90	177.10	155.20	73.90	108.90	1.20	63.30
V	681.60	302.20	436.90	262.90	309.90	210.40	230.50	261.50	317.10	191.80	259.90	25.10	157.50
Au	28.00	10.00	28.00	10.00	37.00	11.00	15.00	66.00	36.00	0.01	15.00	11.00	35.00
Sc	39.50	44.40	31.10	44.10	37.90	28.90	59.80	48.90	31.30	23.60	56.90	11.70	19.40
Co	33.10	48.40	50.30	26.50	35.30	22.00	17.90	53.70	63.70	36.80	47.90	25.30	49.70
Zn	21.10	98.80	13.00	75.60	25.30	106.50	143.40	78.60	13.70	109.10	180.40	36.80	48.50
Cu	44.10	80.10	14.60	47.80	21.30	108.60	32.50	81.30	4.10	2.30	26.40	1.80	68.60
Ni	22.80	51.40	24.00	84.50	9.50	182.00	24.90	82.40	0.80	40.20	30.60	4.60	42.60
Rb	63.90	0.01	38.30	13.10	56.30	13.90	23.70	27.80	67.70	19.70	11.90	178.20	1.60
K	25481.00	415.00	13778.00	6308.00	19671.00	6806.00	10790.00	12201.00	24070.00	7968.00	5229.00	36188.00	249.00
Ba	1084.60	28.60	784.00	169.70	721.80	309.80	595.40	204.90	973.90	416.20	285.70	1822.90	11.70
Pb	30.00	8.30	33.30	0.20	16.30	9.10	17.10	15.90	44.20	12.00	5.00	18.20	8.70
Sr	174.10	381.60	134.50	276.10	154.30	231.70	95.20	206.20	105.00	183.80	68.90	119.70	267.30
Th	5.50	0.50	7.70	0.20	6.30	3.10	3.00	0.00	3.80	3.30	7.40	16.20	1.00
U	27.00	0.10	28.70	0.00	7.00	2.20	1.20	0.00	6.80	0.50	2.40	6.10	2.70
Zr	175.70	112.10	188.70	86.00	234.10	144.70	149.40	86.90	164.00	135.60	127.70	302.00	56.00
Ti	6463.21	9776.65	6527.96	8854.62	10463.67	13363.45	12411.45	8550.67	5072.97	6267.17	10805.39	2515.50	4939.88
Nb	12.30	7.10	13.10	5.60	17.70	9.90	9.90	4.70	11.80	11.70	8.50	21.50	4.70
Y	12.50	34.40	17.00	25.60	34.80	35.50	40.90	25.80	28.90	24.20	38.30	22.70	17.40
La	0.00	0.00	0.00	0.00	6.80	0.80	0.00	0.00	4.00	8.20	2.40	33.60	0.00
S	6211.00	46.00	1210.00	21.00	1703.00	127.00	517.00	56.00	4725.00	86.00	75.00	10.00	166.00
As	85.00	34.00	21.00	25.00	37.00	28.00	224.00	47.00	19.00	24.00	365.00	6.00	11.00
Ga	20.20	19.40	13.20	14.90	19.40	21.30	16.50	16.20	16.70	15.50	19.50	16.50	14.90
Nd	6.70	0.00	3.20	0.00	21.20	0.00	7.70	0.00	4.40	16.80	0.00	26.50	0.00
Ce	8.10	13.10	10.50	5.00	42.10	14.40	21.90	0.00	26.70	42.30	7.30	64.00	0.00

metallic elements
transition elements
low field strength elements/LIL
high field strength elements

Appendix G2 Hildreth plots (1,2,3) of enrichment/depletion in host rocks to the alteration zone, at varying distances from the veined zone and normalized to sample PH20 - considered typical of the relatively unaltered meta-gabbro/meta-norite. Plot 4 indicates the dominant depletion of Al, Fe, Mg, Ca, Pb, Cu, Zn, Ni and As of the aplite/gneiss in the vicinity of the altered zone